

24th INTERNATIONAL MULTIDISCIPLINARY SCIENTIFIC GEOCONFERENCE - SGEM 2024

01 – 07 July 2024 - Albena, Bulgaria

CONFERENCE PROCEEDINGS OF SELECTED PAPERS in

ENERGY AND CLEAN TECHNOLOGIES

ISSUE 4.1

DISCLAIMER

The **International Multidisciplinary Scientific GeoConference SGEM (Survey, Geology, Ecology, and Management)** serves as a global platform for pioneering research and scientific dialogue across the diverse fields of geosciences. It is dedicated to advancing interdisciplinary solutions for the most pressing environmental challenges of our time — **Global Warming, Climate Change, CO_2 Reduction, Biodiversity Conservation, and the Development of Green Technologies**. By fostering a collaborative exchange of knowledge and **aligning its objectives** with the **United Nations Sustainable Development Goals (SDGs), SGEM aims to inspire scientific excellence and drive sustainable practices toward a greener, more resilient future for our planet.**

Authors are responsible for the content and accuracy of the written papers. Opinions expressed are not meant to represent or reflect the position of the SGEM International Scientific Committee members.

No part of this book may be reproduced or transmitted in any form or by any means, electronic or mechanical, for any purpose, without the express written permission of the SGEM International Scientific Committee on Earth and Planetary Sciences.

Copyright © SGEM WORLD SCIENCE (SWS) Scholarly Society 2024
Haidingergasse 1, C / 1113, Vienna 1030, Austria
Published by STEF92 Technology
Total print: 5000

E-mail: **sgem@sgem.org** | URL: **www.sgem.org**

ISBN 978-619-7603-71-2

ISSN 1314-2704

DOI: 10.5593/sgem2024/4.1

FOREWORD

Dear Readers,

It is with great pride that we introduce the fourth issue of the **24th volume** of the **SGEM GeoConference 2024 Conference Proceedings**, which focuses on **Nuclear Technologies, Renewable Energy Sources and Clean Technologies, Recycling, and Air Pollution and Climate Change**. This collection of papers is a testament to the transformative potential of innovation in addressing some of the most pressing global challenges, from transitioning to clean energy to mitigating climate change impacts and promoting sustainable resource use.

Advancing Sustainable Solutions Through Innovation

The research presented in this edition highlights the critical role of technological advancements in shaping a more sustainable future. Topics range from **cutting-edge developments in nuclear diagnostics and renewable energy systems to innovative recycling techniques and strategies for reducing air pollution**. These studies contribute to global efforts to meet the United Nations Sustainable Development Goals (SDGs), including affordable and **clean energy (SDG 7), industry, innovation, and infrastructure (SDG 9), sustainable cities and communities (SDG 11), and climate action (SDG 13).**

Highlights

- Nuclear Technologies: This section explores advancements in nuclear diagnostics and **irradiation specifications**, demonstrating their **potential for safer and more efficient applications in energy and industry**.
- **Renewable Energy Sources and Clean Technologies**: Here, researchers delve into innovations in hydrogen fuel cells, solar and wind energy systems, and wave power, emphasizing the importance of **sustainable energy solutions for reducing carbon emissions**.
- **Recycling**: Studies in this section **investigate novel methods for waste valorization**, including the use of industrial by-products in construction and the development of **sustainable fuels** from biomass and other organic materials.
- **Air Pollution and Climate Change**: This section addresses the urgent need to **mitigate air pollution** and its impacts on **public health** and the environment. Topics include **alternative fuels**, **emission reduction** technologies, and the analysis of climate change patterns, providing actionable insights for **policymakers** and industry leaders.

Commitment to Scientific Excellence

Each paper in this special collection of papers has undergone a **rigorous peer review process**, ensuring that the research presented meets the highest standards of scientific rigor, originality, and relevance. This commitment to excellence reflects our shared **dedication to advancing knowledge and driving innovation in fields critical to sustainable development.**

A Call for Collaboration and Action

As we face the dual challenges of climate change and resource scarcity, the findings and innovations presented in this issue highlight the importance of collaboration across

disciplines and sectors. By **fostering dialogue** and **sharing knowledge**, we can develop solutions that not only **address immediate challenges but also pave the way for a more sustainable and resilient future.**

We would like to extend our deepest gratitude to all the authors, reviewers, and conference organizers for their invaluable contributions to this volume. It is our hope that the insights and advancements contained within these pages will **inspire further research, innovation, and action in the pursuit of sustainability.**

Sincerely yours,

Prof. Dr. hab. oec. Baiba Rivza
Editor-in-Chief of XXIV SGEM GeoConference Proceedings
Member of the Presidium of the Latvian Academy of Sciences, LATVIA
President of the Latvian Academy of Agricultural and Forestry Sciences
Vice-chair of the Latvian Council of Higher education
President of Latvian universities professors' association
Expert from the European Academy of Sciences Academic Advisory Board (EASAC)

Prof. DSc. Oleksandr Trofymchuk
Editor-in-Chief of XXIV SGEM GeoConference Proceedings
National Academy of Sciences of Ukraine, UKRAINE

CONFERENCE PROCEEDINGS CONTENTS

NUCLEAR TECHNOLOGIES

1. DIAGNOSTICS OF UNDERGROUND MASOURY, Dr. Richard Balaz, Dr. Stanislav Toth.....3

2. IRRADIATION SPECIFICATIONS, Assoc. Prof., Ing. Ph.D., MBA, LL. M. Martin Hrinko, Ing. Ph.D. Pavel Svec, Assoc. Prof., RNDr. CSc. Jiri Svec.....13

RENEWABLE ENERGY SOURCES AND CLEAN TECHNOLOGIES

3. ANALYSIS OF THE AIR FLOW IN THE RENOVATED TEST SECTION OF BSHC SMALL WIND TUNNEL, Nikita Dobin.....23

4. APPLICATION OF THE PROTON-EXCHANGE MEMBRANE HYDROGEN FUEL CELL AS A MOBILE POWER UNIT FOR THE HYDRIVE 1 VEHICLE, Maksymilian Zarychta.....31

5. APPLICATIONS OF HYDROGEN ENERGY IN THE FIELD OF TRANSPORT, Eng. Sorin Echim, Assoc. Prof. Dr. Eng. Sanda Budea.....39

6. CAN BIOGAS CONTRIBUTE TO PURE HYDROGEN COMBUSTION?, Assoc. Prof. Dr. Isabel Amez, Assoc. Prof. Dr. Blanca Castells, Assoc. Prof. Dr. David Bolonio, Assoc. Prof. David Leon, Prof. Marcelo F. Ortega.....47

7. CLIMATE CHANGE, WASTE MANAGEMENT, AND COAL ABANDONMENT: THREE PILONS OF SUSTAINABILITY, Sofia Fourkioti, Konstantinos Panitsidis, Konstantinos Spinthiropoulos, Marina Vezou.....55

8. DESIGN AND SIMULATION OF STATIC REQUIREMENTS IN THE CASE OF A WIND TURBINE FIXED ON A MARITIME TRANSPORT SHIP, Assoc. Prof. Dr. Carmen-Penelopi Papadatu, Lect. Dr. Costel Humelnicu, Eng. Radu Aiordachioaiei, Eng. Ionut - Cristian Adam-Papadatu.....61

9. EFFICIENCY ANALYSIS OF THE USE OF SOLAR PHOTOVOLTAIC MODULES BASED ON CLIMATIC ZONES, PhD Ress. Bohirjon Sharifov, Assoc. Prof. Dr. Svetlana Beryozkina, Dr. Anvari Ghulomzoda, Dr. Murodbek Safaraliev, PhD Ress. Shokhrukh Sidikov.....73

10. ESTIMATION OF WAVE POWER AND RECENT DECADAL CHANGES IN BULGARIAN BLACK SEA NEARSHORE AREA, Assoc. Prof. Dr. Nikolay Valchev.....83

11. EXPERIMENTAL MODEL FOR ANALYZING HYDROGEN EXPLOSIONS WITH THE MODIFICATION OF PROPAGATION DIRECTION, Eng. Ligia Ioana Tuhut, Eng. Andrada Matei, PhD. Eng. Vlad-Mihai Pasculescu, PhD. Eng. Daniel-Gheorghe Florea, PhD. Eng. Bogdan Adrian Simon-Marinica.....91

12. FISCHER-TROPSCH SYNTHESIS OVER POLYMER SUPPORTED PROMOTED IRON CATALYSTS, Assoc. Prof. Dr. Mariia E. Markova, Assoc. Prof. Dr. Antonina A. Stepacheva, Prof. Dr. Vladimir P. Molchanov, Assoc. Prof. Dr. Galina N. Demidenko, Prof. Dr. Mikhail G. Sulman.....99

13. FLAME ANALYSIS: UNDERSTANDING THE COMBUSTION OF RENEWABLE FUELS, Assoc. Prof. Dr. Blanca Castells, Assoc. Prof. David Leon, Assoc. Prof. Dr. Isabel Amez, Researcher Roberto Paredes, Assoc. Prof. Dr. David Bolonio 107

14. HYDROSTATIC POWER TRANSMISSION SYSTEM FOR WIND TURBINES, Ph.D. Eng. Catalin Dumitrescu, Ph.D. Eng. Alexandru-Polifron Chirita, Ph.D. Stud. Eng. Stefan-Mihai Sefu, Ph.D. Chem Adriana Mariana Bors, Assist Res. Ana-Maria Carla Popescu.....115

15. INFLUENCE OF THE NATURE OF AROMATIC POLYMER AS A PT PARTICLE STABILIZER ON ITS ACTIVITY AND SELECTIVITY IN THE LIQUID-PHASE HYDROGENATION OF AROMATIC AND POLYAROMATIC SUBSTRATES, Assoc. Prof. Dr. Alexey Bykov, Assoc. Prof. Dr. Galina Demidenko, Assoc. Prof. Dr. Linda Nikoshvili, Ms. Elena Bakhvalova.....123

16. INVESTIGATION OF THE TRANSITION PROCESS OF PARALLEL OPERATION OF A SOLAR POWER PLANT AND THE GRID UNDER EMERGENCY DISTURBANCE, Assoc. Prof. Dr. Svetlana Beryozkina, PhD Ress. Bohirjon Sharifov, Dr. Murodbek Safaraliev, Dr. Anvari Ghulomzoda, PhD Ress. Mukhammadjon Odinabekov 131

17. LIFE-CYCLE ANALYSIS OF FIREWORKS: ENVIRONMENTAL IMPACT AND IMPROVEMENT OPPORTUNITIES, Assist. Prof. David Leon, Assoc. Prof. Dr. David Bolonio, Assoc. Prof. Dr. Isabel Amez, Researcher Roberto Paredes, Assist. Prof. Dr. Blanca Castells 139

18. MONITORING SOLAR FARMS USING DRONES - UTILIZED TECHNIQUES AND BENEFITS, Dr. Eng Tymoteusz Turlej, Assoc. Prof. Dr. Krzysztof Kolodziejczyk, MSc Eng. Jedrzej Minda 149

19. OPTIMIZATION OF PROCESS CONDITIONS FOR THE CATALYTIC CONVERSION OF MICROCRYSTALLINE CELLULOSE INTO SUGAR ALCOHOLS, Dr. Oleg Manaenkov, Dr. Olga Kislitsa, Dr. Antonina Stepacheva, Dr. Linda Nikoshvili, Prof. Valentina Matveeva.....157

20. PHOSPHATE REMOVAL ON BIOCHAR, Drd. Popescu Mihaela Alexandra, Prof. Dr. Elena-Emilia Sirbu, Asst. Prof. Dr. Catalina Calin, Asst. Prof. Dr.Cristina Popa, Dr. Cristina Emanuela Enascuta 165

21. PHOTOVOLTAIC SYSTEM FOR POWERING A REMOTE ACTUATION SYSTEM, PhD. Eng. Radu Rădoi, PhD. Stud. Eng. Liliana Dumitrescu, PhD. Stud. Eng. Bogdan Tudor, Eng. Andrei Benescu, PhD. Stud. Eng. Robert Blejan 173

22. REDUCING CEMENT INDUSTRY EMISSIONS: SYNTHETIC GAS FROM CARBON DIOXIDE AND GREEN HYDROGEN, Assoc. Prof. Dr. David Bolonio, Assist. Prof. Dr. Isabel Amez, Assist. Prof. Dr Blanca Castells, Assist. Prof. David León, Assist. Prof. Enrique García Franco1 181

23. ROUGHNESS EFFECT ON A FULL-SCALE GENERAL CARGO VESSEL TOTAL RESISTENCE AND EFFECTIVE POWER, PhD. Andreea Mandru, Prof. Dr. Liliana Rusu, Assoc Prof. Dr. Florin Pacuraru 189

24. SAWDUST LIQUIEFACTION OVER SCHUNGITE-BASED CATALYST, Assoc. Prof. Dr. Antonina Stepacheva, Assoc. Prof. Dr. Mariia Markova, Assoc. Prof. Dr. Oleg Manaenkov, Assoc. Prof. Dr. Elena Shimanskaya, Prof. DSc. Valentina Matveeva 197

25. STUDY OF CHANGES IN HYDROGEN CONCENTRATION IN SOIL GAS SAMPLES, Paulina Kopera, Anna Twarog, Henryk Sechman.....205

26. THERMOELECTRIC PERFORMANCE OF Na2B4O7-DOPED AND GRAPHENE-DISPERSED Bi2Sr2Co2Oy COMPOSITES, Vakhtang Zhghamadze, Dr. Nikoloz Margiani, Prof. Dr. Masatoshi Takeda, Iamze Kvartskhava, Dr. Giorgi Mumladze 211

27. USING A HEAT PUMP TO COVER PEAK HEAT LOADS IN HARSH CLIMATES, Prof. Dr. Sergey Shcheklein, Prof. Dr. Vladimir. Velkin, Assoc. Prof. PhD Andrey Matveev, Assoc. Prof. PhD Igor Koshkin, Sergey Pushkarev 219

RECYCLING

28. AIR CONVERSION OF PYROLYSIS PRODUCTS OF HYDROCARBON RAW MATERIALS INTO SYNTHESIS GAS (H2+CO) FOR THE PRODUCTION OF ELECTRICAL ENERGY USING SOLID OXIDE FUEL CELLS, Prof. Dr. Sergey Shcheklein, Prof. Dr. Alexey Dubinin, Assoc. Prof. PhD Andrey Matveev, Vyacheslav Filippenkov 229

29. ANALYSIS OF THE EFFECTIVENESS OF VARIOUS TYPES OF BLEACHING EARTHS FOR PARAFFIN REFINING ON THE EXAMPLE OF THE TERRA TRADE COMPANY, Engr. Jan Udaliszczew 243

30. DETERMINATION OF THE PRODUCT DEVELOPMENT DIRECTIONS FOR THE FERTILIZER PRODUCTS MADE FROM PIG FATTENING AND SLAUGHTERING BY-PRODUCTS, Dr. Anita Csiba, Dr. Arpad Ferencz.....251

31. EXPERIENCES WITH THE USE OF CUPOLA FURNACE SLAG IN CONSTRUCTION INDUSTRY, Ing. Patrik Fedorko, prof. Ing. Alena Pribulova, CSc., Assoc. Prof. Ing. Jozef Petrik, PhD, Ing. Peter Blasko, PhD, Assoc. Prof. Ing. Peter Futas, PhD 259

32. FACTORS INFLUENCING SELECTIVE WASTE COLLECTION, M Sc, Eng. Jakub Tytko, Prof. Dr, D.Sc. Eng. Mohamed Alwaeli 267

33. HIGH STRENGTH ZOLOGYPSUM COMPOSITE, Prof. Dr. Victoria Petropavlovskaya, Assoc. Prof. Dr. Kirill Petropavlovskii, Mr. Petr Kalyaskin, Assoc. Prof. Dr. Tatiana Novichenkova.....275

34. LOW CARBON BINDERS WITH ASH MICROSPHERE, Prof. Dr. Victoria Petropavlovskaya, Assoc. Prof. Dr. Kirill Petropavlovskii, Assoc. Prof. Dr. Tatiana Novichenkova, Prof. Dr. Michail Sulman, Prof. Dr. Yury Kosivtsov.....283

35. LOW COST AIRDROP DELIVERY SYSTEM, Ing. Salistean Adrian 291

36. RECYCLING OF BLACK LIQUOR WASTE FROM PULP FACTORIES AND THE DEVELOPMENT OF SUSTAINABLE FUELS, Florian Marin, Dr. Oana Botoran, Prof. Dr. Simona Oancea, Dr. Marius Constantinescu, Dr. Anca Maria Zaharioiu.....299

37. THE EFFECT OF THE AMOUNT OF BINDER ON THE PROPERTIES OF BRIQUETTES PREPARED FROM FOUNDRY DUST, Prof. Ing. Alena Pribulová, CSc., Assoc. Prof. Ing. Peter Futáš, PhD, Ing. Patrik Fedorko, Prof. Ing. Marcela Pokusova, PhD, Assoc. Prof. Ing. Maria Mihalikova, PhD 307

38. THE POTENTIAL COMPLEXING IMPACT OF SOME ORGANIC COMPOUNDS AMINE AND CARBOXYL GROUPS ON TRANSITION METALS, PhD(c).E Adelina Haskaj, PhD(c). Prof.Dr.Musaj Pacarizi, Prof.Dr.Sonja Lepitkova, Berat Sinan, PhD(c), Bahri Sinani, PhD(c), Elida Dreshaj1 315

39. THERMAL DECOMPOSITION OF WOOD WASTE. THERMOGRAVIMETRIC ANALYSIS, Assoc. Prof. Dr. Antonina A. Stepacheva, Assoc. Prof. Dr. Yury V. Lugovoy, Prof. Dr. Vladimir P. Molchanov, Prof. Dr. Yury Yu. Kosivtsov**,** Prof. Dr. Mikhail G. Sulman 323

40. UTILIZATION OF ASH FROM THE COMBUSTION OF KUZNETSK AND EKIBASTUZ COALS, Dr. Leonid Delitsyn, Prof. Dr. Mikhail Sulman, Dr. Ruslan Kulumbegov, Prof. Dr. Oleg Popel, Dr. Alexander Sidorov.....331

41. VALORIFICATION OF PRUNUS CERASIFERA FRUITS (PULP, PEEL, WHOLE FRUIT) FOR YOGURT PRODUCTION, PhD. Mădălina Moga, Dr. Mihaela Tița, Dr. Adelina Constantinescu, Dr. Ovidiu Tița.....339

AIR POLLUTION AND CLIMATE CHANGE

42. AEROSOL FORMATION DURING THE HANDLING OF BEECH-PLASTIC PELLETS, Ing. Nikola Čajová Kantová, PhD., Ing. Alexander Čaja, PhD., prof. Ing. Radovan Nosek, PhD., Ing. Alexander Backa2 351

43. AGRICULTURE AS A DRIVER FOR CLIMATE CHANGE, Lecturer Dr. Carmen Simona Dumitrescu, Prof. Dr. Sorin Mihai Stanciu, Lecturer Dr. Raul Pașcalău, Assoc. Prof. Dr. Cosmin Sălășan.....359

44. AIRBORN MICROORGANISMS IN HOT POINT AND GREEN AREAS AT DIFEERENT HIGHT OF GROUND AIR, Asen Peshev, Assist. Prof. Dr. Bilyana Grigorova-Pesheva, Assist. Prof. Dr. Georgi Kadinov 367

45. ASSESSMENT OF HEAVY METAL POLLUTION IN SNOW SAMPLES COLLECTED AT VARIOUS DISTANCES FROM ROAD SECTIONS: CASE STUDY JELGAVA, PhD Kristine Valujeva, PhD Candidate Jovita Pilecka-Ulcugaceva, Mg.sc.ing. Sindija Liepa, Dr.geogr. Oskars Purmalis, Assoc. Prof. Ph.D Inga Grinfelde.....375

46. BIOMONITORING OF HEAVY METALS IN THE CITY OF JELGAVA, LATVIA USING LICHEN, XANTHORIA PARIETINA, PhD Candidate Jovita Pilecka-Ulcugaceva, PhD Candidate Anda Bakute, Dr.geogr. Oskars Purmalis, Bc.sc.ing. Kristaps Siltumens, Assoc. Prof. Ph.D Inga Grinfelde.....381

47. CHALLENGES AND RISKS FOR ROMANIAN FARMERS, Lecturer Dr. Carmen Simona Dumitrescu, Lecturer Dr. Cosmina Simona Toader, Assoc. Prof. Dr. Cosmin Sălășan 389

48. EVALUATING THE IMPACT OF AUTOMOBILE POLLUTION ON THE HEALTH OF THE ROMANIAN POPULATION THROUGH STATISTICAL METHODS, Assoc. Prof. Dr. Eng. Rus Madalina, Assoc. Prof. Dr. Eng. Veresiu Silvia, Prof. Dr. Eng. Mereuta Elena, Assoc. Prof. Dr. Eng. Valentin Amortila, PhD Eng. Balasoiu George 395

49. FACTORS AFFECTING INDOOR AIR QUALITY IN KINDERGARTEN, Petra Stiborova, Andrea Badurova, Iveta Skotnicova 403

50. IMPACT OF THE BUILT-UP AREA OF A CITY ON THE DIURNAL PATTERN OF TEMPERATURES DURING TROPICAL DAYS, Ing. Martin Minárik, Dr. Vladimír Kišš, Assoc. Prof. Dr. Martin Prčík, Assoc. Prof. Dr. Ján Čimo, Mgr. Maroš Turňa 411

51. NEURAL NETWORK MODELING OF THERMAL ENGINES POWERED BY ALTERNATIVE FUELS FOR THE PURPOSE OF REDUCING ATMOSPHERIC POLLUTION, Assoc. Prof. Dr. Eng. Constantin Georgescu, Assoc. Prof. Dr. Eng. Valentin Amortila, Assoc. Prof. Dr. Eng. Cristian Muntenita 419

52. OPERATION CHARACTERISTICS OF A SMART MINI HYBRID HEAT PUMP USED FOR THE ENERGY ACCUMULATION, Ing. Alexander Čaja, PhD., Ing. Nikola Čajová Kantová, PhD., prof. RNDr. Milan Malcho, CSc., Ing. Patrik Nemec, PhD. 427

53. RECENT CHANGES IN THE SNOW COVER DURATION IN BULGARIA – PRELIMINARY RESULTS, Assist. Prof. Dr. Dimitar Nikolov, Assist. Prof. Dr. Cvetan Dimitrov, Msc. Radoslav Evgeniev 435

54. SOLUTIONS FOR REDUCING THE AIR POLLUTION GENERATED BY VEHICLE, Assoc. Prof. Dr. Eng. Mihai Gingarasu, Prof. Dr. Eng. Elena Mereuta, Assoc. Prof. Dr. Eng. Valentin Amortila, Assist. PhD. Ress.. Eng. George Balasoiu 443

55. STUDY ON THE INFLUENCE OF THE ENERGY INDUSTRY ON THE LEVEL OF POLLUTION OF WASTEWATER IN ROMANIA, Assoc. Prof. Dr. Eng. Silvia Veresiu, Assoc. Prof. Dr. Eng. Madalina Rus, Prof. Dr. Eng. Elena Mereuta, Assoc. Prof. Dr. Eng. Valentin Amortila, Assoc. Prof. Dr. Eng. Mihai Gingarasu.....451

56. THE PREDICTION AND OPTIMIZATION OF ALTERNATIVE FUEL CONSUMPTION IN VEHICLES USING ARTIFICIAL NEURAL NETWORKS WITH THE AIM OF REDUCING ATMOSPHERIC POLLUTION, Assoc. Prof. Dr. Eng. Amortila Valentin, Prof. Dr. Eng. Mereuta Elena, Assoc. Prof. Dr. Eng. Veresiu Silvia, Assoc. Prof. Dr. Eng. Rus Madalina, PhD Eng. Balasoiu George.....459

57. ANALYSIS OF DIFFERENT FACTORS IMPACT ON PARTICULATE MATTER FORMATION DURING THE REFUSED DERIVED FUELS COMBUSTION, Radovan Nosek, Michal Sramka, Nikola Čajová Kantová 467

58. VARIATION OF CRITICAL VELOCITY OF DOWNWARD VENTILATION IN INCLINED ROAD TUNNELS, Prof. Omar Lanchava, Prof. Nino Ratiani, Assoc. prof. Zaza Khokerashvili, Assoc. prof. Nino Arudashvili 475

SECTION

NUCLEAR TECHNOLOGIES

DIAGNOSTICS OF UNDERGROUND MASOURY

Dr. Richard Baláž[1]

Dr. Stanislav Tóth[2]

[1] Technical University of Košice, Civil Engineering Faculty, Institute of Architectural Engineering, Department of Architectural Engineeringy. **Slovakia**

[2] Technical University of Košice, Civil Engineering Faculty, Institute of Architectural Engineering, Department of Architectural Engineeringy. **Slovakia**

ABSTRACT

The masonry moisture sanation process does not end, when the building job is over. This article contains results from long-term measurements of moisture levels in underground areas of several old buildings. These results can help in diagnostics and design of repairs in other buildings.

Keywords: Diagnostics building, chemical and moisture analysis of masonry, metods of dehumidifications of masonry, old and historical building, underground spaces.

INTRODUCTION

In recent years, new remedial materials and technologies have been implemented. Due to insufficient knowledge about the properties and behaviour of these materials in different environments, and due to improper application of some remedial measures, re-emergence of defects often occurs shortly after repairs. This leads to significant and sometimes irreparable damage. Such unqualified reconstructions result in a shorter lifespan of buildings and potentially increase the costs of their renovation and maintenance. The project's aim is to verify the effectiveness of various dehumidification methods, particularly in the underground spaces of buildings, through in-depth diagnostics and analysis of implemented remedial measures on specific historical and classical buildings. Another main objective is to investigate, under laboratory conditions, the possibilities of using newer injection materials and technologies for more porous materials that were used in masonry in the second half of the 20th century and today. This focus is primarily due to frequent waterproofing failures, not only in historic buildings but also in new constructions.

OBJECTIVES

Nearly all buildings in city centers need to address the issue of reducing moisture in masonry to an acceptable level. When it comes to maintaining historical buildings, solving the problem of increased masonry moisture presents more complex challenges and limited options for remediation methods. Furthermore, most investors wish to utilize or operate underground spaces. The proposal for an optimal solution to a comprehensive remediation system depends on the designer's experience, the surrounding development, and the financial capabilities of the investor, as older buildings often suffer from neglected maintenance. When deciding on a method to

https://doi.org/10.5593/sgem2024/4.1/s16.01

eliminate moisture, it is necessary to identify the primary causes of its presence in the observed building and consider the advantages and possible drawbacks of each method.

The building owner's requirement is to assess or diagnose the moisture in the masonry of underground spaces to propose measures to eliminate moisture from the walls.

SUBJECT OF DIAGNOSING

The subject of this diagnostic assessment is the subterranean spaces of the building located on parcel no. 2263/1 in the cadastral area of Stredné Mesto, Košice I - Staré Mesto district, with the main entrance at 27 Kmeťova Street. The building is three stories high. During excavation and construction work on the new building on the adjacent parcel no. 2262 (building of ŽSR), a collapse occurred in the lateral part of the subject building, necessitating the restoration of the entrance and internal staircase. Simultaneously, the building's use was also altered. Prior to the reconstruction, the building was utilized for commercial purposes. The basement housed a relaxation center with a swimming pool, sauna, and fitness center. On the ground floor, there was a language school. The upper floor and attic served the needs of a bailiff's office.



Fig. 1: View of the facade of the subject building.

Post-reconstruction, the building will contain a single residential unit (basement, ground floor, and part of the upper floor) and office spaces (part of the upper floor and attic). The basement will be used for a boiler room, laundry room, sauna, and gym. The ground floor will be designated for residential purposes, including living rooms (kitchen, utility room, pantry, common rooms, parents' bedroom, parents' dressing room, sanitary facilities, and hall with staircase). The ground floor will be connected to the basement by a single-flight internal staircase. The upper floor will be partially used for residential purposes and partially for office purposes. There will be children's rooms with changing rooms and sanitary facilities. The ground floor and upper floor will be connected by a double-flight internal staircase located in the entrance hall. The office spaces will have a separate entrance designed to minimize disturbance to the residential areas. The attic will house office spaces with sanitary facilities, a kitchenette, and

storage spaces, accessible via a staircase. The total built-up area is 307,0 m². The existing building has an L-shape, with a two-bay masonry structure facing the street and a longitudinal load-bearing system. The courtyard wing consists of a ssingle bay. Both parts of the building are accessible from a courtyard gallery that lines the inner perimeter of the structure. The courtyard galleries are on two height levels, allowing access to the ground floor and the upper floor. The street-facing roof has a double-pitched design with a 33° slope. The courtyard section above the single-bay has a monopitch roof with a 30° slope. The double-pitch and monopitch parts of the roof are continuous and extend to the gable walls of the building. The roof's load-bearing structure consists of a wooden truss with a standing frame. The building is subject to Act No. 49/2002 coll. on the Protection of the Monument Fund and is listed as an object within the protective zone of the Urban Monument Reserve of Košice, although the building itself is not a protected monument. [1]

DESCRIPTION OF BASEMENT STRUCTURES AND MOISTURE ANALYSIS.

In the basement, the perimeter walls are 650 mm thick, and the internal load-bearing wall is 710 mm thick. The perimeter walls facing the courtyard are composed of mixed masonry - brick and interlaid stone, with stone foundations. The transverse walls are 550 mm and 650 mm thick. Above the window openings in the basement, there are straight lintels. The ceiling above the basement consists of brick vaults supported by I-shaped rolled steel beams resting on the load-bearing walls, with an overall ceiling thickness ranging from 400 mm to 610 mm. The ceiling height varies between 2070 mm and 2230 mm. During the last building modification, the basement spaces were adapted for commercial use as a relaxation center, which included the installation of a new floor with ceramic tiles. A waterproofing layer of asphalt strips was placed between the base concrete and the subsequent concrete layer. The walls were plastered and partially covered with white earthenware tile cladding. At the time of the inspection, some of the wall plaster had been removed, particularly in areas that were significantly damp. Partial demolition work had also been carried out according to the drawing documentation (see Fig. 2 – Basement – Existing Condition at the Time of Inspection). According to the reconstruction project, an English courtyard was initially proposed for the courtyard side of the building. However, the building owner did not prefer an open English courtyard. Consequently, alternative solutions were explored for modifications in the courtyard area, including possibilities for enlarging the window structures to enhance the natural lighting of the basement spaces. [2]



Fig. 2. Basement – Existing Condition at the Time of Inspection

https://doi.org/10.5593/sgem2024/4.1/s16.01

To develop a proposal for modifications to eliminate moisture, an inspection of the building and a visual diagnosis of the basement structures were conducted. Additionally, eight samples were taken for laboratory moisture determination, at heights of 500 mm and control samples at a height of 1000 mm from the floor. During the inspection, the internal drainage system had already been restored, including the horizontal conduit towards Kmeťova Street. The old pipes were cracked and clogged, likely serving as a constant source of moisture under the building.

MEASUREMENT METHODS

Regarding the evaluation of masonry moisture, no specific standard has been adopted in Slovakia to date. However, we can refer to the standard accepted in the Czech Republic. According to informative appendix A of the Czech standard ČSN 73 0610 "Hydroizolace staveb – sanace vlhkého zdiva" (Building Waterproofing – Remediation of Damp Masonry), moisture content in masonry is classified by weight percentage as follows: [3]

w < 3% - very low moisture

3 % < w < 5% - low moisture (In Slovak literature, the symbol "u_m" is used

5 % < w < 7,5% - increased moisture for material moisture)

7,5% < w < 10% - high moisture

w > 10% - very high moisture

The moisture content in weight percentage is calculated according to the aforementioned standard as follows:

$$w = \frac{m_v - m_s}{m_s} * 100 \quad [\%] \qquad (1)$$

Where: m_v = weight of the wet sample in *kg*

m_s = weight of the dry sample in *kg*

Based on the determination of the actual moisture content of the masonry during the inspection as indicated in Table No. 2, it was found that the masonry in direct

contact with the ground from the courtyard side had a very high moisture content. Therefore, it was necessary to insulate this masonry not only horizontally but also vertically from the outside.

The horizontal insulation of the floors implemented during the previous renovation of the underground spaces altered the moisture regime in the substructure. Previously, ground moisture that could evaporate through the earthen floor treatments in the basements has, in recent years, penetrated more into the walls. Additionally, the clay tile cladding hindered its gradual evaporation from the masonry, causing moisture to rise to almost the entire height of the basement walls. Operational moisture likely contributed significantly, leading to surface condensation in some areas. The evaporation of moisture and the drying of the masonry, especially in the upper foundation area, will be a long-term process spanning several years, even after the additional waterproofing of the masonry is implemented. [4]

Table 1. Preliminary overview of methods and their applications.

I. METHOD	II. CAUSE AND TYPE OF MAISTURE						
	III. MOISTURE INGRESS				IV. ATMOSPHERIC MOISTURE	V. OPERATIONAL HUMIDITY	VI. CONDENSING HUMIDITY
	VII. LOW 3%<u<5%	VIII. INCREASED 5%<u<7,5%	IX. HIGH 7,5%<u<10%	Very high u>10%			
X. INSERTING ADDITIONAL WATERPROOFING STRIPS, BOARDS, FOILS, SHEETS	**XI.**	**XII.** ●	**XIII.** ○	**XIV.**	**XV.**	**XVI.**	**XVII.**
XVIII. APPLICATION OF SPECIAL COATINGS, PLASTERS, OTHER MATERIALS, DIFFUSION AND SEALING TREATMENTS	**XIX.** ●	**XX.** ○	**XXI.**	**XXII.**	**XXIII.** ○	**XXIV.** ●	**XXV.** ●
XXVI. ELECTROOSMOSIS	**XXVII.**	**XXVIII.**●	**XXIX.**	**XXX.**	**XXXI.**	**XXXII.**	**XXXIII.**
XXXIV. AIR TREATMENT	**XXXV.** ●	**XXXVI.**○	**XXXVII.**	**XXXVIII.**	**XXXIX.**○	**XL.**	**XLI.**
XLII. HORIZONTAL AND VERTICAL BARRIERS WITH INFUSION DRILLING	**XLIII.**	**XLIV.** ●	**XLV.**	**XLVI.**	**XLVII.**	**XLVIII.**	**XLIX.**
L. CONSTRUCTION MODIFICATIONS OF THE SURROUNDINGS, RECONSTRUCTIONS, DRAINAGE, LAYOUTS	**LI.** ○	**LII.** ○	**LIII.** ○	**LIV.** ●	**LV.** ●	**LVI.** ○	**LVII.** ○

https://doi.org/10.5593/sgem2024/4.1/s16.01

Table. 2. Results of laboratory evaluation of masonry moisture content in % by the weight in the basement masonry of the building in evaluation.

Sample number	Location in the building	Material	Humidity in % of weight	Sampling height position
1a	Exterior wall, west side inside.	brick	**15,5**	500 mm above the floor
2a	Pillar on outer wall, inside, west side	brick	**1,0**	500 mm above the floor
2b	Pillar on outer wall, inside, west side	brick	**1,25**	1000 mm above the floor
3a	East outer wall, inside towards the courtyard	brick	**14,5**	500 mm above the floor
3b	East outer wall, inside towards the courtyard	brick	**8,4**	1000 mm above the floor
4a	South side, outer wall from the inside, under the window	brick	**13,2**	500 mm above the floor
5	South side, outer wall inside, pillar	brick	**1,9**	1000 mm above the floor
6a	North side, outer wall, boiler room	brick	**1,0**	800 mm above the floor



Fig. 3. View of masonry samples – colour scale according to the moisture content of the brick masonry

DESIGN OF BUILDING MODIFICATIONS TO REMOVE MOISTURE IN MASONRY.

Based on the analysis of the causes of very high moisture in the exterior masonry, which was in direct contact with the ground, it was recommended to implement new waterproofing of the exterior basement walls, including vertical insulation from the outside. Firstly, it was necessary to excavate a trench at the masonry around the courtyard side of the house. Due to concerns about weakening the masonry along the entire house at once, it was recommended to carry out the excavation in stages, requiring precise measurement and installation of drainage pipes to ensure a 1% slope towards inspection shafts with a sand trap Ø 300 mm and connection to the sewer. The excavation also needed to be sloped away from the building at a 15-degree angle. After removing the soil, the vertical walls were cleaned - scraped to a depth of 20-30 mm to remove the most damaged mortar. The scraped areas then needed to be filled with new cement mortar, and the vertical surface had to be levelled with mortar. Since a smooth surface was required for applying the vertical waterproofing silicate plaster (PCI-Dichtschlämme) with a thickness of 4 mm, the plaster needed to be applied in two layers, each covering the previous layer. The waterproofing needed to extend above the modified terrain to a height of 300 mm. During application, it was necessary to adhere to the manufacturer's technological recommendations, including allowing the excavation to be backfilled only after sufficient curing (i.e., after 4-5 days).

The protection of the vertical insulation was achieved using dome-shaped polyethylene foil (Platon) along the entire height of the wall, extending down to the ground next to the drainage pipe. Vertical joints with a width of at least 100 mm were overlapped and joined using special double-sided adhesive tape. The foil was terminated - fixed at ground level with a PVC termination strip.

Prior to design work, it was determined by probing that the surrounding soil in the courtyard area had low permeability. Therefore, it was recommended to install drainage pipes to capture rainwater runoff, which could act as occasional pressure water. The drainage pipe (from ACO building components - Frankeniscke Strasil system) was laid in a gravel bed 300 mm high and wrapped in geotextile (Filtex 300) to protect it from fine particles. The drainage system's functionality should be checked and cleaned with pressurized water at least once a year, using inspection shafts placed at bends - transitions. The drainage pipe was connected to the horizontal sewer line via a backflow preventer to prevent the outside street sewer from backing up and flooding the drainage system during heavy rains.

The exterior finish of the courtyard area consisted of concrete paving on sand - a so-called "breathing" finish with a minimum slope of 1% away from the exterior walls.

Horizontal insulation of the exterior walls was carried out after the vertical insulation was completed using chemical injection by a specialized company authorized for such work. After horizontal insulation was applied, it was recommended to leave the walls without plaster for at least 6 months to allow for partial evaporation of moisture from the surface layers of the walls. It was anticipated that nitrates (leakage from sewers) - salts that cannot be removed from the walls - might occur in the rear part of the building. During slow drying, these salts could crystallize on the surface of the brick masonry, and they could be mechanically removed with a brush or washed with

https://doi.org/10.5593/sgem2024/4.1/s16.01

pressurized water. Adequate cross-ventilation of the basement spaces should be ensured over the next 2-3 years for quality gradual drying of the walls.

After 6 months from the completion of the horizontal insulation and after any partial crystallization of salts from the masonry, it was recommended to apply remedial plaster, which, with its structure, would facilitate further drying of the masonry without undesired moisture patches (salts act hygroscopically, absorbing moisture from the air). Remedial plasters (e.g., the SANO system) were not applied where wall tiles would be installed. Gypsum should not be used to attach electrical installations. [5]

Remedial plasters do not replace water and rising damp insulation. The proposed multi-layer remedial system SANO, as a specific proposal for the building in question, was supplied in the form of dry mortar mixtures according to DIN 18557 and also met the new WTA 2-2-91 guideline. [6]

The further process of applying remedial plaster was as follows:

1. A remedial base coat (SANO 04) was applied to the masonry to create a discontinuous (network) layer covering a maximum of 50% of the treated surface, with a thickness of approximately 1.5 - 2 mm, and allowed to dry sufficiently for 20 - 24 hours.
2. After the masonry treated with the base coat (SANO 04) dried, the core plaster (SANO 02) was applied in layers of no more than 20 mm. Each layer had to dry for a minimum of 20 - 24 hours, depending on the temperature, before applying the next layer. Individual layers were smoothed only with a batten. In any case, they must not be smoothed with a trowel.
3. After the core plaster dried (approximately 21 days), the final layer (SANO 01 - stucco) was applied. This layer was final.
4. COLOR SURFACE TREATMENTS: For any colour treatment of the masonry, RELIUS paints based on silicone or silicate should be used. Under no circumstances should dispersion paints be used on treated masonry.

CONCLUSION

Based on the inspection, a proposal was made to create additional insulation for the perimeter walls that are in contact with the ground and currently have a high moisture content. Even after the insulation is installed, the process of drying out the masonry is long-term and may take several years. The remediation process is considered effective if the moisture content decreases by half after two years. To ensure proper gradual drying of the walls, sufficient cross ventilation of the basement spaces should be provided over the next 2-3 years.

REFERENCES

[1] Zákon NR SR číslo 272/1994 Z. z. o ochrane zdravia v znení neskorších predpisov a vyhláška č. 326/2002 MZ SR, ktorou sa ustanovujú najvyššie prípustné hodnoty zdraviu škodlivých faktorov vo vnútornom ovzduší budov.

[2] VLČEK, M., BENEŠ, P.: *Poruchy a rekonstrukce staveb II*., Vydavateľstvo ERA

group, spol.s r.o., Brno 2005, ISBN 80-7366-013-X

[3] Smernica WTA 4-6-98. „*Dodatečná hydroizolace stavebních konstrukcí ve styku se zeminou*“– preklad z nemeckého originálu, Česká stavební společnost - WTA CZ, Praha 2004

[4] ŐNORM B 3355–1. Vysušovanie vlhkého muriva, diagnostika stavieb a zásady plánovania.

[5] ČSN.73 0610 Hydroizolace staveb – sanace vlhkého zdiva- základní ustanovení: Praha , 2000.

[6] Flimel, M.: Fyzikálne faktory pracovného prostredia. Prešov: TU-FVT, 2003. 105 s. ISBN 80-7099-499-1.

https://doi.org/10.5593/sgem2024/4.1/s16.01

IRRADIATION SPECIFICATIONS

Assoc. Prof., Ing. Ph.D., MBA, LL.M. Martin Hrinko[1]

Ing. Ph.D. Pavel Švec[1]

Assoc.Prof., RNDr. CSc. Jiří Švec[1]

[1]Vysoká škola CEVRO, Praha**, Czech Republic**

ABSTRAKT

Radiation technologies using ionising radiation and radionuclides are now widely used in all areas of human activity. These include applications in medicine, industry, nuclear energy, and science. Exposure to ionising radiation therefore affects radiation workers employed at these sites, a large group of people who are in the vicinity of the sites in the course of their work, and people who live and work in the vicinity of the sites.

However, the positive properties of ionising radiation and radionuclides that we use in practical applications can be accompanied by negative effects of ionising radiation from which we must protect ourselves with well-developed and effective radiation protection. However, the negative effects of ionising radiation, which can occur with uncontrolled exposure, are quite different from other pollutants that affect humans, such as noise, dust, light or heat fields, toxic substances, etc. varies considerably. For example, by the fact that humans have no sense to alert them that they are in a radiation field. This is a fact that greatly affects all radiation activities and all contact with ionizing radiation.

This paper deals with the differences and specifics of irradiation. He gradually discusses them, looking for their mutual connections and links. It discusses their significance and seriousness. It also discusses their impact on radiation safety and the provision of effective and reliable radiation protection for radiation workers and the public.

In view of the widespread use of radiation technologies, good knowledge and awareness of ionising radiation can contribute to working responsibly in radiation workplaces and to minimising the emergence of various rumours and untruths among the public.

Keywords: Ionising radiation, radioactivity, radiation effects, radiation protection

INTRODUCTION

Radiation technologies using ionising radiation and radionuclides are now widely used in all areas of human activity. These are applications in medicine (radiodiagnostics, nuclear medicine, radiotherapy), in industry (technological measurements - thickness gauges, level gauges, moisture gauges, density gauges, etc., defectoscopy, carousel measurements, tracking methods, radiation technology), in nuclear energy, in science (methods of substance analysis, quantum physics).

https://doi.org/10.5593/sgem2024/4.1/s16.02

The main benefits of radiation technologies are [1]:

- The radioactive transformation that produces ionising radiation is independent of external conditions (pressure, temperature, humidity).
- Possibility to measure without sampling and with non-contact measuring methods.
- High sensitivity measurement.
- The outputs from the detectors are mostly electrical signals. These can be used for direct measurement of quantities, optical or acoustic signalling, as well as control circuits for automation processes.

Workplaces with sources of ionising radiation are therefore part of many technological plants, medical facilities and scientific research institutes. Thus, not only the radiation workers who are employed at these sites come into contact with ionising radiation, but also a large group of people who are in the vicinity of radiation sites as part of their duties. In all these cases, ionising radiation and radionuclides exploit their positive properties. However, these may be accompanied by negative effects of ionising radiation related to possible uncontrolled exposure and thus uncontrolled ionisation of tissues and organs of the human body [2],[3]. However, the negative effects of ionising radiation are quite different from the effects of other pollutants that affect humans, such as noise, dust, light or heat fields, toxic substances, etc, are quite different. For example, the fact that humans have no senses that would alert them to the fact that they are in a radiation field, and also the fact that the radioactive transformation that produces ionising radiation cannot be influenced or, above all, stopped by external conditions, which is possible with most sources of pollution.

The present paper deals with the differences and specifics of irradiation. It discusses them in turn and considers their importance and relevance to radiation protection and the protection of radiation workers and the public.

SPECIFICS OF IRRADIATION

In all nuclear technologies, the radiation protection of workers and the public must be ensured. The following peculiarities of the negative effects of ionising radiation must be considered.

1. **The radioactive transformation that is the source of ionising radiation is independent of external conditions.**

Thus, the radioactive transformation of a given radionuclide proceeds in the same way (given by the type of transformation) and at the same rate (given by the half-life of the radionuclide) under all conditions. No external intervention can change the type of conversion and accelerate, slow down or stop the radioactive conversion.

On the one hand, this allows wide use of radionuclides in technology, medicine, science, etc., but on the other hand, it causes great complications in dealing with emergencies where radiation exposure may occur [4]. In this case, the primary source of the problem - the emission of ionising radiation - cannot be reduced or stopped. We can only protect

ourselves from ionising radiation, for example, by shielding ourselves or keeping a sufficient distance from the radiation source.

A similar situation arises concerning the management of radioactive waste that is generated by nuclear technologies. The basic negative characteristic of radioactive waste must be considered, i.e. the radioactive transformation cannot be influenced in any way, nor can it be disposed of in an ideal way. This is a major difference compared to dealing with other wastes. Radioactive waste can only be converted into a form which is as environmentally resistant as possible (e.g. glass or ceramics) and stored safely. It is then necessary to wait until all the radionuclides in the waste have been transformed into stable elements. This can take thousands of years. This is the main problem with radioactive waste because mankind has no practical experience with storing anything for so long.

2. The human senses cannot detect ionising radiation.

If a person is in a field of ionizing radiation, then even at high doses - unless he has the appropriate measuring device - he does not detect or feel the presence of the radiation field. This means that he or she also has no way of assessing the danger of the situation. This is not true for most pollutants. For example, when fighting a fire, an experienced firefighter can tell from visual (height, colour and contours of fire and smoke) and acoustic sensations what may be burning in each area and what the danger is. In the event of an emergency involving a source of ionising radiation, this is not possible. This of course complicates the management of such a situation.

However, these may not only be radiation incidents and accidents but also industrial and technological emergencies (fire, explosion) [5]. Given the widespread use of radiometry, it is likely that radiometric thickness gauges, density gauges, level gauges, etc. will be present in the affected area. The protective casing or shielding of these devices can be damaged by heat or mechanical force. Unwanted emission of radiation or scattering of the radionuclide may occur. This adds a radiation field to the pollutants in the area, which will not be sensibly detected by the intervening workers. To prevent this from happening, the emergency services must have sufficient information about the area in which the accident has occurred and must also be equipped with appropriate measuring equipment.

The sensory undetectability of ionizing radiation represents one source of fear of ionizing radiation – radiophobia. There is speculation about the risks of radiodiagnostics and radiotherapy, the negative effects of uranium mining, the safety of nuclear power stations, etc. In cases of radiophobia, some existing negative effects of ionizing radiation are intentionally exaggerated and misinterpreted. In many cases, the effects of radiation are also confused with the toxicity of radionuclides [6],[7]. Radiophobia can only be eliminated through a permanent open information policy.

3. The effects of ionizing radiation are threshold (non-stochastic, deterministic) and non-threshold (non-stochastic)

The essence of the biological effects of ionising radiation is its ability to ionise and excite the atoms and molecules of the exposed organism. The observable effects of ionising

https://doi.org/10.5593/sgem2024/4.1/s16.02

radiation on living matter always have their origin in the processes that are induced by ionising radiation in the cells.

Damage to the cell can occur in two ways [6]:

a) Cell death (or loss of the cell's ability to divide)
b) by changing the genetic information of the cell while maintaining further cell division; radiation thus induces mutations, resulting in various malignant neoplasms (cancers).

The biological effects are divided into:

- early (manifested in a short time after exposure to large single doses) and late (manifested after a longer interval; ionising radiation can affect human health even very long after exposure).
- somatic (in relation to the irradiated individual) and genetic (in relation to the offspring of the irradiated individual),
- stochastic (threshold, deterministic) and stochastic (threshold).

We divide the biological effects into:

- early (appears in a short time after irradiation with larger single doses) and late (appears after a longer period, ionizing radiation can affect human health even after a very long time after irradiation),
- somatic (relating to the irradiated individual) and genetic (relating to the offspring of the irradiated individual),
- Non-stochastic (threshold, deterministic) and stochastic (non-threshold).

Non-stochastic (deterministic) effects

These are effects that occur as a result of the death or loss of the ability to divide large numbers of irradiated cells.

These are threshold effects. They occur only after a certain threshold dose is exceeded (this is different for different organs, for a single irradiation it ranges from 1 to 3 Gy). The effect does not appear when exposed below the dose threshold. After exceeding the threshold dose, the severity of the damage increases approximately linearly with the size of the dose (Fig. 1 [8]). Deterministic effects include various forms of acute radiation sickness, radiation skin damage, fertility damage (early effects), chronic radiodermatitis, and eye lens damage (late effects).

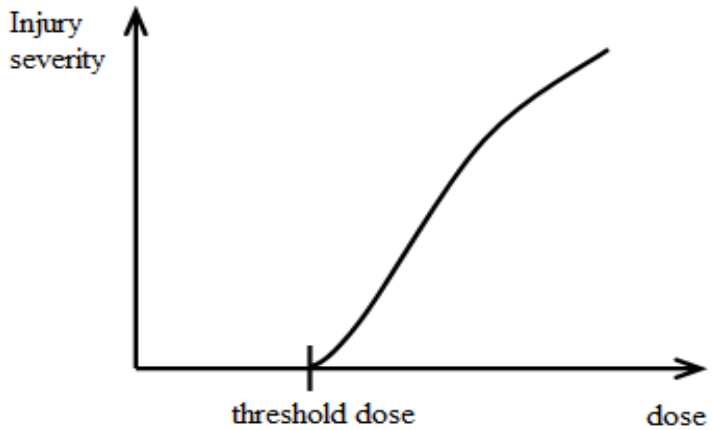


Figure 1. Deterministic effects

Stochastic effects

These are effects that are caused by changes in the genetic information (mutations) of cells that result from the action of ionising radiation on cells.

These are threshold-free effects. The severity of damage does not increase with increasing effective dose, but the probability of damage occurring in the exposed population does (Fig. 2 [8]). Stochastic effects include malignant neoplasms (somatic effects) and genetic effects. In both cases, the effects are delayed, and the latency period can be many years.

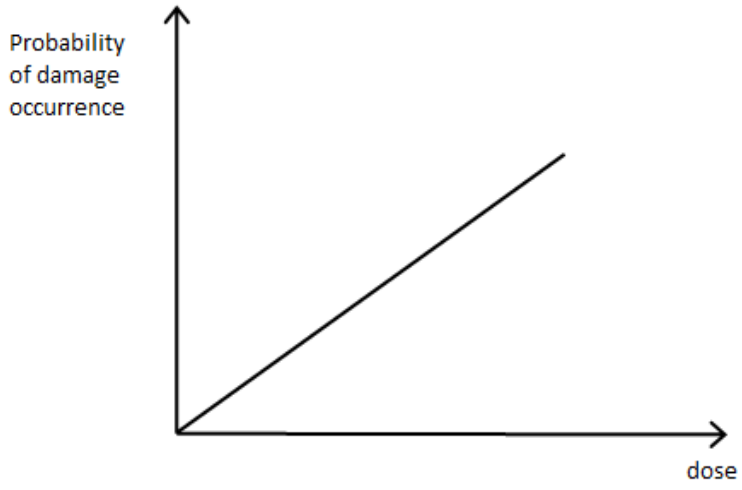


Figure 2. Stochastic effects

From the point of view of radiation protection [9], it is important that radiation threshold effects can be avoided by setting maximum permissible doses (limits) that are much lower than the threshold effects. This is not possible for non-threshold effects. This means that any exposure can be dangerous to humans. It is therefore necessary to reduce exposure in all cases where possible.

4. The effects of radiation can be both genetic and somatic.

Somatic effects affect the irradiated individual, while genetic effects affect their offspring. In the case of exposure, the damage can be passed on in the form of genetic effects to subsequent generations of the exposed individual. The offspring of irradiated persons are affected by mutations in germ cells. The mutated gene can reproduce during cell division and the mutation is passed on to the next generation. It is estimated that the mutated gene will remain in the population for as long as 40 generations. This is a very significant difference from most pollutants that affect humans. Estimating the likelihood of genetic damage as a function of dose is only possible indirectly, as primary data on affected human populations are not available.

5. The level of knowledge of radioactivity and ionising radiation in the general population is very low.

Little knowledge of this issue leads to various rumours and misinformation. This can lead to underestimation or overestimation of radiation protection in radiation emergencies. The same applies when human exposure occurs. This can only be changed by a very sophisticated information system. It is mainly about the properties and effects of ionising radiation, radiation safety and behaviour in radiation emergencies. This includes not only

https://doi.org/10.5593/sgem2024/4.1/s16.02

radiation workers, but also a large group of people who, as part of their work duties in the vicinity of radiation sites, move or live in the vicinity of nuclear installations.

It is also very important that correct information about ionising radiation is available to patients undergoing medical exposure [8].

The low level of knowledge of radioactivity and ionising radiation also contributes - in combination with the sensory undetectability of ionising radiation - to radiophobia.

6. Little experience in dealing with incidents involving sources of ionising radiation.

This is the so-called "good and bad" situation at the same time. It is certainly a good thing that there are not too many of these emergencies in the world today. On the other hand, the teams dealing with these emergencies have little or, in extreme cases, no experience at all [10]. It is therefore very important to have well-prepared emergency documentation (emergency plan, emergency regulations, emergency instructions) and adequate training and knowledge of the emergency personnel. Emphasis is also placed on the implementation of emergency drills and habits and verification of the functionality of all technical means, systems, and devices necessary for intervention.

It is necessary to mention here radiological terrorism, i.e. the misuse of radionuclides for terrorist purposes. Contrary to initial predictions, the terrorist misuse of radionuclides occurs only in very rare cases (e.g. the murder of the agent A. Litvinenko in 2006). The widespread misuse of radionuclides is hampered by their very easy detection and thus their detection.

7. The initial symptoms of radiation sickness are no different from those of ordinary diseases.

These initial symptoms are no different from the initial symptoms of the flu, for example (increased temperature, headache, and feeling unwell). Unless the treating physician has information that the patient may have been exposed to radiation, he or she may not be able to tell from the initial symptoms that the patient is suffering from radiation exposure. This can, of course, bring some problems and complications for further treatment. However, it should be noted that radiation sickness is a deterministic effect with a threshold of 1 to 3Gy [8]. However, this is a large exposure that is only relevant in the case of large-scale radiation accidents.

8. Incorrect estimation of the results of the calculation

In common practice, people usually estimate the dimensions, volume and weight of objects and time intervals. This is not the case for radiation protection calculations. When calculating a worker's dose, there is no obvious way to verify the accuracy of the calculated value. This is related to the sensory imperceptibility of ionising radiation. All calculations concerning radiation protection must therefore be very well checked and verified (control calculations, statistical tests) [11].

CONCLUSION

The expanding use of nuclear technologies means that workplaces with sources of ionizing radiation are part of many technological plants, medical facilities, and scientific research institutes. Contact with ionising radiation thus involves radiation workers who are employed at these sites, a large group of people who are in the vicinity of the sites as part of their duties, and people who live and work near the sites.

However, exposure to ionising radiation is very different from physical fields that affect humans, such as noise, dust, light or heat fields, toxic substances, etc. varies considerably. This fact accompanies all activities and contacts of radiation workers and the public with radionuclides and ionising radiation.

Some of the more important differences are that the radioactive transformation that produces ionising radiation is independent of external conditions and that ionising radiation is not detectable by the human senses.

The radioactive transformation of a given radionuclide therefore proceeds in the same way and at the same rate under all conditions. No external intervention can change the type of conversion and accelerate, slow down or stop the radioactive conversion.

When a person is in a field of ionising radiation, even at high doses, the presence of the radiation field cannot be detected or felt. This means that he or she has no way of assessing the danger of the situation.

This can have a very negative impact on industrial and technological emergencies (fire, explosion). Violation of radiometric equipment that may be present in the affected area may result in unwanted emission of radiation or scattering of radionuclides. This adds a radiation field to the pollutants in the area, which will not be sensibly detected by the intervening workers. The responders must be sufficiently informed about the area in which the accident occurred and equipped with appropriate measuring equipment.

The undetectability of ionising radiation by the senses is a source of fear of ionising radiation - radiophobia - where some of the real negative effects of ionising radiation are deliberately overestimated and misinterpreted. Only a permanent open information policy can eliminate radiophobia. This is very important for patients undergoing medical radiation.

The effects of ionising radiation are divided into threshold and non-threshold effects. From a radiation protection point of view, it is important that radiation threshold effects can be avoided by setting maximum permissible doses (limits) that are much lower (about 50 times) than the threshold effects. This is not possible for non-threshold effects. This means that any exposure can be dangerous to humans. It is therefore necessary to reduce exposure in all cases where possible.

The effects of radiation can also be genetic, where the damage can be passed on to future generations of the irradiated individual. This is a very significant difference from most pollutants that affect humans.

Little knowledge of this issue leads mainly among the population to various rumours and misinformation and underestimation or overestimation of radiation protection, or the

https://doi.org/10.5593/sgem2024/4.1/s16.02

consequences of human exposure. This can only be changed by a very sophisticated information system.

It can be concluded that exposure to ionising radiation has certain specificities that concern not only radiation workers in the provision of radiation protection at the workplace but also a large part of the population that may come into contact with ionising radiation.

REFERENCES

[1] Hála, J., Radioaktivita, ionizující záření, jaderná energie. Brno: Konvoj 1998

[2] Nekula, J. et al., Radiobiologie. Olomouc: UP 2001

[3] Cember, H., Introduction to Health Physics. New York: Mc Graw-Hill-eBooks 2009

[4] Prouza, Z., Švec, J., Zásahy při radiační mimořádné události. Ostrava : Edice SPBI Spektrum, 2008

[5] Lukáš, L., a kol., Bezpečnostní technologie, systémy a management III. Zlín: VeRBuM, 2013

[6] Kubinyi, J. et al., Principy radiační ochrany v nukleární medicíně. Praha:Grada Publishing, a.s. 20018

[7] ICRP 105 Radiological Protection in Medicine, 2007

[8] Klener, V. (ed.), Principy a praxe radiační ochrany. Praha: SÚJB/AZIN 200

[9] ICRP1997b General Principles for the Radiation Protection for Workers, Publication No. 75, Oxford, Pergamon Press 1997

[10] Security of Radioactive Sources, Procesings of an International Conference, IAEA, Vienna, March 2003

[11] Meloun, M., Militký, J., Statistická analýza experimentalnich dat. Praha:Academia, 2004

SECTION

RENEWABLE ENERGY SOURCES AND

CLEAN TECHNOLOGIES

ANALYSIS OF THE AIR FLOW IN THE RENOVATED TEST SECTION OF BSHC SMALL WIND TUNNEL

Nikita Dobin[1]

[1]Institute of Metal Science, Equipment, and Technologies with Center for Hydro- and Aerodynamics "Acad. A. Balevski" at the Bulgarian Academy of Sciences – (IMSETHC-BAS), Varna, **Bulgaria**

ABSTRACT

The existing at Bulgarian Ship Hydrodynamics Centre (BSHC) wind tunnel named MINIAT is under upgrade, in order to expand the range of the Center's capabilities and the scope of aerodynamic research by enlarging the working section sizes and closing the air flow. This renovation is inspired by recent development of modern technologies for renewable wind energy conversion and necessity for comprehensive investigation of environmental effects.

The objective of this study was to theoretically calculate a new aerodynamic contour and subsequently develop a computer model for the new constrictor and diffusor sections of the wind tunnel. To make the final decision, a series of computational fluid dynamics (CFD) simulations has been performed in ANSYS Fluent to confirm the adequacy of the sizes of the new wind tunnel elements selected using the theoretical method. The behavior of the flow in these areas was also studied using CFD methods in ANSYS fluent. Static pressure contours and velocity field contours are presented in transverse and longitudinal sections, to illustrate the homogeneity of the flow. The results will be illustrated and presented graphically.

This research is significant within the context of Renewable Energy Sources and Clean Technologies. By optimizing the wind tunnel design, the study enhances its application for renewable energy studies, particularly in wind energy conversion. The novelty of this research lies in its comprehensive approach, combining theoretical design with advanced CFD simulations to achieve an optimal aerodynamic contour for the upgraded wind tunnel sections. The authors' contributions include the theoretical calculations, development of the computer model, and the extensive CFD analysis that validated the design, ensuring its effectiveness for future aerodynamic and environmental research. The results will be graphically illustrated to provide a clear understanding of the improvements achieved through this upgrade.

Keywords: wind tunnel design, wind tunnel testing, aerodynamics, CFD

INTRODUCTION

The groundwork for the upgrade of the small wind tunnel « MINIAT» goes back more than 15 years, when BSHC first began discussing the possibility of modifying the working section.

The main motivation for this task is the future design and construction of a new working section of the small wind tunnel at the BSHC for wider use of the existing

https://doi.org/10.5593/sgem2024/4.1/s17.03

infrastructure, broadening the horizons of scientific activity and training young specialists.

The creation of the gradient flow is necessary due to the increasing interest in the world to determine the aerodynamic performance of transport, industrial, residential, construction and other sites exposed to strong wind.

If we look at the types of experimental investigations that can be done in wind tunnels with boundary layer modelling capability, we can summarize their activities in the following directions:

- Wind loading of objects in the flow;
- Renewable Energy;
- Civil architecture and construction;
- Verification and calibration of instruments and sensors;
- Training.

From the perspective of Renewable Energy Sources and Clean Technologies, this research is crucial. The upgraded wind tunnel will play a vital role in advancing wind energy conversion technologies. It will enable detailed aerodynamic studies, essential for optimizing the design and performance of wind turbines and other renewable energy systems.

According to forecasts by the European Wind Energy Association (EWEA) [3],[4], Europe could install up to 450 GW of new wind turbines by 2030, potentially supplying up to 32% of the EU's electricity. By 2050, this capacity could reach 1 TW, meeting up to 50% of the EU's electricity needs. Consequently, the EU's long-term strategic development programs prioritize research in wind turbine technology, the integration of wind energy, and offshore development. This focus has led to increased interest from aerodynamic laboratories in studying the aerodynamics of wind turbines.

BASIC REQUIREMENTS

- The ability to model the phenomena themselves depends on compliance with the laws of similarity theory.
- In low velocity wind tunnels, an open test section is used. To reduce the losses and the power dissipation, a closed test sections is used, the aerodynamic characteristics of such test sections are higher than the open type. [6]
- The effort to realize the similarity of the model tests with the field tests leads to the creation of low-turbulence wind tunnels, in which the degree of turbulence is close to the turbulence of the free atmosphere.
- At present, the turbulence degree of modern wind tunnels reaches 0.2%, and the recommended requirement for the turbulence degree in the test sections of wind tunnels is Tu<0.5% for conducting tests from the directions described above.
- Model tests of ships and marine objects are usually carried out in a low-speed closed-loop WT with a rectangular cross-section of the test section, with a uniform velocity field in the section +/-0.5%.
  Typical aerodynamic tests in shipbuilding and marine engineering:

  - Investigation of aerodynamic forces and moments on underwater and abovewater parts of a floating vessel or other marine object and calculation of dimensionless drag coefficients;
  - Exhaust and smoke propagation on decks and funnel optimization;
  - Visualization of flow lines and study of pressure distribution over the hull surface.
- Specialized boundary layer wind tunnel is required to solve problems in architecture and civil engineering; such tunnels require a long working section $L/D_H > 5$ to adequately model the flow characteristics.
- The new working section should have a rectangular cross-section and the flow velocity in it should not be less than 30 m/s.
- Considering that we will not be designing a completely new aerodynamic loop, but only changing the working section, contraction and diffuser of the existing WT, the size of the working area will be limited. According to preliminary estimates, the dimensions of the new working section with a boundary layer of the above dimensions will allow the testing of models at a scale of 1:300-1:500

ANALYSIS

Information on the existing wind tunnel:

MINIAT is a subsonic aerodynamic wind tunnel with an open working section. The circuit of the MINIAT is vertical in space, so that the working section of the chamber is above the return duct to the tunnel. The tunnel sizes are 1.4 m (width) x 2.47 m (height) x 8.1 m (length), with elliptical working section 0.8 x 0.466 m, length 0.95 m.

The sketch of MINAT is shown in Fig.1.

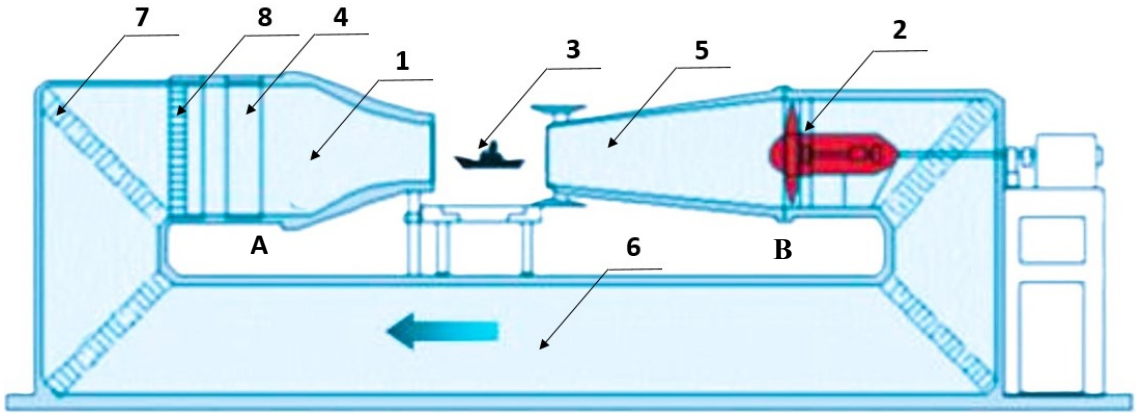


Fig. 1. A sketch of existing MINAT tunnel at BSHC
1 - constrictor (nozzle); 2 - impeller; 3 - test section; 4 - setting chamber; 5 - diffuser; 6 - return duct; 7 – corner

https://doi.org/10.5593/sgem2024/4.1/s17.03

This sets the following boundaries for the renovated section:

- The new working section of the wind tunnel can be located between sections A-A and B-B (i.e. from the end of the setting chamber to the entrance of the adapter). The total length of the new structure should be L=4110 mm;
- The available fan unit with power N=60 kW should provide an air flow velocity of at least 30 m/s.

Calculation of new aerodynamic contour elements:

First, let's use the continuity equation to determine the preliminary dimensions of the working section:

$$A_1V_1=A_2V_2 \quad (1)$$

It follows that the cross-sectional area of the new working section should not exceed Smax= 0.585 m^2 in order to satisfy the required flow velocity condition.
Knowing that the adapter diameter da= 890 mm, in order to avoid changing the flow pattern in the working section, the maximum width of the new working section at its inlet should not exceed b=840mm.
In the existing wind tunnel there is also a limitation on the height of the working section due to the presence of the base plate. This limitation is h= 600 mm.
The result of all this is:

B_{TS}=840mm. H_{TS}= 600 mm. S_{TS}= 0.504 m^2 < S_{max},

According to [1], the length of the test section should not be less than 0.5 of its hydraulic diameter to ensure uniform airflow at the nozzle outlet, and not more than 3 times the equivalent hydraulic diameter to avoid boundary layer separation at the test section outlet.

$$D_H = 4A/P \quad (2)$$

where A is the cross-sectional area of the fluid flow and P is the wetted perimeter of the flow cross-section. This gives $D_H = 0.7$ and the optimum length of the working section becomes $L_{TS} = 1.5$ m.
The constrictor or 'nozzle' is the most important part of the wind tunnel design; it has the greatest influence on the quality of the flow in the working section. Its purpose is to accelerate the flow from the setting chamber to the working section and to reduce turbulence and irregularities in the working section. The acceleration of the flow and the reduction of irregularities depend mainly on the so-called narrowing factor N between the inlet and outlet zones.

N_{con} =A_1/A_2 – which is the ratio of the cross-sectional area of the inlet to the cross-sectional area of the outlet of the nozzle, is directly related to the quality of the flow.

In our case we get N ≈ 3.

By practical experience, if both the constrictor half-angles, α/2 and β/2, take values of the order of 12º, the contraction has good fluid dynamic behavior. However, with such a slow contraction, the constrictor arc increases significantly, which is impractical in our case. Therefore, we take the length of the constrictor to be $L_{con} = 1$ m, and as a consequence, the two semi-angles will be of the order of about 15° each.

According to [2], among the polynomials they tested, the fifth-order polynomial emerges as optimal. It exhibits no flow separation either at the centerline or along the corners, meets minimum Reynolds number criteria, and ensures highly uniform flow.

$$Y(X) = H_i - (H_i - H_e)[6\left(\frac{X}{L}\right)^5 - 15\left(\frac{X}{L}\right)^4 + 10\left(\frac{X}{L}\right)^3] \quad (3)$$

where:
H_i - nozzle inlet height
H_e - nozzle exit height
X - Coordinates of points along the x axis
L - Nozzle length
The results of calculating polynomial curves are shown in Figures 2 and 3.

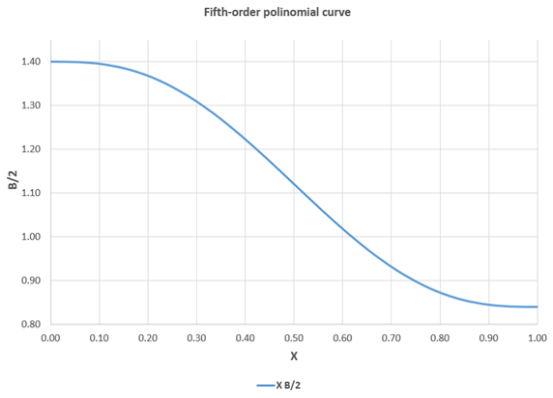


Fig. 2. Results of calculating a polynomial curve along the width

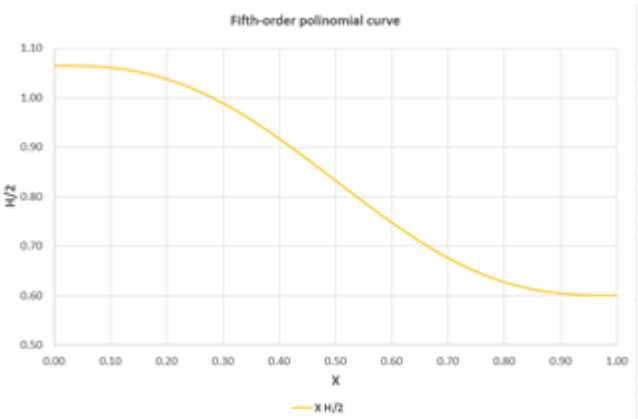


Fig. 3. Results of calculating a polynomial curve along the height

A diffuser is a gradually widening channel located after the test section where the flow rate decreases and the pressure increases. In the event of flow separation, pressure pulsations are transmitted upward in a test section, resulting in pressure and velocity non-uniformity. Barlow, Rae and Pope [1] says, that the divergence angle of the diffuser walls should be less than 7° to avoid flow separation.

Knowing that we selected the nozzle length and the test section length, and the overall length of the design was limited by the existing parts, diffuser length L_{diff}=*1610 mm.*

To make the final decision a series of CFD simulations were performed in ANSYS Fluent [5] to confirm the adequacy of the sizes of the new wind tunnel elements selected.

RESULTS

The new aerodynamic contour was calculated using the proposed method, and the new dimensions are shown in Table 1. After calculating the dimensions of the new wind tunnel elements, a 3D model of the aerodynamic contour was created. Fig. 4. The ANSYS Fluent software package was used to simulate the flow in a new test section. The modeling results confirmed the correctness and adequacy of the previously chosen

https://doi.org/10.5593/sgem2024/4.1/s17.03

method for calculating new elements. Thus, Figure 5 shows the pressure distribution along the outer contour of the studied elements, as we can see - there are no zones with a sharp change in pressure in the test section, which indicates the absence of zones with separation of the boundary layer. Figures 6, 7 and 8 show the velocity contours in three different cross sections - directly at the entrance of the test section, in the middle of the test section and at the exit of the test section. An analysis and comparison is also provided for two corner options - straight and rounded. Figures 6, 7, and 8 clearly show that rounding the corners of the aerodynamic contour has a positive effect on the velocity distribution in the test section.

Table 1. Geometry dimensions of the new element of the tunnel

Element of aerodynamic contour	length, mm.	Entrance section, mm	Output section, mm.
Constrictor	1000	1400x1066	840x600
Test section	1500	840x600	840x600
Diffuser	1610	840x600	Φ 890

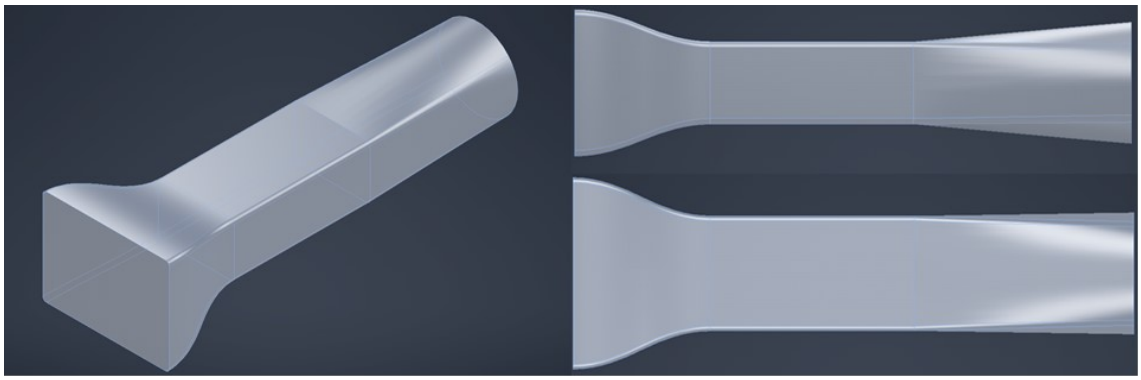


Fig. 4. 3D model of the new test section with nozzle and diffuser.

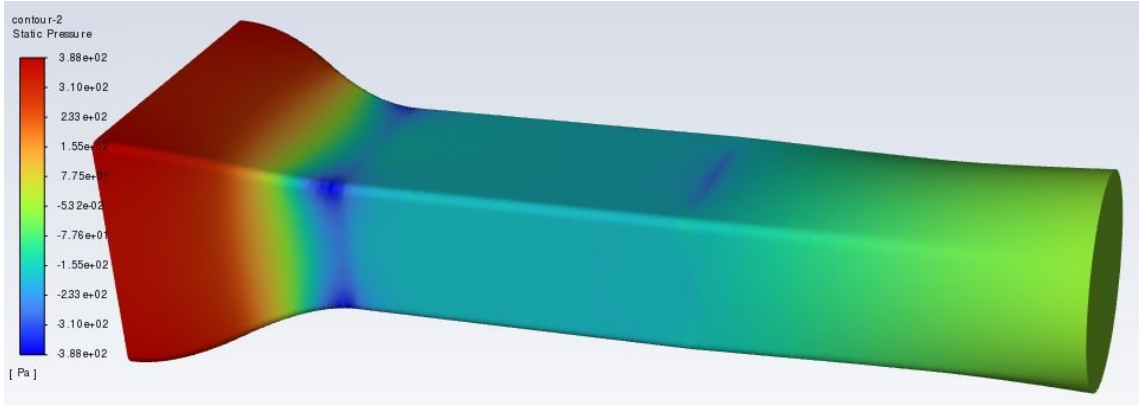


Fig. 5. Distribution of static pressure along the walls of a new wind tunnel section.

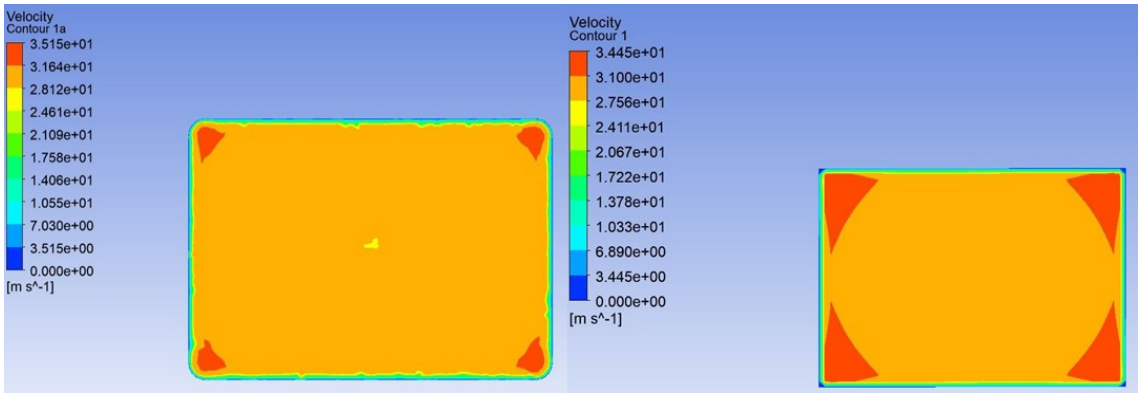


Fig. 6. Comparison of velocity fields at the entrance of the test section. (With and without rounded corners).

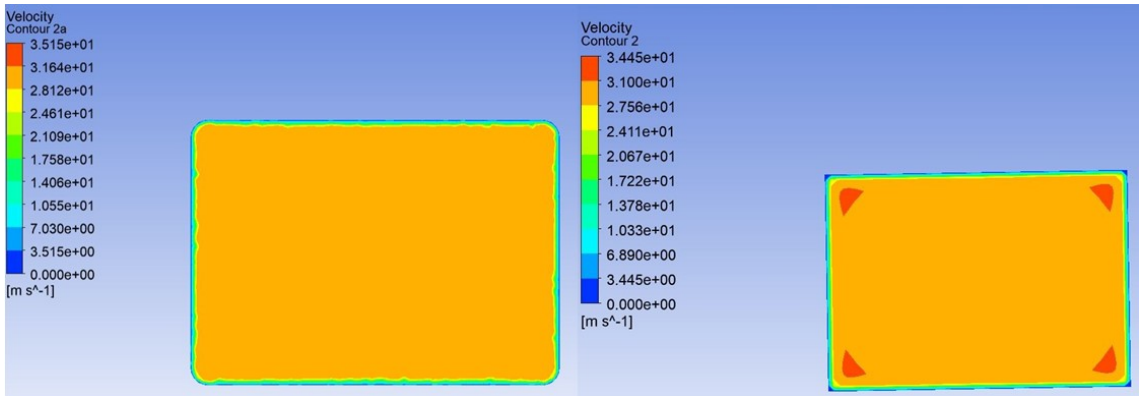


Fig. 7. Comparison of velocity fields in the middle of the test section. (With and without rounded corners).

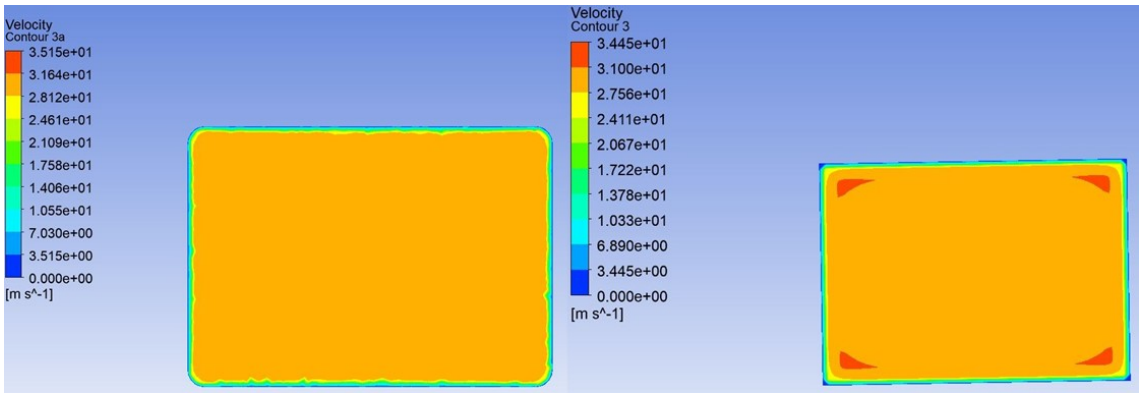


Fig. 8. Comparison of velocity fields at the end of the test section. (With and without rounded corners).

DISCUSSION

The purpose of this work was primarily to calculate a new section of the aerodynamic contour for the subsequent renovation of the existing wind tunnel at the BSHC, and as can be seen from the data provided, this goal was achieved and the optimal contour was selected. We can also note that there is a fairly large number of published works in the public domain on the design of new wind tunnels, but there is practically no information on the renovation of existing installations, which adds to the uniqueness of this work.

https://doi.org/10.5593/sgem2024/4.1/s17.03

CONCLUSION

In this work, the CFD calculations were used to analyze forms and dimensions of a new working section of aerodynamic contour in the process of the renovation of an existing wind tunnel. Three parts of the aerodynamic contour, such as the nozzle, working section and diffuser, were calculated and created in the form of a 3D computer model and then studied using ANSIS Fluent software. As a result of the studies, the adequacy of the chosen method for calculating the aerodynamic contour was proven and the geometry of the contour cross section was optimized in order to obtain a more uniform flow in the test section. Static pressure contours and velocity field contours were plotted to illustrate the homogeneity of the flow. The results were illustrated and presented graphically. The final dimensions of the new wind tunnel section have been selected and approved. It should also be noted that the data obtained will become the basis for further development of the project. The calculated dimensions will be used in the technical design stage, and the computer 3D model will be used for further research to prove the possibility of modeling the atmospheric boundary layer in a small wind tunnel with a short test section.

REFERENCES

[1] Barlow J. B., Rae W. H. Jr.- Pope A. Low Speed Wind Tunnel Testing. 3rd Ed. Wiley-Interscience: New York, 1999. ISBN: 978-0-471-55774-6

[2] James H. Bell and Rabindra D. Mehta CONTRACTION DESIGN FOR SMALL LOW-SPEED WIND TUNNELS, Stanford University Department of Aeronautics and Astronautics Stanford, CA 94305, 1988, pp 13-15

[3] The European Wind Energy Association | EWEA | Wind energy scenarios for 2030

[4] The European Wind Energy Association | EWEA | 2050: Facilitating 50% Wind Energy

[5] John E. Matsson, An Introduction to ANSYS Fluent 2021, SDC Publications, 2021, 552 p. ISBN: 9781630574628

[6] Bradshaw, P., and R. C. Pankhurst. The Design of Low-Speed Wind Tunnels. Jan. 1964, https://doi.org/10.1016/0376-0421(64)90003-x.

APPLICATION OF THE PROTON-EXCHANGE MEMBRANE HYDROGEN FUEL CELL AS A MOBILE POWER UNIT FOR THE HYDRIVE 1 VEHICLE

Maksymilian Zarychta[1]

[1] AGH University of Science and Technology, **Poland**

ABSTRACT

This paper extensively explores the technology of Proton Exchange Membrane (PEM) hydrogen fuel cells, delving into its theoretical foundations, operational intricacies, and its specific application in the HYDRIVE 1 bolide. The PEM fuel cell plays a crucial role in the vehicle's power ecosystem by converting hydrogen and oxygen into electricity, which is then utilized to energize the electrical system, telemetry, and engine. The drive system's specifications are meticulously presented, encompassing considerations of efficiency and safety.

Choosing a hydrogen cell as the propulsive force for an automobile necessitates a comprehensive understanding of its operations. The study incorporates a thorough examination of various factors influencing the cell's performance, including operating conditions and the hydrogen supply system. Years of research have been dedicated to scrutinizing these aspects, facilitating a comprehensive analysis. The findings are then systematically compared with the manufacturer's data, enabling a holistic evaluation of the PEM hydrogen fuel cell's viability and effectiveness in the automotive domain.

Keywords: hydrogen, fuel cell, efficiency.

INTRODUCTION

Research on hydrogen as an alternative fuel gained traction in the 1990s. Today, hydrogen fuel cell technology is rapidly advancing, particularly in transportation. In response, MechaniCAD students aspire to construct HYDRIVE 1, an eco-friendly race car, for the Shell Eco-marathon [5], promoting sustainable energy. Their study aims to meticulously evaluate hydrogen fuel cell efficiency, comparing actual performance with manufacturer specifications to provide a comprehensive analysis of its practical value.

ANALYSIS OF THE ENERGY SUPPLY SYSTEM IN THE HYDRIVE 1 CAR

The basis for research in the analysis of the hydrogen fuel cell efficiency was a thorough understanding of its operation. The PEM (Proton-Exchange Membrane) fuel cell powering the HYDRIVE 1 car is a product from Horizon, model H-500 XP [1]. It is a 500-watt, self-humidifying, low-temperature fuel cell powered by hydrogen with 99.99% purity.

https://doi.org/10.5593/sgem2024/4.1/s17.04

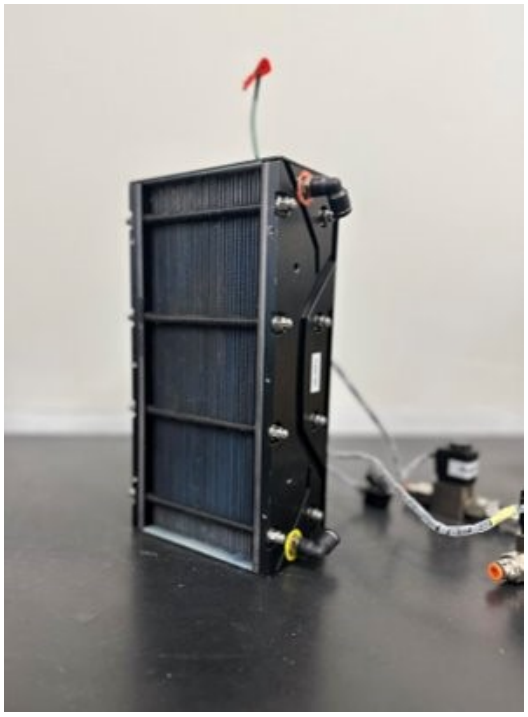


Fig. 1. Horizon H-500 XP hydrogen fuel cell with visible membranes [4].

PEMFC (Proton Exchange Membrane Fuel Cells) consists of a cathode, an anode, and a polymer membrane. Protons generated at the anode are transported through the polymer membrane to the cathode, where oxygen reduction occurs. Membranes are often constructed from materials such as Nafion [2]. The Horizon H-500 XP cell has 30 layers of polymer membranes [1].

The energy supply system of the HYDRIVE 1 car (Figure 2) begins with a high-pressure hydrogen tank serving as fuel storage. A two-stage regulator maintains system pressure at 0.5 bars, ensuring safe operation. Steel pipes transport hydrogen efficiently to subsequent components. Electrovalves regulate hydrogen flow, crucial for precise fuel control and safety, shutting off supply in case of leaks. The purge eliminates impurities and moisture, preventing pressure spikes that could affect system efficiency and durability. A flow meter enables precise fuel adjustment. The hydrogen fuel cell converts hydrogen to electrical current, powering the vehicle's electrical system and BLDC motor. Strategically located, the cell operates optimally. The cell controller manages system operation, monitoring parameters and ensuring optimal conditions. This integrated approach enhances efficiency and minimizes environmental impact, showcasing HYDRIVE 1 as an innovative solution in mobile unit technology.

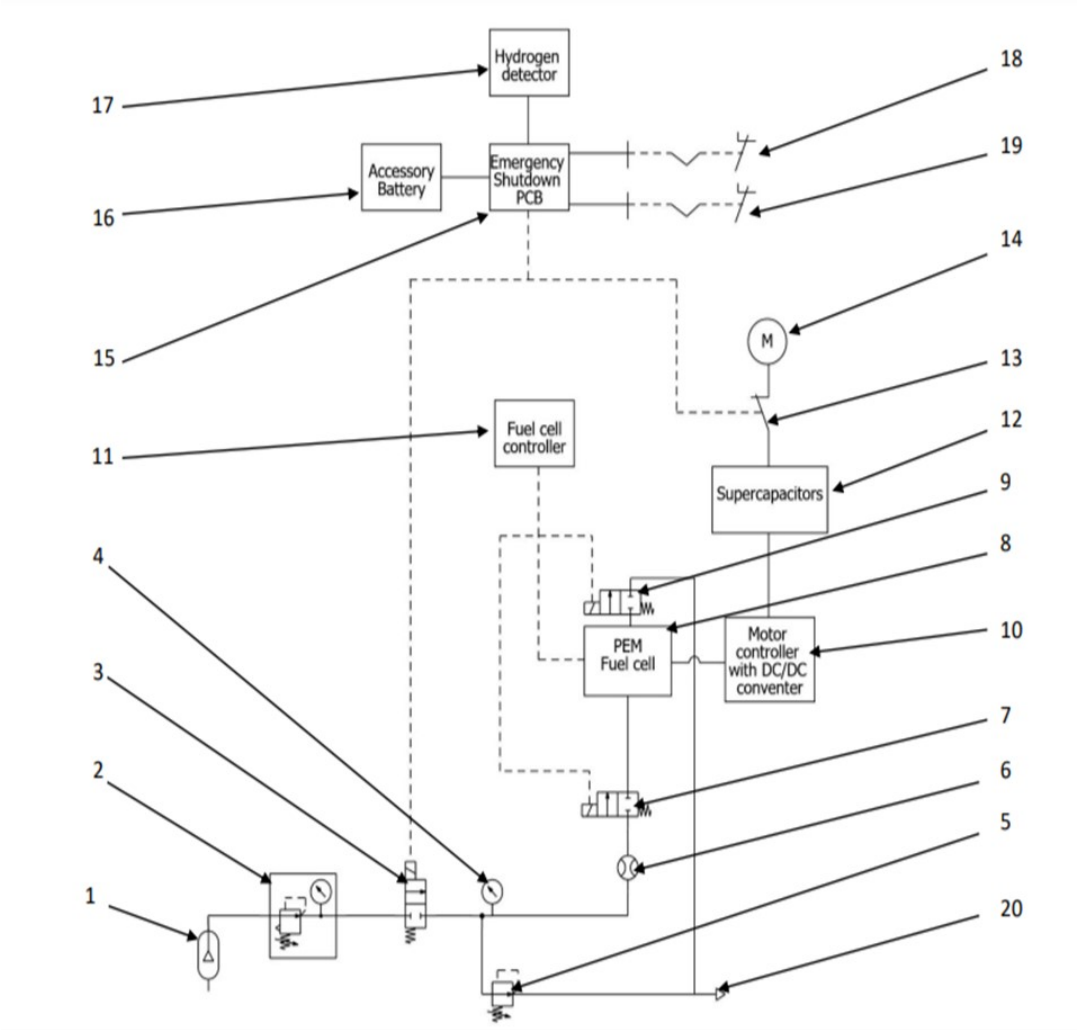


Fig. 2. Diagram of the energy supply system in the HYDRIVE 1 car [4].

Table 1. Elements in the diagram of the energy supply system in the HYDRIVE 1 car. [4]

Nr.	Name	Nr.	Name
1	Hydrogen tank	11	Cell controller
2	Pressure regulator	12	Supercapacitor stack
3	Emergency shut-off valve	13	Engine power switch
4	Pressure gauge	14	BLDC motor
5	Electrovalve	15	PCB with emergency switch
6	Flow meter	16	Auxiliary battery
7	Hydrogen cell inlet valve	17	Hydrogen sensor
8	HP X500 Fuel Cell	18	External emergency button
9	Hydrogen fuel cell purge valve	19	Intternal emergency button
10	Motor controller with DC/DC converter	20	Outlet (purge)

https://doi.org/10.5593/sgem2024/4.1/s17.04

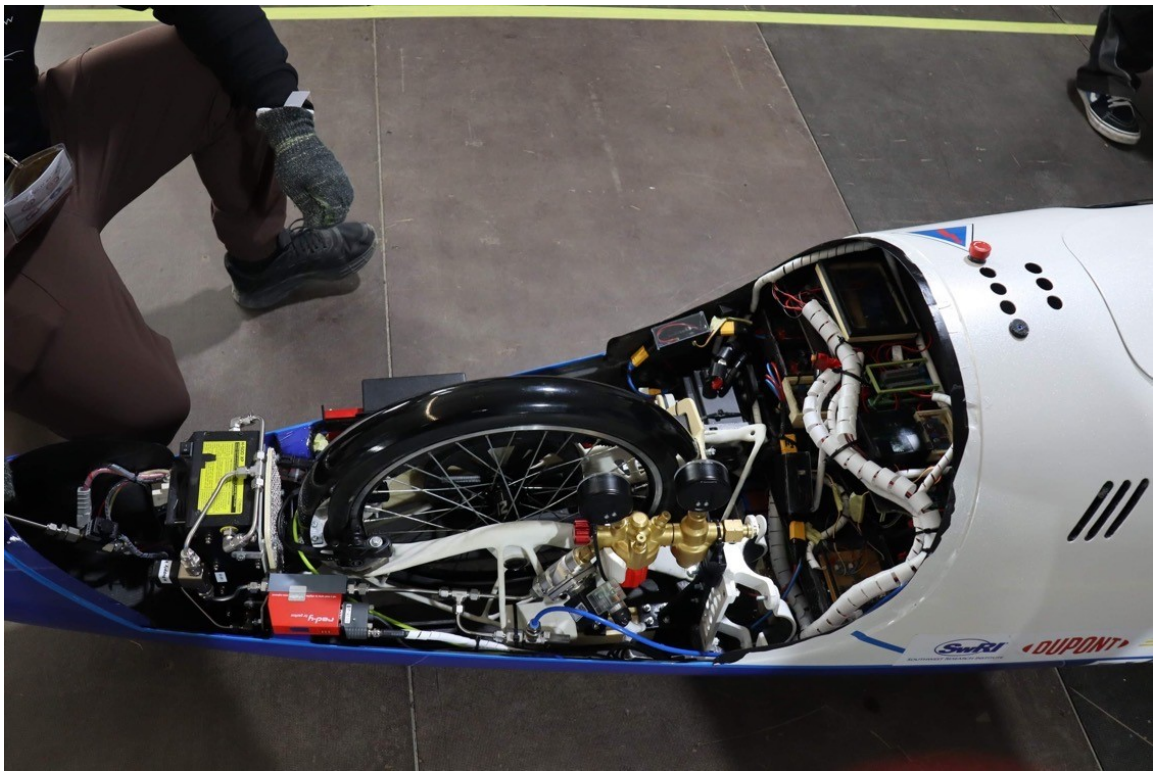


Fig. 3. Photograph of the actual hydrogen supply system in the HYDRIVE 1 car [4].

RESEARCH METHODOLOGY

Over the years, several fuel cell tests have been conducted. During the conducted tests, the focus was on analyzing the hydrogen fuel cell to assess its efficiency. In this context, the cell was connected both to a load, which allowed control of the current and recording of the gross power generated P_FC, and to the hydrogen supply system. To monitor the supplied hydrogen, a flow meter was used, which precisely recorded the flow rate in standard liters per minute.

During the experiments aimed at obtaining a comprehensive assessment of the cell, attention was paid to the set current and the voltage value generated by the cell under various load conditions. Additionally, the fuel cell current I_FC, which is the generated current value reduced by the current consumed for the cell's own needs I_PW, was read from the cell controller.

By integrating these diverse measurements, a complete picture of the hydrogen fuel cell operation was obtained, as well as correlation with the supplied hydrogen. The results were analyzed and used for further calculations of the actual system efficiency. Below is a table of data from one of the sample tests:

Table 2. Study from June 10, 2023. [4]

I_ST [A]	U_FC [V]	P_FC [W]	I_FC [A]	I_PW [A]	P_PW [W]	P_NET [W]	EFF [%]	Flow [ln/min]
1	22,3	22,3	2,1	1,1	13,2	9,1	6,38	0,8
1,5	21,8	32,7	2,3	0,8	9,6	23,1	14,39	0,9
2	21,4	42,8	3,1	1,1	13,2	29,6	16,59	1
2,5	21,2	53	3,3	0,8	9,6	43,4	22,12	1,1
3	20,9	62,7	4,1	1,1	13,2	49,5	23,12	1,2
3,5	20,7	72,45	4,3	0,8	9,6	62,85	27,10	1,3
4	20,5	82	5,1	1,1	13,2	68,8	27,55	1,4
4,5	20,3	91,35	5,3	0,8	9,6	81,75	30,55	1,5
5	21	105	6,1	1,1	13,2	91,8	32,16	1,6
5,5	20	110	6,3	0,8	9,6	100,4	33,11	1,7
6	19,8	118,8	7,1	1,1	13,2	105,6	32,89	1,8
6,5	19,7	128,05	7,3	0,8	9,6	118,45	34,95	1,9
7	19,5	136,5	8,1	1,1	13,2	123,3	34,56	2
7,5	19,4	145,5	8,4	0,9	10,8	134,7	35,96	2,1
8	19,3	154,4	9,1	1,1	13,2	141,2	35,98	2,2
8,5	19,2	163,2	9,4	0,9	10,8	152,4	37,14	2,3
9	19	171	10,1	1,1	13,2	157,8	36,86	2,4
9,5	18,9	179,55	10,4	0,9	10,8	168,75	37,84	2,5
10	18,8	188	11,1	1,1	13,2	174,8	37,69	2,6
11	18,5	203,5	12,1	1,1	13,2	190,3	39,51	2,7
12	18,3	219,6	13,1	1,1	13,2	206,4	38,57	3
13	18,1	235,3	14,1	1,1	13,2	222,1	40,16	3,1
14	17,8	249,2	15,1	1,1	13,2	236	40,09	3,3
15	17,6	264	16,2	1,2	14,4	249,6	39,98	3,5
16	17,4	278,4	17,2	1,2	14,4	264	40,00	3,7
17	17,1	290,7	18,2	1,2	14,4	276,3	39,71	3,9

I_ST – current set on the load, controlling the cell's operation [A]

U_FC – measured voltage of the hydrogen cell [V]

P_FC – gross power generated by the hydrogen cell [W]

I_FC – measured current of the hydrogen cell [A]

I_PW - measured current for the cell's own needs [A]

P_PW – power for the cell's own needs [W]

P_NET – net power generated by the hydrogen cell [W]

EFF – calculated actual efficiency of the cell

Flow – measured flow of hydrogen in the system through the flow meter

ANALYSIS OF THE EFFICIENCY OF THE HYDROGEN FUELL CELL

In the first stage of the analysis, manufacturer data regarding the electrical energy content in 1 kg of hydrogen are utilized. Based on this, the amount of energy is

https://doi.org/10.5593/sgem2024/4.1/s17.04

converted into kilowatt-hours (kWh), which allows for a better understanding of the energy potential of the supplied fuel.

The energy content in 1 kg of hydrogen is $120{,}1\ MJ\ (LHV) \approx 33{,}3\ kWh$ [3]. The application of the formula for the molar volume of hydrogen allows the identification of the correlation between the fuel potential and the amount of energy generated:

$$V = n \cdot \Phi \tag{5}$$

$$\left(\frac{1000\ g}{2\ g/mol}\right) \cdot 22{,}4\ \frac{L}{mol} = 11200\ L$$

$$11200\ L - 33300\ Wh$$

$$1L/\min - x\ W$$

$$x = \frac{1\ L/min \cdot 33300\ W \cdot 60\ min}{11200\ L} = 178{,}393\ W$$

1 L/min enables the attainment of $178{,}393\ W$ of electrical power [1].

Taking into account the point P_NET = 174.8 W (current set on the load I_ST) from table 2, at which the flow meter indicated a consumption of 2.6 L/min for this power draw, it was calculated that such an amount of hydrogen is capable of generating:

$$P_c = 2{,}6 \cdot 178{,}393 = 463{,}82\ W$$

Calculation of efficiency:

$$\eta = \frac{P_{net}}{P_c} \cdot 100\% \tag{6}$$

$$\eta = \frac{174{,}8}{463{,}82} \cdot 100\%$$

$$\eta = 37{,}69\ \%$$

The efficiency of the cell at the selected point was η = 37.69%.

APPLICATION OF QUADRATIC APPROXIMATION

In order to compare the calculated efficiencies of the tested cell with the manufacturer's values, more data are needed. Based on the measurements from the flow meter, the manufacturer provided ten operating points. The flow meter in the car measures to tenths, while the Horizon company used a different device with accuracy to hundredths.

Table 3. Values of generated power depending on the flow rate [1].

Generated power [W]	0	35,34	78,79	98,03	120,2	149,94	196,27	295,72	397,56	497,41
Flow [ln/min]	0,108	0,466	0,893	1,108	1,306	1,666	2,218	3,262	4,51	5,69

Quadratic approximation enabled us to estimate results for missing points, enhancing our understanding of how our measurements align with the manufacturer's data. Comparing forecasted values with actual measurements was essential for accurately assessing and comparing cell efficiency under different operating conditions.The general formula for quadratic polynomial approximation is:

$$f(x) = ax^2 + bx + c \tag{7}$$

Where the values of a, b, and c are the coefficients of the quadratic polynomial.

Using the MATLAB program, quadratic approximation was performed with the polyfit() function, considering the data provided by the manufacturer listed in Table 3. The polyval() function was used to calculate the polynomial values for the set of points. Applying the approximation, the coefficient of determination was calculated, with a value of $R^2 \in [0;1] = 0{,}9998$.

RESULTS

The results of the hydrogen fuel cell efficiency analysis are illustrated in Figure 8, where the efficiency curves of the tested cell obtained during the research over the years are compared with the manufacturer's efficiency curve.

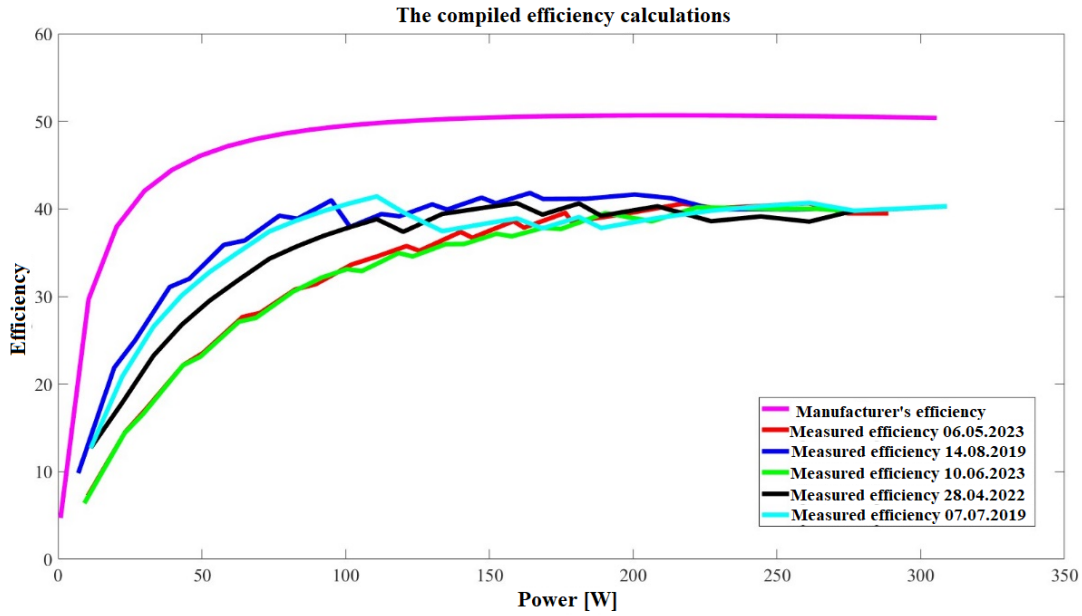


Fig. 4. Comparison of compiled efficiencies of the hydrogen fuel cell.

https://doi.org/10.5593/sgem2024/4.1/s17.04

CONCLUSION

The graph illustrates the variation in cell efficiency relative to the generated power. A notable disparity exists between the results obtained by the MechaniCAD Scientific Group's research and the manufacturer's data. Clear discrepancies in efficiency were evident in the 0 to 200 W range, suggesting fluctuations in efficiency over time. Between 100 to 250 W, fluctuations were observed in the calculated data, eventually stabilizing at the nominal operating point of 300 W. Efficiency demonstrates an upward trend with increasing power, peaking between 38-41%. At the nominal operating point, differences in efficiency are minimal. These findings deviate from the expected consistency in cell efficiency as claimed by the manufacturer. Other investigators may not have reported similar findings, possibly due to variations in testing conditions or reliance on manufacturer-provided data. These unexpected discrepancies could stem from factors such as changes in cell performance over time or differences in testing methodologies.

REFERENCES

[1] Horizon, H-500 XP Fuel Cell Stack, https://www.horizoneducational.com/h-500-xp-fuel-cell-stack/p1405

[2] Joanna Banaś-Gac, Materiały dydaktyczne z przedmiotu Elektrochemia Ciała Stałego, https://home.agh.edu.pl/~jbanas/2.pdf

[3] Ludwig-Bölkow-Systemtechnik, Wasserstoff Daten, http://www.h2data.de/

[4] Own study, SKNK MechaniCAD.

[5] Shell, About Shell Eco-marathon, https://www.shellecomarathon.com/about.html

APPLICATIONS OF HYDROGEN ENERGY IN THE FIELD OF TRANSPORT

Eng. Sorin Echim[1]
Assoc. Prof. Dr. Eng. Sanda Budea[2]
[1] National Research & Development Institute for Gas Turbines-COMOTI Bucharest, **Romania**
[2] National University of Science and Technology Politehnica Bucharest, **Romania**

ABSTRACT

In the REPowerEU strategy, the European Commission proposes accelerating renewable hydrogen production by 2030 to produce more affordable, safer, and sustainable energy. Hydrogen energy has significant potential in the future of transportation. Its many benefits include reducing pollution, diversifying energy sources, having higher energy density than batteries, and being used for long-distance or high-tonnage transport.

The present article proposes an analysis of the use of hydrogen energy in transport between potential and perspectives. The benefits are highlighted, and the technologies for obtaining H2 as an energy source are presented. Depending on the source and extraction method, four methods and technologies for securing hydrogen and four main types of H2 (green, gray, blue, and turquoise) exist. Although green H2 is the only type obtained with zero polluting gas emissions, the most widespread is gray H2 (from natural gas or waste coal) - 96% today.

The main applications of hydrogen in transport are presented:

1. Road-Fuel Cell Vehicles (FCEVs) that offer zero emissions and range similar to vehicles with conventional engines and short recharging time. 65% of buses must be zero-emission by 2025 and 30% of trucks by 2030. The Mercedes-Benz city bus runs entirely on energy from two sources - state-of-the-art electric batteries and hydrogen-based fuel cells, which protect the energy supply on the road - without intermediate charging. In cars, Toyota's Fuel Cell System is one of the most advanced technologies in the field.

2. Rail—Hydrogen use in rail vehicles offers a clean alternative to diesel or electric locomotives, significantly reducing gas emissions. Alstom's Coradia iLint, manufactured in 2016, is the world's first passenger train powered by fuel cells and H2.

3. Maritime transport—Hydrogen fuel cells can propel ships or power other energy systems. The HySeas III project demonstrates that fuel cells can be successfully integrated with a marine hybrid electric propulsion system (electric propulsion, controls, batteries, etc.) and associated hydrogen storage facilities. Hydrogen ferries—Norwegian Ship Design has designed RoPax with this in mind.

4. Air transport must operate with clean energy. ZeroAvia's 19-seat twin-engine Dornier 228 aircraft completed a test flight of around 10 minutes in the UK.

This article proposes an analysis of hydrogen technologies and their applications in transport, following the potential, challenges, and immediate prospects of implementation, as well as specific economic and environmental aspects.

Keywords: hydrogen energy, production technologies, use in transport.

https://doi.org/10.5593/sgem2024/4.1/s17.05

INTRODUCTION

Hydrogen accounts for around 2% of the EU's energy mix, of which 95% is produced by burning fossil fuels, which releases 70-100 million tonnes of CO2 annually. According to research, renewable energies could provide a substantial part of the European energy mix until 2050. In this mix, hydrogen could represent up to 20%, respectively between 20-50% of energy needs in transport and between 5-20% of needed in industry [1].

To achieve the objectives of the REPowerEU strategy to accelerate the production of renewable hydrogen until 2030, the European Commission proposes the production of energy under more accessible, safer, and more sustainable conditions. Part of this plan represents the acceleration of renewable hydrogen production until 2030, raising the level of hydrogen to 20 megatons per year from 10 megatons per year as proposed in the 2020 Hydrogen Strategy. In 2021, the EU had 136 hydrogen refueling points, and MEPs are calling for such stations to be created every 100 km along major EU roads by 2028 [1].

The most significant demand potential in the future is as an existing raw material in the industry, where the US will increase its potential, while Europe will decrease. The most significant difference between the potential of the years 2030 - 2050 is transport, where demand will grow exponentially in both the US and Europe [2,3]. Thus, in the scenario of the announced commitments, hydrogen is mainly used in sectors such as industry and transport, with the effect of increasing the penetration of renewable energy becoming more pronounced, as it is designed for net zero carbon emissions.

It should be noted that the cost of hydrogen fuel, both in terms of effective price and environmental impact, is independent of the hydrogen fuel cell technology used, significantly impacting the potential applications and competitiveness of hydrogen propulsion [4].

Developing research on technologies for obtaining hydrogen, transport, storage, and use in transport applications faces several technical, economic, and environmental challenges. Solving these challenges will strengthen the prospects for implementation.

MATERIALS AND METHODS

Hydrogen production technologies

In the analysis of hydrogen production, we summarize four methods and technologies for obtaining hydrogen, which provide green, gray, blue, and turquoise H2 depending on the source and extraction method. Several technologies are used for hydrogen production, including thermochemical, electrochemical, biological, and photocatalytic.

Thermochemical hydrogen production technologies involve high-temperature reactions with feedstocks to produce hydrogen.

These methods are widely used for large-scale hydrogen production. Key thermochemical processes include steam methane reforming (SMR), partial oxidation (POX), auto thermal reforming (ATR), and biomass gasification. SMR is the most common method of large-scale hydrogen production. It involves the reaction of natural gas (methane) with steam at high temperatures (about 700–1000 °C) in the presence of a catalyst, usually based on nickel [5]. Thermochemical processes are among the various methods used to produce hydrogen. These processes offer several industrial applications and advantages. Thermochemical processes can produce hydrogen for power generation in fuel cells or

direct combustion in engines. Hydrogen produced by thermochemical processes is used as a raw material in various chemical processes. Thermochemical processes have high conversion efficiencies and can produce large amounts of hydrogen [6].

Electrochemical hydrogen production technologies involve using electricity to drive reactions that produce hydrogen. These methods offer a clean and sustainable approach to hydrogen production, with the potential for large-scale implementation if powered by renewable energy sources. Water electrolysis is the most common method among the electrochemical technologies for hydrogen production [7]. It involves passing an electric current through water to break it into hydrogen and oxygen. The process occurs in an electrolyzer, which consists of two electrodes (anode and cathode) separated by an electrolyte. An electric current is applied to the anode and cathode, which are immersed in the electrolyte. At the anode, water molecules are oxidized, producing oxygen gas and hydroxide ions (OH-) in alkaline electrolyte, protons (H+) in proton exchange membrane (PEM) electrolysis, or oxygen ions (O2–) in oxide electrolysis solid (SOE). The ions produced at the anode migrate through the electrolyte to the cathode. The ions are reduced at the cathode, forming hydrogen gas [8]. The hydrogen and oxygen gases produced are separated, collected, and compressed or liquefied for storage and transport.

Biological hydrogen production technologies use microorganisms or their enzymes to produce hydrogen through biological processes. These processes are generally more sustainable and environmentally friendly than conventional thermochemical and electrochemical methods. Standard biological technologies for hydrogen production include fermentation in the absence of light and fermentation in the presence of light (photofermentation).

Both fermentation in the absence of light and fermentation in the presence of light promise technologies for producing biological hydrogen. Some of the latest biological technologies for hydrogen production have been researched and developed.

Biological processes for hydrogen production involve using living organisms to generate hydrogen through metabolic processes. Hydrogen produced using biological processes can be used in the agricultural sector for energy generation or as a raw material for producing biofertilizers and biofuels [9].

Photocatalytic hydrogen production technologies involve using photocatalysts (light-absorbing materials) to facilitate the dissociation of water into hydrogen and oxygen upon exposure to sunlight. The most common photocatalytic technology for hydrogen production is water splitting using semiconductor photocatalysts [10]. Hydrogen produced by photocatalytic processes can store solar energy for later use, providing a means for grid stability and energy management. However, the current efficiency of photocatalytic hydrogen production is relatively low compared to other hydrogen production technologies such as SMR and electrolysis [11].

Applications of hydrogen energy in transport

Hydrogen energy has various applications, with multiple direct and indirect uses, for decarbonizing all sectors, including transport. The potential and prospects of using hydrogen energy in this field are being further analyzed.

1. *Road transport*—Using hydrogen in fuel cell vehicles (FCEVs) enables efficient and clean electricity production, using hydrogen as fuel and generating water as the only emission.

https://doi.org/10.5593/sgem2024/4.1/s17.05

Typical fuel cells are proton exchange membrane fuel cells (PEMFCs), solid oxide fuel cells (SOFCs), phosphoric acid fuel cells (PAFCs), and alkaline fuel cells (AFCs) - depending on the electrolyte. Of these, PEMFC dominates the choice of automotive fuel cells; PEMFCs reach regular operation quickly, have stable working pressure due to a relatively simple operation mechanism, and can use electrolytes without involving complex chemical changes, but high cost and short lifetime are vital issues to be solved to ensure industrialization at scale wide range of fuel cell cars [12].

Japan was one of the first countries in the world to launch a national hydrogen strategy in 2017. Its goals were to build an H2 supply network to produce 300,000 t H2 and expand H2 mobility by 2030 [13].

A relevant example of a fuel cell application is the Toyota Fuel Cell System concept, one of the most advanced technologies in the field and is used in the Mirai model. Decades of research and development of hybrid propulsion technology have made Toyota the first in the world to achieve a system with a power density of 3.1 kW/l, which can be used not only to power vehicles but also to buses, taxis, forklifts, or even for powering homes. A Mirai vehicle can supply an average home for about a week in an emergency [14].

Another example is fuel cell buses; in this case, the contribution to reducing air pollution and noise in the urban environment is significant. The Mercedes-Benz eCitaro fuel cell city bus is designed for a pressure of 350 bar. It runs on energy from two sources: state-of-the-art electric batteries and hydrogen-based fuel cells, which ensure the continuity of the energy supply on the road without the need for intermediate charging. The modular system of the eCitaro fuel cell allows different combinations of the battery system and hydrogen tanks, thus ensuring the correct configuration for any transport requirement: solo bus - available with five hydrogen tanks with a total H2 capacity of 25 kg + 3 accumulators of 294 kWh, or the articulated bus - equipped with 6-7 hydrogen tanks with a total capacity of 30 or 35 kilograms and 3-4 batteries with a maximum energy content of 392 kWh [15].

2. *Rail transport* - using hydrogen in rail vehicles offers a clean alternative to diesel or electric locomotives, significantly reducing gas emissions.

The Korea Railway Research Institute announced in April 2021 (and the research is expected to continue until 2025) that for a liquid hydrogen-powered train running at 150 km/h, the estimated range is 1.6 times higher than that of gaseous hydrogen-fueled trains at 700 bar. The time required to refill with liquid hydrogen is expected to be 20% less than with gaseous hydrogen fueling.

Germany was the first country in the world to use hydrogen-powered trains (14 trains in 2022) commercially. In 2016, the Coradia iLint, manufactured by the French company Alstom, became the first passenger train powered by fuel cells and H2. The train produces no emissions, only steam, and is quiet [16].

3. *Maritime transport* - hydrogen fuel cells can propel ships or power other energy systems on board.

Fuel cell-powered ships are becoming a promising, environmentally friendly technology in the maritime industry, with more and more theoretical studies and industrial applications exploring their availability and efficiency. However, for these technologies to become commercially viable and widely adopted in the maritime sector, comprehensive and well-defined regulations must be established internationally [17].

A research project supported by the EU through the Horizon 2020 research program is Hyseas III, which aims to demonstrate that fuel cells can be successfully integrated with a marine hybrid electric propulsion system (electric propulsion, control devices, batteries, etc.), together with the associated hydrogen storage facilities. In some cases, the fuel cells used in HySeas III have reached over 30,000 hours of operation [18]. Research in the field has resulted in the development of two of the world's largest hydrogen-powered ferries - RoPax, designed by Norwegian Ship Design, each vessel with a length of approximately 117 meters, with a transport capacity of 120 cars and 599 passengers, which will operate entirely on hydrogen, requiring daily 5 - 6 t of H2 [19].

Other marine projects where fuel cells are used as part of the hybrid power system for ship propulsion are summarized in Table 1.

Table 1. Examples of fuel cell designs for marine propulsion [20]

Project	FC Type	Type of Vessel	FC Power Rating	R&D Partners	Fuel
FellowSHIP	MCFC	Offshore supply vessel	320 kW	DNV-GL and Wartsila	LNG
FCSHIP	MCFC SOFC PEMFC	Passenger ferry	Up to 1 MW	DNV-GL	Hydrogen for PEMs Hydrocarbons for MCFCs and SOFCs
ZEMSHIP	PEMFC	Passenger ferry	96 kW	Proton Motor	Hydrogen
Nemo H2	PEMFC	Passenger ferry	60 kW	Alewijnse	Hydrogen
MARANDA	PEMFC	Research vessel	Two 82.5 kW (165 kW)	ABB and VTT	Hydrogen
Raicho Project for Next-Generation Water Transportation	PEMFC	Research vessel	30 kW	Tokyo University of Marine Science and Technology and Toshiba	Hydrogen
Hybrid Power Lab at NTNU	PEMFC	Laboratory scale demo	Two 30 kW (60 kW)	ABB, SINTEF Ocean, NTNU	Hydrogen

4. *Air transport*: The development of hydrogen aircraft aims to reduce carbon emissions and provide a sustainable alternative to internal combustion aircraft.

Currently, hydrogen combustion propulsion and fuel cells are the two main options for hydrogen-powered aircraft propulsion systems, the latter being the way to get close to "zero emissions." Figure 1 illustrates how the fuel cell propulsion system works, and a battery can be added to the system to provide a backup or extra power [21].

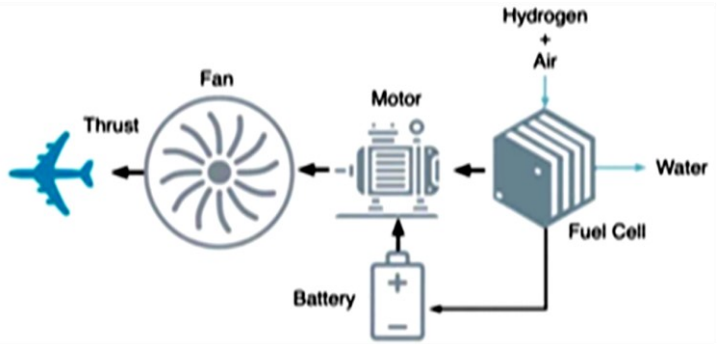


Figure 1. Fuel cell propulsion system [21]

ZeroAvia's twin-engine Dornier 228 - H2 fuel cell aircraft is a step forward in aviation technology. It has completed a test flight of around 10 minutes in the UK. This is part of

https://doi.org/10.5593/sgem2024/4.1/s17.05

the race to decarbonize the aviation industry, which accounts for around 2.5% of global carbon emissions [22].

RESULTS

Table 2 comprehensively compares the four leading hydrogen production technologies, outlining their advantages, disadvantages, state of development, and prospects.

Table 2. Summary and comparison of various hydrogen production technologies [23].

Technology	Advantages	Disadvantages	Development stage	Future outlook
Thermochemical production	Well-established Scalable Efficient	GHG emissions Non-renewable resources	Mature	Integration of CCS Transition to sustainable feedstocks
Electrochemical production	Clean Renewable Adjustable output	Efficiency Cost-effectiveness	Advanced	Improved efficiency Cost reduction Large-scale adoption
Biological production	Environmentally friendly Potential use of waste	Low yield Scalability challenges	Developmental	Biotechnology breakthroughs Process optimization
Photocatalytic production	Renewable Clean Sunlight-driven	Early development Material limitations	Early stage	Advances in materials Improved reaction efficiency

DISCUSSION

At fuel stations, H2 can be stored in gaseous form in tanks at 45 bar, 200 bar, or most often in liquid hydrogen storage tanks at -253 ˚C. The hydrogen must then be compressed to the required pressure of 350 or 700 bars, depending on the vehicle's fuel cell technology, which can increase fuel costs and time. In the challenge to reduce costs and develop storage/supply technologies for equipment in hydrogen refueling stations, companies in the field have notable results (e.g. Linde offers two solid and innovative refueling technologies: liquid hydrogen cryogenic pump and compressor ionic for compressed hydrogen, both technologies managing to keep fueling times to 3-4 minutes).

CONCLUSION

As environmental concerns increase due to greenhouse gas emissions, hydrogen is proving to be a viable fuel for multiple fuel cell applications in transportation.

The costs of hydrogen production are still significant, especially for the production of green hydrogen. Still, they can be lowered with appropriate investments in research, technological development, and technologies related to hydrogen production, transport, storage, and use. In this sense, green hydrogen, produced from renewable energy, should have priority over the other types of hydrogen, especially in the context of decreased production costs.

Green hydrogen is produced by electrolysis of water using renewable electricity. As the production and share of green hydrogen increase globally, it is expected to be cost-competitive with gray hydrogen produced from fossil fuels.

Fuel cell technologies are constantly developing, and the long time spent researching and developing hydrogen technology seems to be paying off. Hydrogen technology can successfully compete with competing technologies for most applications, although costs

are still higher. As the volume of products/technology increases, production costs will become economically profitable.

Despite fuel cells' significant potential, there is a regulatory gap, particularly in shipping. Fuel cells are entering the scope of commercial use in marine applications, so regulations in the field and technical standards regarding fuel cells must exist, be developed, and be constantly updated.

REFERENCES

[1] Energy from hydrogen: what are the benefits for EU? [(accessed on 15 April 2024, 17.00)].https://www.europarl.europa.eu/pdfs/news/expert/2021/5/story/20210512STO04004/20210512STO04004_ro.pdf

[2] IEA G20 The Future of Hydrogen. [(accessed on 03 May 2024, 20.00)], pp.203. Available online: https://www.iea.org/reports/the-future-of-hydrogen

[3] Eriksen R., Hydrogen Forecast to 2050. [(accessed on 03 May 2024,21.00)]. Available online:https://aben.com.br/wpcontent/uploads/2022/06/DNV_Hydrogen_Report_2022_Highres_single1.pdf

[4] Gis W., Menes M., Pielecha J., et al., Implementation of vehicles equipped with fuel cells and hydrogen refueling infrastructure in Europe. Combustion Engines. 2015, 162(3), pp.782-787.

[5] Boretti A., Banik B.K., Advances in Hydrogen Production from Natural Gas Reforming. Adv Energy Sustain Res 2021; 2(11):2100097. https://doi.org/10.1002/aesr.202100097.

[6] Inayat A., Tariq R., Khan Z., Ghenai C., Kamil M., Jamil F., et al., A comprehensive review on advanced thermochemical processes for bio-hydrogen production via microwave and plasma technologies. Biomass Convers Biorefin 2020. https://doi.org/10.1007/s13399-020-01175-1.

[7] Anwar S., Khan F., Zhang Y., Djire A., Recent development in electrocatalysts for hydrogen production through water electrolysis. Int J Hydrogen Energy 2021; 46 (63):32284, pp.317. https://doi.org/10.1016/j.ijhydene.2021.06.191.

[8] Al-Shara N.K., Sher F., Iqbal S.Z., Curnick O., Chen G.Z., Design and optimization of electrochemical cell potential for hydrogen gas production. J Energy Chem 2021; 52:421, pp.7. https://doi.org/10.1016/j.jechem.2020.04.026.

[9] Sharma P., Gaur V.K., Kim S-H, Pandey A., Microbial strategies for bio-transforming food waste into resources. Bioresour Technol 2020; pp.299:122580. https://doi.org/10.1016/j.biortech.2019.122580.

[10] Ishaq T., Yousaf M., Bhatti I.A., Batool A., Asghar M.A., Mohsin M., et al., A perspective on possible amendments in semiconductors for enhanced photocatalytic hydrogen generation by water splitting. Int J Hydrogen Energy 2021; 46(79): 39036–57. https://doi.org/10.1016/j.ijhydene.2021.09.165.

[11] Oh V.B.Y, Ng S.F., Ong W.J,. Is photocatalytic hydrogen production sustainable? – Assessing the potential environmental enhancement of photocatalytic technology against steam methane reforming and electrocatalysis. J Clean Prod 2022; 379: 134673. https://doi.org/10.1016/j.jclepro.2022.134673.

https://doi.org/10.5593/sgem2024/4.1/s17.05

[12] Hu D.H., Wang Y.T., Li J.W., Yang Q., Wang J., Investigation of optimal operating temperature for the PEMFC and its tracking control for energy saving in vehicle applications. Energy Convers. Manag. 2021, pp. 249, 114842. http://doi.org/10.1016/j.energy.2020.119744

[13] https://www.linde-gas.ro/ro/hydrogen/mobilizing-public-buses-and-trains-with-h2.html, [(accessed on 03 May 2024, 16.00)];

[14] https://www.toyota.ro/discover-toyota/environment/cleaner-mobility/fuel-cell, [(accessed on 03 May 2024, 22.00)];

[15] https://www.mercedes-benz-bus.com/ro_RO/models/ecitaro-fuel-cell.html, [(accessed on 04 May 2024, 11.00)];

[16] Wang J., Gao Y., Sun S., Lei Shi H., Safety Technologies and Challenges of Hydrogen-Powered Rail Transport. (Eds.): WHTC 2023, SPPHY 393, pp. 100–107, 2024. https://doi.org/10.1007/978-981-99-8631-6_11.

[17] Inal O. B., Decarbonization of shipping: Hydrogen and fuel cells legislation in the maritime industry, Brodogradnja Volume 75, Number 2 (2024) 75205; pp.11 https://www.researchgate.net/publication/378394033;

[18] https://www.hyseas3.eu/the-project/, [(accessed on 04 May 2024, 12.00)];

[19] https://www.norwegianshipdesign.no/archive/p1906contractsigning-bbj3r, [(accessed on 04 May 2024, 13.00)];

[20] Shakeri N., Zadeh M., Nielsen J.B., Hydrogen Fuel Cells for Ship Electric Propulsion IEEE Electrification Magazine / JUNE 2020 10.1109/MELE.2020.2985484, pp.32;

[21] Dawei Xu, Technologies and challenges of hydrogen-powered aviation, Beijing Institute of Technology, Zhuhai, School of Aviation, Zhuhai, China, 519000 CONF-MCEE 2023, IOP Publishing;

[22] Pop A., A small hydrogen-powered electric plane could be the key to zero-carbon flight, Un mic avion cu motor electric cu hidrogen ar putea fi cheia zborului cu zero emisii de carbon, Newsweek Romania/International, updated 21.01.2023, 17.48 https://newsweek.ro/international/un-mic-avion-cu-motor-electric-cu-hidrogen-ar-putea-reprezenta-cheia-zborului-cu-zero-carbon-emisii;

[23] Lei Zhang, Cunqi Jia, Fuqiao Bai, Wensen Wang, et al., A comprehensive review of the promising clean energy carrier: Hydrogen production, transportation, storage, and utilization (HPTSU) technologies, Fuel 355 (2024) 129455 pp.7, https://doi.org/10.1016/j.fuel.2023.129455.

CAN BIOGAS CONTRIBUTE TO PURE HYDROGEN COMBUSTION?

Assist. Prof. Dr. Isabel Amez[1,2]

Assist. Prof. Dr. Blanca Castells[1,2]

Assoc. Prof. Dr David Bolonio[1,2]

Assist. Prof. David León[1,2]

Prof. Marcelo F. Ortega León[1,2]

[1] Department of Energy and Fuels, E.T.S. Ingenieros de Minas y Energía, Universidad Politécnica de Madrid, Ríos Rosas 21, 28003 Madrid, **Spain**
[2] TECMINERGY Technical University of Madrid, Spain, C/Eric Kandel, 1 (TECNOGETAFE), Parque Científico y Tecnológico de la UPM, 28906 Getafe, **Spain**

ABSTRACT

Hydrogen combustion is presented as a potential solution to cover the heat demand with renewable energies. However, current technologies do not allow the combustion of pure hydrogen and it must often be mixed with fossil fuels. Carbon dioxide (CO_2) has proven to be useful for stabilizing hydrogen combustion, as has methane (CH_4). Therefore, this research proposes the use of biogas as a stabilizer of pure hydrogen combustion. For this purpose, experimental tests were carried out, burning a lean biogas (BG 50% CH_4) and a medium biogas (BG 60% CH_4). Each biogas was burned in a commercial biogas burner with different percentages of hydrogen. Afterwards, the combustion temperature and the difference in temperatures obtained before and after combustion were analyzed. These parameters allow to study the dual effect between H_2 and CO_2. The results show that the balance between the percentage of CO_2 and H_2 is vital for efficient combustion. Therefore, this study significantly contributes to the advancement of sustainable combustion systems.

Keywords: Hydrogen, biogas, combustion, flame analysis, emissions

INTRODUCTION

Fossil fuels, such as oil, natural gas and coal, are the main sources of thermal energy in industry [1]. However, their combustion generates a significant amount of greenhouse gas (GHG) emissions, such as carbon dioxide (CO_2), methane (CH_4) and nitrogen oxide (NOx), which contribute to climate change and air quality degradation. In addition, the exploitation and transport of these fuels present risks of spills and accidents that can cause serious environmental damage [2].

In this context, hydrogen emerges as a promising energy carrier to meet the thermal energy demand of industry [3]. Hydrogen is the most abundant element in the universe and its combustion produces mainly water vapour. Given the use of air as an oxidant, NOx is also generated to a lesser extent than fossil fuels, thus eliminating CO_2 and CO emissions, particulates, volatile organic compounds (VOC), etc. In addition, hydrogen can be produced from a variety of sources, including renewable sources such as electrolysis of water using solar or wind energy, making it a sustainable option in the long term. Recent advances in hydrogen combustion in industrial furnaces and boilers

https://doi.org/10.5593/sgem2024/4.1/s17.06

have shown significant progress in terms of efficiency and emission reductions [4], [5]. For example, hydrogen-specific burners have been developed that optimise the combustion process, achieving more complete and efficient combustion. In addition, research into high temperature and corrosion resistant materials has led to the development of more durable and safer equipment for hydrogen combustion [6].

However, the combustion of pure hydrogen presents several challenges [7]. One of the main problems is the high flame temperature, which can cause damage to equipment materials and increase the risk of NOx formation, a pollutant harmful to human health and the environment. In addition, the low energy density of hydrogen compared to fossil fuels poses challenges in storage and transport [8]. To address these problems, one proposed solution is the addition of CO_2 to hydrogen during combustion [9]. This technique, known as co-combustion or blending, can help moderate flame temperature and reduce NOx formation, while improving combustion efficiency. The addition of CO_2 acts as a diluent, reducing the reactivity of hydrogen and better controlling the combustion process [10], [11].

The sources from which CO_2 can be obtained for these processes are diverse. CO_2 can be captured from existing industrial emissions, such as power plants and factories, through carbon capture and storage (CCS) technologies [12]. Another potential source is direct air capture, although this technique is still under development and expensive. In addition, CO_2 can be obtained from biological processes, such as fermentation in bioethanol production and wastewater treatment [13].

Biogas stands out as a viable and sustainable source of CO_2. Biogas, produced from anaerobic digestion of organic waste, contains approximately 50-70% methane and 30-50% CO_2. This CO_2 can be separated and used in co-firing with hydrogen. In addition, the use of biogas contributes to waste management and the reduction of methane emissions, another potent GHG [14].

Therefore, in this study, different biogas mixtures will be analysed, at 40 (BG60) and 50% (BG50) of CO_2, and hydrogen percentages will be added at 5, 10, 15, 15, 20 and 25%. Parameters of maximum combustion temperature and heat exchange to the cooling water will be analysed. The objective will be to analyse the dual effect of H_2 and CO_2 in combustion, to analyse the potential of using biogas as a H_2 combustion enhancer.

MATERIALS AND METHODS

Experimental set-up

The experimental configuration is designed for analyse the combustion properties and water heat. Biogas is emulated using a mixture of carbon dioxide (CO_2) and methane (CH_4). Mass flow controllers are employed to blend synthetic biogas with hydrogen (H_2). The concentration control system manages three slow-opening gas valves. The fuel mixture is delivered to the burner inlet at a pressure of 4 mbar. Atmospheric air is supplied to the gas burner by an integrated fan. The burner has a thermal capacity of 33 kW and the fuel consumption rate of approximately 3 Nm^3/h. The gas burner utilized is a Bentone BFG1 H3, designed in compliance with the European standard EN 676 [15].

In addition, the burner is connected to a water test bench with a capacity of 40 kW. The test bench has thermocouples for the combustion chamber inlet and outlet water and

regulates the water flow through the combustion chamber. Figure 1 shows the experimental set-up.

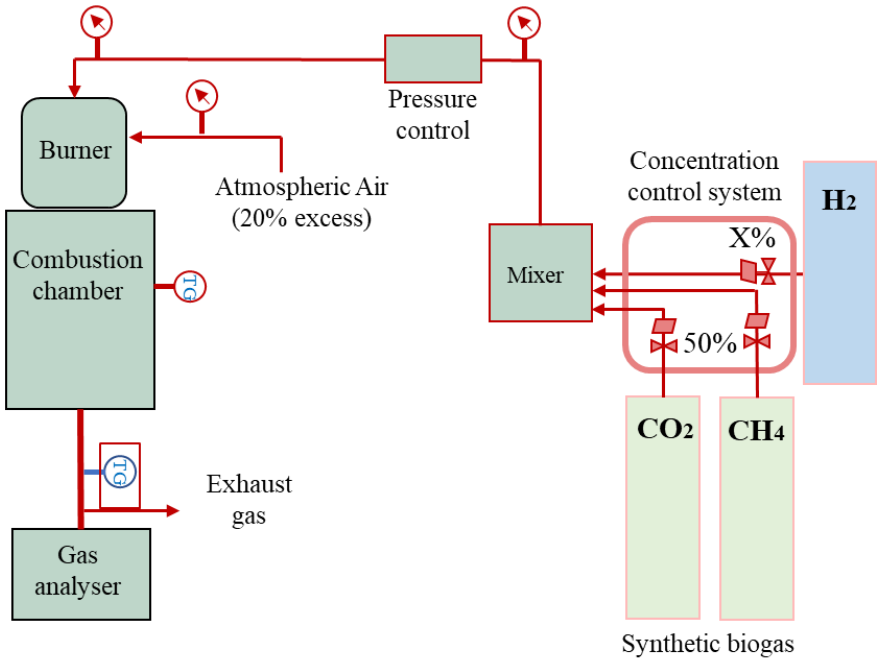


Fig. 1. Scheme of the experimental set-up for combustion.

Experimental methodology

The experimentation is carried out for a lean BG50 and BG40. Subsequently, hydrogen was added at 5 % intervals until 25% hydrogen in the mixture was reached. The blend is set in the mixture control system, taking into account certain considerations. Since different gases are used, a conversion factor must be applied. These factors will be 1.001 for hydrogen, 0.76 for methane and 0.74 for CO_2. As we have three gases, we must apply the equations 1, 2 and 3:

$$Q_{real} = Q \cdot F \qquad eq.\ (1)$$

$$Q_{real} = A \cdot Q \cdot F \qquad eq.(2)$$

$$Ci = Q_{real\ i} / (Q_{real\ i+1} + Q_{real\ i+2} + Q_{real\ i+3}) \qquad eq.(3)$$

Where:

- Q_{real}: Final actual flow rate that lets the mass flow for a certain valve opening.
- A: The percentage of opening of the mass flow valve.
- Q: Full scale, i.e., the design flow rate of the mass flow controller for a factor of 1.
- F: Gas conversion factor.
- Ci: Concentration of gas 1.
- $Q_{real\ i}$: Actual flow rate for a given opening of gas 1.
- $Q_{real\ i+2}$: Actual flow rate for a given opening of gas 1.
- $Q_{real\ i+3}$: Actual flow rate for a given opening of gas 1.

https://doi.org/10.5593/sgem2024/4.1/s17.06

Since the actual flow rates and openings of the three mass controllers are not known, tools such as Solver must be used to obtain the openings and set the desired mixture. Once the mixture has been calculated and set, the burner is started. The initial water temperature values are recorded and combustion begins.

RESULTS

Fuel properties

Figure 2 presents the Wobbe Index and Calorific Value calculations based on the theoretical method outlined in standard EN ISO 6976 [16]. These calculations are carried out to ensure that the mixture used has a calorific value greater than 6 MJ/m^3. Below this value, the burner cannot operate.

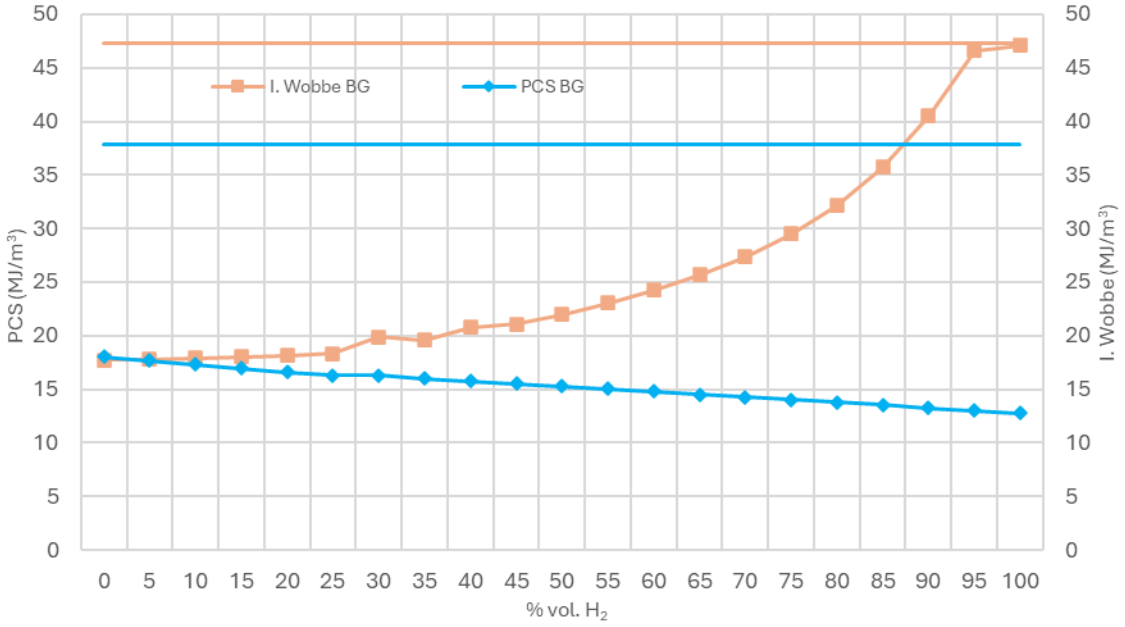


Fig. 2. Results of the analysis of the quality of the mixtures according to EN ISO 6976.

Afterwards, an analysis of the temperature rise of the cooling water was carried out. The initial values of the water before combustion and the peak obtained during the test were taken. Figure 3 shows a graph comparing the CO_2 concentration in the mixture and the H_2 concentration with the recorded water temperature increases.

On the other hand, the combustion temperature of the different mixtures was analysed. Figure 4 again compares the CO_2 concentration in the mixture and the H_2 concentration with the maximum combustion temperature recorded in the combustion.

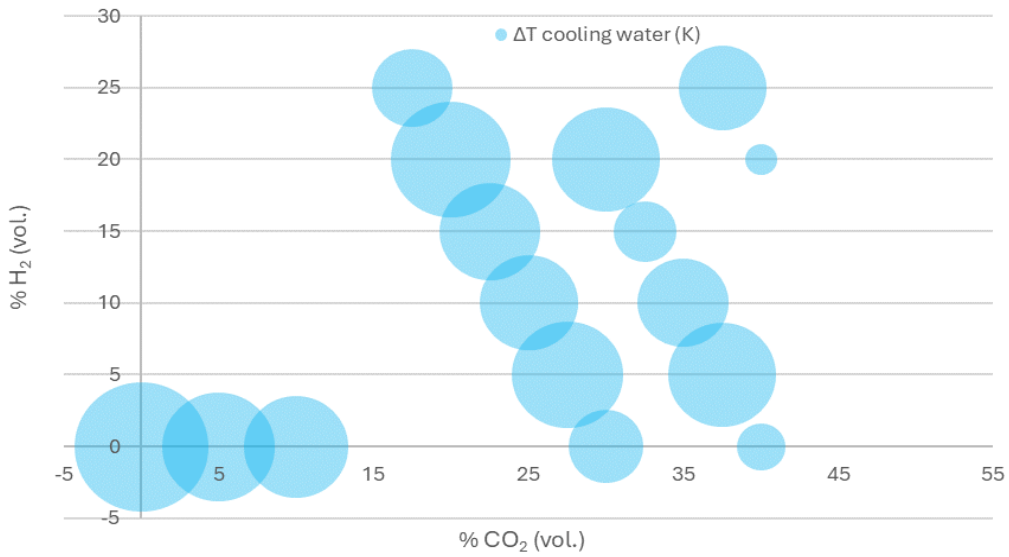


Fig. 3. Cooling temperature increase vs. CO_2 and H_2 concentration in the mixture.

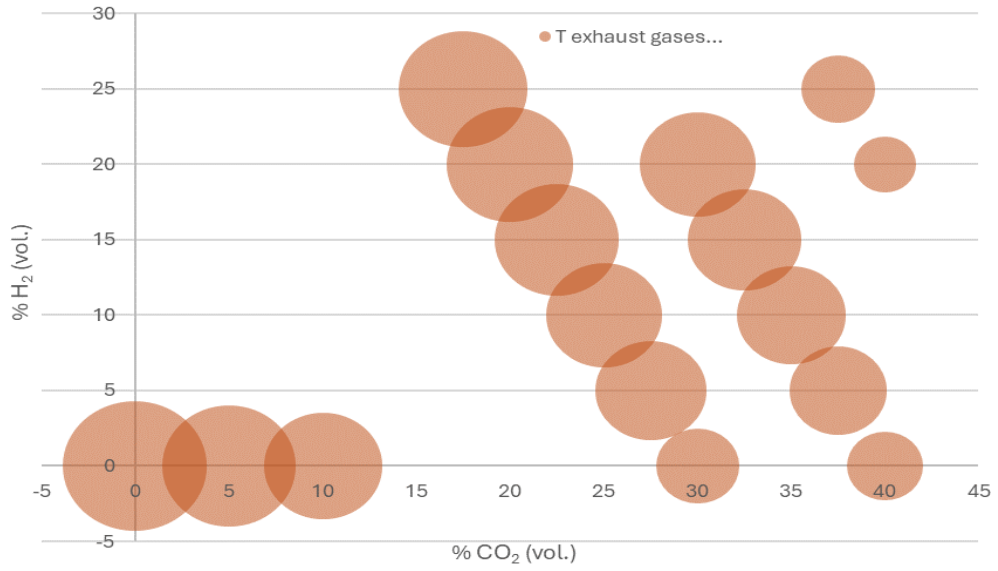


Fig. 4. Cooling temperature increase vs. CO_2 and H_2 concentration in the mixture.

DISCUSSION

The Wobbe Index is a key parameter for assessing the interchangeability of fuels. Generally, since current systems are designed for natural gas, it is an interesting benchmark when studying new fuels. The two straight lines in Figure 2 represent the Higher Calorific Value of natural gas (blue) and the Wobbe Index of Natural Gas (Orange). As can be seen, only pure hydrogen is able to reach the Wobbe index of natural gas, and contrary to what is observed in the results (Figures 3 and 4) the Upper Heating Value of the mixture decreases as the percentage of H_2 increases. This is due to the low energy density of H_2 per unit volume.

The dual effect of CO_2 and H_2 on combustion can be studied in figures 3 and 4. The size of the circles represents in each case the variable to be analysed. In Figure 3, the larger the size of the circle, the greater the temperature difference recorded, and therefore the

https://doi.org/10.5593/sgem2024/4.1/s17.06

greater the heat exchange in combustion. In Figure 4, the larger the size of the circle, the higher the maximum combustion temperature recorded. Both parameters are closely related, however, some differences are observed. The most optimal combustion would be expected to obtain the largest circle size, which in both cases coincides with the combustion of pure methane. But when we have H_2 and CO_2 in the mixture, the trend changes. It seems that an increase in combustion temperature is related to the increase of H_2 in the mixture, and that too much CO_2 is no longer beneficial. This trend is not so clearly observed with increasing cooling temperature. Figure 3 shows that it is best to maintain low H_2 values for high CO_2 values and vice versa. This can be explained by the oxygen demand of H_2 and CH_4 in the mixture, while CO_2, an inert gas, displaces the fuel volume.

CONCLUSION

Hydrogen combustion is proposed as a potential solution to meet industrial heat demand through renewable energies. Current technologies, however, do not support pure hydrogen combustion, necessitating its mixture with other fuels.

The results indicate that the balance between the percentages of CO_2 and H_2 is crucial for efficient combustion. An optimal ratio enhances combustion performance and efficiency. Moreover, using hydrogen as a fuel significantly reduces emissions compared to fossil fuels, eliminating CO_2 and reducing NOx emissions due to its combustion properties. This makes hydrogen a cleaner alternative for industrial heat production.

Adding CO_2 to hydrogen during combustion can mitigate these issues by lowering flame temperatures and NOx formation while improving combustion efficiency. CO_2 acts as a diluent, reducing hydrogen's reactivity and better controlling the combustion process. This study finds that enriching biogas with hydrogen at different levels (5-25%) can improve the combustion properties of the biogas. However, the optimal mixture must be carefully balanced to achieve the desired combustion performance.

ACKNOWLEDGEMENTS

This project has received funding from the Spanish Government, in the 2021 call “Proyectos de Transición Ecológica y Transición Digital” with the project number of: TED2021-132181B-I00.

REFERENCES

[1] H. A. Daggash *et al.*, “Closing the carbon cycle to maximise climate change mitigation: Power-to-methanol: vs. power-to-direct air capture,” *Sustain. Energy Fuels*, vol. 2, no. 6, pp. 1153–1169, 2018, doi: 10.1039/c8se00061a.

[2] M. Talibi, P. Hellier, and N. Ladommatos, “Combustion and exhaust emission characteristics, and in-cylinder gas composition, of hydrogen enriched biogas mixtures in a diesel engine,” *Energy*, vol. 124, pp. 397–412, 2017, doi: 10.1016/j.energy.2017.02.070.

[3] P. C. Slorach and L. Stamford, “Net zero in the heating sector: Technological options and environmental sustainability from now to 2050,” *Energy Convers.*

Manag., vol. 230, p. 113838, 2021, doi: 10.1016/j.enconman.2021.113838.

[4] M. A. M. Costa, N. C. B. Schiavon, M. P. Felizardo, A. J. D. Souza, and K. J. Dussán, "Emission analysis of sugarcane bagasse combustion in a burner pilot," *Sustain. Chem. Pharm.*, vol. 32, no. February, p. 101028, 2023, doi: 10.1016/j.scp.2023.101028.

[5] M. Sekar, T. A. Alahmadi, and S. Nithya, "Numerical simulation of industrial gas burners fueled with hydrogen-methane mixtures for enhanced combustion efficiency and reduced greenhouse gas emissions," *Fuel*, vol. 370, no. May, p. 131807, 2024, doi: 10.1016/j.fuel.2024.131807.

[6] E. E. Fordoei, K. Mazaheri, and A. Mohammadpour, "Effects of hydrogen addition to methane on the thermal and ignition delay characteristics of fuel-air, oxygen-enriched and oxy-fuel MILD combustion," *Int. J. Hydrogen Energy*, vol. 46, no. 68, pp. 34002–34017, 2021, doi: 10.1016/j.ijhydene.2021.07.065.

[7] M. El-Adawy, M. A. Nemitallah, and A. Abdelhafez, "Towards sustainable hydrogen and ammonia internal combustion engines: Challenges and opportunities," *Fuel*, vol. 364, no. January, p. 131090, 2024, doi: 10.1016/j.fuel.2024.131090.

[8] A. G. Olabi, T. Wilberforce, and M. A. Abdelkareem, "Fuel cell application in the automotive industry and future perspective," *Energy*, vol. 214, p. 118955, 2021, doi: 10.1016/j.energy.2020.118955.

[9] S. Carpenella *et al.*, "Large Eddy Simulation of Hydrogen/Air MILD combustion in a cyclonic burner," *Appl. Therm. Eng.*, vol. 244, no. November 2023, p. 122733, 2024, doi: 10.1016/j.applthermaleng.2024.122733.

[10] F. Yan, L. Xu, and Y. Wang, "Application of hydrogen enriched natural gas in spark ignition IC engines: from fundamental fuel properties to engine performances and emissions," *Renew. Sustain. Energy Rev.*, vol. 82, no. June 2017, pp. 1457–1488, 2018, doi: 10.1016/j.rser.2017.05.227.

[11] R. Bouguessa, L. Tarabet, K. Loubar, T. Belmrabet, and M. Tazerout, "Experimental investigation on biogas enrichment with hydrogen for improving the combustion in diesel engine operating under dual fuel mode," *Int. J. Hydrogen Energy*, vol. 45, no. 15, pp. 9052–9063, 2020, doi: 10.1016/j.ijhydene.2020.01.003.

[12] D. G. Faria, M. M. O. Carvalho, M. R. V. Neto, E. C. de Paula, M. Cardoso, and E. K. Vakkilainen, "Integrating oxy-fuel combustion and power-to-gas in the cement industry: A process modeling and simulation study," *Int. J. Greenh. Gas Control*, vol. 114, no. May 2021, 2022, doi: 10.1016/j.ijggc.2022.103602.

[13] C. Mao, Y. Feng, X. Wang, and G. Ren, "Review on research achievements of biogas from anaerobic digestion," *Renew. Sustain. Energy Rev.*, vol. 45, pp. 540–555, 2015, doi: 10.1016/j.rser.2015.02.032.

[14] N. Ketsub *et al.*, "A systematic evaluation of biomethane production from sugarcane trash pretreated by different methods," *Bioresour. Technol.*, vol. 319, 2021, doi: 10.1016/j.biortech.2020.124137.

[15] C. 131, *EN 676 Forced draught burners for gaseous fuels*, vol. 10, no. 1025.

https://doi.org/10.5593/sgem2024/4.1/s17.06

2020, pp. 2012–2013.

[16] E. C. for Standardization, *EN ISO 6976:2016 Natural gas - Calculation of calorific values, density, relative density and Wobbe indices from composition*. European Union, 2017.

CLIMATE CHANGE, WASTE MANAGEMENT, AND COAL ABANDONMENT: THREE PILONS OF SUSTAINABILITY

Sofia Fourkioti
Konstantinos Panitsidis
Konstantinos Spinthiropoulos
Marina Vezou
Department of Management Science and Technology, University of Western Macedonia, Kozani**, Greece**

ABSTRACT

The negative results of irrational human activity have been visible throughout the last decades in the environment. Air, water, and land pollution are significant variables of this equation and have a major share in climate change. To obtain control of the situation, Europe tried to take action by presenting new environmentally friendly plans, such as "The Green Deal Industrial Plan" or "Recovery Plan for Europe". One of the greatest aims of our century is the transition to a Circular Economy and the abandonment of previous years' practices. Also, digitalization is a significant parameter that is used to accelerate procedures, such as remote work, data exchange, automation, etc. The current survey deals with the case of Western Macedonia, Greece. The study case of Western Macedonia is quite important, as this region has been the major energy producer in Greece, and it is very interesting to examine the various social and economic changes that the circular economy and decarbonization will bring. The methodology that was followed for this survey was the Tollgate approach in combination with R programming for the statistical analysis. More specifically, the papers that were reviewed for this research were collected by digital libraries using the tollgate approach. This method uses specific characteristics that are valuable for the survey and then organizes the papers in specific categories. The final number of papers that were reviewed more closely was 50. Then, the collected data were analyzed using R programming. The results showed that the transition from a linear to a circular economy will have positive effects on many sectors and revealed a strong connection between the circular economy and climate, waste management, energy, and other sectors, such as the health sector. The review of these surveys contributes to understanding the situation in Western Macedonia, comparing it with other regions, and applying various measures that are suitable for this area. Consequently, all nations that wish for a greener future must create awareness regarding subjects such as environmental pollution, climate change, linear and circular economies, zero waste, decarbonization or abandonment of fossil fuels, transition to renewable energy sources, and digitalization.

Keywords: circular economy; climate change; pollution; digitalization; decarbonization

INTRODUCTION

Human activity has resulted in the extended pollution of the environment, and these practices, which have been followed for decades, are the most significant variables for climate change. Additionally, irrational activities have various indirect effects since they affect living organisms and generally life. Europe's efforts to take action led to the

https://doi.org/10.5593/sgem2024/4.1/s17.07

presentation of various recovery plans regarding energy transition, climate change, waste management, and green practices for materials' saving. As a result, the majority of European countries try to comply with the new policies and contribute to environmental recovery.

Greece focuses mainly on energy transition and waste management. The main source of energy production in Greece was based on coal exploitation, and the affected areas were Western Macedonia, Megalopolis (Arkadia), and Aliveri (Evoia). The research is dealing with Western Macedonia's case and presents the current situation of coal mines, the new RES investments, the climate change of the area due to pollution, and the effects on the health of residents. Surveys conducted in the region of Western Macedonia showed that this area is severely affected by pollutants and heavy metals due to the coal exploitation [1]. Although, the energy transition, that caused the shutdown of some coal mines, showed that the air quality of these areas has improved significantly [2] These results show that affected areas have a higher degree of contamination than areas that are far from lignite power plants. As a result, these areas will finally be relieved when air pollution reduces, due to the energy transition. Although these are very positive results for the environmental recovery, insecurity for the future of Western Macedonia has developed. The residents of this region are concerned that job insecurity and unemployment will occur by the closure of the mines [3].

Regarding waste management, it is known that Greece is below the European average in terms of recycling. The recycling rate is 21%, which means that a significant increase is crucial. The results of this study show that if the waste can be used as a resource for energy or materials, then a near-zero pollution future is possible. For this moment, this study is not applicable, but it can be used as an inspiration for humans to change their perception of waste management.

Waste management and recycling are very significant factors in the circular economy. For the moment, in Greece, waste management is concerned mostly with the sorting of waste and recycling. Additionally, to reduce the volume of waste, in some areas, there are waste-to-energy plants, but it is a practice that is controversial. Studies revealed that some indicators, such as air pollution, solid waste or the existence of industry in an urban area, can help in measuring the sustainability of this area [4].

Another important subject that is being discussed in this paper is the digital development. Digital Development is the key to the Circular Economy. The various digital tools, such as the Internet of Things (IoT), artificial intelligence (AI), digital platforms, data analytics or blockchain technology, can be very helpful to a sustainable future.

Digital technologies could be very helpful in designing a strategy for waste management of the abandoned coal mines of Western Macedonia, or data collection from dangerous zones using IoT. Additionally, digital tools, such as web platforms can create awareness and inform the residents regarding the situation and positively contribute to the energy transition.

MATERIALS AND METHODS

For this research both literature and empirical review took place. For the literature review, a great number of research papers were reviewed, and their conclusions were very useful for this research. Also, data from organizations based in Greece were excluded.

The tollgate approach was used to come up with the investigation's results [5]. The tollgate approach is an academic material organizing methodology that helps in article concentration, review, and evaluation of the examined material. The significance of this methodology refers to the selection of specific characteristics that are essential to an investigation. The concentrated data are being examined, and then they can be evaluated as useful or irrelevant to the research.

This approach is a great choice of reviewing material as it offers the following:

- Using keyword research, an author can understand the demand for exploration of a thematic field. This can be understood by the number of relevant articles that come up as a result from the research.
- Additionally, an author can categorize the selected articles by field.
- Using the tollgate methodology, an author can set various approval points for the articles that are reviewed. These approval points have been determined by the author, and they represent each article's purposes.

The source of the investigation were digital libraries. These libraries have a great selection of books, magazines, and any other material that could be a source of information and can be managed electronically. The selected libraries were : Scholar, Science Direct, ACM Digital Library, MDPI, IOP, IEEE Xplore, Wiley Online Library, IET Digital Library and Mendeley. The access to a digital library is very important for an author as it offers a richer and broader source of information, comparing to a physical library. Additionally, authors of the academic environment can have access to these digital libraries via their institutional accounts, giving them the opportunity to review multiple articles with no fees. The selection of the digital libraries was based on the fact that these libraries are universal, updated and they contain a rich amount of academic material.

Regarding the use of the keywords for this research, we created two categories of keywords, based on the number of words that were used for the research.

The first step of the research was gathering the papers that seemed to be suitable for the literature review. The research took place in various digital libraries, using the various relevant keywords. After that, a categorization of the papers followed to better organize the research material. The final number of papers that were used were 50.

- The first one was regarding a research based on the selected keywords, where 371 papers were found.
- The next step was the selection of information by title or abstract, where the number of papers were 200.
- Also, 76 papers were found to be related to the selection based on the full article.
- Additionally, these papers were examined by their conclusions, 55 papers appeared related to our investigation.

After the final selection, the objectives of the papers were referring to the decarbonization of Western Macedonia, the transition of conventional energy sources to renewable ones, climate change, the pollution from greenhouse gases, and the transition to the circular economy in the energy sector.

Except for the literature review, an empirical review was also conducted. For the empirical review, both quantitative and qualitative data were used.

https://doi.org/10.5593/sgem2024/4.1/s17.07

The quantitative data were extracted from organizations such as IPTO – Independent Power Transmission Operator (ADMIE in Greek), to create tables and graphs useful to this research. The qualitative data used in this paper were obtained from surveys.
For the statistical analysis of the content, R programming was used. This software is suitable for statistical computing and data visualization. In this research, R was used to organize the data, which were collected from the selected papers. The data analysis was conducted with Descriptive Statistics to compare the results. For easy and efficient comparison of the data, pie charts and histograms were created. Excel was also used for the development of the final form of the graphical content.

RESULTS

The objects that have been discussed in the body of this paper divide in two main categories. The first category is concerning Western Macedonia and generally Greece and the points of investigation were the following [6–9]:

- The energy production in Western Macedonia the previous years.
- The degree of pollution and PMs in Western Macedonia due to the lignite mines.
- The pollution in Greece due to conventional sources of energy.
- The climate change of the region of Western Macedonia due to the conventional energy sources.
- The energy transition and its impact in the area.
- The future of energy in Western Macedonia and the Renewable Energy investments.
- The public awareness of the lignite impacts in their region.
- The job insecurity due to the closure of the mines and the future job opportunities.
- The current policies and the future strategies.

The second category concerns the situation in the rest of the World. The selected papers were mainly case studies and the objects investigated were the following:

- Studies that have been conducted in Europe that show the strong connection between air pollution and the energy sector.
- The goal of Europe is to achieve climate neutrality by 2050.
- Covid-19 crisis and Circular Economy in the health sector.
- The role of digitalization in sustainability.
- E-waste management and digital tools.
- The indicators that are affected due to an economic transition.
- The understanding of consumers' behavior to create strategies for waste management by the principle of the Circular Economy.
- The role of AI in Water, Food, and Energy.
- Green-IoT and Edge-AI as enablers of sustainability.
- Lifestyle changes to reduce carbon footprint.

The results of the study showed that the Circular Economy is one of the most significant subjects of our century and it affects each sector in a different way. The academic articles review suggested that almost every country in Europe tries to apply the principles of the Circular Economy to reduce its carbon footprint. Additionally, in the reviewed studies we notice that significant efforts are being made by developing countries too.

Also, the reviewed studies are referring in a combination of subjects at a time, which indicates the connection of the Circular Economy with various sectors. Leadership can play a crucial role in decision making and sustainable transition. Some of the top subjects are Climate Change, Energy Transition, Decarbonization, Waste Management, Digitalization, Economy, Zero Waste and Health. Another significant characteristic is that most of the papers that were reviewed for the current study are published after 2018. This this shows that our research is up to date.

The strategies and measures that are applied in other countries can be an example for local and regional authorities of Western Macedonia and contribute to the right decisions for the area, create more job opportunities in a carbon-free future, relieve residents' concerns and help Western Macedonia to be once more the greatest power in the energy sector.

Future research could deal with the renewable energy extensions in the area, decarbonization, the results of lignite usage in residents health, waste management, e-waste management on the abandoned coal mines and restoration of the area.

DISCUSSION

Although Western Macedonia is facing great changes in the energy sector, we must keep in mind that new investments are being discussed regarding renewable energy sources. These investments promise to help the area to become once again the major energy power of Greece. The closure of the lignite mines may provoke negative emotions to the residents of Western Macedonia due to the job insecurity, but it is also introducing new ways to exploit the degraded land that cannot be used for agriculture. Thus, new job opportunities arise from renewable energy investments in the degraded lands and give the chance to the residents to remain to their birth places and do not emigrate for professional reasons.

Circular economy policies in the energy sector focus on green energy production, reduction of waste, decreasing of land, water, and air pollution, promote the energy efficiency and renewable energy. Additionally, can lead to investments on energy storage technologies, which is a highly important subject of our century and will give a solution to various energy restrictions. Finally, these policies will help the country become energy efficient, without adding more pollution to the planet.

CONCLUSION

To summarize, the current paper's subject is studying the effects of the Circular Economy, Energy Transition, Waste Management and Climate Change in Western Macedonia.
The methodology that was followed to select the papers that were suitable for the survey was the tollgate approach. Selected keywords were used to search articles through digital libraries. The final selection was made by separating the articles based on certain specific criteria, such as whether they had a title related to the topics of interest or whether they had an interesting abstract. The articles resulting from the selection were about 55.
Additionally, the 55 articles were categorized based on specific characteristics, such as their topic or the year of publication.
The significance of this research is to understand the current situation in Western Macedonia. It is important to identify the degree of pollution, the climate change and find ways to be more sustainable and environmentally friendly. Also, by reviewing the policies that are followed in Europe or the rest of the World, we can adjust them to Western Macedonia's and generally Greece's needs [10].

https://doi.org/10.5593/sgem2024/4.1/s17.07

REFERENCES

[1] Evagelopoulos, V.; Begou, P.; Kassomenos, P.; Zoras, S. Investigation of the Particulate Air Pollution and the Ratio of PM $_{2.5}$ to PM $_{10}$ Concentrations in the Atmosphere over the Lignite Mining and Lignite-Fired Power Plants Region of Western Macedonia, Greece. *IOP Conf Ser Earth Environ Sci* **2022**, *1123*, 012077, doi:10.1088/1755-1315/1123/1/012077.

[2] Sachanidis, C.; Pavloudakis, F.; Roumpos, C. Correlation of Ambient Air Quality with the Sudden Reduction in Mining Activity in a Complex of Lignite Mines.; MDPI AG, 2022; p. 102.

[3] Triantafyllou, A.G.; Krestou, A.; Matthaios, V. Lignite Power Plant's Contribution to the Particulate Pollution in the Grater Western Macedonia Area, Greece 2013, 1245–1250.

[4] Moussiopoulos, N.; Achillas, C.; Vlachokostas, C.; Spyridi, D.; Nikolaou, K. Environmental, Social and Economic Information Management for the Evaluation of Sustainability in Urban Areas: A System of Indicators for Thessaloniki, Greece. *Cities* **2010**, *27*, 377–384, doi:10.1016/J.CITIES.2010.06.001.

[5] Li, Z.; Anming, X.; Naiyue, Z.; Jianbin, H.; Zhong, C. A SOA Modernization Method Based on Tollgate Model. In Proceedings of the 2009 International Symposium on Information Engineering and Electronic Commerce; IEEE, May 2009; pp. 285–289.

[6] Energy_Report_202304_v1_gr.

[7] Sharma, M.; Joshi, S.; Govindan, K. Issues and Solutions of Electronic Waste Urban Mining for Circular Economy Transition: An Indian Context. *J Environ Manage* **2021**, *290*, 112373, doi:10.1016/j.jenvman.2021.112373.

[8] Sartori, I.; Hestnes, A.G. Energy Use in the Life Cycle of Conventional and Low-Energy Buildings: A Review Article. *Energy Build* **2007**, *39*, 249–257, doi:10.1016/J.ENBUILD.2006.07.001.

[9] Li, D.H.W.; Yang, L.; Lam, J.C. Zero Energy Buildings and Sustainable Development Implications – A Review. *Energy* **2013**, *54*, 1–10, doi:10.1016/J.ENERGY.2013.01.070.

[10] Tranoulidis, A.; Sotiropoulou, R.E.P.; Bithas, K.; Tagaris, E. Decarbonization and Transition to the Post-Lignite Era: Analysis for a Sustainable Transition in the Region of Western Macedonia. *Sustainability (Switzerland)* **2022**, *14*, doi:10.3390/su141610173.

DESIGN AND SIMULATION OF STATIC REQUIREMENTS IN THE CASE OF A WIND TURBINE FIXED ON A MARITIME TRANSPORT SHIP

Assoc. Prof. Dr. Carmen-Penelopi Papadatu[1]

Lect. Dr. Costel Humelnicu[1]

Eng. Radu Aiordachioaiei[1]

Eng. Ionut - Cristian Adam-Papadatu[1]

[1] "Dunarea de Jos" University from Galati, **Romania**

ABSTRACT

Maritime transport plays a crucial role in the global economy, ensuring the transport of around 80% of world trade. However, shipping is responsible for a significant portion of greenhouse gas emissions, accounting for approximately 2.5% of total global emissions. In this context, the efficiency of fuel consumption in ships using the renewable energy sources can bring significant benefits for the environment and contributes to the achievement of the objectives of reducing greenhouse gas emissions. The opportunity of the work consists in the fact that it aims to improve the efficiency of the fuel consumption of the ships through renewable energy sources.

The integration of a hybrid system consisting of 4 wind turbines on a board ship can increase the energy efficiency. Wind turbines can capture the power of the wind to generate electricity, while kites can be used to capture energy from air currents at higher altitudes. Research can explore the possibilities of integrating the hybrid system with other renewable energy sources such as solar panels.

This paper also presented a simulation of the static loads used in Inventor 2022.

Keywords: Conservation of the energy, simulation, wind turbine, maritime transport, unconventional energy.

INTRODUCTION

Container transport is regarded as the world's truly global supply chain. A single cargo-laden container can be moved by different transport vehicles (e.g.,vessels, trains, and trucks). These are handled by various types of handling equipment and facilities (e.g., terminals, cranes, trailers, wagons, and depots) from the point of departure to the destination along the entire from one end to the other supply chain.

The importance of the container shipping sector is supported by the fact that over 70% of world trade and over 50% of world's seaborne trade by value is carried by container ships according to the 2018 annual review of maritime transport by The United Nations Conference on Trade and Development [1, 2]. The container shipping supply chain (CSSC) consists of several key stakeholders such as the shipper, freight forwarder, shipping line, port/terminal operator, inland carrier, and intermodal terminal/depot operator [2].

https://doi.org/10.5593/sgem2024/4.1/s17.08

CSSC can be classified into five segments [2, 3, 4]: Shipping arrangement; Container management; Maritime transport proper with cargo ships; Port and terminal management; Inland transport and cargo storage.

The term *Container Logistics* refers to the efficient management of container flows and storage in transport networks to meet customer requirements. It is desired to use the maritime container fleet to the maximum, but also to save costs related to fuel, wanting to avoid excessive pollution as much as possible. According to Drewry Shipping Consultant, the world's container fleet exceeded 37 million equivalent units (TEU) in 2018, which were mainly held by cargo shipping lines and container lessors, roughly on a 50:50 split. The container fleet is the most important for container shipping companies in terms of capital investment [2]. The massive pollution due to transport and, implicitly, cargo ships, led to the involvement of the world's states in policies to reduce the greenhouse effect emissions. Carbon dioxide, as one of the most important greenhouse gases (GHG) emitted by human activities, has attracted the attention of the IMO (International Maritime Organization) for a long time. IMO sponsored four extensive studies on GHG emissions from shipping, which were published in 2000, 2009, 2014, respectively 2020 [2]. Of all the shipping sectors, container ships are the largest sources of CO2 emissions, representing 23% of the total CO2 emissions from maritime transport [5].

According to the 2016 Paris Climate Summit, GHG emissions from cargo shipping were unregulated until 2023. But the decarbonization it was always on the IMO agenda. The shipping industry and IMO Member States have considered a series of measures to reduce greenhouse gases generated by shipping in recent years. Measures to reduce maritime emissions can be classified into four categories: operational measures, technical measures, market-based measures and alternative fuels possibly renewable energies [2, 3, 6, 7]. Operational measures focus on energy reduction and operational improvement productivity by performing appropriate operational activities for marine transport vessels [2]. Replacing the conventional energy with green energy, captured from the marine environment, can help reduce pollution and save fossil fuels in the shipping sector. Shipbuilders are aware of the negative impact of emissions of harmful gases and hazardous chemicals on human health and the environment, which is why they are focusing on reducing marine pollution and implementing international requirements for the protection of the marine environment. Unconventional energy captured from the marine environment, through sources such as solar and wind power, can help conserve fossil fuels and preserve them for future use, thus protecting the planet's fossil fuel reserves. Research and development of renewable and green energy technologies, both in the marine and onshore sectors, are encouraged and supported to create a dynamic market for alternative sources of either electrical, green, or ecological energy, thus contributing to a cleaner and more sustainable environment with lower costs and less pollution and noise [8].

MARPOL is the acronym for the International Convention for the Prevention of Pollution from Ships or short for "marine pollution". This convention was adopted in 1973 by the International Maritime Organization (IMO) and has been amended several times since then to include new regulations and to keep pace with new technologies and developments in the maritime industry [9, 10, 12]. The International Convention for the Prevention of the Pollution of the Marine Environment from the Use of Ships (MARPOL) sets international standards for preventing pollution of the marine

environment from ships by regulating emissions and discharges from ships. This includes regulations for the management of waste and wastewater, as well as for the prevention of pollution by hydrocarbons and other hazardous substances. The main purpose of MARPOL is to protect the marine environment and human health [11].

ORIGINAL ELEMENTS OF THE RESEARCH

Maritime transport is an important source of greenhouse gases (GHGs) due to emissions of carbon dioxide (CO2), which is the most important greenhouse gas. CO2 emissions from shipping are estimated to represent approximately 2.5% of total global greenhouse gas emissions. Nitrogen oxides (NOx) and sulfur dioxide (SO2) are two main gases emitted by ships. They are released into the atmosphere when fuel is burned to generate power for ships. NOx and SO2 are responsible for the formation of acid rain and can lead to negative effects on human and animal health as well as on ecosystems. Ships also emit fine particles, including PM2.5 and PM10, which then are released by ships and can travel long distances, affecting air quality in regions other than where the ships emit the gases. These particles can cause respiratory problems such as asthma and other respiratory conditions and contribute to cardiovascular disease and increased mortality. Fine particles can also affect animal health and lead to decreased soil quality and loss of biodiversity.

In addition, ships can also cause water pollution through emissions of toxic substances, including hydrocarbons, heavy metals and other chemicals that are released through the sewage system and through fuel and other chemical leaks during loading and unloading, but also noise pollution, which can affect marine life and can lead to the disruption of natural habitats and the migration of marine animals. In order to reduce the environmental pollution caused by maritime traffic, various studies have been carried out over time [9, 11, 12].

CONFIGURATION OF THE HYBRID SYSTEM CONSISTING OF FOUR VERTICAL AXIS WIND TURBINES AND A KITE

The proposed hybrid wind power system for commercial ship is an innovative and sustainable solution for the generation of electricity at sea. Integrating four vertical axis wind turbines and a kite-inspired concept, this system exploits the potential of wind energy in an efficient and maritime environment-friendly way.

Vertical axis wind turbines are the backbone of this hybrid system. Strategically placed on the ship's superstructure, these specially designed turbines can capture wind energy efficiently even in variable sea conditions. They are designed to withstand the forces and motions of the ship, thus maximizing the generation of electrical energy while sailing. An innovative component of this system is the addition of the kite concept, adapted to the maritime environment. Instead of a classic kite, alternative technologies such as sails are used to capture wind energy during sailing. These aerodynamic elements, integrated into the ship's design, allow the kinetic energy of the wind to be converted into mechanical energy, opening up new opportunities for power generation at sea. The hybrid system is complemented by a centralized energy generation and storage system. The electric generators attached to the wind turbines and the kite concept that tows the ship with the help of the wind. Storing energy in battery banks allows electricity to be used later when there is not enough wind or to meet energy

https://doi.org/10.5593/sgem2024/4.1/s17.08

demand during periods of low wind. The hybrid system ensures intelligent energy management with the help of an advanced control system. It regulates the power generated based on the availability and performance of the wind turbine so that the generators operate at optimal capacity, avoiding overuse and saving fuel. Synchronization with the ship's energy demand allows efficient use of resources and a reduction in evening gas emissions.

THE PLACEMENT OF TURBINES ON BOARD THE SHIP AND THEIR INFLUENCE ON THE STABILITY OF THE SHIP

Vertical axis wind turbines are designed to be lightweight compared to other marine construction equipment such as containers. Typically, these turbines are made from lightweight materials such as aluminium and composite materials to reduce overall weight. By comparison, containers are made of steel [14] or other heavy materials, which means that their weight will be much greater than that of wind turbines [11]. The wind turbines are placed symmetrically on the ship, which means that their weight will be evenly distributed on the ship. Thus, significant imbalances caused by wind turbines will not occur. Conversely, containers, which may be irregularly loaded onto the ship, can create larger imbalances. However, the ship's stability is designed to cope with these weight variations and to keep the ship in a stable position while sailing. To maintain the stability of the ship, it is important to consider the distribution of weight on the ship. This is done by properly loading and arranging the containers on the ship's deck. In general, heavier containers are placed at the bottom of the ship, while lighter containers are placed on top of them. Thus, the total weight is distributed evenly and evenly throughout the vessel, helping to maintain stability.
In conclusion, placing 4 wind turbines on a commercial cargo ship should not affect the stability of the ship, considering that the turbines are light and symmetrically placed, and the ship is loaded with much heavier containers [11].

VERTICAL AXIS WIND TURBINE DESCRIPTION AND PERFORMANCE PARAMETERS

Vertical axis wind turbines are mainly of two types - lifting models and resistance models. In these, the axis of rotation is kept vertical, i.e. perpendicular to the ground. The other mechanical and electrical components are placed close to the ground, i.e. below the turbines, using a shaft. Since they are not placed parallel to the ground, they have a high capacity to capture wind from all directions. The power and other parameters of VAWTs can be calculated using the following equations. The kinetic energy present in the wind is considered as the power available in the wind and is assumed to be proportional to the air density, wind speed and surface area of capture of the wind turbine.

The power available in the wind is given by Pw:

$$Pw=12\cdot\rho\cdot A\cdot v^3 \quad (1)$$

Mentions:
ρ is the density of air, i.e. 1,225 kg/m^3
A represents the area corresponding to the wind turbine
v represents the wind speed.

According to a German physicist, Albert Betz [15], no wind turbine can convert the kinetic energy of the wind into mechanical energy at a rate higher than 59.3%. This conversion limit was later called the Betz limit. Therefore, the mechanical power generated by the wind turbine is given as the power available at the turbine, Pt.

$$Pt=12\cdot\rho\cdot Cp\cdot A\cdot v^3 \quad (2)$$

The constant 16/27 ≈ 0.593 is known as the Betz coefficient [15]. The electricity generated by the wind turbine system represents 59.3% of the input wind energy. Thus, the wind turbine coefficient or power coefficient, Cp, can be defined as the ratio of the electricity produced by the wind turbine to the total power available in the wind. Thus, the wind turbine coefficient or power coefficient, Cp, can be defined as the ratio of the electrical energy produced by the wind turbine to the total power available in the wind.

The conversion to electricity would be 70% of 59.3%, i.e. the Cp value can be calculated as 0.70 * 0.593 ≈ 0.41, which gives the approximate efficiency of good turbines of 41%. In general, the efficiency range of good quality turbines is between 35% and 45%. The captured area of the VAWT is given as the product of the rotor height and the rotor diameter.

$$A=H\cdot D \quad (3)$$

Mentions:

H is the height of the VAWT rotor in meters and D is the diameter of the VAWT rotor in meters.

The tip speed ratio (TSR) or λ for wind turbines is the ratio of the tangential blade tip speed to the actual wind speed. TSR can be calculated using the relationship:

$$TSR= (\omega \cdot R)/ v \quad (4)$$

Where ω is the rotor rotation speed in radians per second, R is the rotor radius in meters and v is the actual wind speed. TSR can also be referred to as the Lambda parameter. The number of vanes varies between 3, 5 and 8 and the performance in terms of power output is also studied. With a larger number of vanes, the TSR (Tip Speed Ratio) value is reduced. Thus, increasing the drag force leads to less power and basically less efficiency. The relationship between TSR and the number of pallets used can be deduced using the following formula:

$$TSRmax= (4 \cdot \pi)/ N \quad (5)$$

The solidity of a wind turbine (S) is used to "define the geometry of the VAWT" and is calculated using the equation as follows. It is a unitless parameter.

$$S = (N \cdot C) /D \quad (6)$$

In rel. (6): N is the number of vanes used in the design of the VAWT; C is the chord length of the air foil; D is the rotor diameter.

Next level consists of a vertical axis turbine presentation, a project that one of the authors [11] developed using the Solidworks application. This turbine represents an innovative solution for power generation in environments with wind flows. The vertical axis tube we designed has a height of 15 m from the ground flange to the end of the blade, a blade height of 9 m and a diameter of 7 meters. These dimensions were chosen according to the characteristics of the environment in which the tube will be placed. To ensure optimal energy capture efficiency, the NACA4412 blade turbine was designed.

https://doi.org/10.5593/sgem2024/4.1/s17.08

The Tubercle NACA4412 air foil is used in the design of aircraft wings and wind turbine blades. The blade model was taken from an online library [11, 13], more precisely the coordinate points to make the 2D model of the blade, which was then transformed into a 3D model.

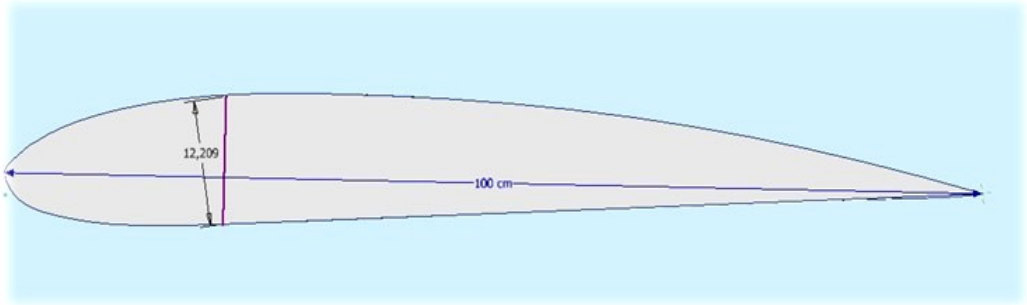


Figure 1. The 2D model of the blade NACA 4412 [11]

This provides an aerodynamic profile, which allows maximum conversion of kinetic energy into mechanical energy. The curved profile of the blades provides increased stability during operation, minimizing vibrations and disturbances.

The 2D model of the blade NACA 4412 [11] can be observed in figure 1 and in figure 2, the 3D model of the blade NACA 4412 [11] can be observed too.

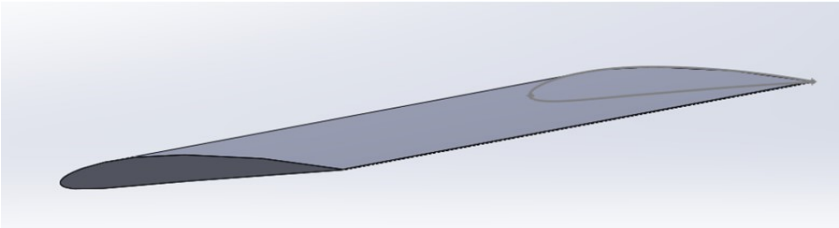


Figure 2. The 3D model of the blade NACA 4412

In figure 3, the 3D model of the vertical axis wind turbine assembly has been presented. General drawing of the wind turbine has been presented in figure 5, with the following mentions: 1- main pillar; 2- clamping flange; 3- generator; 4- attachment pillar for blade 2; 5- wind blade; 6- fastening screw for the wind turbine blade; 7- flange fixing screw. In figure 4, a simplified scheme of the system has been presented and in the figure 6 - the execution drawing of the NACA 4412 blade has been presented.

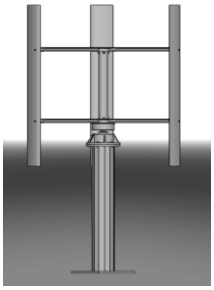


Figure 3. The 3D model of the vertical axis wind turbine assembly [11,13]

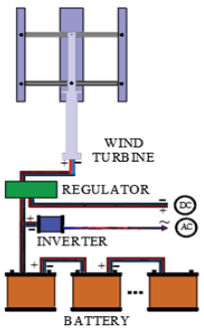


Figure 4. The scheme of the system

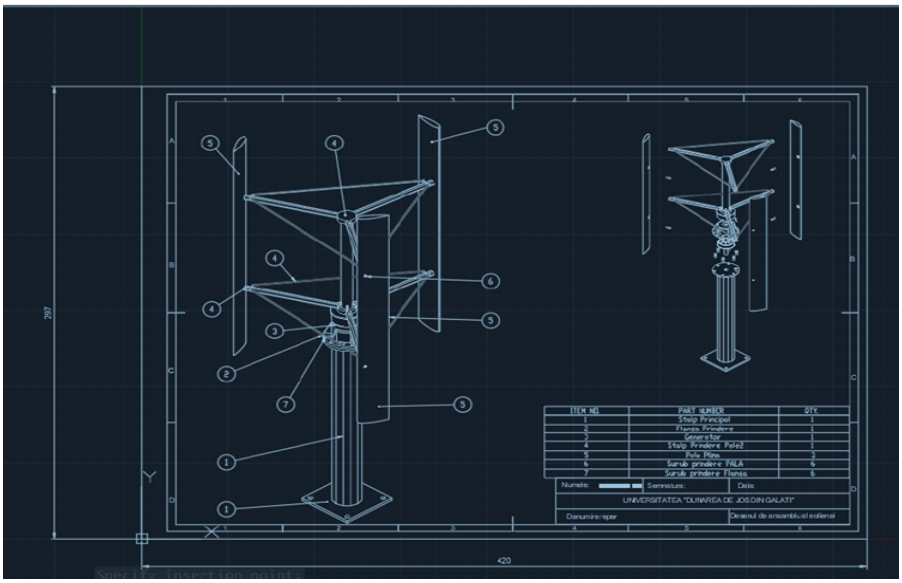


Figure 5. General drawing of the wind turbine [11]

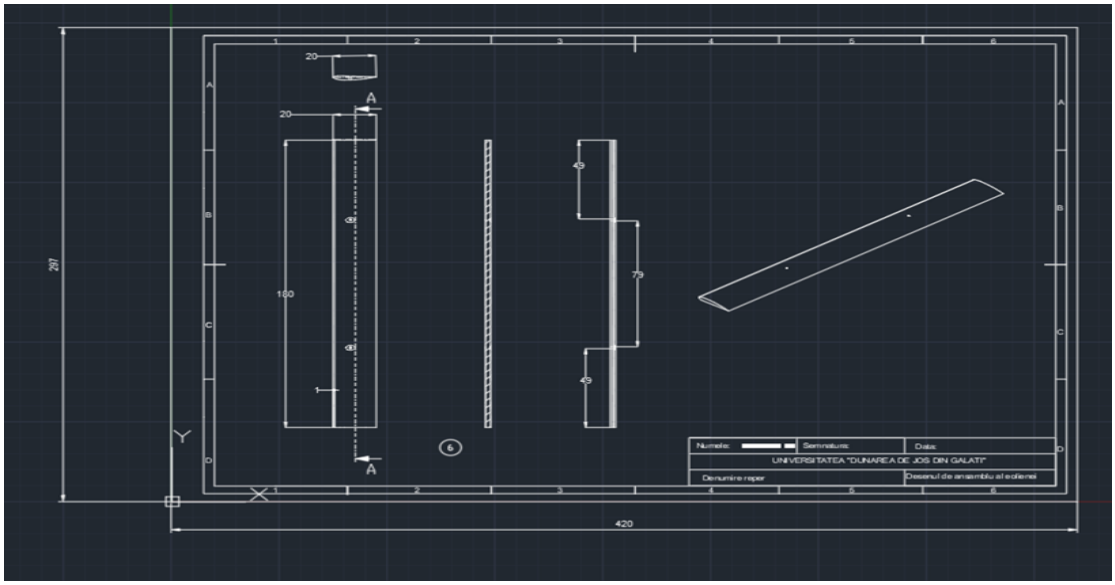


Figure 6. The execution drawing of the NACA 4412 blade [11]

THE USING OF THE INVENTOR PROGRAM TO CALCULATE THE STATIC STRESSES IN THE PILLAR OF THE WIND TURBINE

The Autodesk Inventor – Assembly program was used to determine the static stresses acting on the pillar of the wind turbine. This component was chosen because it has the smallest section, the longest length and supports the weight of all the blades as well as their connecting elements.

In order to carry out the study, the constraints of the components were made, also a material was assigned to each segment of the assembly, material that can be found in the library of the Inventor program. The main leg and clamping flange were attributed to a carbon steel [14], and on the secondary post, the lamella and clamping supports, it was attributed to Aluminium 6061 Welded. The assembly was fixed at the bottom, on the clamping plate, and a pressure of 2.75 MPa was placed on the secondary post (to which

https://doi.org/10.5593/sgem2024/4.1/s17.08

the blades are fixed). This pressure was calculated using the value of 1013 mbar - this being the pressure at the ocean level.

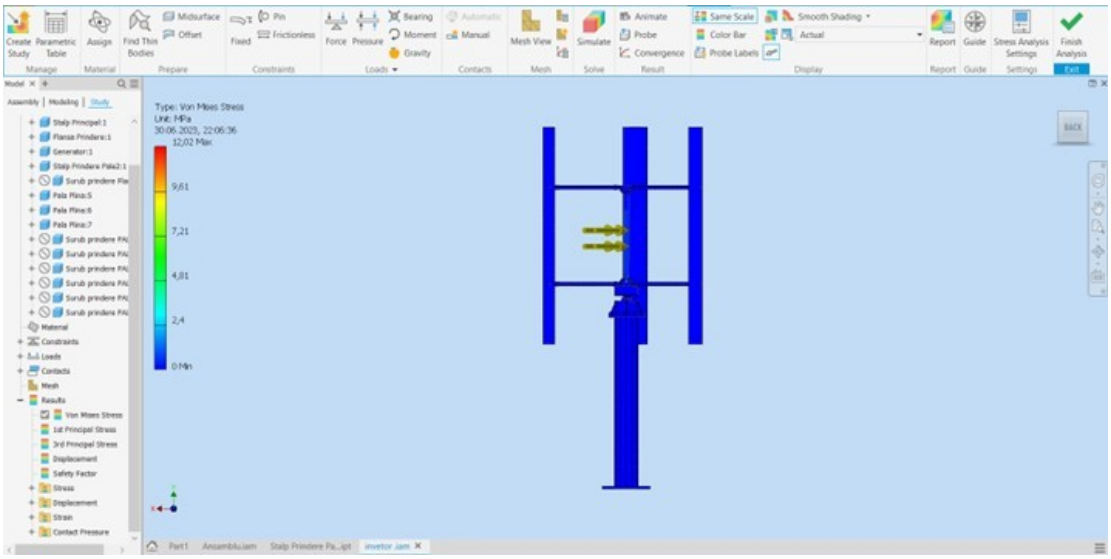


Figure 7. Von Mises Stress

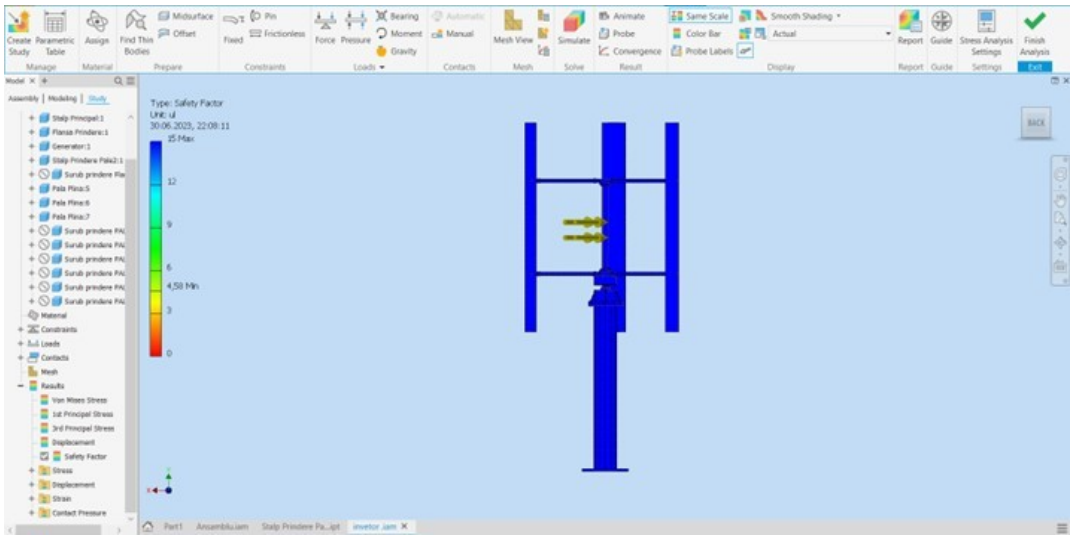


Figure 8. Safety Factor

RESULTS: After the static action of simulation, it was found that the Von Mises stress was 12.02 MPa (fig. 7) and the minimum safety factor was 4.58 (fig. 8). In the specialized literature, a minimum safety factor for aluminium used in the naval field is specified with a minimum value of 6. Since the resulting minimum safety factor is located below this value, for optimization, two possibilities were considered: 1. Axis resizing; 2. Assignment of another material with higher mechanical properties. Since the use of the first option would lead to an increase in the mass of the assembly, the second option was chosen. Consequently, Aluminium 6061 AHC was chosen.

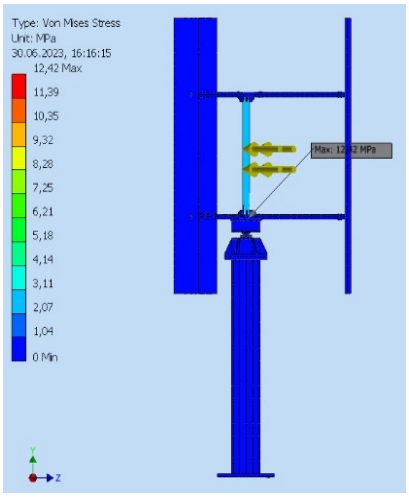


Figure 9. Von Mises Stress evolution

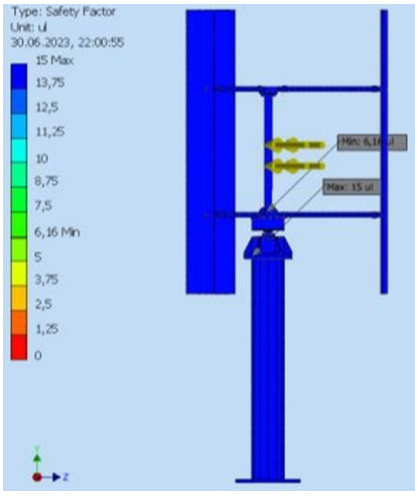


Figure 10. Safety Factor

After the second simulation a Von Mises Stress of 12.42 MPa resulted (fig. 9), and the minimum Safety Factor has a value of 6.16, visible in figure 10.

CONCLUSION

The integration of a hybrid system consisting of 4 wind turbines on the board of the ships can increase their energy efficiency.

The main advantages are:
Reduction of fuel consumption: The implementation of a hybrid system can contribute to the reduction of fuel consumption of ships.
Sustainability: The use of wind energy can bring a more sustainable approach to shipping, reducing environmental impact and greenhouse gas emissions.
Flexibility: The hybrid system can provide greater flexibility in managing energy sources by adapting to variations in weather conditions and the availability of wind and air currents.

Possible research directions: Improving the design and efficiency of the wind turbines; Making an efficient and reliable aeolian energy harvesting kite can be technically challenging and requires research and development in materials, control algorithm and clamping the systems; Integration with other renewable energy systems: Research can explore the possibilities of integrating the hybrid system with other renewable energy sources such as solar panels.

In conclusion, the use of a hybrid wind turbine system on the board of ships can bring significant energy and sustainability benefits, but it requires further research and development to optimize performance and ensure effective integration into the naval environment.

https://doi.org/10.5593/sgem2024/4.1/s17.08

REFERENCES

[1] Lee, C.-Y.; Song, D.-P. Ocean container transport in global supply chains: Overview and Research opportunities, Transportation Research, Part B Methodol. WOS:000392792700021, https://doi.org/10.1016/j.trb.2016.05.001, vol. 95, pp.442–474, 2017, Online ISSN: 1879-2367, Print ISSN: 0191-2615.

[2] Song, D. A Literature Review, Container Shipping Supply Chain: Planning Problems and Research Opportunities. **Logistics**, MDPI WOS:000668202300001, https://doi.org/10.3390/logistics5020041, 5, p. 41, 2021, ISSN: 2305-6290.

[3] Song, D.P. Container Logistics and Maritime Transport; Routledge: London, UK, WOS:001056525900008, https://doi.org/10.4324/9780429320996, 2021.

[4] Verweij, K. Synchronic modalities: Critical success factors. In *Logistics* Handbook 2011; Van der Sterre, P.J., Ed. Feico Houweling, Rotterdam, The Netherlands, pp. 75–92, 2011.

[5] Olmer, N.; Comer, B.; Roy, B.; Mao, X.; Rutherford, D. Greenhouse Gas Emissions from Global Shipping, 2013–2015; International Council on Clean Transportation: Washington, DC, USA, 2017.

[6] Bouman, E.A.; Lindstad, E.; Rialland, A.I.; Strømman, A.H. State-of-the-art technologies, measures, and potential for reducing GHG emissions from shipping—A review. Transp. Res. Part D Transp. Environ. https://doi.org/10.1016/j.trd.2017.03.022 ,WOS:000401398400029, 52, pp. 408–421, 2017, ISSN: 1361-9209.

[7] Shi,W.; Xiao, Y.; Chen, Z.;McLaughlin, H.; Li, K.X. Evolution of green shipping research: Themes and methods. Maritime Policy & Management, https://doi.org/10.1080/03088839.2018.1489150, WOS:000443903900003, **2018**, 45, pp. 863–876, Print ISSN: 0308-8839, Online ISSN: 1464-5254.

[8] Rutherford, D.; Comer, B. The International Maritime Organization's Initial Greenhouse Gas Strategy; International Council on Clean Transportation: Washington, DC, USA, 2018.

[9] Copeland C., Cruise Ship Pollution: Background, Laws and Regulations, and Key Issues, Congressional Research Service, 1 July 2008, Archived from the original (PDF) on 25 April 2013, Order Code RL32450.

[10]. www.imo.org, *International Convention for the Prevention of Pollution from Ships (MARPOL),* Archived from the original on 4 October 2019, retrieved 23 July 2015. Last accessed: 04.02.2024.

[11] Aiordachioaei, R., Undergraduate project, Coordinating teacher: Assoc. Professor Papadatu C.P., PhD., "Dunarea de Jos" University, Galati, Romania, 2023.

[12] Papadatu, C.-P., The Environment Politics in Balkans (Politici de Mediu în Balcani), Editura Fundației Universitare „Dunărea de Jos", Galati, Romania, 2008, ISBN: 978-973-627-414-5.

[13] http://airfoiltools.com/plotter/index.

[14] Papadatu, C.P., Posibilitati de imbunatatire a calitatii unor oteluri utilizate in industria metalurgica, Editura Fundatiei Universitare Dunarea de Jos, Galati, Romania, 2006, ISBN 978-973-627-371-1.

[15] Betz, A. The Maximum of the Theoretically Possible Exploitation of Wind by Means of a Wind Motor, Journal article, *Wind Engineering,* Vol. 37, No. 4 pp. 441-446 (6 pages), Published By: Sage Publications, Ltd., 2013 (Translation of: *Das Maximum der theoretisch möglichen Ausnützung des Windes durch Windmotoren, Zeitschrift für das gesamte Turbinenwesen*, Heft 26, 1920).

https://doi.org/10.5593/sgem2024/4.1/s17.08

EFFICIENCY ANALYSIS OF THE USE OF SOLAR PHOTOVOLTAIC MODULES BASED ON CLIMATIC ZONES

PhD Ress. Bohirjon Sharifov[1]

Assoc. Prof. Dr. Svetlana Beryozkina[2]

Dr. Anvari Ghulomzoda[3]

Dr. Murodbek Safaraliev[4]

PhD Ress. Shokhrukh Sidikov[3]

[1] Tajik Technical University named after Academician M.S. Osimi, **Tajikistan**
[2] College of Engineering and Technology, American University of the Middle East, **Kuwait**
[3] Novosibirsk State Technical University, **Russia**
[4] Ural Federal University, **Russia**

ABSTRACT

Currently, solar energy is one of the most widely used types of green energy in the world. In different parts of the earth, solar insolation is not constant. Therefore, this study aims to determine the main characteristics of solar insolation in the different climatic zones. This paper analyzes the prospects for using solar energy in subtropical, temperate-continental, continental, sharp-continental, and monsoon climate zones. The efficiency of converting solar radiation into electrical energy is estimated considering seven regions located in these climatic zones. The analysis is based on the results of an annual study of a test photovoltaic station installed at the Ufa State Aviation Technical University. Based on the analysis results, temperature characteristics, solar insolation, solar energy conversion efficiency, and specific electricity generation were obtained for each region. The study found that the efficiency of solar energy conversion of photovoltaic modules in climatic zones ranges from 60% to 85% of the nominal value. The average value of solar radiation in the remote northern regions is 810 kWh/m^2, in the southern regions it is in the range of 1350-1400 kWh/m^2. The technical potential of using solar energy is very high, the most favorable are the subtropical and continental climate zones.

Keywords: autonomous solar power plants, conversion efficiency, photovoltaic modules, solar insolation, solar energy.

INTRODUCTION

Photovoltaic solar energy conversion is considered one of the fastest-growing renewable energy applications in the world. Currently, the total capacity of installed solar photovoltaic systems is over 38 GW. The annual growth rate over the past 5 years is 30%. The leaders in this direction are China (10 GW), Japan (9.7 GW), USA (6.2 GW), Great Britain (2.4 GW), Germany (1.9 GW) [1-4].

Russia has enormous potential for almost all types of renewable energy sources (RES), including solar. There are quite a few regions in Russia where the average annual solar radiation is 4-5 kWh per 1 m^2 per day (this figure is comparable to the south of

https://doi.org/10.5593/sgem2024/4.1/s17.09

Germany and the north of Spain - countries that are leaders in implementing photovoltaic systems).

Russia has enormous potential in almost all types of renewable energy sources (RES), including solar. According to the classification, the territory of Russia is divided into the following climatic zones: Arctic, subarctic, temperate continental, continental, sharply continental, monsoon, and subtropical climate zones [5].

According to official statistics presented by the Institute of Energy Strategy, the total potential of solar energy is 2,300,000 million tons of fuel equivalent, and the technical potential is 2,300 million tons of fuel equivalent. (this is 2 times the total energy consumption in the country) and economic – 12.5 million t.e. [6]. These data refute existing opinions about the insufficient potential of Russian solar energy and the inexpediency of its development in Russia. It should be noted that high levels of insolation in Russia are observed not only in the North Caucasus but also in the Far East, as well as in the south of Siberia (Fig. 1).

In this regard, the purpose of this work is to analyze and evaluate the effectiveness of the use of solar photovoltaic installations in the climatic conditions of the Russian Federation (RF).

PROBLEM STATEMENT

This research was carried out at the Ufa State Aviation Technical University (USATU) based on a test photovoltaic system (TPS) [7-10]. TPS is designed to test photovoltaic modules (PVM) under real lighting and climatic conditions in 7 regions of the Russian Federation: Astrakhan, Vladivostok, Gorno-Altaisk, Makhachkala, St. Petersburg, Ufa, Yakutsk.



Figure 1. Level of solar insolation by regions of the Russian Federation

Table 1. Main operational characteristics of PVM

Parameter	PramacLuce (LLC «Hevel»)	TCM-210SB
Rated power	125 W	223 W
Open circuit voltage	71 V	44 V
Operating voltage	56 V	38 V
Operating current	2.23 A	5.87 A
Efficiency	8.74%	17.34%
Surface area	1.43 m^2	1.286 m^2
Weight	20 kg	15 kg

The objects of study are two PVMs manufactured using different technologies. Thin-film PVM (PramacLuce) made based on amorphous and microcrystalline silicon has a thickness of active layers of no more than 1.5 micrometers. The second PVM (TCM-210SB) is made based on crystalline silicon wafers and has an active layer thickness of at least 180 micrometers, which provides the maximum conversion rate of light energy into electrical energy, but at the same time significantly increases the cost of production. The main operational characteristics of PVM are given in Table. 1.

EXPERIMENTAL STUDIES AND THEIR RESULTS

Based on the data obtained, an analysis of the operating efficiency, a comparison of energy indicators for the considered PVMs, and a comparison of climatic conditions in the regions of the Russian Federation for the period from January 2015 to December 2015 were carried out. During the experiment, measurements of the average daily ambient temperature were made in 7 regions of the Russian Federation (Fig. 2).

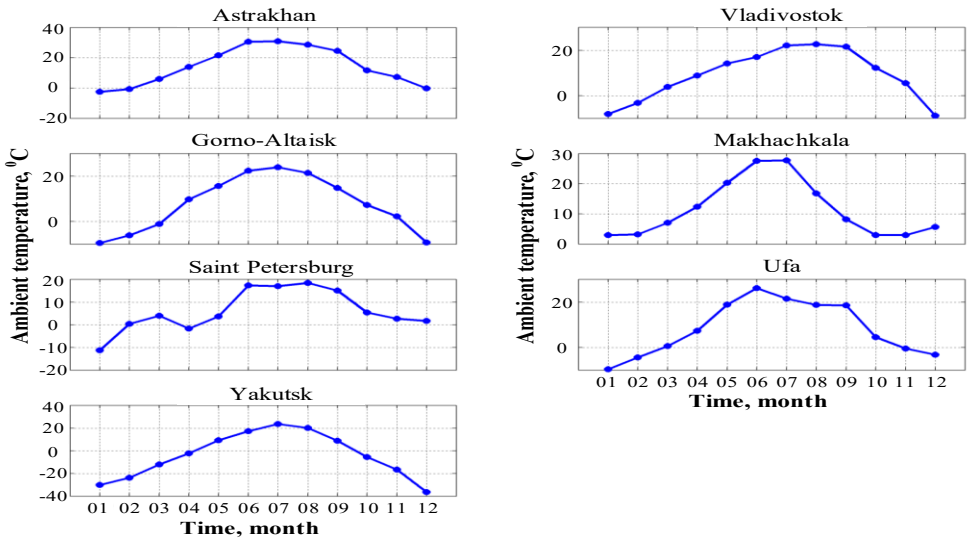


Figure 2. Average values of ambient temperature at monitoring points (^{0}C) for 2015

The graphs in Fig. 2 show that in the climatic conditions of Yakutsk, the average daily temperature during the winter monitoring period ranges from -10 ^{0}C to -40 ^{0}C. In summer, this indicator varies from +15 ^{0}C to +32 ^{0}C. Thus, the average annual ambient temperature in Yakutsk is -3.96 ^{0}C. The average daily temperature in Astrakhan varies

https://doi.org/10.5593/sgem2024/4.1/s17.09

from -1 ^{0}C (January 2015) to +32 ^{0}C (July 2015). For Astrakhan, the average annual temperature is +14.34 ^{0}C. Further, for other regions of the Russian Federation, the ambient temperature values are Vladivostok from -8 ^{0}C (January 2015) to 22 ^{0}C (July 2015), average annual temperature +8.9 ^{0}C; Gorno-Altaisk from -9 ^{0}C (January 2015) to +24 ^{0}C (July 2015), average annual temperature +7.6 ^{0}C; Makhachkala from +7 ^{0}C (January 2015) to +27 ^{0}C (July 2015), average annual temperature +11.4 ^{0}C; St. Petersburg from -11 ^{0}C (January 2015) to +18.4 ^{0}C (July 2015), average annual temperature +6 ^{0}C; Ufa from -9 ^{0}C (January 2015) to +26 ^{0}C (July 2015), average annual +8.2 ^{0}C.

As part of this work, solar radiation indicators were also measured in the regions of the Russian Federation and compared with tabular data from NASA databases [7] (Table 2). On average, the deviation of the measured values from the tabulated data on NASA databases does not exceed 13% of the daily average value. The deviation of the measured values from the tabulated ones in the winter months is due, among other things, to the presence of precipitation in the form of snow, and in the summer to the presence of cloudy weather, since the NASA database gives the average value of solar radiation for the period 1983-2005.

Table 2. Average monthly level of solar radiation, kWh/m^2

Month	**Astrakhan**		**Vladivostok**		**Gorno-Altaisk**		**Makhach-kala**		**St. Petersburg**		**Ufa**		**Yakutsk**	
	TPS	NASA	TPS	NASA	TPS	NASA	TPS	NASA	TPS	NASA	TPS	NASA	TPS	NASA
1	2.05	2.13	3.97	2.35	1.48	1.21	2.21	1.77	0.63	0.43	1.47	0.79	0.24	0.36
2	3.18	3.36	4.72	3.41	2.59	2.15	2.56	2.50	0.62	1.19	2.38	1.62	2.77	1.37
3	5.03	4.93	4.92	4.45	3.7	3.58	2.61	3.37	2.9	2.46	5.69	3.08	4.53	3.34
4	5.84	6.39	5.1	5.01	5.66	4.53	4.87	4.30	3.42	2.92	4.60	4.49	6.05	5.75
5	5.87	7.42	4.2	5.31	5.96	5.46	5.4	5.09	4.86	5.20	5.04	5.32	5.71	7.67
6	7.19	7.73	3.43	5.36	6.55	5.87	6.28	5.56	5.98	5.59	6.52	5.64	5.54	7.35
7	7.15	7.55	4.1	4.55	5.88	5.67	6.02	5.45	4.90	5.30	4.79	5.57	6.3	7.68
8	7.10	6.55	2.71	4.30	5.58	4.98	5.39	4.81	4.14	4.23	4.44	4.30	4.97	5.99
9	5.84	5.29	5.29	4.09	4.24	3.59	5.78	4.03	2.67	2.62	4.64	2.91	4.55	3.81
10	4.65	3.57	4.57	3.27	2.30	2.25	2.53	2.97	2.34	1.31	1.49	1.50	1.85	1.90
11	3.18	2.31	3.24	2.33	1.31	1.33	3.16	1.93	0.45	0.56	0.78	0.92	1.21	0.56
12	1.35	1.77	3.22	1.98	1.09	0.89	1.88	1.48	0.35	0.26	0.48	0.66	0.11	0.17
The average for the year	4.86	4.92	4.12	3.86	3.94	3.46	3.99	3.61	2.75	2.67	3.52	3.10	3.65	3.83

Analysis of the data obtained showed that the minimum level of solar radiation was recorded in St. Petersburg (0.63 kWh/m^2, January 2015), and the maximum in Astrakhan (7.15 kWh/m^2, July 2015).

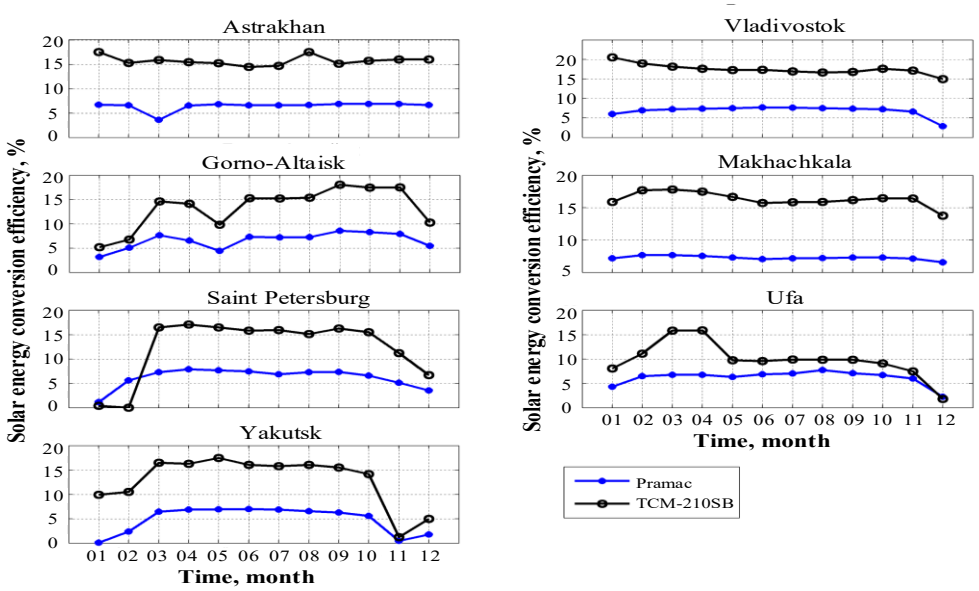


Figure 3. Solar energy conversion efficiency by month

Also, for the studied PVM, an analysis and comparison of the effectiveness of the transformation of solar energy for the period from January 2015 to December 2015 (Fig. 4) was analyzed. From the figure, it follows that this indicator for Pramac PVM changes in the range from 0.08% (Yakutsk, January 2015) to 7.74% (Vladivostok, June 2015). For the TCM-210SB PVM, this indicator varies in the range of 0.43% (St. Petersburg, January 2015) to 20.56% (Vladivostok, January 2015).

The efficiency of solar energy conversion for the southeastern part (Vladivostok) and the southwestern part of the Russian Federation (Astrakhan, Makhachkala) increases to a maximum in the winter-spring period. For Pramac PVM these values are 6.02-7.5%, and for TCM-210SB PVM 15.26-20.56%. In summer, this indicator varies in the range of 6.61-7.05% for Pramac PVM and 14.5-18.08% for TCM-210SB PVM. In hot summers, the PVM surface is heated to 40-45^{0}C, which will lead to a significant decrease in the efficiency of solar energy conversion by 5-10% of the nominal value [7]. In the autumn period, as the temperature decreases, a slight increase in the considered indicator for PVM is observed.

In the conditions of the southern part of Siberia (Gorno-Altaisk), the efficiency of solar energy conversion for Pramac PVM ranges from 3.02% (January 2015) to 8.7% (September 2015), and for TCM-210SB PVM from 5.02% (January 2015) 18.08% (September 2015). The maximum of this PVM indicator is observed in the autumn period around 17.5% for the TCM-210SB PVM and 8% for the Pramac PVM. In winter, this figure for Pramac PVM decreases to 3-5%, and for TCM-210SB PVM to 5-10%. This is explained by a possible increase in the number of cloudy and rainy days, which is typical for the climate of Gorno-Altaisk, and the presence of snow cover on the surface of the PVM. In spring, there is a significant increase in the solar energy conversion efficiency of PVMs up to 7.5% for Pramac PVMs, and 14.5% for TCM-210SB PVMs. In summer, this figure is at the level of 7.5% for Pramac PVM and 15% for TCM-210SB PVM.

In the conditions of the central zone of the Russian Federation (Ufa), the average values of the solar energy conversion efficiency of thin-film PVM in the summer months were

https://doi.org/10.5593/sgem2024/4.1/s17.09

in the range of 6-7.7%, in the winter 2-6%, while the average value for the year was 6.19%. The average value of the indicator for PEMs based on silicon wafers was 9.86%. In summer, a change in the efficiency of solar energy conversion was recorded within the range of 9.5-9.8%. In winter, this figure is in the range of 2-7%. It should be noted that starting from May 2015, due to burnout of metal contacts and partial short-circuiting of metal contacts of the PVM TCM-210SB, a decrease in efficiency indicators by 40% of the nominal value (17.34%) was recorded. At the same time, in other monitoring cities across Russia, the TCM-210SB PVM works properly, which makes it possible to assume that there is a defect in this particular module. A more detailed analysis of the effectiveness of using PVM for the climatic conditions of the central zone of the Russian Federation was carried out in works [7,9].

For the northeast of the Russian Federation (Yakutsk), the efficiency of solar energy conversion in summer for PVM was in the range of 6.3-6.9%, in winter this figure is in the region of 0.1-2%. For PVM TCM-210SB, a change in the indicator was recorded within the range of 15-17% in summer and 5-10% in winter. The average annual value of the indicator for PVM Pramac is 4.76%.

An analysis of solar energy conversion efficiency indicators in the conditions of the northwestern part of the Russian Federation (St. Petersburg) was also performed. In the summer, the values of the considered indicator for the Pramac PVM were 7-7.7%, and for the TCM-210SB PVM, they varied in the range of 16-17%. In winter, this figure for the Pramac PVM was in the range of 1.2-6%, and for the TCM PVM-210SB 0.5-7%.
For Pramac PVM, solar energy conversion efficiency values varied in the range of 1.2% to 7.46%, with an average value for the entire monitoring period of 6.16%. For the TCM-210SB solar panel, the specific energy production values ranged from 0.5% to 16, with an average value for the entire monitoring period of 12.26%. The change in the annual efficiency of solar energy conversion for the studied PVMs is shown in Fig. 4.

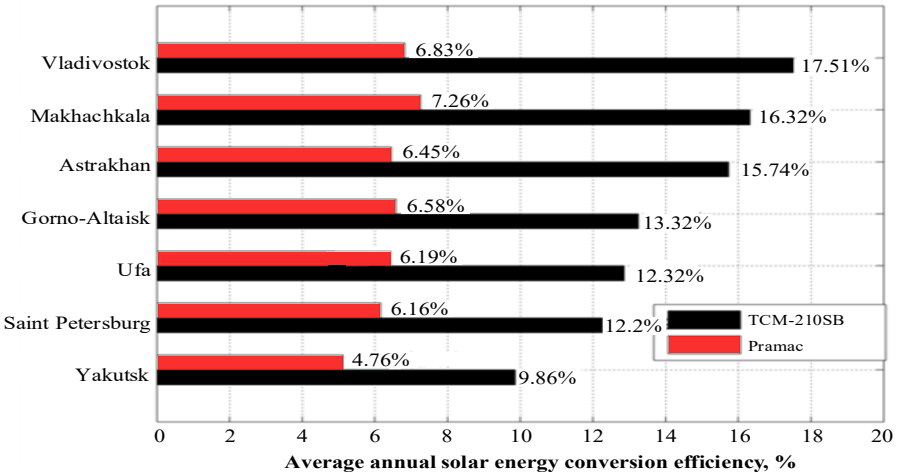


Figure 4. Average annual solar energy conversion efficiency

From Fig. 4 it follows that the average annual solar energy conversion efficiency for Pramac PVM is in the range of 0.6 (Yakustk) to 0.85 (Vladivostok), with the average value for all regions being 0.81 of the nominal value. For PVM TCM-210SB this indicator varies from 0.7 (St. Petersburg) to 1.01 (Vladivostok), with an average annual value of 0.81 from the nominal value.

During the experiment, an analysis of specific energy production indicators for the studied PVMs from January to December 2015 was also carried out.
Specific energy production in the climatic conditions of the southwestern part of the Russian Federation (Astrakhan, Makhachkala) varies from 32 kWh (January 2015) to 172 kWh (July 2015), with an average annual value of 105.94 kWh for thin-film PVM. The specific energy output for PVM based on crystalline silicon ranges from 38 kWh (January 2015) to 186 kWh (July 2015), with the average annual specific energy output for this module being 119 kWh. In summer, the specific energy production value for the Pramac PVM is 128-186 kWh, and for the TCM-210SB PVM is 163-172 kWh. In winter, the specific energy production for the Pramac PVM is in the range of 32-64 kWh, and for the TCM-210SB PVM, it is 52-71 kWh.

The value of specific energy production in the climatic conditions of Vladivostok varies from 21 kWh (January 2015) to 108 kWh (June 2015) for the Pramac FEM, and for the TCM-210SB FEM from 80 kWh (July 2015) to 153 kWh (August 2015). The average annual value of specific energy production is 81 kWh for the Pramac FEM, 121 kWh for the TCM-210SB FEM (Fig. 5).

Specific energy production in the climatic conditions of Gorno-Altaisk varies in the range from 16.34 kWh (January 2015) to 154 kWh (June 2015), with an average annual value of 81 kWh for Pramac PVM. For PVM TCM-210SB, the value of specific energy production varies from 28 kWh (January 2015) to 164 kWh (May 2015), with the average annual value being 86 kWh.

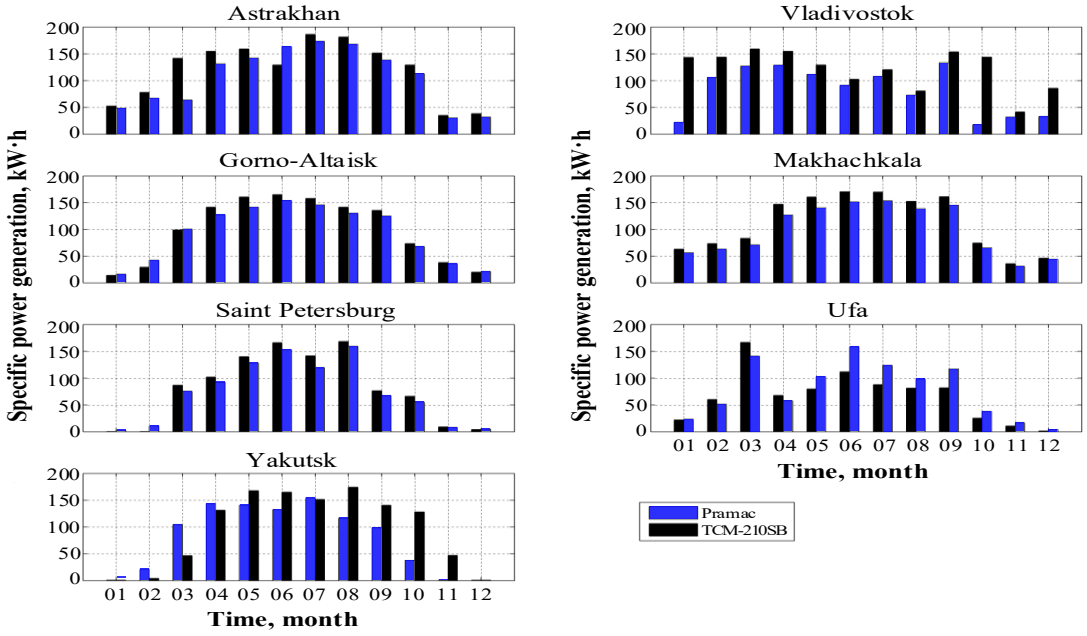


Figure 5. Specific energy production by month

In the climatic conditions of the northwestern part of the Russian Federation (St. Petersburg), the average value of specific energy production for the Pramac PVM was 67 kWh, and for the TCM-210SB PVM, it was 73 kWh. In winter, the solar energy conversion efficiency for the Pramac PVM was in the range of 4-10, and for the TCM PVM-210SB in the range of 0.5-4, respectively. In summer, the average values of specific energy production changed from 128 kWh (May 2015) to 160 kWh (July 2015)

https://doi.org/10.5593/sgem2024/4.1/s17.09

for the Pramac PVM, and for the TCM-210SB PVM from 140 kWh (May 2015) to 166 kWh (June 2015).

The average value of specific energy production in the conditions of Ufa for the Pramac PVM is in the region of 72-75 kWh and for the TCM-210SB PVM in the range of 79-81 kWh. In winter, a change in the specific energy output for thin-film PVMs was recorded in the range of 10-21 kWh, and for PVMs based on crystalline silicon in the range of 20-32 kWh. During the summer observation period, the maximum specific energy production for the Pramac PVM was 153 kWh (June 2015), and for the TCM-210SB PVM 163 kWh (June 2015). In summer, specific energy production fluctuates in the range of 100-153 kWh for the Pramac PVM, and in the range of 130-165 kWh for the TCM-210SB PVM.

Despite the severe cold weather in the northeastern part of the Russian Federation (Yakutsk), the energy indicators of PVM are in no way inferior to other regions. In the climatic conditions of Yakutsk in summer, the specific energy production for the Pramac PVM reaches up to 153 kWh (July 2015), and for the TCM-210SB PVM, it was 165 kWh (July 2015). In winter, a change in the specific energy production for the Pramac PVM is observed in the range of 6-8 kWh, and for the TCM-210SB PVM in the range of 5-9 kWh. The average annual value of specific energy production for a thin-film PVM is 71 kWh, and for a TCM-210SB PVM, it is 81 kWh.

CONCLUSION

1. Analysis of the distribution of solar radiation power on the territory of the Russian Federation allowed us to draw the following conclusions:
- maximum values of solar insolation are observed at low latitudes (Astrakhan, Vladivostok, Makhachkala, Gorno-Altaisk). As the latitude of the area increases, the amount of solar radiation decreases (Ufa, Yakutsk, St. Petersburg).
- the average value of solar radiation in remote northern regions is 810 kWh/m^2, in the southern regions it is in the range of 1350-1400 kWh/m^2.

2. The technical potential for using solar energy is very high, the most favorable are the southwestern and southeastern regions of the country.

3. As part of the study, it was established that the efficiency of solar energy conversion of PVMs in the climatic conditions of the Russian Federation is in the range from 60% to 85% of the nominal value.

REFERENCES

[1] Nizhegorodtsev. R.M., Ratner S.V., Trends in the development of industrially developed renewable energy technologies: the problem of resource limitations / Thermal Energy, 2016, No. 3, pp. 43-53.
[2] Asanov M.S., Safaraliev M.Kh, Zhabudaev T.Zh, et al. Algorithm for calculation and selection of micro hydropower plant taking into account hydrological parameters of small watercourses mountain rivers of Central Asia / International Journal of Hydrogen Energy, 2021, No 75, pp. 37109-37119.

[3] Manusov V., Matrenin P., Nazarov M., et al. Short-Term Prediction of the Wind Speed Based on a Learning Process Control Algorithm in Isolated Power Systems / Sustainability, 2023, No 2, Art. 1730.
[4] Bumtsend U., Safaraliev M., Ghulomzoda A., et al. The Unbalanced Modes Analyze of Traction Loads Network / Ural Symposium on Biomedical Engineering, Radioelectronics and Information Technology (USBEREIT), Russia, 2020, pp. 0456-0459.
[5] Climate zones of Russia. Available online: https://gotonature.ru/1556-klimaticheskie-poyasa-rossii.html.
[6] Kerimov I.A., Debiev M.V., Magomadov. A.M., et al. Solar and wind energy resources of the Chechen Republic / Engineering Bulletin of the Don, 2012, No. 1, pp. 302-312.
[7] Ismagilov F.R., Gaysin. B.M., Sharifov B.N., Teregulov T.R., Investigation of the efficiency of solar photovoltaic installations in the climatic conditions of the Republic of Bashkortostan / Bulletin of the Ufa State Aviation Technical University, 2016, No. 2, pp. 111-116.
[8] Sharifov B.N., Teregulov T.R., Modeling a solar panel in Matlab/Simulink / Bulletin of the Ufa State Aviation Technical University, 2015, No. 4, pp. 77-83.
[9] Ismagilov F.R., Sattarov R.R., Gaysin B.M., et al. Study of the characteristics of autonomous sources of electricity based on photoelectric modules in the conditions of middle latitudes of Russia / Elektrotechnique complexes and systems, 2015, No. 1, pp. 51-57.
[10] Voronin S.M., Taran A.A., Autonomous power supply system based on a solar power plant / Mechanization and electrification of agriculture, 2007, No. 3, pp. 24-25.

https://doi.org/10.5593/sgem2024/4.1/s17.09

ESTIMATION OF WAVE POWER AND RECENT DECADAL CHANGES IN BULGARIAN BLACK SEA NEARSHORE AREA

Assoc. Prof. Dr. Nikolay Valchev[1]

[1] Institute of Oceanology – Bulgarian Academy of Sciences, **Bulgaria**

ABSTRACT

The study deals with estimation of theoretical wave power resources and their spatial variability in transitional waters along the Bulgarian Black Sea coast. It is based on wave climate data obtained by means of hindcast of wave conditions during 2013-2022. Numerical simulations were performed using the third-generation spectral wave model SWAN and the theoretical wave power was computed using the spectral output in terms of energy transport per unit of the wave crest length. Estimates for wave power means and maxima as well as for the total wave energy are presented for twenty locations along the study area. They assert the high spatial variability of wave power as well as its slight decrease compared to the previous decade. Results point out changes in wave energy potential compared to previous decade expressed in a minor decrease along almost the entire Bulgarian Black Sea nearshore area.

Keywords: renewable energies, theoretical wave power, wave exposure

INTRODUCTION

The Ocean is a huge energy reservoir. Ocean energy can be derived from tides, currents, waves, thermohaline gradients and its chemical composition. The external energy input to the geobiosphere is considered renewable to contrasting to the internal one (non-renewable). The main external sources are solar energy. Through processes in the atmosphere-ocean boundary layer, solar energy generate secondary– winds and tertiary renewables – wind waves. Among these options, perhaps the most challenging is collection of energy from the waves [1].

Wave energy alongside the energy harvested from winds have a key role in meeting world's necessity for renewable sources. It is in abundance and although not as easily predictable as the tidal power, wave forecast is more reliable than wind or solar energy [2]. As of 2023, wave power is not widely employed for commercial applications, after a long series of experimental projects. Attempts to use this energy reportedly began in 1890 or even earlier [3], mainly due to economic reasons. Certainly, wave energy is profitable since the power density is much compared to other renewable sources, which allows collection of more quantity out of a smaller surface [4]. Just below the ocean water surface the wave energy flow, in time-average, is typically five times denser than the wind energy flow 20 m above the sea surface, and 10 to 30 times denser than the solar energy flow.

Capacity of the global wave energy potential is calculated to 3.702 TW, which is limited to deep water off the coastlines. Thus, excluding low-energy coastlines as well as areas, which may experience ice coverage, the above estimation drops drastically to 2.985 TW in comparison to earlier estimation [5]. Therefore, the main goal of this paper is to

https://doi.org/10.5593/sgem2024/4.1/s17.10

evaluate theoretical wave power resource along the Bulgarian Back Sea coast as inferred by recent wave climate and to highlight changes compared to previous periods.

Wave climate is a unique combination of mesoscale processes in the atmospheric-ocean boundary layer and influence of the local geomorphic settings. It often exhibits significant short-term, monthly, seasonal, and inter-annual variation. Climate can be evaluated based on systematic and continuous measurements, application of numerical models or joint use of both approaches. The result is a series of representative data on the sea states. Long-term direct wave measurements in the Black Sea are insufficient to obtain representative climatic characteristics. The same largely applies to satellite (altimetry) measurements, which have been actively used in the last few decades. They suffer partial coverage and not sufficiently high for estimation of local wind and wave climate resolution, particularly near the coast [6]. Since the amount of wave energy that can be collected by contemporary WECs varies depending on location and weather conditions, the most effective method for assessment of energy potential is reconstruction of the past wave climate. Usually, it is done by means of wave modelling forced with gridded data of atmospheric fields - wind and atmospheric pressure – that is by hindcasting. Notable example is the study of global wave energy resources based on hindcasting [7]. Such an assessment for the Black Sea was done in [8, 9, 10]. These studies reveal western and south-western shelf of the Black Sea as particularly perspective in terms of wave energy potential.

MATERIALS AND METHODS

Waves are generated by wind blowing over the sea surface. If the waves propagate slower than the wind speed just above them, an energy transfer from the wind to the waves takes place. Both air pressure differences between the upwind and the lee side of a wave crest and wind friction on the water surface, producing shear stress, cause the growth of the waves [11]. Sea state properties have a random nature. The waves in a sea state may differ in shape, height, frequency, and direction of propagation. Hence, wind waves can be described as a stochastic process, in combination with the physics governing their generation, growth, propagation and decay. For description of the wave climate in a certain area, temporal, directional and spectral characteristics are used, which are preconditioned by the wave spectrum of the individual sea states.

To achieve the study goal, recent wind wave climate was estimated by means of hindcasting spanning a period of 10 years (2013-2022) using the wind fields obtained with GFS global atmospheric model at 0.5 resolution [12]. Wind wave properties were obtained by numerical modelling of wave conditions on the western Black Sea shelf. To this end, a coupled system of third generation spectral wave models WAM-SWAN was employed. The SWAN Cycle III model, version 40.91 [13] was set up for wave simulations in the western shelf area at a horizontal resolution of about 3 km. SWAN was run in the third-generation mode accounting for the following deep and shallow water processes: generation by wind; dissipation by whitecapping, bottom friction and depth-induced breaking; and non-linear wave-wave interaction (quadruplets and triads). Details on the model set-up and validation are described in [14]. The availability of long-term numerical simulations allowed for extraction multi-annual time series of various wave properties, which were statistically processed.

Herein, theoretical wave power resource was computed using the spectral output of the numerical wave model as energy transport per unit of the wave crest length, given in kW m^{-1} [13]:

$$P_w = \rho g \int_0^{2\pi} \int_{\sigma_{min}}^{\sigma_{max}} c_g \, S(\sigma, \theta) \, d\sigma d\theta \quad (1)$$

where ρ is sea water density; g – acceleration of gravity; $S(\sigma,\Theta)$ – directional wave variance density spectrum; c_g – wave group velocity; σ – wave frequency; Θ – direction of the spectral components propagation.

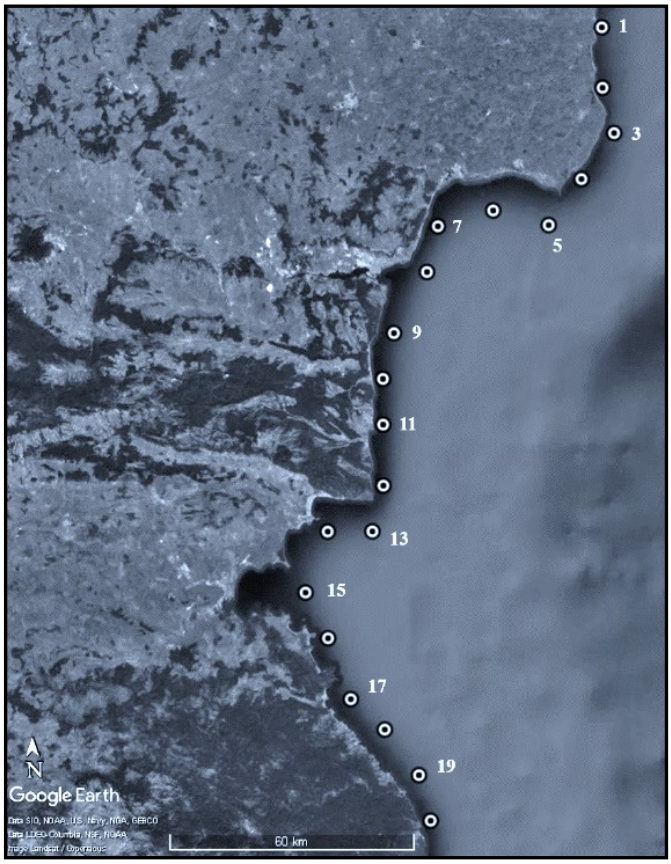


Figure 1. Scheme of the study area and location of points for which theoretical wave power resource are estimated

The evaluation the wave energy potential is further based on the wave climate assessment in terms of significant wave height (H_S) and wave energy period (T_E). For this purpose, the continuous wave time series were divided into two-dimensional clusters, as each of them covers H_S and T_E bands with discretization of 1 m and 0.5 s, respectively. Thus, each cluster represents regimes with different wave energy potential. Mean annual P_W was estimated for each wave cluster. Additionally, probability of occurrence for waves falling in each (H_S–T_E) cluster was determined as well as the duration in hours of each wave regime within a statistical year. Statistical year is an engineering concept according to which the whole data temporal coverage is squeezed to duration of a year in a way that the wave action in each cluster takes place during a certain number of hours depending on the corresponding frequency of occurrence. Thus, the total wave energy E_W was obtained.

https://doi.org/10.5593/sgem2024/4.1/s17.10

Temporal variability of wind climate at each point is characterized in terms of seasonal variability (*SV*) and monthly variability (*MV*) of wave power resource. The lower the values of these indices the more stable the wave power potential and the more appropriate a site is for location of WEC. *MV* and *SV* are defined as follows [10]:

$$MV = \frac{P_{max,M} - P_{min,M}}{P_{year}} \ [\text{kW m}^{-1}] \quad (2)$$

$$V = \frac{P_{max,S} - P_{min,S}}{P_{year}} \ [\text{kW m}^{-1}] \quad (3)$$

where $P_{(max,M)}/P_{(max,S)}$ and $P_{(min,M)}/P_{(min,S)}$ are the mean wave power in the most and less energetic month/season in a statistical sense, while P_{year} is the mean annual estimate of the wave power.

The study area comprises the shallow shelf and coastal zone along the Bulgarian Black Sea seaside. The theoretical wave power resource is estimated for twenty points indicated in Fig. 1. They are almost evenly distributed to form a strip along the coastline at offshore distances varying between 2 and 10 km with water depths in the range of 20 to 70 m (Table 1). Except for points 14 and 19, all other points are in transitional waters.
In the western Black Sea, considerable seasonal variability is the most marked feature of wind and wave climate. Winds from the eastern quarter are important for wave generation as northeastern are predominant. Following wind pattern, high waves most frequently propagate from northeast, east and southeast [14].

RESULTS AND DISCUSSION

Detailed information about theoretical wave power resource and its seasonal and monthly variation for all selected locations is presented in Table 1. Results show that wave power resources vary in broad range from 0.12 to 2.02 kWh m^{-1} (for means) and from 12.55 to 140.56 kWh m^{-1} (for maxima) thus indicating the large spatial variability of theoretical wave power in Bulgarian Black Sea territorial waters. The same is valid for the total wave energy, which theoretical quantity ranges between 1.18 and 17.63 MWh m^{-1}.

The most and the less energetic seasons over the investigated period were winter and summer, respectively. Winter season includes December, January, and February, while summer months are June, July and August. The most energetic month is January, while the less energetic one is June. Prevailingly, values of $P_{(max,M)}$–$P_{(min,M)}$ and $P_{(max,S)}$–$P_{(min,S)}$ considerably surpass P_{year}. As a result, seasonal and monthly variability indices are greater than one, which suggest large inter-seasonal and intra-annual variability of wave energy (Table 1). In addition, it is noticed that the wave power maxima exceed the means 70-90 times. These circumstances significantly reduce the accessibility to wave energy resources and hampers their reliable integration into energy-transmission systems due to low efficiency of WECs operation.

Distribution of theoretical wave power resources by significant wave height bands is presented in Fig. 2. For almost all locations the most energetic wave band is $1 \leq H_s < 2$ m. The energy content in this band varies from 24 to more than 40% (point 9). The exceptions are five points for which the theoretical wave power is less than 0.5 kW m^{-1} (points 5-7, 8 and 14). The reason is they are situated in sheltered areas with pronounced shoaling, which determines marked wave transformation relatively far from the shore. The

maximum wave energy content in bands of $H_S \geq 3$ m is 34.4% for the most southern point of the strip and decreases irregularly northward. The amount of wave power contained in the bands of $H_S < 3$ m is 16.38 kW m^{-1} and in those of $H_S \geq 3$ m – 4.67 kW m^{-1}, i.e. 3.5 times lower.

Table 1. List of examined locations with their offshore distance (L_{off}), key wave properties – significant wave height (H_S) and wave energy period (T_E) maxima, as well as theoretical wave power (P_W) means and maxima, total wave energy (E_W) and their seasonal (*SV*) and monthly (*MV*) variability

Point		L_{off}	H_S max	T_E max	P_W [kW m^{-1}]		E_W [MWhm^{-1}]	SV	MV
No	Location	[km]	[m]	[s]	mean	max	mean	-	-
1	Durankulak	2.5	6.15	8.1	1.16	89.60	10.17	0.92	1.22
2	Shabla	2.5	6.20	8.2	1.17	90.28	10.25	0.92	1.22
3	Tyulenovo	4.0	6.20	8.1	1.16	89.62	10.16	0.92	1.22
4	Rusalka	2.5	6.10	7.8	1.14	88.11	10.13	0.92	1.22
5	Kaliakra	9.0	2.95	7.0	0.20	13.98	1.78	1.00	1.00
6	Balchik	8.0	3.02	6.7	0.21	16.32	1.90	0.65	0.82
7	Golden sands	4.0	3.59	7.3	0.28	27.24	2.64	0.35	0.70
8	Sunny day	6.0	4.45	7.1	0.60	50.52	5.27	0.65	0.95
9	Pasha dere	4.5	4.76	7.1	0.63	54.11	5.59	0.90	1.25
10	Shkorpilovtsi	3.0	5.22	7.3	0.75	60.07	6.62	1.02	1.35
11	Byala	3.0	5.62	7.4	1.06	83.74	9.54	0.92	1.22
12	Obzor	3.5	6.08	7.9	1.25	91.24	11.16	1.10	1.35
13	Emine	7.0	6.16	8.0	1.27	92.36	11.34	1.10	1.35
14	Nesebar	5.0	2.65	5.5	0.12	12.55	1.18	0.95	1.15
15	Pomorie	10.5	5.48	8.0	0.88	72.07	7.76	0.90	1.25
16	Kavatsite	5.0	6.20	8.3	1.36	108.03	12.15	1.00	1.35
17	Primorsko	7.0	6.15	8.1	1.55	130.42	13.59	1.10	1.45
18	Tsarevo	7.5	6.36	8.3	1.81	139.50	15.72	1.20	1.50
19	Sinemorets	6.5	6.72	8.4	2.01	139.70	17.55	1.20	1.50
20	Rezovo	3.0	6.74	8.5	2.02	140.56	17.63	1.20	1.50

A large spatial variability of the mean wave power is observed following well-pronounced alteration along the shore. The highest potential is marked in the endmost northern (1-4), central (9-13) and southern (15-20) parts of the study area, which are exposed to the winds with the largest fetch and persistence – those of the eastern quarter. This allows for full development of wave field and low rate of wave transformation even close to the shore, especially to the south.

In between, lower energy potential areas stretch, which are confined predominantly within Varna and Burgas bays and the adjacent areas but are also sheltered by jutted out capes such as Kaliakra and Emine as well as by Pomorie peninsula. This highlights the importance of the local geomorphic settings such as shelf width and depth, shoaling conditions, and coastal slope, which may considerably influence the wave field transformation, e.g. by refraction or bottom friction. In the above cases, waves start their transformation relatively far from the shore and as a result, waves arrive at the selected

https://doi.org/10.5593/sgem2024/4.1/s17.10

locations already smaller in height and with lower energy potential. This is particularly valid for points 5-7 and 14-15.

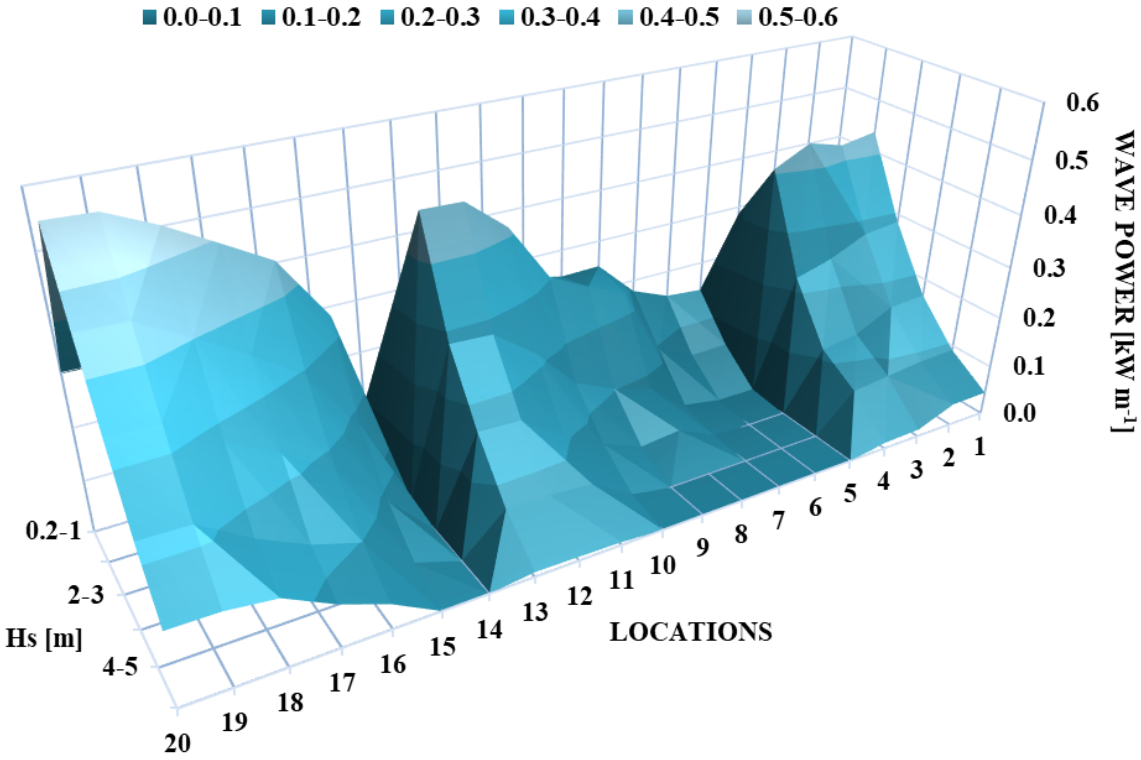


Figure 2. Mean wave power in [kW m^{-1}] by significant wave height bands

Compared to recent studies, a minor decrease of wave power is detectable along almost the entire Bulgarian Black Sea coastal area, which is most pronounced for locations 9-13. Nevertheless, wave power marks an increase for locations 3, 4, and 16. These results conform very well with findings about the wave exposure of the Bulgarian Black Sea coast [14].

CONCLUSION

This study provides an insight into the recent theoretical wave power resources and its spatial pattern along the Bulgarian Black Sea coast. To this end, wave hindcast data spanning 10-yr period were processed to obtain estimates of mean wave power and total wave energy at twenty locations situated in transitional waters. Results shows that mean wave power varies in broad range from 0.12 to 2.02 kW m^{-1}, while the total wave energy quantity ranges between 1.18 and 17.63 MWh m^{-1}. A large spatial variability of the mean wave power is observed, which is defined by distinct alteration of wave energy potential along the shore. The highest potential is marked in the endmost northern, central, and southern parts of the study area. Main role in spatial variability pattern plays wind and wave climate but nonetheless the local geomorphic settings such as shelf width and depth, shoaling conditions, and coastal slope, which may considerably influence the wave field transformation and subsequent energy dissipation. The study highlights changes in wave energy potential compared to previous decade. It finds expression in a slight decrease of the order of 4-5% detected along almost the entire Bulgarian Black Sea coastal area,

which is most pronounced for the stretch Pasha dere – Emine. Nevertheless, wave power marks an increase in the areas surrounding Tyulenovo, Rusalka and Kavatsite.

ACKNOWLEDGEMENTS

The study has been performed within the project "Coastal HYdro-Morphological Regime changes in mAn-modified environment – CHYMERA", funded by Bulgarian National Science Fund under the Ministry of Education and Science of Republic of Bulgaria, Contract No КП-06-Н54/8/01.12.2021.

REFERENCES

[1] Odum H.T., Handbook of eMergy Evaluation: eMergy of Global Processes, University of Florida, Environmental Engineering Sciences, Center for Environmental Policy, 2000, p 29;

[2] Tucker M.J., Pitt E.G., Waves in ocean engineering, New York: Elsevier, 2001, p 548;

[3] Miller C., A Brief History of Wave and Tidal Energy Experiments in San Francisco and Santa Cruz, 2004, http://www.outsidelands.org/wave-tidal3.php;

[4] Thorpe T.W., A Brief Review of Wave Energy, Report ETSU-R120. Department of Trade and Industry, 1999, p 187;

[5] Mørk G., Barstow S., Kabuth A.K., Pontes M.T., Assessing the global wave energy potential, 29th Int. Conf. on Ocean, Offshore Mechanics and Arctic Engineering, Shanghai, China, 2010, p 9, DOI: 10.1115/OMAE2010-20473;

[6] Vignudelli S., Cipollini P., Roblou L., Lyard F., Gasparini G., Manzella G.M.R., Astraldi M., Improved satellite altimetry in coastal systems: case study of the Corsica Channel (Mediterranean Sea), Geophys. Res. Lett., vol. 32, L07608, doi:10.1029/2005GL022602, p 5, 2005;

[7] Cornett, A.M., A Global Wave Energy Resource Assessment, 18th International Offshore and Polar Engineering Conference, Vancouver, Canada, Paper No. ISOPE-2008-TPC-579, 2008, p 9;

[8] Valchev N., Andreeva N., Valcheva N., Assessment of offshore wave energy in the Black Sea on the basis of long-term wave hindcast. In: Developments in Maritime Transportation and Exploitation of Sea Resources (Soares, C.G. & López Peña, F., Eds.), CRC Press: Taylor and Francis Group, London, 2014, ISBN:978-1-138-00124-4, pp 1021-1027;

[9] Akpınar A., Bingölbali B., van Vledder G.Ph., Long-term analysis of wave power potential in the Black Sea based on 31-year SWAN simulations, Ocean Eng., vol. 130, pp 482-497, 2017;

[10] Rusu L., Ganea D., Mereuta E., A joint evaluation of wave and wind energy resources in the Black Sea based on 20-year hindcast information, Energy Exploration & Exploitation, vol. 36/issue 2, pp 335–351, 2018;

[11] Holthuijsen L.H., Waves in oceanic and coastal waters, Cambridge University Press, 2007, p 387.

https://doi.org/10.5593/sgem2024/4.1/s17.10

[12] Wang J.A., Sardeshmukh P.D., Compo G.P., Whitaker J.S., Slivinski L.C., McColl C.M., Pegion P.J., Sensitivities of the NCEP Global Forecast System, Mon. Wea. Rev., vol. 147, pp 1237–1256, 2019, https://doi.org/10.1175/MWR-D-18-0239.1;

[13] SWAN Team, SWAN Cycle III version 41.31, User Manual, Delft University of Technology, Delft, The Netherlands, 2021;

[14] Valchev, N., Andreeva N., Prodanov B., Valcheva N., Eftimova P., Spatial and multiannual alteration of wave exposure along the Bulgarian coast as inferred by numerical modelling of wave energy transfer, Proc. of 23rd International Multidisciplinary Scientific GeoConference SGEM 2023, Bulgaria, vol. 23/issue 3.1, 2023, pp 149-158.

EXPERIMENTAL MODEL FOR ANALYZING HYDROGEN EXPLOSIONS WITH THE MODIFICATION OF PROPAGATION DIRECTION

Eng. Ligia Ioana Tuhut[1]

Eng. Andrada Matei[1]

PhD. Eng. Vlad-Mihai Pasculescu[1]

PhD. Eng. Daniel-Gheorghe Florea[1]

PhD. Eng.Bogdan Adrian Simon-Marinica[1]

[1]Institutul Naţional de Cercetare-Dezvoltare pentru Securitate Minieră şi Protecţie Antiexplozivă -INSEMEX Petroşani, **Romania**

ABSTRACT

In this study, we present the design and implementation of an experimental stand tailored for the analysis of hydrogen explosions with the capability of modifying the propagation direction.

Hydrogen explosions pose significant safety concerns in various industrial settings, and understanding their behavior under different conditions is crucial for risk assessment and mitigation strategies. The experimental setup integrates precise control mechanisms to manipulate the direction of explosion propagation, allowing for systematic investigation of explosion dynamics and their effects on surrounding environments.

We describe the key components of the experimental stand, such as the ignition mechanism, confinement chamber, and data acquisition system, including Schlieren techniques mainly used for capturing images of the flame front behavior.

Additionally, we outline the experimental procedures for conducting controlled explosion tests with varying propagation directions. The versatility of the experimental stand enables researchers to explore diverse scenarios and assess the impact of propagation direction on explosion characteristics such as pressure dynamics and flame velocity. Through comprehensive analysis of experimental results, insights can be gained to enhance the safety measures and design considerations for hydrogen handling facilities and related industrial processes

Keywords: hydrogen, explosion, Schlieren, risk, experiment

INTRODUCTION

Hydrogen, hailed as the most abundant element in the universe, has garnered significant attention due to its potential as a clean and efficient energy carrier. Its properties, such as high energy content and environmentally friendly combustion byproducts, make it a promising candidate for various applications, including fuel cells, transportation, and industrial processes. However, the safe handling and utilization of hydrogen are crucial, given its flammable nature and the associated risks, particularly concerning explosion hazards.

https://doi.org/10.5593/sgem2024/4.1/s17.11

In recent years, research efforts have focused on understanding the behavior of hydrogen explosions to enhance safety measures and mitigate potential risks. Hydrogen explosions, though rare, can result in catastrophic consequences, making their analysis and prevention paramount. [1] Traditional models for analyzing hydrogen explosions typically consider propagation in a single direction, overlooking potential scenarios where modification of propagation direction may occur due to various factors such as obstacles, ventilation conditions, or geometric constraints. [2]

This paper presents an experimental model aimed at analyzing hydrogen explosions with the modification of propagation direction. By investigating scenarios where hydrogen propagation deviates from the conventional path, we aim to enhance our understanding of explosion dynamics and improve safety protocols. The experimental setup allows for controlled testing under various conditions to simulate real-world scenarios and evaluate the effectiveness of safety measures.

Properties of Hydrogen:

1. **High Energy Content:** Hydrogen has the highest energy content per unit mass of any fuel, making it an efficient energy carrier.
2. **Lightweight:** Hydrogen is the lightest element, which makes it valuable for applications requiring lightweight materials.
3. **Clean Combustion:** When hydrogen combusts, it produces only water vapor as a byproduct, making it environmentally friendly.
4. **Highly Flammable:** Hydrogen is highly flammable and can form explosive mixtures with air within a wide range of concentrations.
5. **Low Density:** Hydrogen gas has low density, which affects its storage and transportation methods.

Uses of Hydrogen:

1. **Fuel Cells:** Hydrogen fuel cells generate electricity through a chemical reaction between hydrogen and oxygen, with applications in vehicles, stationary power generation, and portable devices.
2. **Industrial Processes:** Hydrogen is used in various industrial processes, including petroleum refining, ammonia production for fertilizers, and methanol production.
3. **Transportation:** Hydrogen is being explored as a clean fuel for transportation, including hydrogen-powered vehicles such as cars, buses, trucks, and trains.
4. **Energy Storage:** Hydrogen can be used for energy storage and grid balancing, particularly in conjunction with renewable energy sources like wind and solar power.
5. **Chemical Industry:** Hydrogen serves as a feedstock for chemical synthesis, including the production of hydrogen peroxide, hydrochloric acid, and various organic compounds.
6. **Aerospace:** Hydrogen has historically been used as a propellant in rockets due to its high energy content and lightweight nature.

7. **Food Industry:** Hydrogenation is a process used in the food industry to convert unsaturated fats into saturated fats, improving shelf life and texture of food products.

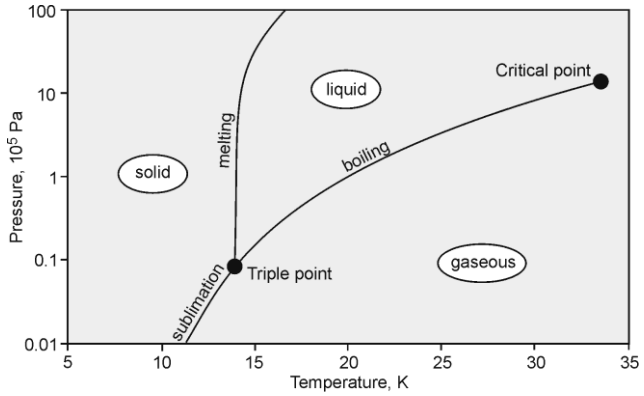


Fig. 1. Phase diagram of hydrogen (Molkov, 2012).

MATERIALS AND METHODS

Application of Schlieren Techniques

Schlieren techniques are optical methods used to visualize density variations in transparent media, such as gases or liquids, that occur due to variations in refractive index. These variations in density typically occur as a result of changes in temperature, pressure, or composition, making Schlieren techniques particularly useful for studying phenomena like shock waves, heat transfer, and fluid dynamics. [3]

In a basic Schlieren setup, a light source, typically a collimated beam of light, is passed through a lens system to produce a parallel light beam. This beam is then directed through the test section, where the density gradients cause slight deviations in the light's path. A knife-edge or other optical component is used to block part of the light beam, creating a shadow that corresponds to the density variations in the test section. A second lens system focuses the light onto a viewing screen or camera, allowing the density gradients to be visualized.

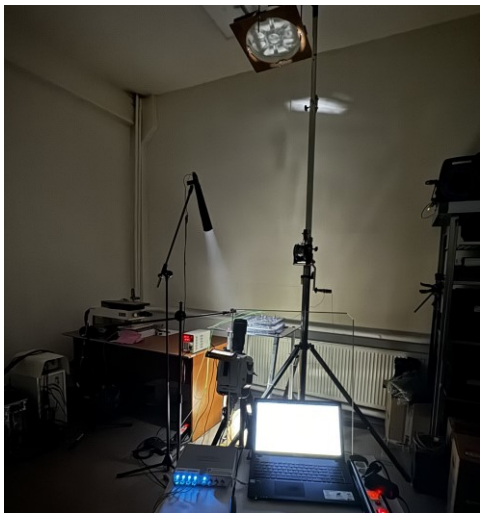


Fig. 2. The Schlieren ensemble used for the stand experiment

https://doi.org/10.5593/sgem2024/4.1/s17.11

To construct an experimental stand for Schlieren imaging, several key components are required:

1. **Light Source**: A bright, collimated light source is essential for generating the parallel light beam needed for Schlieren imaging. This can be achieved using a laser, a high-intensity lamp, or other specialized light sources.

2. Optics: A series of lenses and mirrors are used to collimate and focus the light beam, as well as to direct it through the test section and onto the viewing screen or camera.

3. Test Section: This is the region where the density gradients of interest occur. It may contain the object or phenomenon being studied, such as a shock wave or fluid flow.

4. Knife-Edge or Spatial Filter: This optical component is used to block part of the light beam, creating a sharp shadow that reveals the density variations in the test section.

5. Viewing Screen or Camera: The density gradients visualized by the Schlieren setup can be observed directly on a viewing screen or captured using a camera for later analysis.

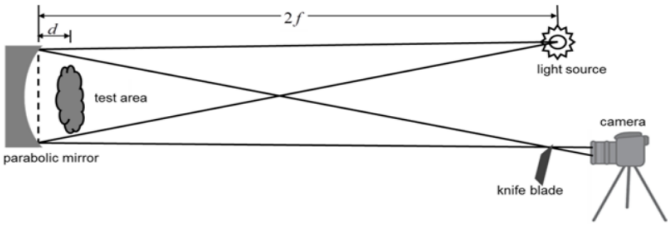


Fig. 3. Simple Schlieren configuration

Development of the stand construction for analysing the hydrogen explosion with modification of propagation direction

The construction of the experimental stand must be carefully designed to ensure alignment and stability of the optical components, as well as to provide access to the test section for introducing experimental setups or samples. Additionally, considerations such as environmental control (e.g., temperature and vibration) may be necessary to minimize disturbances to the measurements.

A square spiral stand, comprising of four interconnected chambers, was developed for conducting physical experiments on air-hydrogen mixture explosions. The experimental model for evaluating the modified propagation of explosions utilized a 20 mm thick sheet of polycarbonate as the construction material as shown in Figure 4.

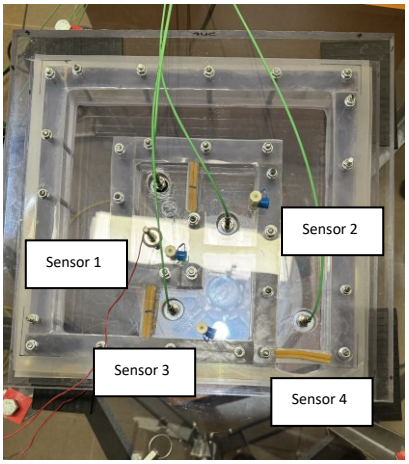


Fig. 4. The polycarbonate model with its corresponding sensors

Polycarbonate was chosen for its transparency and exceptional resistance to shocks and high pressures. [4] Considering the safety precautions for conducting the experiments, the internal section of the explosion tunnel was set at dimensions of 50 x 30 mm.
Given this information, the only limitation was determined by the diameter of the parabolic mirrors utilized in recordings using Schlieren techniques. Therefore, a spiral with 20 mm walls and a 50 mm width was constructed around the ignition chamber, which also houses the source of initiation for the explosive mixture. This spiral extends to the end of a circular portion with a diameter of 412 mm, matching the diameter of the parabolic mirrors shown in Figure 2. The spiral's median line was 1040 mm in length, while its internal volume was 1.56 liters.

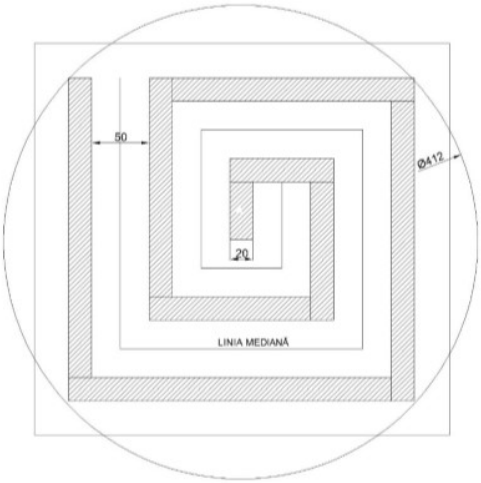


Fig. 5. Construction sketch of the spiral model

To seal the spiral, gaskets were made on the upper and lower closing plates of the model, and at various distances along the median line, three rectangular baffles were also constructed and installed, each consisting of two plates with two holes of 12 mm diameter. [5] Food-grade film was inserted between the plates to separate the spiralled tunnel into distinct chambers (Figure 6).

https://doi.org/10.5593/sgem2024/4.1/s17.11

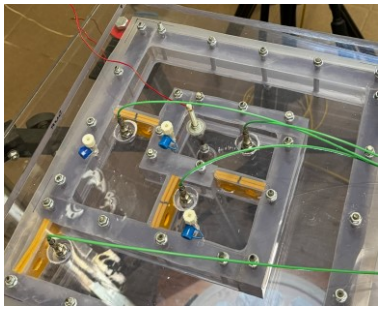


Fig.6. Highlighting the rectangular baffles (yellow colour)

The first chamber, for initiating the air-hydrogen mixture, was equipped with electrodes for generating electric sparks, a capped device for introducing hydrogen, and a pressure sensor (Figures 7 and 8).

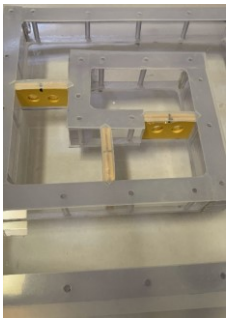


Fig. 7. Mounting the gaskets and the 3 baffles

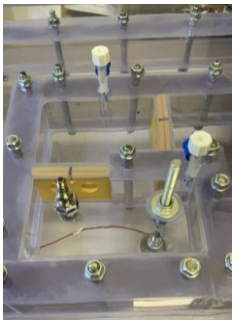


Fig. 8. First chamber

The other two sealed chambers were also equipped with fuel gas loading devices and pressure sensors. The remaining spiral path was intentionally left open to release explosion overpressures.

For charging the chambers with explosive atmosphere, concentrations of 20% volume hydrogen in air were used for loading the three chambers separated by the previously described perforated baffles. The volumes of the three chambers were 157.5 ml (chamber 1), 138 ml (chamber 2), and 193.5 ml (chamber 3), with the rest of the explosion path left open to clean air.

Video recordings were made using a high-speed Phantom camera, at a frequency of 30,000 fps.

RESULTS

The results highlighted the initiation and development of the air-hydrogen mixture explosion and the propagation of the flame front through the three chambers (by rupturing the films of the baffles), the passage of the flame front into the space beyond the baffles, and its extinguishment once the fuel support was consumed.

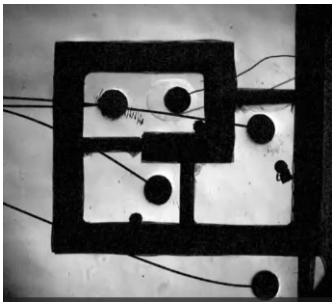


Fig. 9. Initiation of the explosive mixture

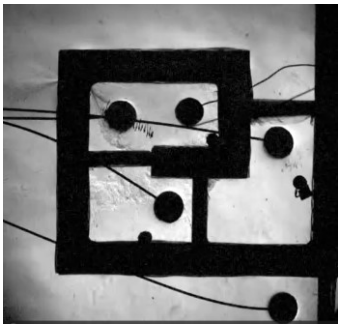


Fig. 10. Propagation of the flame in chamber 2

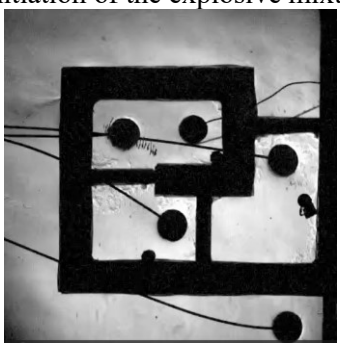


Fig. 11. The advance of the flame front in the third chamber

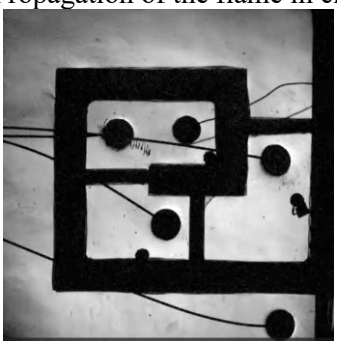


Fig.12. Expansion of the explosion in the last chamber

The graph in Figure 12 displays the recorded pressure values. As we progress along the spiral trajectory, there is a noticeable rise in pressures. Further research could focus on doing a thorough analysis of the characteristics and patterns exhibited by the pressure waves created within the experimental setting. The graph in Figure 13 displays the recorded pressure values. As we progress along the spiral trajectory, there is a noticeable rise in pressures, with the highest pressure recorded by Sensor 3 in chamber 3 (3,56bar).

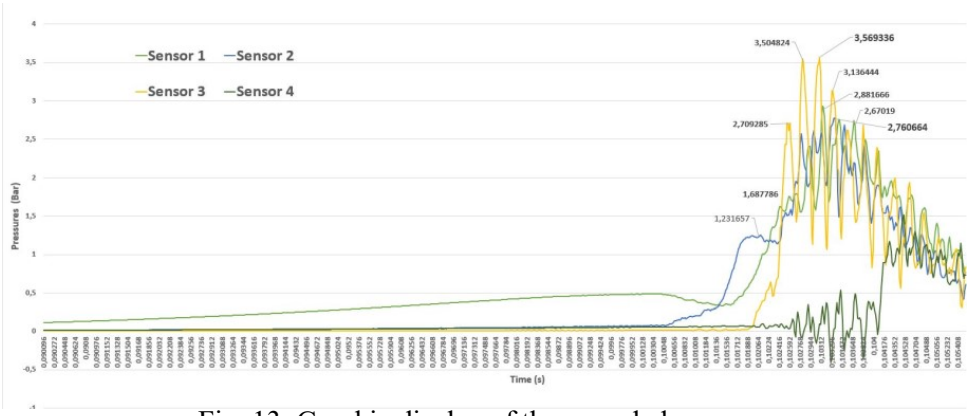


Fig. 13. Graphic display of the recorded pressures

CONCLUSION

The observed initiation and dynamic progression of the air-hydrogen mixture explosion, coupled with the flame front's propagation through the chambers via ruptured baffles' films, strongly validate the efficacy of the experimental setup in accurately simulating real-world explosion scenarios. The passage of the flame front into the space beyond the baffles and its subsequent extinguishment after the fuel support was consumed highlight

https://doi.org/10.5593/sgem2024/4.1/s17.11

the dynamic nature of explosion propagation and the importance of containment measures.

Analysis of the recorded pressure values, particularly the noticeable rise along the spiral trajectory with the highest pressure recorded in chamber 3, underscores variations in explosion intensity and dynamics within the chambers [6].

The findings suggest the need for further research to conduct a thorough analysis of the characteristics and patterns exhibited by the pressure waves created within the experimental setting [7].

Future investigations could focus on refining safety measures and protocols based on a deeper understanding of explosion dynamics and pressure wave behavior, thereby enhancing safety in hydrogen-related applications.

ACKNOWLEDGEMENTS

This work was carried out through the ”Nucleu” Program within the National Plan for Research, Development and Innovation 2022-2027, with the support of the Romanian Ministry of Research, Innovation and Digitalisation, project no. 23 32 02 02, title: Numerical modelling on the ignition and propagation of explosions generated by air-hydrogen mixtures – H2Model.

REFERENCES

[1] Takuma, T. (Ed.) Hydrogen Safety Engineering II. Springer. https://doi.org/10.1007/978-3-030-39052-0, 2020

[2] Sandrock, G., Hehemann, D. G., & Nørskov, J. K. (2019). Recent Advances in the Science and Technology of Hydrogen. ACS Catalysis, 9(12), 11136–11153. https://doi.org/10.1021/acscatal.9b02851

[3] Pasculescu V.M., Suvar M.C., Tuhut L.I., Munteanu L., Numerical modelling of hydrogen release and dispersion, 9th edition of the International Multidisciplinary Symposium “UNIVERSITARIA SIMPRO 2021, 342, Romania, 2021

[4] Niculescu T, Pasculescu D, Pasculescu VM, Stoica IO., „Evaluation of electrical parameters of intrinsic safety barriers of the electrical equipment intended to be used in atmospheres with explosion hazard”, International Multidisciplinary Scientific GeoConference Surveying Geology and Mining Ecology Management. 1(2):169-76, 2014;

[5] Tuhut L.I., Florea G.D., Simon-Marinica B.A., Prediction of structural deformations in a research stand for the study of hydrogen explosions, MATEC Web of Conferences (Vol. 389, p. 00075). EDP Sciences, 2024

[6] Niculescu T, Pasculescu D., „Use of numerical simulation to study capacitive loads which is connecting to an AC power source”, In 15th International Multidisciplinary Scientific Geoconference SGEM 2015 (pp. 391-398), 2015

[7] Pana L, Grabara J, Pasculescu D, Pasculescu VM, Moraru RI., „Optimal quality management algorithm for assessing the usage capacity level of mining transformers”, Polish Journal of Management Studies;18(2):233-44, 2018

FISCHER-TROPSCH SYNTHESIS OVER POLYMER SUPPORTED PROMOTED IRON CATALYSTS

Assoc. Prof. Dr. Mariia E. Markova

Assoc. Prof. Dr. Antonina A. Stepacheva

Prof. Dr. Vladimir P. Molchanov

Assoc. Prof. Dr. Galina N. Demidenko

Prof. Dr. Mikhail G. Sulman

Tver State Technical University, **Russia**

ABSTRACT

In recent decades, the interest of researchers has focused on the development of methods for obtaining alternative energy sources. Fischer-Tropsch synthesis is one of the methods for obtaining a wide range of hydrocarbons and their derivatives. Ru, Ni, Fe and Co are the widely used catalytically active metals in FTS. To increase the activity of the catalyst, as well as increase the yield of target products, promoters are introduced into catalytic systems. In FTS, oxides of alkaline and rare earth metals, oxides of lanthanides and actinides, and noble metals are used as modifiers.

In this work, we studied the effect of Fe promotion with Ni, Co, and Ru on the CO conversion and the formation of gasoline-range hydrocarbons in the liquid-phase FTS. Novel catalysts supported on the aromatic polymer matrix characterized by the high specific surface area and fine distribution of the active phase were developed. The addition of Ru to the Fe catalyst was shown to increase both CO conversion and selectivity toward the formation of gasoline-range alkanes compared to the monometallic catalysts.

Keywords: Fischer-Tropsch synthesis, hydrocarbons, iron-containing catalysts, polymer support

INTRODUCTION

The oil and gas industry are one of the largest sectors of the economy of the Russian Federation. According to experts, the contribution of this industry to the formation of the Federal Budget is about 30%, but according to forecasts of the Accounts Chamber of the Russian Federation, this number will decrease [1]. To date, the oil complex has more than 295 oil production and refining organizations [2]. The reserves of explored oil and gas fields currently amount to more than 30 billion tons (12% of the world's oil reserves). Based on the rates of oil production and refining, various experts estimate the availability of oil reserves in 30-50 years [3-8]. In this regard, the interest of scientists is focused on the development of technologies for obtaining alternative energy sources. The Fischer-Tropsch synthesis (FTS) is one of the methods for obtaining a wide range of hydrocarbons and their derivatives.

The effectiveness of various catalyst metals in FTS primarily depends on the nature of the adsorption of CO and H_2 on their surface. The transition metals Ru, Ni, Fe and Co

https://doi.org/10.5593/sgem2024/4.1/s17.12

are most often used as catalysts in the Fischer-Tropsch synthesis. To increase the activity of the catalyst, as well as increase the yield of target products, promoters are introduced into catalytic systems. The following compounds are used as energy promoters: oxides of alkaline and rare earth metals, oxides of lanthanides and actinides, VIII-group noble metals etc. [9].

For iron-containing catalysts, alkali metal ions are most often used as promoters. It affects the electronic structure of iron increasing CO chemisorption and inhibiting H_2 adsorption. The last one reduces the rate of FTS but increases the molecular weight of the products formed as well as increases the yield of olefins. In addition, it was found that Na^+ and K^+ ions increase the activity of iron-containing catalysts in both FTS and water gas shift reaction, whereas Cs^+, Rb^+ and Li^+ at low CO content can act as catalytic poisons [10-12]. The promoting effect of manganese for iron-containing catalysts is to increase the dispersion of the metal, as well as to increase the selectivity of the process with respect to light alkenes [13].

The addition of copper and ruthenium contributes to an increase in the density of active sites, leading to a decrease in the distance for oxygen diffusion of the Fe_2O_3 crystal lattice during the transition from oxide to carbide. It provides higher stationary velocity in the gas-phase FTS [14-16]. It should be noted that the modification of the surface with copper suppresses the sintering of iron particles due to a decrease in the reduction temperature, thereby increasing the stability of the catalyst [17]. In the work of Z. Teimouri et al., iron-containing Fischer-Tropsch synthesis catalysts promoted by Mo and Cu were investigated. The introduction of promoters made it possible to increase the activation energy to 51.9 kJ/mol and achieve higher values of CO conversions from 46.7 to 78.8% compared with the non-promoted catalyst [18].

Nickel-promoted iron-based catalysts show higher CO conversion activity compared to monometallic catalytic systems. The addition of nickel increases the rate of iron reduction, blocking the possibility of carbide formation. At the same time, there is a shift in the selectivity of the process towards the formation of methane and light hydrocarbons, since nickel facilitates the dissociative adsorption of hydrogen and has a higher hydrogenating activity. In addition, blocking the formation of carbides leads to a decrease in the possibility of chain growth [19].

Bimetallic cobalt-iron catalysts synthesized by the hydrothermal method showed a high degree of CO conversion and a shift in the selectivity of the process to the formation of light olefins C_2-C_4, which is explained by the high surface area and structure of the active phase consisting of Hagg carbide and metallic cobalt [20].

In this work, we studied the effect of Fe promotion with Ni, Co, and Ru on the CO conversion and the formation of gasoline-range hydrocarbons in the liquid-phase FTS. Novel catalysts supported on the aromatic polymer matrix characterized by the high specific surface area and fine distribution of the active phase were developed.

MATERIALS AND METHODS

The synthesis of mono- and bimetallic catalysts was carried out by the precipitation of metal-containing particles in a subcritical water medium. A high-pressure reactor Parr-4307 (Parr Instrument, USA) was used for the synthesis. Nonfunctionalized hyper-crosslinked polystyrene (HPS) of the MN 270 brand (Purolite Inc., Great Britain) with a granule size of less than 75 μm, pre-washed with acetone and dried to a constant weight

at 70 ° C in air was used as a support. 1.0000 g of HPS, an accurately calculated amount of metal precursor salt, 0.1000 g of sodium bicarbonate ($NaHCO_3$, c.g., Reachim, Russia) as a mineralizer, and 15 mL of distilled water were introduced into the reactor. The following precursors were used: nickel nitrate hexahydrate ($Ni(NO_3)_3 \times 6H_2O$, c.g., Reachim, Russia), iron nitrate nonahydrate ($Fe(NO_3)_3 \times 9H_2O$, c.g., Reachim, Russia), , cobalt nitrate hexahydrate ($Co(NO_3)_2 \times 6H_2O$, c.g., Reachim, Russia), and ruthenium hydroxotrichloride trihydrate ($RuOHCl_3 \times 3H_2O$, c.g., Reachim, Russia). The working pressure of hydrogen was set to 6.0 ± 0.5 MPa. The temperature of catalyst synthesis was 200 ± 10°C. The process time was 15 minutes. The synthesis was carried out with constant stirring at a rate of 750 rpm. After the end of the process, the reactor was cooled to room temperature. After extraction from the reactor, the mixture was filtered and washed with distilled water to remove chloride, nitrate and carbonate ions, as well as sodium ions.

The thermal stability of the polymer was studied by thermogravimetry. The sample, pre-weighed to a constant mass with an accuracy of 10^{-7} g, was placed on thermal weights TG 209 F1 (Netzsch, Germany). Then, a heat treatment program was started. At the first stage, the temperature was increased from 30 to 105 °C at a rate of 10 °C/min, followed by exposure for 2 hours at a temperature of 105 °C. Then, heating was carried out to 150 ° C at a speed of 10 °C / min, followed by 2 hours of exposure at a temperature of 150 °C. The third stage included heating to 200 °C under similar conditions.

The stability of the polymer under conditions of synthesis of catalytic systems was studied by infrared spectroscopy. The spectra of the samples were obtained using an IR-Prestige-21 Fourier transform infrared spectrometer (Shimadzu, Japan). The crushed analyzed sample was placed in an open steel cuvette of the DRS-8000 diffuse reflection device. The spectra were recorded in the range of 4200-400 cm^{-1}, in increments of 4 cm^{-1}.

The specific surface area and porosity were determined using the Beckman Coulter SA 3100 surface area and pore size analyzer (Coulter Corporation, USA) and a sample preparation device: Beckman Coulter SA-PREP (Coulter Corporation, USA).

To evaluate the qualitative composition of the surface and determine the valence state of the metal, X-ray photoelectron spectroscopy (XPS) of the samples was performed. The XPS spectra were obtained using an ES 2403 M-T spectrometer of the SCB AP RAS equipped with a PHOIBOS 100-5MCD energy analyzer (Specs, Germany) and an XR-50 X-ray source (Specs, Germany). The characteristic Mg K*a* radiation (hν = 1253.6 eV) was used for photoelectronic excitation. The power of the radiation source is 250 watts. The spectra were recorded at a pressure of 2×10^{-6} Pa from samples previously degassed in ultrahigh vacuum. The C 1s peak (285.0 eV) was used as a reference peak. The survey spectra were recorded in energy increments of 0.5 eV with an analyzer transmission energy of 40 eV. High-resolution spectra were recorded in energy increments of 0.05 eV at an analyzer transmission energy of 7 eV, which corresponds to Ag $3d_{5/2}$ (0.85 eV).

The catalytic systems were tested in the liquid-phase Fischer-Tropsch synthesis using n-dodecane as a solvent. The process was carried out in a periodic mode in a steel reactor PARR-4307 (Parr Instrument, USA) at a temperature of 200 °C and a pressure of 2 MPa. The ratio of CO to H_2 was 1:4.

https://doi.org/10.5593/sgem2024/4.1/s17.12

The liquid and gas phases of the reaction mixture were analyzed by gas chromatography (Crystallux 4000M (Metachrome, Russia)) and gas chromatography-mass spectrometry QP2010S (Shimadzu, Japan).

RESULTS AND DISCUSSION

In this work, monometallic composites and catalytic systems promoted by transition metals were synthesized. Nonfunctionalized HPS was chosen as the support. The choice of the support was due to its high surface area, developed structure, chemical and thermal stability.

Figure 1a shows thermograms of the initial and treated under catalyst synthesis conditions polymers. Significant weight loss of the polymer sample begins at a temperature of 400 °C. At a temperature of 500 °C, the weight loss of the polymer is about 50%. According to differential thermogravimetry (Figure 1b), the decomposition temperature of the initial and treated polymer is about 350 °C. The thermograms obtained for HPS and treated polymer, as well as for catalysts, practically do not differ (Figure 1). A slight weight loss at temperatures below 100 °C can be explained by the evaporation of capillary moisture. Based on the results obtained, it can be concluded the that polymer remains stable at a catalyst synthesis and FTS temperature of 200 °C.

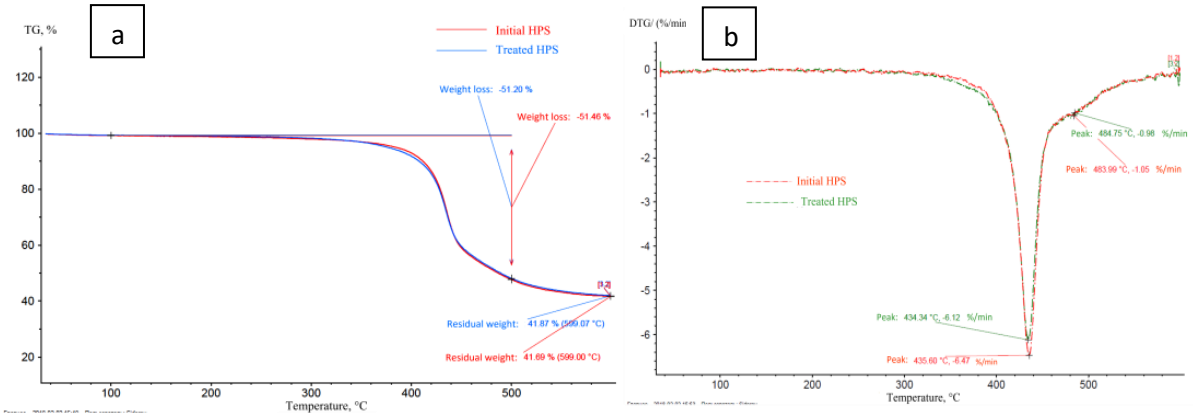


Figure 1. Thermograms (a) and DTG curves (b) for the initial HPS and treated under the conditions of catalyst synthesis

Figure 2 shows the FTIR spectra of samples of the initial and treated under the catalyst synthesis conditions HPS. The main absorption bands correspond to fluctuations of CH-, CH_2-groups, benzene rings, which are part of the polymer matrix. It can be seen from the presented data that the spectra of the initial and treated samples practically do not differ. This may indicate the stability of the polymer during the synthesis of catalytic systems.

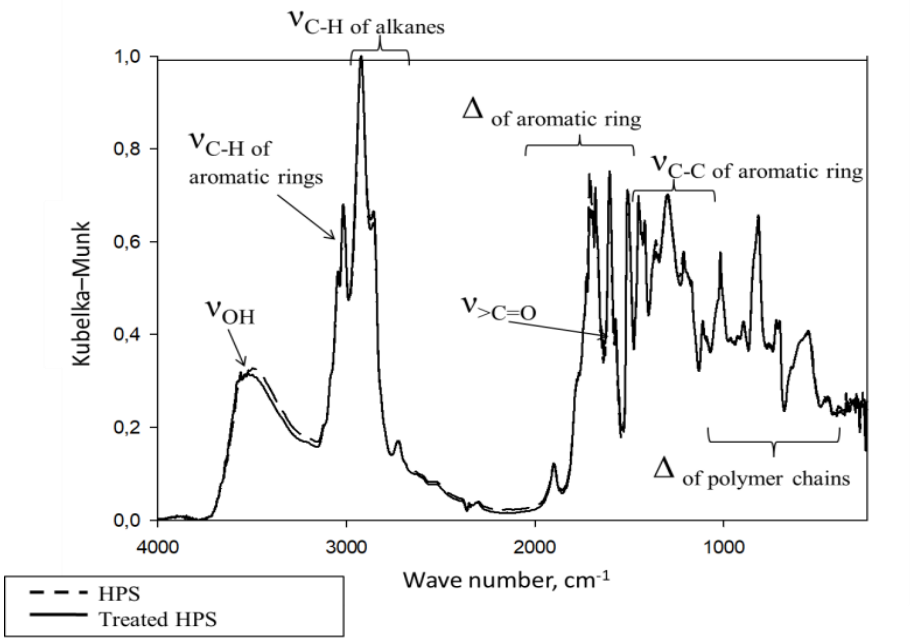


Figure 2. IR spectra of samples of the initial HPS and treated under the conditions of catalyst synthesis

The deposition of the active phase was carried out by precipitation in subcritical water. This method allows the particle size of the active phase to be controlled and ensures its uniform distribution. The proposed synthesis method is considered to be environmentally friendly, since precipitation occurs in an aqueous medium.

A study of the porosity of samples of catalytic systems is presented in Table 1. From the data presented, it can be seen that there is no significant decrease in the specific surface area during the synthesis of catalysts by precipitation under superheated water conditions.

Table 1. Structural characteristics of synthesized samples

Sample	Total pore volume V_p, cm^3/g	Specific surface area			
		Langmuir Model S_L, m^2/g	BET Model S_{BET}, m^2/g	t-plot m^2/g	
				mesopore	micropore
treated HPS	0.69	1276	1163	247	915
1%Ru/ HPS	0.82	1076	948	228	749
2%Ni/ HPS	0.89	1286	1161	260	900
2%Fe/ HPS	0.89	1179	1048	236	806
2%Co/ HPS	0.74	1286	1171	234	936
2%Fe-2%Co/HPS	0.85	1228	1109	235	871
2% Fe-2%Ni/ HPS	0.89	1232	1108	250	856
2%Fe-1%Ru/ HPS	0.89	1217	1092	264	821

https://doi.org/10.5593/sgem2024/4.1/s17.12

According to the X-ray photoelectron spectroscopy, the surface composition of the samples is presented by oxidized forms of metals, namely mixed oxides, hydroxides and oxohydroxides (Table 2).

Table 2. Surface composition of catalysts according to XPS data

Sample	Metal compounds
1%Ru/HPS	RuO_2, $Ru(OH)_3$, Ru
2%Ni/HPS	β-NiOOH
2%Fe/HPS	Fe_3O_4
2%Co/HPS	Co_3O_4
2%Fe-2%Co/HPS	Fe_3O_4, Co_3O_4
2% Fe -2% Ni/HPS	Fe_3O_4, β-NiOOH
2%Fe-1%Ru/HPS	Fe_3O_4, RuO_2, $Ru(OH)_3$, Ru

The results of testing synthesized samples in Fischer-Tropsch liquid-phase synthesis are presented in Table 3. The introduction of Ni and Co into the iron-containing system leads to a decrease in CO conversion, as well as to an increase in the selectivity of the process to low molecular weight products. The decrease in CO conversion may be due to the partial reduction of the metal-containing phase during the Fischer-Tropsch liquid-phase synthesis. To confirm this hypothesis, studies of the surface composition of catalysts by the XPS method were carried out after 1.5 hours of Fischer-Tropsch synthesis (Table 4). According to the analysis, in the sample of 2%Fe-2%Co/HPS, in addition to Co_3O_4, $Co(OH)_2$ is present. Nickel (II) oxide was also detected in a sample of 2% Fe -2% Ni/HPS. The promotion of iron catalysts with ruthenium led to an increase in CO conversion by 5%, while the selectivity of the process to the formation of C_5-C_{11} alkanes increased.

Table 3. Integral selectivity by product groups of Fischer-Tropsch synthesis in the presence of the studied catalysts

Sample	Conversion CO*, mol. %	Selectivity**, mol. %					
		CH_4	C_2-C_4	C_5-C_{11}	C_{13}-C_{14}	Oxygenates C_1-C_5	Olefins
1%Ru/ HPS	25.9	0.1	0.2	94.1	2.3	0.7	2.6
2%Ni/ HPS	15.8	7.5	14.9	75.4	0.0	0.2	1.9
2%Fe/ HPS	24.5	4.6	8.9	78.2	0.0	6.6	1.7
2%Co/ HPS	17.5	5.2	7.6	84.2	1.2	0.4	1.4
2%Fe-2%Co / HPS	7.9	5.0	9.5	78.0	0.0	6.2	1.3
2% Fe -2% Ni / HPS	13.6	5.9	9.4	80.1	0.0	3.5	1.1
2%Fe-1%Ru / HPS	29.8	0.7	3.3	95.8	0.0	0.1	0.1

* The conversion is calculated at 6 hours of the process

** The selectivity is calculated at 6 hours of the process

Table 4. Surface composition of catalysts 2%Fe-2%Co/HPS and 2% Fe -2%Ni/HPS after 1.5 hours of Fischer-Tropsch synthesis according to XPS data

Sample	Metal compounds
2%Fe-2%Co /СПС	Fe_3O_4, Co_3O_4, $Co(OH)_2$
2% Fe -2% Ni /СПС	Fe_3O_4, β-NiOOH, NiO

CONCLUSION

In this work, monometallic composites and catalytic systems promoted by transition metals were synthesized. Nonfunctionalized hyper-crosslinked polystyrene characterized by a high specific surface area, developed structure, chemical and thermal stability was chosen as the carrier. The deposition of the active phase of the catalyst on the polymer support was carried out using the method of precipitation in subcritical water. The polymer was shown to be stable in the catalyst synthesis and FTS conditions. The specific surface area of the synthesized catalytic systems was found to decrease slightly in comparison with the initial support. The catalyst synthesis method provides the fine distribution of the active phase on the support. The surface composition of the catalyst is presented by the oxidized forms of the metals. Testing of the synthesized catalysts in the liquid-phase FTS showed the possibility of increasing of CO conversion and the selectivity regarding to the gasoline-range hydrocarbons while promoting the Fe-containing catalyst with Ru.

ACKNOWLEDGEMENTS

The work is financially supported by the Russian Science Foundation (grant 23-23-00653).

REFERENCES

[1] The auditors explained the decrease in the share of oil and gas budget revenues to a minimum. Sanctions have not become the main factor in such dynamics / Economics, 2023 / URL: https://www.rbc.ru/economics/23/11/2023/655dcfa69a79471d752b6f80 (in Russian).
[2] Kurakin V.I., Abramchikova N.V. Analysis of the peculiarities of the formation of the structure of the Russian oil and gas industry / Economic Sciences, Russia, vol. 2/issue 195, pp. 101 – 108, 2021 (in Russian).
[3] Fry M.E. Assessment of the current state of the Russian oil industry // Bulletin of the Udmurt University of Economics and Law, Russia, vol. 25 /issue 2. pp. 75-85, 2015 (in Russian).
[4] Russia is provided with proven oil reserves of the fields under development, excluding TRIZ, for no more than 20 years / URL: http://www.Neftegaz.ru . (in Russian).
[5] Discoveries of the year: new fields in Russia and the world / Drilling and Oil, 2016.URL: http://burneft.ru/main/news/15958. (in Russian).
[6] Sinyak Yu.V. Economic assessment of the potential of world oil and gas reserves // Problems of forecasting, Russia, vol. 6, pp. 86-107, 2015(in Russian).

https://doi.org/10.5593/sgem2024/4.1/s17.12

[7] Muslimov R.H. A new classification of reserves and resources of oil and combustible gases – moving forward or backward? // Geo resources, Russia, vol. 18. /issue 2, pp. 80-87, 2016 (in Russian).
[8] Berezina E. Is there a life without oil? // Rossiyskaya Gazeta - Federal issue, Russia, vol. 55 /issue.6923, pp. 5, 2016 (in Russian).
[9] A review of advanced catalyst development for Fischer–Tropsch synthesis of hydrocarbons from biomass derived syn-gas / H. Jahangiri, J. Bennett, P. Mahjoubi, K. Wilson, S. Gu // Catal. Sci. Technol. Vol. 4, pp. 2210-2229, 2014.
[10] Bimetallic synergy in cobalt ruthenium Fischer-Tropsch synthesis catalysts / E. Iglesia, S.L. Soled, R.A. Fiato, G.H. Via // J. Catal. Vol. 143, pp. 345-368, 1993.
[11] Raje A., O'Brien R.J., Davis B.H. Effect of potassium promotion on iron-based catalysts for Fischer-Tropsch synthesis // J. Catal. Vol. 180/issue.1, pp. 36-43, 1998.
[12] Fischer-Tropsch synthesis: activity and selectivity for group I alkali promoted iron-based catalysts / W. Ngantsoue-Hoc, Y.Q. Zhang, R.J. O'Brien, M.S. Luo, B.H. Davis // Appl. Catal. A. Vol. 236, pp. 77–89, 2002.
[13] Slurry phase Fischer-Tropsch synthesis over manganese-promoted iron ultrafine particle catalyst / L. Bai, H. W. Xiang, Y. W. Li, Y. Z. Han, B. Zhong // Fuel. Vol. 81, pp. 1577–1581, 2002.
[14] Design, Synthesis, Site Densities, and Catalytic Properties / S. Li, S. Krishnamoorthy, A. Li, G.D. Meitzner, E. Iglesia // J. of Catalysis. Vol. 206, pp. 202–217, 2002.
[15] Liuzzi D., P´erez-Alonso F.J., Rojas S. Full Length Article Ru-M (M = Fe or Co) Catalysts with high Ru surface concentration for Fischer-Tropsch synthesis //Fuel. Vol. 293, pp. 120435 – 120460, 2021.
[16] Investigating the Stability of Ru-promoted Fe-based Fischer-Tropsch Catalyst at high Synthesis Gas Conversion / I. Fraser, A.M. Rabiu, E. van Steen // Energy Procedia, vol. 100, pp. 210 – 216, 2016.
[17] Enhancement of the catalytic performance of silica nanosprings (NS)-supported iron catalyst with copper, molybdenum, cobalt and ruthenium promoters for Fischer-Tropsch synthesis / A. Alayat, E. Echeverria, D N. Mcllroy, A.G. McDonald // Fuel Processing Technology, vol. 177, pp.89–100, 2018.
[18] Insights to the reaction kinetics of Fischer-Tropsch synthesis using an integral system over Cu-Mo promoted Fe catalyst / Z. Teimouri, N. Abatzoglou, A.K. Dalai// Fuel, vol. 360, pp. 130512, 2024.
[19] Study on an iron–nickel bimetallic Fischer–Tropsch synthesis catalyst / T. Li, H. Wang, Y. Yang, H.Xiang, Y. Li // Fuel Processing Technology, vol. 118, pp. 117-124, 2014.
[20] M¼Fe, Zn, Ni and Co) nanoparticles: Facile synthesis approach and their superb stability and catalytic performance in Fischer-Tropsch synthesis / M. Abbas, J. Zhang, T.S. Mansour, J. Chen // International journal of hydrogen energy, vol. 45, pp. 10754 – 10763, 2020.

FLAME ANALYSIS: UNDERSTANDING THE COMBUSTION OF RENEWABLE FUELS

Assist. Prof. Dr Blanca Castells[1,2]

Assist. Prof. David León[1,2]

Assist. Prof. Dr. Isabel Amez[1,2]

Researcher Roberto Paredes[1]

Assoc. Prof. Dr. David Bolonio[1,2]

[1] Department of Energy and Fuels, E.T.S. Ingenieros de Minas y Energía, Universidad Politécnica de Madrid, Ríos Rosas 21, 28003 Madrid, **Spain**
[2] TECMINERGY, Technical University of Madrid, Spain, C/Eric Kandel, 1 (TECNOGETAFE), Parque Científico y Tecnológico de la UPM, 28906 Getafe, **Spain**

ABSTRACT

Due to the increase of global concerns over environmental degradation, the search for sustainable energy sources has led to increased utilization of renewable fuels such as biogas and biodiesel. Despite their advantages in terms of sustainability, challenges persist in their efficient utilization. An easy method to approach these challenges is addressing the characteristics of flames produced during these fuels' combustion. This study aims to address these challenges by developing a MATLAB-based flame analysis tool capable of determining flame shape and colour areas. By assessing a diverse dataset of digital images and videos capturing flames from various fuel sources, this tool enables comprehensive comparisons between flames produced by renewable fuels and traditional fuels. Moreover, thermography pictures were also assessed in order to properly define the areas in terms of temperature. A key contribution of this research is the introduction of a novel parameter noted as "shape factor," which quantifies flame morphology and dispersion. Through rigorous analysis, this parameter serves as a valuable metric for assessing flame stability and transition points. Through the study of the diferent features of renewable fuel flames, this study offers valuable insights crucial for optimizing combustion processes and advancing sustainable energy solutions. The proposed methodology not only aids in evaluating the performance of renewable fuels but also facilitates informed decision-making in energy transition initiatives. Ultimately, this research represents a significant step towards mitigating environmental impact and fostering a more sustainable energy landscape.

Keywords: combustion analysis, flame characteristics, biogas

INTRODUCTION

In the last decades, the global concern regarding the environmental degradation has significantly grown leading to an increase in the search for new sustainable energy resources. In this context, the use of biomass, biogas and biodiesel presents several advantages that can mitigate the main global warming causes [1]. These fuels, derived from organic waste, can be considered promising alternatives to the traditional fossil fuels, duel to their potential to reduce greenhouse gas emissions and dependency of non-

https://doi.org/10.5593/sgem2024/4.1/s17.13

renewable fuels. However, despite these benefits, there are still several challenges associated with these fuels in terms of energetic efficiency, especially related to combustion processes [2].

Although renewable fuels combustion is more sustainable, it presents some specific characteristics that require a detailed analysis in order to optimize the process. Understanding the behaviour of the flames produced during the combustion of these fuels is a key parameter to approach the combustion efficiency challenge [3]. Flame characteristics such as shape, colour, temperature distribution, etc., provide critical information regarding combustion process stability of and efficiency [4]. However, despite the importance of these parameters, systematic and quantitative flame analysis is still an uncommon research topic.

Indeed, previously published literature regarding combustion process [5], has mainly focused on fossil fuels combustion, given that these fuels predominate in industrial facilities. However, as mentioned above, the recent tendency change in fuels combustion derived from the climate change concern, has led to increase the number of studies that focus on renewable fuels combustion, focusing on thermal efficiency, gas emissions and physical flame characteristics [6].

The variability in the composition and the presence of impurities are the main factors that influence combustion efficiency and lead to a complex reaction [7]. Regarding gaseous biofuels biogas and hydrogen are the most commonly used. Biogas is composed mainly of methane (CH_4) and carbon dioxide (CO_2). Several studies have pointed out that biogas flame tends to be more diffuse and has greater variability in shape and colour if compared to fossil fuel flames [8]. Hydrogen is commonly used in mixed with other gases to improve their properties, therefore, the flame significantly varies depending on the other gases [9]. On the other hand, biodiesel produced from vegetable oils and animal fats through transesterification also presents differences when comparing the flame to conventional diesel. More specifically, biodiesel flames present a different temperature distribution and are typically more luminous [10]. Previously published research indicated that biodiesel might produce a cleaner combustion, with less amount of emitted particles and nitrogen oxides [11].

Nevertheless, the most heterogeneous biofuel is biomass, as it includes waste from different sources and origins, leading to a variable composition and physic-chemical properties. Because of that, biomass flames present less uniform profile and significant variations in terms of shape and colour [12]. Moreover, biomass combustion might produce greater amounts of ashes, a parameter that also influences flame efficiency and stability. However, solid biofuels flame behaviour has been widely studied which means that parameters and characteristics that can be obtained from flame analysis (such as stability, flame areas, temperature, etc.) are well known [13]. However, the ignition of the dust cloud produced when the biomass dust is dispersed in the air is a topic of high relevance due to the accidents produced in the industry because of biomass ATEX (explosive atmosphere) characteristics. Some authors have already focused on the use of thermography and image analysis when performing ATEX characterization tests, however this techniques and methods are not commonly used for solid biofuels.

Therefore, it is clear that new flame analysis tools should be developed in order to properly address the combustion process. Because of that, this study presents the use of a Matlab® code which allows the determination of the different colour areas and

regions in the flame, allowing to carry out a detailed assessment of flame images and videos, so specific metrics can be determined. Moreover, a “shape factor” has been defined in order to address the variation of the flame shape which allows to assess stability and turbulence. Besides that, thermographic images and videos have been also studied as it provides additional information regarding flame temperature profile, which can be related to understand thermal efficiency. The combination of these parameters provides a deep analysis of biofuels flame behaviour, and reaction insights that help optimize combustion process and develop new sustainable energetic solutions.

MATERIALS AND METHODS

Biofuels and test apparatus

Flame analysis can be used in a wide range of tests related to flammability and burning characterization. In the present research different tests and biofuels were used in order to address the possibilities and uses of the method. Specifically, this study focuses on gaseous and solid biofuels.

For gaseous biofuels, a mixture of 70% methane and 30% carbon dioxide was produced in order to simulate biogas. The combustion was performed in a Bentone BFG1 H3 industrial burner generating an open flame. Moreover, the combustion was produced also in a carbon dioxide atmosphere enriched with oxygen in order to produce an oxy combustion process. In the present study, two different oxygen concentrations were used: 24% and 31% in order to see different flame behaviours. The flame was recorded using a digital camera; therefore, two videos were obtained (BG24 and BG31 for 24% and 31% oxygen concentrations respectively).

On the other hand, for solid biofuels as mentioned before, the use of flame analysis in ATEX characterization tests is not usually studied. Among the different test commonly used to define the ATEX characteristics of a dust, two of them produce a dust ignition that can be easily recorded and analysed using a FLIR T530 thermographic camera. Minimum ignition energy (MIE) and minimum ignition temperature of a dust cloud (MITc). MIE was carried out using a MIKE 3 apparatus while MITc was performed using a GG vertical furnace. Although both tests are standardized [14], the complete procedure was not performed as the test conditions were selected just to obtain the flame image required for the analysis. Therefore, for MIE 1200 mg of sample and 1000 mJ were used, while 650 ºC and 300 mg were used for MITc. In both tests, the selected biomass was corn starch.

Image and video analysis

Image and video analysis was performed using Matlab®. For image analysis, the colour of each pixel is determined as RGB vector and then the area of each colour is determined. On the other hand, video analysis intends to define turbulence by implementing a dimensionless parameter defined as “shape factor”. This parameter measures the variation of the flame area. Comparing the evolution of the flame to the first frame of the video, when shape factor is close to 1 the shape variation is minimum, when is negative the area has decreased and when positive the flame area has increased.

https://doi.org/10.5593/sgem2024/4.1/s17.13

RESULTS

The results obtained from the video analysis of biogas oxy-combustion can be seen in figures 1 and 2. Figure 1 shows the evolution of the shape factor versus time while figure 2 shows flame pictures of both samples at different times.

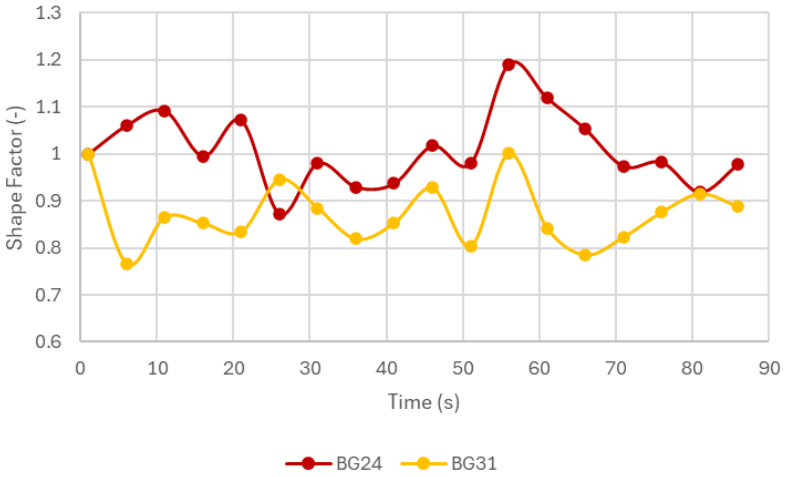


Figure 1: biogas oxy-combustion shape factor

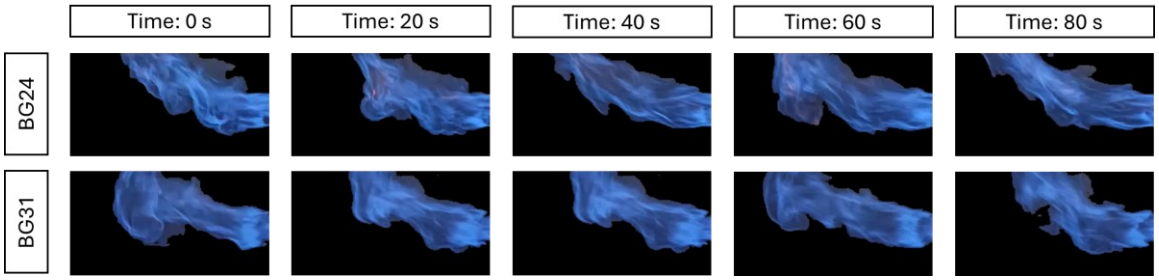


Figure 2: flames produced during biogas oxy-combustion

It is clear that BG24 presents more variability than BG31. Moreover, it can be noticed that BG31 shape factor is negative which is consistent with the pictures depicted in figure 2, where the area decreases. In both samples, there is an increase in the shape factor between 50 and 60 s which indicates an increase in the turbulence of the flame. Regarding the turbulence, the variability of BG24 indicates more flame turbulence which indeed can be noticed also in figure 2.

Regarding the ATEX tests for corn starch, the results are presented in figures 3 and 4. Figure 3 shows the MIE results with the thermographic images and the colour analysis. On the other hand, the MITc results are plotted in figure 4. In both tests blue represent ambient temperature, therefore blue represents the maximum density of pixels in both tests and times besides the moment in which the dust ignition takes place.
In both cases it is noticed that the explosion takes place in two different steps. In the first one takes place the main ignition producing a violent and fast combustion, afterwards there is a second smaller ignition in the vacuum that follows the first ignition. This second stage can be clearly seen in picture number 11 in figure 3 and picture number 4 in figure 4.

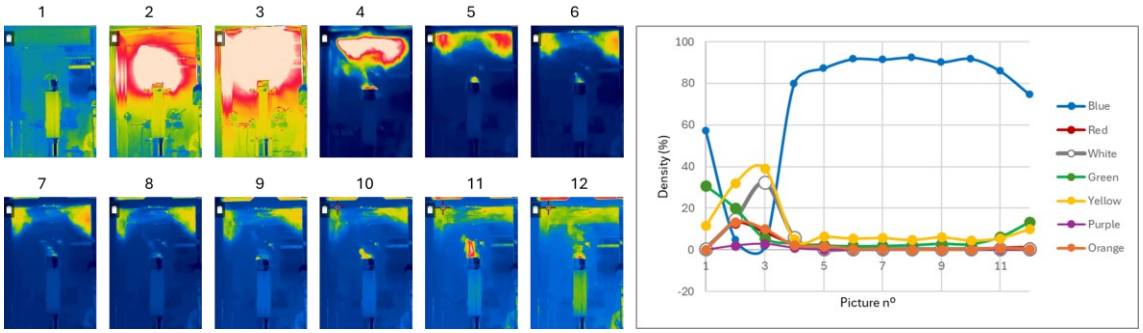


Figure 3: MIE ignition pictures and colour analysis

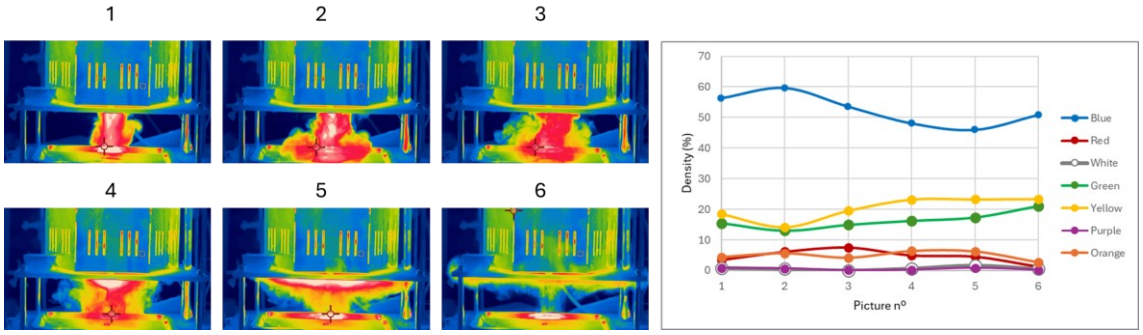


Figure 4: MITc ignition pictures and colour analysis

DISCUSSION

As mentioned before, samples BG24 presents more variability than sample BG31. This variability is noticed in the shape factor which indicates a more turbulent and less stable flame. On the other hand, BG31 presents a negative shape factor due to the decrease of the area. Those results indicate that higher oxygen percentages lead to more stable combustion reactions, therefore oxy combustion can produce more efficient reactions than traditional combustion and improve the energetic conversion of biogas.

From the pictures showed in figure 2, it can be noticed that biogas flames are almost completely blue with just a few orange pixels as noticed in BG24 sample for 20 s and 60 s time. Because of that the use of the image analysis to obtain the colour density did not provide any relevant information. However, it is known that biogas can present different carbon dioxide contents therefore further studies should consider the simulation of biogas using different CO_2 concentrations and evaluate if there are important differences in the colour and shape of the flames.

Regarding the ATEX test the implementation of image processing analysis presents a significant advantage. As mentioned in the standard, MITc and MIE ignition is determined visually, therefore, there is a subjectivity attached to these tests as the determination of whether there is ignition or not depends on the test technician. The implementation of image analysis can eliminate this subjectivity as the ignition would be determined by image colour processing.

If the colour densities and their evolution is considered it can be noticed that blue pixels are the most commonly present in the pictures as they represent ambient temperature,

https://doi.org/10.5593/sgem2024/4.1/s17.13

therefore, when no ignition is produced thermographic images do only show ambient temperature. In the MIE test when the ignition is produced (pictures number 2 and 3), the blue density heavily decreases while yellow, orange and red densities increase. The same fact takes place in the second stage of the ignition, shown in pictures number 11 and 12 from figure 3, however this time the ignition is significantly lower and so it is the decrease in the blue area and the increase in the remaining ones. The plot with the colour densities shown in figure 3 perfectly identifies this process which means that image analysis can improve this test performance.

The same tendency can be observed in MITc, however in this case less amount of pictures has been treated and so the ignition is not so well characterized. Nevertheless, it can be noticed that as the ignition area increases so it does the colours related to the higher temperatures (i.e. red, orange and yellow). The colour density analysis can be also performed in normal videos recorded with a digital camera instead of thermographic videos, however, the image processing tool defined in this study is especially interesting when using thermographic pictures as it perfectly defines the temperature ranges and the temperatures of each area.

CONCLUSION

Flame analysis using image processing tools and thermography has proved to be an efficient methodology to assess renewable biofuels combustion. This study has focused on the characterization of oxy-combustion biogas flames and biomass combustion, by determining colour areas and flame shape.

The results showed that biogas oxy-combustion produced significant variations in flame stability and turbulence, and that an increase in the oxygen percentage leads to a more stable combustion. This tendency was not only noticed in the videos but also in the shape factor results.

Regarding ignition sensitivity tests using corn starch, the use of thermographic pictures allowed an accurate characterization of the ignition process erasing the subjectivity inherent in the methodology defined in the standards. Colour density analysis was proved to be an efficient tool to identify and characterize ignition transition and combustion stages, which provides a better comprehension of biomass combustion.

It is clear that a key contribution in this research is the definition of the shape factor, as this parameter allows to quantify flame morphology and dispersion. The application of this parameter to the tests and samples mentioned above proved the important metric value that the shape factor presents and allows to assess flame stability and transition points. This fact shows an important potential when addressing renewable fuels combustion as it simplifies the study of the flame behaviour and combustion mechanisms.

In summary, the implementation of image analysis and thermography tools provides a detailed and objective evaluation of biofuels combustion, contributing to the development of more efficient and sustainable combustion processes. Future research could focus on the variability of biogas composition and its impact on the shape and color of flames, as well as the application of these methods to other types of renewable fuels. These improvements will help optimize combustion processes and promote sustainable energy solutions, reducing environmental impact and moving towards a more sustainable energy landscape.

ACKNOWLEDGEMENTS

This project has received funding from IV Convocatoria Catedra Empresa Fundación Cepsa de Energía y Medio Ambiente de la Escuela de Minas y Energía (UPM). – Proyecto OTT CAT200600041P.

REFERENCES

[1] M. Shahbaz, C. Raghutla, K.R. Chittedi, Z. Jiao, X.V. Vo, The effect of renewable energy consumption on economic growth: Evidence from the renewable energy country attractive index, Energy. 207 (2020) 118162. https://doi.org/https://doi.org/10.1016/j.energy.2020.118162.

[2] S. V. Vassilev, D. Baxter, L.K. Andersen, C.G. Vassileva, An overview of the composition and application of biomass ash.: Part 2. Potential utilisation, technological and ecological advantages and challenges, Fuel. 105 (2013) 19–39. https://doi.org/10.1016/j.fuel.2012.10.001.

[3] P. Sabia, G. Sorrentino, G.B. Ariemma, M. V Manna, R. Ragucci, M. de Joannon, MILD Combustion and Biofuels: A Minireview, Energy & Fuels. 35 (2021) 19901–19919. https://doi.org/10.1021/acs.energyfuels.1c02973.

[4] Y. Yin, P.R. Medwell, A.J. Gee, K.K. Foo, B.B. Dally, Fundamental insights into the effect of blending hydrogen flames with sooting biofuels, Fuel. 331 (2023) 125618.

[5] Q. Zhao, X. Chen, Y. Li, H. Dai, Suppression mechanisms of ammonium polyphosphate on methane/coal dust explosion: Based on flame characteristics, thermal pyrolysis and explosion residues, Fuel. 326 (2022) 125014.

[6] T. Sathish, D.K. Singaravelu, Combustion analysis using third generation biofuels in diesel engine, (2020).

[7] B. Rotavera, C.A. Taatjes, Influence of functional groups on low-temperature combustion chemistry of biofuels, Prog. Energy Combust. Sci. 86 (2021) 100925.

[8] Q. Zhang, J. Xia, J. Wang, Z. He, W. Zhao, Y. Qian, L. Zheng, R. Liu, X. Lu, Experimental study on ignition and combustion characteristics of biodiesel-butanol blends at different injection pressures, Renew. Sustain. Energy Rev. 160 (2022) 112289.

[9] X. Yang, W. Yang, S. Dong, H. Tan, Flame stability analysis of premixed hydrogen/air mixtures in a swirl micro-combustor, Energy. 209 (2020) 118495. https://doi.org/https://doi.org/10.1016/j.energy.2020.118495.

[10] S.H. Pourhoseini, M. Namvar-Mahboub, E. Hosseini, A. Alimoradi, A comparative exploration of thermal, radiative and pollutant emission characteristics of oil burner flame using palm oil biodiesel-diesel blend fuel and diesel fuel, Energy. 217 (2021) 119338.

[11] T.N. Verma, P. Shrivastava, U. Rajak, G. Dwivedi, S. Jain, A. Zare, A.K. Shukla, P. Verma, A comprehensive review of the influence of physicochemical properties of biodiesel on combustion characteristics, engine performance and emissions, J. Traffic Transp. Eng. (English Ed. 8 (2021) 510–533.

https://doi.org/10.5593/sgem2024/4.1/s17.13

[12] S. Wang, C. Zou, C. Lou, H. Yang, M. Mei, H. Jing, S. Cheng, Effects of hemicellulose, cellulose and lignin on the ignition behaviors of biomass in a drop tube furnace, Bioresour. Technol. 310 (2020) 123456.

[13] J. Mularski, J. Li, A review on biomass ignition: Fundamental characteristics, measurements, and predictions, Fuel. 340 (2023) 127526. https://doi.org/https://doi.org/10.1016/j.fuel.2023.127526.

[14] European committee for standardization CEN-CENELEC, ISO/IEC 80079-20-2:2016 Explosive atmospheres - Part 20-2: Material characteristics - Combustible dusts test methods, 2016.

HYDROSTATIC POWER TRANSMISSION SYSTEM FOR WIND TURBINES

Ph.D. Eng. Cătălin Dumitrescu[1]

Ph.D. Eng. Alexandru-Polifron Chiriță[1]

Ph.D. Stud. Eng. Ștefan-Mihai Șefu[1]

Ph.D. Chem. Adriana Mariana Borș[1]

Assist Res. Ana-Maria Carla Popescu[1]

[1] National Institute of Research & Development for Optoelectronics/INOE 2000, Subsidiary Hydraulics and Pneumatics Research Institute/IHP, **Romania**

ABSTRACT

In 2023, 18.3 GW of new wind energy conversion capacity was installed in Europe; most of them (79%) represent onshore capacities. Most of this energy production is achieved with horizontal axis wind turbines. For this type of turbine, the location of the transmission coupled with an electric generator or a hydraulic group, in the turbine platform, leads to a significant increase in the mass of the platform, and implicitly in the mass of the pillar that supports the turbine. In addition, turbine maintenance becomes more difficult as the rotor diameter and installation height increase. The platform (excluding the rotor) represents between 20 ... 35% of the total weight of a large turbine reaching hundreds of tonnes in some cases. In the case of the VESTAS V90 turbine, the platform weighs 75 tonnes, the rotor 40 tonnes, and the tower 152 tonnes. For this reason, methods of reducing the suspended mass, mainly by placing the electric generator on the ground, have been and are being intensively studied in the last decades. If at the beginning large power turbines were studied, recently medium and small sized turbines are also being considered. The paper presents a solution for hydrostatic transmission of energy from the turbine rotor to the generator, validated by numerical simulation with Simcenter Amesim.

Keywords: renewable, wind energy, hydrostatic transmission, wind turbine, numerical simulation

INTRODUCTION

Obtaining energy from renewable sources and increasing its share of the total energy consumed worldwide are current trends, which are quantified in various European and world documents; for example, the Renewable Energy Directive, adopted in 2023, proposes that in 2030 at least 42.5% of the total energy consumed at EU level should come from renewable sources, and greenhouse gas emissions should be reduced by at least 55 %. For the year 2050, the target is even more ambitious, the proposal being that Europe becomes a climate-neutral continent [1].

Worldwide, the share of energy produced from renewable sources in 2021 was 12.6%; in terms of electricity, 30% of its total is produced from renewable sources, and of this almost half is produced from solar and wind energy. There are countries where electricity is mostly produced from renewable resources (Denmark 61%, of which 55%

https://doi.org/10.5593/sgem2024/4.1/s17.14

from wind energy and 6% from solar energy). Both fields have continuous and strong development; in the year 2022, the total capacity of installed wind turbines increased by 77 GW, to a total of 906 GW [2].

This was also possible due to the continuous increase in the power of installed wind turbines, most of which are horizontal axis turbines. The current record for an offshore turbine in operation is 16 MW, and it produces 80 GWh of electricity annually; these records also bring a number of challenges to those who design, build and install them.

A significant part of the weight of a turbine is the support tower and nacelle; to these one needs to add the weight of the foundation, proportional to the power of the turbine and the mass suspended above the ground. For example, the Enercon E-126 onshore turbine, with a power of 7.6 kW, has a nacelle that weighs 348 tonnes, and the tower together with the foundation weighs 2800 tonnes [3].

As for offshore turbines, they are of higher power, but the weight of the main components is also higher. Representative is the case of the MySe 16-242 turbine (16 MW, 242 m rotor diameter), which declares a nacelle weight below 37 t/MW (or less than 592 tonnes for nacelle weight) [4].

Since the power of the turbine is proportional to the diameter of the rotor, as this diameter increases, so does the distance between the ground and the nacelle, where most of the turbine components are located.

The safe support of these components, some located at heights of over 100 m, involves the construction of complex structures, with a high consumption of material; in addition to the cost of the materials, lately there is also the problem of environmental pollution for the production of these quantities of materials and the pollution caused by the transport to the location [5,6].

If certain components of the turbine, such as the rotor or nacelle, must be elevated, other components, such as the electric generator, can be located on the ground using various solutions. The reduction of suspended masses in the structure of wind turbines has beneficial consequences from several points of view:

- Resistance structures are made with less material consumption, especially steel and concrete.
- Less environmental pollution when manufacturing materials.
- Easier transport and assembly.
- Generator maintenance becomes significantly easier.

If the generator is located on the ground, the mechanical transmission of energy between the rotor and the generator, including the adaptation of the rotation speeds of the two components, can be achieved by hydraulic means; it is a solution that has been under the attention of research scientists for several decades, with promising results. The proposed solutions use classic hydraulic equipment [7,8] or equipment in digital construction [9,10].

MATERIALS AND METHODS

To reduce the mass of components in the nacelle of a wind turbine, mechanical components such as the speed reducer and the gearbox were replaced with hydrostatic transmissions (HSTs) because they have a higher power density.

In order to maintain the constant speed of the synchronous electric generator, instead of a closed-circuit hydrostatic transmission with secondary regulation, which is complex, expensive and unnecessary, it was decided to equip the wind turbine with two open-circuit hydrostatic transmissions.

The first of these, HST1, is located in the nacelle of the wind turbine and has the role of multiplying the speed of the rotor of the wind turbine 30 times so that the hydraulic pump of HST2 located on the ground is driven to a suitable speed. The connection between HST1 and HST2 is made through a shaft that connects the hydraulic motor of HST1 with the hydraulic pump of HST2.

HST1 has in its structure an orbital hydraulic motor, with a capacity of 1000 cc/rev, used as a hydraulic pump; this orbital motor is driven by the rotor of the wind turbine with a speed between 30-150 RPM. The other positive displacement machine of this transmission is one with axial pistons and fixed capacity of 34 cc/rev. The scheme of this transmission also includes a pressure valve set at maximum pressure of 300 bar as a safety valve, a hydraulic volume (chamber), hydraulic tank and hydraulic pipes.

The HST2 is with secondary regulation and has in its structure two positive displacement hydraulic machines – a pump with a fixed capacity of 34 cc/rev, and a motor with variable capacity and the maximum value of 49 cc/rev. The variable capacity of the hydrostatic motor in the structure of HST2 allows constant maintenance of the hydraulic motor speed and implicitly of the synchronous electric generator whose frequency is dependent on the speed.

The simulation network of the wind turbine with a rotor diameter of 15 m equipped with hydrostatic transmission and their parameters are presented in Figure 1. The numerical simulation was performed in Simcenter Amesim and had the following settings: start time 0, end time 100 s, number of points 10001, sampling frequency 100 Hz and print interval 0.01 s.

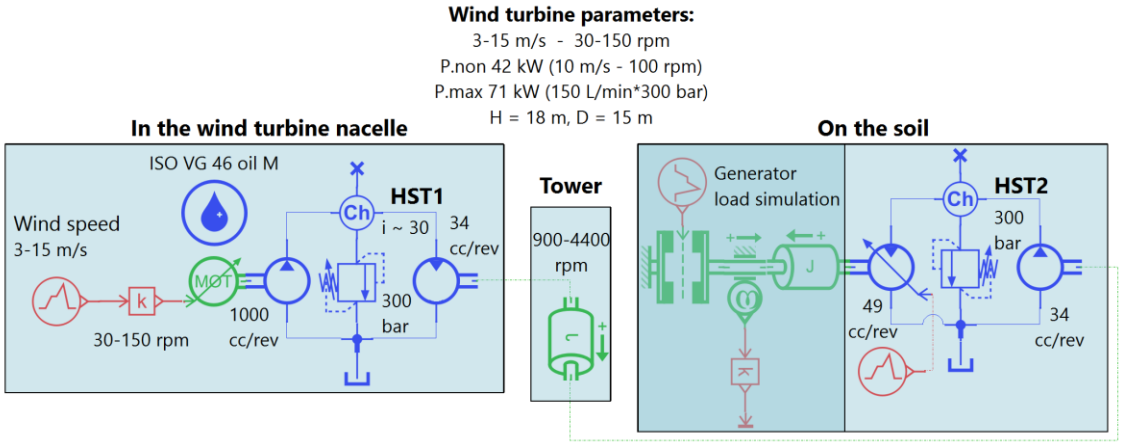


Figure 1. Numerical simulation network of the wind turbine equipped with hydrostatic transmissions.

https://doi.org/10.5593/sgem2024/4.1/s17.14

RESULTS & DISCUSSION

After running the numerical simulation model of the wind turbine equipped with hydrostatic transmissions, the graphs presented in this section of the paper result.

Figure 2 shows the theoretical variations of the power developed by the wind turbine depending on the wind speed, the rotation speed of the wind turbine shaft, as well as the rotational speed of the hydraulic pump in the structure of HST2.

In this figure, one can see that the wind turbine produces 42 kW at a wind speed of 10 m/s and a speed of wind turbine shaft of 100 RPM.

The maximum power of the wind turbine is 71 kW; it is reached at a wind speed of 15 m/s and a rotation speed of the turbine shaft of 150 RPM or at a rotation speed of 4400 RPM of the hydraulic pump in the structure of HST2.

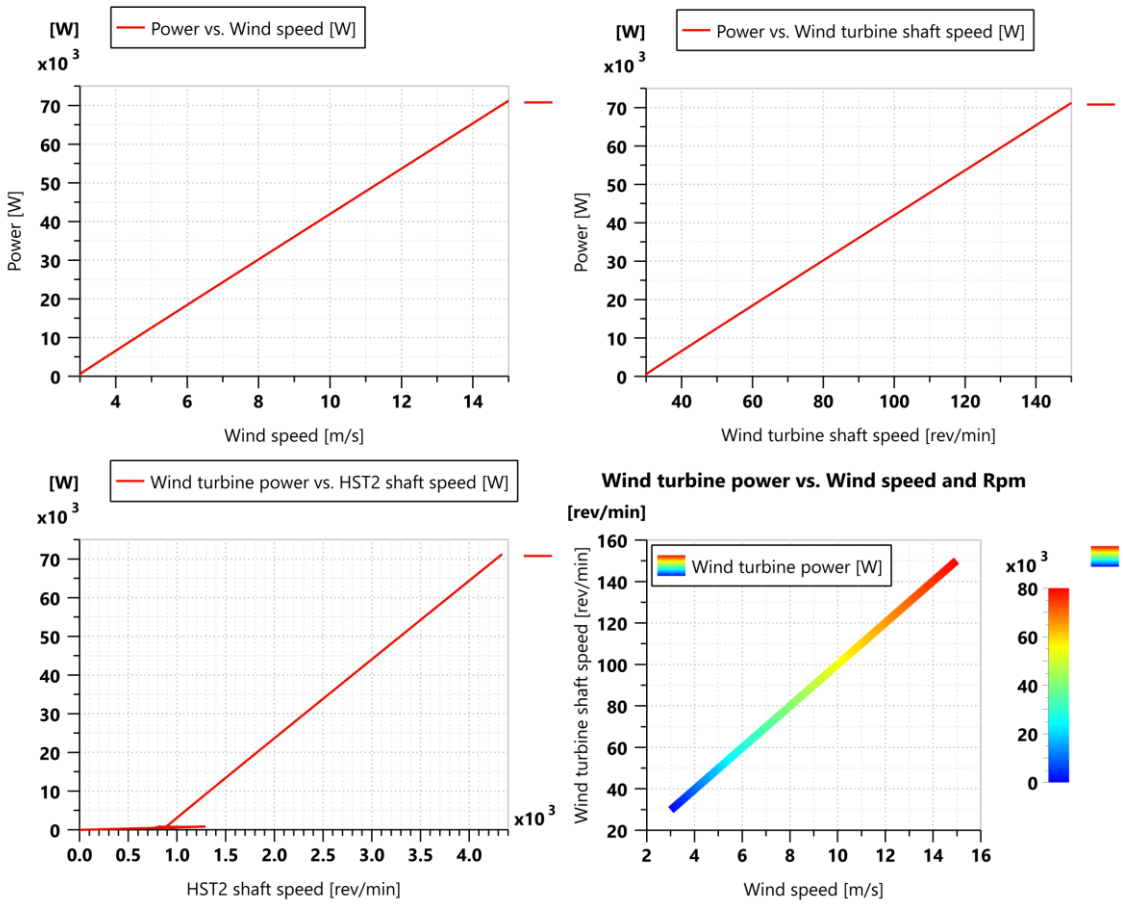


Figure 2. Power as a function of wind speed, wind turbine shaft speed and speed of the hydraulic pump in the structure of HST2.

The dynamic variation over time of the pressures and the flow rates of the two hydrostatic transmissions in the structure of the wind turbine are presented in Figure 3.

The capacities of the positive displacement machines were chosen so that the maximum pressure of the two HSTs never exceeds 300 bar so that the volume losses are as small as possible and the nominal diameter of the pipes is DN16, so that the linear losses are also as small as possible. Moreover, in Figure 3 one can see that the flow rate of the two transmissions varies from 30 to 150 l/min.

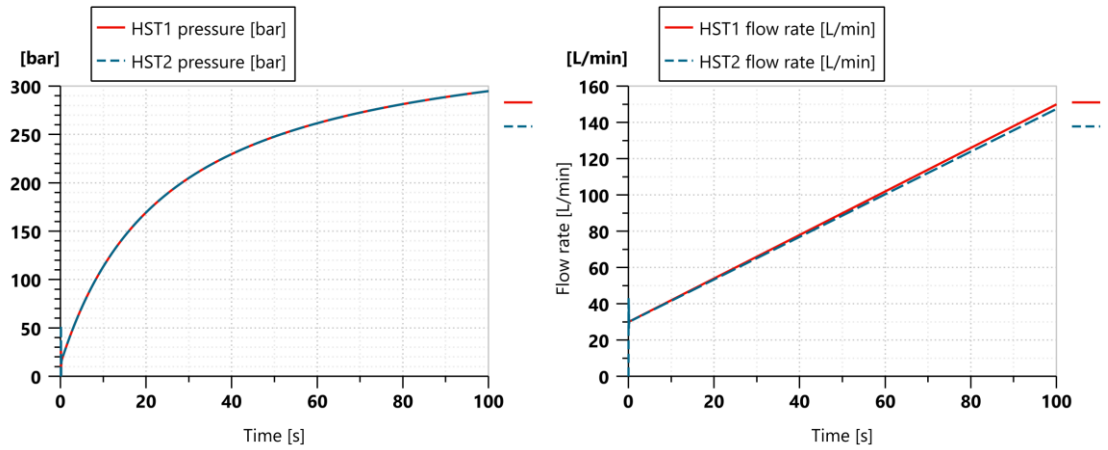


Figure 3. Dynamic variation over time of pressures and flow rates of the two hydrostatic transmissions.

The dynamic variation over time of the speed of the synchronous electric generator and its frequency are presented in Figure 4.

In the graphs in this figure, one can see that regardless of the rotor speed of the wind turbine and the resisting torque to the shaft of the electric generator, changing the volumetric capacity of the hydraulic motor in the range from 20% to 100%, the speed of the electric generator remains approximately constant around the value of 3000 RPM, as well as its frequency, around 50 Hz, the error being less than 1 Hz.

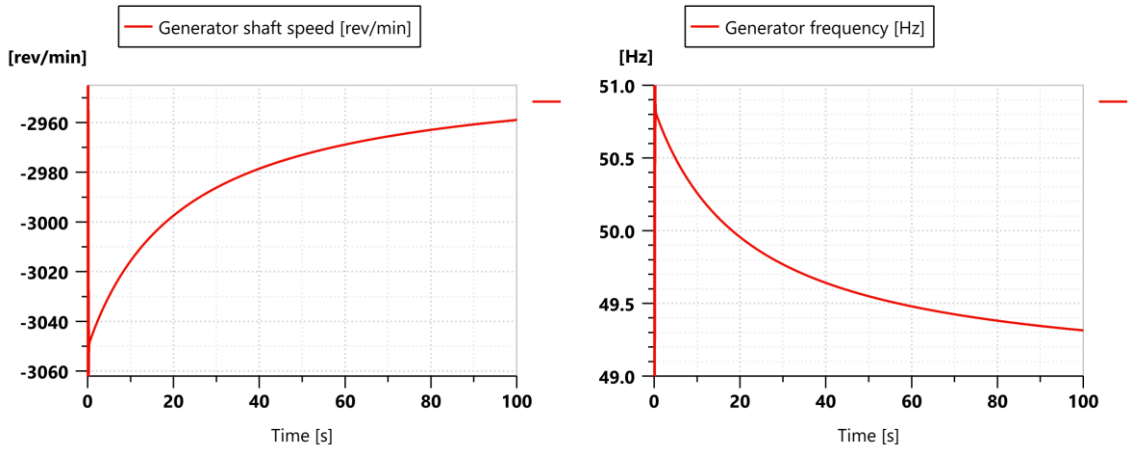


Figure 4. Speed of the synchronous electric generator and its frequency.

CONCLUSION

The paper presents a solution for transmission of energy from the turbine rotor to the generator in wind turbines, which has been validated by numerical simulation using Simcenter Amesim. The proposed system consists of two open-circuit hydrostatic transmissions, HST1 and HST2, which are located in the nacelle of the wind turbine and on the ground, respectively. HST1 multiplies the speed of the wind turbine rotor 30 times, driving the hydraulic pump of HST2 located on the ground, while HST2 maintains a constant speed of the synchronous electric generator.

The results of the numerical simulation show that the wind turbine can produce a maximum power of 71 kW at a wind speed of 15 m/s and a rotation speed of 150 RPM

https://doi.org/10.5593/sgem2024/4.1/s17.14

or at a rotation speed of 4400 RPM of the hydraulic pump in the structure of HST2. The dynamic variation over time of the pressures and flow rates of the two hydrostatic transmissions shows that the capacities of the positive displacement machines were chosen so that the maximum pressure of the two HSTs never exceeds 300 bar, and the nominal diameter of the pipes is DN16. The dynamic variation over time of the speed of the synchronous electric generator and its frequency shows that the speed of the electric generator remains approximately constant around the value of 3000 RPM, as well as its frequency, around 50 Hz, and the error is less than 1 Hz.

The proposed hydrostatic power transmission system for wind turbines has several advantages, such as reducing the suspended mass of the turbine, reducing the cost of the transmission system, and improving the efficiency of the system. However, further research is necessary to validate the proposed system experimentally and to evaluate its performance under different operating conditions. Additionally, the system durability and maintenance requirements need to be studied to ensure its long-term viability.

In conclusion, the proposed hydrostatic power transmission system for wind turbines has the potential to reduce the suspended mass of the turbine, reduce the cost of the transmission system, and improve the efficiency of the system. The results of the numerical simulation are promising, but further research is necessary to validate the proposed system experimentally and to evaluate its performance under different operating conditions. The proposed system has the potential to contribute to the advancement of wind energy technology and the reduction of greenhouse gas emissions.

ACKNOWLEDGEMENTS

This work was carried out through the Core Program within the National Research Development and Innovation Plan 2022-2027, carried out with the support of the Romanian Ministry of Research, Innovation and Digitalization (MCID), project no. PN 23 05. The research was financially supported by a project funded by MCID through Programme 1 – Development of the national research & development system, Sub-programme 1.2–Institutional performance–Projects financing the R&D&I excellence, Financial Agreement no. 18PFE/30.12.2021.

REFERENCES

[1] European Commission, Renewable energy targets, accessed on April 18, 2024, https://energy.ec.europa.eu/topics/renewable-energy/renewable-energy-directive-targets-and-rules/renewable-energy-targets_en.

[2] REN21 (Renewable Energy Policy Network for the 21st Century), Renewables 2023. Global Status Report, accessed on April 18, 2024, https://www.ren21.net/gsr-2023/.

[3] The Wind Power, accessed on April 22, 2024, https://www.thewindpower.net/turbine_en_223_enercon_e126-6000.php.

[4] The Maritime Executive, LLC, Design for the world's largest wind turbine, 16MW from China, accessed on April 23, 2024, https://maritime-executive.com/article/design-for-the-world-s-largest-wind-turbine-16mw-from-china.

[5] Rajaei M., Tinjum J.M., Life cycle assessment of energy balance and emissions of a wind energy plant, Geotechnical and Geological Engineering, vol. 31, pp 1663-1670, 2013. DOI: 10.1007/s10706-013-9637-3.

[6] Mello G., Dias M.F., Robaina M., Wind farms life cycle assessment review: CO2 emissions and climate change, Energy Reports, vol. 6/supplement 8, pp 214-219, 2020. DOI: 10.1016/j.egyr.2020.11.104.

[7] Vukovic M., Murrenhoff H., The next generation of fluid power systems, Procedia Engineering, vol. 106, pp 2-7, 2015. DOI: 10.1016/j.proeng.2015.06.002.

[8] Popescu T.C., Dumitrescu I.-C., Considerations regarding the use of hydrostatic transmissions in wind turbines, 25th International Conference on Hydraulics and Pneumatics HERVEX, Băile Govora, Romania, November 13-15, pp 111-119, 2019.

[9] Piña Rodriguez I.G., Hydraulic drivetrains for wind turbines: Radial piston digital machines, Graduation project for M.Sc. in Sustainable Energy Technology, Delft University of Technology, July 2012.

[10] Sheng Y., Escobar-Naranjo D., Stelson K.A., Feasibility of hydrostatic transmission in community wind turbines, Actuators, vol. 12/issue 11, ID 426, 2023. DOI:10.3390/act12110426.

https://doi.org/10.5593/sgem2024/4.1/s17.14

INFLUENCE OF THE NATURE OF AROMATIC POLYMER AS A PT PARTICLE STABILIZER ON ITS ACTIVITY AND SELECTIVITY IN THE LIQUID-PHASE HYDROGENATION OF AROMATIC AND POLYAROMATIC SUBSTRATES

Assoc. Prof. Dr. Alexey Bykov

Assoc. Prof. Dr. Galina Demidenko

Assoc. Prof. Dr. Linda Nikoshvili

Ms. Elena Bakhvalova

Tver State Technical University, **Russian Federation**

ABSTRACT

A series of platinum catalytic systems stabilized in aromatic polymers were obtained in this work. Commercially available styrene-divinylbenzene (MN100) and polymers synthesized by one-stage crosslinking by the Friedel-Crafts reaction from benzene, naphthalene, and an equimolar benzene-naphthalene mixture were used as polymers. The obtained systems were tested in liquid-phase hydrogenation reactions of benzene, toluene, and benzene-toluene mixture, as well as anthracene in a dodecane medium. The reaction products were studied using GC-MS. Polymers and catalytic systems were studied using diffuse reflection IR spectroscopy, XPS, low-temperature nitrogen physisorption, thermogravimetry coupled with mass spectrometry, and TEM.

The study of polymers by XPS and FTIR showed the presence of oxygen-containing functional groups with a similar nature in all polymers. The range of thermal stability of polymers was determined. The catalytic activity of 1%Pt/polymer systems in liquid-phase hydrogenation of solutions of pure benzene, toluene, and anthracene in dodecane, as well as an equimolar benzene-toluene mixture in dodecane, were compared. The dependence of the reaction rate, as well as the selectivity in the case of anthracene, on the nature of the aromatic blocks in the polymer matrix, was shown. The selectivity for cycloalkanes during hydrogenation of mononuclear arenes was 100%, regardless of substrate conversion. The selectivity of obtaining 9,10-dihydroanthracene at 90% anthracene conversion was found to be above 80% for all studied systems. In addition, the possibility of obtaining smaller diameter metal particles in the synthesized polymers in comparison with the industrial polymer MN100 was shown.

Keywords: hydrogenation of arenes, crosslinked polymer, platinum

INTRODUCTION

Polymer matrices based on the aromatic structures find a wide application as catalyst supports in fine organic synthesis, and chromatography [1-3]. They are widely used as sorbents for the removal of pollutants from gaseous and liquid industrial flows. The application of aromatic polymers as reservoirs for the storage of gas and volatile compounds is well known [4-10]. In most cases, non-functionalized and functionalized

https://doi.org/10.5593/sgem2024/4.1/s17.16

polystyrene, crosslinked polystyrene, and copolymers of styrene-divinylbenzene are used as such polymers. The industrial styrene-divinylbenzene polymers MN100, and MN-270, and their analogs are known to be used as supports for hydrogenation catalytic systems [11, 12].

In this work, the aromatic polymer matrices were obtained by the crosslinking of benzene, naphthalene, and their equimolar mixture with methylal in the presence of iron chloride. The work is focused on the study of the possibility of application of such polymers as supports for the catalysts of arene hydrogenation. The activity of the catalytic systems containing platinum was evaluated. The influence of the composition of the polymer network on the activity of catalytic systems was studied.

MATERIALS AND METHODS

Polymer Synthesis

Polymer matrices were obtained by the crosslinking of 0.02 mol of aromatic substrate with methylal (0.06 mol) in the medium of 1,2-dichloroethane in the presence of iron III chloride. The cross-linking was carried out as follows: methylal was dropped in the well-stirring mixture of substrate, iron chloride, and dichloroethane for 1 h at 40 °C. The mixture was then stirred for 5 h at 45 °C. After that, the temperature was raised to 80°C and the synthesis was performed for 19 h. The polymer obtained was washed in the Soxhlet apparatus for 24 h and dried in a vacuum at 60°C for 24 h. The polymers were signed as PB (polymer obtained from benzene), PN (polymer obtained from naphthalene), and PBN (polymer obtained from benzene and naphthalene). The synthesized polymers were found to be fine powders.

The industrial styrene-divinylbenzene copolymer MN100 was milled and the fraction with the particle size below 63 μm was used. The polymer was washed consecutively with water and acetone and dried at 70°C in the air.

Catalyst Synthesis and Characterization

Catalytic systems Pt/PBN, Pt/PN, Pt/PB, and Pt/MN100 containing 1 wt. % of Pt were synthesized by wetness impregnation using a solution of hexachloroplatinum acid in tetrahydrofuran. The obtained composites were dried at 70°C in the air.

The reduction of the catalysts was carried out in a tube reactor at 300±10°C in a hydrogen flow of 100 mL/min for 3 h. The cooling of the catalysts was performed in a nitrogen atmosphere.

Low-temperature nitrogen physisorption was carried out using a Beckman Coulter SA 3100 (Coulter Corporation, Miami, FL, USA). Before the analysis, each sample was placed in a quartz cell installed in the Beckman Coulter SA-PREP. The samples were pretreated over 60 min under nitrogen at 120°C. Once the pretreatment was completed, the cell was cooled and weighed and then transferred to the analytical port. Analysis was performed at -196°C and at a relative pressure of 0.9814 (for pores less than 100 nm in diameter) to obtain a PSD (ADS) profile.

DRIFTS was carried out using an IRPrestige-21 FTIR spectrometer (Shimadzu, Kyoto, Japan) equipped with a DRS-8000 diffuse reflectance accessory (Shimadzu, Kyoto, Japan). The background sample was a mirror of the material of the optical system of the

DRS-8000 accessory. All spectra were recorded in the 4000–500 cm^{-1} range of wavenumbers at a resolution of 4 cm^{-1}.

TG-MS data were obtained as follows. The thermogravimetric analysis of the samples was carried out using TG 209 F1 YRIS (Netzsch, Germany). Argon (high purity) was used as a medium. The analysis was performed according to the following temperature program: 40°C (5 min) → 10°C/min (600°C) → 600°C (10 min). Active argon flow through the furnace of thermal weights was 20 mL/min, and the protective flow rate was maintained at 20 mL/min during the analysis. A part of the vapor-gas flow from the thermal weights was diverted through a heated quartz capillary to the electron-impact ionization chamber of the mass spectrometer QMS 403 D (Netzsch, Germany). Analysis of the vapor-gas flow was carried out by the cyclic scanning of the ions in the range of 15-135 m/z.

XPS data were obtained using Mg Kα (hν = 1253.6 eV) radiation with an ES-2403 spectrometer (Institute for Analytic Instrumentation of RAS, Saint Petersburg, Russia) equipped with an energy analyzer PHOIBOS 100-MCD5 (SPECS, Berlin, Germany) and X-ray source XR-50 (SPECS, Berlin, Germany). All the data were acquired at an X-ray power of 250 W. Survey spectra were recorded at an energy step of 0.5 eV with an analyzer pass energy of 40 eV. High-resolution spectra were recorded at an energy step of 0.05 eV with an analyzer pass energy of 7 eV. Samples were outgassed for 180 min before analysis and were stable during the examination. The data analysis was performed via Casa XPS. Binding energies (BEs) were determined with the error ±0.1 eV.

STEM characterization was carried out using the FEI Tecnai Osiris instrument (Thermo Fisher Scientific, Waltham, MA, USA) operating at an accelerating voltage of 200 kV, equipped with a high-angle annular dark field (HAADF) detector (Fischione, Export, PA, USA) and an energy-dispersive X-ray (EDX) microanalysis spectrometer (EDAX, Mahwah, NJ, USA). Samples were prepared by embedding them in epoxy resin followed by microtoming (ca. 50 nm thick) at ambient conditions. For the image processing, Digital Micrograph (Gatan, Pleasanton, CA, USA) software and TIA (Thermo Fisher Scientific, Waltham, MA, USA) were used. A Holey carbon/Cu grid was used as a sample support.

Aromatic Substrate Hydrogenation

0.1000 g of the preliminary reduced catalyst, aromatic substrate, and 40 mL of dodecane were placed into the reactor autoclave equipped with a magnetic stirrer. The initial concentration of substrates in each experiment was 0.25 mol/L. The reactor was sealed and purged with nitrogen. The initial nitrogen pressure was set at 3.0 MPa. The reactor was heated up to 230°C at a constant stirring of 1000 rpm. After reaching the reaction temperature, the sampling of the reaction mixture was carried out, and the atmosphere was replaced by hydrogen. The hydrogen partial pressure was 5.0 MPa. 7 samples were taken during the reaction in each experiment.

GC-MS data were obtained as follows. Samples of the reaction mixture were analyzed via GC-MS (Shimadzu GCMS-QP2010S) equipped with a capillary column HP-1MS (100 m × 0.25 mm i.d., 0.25 μm film thickness). Helium was used as a carrier gas at a linear velocity of 20.0 cm/s. The oven temperature was programmed: 50°C (8 min) →15°C /min (180°C). The temperature of the injector, interface, and ion source was at 260°C, ranging from 10 up to 500 m/z.

https://doi.org/10.5593/sgem2024/4.1/s17.16

RESULTS AND DISCUSSION

Three types of the polymer were synthesized by the benzene (PB), naphthalene (PN), and benzene-naphthalene (PBN) crosslinking with methylal in 1,2-dichloroethane. The thermal stability of the polymers obtained was studied using TG-MS in argon medium. Fig. 1 shows the presence of three similar areas of weight loss during the heating of the polymers up to 600°C. An increase in the naphthalene concentration in the polymer was noted to decrease the total polymer weight loss. Mass spectra of the vapor-gas flow formed at the polymer heating were similar for all studied polymers. Fig. 1b shows the mass spectra in the areas of weight loss for PB polymer. The weight loss of the polymer in the temperature range of 100-260°C correlates to the evaporation of 1,2-dichloroethane. The temperature range of the weight loss of 300-400°C correlates with the elimination of 2-chloroellyl radicals from the network structure. The third range above 400°C can be explained by the decomposition of the polymer aromatic matrix.

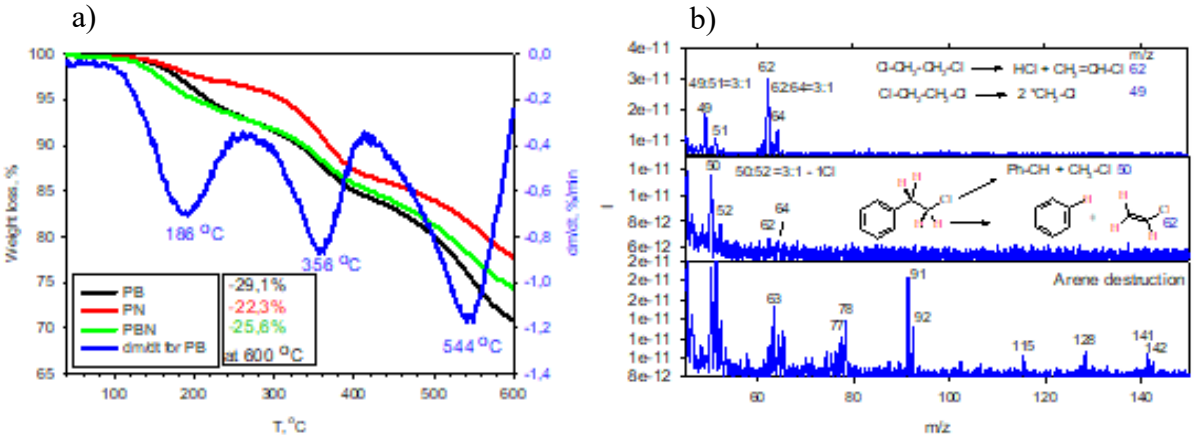


Figure 1. Thermograms of PB, PN, and PBN polymers (a), and mass-spectra of vapor-gas flow in the areas of weight loss for PB polymer (b)

The synthesized polymers were analyzed by diffuse infrared spectroscopy. The IR diffuse reflection spectra normalized by 1604 cm^{-1} are shown in Fig. 2a. The absorption bands at 3046, 3019, and 3007 cm^{-1} correspond to valence vibrations of the C-H bond of aromatic structures. The bands at 1604 and 1502 cm^{-1} correspond to the valence vibrations of C-C aromatic structures. The low-intensity band at 1910 cm^{-1} can be related to the overtones and combined frequencies of vibrations of aromatic structures. The area of about 3500 cm^{-1} corresponds to the valence oscillations of the OH bond. The bands at 1770, 1725, and 1699 cm^{-1} are related to carbonyl groups in the composition of aromatic ester groups and carboxyl groups. 1262 and 1100 cm^{-1} correspond to the bonds of C-O-aromatic and aliphatic ether. The bands in the region of 1440 and 1370 cm^{-1} are related to the deformation vibrations of the CH_2 and CH_3 groups. The 1037 cm^{-1} band corresponds to valence vibrations of the C-Cl bond of CH_2-Cl side radicals that have not completed the formation of methylene bridges during cross-linking. The last one well correlates with mass spectrometry data.

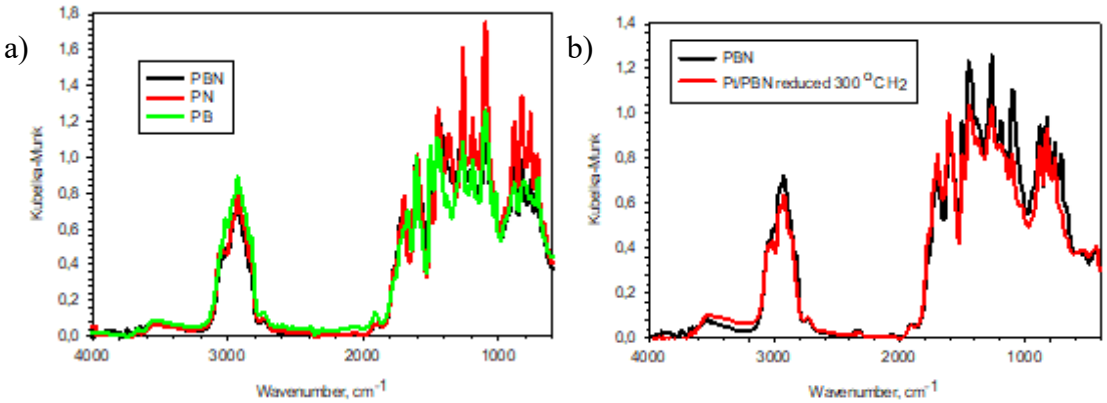


Figure 2. DRIFT spectra of PB, PBN, PN polymers (a), and DRIFT spectra of PBN polymer and catalytic system Pt/PBN reduced at 300°C in a hydrogen flow (b)

The changes in the absorption bands of all polymers during the synthesis and reduction of catalytic systems at 300°C in the hydrogen flow are of the same type and are associated with a decrease in the intensity of the bands 1770, 1725, 1699, 1262, and 1100 cm^{-1} corresponding to the content of ester and ether groups. An example of such a change is shown for the PBN polymer and the reduced Pt/PBN system (Fig. 2b).

Analysis of polymers by low-temperature nitrogen physisorption showed that the specific surface area of polymers was found to be 1066, 1044, and 943 m^2/g for PB, PBN, and PN, respectively (Fig.3a). The specific volume of micropores in the same series was 0.26, 0.27, and 0.20 cm^3/g. An increase in the proportion of naphthalene in the polymer leads to a certain decrease in the specific surface area and specific volume. The introduction of naphthalene into the polymer structure leads to a shift in the pore distribution towards a larger volume (Fig. 3b).

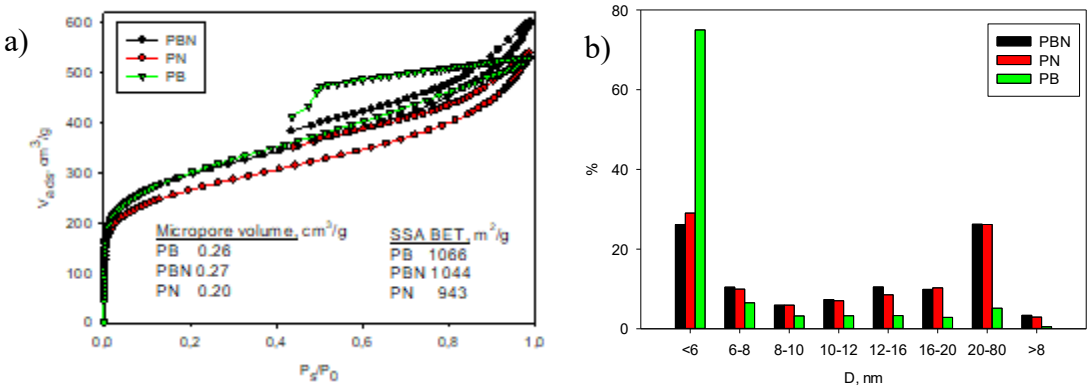


Figure 3. Adsorption-desorption isotherms (a) and pore-size distribution (b) for PB, PN, and PBN polymers

The synthesized polymers were used for the synthesis of platinum-containing catalysts. The analysis of the size of the active phase in the obtained catalytic systems Pt/PB, Pt/PNB, Pt/PN, and the reference Pt/MN100 [11, 13] showed that in all cases a bimodal size distribution of platinum particles was observed (Fig. 4). This effect is seen for Pt/MN100 and Pt/PBN systems. Pt/MN100 has distribution maxima of about 3.9 and 11.7 nm. For Pt/PBN, the distribution maxima are observed at 3.4 nm and 10.9 nm. For Pt/MN100, a significant proportion of larger particles is seen in comparison with

https://doi.org/10.5593/sgem2024/4.1/s17.16

Pt/PBN. The Pt/PB system forms particles with an average size of about 3.1 nm and a certain number of aggregates. The Pt/PN system has particles with a mean size of about 4.3 nm and 8.7 nm, respectively.

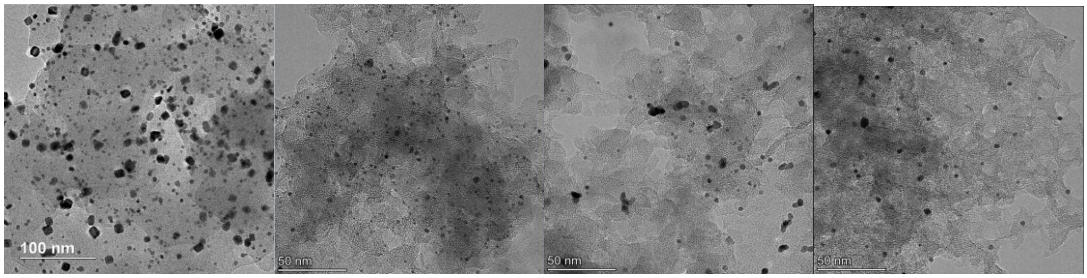


Figure 4. HRTEM images of the reduced catalytic systems Pt/MN100, Pt/PB, Pt/PNB, Pt/PN (from left to right)

XPS analysis of the surface of the initial and reduced catalytic systems showed that during the reduction process, the chlorine content on the surface decreases by a third from 2.6-2.8 at. % to 1.7-1.8 at. %. This correlates with mass spectrometry data. For all initial systems, the Pt 4f7/2 73.7 eV state which can be attributed to PtO and $PtCl_2$ formed as a result of the reduction of hexachloroplatinic acid by tetrahydrofuran during the synthesis of catalysts is observed. For all reduced systems, the Pt 4f7/2 71.8 eV state which can be attributed to platinum metal nanoparticles is observed [14]. For all reduced catalytic systems, a decrease in the oxygen content on the surface by 0.5-1 at. % is also observed. This correlates well with DRIFT spectroscopy data indicating a decrease in the content of ester bonds.

The catalytic activity of the obtained systems was studied in the liquid-phase hydrogenation of benzene, toluene, and anthracene, as well as an equimolar benzene-toluene mixture in n-dodecane. The initial reaction rates for each substrate are shown in Table 1.

During the hydrogenation of benzene, toluene, and their mixtures, only products of complete saturation of the cycles with hydrogen – cyclohexane and methylcyclohexane, respectively – are formed. The main product of anthracene hydrogenation in all cases is the product of hydrogen saturation of the central cycle 9,10-dihydroanthracene. At 90% anthracene conversion, the integral selectivity for 9,10-dihydroanthracene was found to be 86.4, 80.3, 80.1, and 79.5% for Pt/MN100, Pt/PBN, Pt/PN, Pt/PB, respectively.

The relative rate of benzene and toluene solution hydrogenation for the Pt/MN100 system was found to be the highest during the hydrogenation of toluene and the lowest during the hydrogenation of benzene. The relative rate of hydrogenation of benzene and toluene increases in the range of Pt/PBN < Pt/PN < Pt/PB. The initial rate of anthracene hydrogenation decreases in the same range.

Table 1. Initial rates of hydrogenation of aromatic substrates [mol(substrate)/(mol(Pt)*L*s)]

	Pure substrates			Benzene-toluene mixture	
	Benzene	Toluene	Anthracene	Benzene	Toluene
Pt/MN100	0,17	1,37	0,72	0,44	0,55
Pt/PBN	0,97	0,67	1,17	1,29	0,81
Pt/PN	1,03	1,03	0,92	3,88	2,97
Pt/PB	1,39	1,08	1,01	1,75	0,25

The ratio of the initial rates of hydrogenation of benzene/toluene, and their equimolar mixtures is in the range of 0.8 : 1.3 : 1.6 : 7 for systems Pt/MN100 : Pt/PN : Pt/PBN : Pt/PB. For the synthesized polymers, it corresponds to the transition from a polymer based on crosslinked naphthalene, through an equimolar mixture of naphthalene+benzene to a polymer based on crosslinked benzene. In this range, the elementary building block of the polymer reduces but increases the conformational mobility of the final polymer mesh. Thus, a polymer grid with a small elementary block makes it possible to increase the selectivity of benzene hydrogenation relative to toluene in their mixtures. An increase in a single block size to naphthalene leads to preferential hydrogenation of toluene.

CONCLUSION

Catalytic systems based on benzene, naphthalene, and benzene-naphthalene mixture crosslinked with methylal can be used as supports for catalytic systems for arene hydrogenation. The composition of the mixture of cross-linked arenes affects the micro- and mesoporous structure of the polymer. The last one affects the size distribution of the active phase of the catalytic system and affects the activity of the resulting system in the hydrogenation of mononuclear and polynuclear aromatic substrates.

In addition, the obtained polymers exhibit the stability of the polymer framework in a non-oxidizing environment up to temperatures of about 400°C regardless of the aromatic monomers used for crosslinking. During the synthesis of such polymers, chloroethyl radicals which are largely eliminated in a non-oxidizing environment in the temperature range of 300-400°C without damaging the structure of the polymer mesh are formed.

ACKNOWLEDGEMENTS

The work is financially supported by the Russian Science Foundation, grant 23-23-00090.

REFERENCES

[1] Fontanals N., Marcé R.M., Borrulla F., Cormack P.A.G., Hypercrosslinked materials: preparation, characterization, and applications, Polymer Chem 6 (41), pp. 7231-7244, 2015.

2. Tsyurupa M.P., Tarabaeva O.G., Pastukhov A.V., Davankov V.A., Sorption of ions of heavy metals by neutral hypercrosslinked polystyrene, Intl J Polym Mater Polym Biomater 52 (5), pp- 403-414, 2003.

https://doi.org/10.5593/sgem2024/4.1/s17.16

[3] Bratkowska D., Fontanals N., Borrull F., Cormack P.A.G., Sherrington D.C., Marcé R.M., Hydrophilic hypercrosslinked polymeric sorbents for the solid-phase extraction of polar contaminants from water, J Chromatography A 1217 (19), pp. 3238–3243, 2010.

[4] Chang C.-F., Chang C.-Y., Hsu K. E., Lee S.-C., Holl W., Adsorptive removal of the pesticide methomyl using hypercrosslinked polymers, J Hazard Mater 155 (1-2), pp. 295–304, 2008.

[5] Wood C.D., Tan B., Trewin A., Niu H., Bradshaw D., Rosseinsky M.J., Khimyak Y.Z., Campbell N.L., Kirk R., Stockel E., Cooper A.I., Hydrogen Storage in Microporous Hypercrosslinked Organic Polymer Networks, Chem Mater 19 (8), pp. 2034-2048, 2007.

[6] Li B., Su F., Luo H.-K., Liang L., Tan B., Hypercrosslinked microporous polymer networks for effective removal of toxic metal ions from water, Micropor Mesopor Mater 138, pp. 207–214, 2011.

[10] Tsyurupa M.P., Davankov V.A., Porous structure of hypercrosslinked polystyrene: State-of-the-art mini-review, React Functl Polymers 66 (7), pp. 768-779, 2006.

[11] Bykov A.V., Alekseeva D.V., Demidenko G.N., Vasiliev A.L., Nikoshvili L., Kiwi-Minsker L., New Approach to Synthesis of Tetralin via Naphthalene Hydrogenation in Supercritical Conditions Using Polymer-Stabilized Pt Nanoparticles. Catalysts, 10, pp.1362, 2022.

[12] Manaenkov O., Nikoshvili L., Bykov A., Kislitsa O., Grigoriev M., Sulman M., Matveeva V., Kiwi-Minsker L. An Overview of Heterogeneous Catalysts Based on Hypercrosslinked Polystyrene for the Synthesis and Transformation of Platform Chemicals Derived from Biomass, Molecules 28, pp. 8126, 2023.

[13] Bakhvalova E.S., Pinyukova A.O., Mikheev A.V., Demidenko G.N., Sulman M.G., Bykov A.V., Nikoshvili L.Z., Kiwi-Minsker L, Noble Metal Nanoparticles Stabilized by Hyper-Cross-Linked Polystyrene as Effective Catalysts in Hydrogenation of Arenes, Molecules, 26, 4687, 2021.

[14] Naumkin A. V., Kraut-Vass A., Gaarenstroom S. W., Powell C. J., NIST X-ray Photoelectron Spectroscopy Database, NIST Standard Reference Database Number 20, Gaithersburg MD, 20899: National Institute of Standards and Technology, 2000.

INVESTIGATION OF THE TRANSITION PROCESS OF PARALLEL OPERATION OF A SOLAR POWER PLANT AND THE GRID UNDER EMERGENCY DISTURBANCE

Assoc. Prof. Dr. Svetlana Beryozkina[1]

PhD Ress. Bohirjon Sharifov[2]

Dr. Murodbek Safaraliev[3]

Dr. Anvari Ghulomzoda[4]

PhD Ress. Mukhammadjon Odinabekov[4]

[1] College of Engineering and Technology, American University of the Middle East, **Kuwait**
[2] Tajik Technical University named after Academician M.S. Osimi, **Tajikistan**
[3] Ural Federal University, **Russia**
[4] Novosibirsk State Technical University, **Russia**

ABSTRACT

Solar energy, as one of the types of green energy, is widely studied by researchers from different regions of the world. Practice shows that the generation of clean energy at solar power plants (SPP) is not always constant, and depends on some external factors, for instance, weather conditions, emergency disturbances, etc. Parallel operation of the solar power plant and the grid eliminates some problems, in particular, fluctuations in the frequency of current due to a shortage/excess of electricity, as well as the use of batteries. Therefore, an infinite power grid is a large accumulator that can compensate for such fluctuations. This paper deals with the analysis and investigation of electromagnetic transients during a parallel operation of the SPP and the grid under a short-circuit disturbance. A block diagram and mathematical model of the SPP are developed in the MATLAB package together with Simulink and Power System Blockset. Dynamic and static modes of the parallel operation of the SPP and the grid are analyzed. Waveforms of voltages and currents at the inverter output during a three-phase short circuit are given. The developed model supports the analysis of currents, voltages, and capacities while various disturbances are simulated.

Keywords: converter, electromagnetic transient process, inverter, mathematical model of a solar power plant, solar power plant.

INTRODUCTION

Currently, solar energy plays an important role in the development of the electric power industry. Especially the use of photovoltaic converters in the process of converting solar energy into electrical energy, which opened a new stage in the development of solar photovoltaic power plants. In recent years, the efficiency of photoelectric converters has increased significantly (up to 25-30%), which makes it possible to obtain up to 250 kWh/m2 of electrical energy per year. The contribution of solar energy to global electricity generation does not exceed 0.1%, and among renewable energy sources

https://doi.org/10.5593/sgem2024/4.1/s17.17

(RES) it accounts for only about 1%. However, despite modest successes in the large-scale generation of electricity from solar energy, the rate of increase in capacity at solar power plants over the past 18 years has been very high. For example, the capacity of photovoltaic power plants during the period from 1996 to 2014 increased by more than 81 times (from 0.7 to 57 GW) and continues to grow rapidly (Fig. 1) [1].

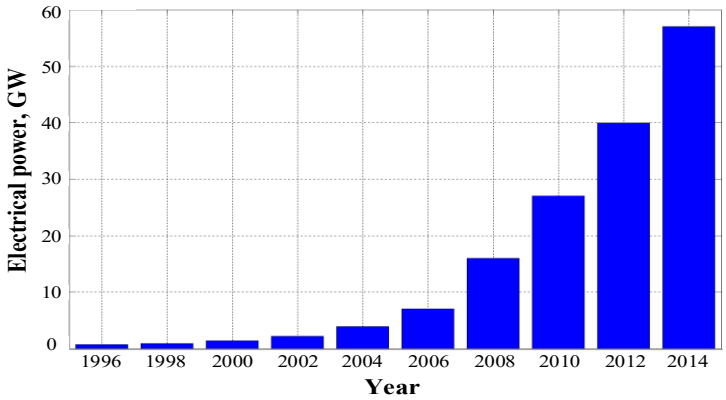


Figure 1. Increase in capacity of solar power plants

A serious disadvantage of autonomous solar photovoltaic power systems is the need to use rechargeable batteries operating in cyclic mode. The number of operating cycles of common lead-acid batteries is small (1500-2000), which requires frequent replacement [2]. The use of industrial batteries with a long service life, for example, nickel-cadmium or lithium-ion, requires a significant increase in financial investments in the construction of solar photovoltaic power systems.

In addition, it must be taken into account that energy losses also occur in batteries. At best, the efficiency of battery charge-discharge processes is 90%, and it deteriorates as they are used.

Parallel operation of the solar photovoltaic power system with the network allows one to avoid many of the disadvantages of autonomous systems, including fluctuations in the frequency of the current due to a shortage/excess of electricity [3,4]. Essentially, an infinite power grid is a large battery that can compensate for such fluctuations.

The purpose of this work is to develop a model and analyze transient processes during the parallel operation of the solar photovoltaic power system with the network under conditions of an emergency disturbance.

PROBLEM STATEMENT

To study the parallel operation of the solar photovoltaic power systems with the network, a simulation model was developed in the Simulink environment, based on a block diagram (Fig. 2) and differential equations that describe electromagnetic transient processes in the solar photovoltaic power systems.

The main element of the solar photovoltaic power systems is the converter. Each converter includes a step-up voltage converter (DC/DC converter) from 200 to 700V, a three-phase inverter made based on IGBT modules using a three-phase bridge circuit, and proportional-integral (PI) current and voltage regulators.

Three-phase inverters as part of the converter perform the following main tasks:

- conversion of direct voltage into alternating voltage at the frequency of the unified power system (UPS);
- synchronization of the frequency of voltage and current of the solar photovoltaic power system with the UPS;
- output voltage stabilization;
- current limitations during overload and short circuits.

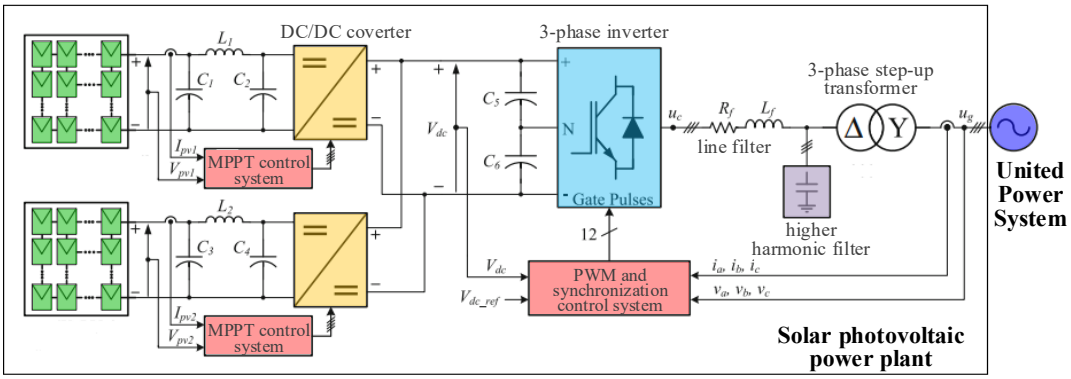


Figure 2. Structural diagram of the solar photovoltaic power systems.

Converter installations are known to be sources of higher harmonics. The commutation of thyristors and transistors distorts the shape of the current and voltage curves in the adjacent AC network, which leads to the appearance of higher harmonics in the network. Higher harmonic filters are used to limit the circulation zones of higher harmonics within substations, eliminate the adverse effects of higher harmonics on the electrical equipment of adjacent systems, and also eliminate radio interference along communication lines. Higher harmonic filters are assigned another task, namely, the delivery of reactive power in the network. The filters contain high-voltage capacitor banks, which are capable of generating reactive power at the main voltage frequency. The need to generate reactive power at a converter substation is because inverters when converting electrical energy, consume significant reactive power from the network.

RESEARCH METHODOLOGY

The study and analysis of transient processes of the solar power system during parallel operation with the UPS is carried out based on the analysis of electromagnetic transient processes on an autonomous inverter (Fig. 3).
The inverter control system consists of the following components:

- algorithm for synchronization with the network;
- d-q axes regulators;
- PI – current regulators;
- bus voltage regulator;
- maximum power point tracking system (Maximum Power Point Tracking System).

https://doi.org/10.5593/sgem2024/4.1/s17.17

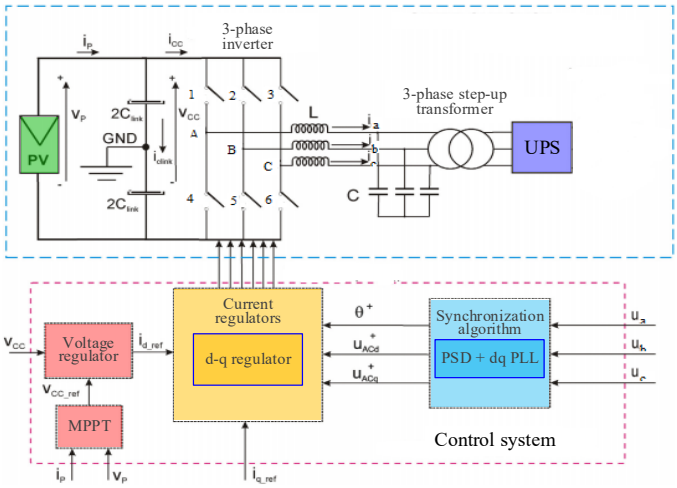


Figure 3. Structural diagram of autonomous inverter

A mathematical model of an autonomous inverter is built based on physical processes occurring in the inverter, which is described by the following equations [5]:

$$\begin{cases} \boldsymbol{U_{Ca}} - U_a = L_a \dfrac{di_a}{dt} + i_a R_a \\ \boldsymbol{U_{Cb}} - U_b = L_b \dfrac{di_b}{dt} + i_b R_b \\ \boldsymbol{U_{Cc}} - U_c = L_c \dfrac{di_c}{dt} + i_c R_c \\ i_p = i_{Clink} + i_{CC} \\ i_{CC} = S_a i_a + S_b i_b + S_c i \\ i_{Clink} = C_{link} \dfrac{dU_{CC}}{dt} \end{cases} \quad (1)$$

where L_a, L_b, L_c – is the inductance of the inverter output filter (H); i_a, i_b, i_c – linear currents of a three-phase system (A); R_a, R_b, R_c – active resistance of the output filter (Ohm); S_a, S_b, S_c – key states of IGBT transistors (1 - on, 0 - off); C_{link} – capacitance of the DC link capacitor (μF); i_p – load current on the DC side (A); i_{Clink} – current on the DC link capacitor (A); i_{CC} – current at the input of the autonomous inverter (A).

Linear currents and voltages are expressed by the following system of equations:

$$\begin{cases} \boldsymbol{U_{Ca}} = E_m \cos\omega t \\ \boldsymbol{U_{Cb}} = E_m \cos(\omega t + \dfrac{2\pi}{3}) \\ \boldsymbol{U_{Cc}} = E_m \cos(\omega t - \dfrac{2\pi}{3}) \\ \boldsymbol{i_a} = I_m \cos(\omega t + \varphi) \\ \boldsymbol{i_b} = I_m \cos(\omega t - \dfrac{2\pi}{3} + \varphi) \\ \boldsymbol{i_c} = I_m \cos(\omega t + \dfrac{2\pi}{3} + \varphi) \end{cases} \quad (2)$$

where E_m – is the phase voltage amplitude (V); I_m – phase current amplitude (A); ω – angular frequency (rad/sec); φ – phase shift (degree). Moreover, in a three-phase current system:

$$i_a + i_b + i_c = 0 \quad (3)$$

Considering equation (1), the voltage at the inverter output is determined as:

$$\begin{cases} \begin{bmatrix} U_a \\ U_b \\ U_c \end{bmatrix} = R \begin{bmatrix} i_a \\ i_b \\ i_c \end{bmatrix} + L \frac{d}{dt} \begin{bmatrix} i_a \\ i_b \\ i_c \end{bmatrix} + U_{dc} \begin{bmatrix} \frac{2S_a - (S_b + S_c)}{3} \\ \frac{2S_b - (S_a + S_c)}{3} \\ \frac{2S_c - (S_a + S_b)}{3} \end{bmatrix} \end{cases} \quad (4)$$

Mathematical model of an autonomous inverter in a two-phase coordinate system

In a symmetrical two-phase system, the axes of the windings are mutually perpendicular, which makes it possible not to take into account the mutual inductive coupling between them and allows one to reduce the number of equations describing transient processes.

It is advisable to study transient processes in three-phase networks, in which phase symmetry is maintained, in a two-phase rotating d-q coordinate system [6].

The spatial representation of coordinate transformation is explained in Fig. 4.

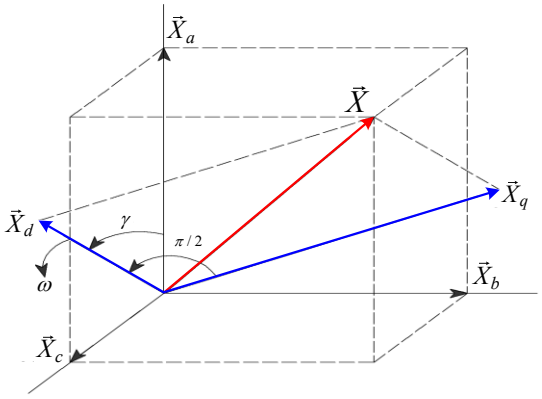


Figure 4. Geometric interpretation of coordinate transformation

where $\vec{X}_a$,$\vec{X}_b$,$\vec{X}_c$ – are vectors representing phase currents, voltage, and flux linkage in a three-phase system; $\vec{X}$ – result vector; $\vec{X}_d$,$\vec{X}_q$ – vectors representing phase currents, voltage, and flux linkage in a two-phase rotating coordinate system d-q; γ – angle of shift of the axes relative to the magnetic axis of phase A; $\omega = 2\pi f$ – angular frequency of rotation.

The transition in the d-q coordinate system is carried out as follows [7]:

$$\begin{cases} f_d = \frac{2}{3}\left[f_a \cos\gamma + f_b \cos(\gamma - \frac{2\pi}{3}) + f_c \cos(\gamma + \frac{2\pi}{3}) \right] \\ f_q = \frac{2}{3}\left[f_a \sin\gamma + f_b \sin(\gamma - \frac{2\pi}{3}) + f_c \sin(\gamma + \frac{2\pi}{3}) \right] \end{cases} \quad (5)$$

$$\begin{cases} f_A = f_d \cos\gamma + f_q \sin\gamma + f_0 \\ f_B = f_d \cos(\gamma - \frac{2\pi}{3}) + f_q \sin(\gamma - \frac{2\pi}{3}) + f_0 \\ f_C = f_d \cos(\gamma + \frac{2\pi}{3}) + f_q \sin(\gamma + \frac{2\pi}{3}) + f_0 \end{cases} \quad (6)$$

where $f_0 = \frac{1}{3}(f_A + f_B + f_C)$ – is the vector of the zero component.

https://doi.org/10.5593/sgem2024/4.1/s17.17

Equality (4) and (5) establish a direct and inverse relationship between actual currents, voltages, and flux linkages in a three-phase system and new changes in the d, q axes.
The system of differential equations in a two-phase rotating coordinate system, under generally accepted assumptions, using the Park-Gorev formula [8] has the form:

$$\begin{cases} u_d = Ri_d + L\dfrac{di_d}{dt} + u_{Sd} - \omega L i_q \\ u_q = Ri_q + L\dfrac{di_q}{dt} + u_{Sq} + \omega L i_d \end{cases} \quad (7)$$

The block diagram of the mathematical model of an autonomous inverter in a fixed coordinate system, taking into account equations (1-7), has the following form:

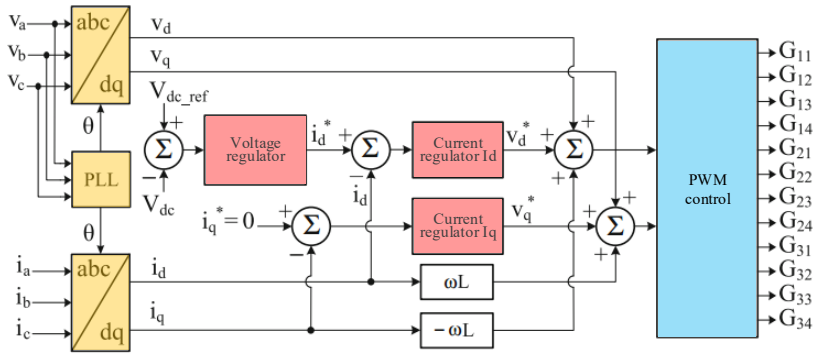


Figure 5. Structural diagram of the mathematical model of the autonomous inverter

RESEARCH RESULTS

The work used the MATLAB environment with the Simulink extension package as one of the most powerful and effective tools for creating a variety of software systems designed to solve scientific and technical problems [8].
Fig. 6 shows a simulation model of the solar photovoltaic power systems, obtained using the MATLAB Simulink program based on a block diagram and differential equations describing electromagnetic transient processes on the solar photovoltaic power systems (1-7).

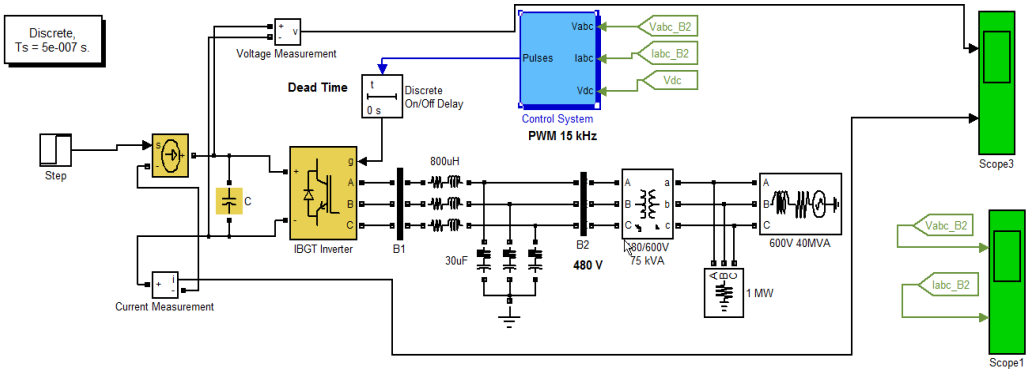


Figure 6. Solar photovoltaic power systems model built in MATLAB Simulink

For the model, Fig. 6, an analysis of the occurrence of transient processes during a short circuit in the UPS was carried out. Fig. 7 shows oscillograms of voltages and currents at the inverter output during a three-phase short circuit in the UPS, the duration of which is 40 ms.

At the initial moment of a short circuit, the high-frequency capacitors of the LC filter of the inverter are discharged through a short-circuited circuit. The discharge process lasts only about 1 us but is accompanied by a current surge that exceeds the amplitude of the periodic component of the short circuit current. The value of the periodic component of the short circuit current is determined not by the resistance of the short circuit, but by the settings of the inverter regulators. Typically, the inverter output current is limited to three times the rated current. The short circuit is switched off by the circuit breaker of the damaged cable line. Due to the untimely operation of the switch poles, overvoltages may occur. In this case, after disconnecting one phase of the damaged circuit, the three-phase short circuit first turns into a two-phase short circuit, and then the remaining phases are disconnected. The overvoltage and its duration depend on the degree of perfection of the inverter regulation system. The best transient performance is achieved by inverters with a high base frequency and fast digital controllers.

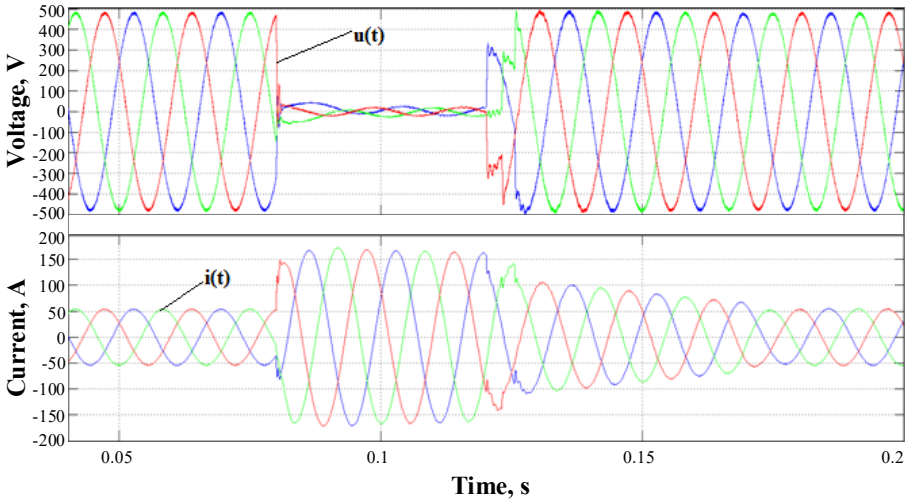


Figure 7. Oscillogram of voltages and currents at the inverter output during a three-phase short circuit lasting 40 ms

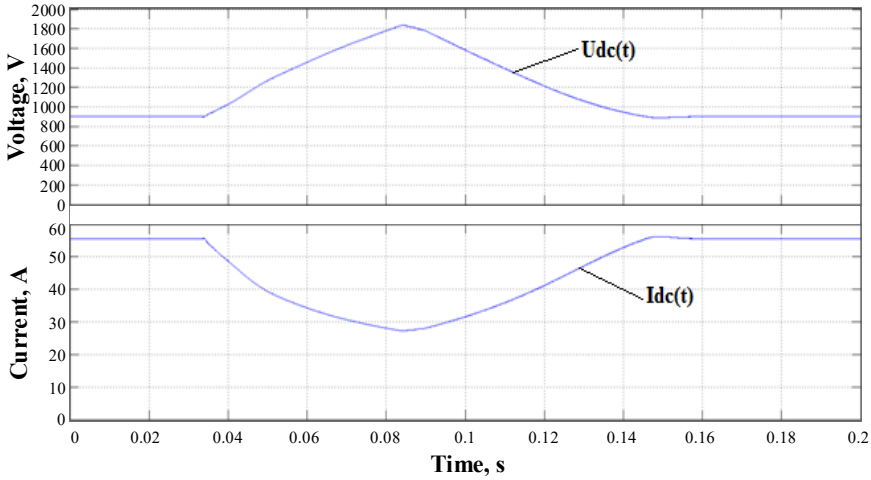


Figure 8. Oscillogram of voltages and currents at the inverter input during a three-phase short circuit lasting 40 ms

Fig. 8 shows oscillograms of voltage and current at the inverter input during a three-phase short circuit in the UPS. The occurrence of a three-phase short circuit at the inverter output leads to idle mode at its input. From the point of view of the balance of

https://doi.org/10.5593/sgem2024/4.1/s17.17

input and output active powers, this mode is quite natural, since during a three-phase short circuit, the active power consumption on the output circuits of the inverter sharply decreases and, accordingly, the direct current at the inverter input.

CONCLUSION

Assessment of emergency modes of solar photovoltaic power systems cannot be carried out using standard methods and requires the use of appropriate dynamic models of solar photovoltaic power systems as part of the UPS, the development of which is an urgent scientific and technical task today.

The presented computer model completely simulates the parallel operation of the solar photovoltaic power systems with the network in all operating modes (static, dynamic) and allows you to analyze the parameters of currents, voltages, and powers during the simulation with subsequent processing of the results obtained.

In the event of a short circuit near a substation, which is accompanied by a significant decrease in network voltage (by more than 10-15%), inverters may lose stability and tip over. To solve this problem, digital automatic control regulators are installed in inverters, which quickly reduce the pulse supply to the transistors when the voltage in the network decreases. The use of digital regulators ensures high performance and the best quality of transient processes during start-up and short circuits.

REFERENCES

[1] Nizhegorodtsev R.M., Ratner S.V., Trends in the development of industrially developed renewable energy technologies: the problem of resource limitations / Thermal Energy, 2016, No. 3, pp. 43-53.

[2] Lakutin B.V., Muravlev I.O., et al. Power supply systems with wind and solar power plants / Tomsk Polytechnic University, Tomsk, 2015, 112 p.

[3] Ghulomzoda A., Gulakhmadov A., Fishov A. et al., Recloser-Based Decentralized Control of the Grid with Distributed Generation in the Lahsh District of the Rasht Grid in Tajikistan, Central Asia / Energies, 2020, issue 14, Art. 3673.

[4] Ghulomzoda A., Safaraliev M., Matrenin P. et al., A Novel Approach of Synchronization of Microgrid with a Power System of Limited Capacity / Sustainability, 2021, issue 24, Art. 13975.

[5] Guerrero-Rodríguez N.F., Herrero-de Lucas L.C. Performance study of a synchronization algorithm for a 3-phasephotovoltaic grid-connected system under harmonic distortionsand unbalances / Electric Power Systems Research, 2014, pp. 252-265.

[6] Bo Yin, Oruganti R., Panda S.K., Bhat A.K.S. A Simple Single-Input-Single-Output (SISO) Model for a Three-Phase PWM Rectifier / IEEE Transactions on Power Electronics, 2009, Vol. 24, pp. 620-631.

[7] Kryuchkov I.P., Starshinov V.A. et al. Transient processes in electrical power systems / MPEI Publishing House, Moscow, 2009, 415 p.

[8] German-Galkin S.G. Computer modeling of semiconductor systems / St. Petersburg: CORONA-print, 2001, 320 p.

LIFE-CYCLE ANALYSIS OF FIREWORKS: ENVIRONMENTAL IMPACT AND IMPROVEMENT OPPORTUNITIES

Assist. Prof. David León[1,2]
Assoc. Prof. Dr. David Bolonio[1,2]
Assist. Prof. Dr. Isabel Amez[1,2]
Researcher Roberto Paredes[1]
Assist. Prof. Dr Blanca Castells[1,2]

[1] Department of Energy and Fuels, E.T.S. Ingenieros de Minas y Energía, Universidad Politécnica de Madrid, **Spain**

[2] TECMINERGY, Technical University of Madrid, Spain, C/Eric Kandel, 1 (TECNOGETAFE), Parque Científico y Tecnológico de la UPM, **Spain**

ABSTRACT

The increasing focus on sustainability necessitates the examination of environmental impacts across all sectors, including pyrotechnics. Pollutant emissions have been extensively studied, but information on sustainability in the pyrotechnics sector is scarce. Thus, a Life Cycle Analysis (LCA) to study two widely used pyrotechnic devices: bangers and shells was carried out, in order to analyze the environmental footprint and detect points where action can be taken. Using SimaPro software and the Product Environmental Footprint (PEF) methodology, the analysis includes all the processes involved from the manufacture of the devices up to their use and end of life, including their distribution. Although the impact on climate change of the devices studied is minimal compared to other products in everyday use, the acquisition of raw materials and their distribution is the stage that contributes the most to the overall environmental impact (60%), while the use of hazardous raw materials, especially potassium perchlorate, and plastics as containers for pyrotechnic compositions, also present important environmental problems. Therefore, measures to reduce the effects of these fireworks should focus on the selection and reduction of raw materials and the elimination of plastic compounds in their designs.

Keywords: Life Cycle Analysis, fireworks, environmental impact, raw materials

INTRODUCTION

Governmental institutions worldwide are moving towards developing a more sustainable planet, driven by different pacts and strategies that will facilitate industrial transformation. One of the most relevant policy frameworks is the 2030 Agenda for Sustainable Development [1]. This plan of action of the United Nations, and assumed by its member states, sets out 17 Sustainable Development Goals (SDGs), with 169 targets, covering the social, economic and environmental spheres. The same applies to the

https://doi.org/10.5593/sgem2024/4.1/s17.18

European Green Pact. It aims to make Europe climate neutral by 2050, focusing on key areas such as clean energy, sustainable mobility, energy efficiency and waste disposal [2].

The need to reduce environmental impact in all sectors is increasingly understood, and in the pyrotechnics sector, studies analysing fewer polluting compositions represent it [3], [4]. Pyrotechnics, present in a multitude of festivities, has a long tradition and a great worldwide recognition. It is a sector known for the quality and artistry in the manufacture of fireworks and other pyrotechnic products [5]. However, the manufacture and use of pyrotechnic products can generate significant environmental impacts due to the generation of air pollutants and waste resulting from the use of non-renewable materials. Hickey et al. have studied the toxicity of particulate matter emitted during the use of fireworks. Toxic metals, such as Pb, were found at extremely high levels [6]. Other researchers such as Singh et al. and Nasir et al. analysed the emissions generated during the Diwali Fireworks period, reporting that fireworks were a potential emitter of metals, organic carbon, elemental carbon and particulate matter, and that SO_2 and NO_X concentrations also increased significantly [7], [8].

Pollutant emissions have been extensively studied, but information on sustainability in the pyrotechnics sector is scarce. There are no circular economy indicators to quantify the impacts of the supply chain of products on the market. These indicators bring together social, economic and environmental aspects, seeking to maximise the value of resources in order to minimise waste throughout the life cycle of products [9]. It also encourages innovation through measures such as eco-design, which can reduce the environmental impact of a multitude of consumer goods [10]. The Life Cycle Assessment (LCA) methodology has emerged as an essential tool for sustainable development. The European Commission has been implementing different life cycle policies for two decades [11], steadily increasing its applications and establishing itself as a fundamental pillar of European sustainable policies.

Every day, more and more research on LCA is revealing important information on sustainability. However, no such analysis has been carried out on pyrotechnic products. Previous studies have analysed the explosives sector which, although they do not use the same compositions as fireworks, can provide useful information due to a similar working principle. Ferreira et al. examine the production of a civil explosive and compare five different compositions based on ammonium nitrate, water, mineral oil, polycarboxylate and XPS. The results show that the highest impact comes from the production of ammonium nitrate, i.e. the raw material phase, and that the addition of sodium nitrate leads to a reduction of impacts ranging from 7% to 14% [12]. Costa et al. provides preliminary results on LCA of RDX production in a military explosives unit. It concludes that hexamine nitration is the most relevant process for the ten environmental impact categories analysed, but stresses the need to develop the study with more specific information on stages such as transport, highlighting the lack of data [13].

In general, the most complicated phase of an LCA is data collection, especially in sectors such as pyrotechnics, due to the limited information available. Therefore, this study carries out a first analysis where a simulation is carried out with theoretical data and assumptions, supported by industry experts and literature, to obtain preliminary results to get an idea of the possible environmental impacts of fireworks. The study analyses the

life cycle of two types of fireworks manufactured in Spain, from the acquisition of raw materials and their distribution, through the manufacturing processes, transport and emissions after use, to the end of life.

MATERIALS AND METHODS

LCA is used as a methodology to study the potential environmental impacts of a product or service. It is regulated by international environmental management standards [14], [15]. These standards define the steps to be followed in order to carry out a life cycle correctly.

Life-Cycle model

The software used in the Life-cycle analysis is SimaPro (Version 9.5), which allows the environmental impacts of products or processes in the value chain to be assessed. The methodology used is the Product Environmental Footprint (PEF). This method studies 16 impact categories, Climate Change (GWP) among them.

The analysis assessed an unfavourable case of manufacture in a hypothetical pyrotechnic factory in Valencia (Spain) and its subsequent use in a pyrotechnic show in Valencia's Town Hall Square during the Fallas festival. The model follows a cradle-to-gate LCA and encompasses the following processes: acquisition of materials, transport, manufacturing, distribution, use and end life. The simplified flow diagram of the model is shown in Figure 1.

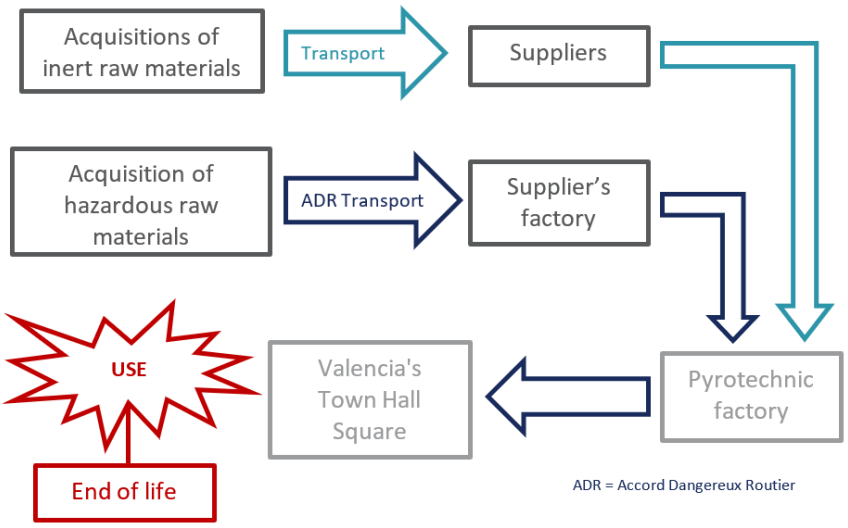


Figure 1. Simplified flow diagram of the Life-cycle model

Two types of fireworks were analysed. One is the flash banger (FB), a simple and widely used product by the general public in Spain. The other is the pyrotechnic shell, a more complex product used by professionals as the main component for night-time fireworks displays in Spain. A comparison between a cardboard (CPS) and a plastic (PPS) case is conducted. This analysis is noteworthy because the choice of packaging can significantly influence the product's environmental impact [16]. The functional units were defined as

https://doi.org/10.5593/sgem2024/4.1/s17.18

shown in Table 1. They have been chosen based on the recommendations of the standards, analysing the following aspects by the Environmental Footprint methodology: their function, their measurement, their quality level and their lifetime.

Table 1. Functional units

Reference	Analysed product	Functional unit
FB	Flash Banger	A flash banger of 5,15 g
CPS	Cardboard Pyrotechnic Shell	A pyrotechnic cardboard shell of 1358,15 g
PPS	Plastic Pyrotechnic Shell	A pyrotechnic plastic shell of 1437,95 g

Life-Cycle Inventory (LCI)

The main system inventory data were developed with the support of industry experts and various manufacturers, although some assumptions have been made. Due to this, life cycle analysis was carried out without information from all actors in the value chain of the products under consideration. The secondary data was obtained from the EcoInvent database, version 3.8.

The quantities of material required for the manufacture of the three functional units analysed, which can be seen in Table 2, were estimated by modelling standard products that can be found on the market. An important part of the FB is their green fuse as a means of ignition. This product is usually imported from China. Therefore, only its composition and its receipt directly at the factory were taken into account for the study. The analysed flash banger had an additional weight of 0.6 g for this green fuse.

Table 2. Quantities of material per functional unit

	Component	FB	CPS	PPS
Inert material	Cotton	0.05	0.2	0.05
	Paper	1.2	83.7	8.7
	Cardboard	2.4	175.9	----
	Plastic bag	----	1.5	----
	Plastic	----	----	309.7
Hazardous material	Aluminum (Al)	0.26	5.285	5.29
	Magnesium (Mg)	----	152.51	152.51
	Sulphur (S)	----	57.0	59.47
	Charcoal (C)	----	86.11	89.88
	Barium Carbonate ($BaCO_3$)	----	42.28	42.28
	Strontium Carbonate ($SrCO_3$)	----	48.32	48.32
	Dextrin	----	26.75	26.86
	Potassium Dichromate ($K_2Cr_2O_7$)	----	6.04	6.04
	Acroids Gum	----	32.50	32.61
	Arabic Gum	----	4.62	4.83
	Potassium Nitrate (KNO_3)	----	325.13	338.61
	Potassium Perchlorate ($KClO_4$)	0.64	310.31	310.31
	TOTAL	**4.55**	**1358.15**	**1435.45**

The energy input makes the difference between the manufacture of flash bangers and the pyrotechnic shells. In the former, there is no energy input flow. This is because the construction of this element in Spain is handcrafted, according to the manufacturers. In contrast, the shells tested consumed energy in the manufacture of the pyrotechnic stars that produced the colour effect. The powder coating of these fireballs is done using a dragee coating machine. The time it takes to complete the process of manufacturing the pyrotechnic stars can vary depending on its speed, the number and size of stars being manufactured simultaneously and the complexity of the design. No real data was available about the actual time of the coating in this sector, so for this analysis, an assumption was made of a working time of 4 hours to achieve 8 kg of product. The consumption of the shell according to the functional unit is 0.6 kWh.

Regarding distribution, since no data on capacity and type is available, neither from value chain actors nor from research, the intermediate data of the typical truck provided by the SimaPro software was chosen. The information was grouped by type of supplier (hazardous material and cotton supplier, paper supplier, cardboard supplier and plastic supplier) for the first stage and by type of material and management for the end of life. Data and locations of common suppliers in the pyrotechnic sector that are usually used by pyrotechnic companies located in the Valencian Community were used.

During a fireworks display, the only outflows are considered to be emissions released into the atmosphere and waste management. Fireworks displays emit particles into the atmosphere in the form of smoke from the combustion reactions of the products. The pollutant compounds typically released into the atmosphere include sulphur dioxide, carbon dioxide, carbon monoxide and suspended metal particles. The information used for the theoretical calculation of the emissions of the analysed products was based on the theoretical chemical reactions [5] that can give an idea of the emissions of the articles under study.

After the explosion of a firework, theoretically, the only waste generated comes from inert material. For the analysis, the ideal scenario was considered. It was taken into account that the waste to be treated consisted of all the inert material of each product. Therefore, after the use of the products in the Fallas of Valencia, the municipal waste management was responsible for collecting and transporting them to their final destination: paper, cotton, cardboard and plastic. The simulation envisaged that paper, cardboard and plastic were sent to a sorting facility and be prepared for recycling. Cotton, on the other hand, was taken to a landfill site.

RESULTS AND DISCUSSION

The interpretation of the results of the different life cycle impact categories provides an in-depth understanding of the environmental impacts of the products under study. The main categories analysed in this study for the different functional units were: Climate change, Particulate matter, Resource use, fossils, Resource use, minerals and metals and Water use. And, the stages under study encompass the whole process: acquisition and distribution of raw materials (1), energy consumption (2), transport to the show (3), emissions (4) and end of life (5). The results obtained are shown in Table 3.

https://doi.org/10.5593/sgem2024/4.1/s17.18

A common conclusion for the categories studied was that end of life stage (5) results in a negative impact. This is due to the ideal scenario in which the hazardous material is completely consumed and all inert waste is recovered and, for the most part, destined for recycling. The results obtained for this stage do not resemble reality, as not all inert materials are recovered and the combustion reactions are not complete. For this reason, the interpretation of the results focused on the remaining phases and the total impact, while future research will focus on analysing an end of life phase closer to reality.

Overall, the impact of the analysed flash banger is only 0.0102 kg CO_2 eq in Climate Change category. The acquisition of raw materials and their distribution (Stage 1) is the stage that contributes the most to all impacts, with 60%. The transport and the emissions of this product generate hardly any effect. This is due to the proximity of the factory analysed to the place where the fireworks were to be fired and to the fact that fireworks generate a much lower amount of emissions during firing than those generated by other emitters [17]. The components which represent the greatest impact are Kraft paper, cardboard, aluminium and potassium perchlorate. The main reason for this is that they account for a higher percentage of the product weight than the rest. Potassium perchlorate is responsible for 63.6% of the impact and accounts for almost 20% of the flash banger, and cardboard is responsible for 25.9%, constituting almost a 50% of the product.

Table 3. Summary results of the Life-Cycle Analysis

Impact category	Unit	Product	Total	1	2	3	4	5
Climate Change	kg CO_2 eq	FB	0.0103	0.012	----	$2.83x10^{-5}$	0	-0.002
		CPS	4.65	4.29	0.18	0.0075	0.32	-0.15
		PPS	3.87	3.86	0.18	0.0071	0.33	-0.51
Particulate matter	Disease inc.	FB	$6.62x10^{-10}$	$9.8x10^{-10}$	----	$2.13x10^{-12}$	0	$-3.2x10^{-10}$
		CPS	$3.89x10^{-7}$	$3.39x10^{-7}$	$3.84x10^{-9}$	$5.61x10^{-10}$	$6.95x10^{-8}$	$-2.33x10^{-8}$
		PPS	$3.26x10^{-7}$	$2.67x10^{-7}$	$3.84x10^{-9}$	$5.92x10^{-10}$	$7.27x10^{-8}$	$-1.86x10^{-8}$
Resource use, fossils	MJ	FB	0.18	0.32	----	0.0004	0	-0.14
		CPS	65.4	71.1	4.49	0.11	0	-10.3
		PPS	50.9	66.0	4.49	0.11	0	-19.7
Resource use, minerals	kg Sb eq.	FB	$1.71x10^{-7}$	$4.29x10^{-7}$	----	$1.27x10^{-12}$	0	$-2.59x10^{-7}$
		CPS	$3.87x10^{-5}$	$5.76x10^{-5}$	$6.21x10^{-8}$	$3.36x10^{-10}$	0	$-1.90x10^{-5}$
		PPS	$4.17x10^{-6}$	$2.34x10^{-2}$	$6.21x10^{-8}$	$3.55x10^{-10}$	0	$-1.93x10^{-5}$
Water use	m^3 depriv.	FB	0.02	0.034	----	$-6.49x10^{-8}$	0	-0.014
		CPS	3.28	4.17	0.13	$-1.71x10^{-5}$	0	-1.02
		PPS	2.09	2.44	0.125	$-1.81x10^{-5}$	0	-0.48

As with flash banger, for the pyrotechnic shell, Stage 1 of raw material acquisition and distribution is responsible for much of the impact in the categories examined. However, in this pyrotechnic article, the effect of energy consumption (Stage 2) appears and Stage 4 emissions have a more notable contribution than in the case of detonating thunder, due to a much higher Net Explosive Content (NEC).

For the cardboard shell, the analysis shows that 92.3% of the impact of the pyrotechnic functional unit comes, as in the flash banger, from the hazardous supplier material. Potassium perchlorate (42.1%) and aluminium magnesium (29.1%) are mainly responsible. In this case, cardboard accounts for 4.17% of the impact. The impact

difference of the plastic pyrotechnic shell in stages is similar to that of cardboard. The individual process emits 0.331 kg CO_2. The hazardous material supplier continues to have the highest impact, with potassium perchlorate and aluminium magnesium. The plastic supplier stands out with 17.7%, well above the impact of cardboard packaging.

As can be seen, the plastic acquisition process generates a significantly higher impact than cardboard (17.7% vs. 4.17%). However, the result does not only depend on the purchase of the material but also on the rest of the processes in the model. Analysing the end of life values, the positive impact is higher for plastic (-13.1%) than for cardboard (-3.17%). This contrast may be one of the reasons why the total impact of the PPS is slightly higher. As the difference between the two carcasses is not excessive, and this simulation depends on several assumptions, no definitive conclusion can be drawn as to which has a greater impact on the environment. It is important to further investigate the end of life scenarios of these products, in order to provide a realistic scenario to compare the two products and their impacts.

Measures that can reduce the effects of this firework should focus on the selection and reduction, if possible, of raw materials. Due to strict pyrotechnical regulations, such changes in hazardous materials are not straightforward and there are many researchers carrying out such studies. However, another way to reduce their impact would be to focus on reducing inert material or replacing it with more sustainable alternatives.

CONCLUSION

An assessment of the environmental impacts associated with two common types of fireworks used in Spain, utilizing the LCA methodology have been carried out. Key findings indicate that the most significant impacts across multiple environmental categories stem from the acquisition and distribution of raw materials, especially hazardous materials like potassium perchlorate and aluminium magnesium. However, the emissions and transport stages have a negligible effect, underlining the importance of material selection.

When comparing the Climate Change impact values of flash bangers and pyrotechnic shells with other everyday products, it can be seen that they are not significant, emitting 0.0102 kg of CO_2 and 4.65 or 3.87 kg of CO_2 (cardboard and plastic), respectively. A can of Coca-Cola emits 0.17 kg of CO_2. Shells, although slightly higher than other everyday products, do not reach for example 15.5 kg CO_2 for 100 g of beef. Despite this, the analysis highlights points in the process where it can contribute to reducing the impact. In particular, the need of focusing on raw material selection and reducing the use of hazardous substances to mitigate the environmental footprint of fireworks. Although strict regulations in the pyrotechnics industry limit changes in hazardous materials, exploring more sustainable inert materials or innovative designs could provide feasible pathways for impact reduction.

The comparison between cardboard and plastic shells reveals that although the plastic shells have a higher initial impact due to the production process, the theoretical recycling scenario suggests potential benefits. However, these assumptions need to be validated with real-world data. Therefore, future research should aim to collect comprehensive real-

https://doi.org/10.5593/sgem2024/4.1/s17.18

world data, particularly for the end-of-life stage, to provide a more accurate and holistic assessment. Additionally, expanding the analysis to include other types of fireworks and exploring alternative materials and manufacturing processes will be crucial for developing sustainable pyrotechnic products.

ACKNOWLEDGEMENTS

We thank Julia Álvarez del Cuadro (Universidad Politécnica de Madrid) for his direct technical help and his willingness to collaborate throughout the duration of the project.

REFERENCES

[1] "RES/70/1. Transforming our world: the 2030 agenda for sustainable development," *Seventieth United Nations General Assembly, New York*, vol. 25, pp. 86–97, 2015.

[2] "The European Green Deal - European Commission." Accessed: Mar. 08, 2024. [Online]. Available: https://commission.europa.eu/strategy-and-policy/priorities-2019-2024/european-green-deal_en

[3] J. J. Sabatini, "Advances toward the development of 'Green' pyrotechnics," *Green Energetic Materials*, pp. 63–102, 2014.

[4] G. Steinhauser and T. M. Klapötke, "'Green' pyrotechnics: a chemists' challenge," *Angewandte Chemie International Edition*, vol. 47, no. 18, pp. 3330–3347, 2008.

[5] M. S. Russell, *The chemistry of fireworks*. Royal Society of Chemistry, 2009.

[6] C. Hickey *et al.*, "Toxicity of particles emitted by fireworks," *Part Fibre Toxicol*, vol. 17, pp. 1–11, 2020.

[7] A. K. Singh and A. Srivastava, "The impact of fireworks emissions on air quality in Delhi, India," *Environmental Claims Journal*, vol. 32, no. 4, pp. 289–309, 2020.

[8] U. P. Nasir and D. Brahmaiah, "Impact of fireworks on ambient air quality: a case study," *International journal of environmental science and technology*, vol. 12, pp. 1379–1386, 2015.

[9] M. Geissdoerfer, P. Savaget, N. M. P. Bocken, and E. J. Hultink, "The Circular Economy–A new sustainability paradigm?," *J Clean Prod*, vol. 143, pp. 757–768, 2017.

[10] D. Polverini, "Regulating the circular economy within the ecodesign directive: Progress so far, methodological challenges and outlook," *Sustain Prod Consum*, vol. 27, pp. 1113–1123, 2021.

[11] M. Damiani, N. Ferrara, and F. Ardente, "Understanding Product Environmental Footprint and Organisation Environmental Footprint methods," *Publications Office of the European Union, Luxembourg, LUX, 34pp*, 2022.

[12] C. Ferreira, F. Freire, and J. Ribeiro, "Life-cycle assessment of a civil explosive," *J Clean Prod*, vol. 89, pp. 159–164, 2015.

[13] D. Costa, E. Galante, I. Andrade, and J. Cunha, "Environmental life-cycle assessment of a military explosive production unit: a preliminary approach," *U. Porto Journal of Engineering*, vol. 1, no. 1, pp. 2–10, 2015.

[14] International Standard Organization, "Environmental management—life cycle assessment, principles and framework, ISO 14040:2006," *European Committee for Standardization CEN, Brussels, Belgium*, 2006.

[15] International Standard Organization, "Environmental management–life cycle assessment, requirements and guidelines, ISO 14044:2006.," *European Committee for Standardization CEN, Brussels, Belgium*, 2006.

[16] R. Abejón, A. Bala, I. Vazquez-Rowe, R. Aldaco, and P. Fullana-i-Palmer, "When plastic packaging should be preferred: Life cycle analysis of packages for fruit and vegetable distribution in the Spanish peninsular market," *Resour Conserv Recycl*, vol. 155, p. 104666, 2020.

[17] "PRTR España | Registro Estatal de Emisiones y Fuentes Contaminantes (PRTR-España)." Accessed: Apr. 02, 2024. [Online]. Available: https://prtr-es.es/

https://doi.org/10.5593/sgem2024/4.1/s17.18

MONITORING SOLAR FARMS USING DRONES - UTILIZED TECHNIQUES AND BENEFITS

Dr. Eng Tymoteusz Turlej[1]

Assoc. Prof. Dr. Krzysztof Kołodziejczyk[1]

MSc Eng. Jędrzej Minda[1]

[1] AGH University of Krakow, **Poland**

ABSTRACT

The article describes commonly used imaging techniques for monitoring solar farms using drones, highlighting the advantages of each method and the benefits of precise flight path planning. Thermal imaging is discussed for its ability to detect temperature variations and identify potential issues like cell degradation and electrical failures without physical inspection. High-resolution imaging provides detailed visual inspections to identify physical damages, dirt accumulation, and shading issues, enhancing maintenance scheduling and operational efficiency. Multispectral imaging captures data across various wavelengths, aiding in performance assessment and identifying aging panels, thereby supporting better maintenance decisions. Intelligent flight path planning algorithms are also highlighted for their role in optimizing drone inspections, ensuring comprehensive data collection, and minimizing inspection time.

The article also summarizes the overall benefits of using drones for solar farm monitoring, including cost-effectiveness by reducing labor and downtime, increased safety by eliminating the need for physical inspections in hazardous areas, and time efficiency due to rapid data collection. Additionally, drones provide comprehensive data collection, supporting informed decision-making and long-term planning, and contribute to environmental sustainability by optimizing the performance and efficiency of solar panels, thus reducing greenhouse gas emissions. Through these advancements, drones play a crucial role in enhancing the management and sustainability of solar farms, driving the transition towards a greener future.

Keywords: UAV, drones, solar farms, inspections

INTRODUCTION

As the world transitions towards renewable energy sources, solar farms are becoming increasingly vital in meeting global energy demands. Efficiently monitoring and maintaining these vast arrays of solar panels is crucial for optimizing performance and longevity. Traditional methods of inspection and maintenance, which often involve manual labor and significant downtime, are being replaced by innovative technologies such as drones [1]. Drones, equipped with advanced sensors and imaging technologies, have emerged as a valuable tool in this endeavor. The selection of appropriate monitoring techniques is critical for identifying and addressing various types of damage and achieving the specific goals of inspections. Different methods are suited to different types of issues, such as thermal imaging for detecting electrical faults and high-resolution imaging for spotting physical damage. The choice of technique influences the

https://doi.org/10.5593/sgem2024/4.1/s17.19

accuracy and efficiency of the inspection process, thereby impacting the overall operational health of the solar farm.

The implementation of standardized inspection protocols is essential for ensuring consistent and reliable data collection. Well-defined inspection schemes facilitate systematic coverage of the entire solar farm, enabling comprehensive analysis and comparison of collected data over time. This systematic approach not only enhances the precision of immediate assessments but also supports long-term maintenance strategies and predictive analytics [2].

By studying thermal imaging, high-resolution imaging, multispectral imaging, LiDAR technology, and the integration of artificial intelligence and machine learning, one can understand how these methods contribute to the effective management of solar farms. It is also important to understand the reasons for using drones, such as cost-effectiveness, safety, time efficiency, comprehensive data collection, and environmental impact.

MATERIALS AND METHODS

In the context of inspecting solar farms, two crucial aspects must be considered to maximize the efficiency and effectiveness of the process. Firstly, the selection of appropriate monitoring technologies is essential. This includes determining the type of imaging technology to be used, such as thermal imaging, high-resolution imaging, or multispectral imaging, each of which offers unique advantages for identifying different types of issues. Secondly, developing appropriate flight patterns and drone routes is vital to fully leverage the potential of the drones. Well-planned flight paths ensure comprehensive coverage of the solar farm, enabling the capture of detailed and accurate data. These optimized routes help in reducing inspection time, minimizing overlaps, and ensuring that all critical areas are thoroughly examined. By combining the right imaging technologies with strategic flight planning, the overall inspection process can be significantly enhanced, leading to better maintenance and management of solar farms.

One of the primary techniques utilized in drone-based monitoring is thermal imaging. Infrared cameras mounted on drones can detect temperature variations across solar panels, providing a crucial diagnostic tool for identifying underlying issues [3]. The principle behind thermal imaging is based on detecting heat emissions; solar panels typically operate at specific temperature ranges, and deviations from these ranges can indicate potential problems. Hot spots detected through thermal imaging are indicative of areas where panels are malfunctioning or damaged. These hot spots often arise from several issues, such as cell degradation, micro-cracks, electrical failures, or shading problems. By identifying these thermal anomalies, maintenance teams can address issues before they escalate into more significant failures that could compromise the efficiency and output of the entire solar farm. Thermal imaging allows for the identification of several critical issues without the need for physical inspection [4]:

- Cell degradation - over time, solar cells can degrade due to exposure to environmental factors such as UV radiation, moisture, and temperature fluctuations. Thermal imaging can detect uneven heating patterns, which are indicative of cell degradation. Early detection allows for timely replacement of affected panels, ensuring the farm operates at optimal efficiency.
- Micro-cracks - these tiny cracks can develop in the silicon cells of solar panels due to mechanical stress or thermal cycling. While micro-cracks are often not visible to

the naked eye, they can significantly impact the panel's performance by increasing electrical resistance. Thermal imaging can reveal these micro-cracks as small, localized hot spots, enabling precise intervention.

- Electrical failures - faulty connections, bypass diode failures, and other electrical issues can cause parts of a solar panel to overheat. These failures are easily detected by thermal imaging, which shows distinct hot spots corresponding to the electrical faults. Addressing these issues promptly prevents further damage and maintains the overall health of the solar farm.
- Shading problems - objects such as dirt, leaves, or bird droppings can create shading on solar panels, reducing their efficiency. Thermal imaging can identify shaded areas that might not be obvious from visual inspection alone, allowing for quick cleaning and restoration of panel performance.
- Mismatch and aging - as panels age, their performance can decline at different rates, leading to mismatches in output. Thermal imaging helps in identifying panels that are underperforming relative to others in the array, providing data necessary for targeted maintenance or replacement.

By utilizing thermal imaging, solar farm operators can conduct regular, non-invasive inspections to maintain and enhance the performance of their installations. This proactive approach minimizes downtime, reduces maintenance costs, and ensures the longevity of the solar farm.

Drones equipped with high-resolution cameras provide detailed visual inspections of solar panels, offering a crucial tool for maintaining the integrity and efficiency of solar farms. High-resolution imaging captures clear, detailed images of the solar panels, enabling the identification of various physical damages and other issues that can affect performance [5]. These high-resolution images help in identifying physical damages such as:

- Cracks and fractures - solar panels can develop cracks and fractures due to mechanical stress, thermal expansion, and contraction, or impact from debris. High-resolution imaging allows for the detection of these cracks, even when they are microscopic, ensuring that damaged panels are identified and replaced or repaired promptly to prevent further degradation.
- Dirt and debris accumulation - accumulation of dirt, dust, bird droppings, leaves, and other debris can significantly reduce the efficiency of solar panels by blocking sunlight. High-resolution imaging can pinpoint areas with high levels of accumulation, allowing maintenance teams to clean the panels more effectively and maintain optimal performance.
- Corrosion and wear: over time, the materials used in solar panels and their supporting structures can corrode or wear down due to exposure to the elements. High-resolution imaging can detect early signs of corrosion and wear, allowing for timely intervention to reinforce or replace affected components and extend the lifespan of the solar farm.
- Connector and cable issues - the electrical connectors and cables that link the panels can also suffer from wear and tear. High-resolution imaging helps in inspecting

https://doi.org/10.5593/sgem2024/4.1/s17.19

these components for signs of wear, ensuring that electrical connections remain secure and efficient.

High-resolution imaging is particularly useful in assessing the overall condition of the solar farm infrastructure. By providing a comprehensive visual record of the site, these images facilitate baseline assessments, regular monitoring, documentation, reporting also secure data integration. High-resolution images can be used to create a baseline assessment of the solar farm's condition when it is first installed. This baseline serves as a reference point for future inspections, making it easier to identify changes and degradation over time. Regular inspections using high-resolution imaging allow for continuous monitoring of the solar farm's condition. This ongoing surveillance helps in detecting emerging issues early, minimizing the risk of major failures and ensuring that the farm operates at peak efficiency. High-resolution images provide valuable documentation that can be used in maintenance reports, regulatory compliance documentation, and warranty claims. Clear visual evidence of panel conditions can support claims and provide proof of proactive maintenance efforts. The detailed visual data from high-resolution imaging can be integrated with other inspection data, such as thermal and multispectral imaging, to provide a more comprehensive understanding of the solar farm's health. This integrated approach enhances the accuracy of diagnostics and the effectiveness of maintenance strategies. By leveraging high-resolution imaging, solar farm operators can ensure that their installations remain in optimal condition, thereby maximizing energy production and extending the lifespan of the solar panels. This technology not only enhances the efficiency and reliability of solar farms but also contributes to more sustainable and cost-effective energy production.

Multispectral imaging involves capturing data at different wavelengths, including visible, near-infrared (NIR), and shortwave infrared (SWIR). This technique provides a multi-dimensional view of the solar panels and the surrounding environment, which is invaluable for assessing the health and performance of solar farms [65]. By utilizing different wavelengths, multispectral imaging can analyze various characteristics of the solar panels and their environment:

- Visible spectrum - captures images in the same range as human vision, providing detailed visual data on the physical condition of the panels. This includes detecting cracks, dirt, and other surface damages that are visible to the naked eye.
- Near-Infrared (NIR) - NIR imaging is sensitive to vegetation and biological materials. It helps in assessing the impact of vegetation around the solar farm. For instance, overgrown plants and weeds can cause shading, which reduces panel efficiency. NIR imaging can identify areas where vegetation management is needed to ensure panels receive maximum sunlight.
- Shortwave Infrared (SWIR) - SWIR imaging penetrates deeper into materials, providing insights into the internal structure of solar panels. It can detect issues like delamination, moisture ingress, and other structural problems that are not visible on the surface. SWIR is also useful for identifying hot spots that indicate internal defects or inefficiencies.

Multispectral imaging helps in assessing the health and performance of solar panels by analyzing vegetation indices and surface reflectance:

- Vegetation Indices - indices such as the Normalized Difference Vegetation Index (NDVI) are calculated using multispectral data to monitor vegetation health around the solar panels. Healthy vegetation reflects NIR light more efficiently, while stressed or unhealthy vegetation reflects less. This information is crucial for managing vegetation to prevent shading and ensure optimal panel performance.
- Surface Reflectance - by measuring how much light is reflected by the surface of the solar panels at different wavelengths, multispectral imaging can assess the cleanliness and condition of the panels. High reflectance in certain wavelengths might indicate dirt or other contaminants, while low reflectance could suggest surface degradation or coating damage [6].

Multispectral data can reveal issues related to panel aging and efficiency degradation:

- Panel aging - multispectral imaging can detect subtle changes in the panels' spectral signatures, indicating aging and wear. This allows for the timely replacement of aging panels to maintain the overall efficiency of the solar farm.
- Efficiency Degradation - multispectral imaging provides detailed insights into these issues by detecting changes in the panels' spectral responses. For instance, a decrease in NIR reflectance might indicate micro-cracks or internal damage, while changes in visible spectrum reflectance can signal surface soiling or coating wear.
- Thermal stress - by combining multispectral data with thermal imaging, operators can identify panels experiencing thermal stress. Thermal anomalies, when correlated with multispectral data, can provide a more comprehensive understanding of the panel's condition, helping to pinpoint the exact nature of the problem.

Multispectral imaging provides a comprehensive toolset for monitoring and maintaining solar farms. By capturing data across multiple wavelengths, it offers a deeper understanding of the panels' condition and performance, enabling proactive maintenance and optimization strategies. This approach ensures that solar farms operate at their highest efficiency, contributing to more sustainable and reliable energy production.

LiDAR technology uses laser pulses to create detailed 3D maps of the solar farm terrain and structures. This sophisticated technique involves emitting laser beams from the drone, which then bounce back upon hitting a surface. The time taken for the laser beams to return is measured, allowing for the precise calculation of distances and the generation of highly accurate topographical maps. These maps provide an intricate view of the solar farm's physical layout, including the elevation and contours of the land, which are crucial for several reasons [7]. LiDAR is invaluable for tracking panel alignment. Solar panels must be precisely aligned to capture the maximum amount of sunlight throughout the day. Any misalignment can significantly reduce their efficiency. LiDAR provides detailed information on the exact positioning of each panel, allowing for adjustments to be made to ensure optimal orientation. This is particularly important in large solar farms where manual alignment checks would be impractical and time-consuming.

Effective flight path planning is essential for maximizing the potential of drones in solar farm inspections. By establishing well-defined flight paths and templates, drones can cover extensive areas systematically, ensuring comprehensive data collection [8]. These

https://doi.org/10.5593/sgem2024/4.1/s17.19

paths are carefully designed to optimize coverage, minimize overlap, and reduce the time required for inspections. Flight paths are typically planned using specialized software that takes into account the layout of the solar farm, the position of the panels, and the topography of the site. The software generates a grid pattern or a series of waypoints that the drone will follow during its flight. These patterns are designed to ensure that the drone's sensors can capture detailed and overlapping images, providing a complete and accurate assessment of the solar panels.

Standardized templates for drone flights are also developed to ensure consistency across inspections. These templates include specific altitude settings, camera angles, and speed parameters tailored to the unique characteristics of each solar farm. By adhering to these templates, operators can ensure that each inspection is performed under consistent conditions, making it easier to compare data over time and identify trends or emerging issues. The use of predefined flight paths and templates allows for automated and repeatable inspections. This automation not only increases efficiency but also reduces the potential for human error. With each flight following the same precise path, the collected data is more reliable and can be seamlessly integrated with historical records for thorough analysis. Meticulous flight path planning and the use of standardized templates are crucial for optimizing the inspection process. They enable drones to fully leverage their capabilities, providing comprehensive, consistent, and accurate data that supports the effective management and maintenance of solar farms.

DISCUSSION

By exploring each of the imaging methods used with drones, one can identify the key benefits specific to each technique. Thermal imaging, a primary technique in drone-based monitoring, leverages infrared cameras to detect temperature variations across solar panels. This technology is crucial for identifying issues such as cell degradation, micro-cracks, and electrical failures without physical inspection. The key benefits of thermal imaging include early detection of potential failures, non-invasive inspection, and significant time and cost savings. By pinpointing hot spots that indicate malfunctioning or damaged panels, thermal imaging allows for prompt and efficient maintenance, thereby enhancing the overall operational efficiency of the solar farm.

High-resolution imaging provides another vital approach, utilizing drones equipped with high-resolution cameras to capture detailed visual inspections of solar panels. This technology excels in identifying physical damages like cracks, dirt accumulation, and shading issues caused by nearby objects or vegetation. The precise detection of physical damage facilitated by high-resolution imaging improves maintenance scheduling and operational efficiency, ensuring that the solar farm infrastructure remains in optimal condition. Multispectral imaging involves capturing data at various wavelengths, including visible, near-infrared, and shortwave infrared. This technique is instrumental in assessing the health and performance of solar panels by analyzing vegetation indices and surface reflectance. The comprehensive performance analysis provided by multispectral imaging enables the identification of aging panels and supports better decision-making for panel replacement. By revealing issues related to panel aging and efficiency degradation, multispectral imaging ensures that solar farms maintain high performance levels over time. LiDAR (Light Detection and Ranging) technology uses laser pulses to create detailed 3D maps of the solar farm terrain and structures. This data is crucial for site planning, tracking panel alignment, and detecting shifts or tilts in the

solar panels. The accurate topographical mapping offered by LiDAR enhances alignment and positioning, preventing structural issues and ensuring that panels are optimally oriented for maximum sunlight exposure. This precise alignment contributes to the overall efficiency and productivity of the solar farm.

The use of drones for solar farm monitoring offers numerous benefits, starting with cost-effectiveness. Traditional manual inspections are both time-consuming and labor-intensive, often necessitating operational shutdowns and the use of scaffolding. Drones mitigate these costs by enabling quick and efficient inspections without interrupting the farm's operations. Although the initial investment in drone technology may be significant, it is quickly offset by long-term savings in maintenance and enhanced operational efficiency.

Safety is another major advantage of drone-based inspections. Conducting manual inspections of large solar farms can pose significant safety risks to personnel, who may need to work at heights or in proximity to electrical hazards. Drones remove the necessity for human inspectors to access these dangerous areas physically, thereby enhancing overall safety and significantly reducing the likelihood of accidents. Time efficiency is greatly improved with the deployment of drones. They can cover extensive areas in a fraction of the time required for manual inspections. This capability allows for more frequent inspections, facilitating the early detection of issues and enabling prompt maintenance actions. Consequently, the overall uptime and productivity of the solar farm are markedly enhanced. Drones are equipped with a variety of sensors, enabling comprehensive data collection that provides a holistic view of the solar farm's condition. This extensive data aids in making informed decisions regarding maintenance, upgrades, and operational strategies. Furthermore, the ability to store and analyze historical data supports trend analysis and long-term planning, ensuring that maintenance strategies are proactive rather than reactive.

The environmental impact of using drones is also significant. By optimizing the performance and efficiency of solar panels, drones contribute to the sustainability of solar farms. Improved monitoring leads to better energy output, ensuring that solar farms operate at their full potential. This efficiency translates to a more effective contribution to the reduction of greenhouse gas emissions, aligning solar energy production with broader environmental goals. The combination of these benefits highlights the essential role of drones in modern solar farm management, promoting efficiency, safety, and sustainability.

CONCLUSION

The combination of thermal imaging, high-resolution imaging, multispectral imaging, LiDAR, and AI-driven data processing provides a comprehensive suite of technologies that significantly enhance the monitoring and maintenance of solar farms. These technologies collectively offer early detection of issues, precise damage identification, comprehensive performance analysis, accurate site mapping, and predictive maintenance capabilities, thereby ensuring that solar farms operate at peak efficiency and longevity.

In addition to these imaging technologies, intelligent flight path planning algorithms are crucial for maximizing the efficiency of drone inspections. These algorithms take into account the layout of the solar farm, the position of the panels, and the topography of

https://doi.org/10.5593/sgem2024/4.1/s17.19

the site to generate optimized flight paths. By ensuring systematic coverage and minimizing overlaps, these smart algorithms enhance the precision of data collection and reduce the time required for inspections. Automated and repeatable flight paths, guided by these algorithms, ensure consistent inspection conditions, facilitating more reliable data analysis and trend identification over time.

As drone technology continues to evolve, its role in supporting the growth and sustainability of solar energy will undoubtedly expand. The integration of advanced imaging techniques, AI, and intelligent flight path planning positions drones as an indispensable tool in the renewable energy sector. These innovations not only improve the efficiency and reliability of solar farm operations but also contribute significantly to the broader goal of transitioning to sustainable energy sources. By continuously advancing these technologies, we move closer to a greener future, where solar energy can be harnessed more effectively and sustainably than ever before.

REFERENCES

[1] Zhang K, Pakrashi V, Murphy J, Hao G. Inspection of Floating Offshore Wind Turbines Using Multi-Rotor Unmanned Aerial Vehicles: Literature Review and Trends. Sensors (Basel). 2024 Jan 30;24(3):911. doi: 10.3390/s24030911;

[2] Rodriguez-Vazquez J, Prieto-Centeno I, Fernandez-Cortizas M, Perez-Saura D, Molina M, Campoy P. Real-Time Object Detection for Autonomous Solar Farm Inspection via UAVs. Sensors (Basel). 2024 Jan 25;24(3):777. doi: 10.3390/s24030777. PMID: 38339494; PMCID: PMC10857385;

[3] Pruthviraj, U.; Kashyap, Y.; Baxevanaki, E.; Kosmopoulos, P. Solar Photovoltaic Hotspot Inspection Using Unmanned Aerial Vehicle Thermal Images at a Solar Field in South India. Remote Sens. 2023, 15, 1914. https://doi.org/10.3390/rs15071914;

[4] G. B. Balachandran, M. Devisridhivyadharshini, M. E. Ramachandran, R. Santhiya, „Comparative investigation of imaging techniques, pre-processing and visual fault diagnosis using artificial intelligence models for solar photovoltaic system – A comprehensive review”, Measurement, t. 232, s. 114683, 2024, doi: https://doi.org/10.1016/j.measurement.2024.114683

[5] M. Meribout, V. Kumar Tiwari, J. Pablo Peña Herrera, i A. Najeeb Mahfoudh Awadh Baobaid, „Solar panel inspection techniques and prospects”, Measurement, t. 209, s. 112466, mar. 2023, doi: 10.1016/j.measurement.2023.112466;

[6] F. Zhu, K. Xie, L. Quan, i D. Gan, „Multispectral compressive light beam induced current method for photovoltaic cell assessment”, Sol. Energy, t. 275, s. 112621, cze. 2024, doi: 10.1016/j.solener.2024.112621;

[7] S. Szabó et al., „Automated registration of potential locations for solar energy production with Light Detection And Ranging (LiDAR) and small format photogrammetry”, J. Clean. Prod., t. 112, s. 3820–3829, sty. 2016, doi: 10.1016/j.jclepro.2015.07.117;

[8] J. Su, X. Zhu, S. Li, i W.-H. Chen, „AI meets UAVs: A survey on AI empowered UAV perception systems for precision agriculture”, Neurocomputing, t. 518, s. 242–270, 2023, doi: https://doi.org/10.1016/j.neucom.2022.11.020;

OPTIMIZATION OF PROCESS CONDITIONS FOR THE CATALYTIC CONVERSION OF MICROCRYSTALLINE CELLULOSE INTO SUGAR ALCOHOLS

Dr. Oleg Manaenkov
Dr. Olga Kislitsa
Dr. Antonina Stepacheva
Dr. Linda Nikoshvili
Prof. Valentina Matveeva
Tver State Technical University, **Russia**

ABSTRACT

The scale of annual reproduction of cellulose-containing biomass in nature allows us to draw an unambiguous conclusion that cellulose is the only source of raw materials for the chemical and fuel industries, representing a real alternative to fossil resources and, first of all, oil. Cellulose is the main component of plant biomass. According to some estimates, almost half of the organic carbon in the biosphere is contained in cellulose. Hydrolytic hydrogenation is a special case of carbohydrate hydrogenation. With regard to cellulose, the essence of the process is to combine the processes of its hydrolysis and hydrogenation of the resulting glucose. Cellulose is a difficult-to-process substrate, which determines the "harsh" reaction conditions for its hydrolytic hydrogenation. In this regard, it is important to optimize the reaction conditions in order to increase the yield of the target products - sorbitol and mannitol. In this study, the reaction conditions for the conversion of microcrystalline cellulose in the presence of Ru-containing polymeric catalysts (temperature, pressure H_2, time, substrate/catalyst ratio, reactor volume) were optimized. As a result, the maximum selectivity for sorbitol was 43.5 %, mannitol - 3.7 % with a cellulose conversion of 64 %. Also, based on the results of the study, a mathematical model was proposed to formally describe the kinetics of hydrogenation/hydrogenolysis of glucose.

Keywords: cellulose, sorbitol, hydrogenolysis, ruthenium catalyst, hypercrosslinked polystyrene

INTRODUCTION

Sugar alcohols are substances with high added value obtained from biomass [1]. Sorbitol is in demand in the food, textile industries, pharmaceuticals and cosmetology [2]; it is used in the synthesis of vitamin C, surfactants, resins, glycols, lactic acid, etc. [3]. Sorbitol is synthesized by hydrogenation of glucose, which can be obtained from starch or cellulose [4]. Cellulose has no nutritional value and is found in large quantities in waste from the paper and wood processing industries and agriculture. One of the most promising options for its processing is hydrolytic hydrogenation to sorbitol [5, 6]. Ru-containing catalysts are among the most active in this process [7]. Thus, the objects of research most often become the carrier of the active phase of a Ru-containing catalyst. For example, Ribeiro L. et al. [8] studied the influence of the nature of the

https://doi.org/10.5593/sgem2024/4.1/s17.21

substrate on the process of direct conversion of cellulose to sorbitol. The authors synthesized eight types of Ru-containing catalysts based on micro- and mesoporous supports. Wang et al. [9] obtained a hexitols yield of 39.4 % on mesoporous Ru/HZSM-5. It has been shown that Brønsted and Lewis acid sites on the surface of mesopores formed after alkaline treatment of the original ZSM-5 zeolite contribute to the hydrolysis of soluble cellulose oligomers formed during the primary hydrolysis of its crystals. A significantly higher yield of hexitols (up to 63.6 %) was obtained using Ni-containing catalysts based on ZSM-5 zeolite [10]. Approximately the same yield of hexitols (60 %) was obtained on Ni/NCC-ZSM-5 [11]. A special feature of this catalytic system is that the synthesis of ZSM-5 zeolite with a mesoporous structure and active acid sites was carried out using nanocrystalline cellulose (NCC) as a matrix. In [12], T-10157 carbon black treated with H_2SO_4 (TSu) was used as a substrate. The Ru-TSu catalyst showed relatively high sorbitol selectivity and reuse stability. In [13], Ru-Ni bimetallic catalysts based on activated carbon and carbon nanotubes were proposed for the direct conversion of cellulose to sorbitol. The promoting effect of nickel is shown, which is caused by the interaction of Ru and Ni particles at the nanoscale. The yield of sorbitol was 50–60 %. It should be noted that carbon materials have been used in cellulose conversion processes for quite a long time, and the more interesting are catalysts based on other types of supports. For example, a highly efficient catalyst based on copper oxide and a CeO_2-ZrO_2 support was proposed by the authors of the study [14]. During the hydrolytic hydrogenation of cellulose in a neutral aqueous medium (245 °C, 750 PSI H_2, 240 min) on CuO/CeO_2-ZrO_2, the cellulose conversion was 92%, the sorbitol selectivity was 99.1%. The catalyst showed stability over five repeated cycles of use. The authors attribute such exceptional characteristics of the catalyst to the mesoporous structure of the support, which facilitates the transport of reagents, as well as to the increased hydrogenation ability of the Cu-containing active phase. We [15] investigated the possibility of using Ru-containing catalysts based on a mesoporous polymer matrix of hypercrosslinked polystyrene (HPS) for cellulose conversion.

The purpose of this study is to optimize the conditions and determine the kinetic patterns of the catalytic conversion of cellulose to sorbitol in the presence of a Ru-containing catalyst based on an HPS polymer matrix.

MATERIALS AND METHODS

Materials. HPS Macronet MN-270 (without functional groups), was purchased from Purolite Int., U.K. and purified by rinsing with water and drying in vacuum. Distilled water, gaseous pure hydrogen, microcrystalline cellulose (degree of crystallinity 75-80%, Chimmedservice, Russia), and ruthenium (IV) hydroxochloride (pure, OJSC Aurat, Russia) were used as received.

Catalyst preparation. The catalysts were prepared via a four-step synthesis according to a procedure described elsewhere [15]. The study used a catalyst containing 3% ruthenium – 3 % Ru/HPS MN270.

Method of cellulose hydrolytic hydrogenation. The experiments were performed in a steel reactor (50 cm^3, Parr Instrument, USA). Microcrystalline cellulose, a catalyst and 30 mL of distilled water were loaded into the steel reactor. Then reactor was flushed three times with hydrogen under pressure. The mixture was heated and stirred (≈100 rpm) to prevent the formation of local hot spots and the catalyst surface was saturated with hydrogen. After reaching the set temperature, the stirrer speed was increased to

600 rpm. This moment was chosen as the reaction starting time. At the end of the experiment the catalyst and non-hydrolyzed cellulose were separated by filtration. The weight of the non-hydrolyzed cellulose was determined as the difference between the weight of the residue on the filter and the catalyst weight. The content of the conversion main products was determined by chromatographic methods in liquid and gas phases. For the analysis of a gas phase, gas chromatograph Crystallux-4000M (MetaKhrom, Russia) was used, while for the liquid phase, UltiMate 3000 (Dionex, USA) was employed. Cellulose conversion was calculated using the formula: $X=(m_{c0}-m_c)/m_{c0}\cdot 100$, where m_c is the weight of non-hydrolyzed cellulose and m_{c0} is the initial weight of cellulose. The selectivity was calculated using the formula $S=m_p/(m_{c0}-m_c)\cdot 100\%$, where m_p is the weight of the reaction product.

RESULTS AND DISCUSSIONS

The study of the influence of temperature was carried out in the range from 175 to 250 °C. The research results are presented in Table 1.

Table 1: Dependence of cellulose conversion (X) and product selectivity on reaction temperature.

°C	X, %	Selectivity, %												
		S	M	G	1,4-S	Xy	E	Gl	PG	EG	CH_4	Et	Pr	iB
175	19.0	3.0	1.5	tr.	2.7	4.3	tr.	0	0	0	0	0	0	0
180	23.1	5.4	1.8	tr.	2.9	4.8	0.2	0	0	0	0	0	0	0
185	27.2	14.3	2.4	tr.	3.6	5.1	0.3	0	0	0	tr.	0	0	0
190	32.5	25.1	3.3	0.03	3.8	5.2	0.4	tr.	tr.	tr.	0.5	0	0	0
195	41.7	31.1	3.5	0.05	3.7	4.9	0.7	1.4	tr.	tr.	0.8	tr.	0	0
200	54.5	36.2	3.6	0.11	3.6	4.6	0.9	2.2	1.1	0.7	1.5	tr.	tr.	0
205	64.0	43.5	3.7	0.18	3.5	4.4	1.1	3.5	2.4	1.3	3.2	0.05	tr.	tr.
210	67.3	39.7	3.5	0.16	2.9	3.8	1.2	4.5	2.6	1.4	4.5	0.07	0.05	0.05
215	71.1	32.0	2.7	0.13	2.6	3.3	1.4	6.3	3.5	1.6	5.3	0.12	0.1	0.1
220	74.4	28.2	2.0	0.12	2.3	2.7	1.4	7.6	4.3	1.8	6.0	0.2	0.2	0.2
225	79.2	26.2	1.8	0.09	2.1	2.4	1.5	7.4	5.1	1.9	8.2	0.4	0.3	0.3
230	82.6	24.0	1.7	0.05	2.1	2.2	1.6	5.5	5.8	2.3	9.4	0.55	0.4	0.4
235	86.3	22.3	1.6	0.02	2.0	2.1	1.7	3.5	7.6	2.7	11.3	0.7	0.45	0.5
240	91.5	20.1	1.4	0.02	1.8	1.8	1.8	2.6	10.2	3.5	12.8	0.85	0.55	0.6
245	100	18.0	1.1	tr.	1.5	1.5	1.8	2.3	11.6	5.3	13.5	1	0.7	0.65
250	100	14.5	0.7	tr.	1.3	1.3	1.9	1.8	12.3	6.3	14.6	1.2	0.8	0.7

S – sorbitol; M – mannitol; G – glucose; 1,4-S – 1,4-sorbitan; Xy – xylitol; E – erythritol; Gl – glycerol; PG – propylene glycol; EG – ethylene glycol; Et – ethane; Pr – propane; iB – isobutane; tr. – trace. H_2 60 bar, 60 min, 600 rpm, Ru/cellulose ratio 0.042/1(mmol/g), catalyst 3 % Ru/HPS MN 270.

Cellulose conversion increases with increasing temperature and reaches 100 % at 245 °C. Maximum selectivity for sorbitol is observed at a temperature of 205 °C. The maximum value of sorbitol selectivity at a temperature of 205 °C is explained by the fact that hydrolysis of the crystalline part of cellulose begins. Moreover, hydrolysis occurs more completely, with the formation of short oligomers and a large amount of glucose, which at a given temperature very quickly, without having time to caramelize, is hydrogenated to sorbitol. Mannitol in the hydrolytic hydrogenation reaction of cellulose is a minor product formed as a result of the hydrogenation of fructose, which accumulates in small quantities in the liquid phase as a result of the glucose isomerization reaction. Selectivity for mannitol under optimal conditions does not exceed 4 %. 1,4-sorbitan is a product of sorbitol dehydration at high temperatures (140 °C and above). It was shown that the selectivity for 1,4-sorbitan does not exceed 4 %

https://doi.org/10.5593/sgem2024/4.1/s17.21

under optimal reaction conditions. Also, C_5-C_2 polyols are formed in small quantities (Table 1): xylitol, erythritol, glycerol, ethylene and propylene glycol. The formation of methane in fairly large quantities (selectivity up to 14 – 15 % at 240-250 °C) is due to the hydrogenolysis of glycerol, propylene glycol and ethylene glycol. At 205 °C, methane selectivity was 3.2 %. The remaining alkanes are present in the gas phase in trace amounts.

The study of the effect of reaction time was carried out in the range from 0 to 120 min. The research results are presented in Table 2. It is shown that the dependence of the degree of cellulose conversion on the process time is less pronounced than the dependence of cellulose conversion on the process temperature.

Table 2: Dependence of cellulose conversion (X) and selectivity for main products on reaction time.

τ,	X,	Selectivity, %												
min	%	S	M	G	1,4-S	Xy	E	Gl	PG	EG	CH_4	Et	Pr	iB
0	41.3	23.9	3.6	9.7	1.4	2.3	0.2	0.5	0.2	0.1	tr.	tr.	tr.	tr.
10	53.5	37.6	4.4	2.8	2.3	5.5	0.5	1.6	1.1	0.9	0.8	tr.	tr.	tr.
20	55.3	41.0	4.3	1.2	2.6	5.6	0.7	2.4	1.6	1.0	1.7	tr.	tr.	tr.
30	57.6	42.7	4.1	0.6	2.8	5.1	0.9	2.8	2.1	1.1	2.3	tr.	tr.	tr.
40	59.5	42.9	4.0	0.4	3.1	4.7	1.0	3.1	2.2	1.2	2.8	tr.	tr.	tr.
50	62.1	43.3	3.8	0.3	3.4	4.5	1.0	3.3	2.3	1.2	3.0	0.03	tr.	tr.
60	64.0	43.5	3.7	0.2	3.5	4.4	1.1	3.5	2.4	1.3	3.2	0.05	tr.	tr.
70	64.7	42.1	3.6	0.2	3.4	4.2	1.1	3.2	2.6	1.3	3.4	0.06	tr.	tr.
80	65.3	39.6	3.4	0.1	3.2	4.0	1.0	2.7	2.7	1.2	3.6	0.07	0.01	0.01
90	66.2	38.7	3.3	0.1	3.2	3.9	0.9	2.5	2.8	1.2	3.8	0.07	0.02	0.01
100	66.8	36.0	3.3	tr.	3.0	3.8	0.9	2.1	2.8	1.2	4.1	0.08	0.03	0.02
110	67.5	33.2	3.2	tr.	2.8	3.6	0.8	2.0	2.9	1.1	4.4	0.1	0.04	0.03
120	68.7	32.5	3.2	tr.	2.7	3.6	0.8	1.8	2.9	1.1	4.5	0.1	0.05	0.04

S – sorbitol; M – mannitol; G – glucose; 1,4-S – 1,4-sorbitan; Xy – xylitol; E – erythritol; Gl – glycerol; PG – propylene glycol; EG – ethylene glycol; Et – ethane; Pr – propane; iB – isobutane; tr. – trace. H_2 60 bar, 205 °C, 600 rpm, Ru/cellulose ratio 0.042/1(mmol/g), catalyst 3 % Ru/HPS MN 270.

After the start of the experiment, the selectivity for sorbitol increases in 10 minutes from 23.9 to 37.6 % due to the fact that the amount of cellulose that has reacted increases. Over time, an increasing amount of glucose is hydrogenated to the target product, and by the 60th minute of the experiment, the selectivity for sorbitol reaches a maximum of 43.5 %. With a further increase in the reaction time, the selectivity for sorbitol decreases due to its hydrogenolysis. The maximum selectivity for mannitol (4.4 %) was observed after 10 min. The maximum selectivity for 1,4-sorbitan (3.5 %) is observed at the optimal duration of the experiment (60 min). The remaining quantifiable reaction products accumulated in the liquid and gas phases of the catalyst in insignificant quantities.

The study of the influence of hydrogen partial pressure was carried out in the range from 40 to 120 bar. The results of the study are presented in Table 3. It has been shown that the optimal value for the partial pressure of hydrogen is 60 bar. As the pressure increases, the conversion increases, but only slightly. This fact can be explained by the fact that with increasing pressure, hydrogen gradually fills the active centers of the catalyst, thereby preventing substrate molecules from accessing the surface of the active phase. At a certain pressure value (in our case 100 - 120 bar), the active centers of the catalyst, on which hydrogen molecules are adsorbed, can be almost completely occupied. Maximum selectivity for sorbitol was observed at a hydrogen partial pressure of 60 bar.

Table 3: Dependence of cellulose conversion (X) and selectivity for main products on the partial pressure of hydrogen.

bar	X, %	Selectivity, %												
		S	M	G	1,4-S	Xy	E	Gl	PG	EG	CH_4	Et	Pr	iB
40	39.6	22.1	1.4	0.10	5.2	4.7	1.8	1.5	2.7	1.8	6.4	tr.	tr.	tr.
60	64.0	43.5	3.7	0.18	3.5	4.4	1.1	3.5	2.4	1.3	3.2	tr.	tr.	tr.
80	68.4	41.6	3.6	0.16	4.1	4.1	1.3	3.9	1.1	0.5	5.1	tr.	tr.	tr.
100	73.4	38.4	3.4	0.14	4.5	3.7	1.5	4.6	0.9	0.2	6.2	tr.	tr.	tr.
120	77.2	36.0	3.4	0.11	4.8	3.2	1.6	4.8	0.7	0.1	6.4	tr.	tr.	tr.

S – sorbitol; M – mannitol; G – glucose; 1,4-S – 1,4-sorbitan; Xy – xylitol; E – erythritol; Gl – glycerol; PG – propylene glycol; EG – ethylene glycol; Et – ethane; Pr – propane; iB – isobutane; tr. – trace. 205 °C, 60 min, 600 rpm, Ru/cellulose ratio 0.042/1(mmol/g), catalyst 3% Ru/HPS MN 270.

When studying the effect of the substrate/catalyst ratio on the process of hydrolytic hydrogenation of cellulose, the Ru/cellulose values varied from 0.021/1 to 0.084/1 (mmol of ruthenium in the catalyst per 1 g of cellulose). The obtained experimental data are presented in Table 4.

Table 4: Dependence of cellulose conversion (X) and sorbitol selectivity on the Ru/cellulose ratio.

Ru/cellulose (mmol/g)	X, %	Selectivity for sorbitol, %
21/1	63.2	13.2
0.042/1	64.0	43.5
0.084/1	65.2	2.6

The optimal ratio has been shown to be 0.042/1 (mmol/g). In this case, the selectivity for sorbitol takes a maximum value of 43.5%.

To evaluate the effect of reactor type on sorbitol selectivity and the resulting cellulose conversion, four types of reactors were used. During the study, it was found that differences in the nature of the process decrease with increasing reactor volume, starting from 50 cm^3 (Table 5). The values of cellulose conversion and sorbitol selectivity obtained in experiments using reactors with a volume of 50, 100 and 150 cm^3 turned out to be very close. When using a reactor with a minimum volume (30 cm^3), the degree of cellulose conversion increases by approximately 10 %, while selectivity for sorbitol, on the contrary, decreases.

Table 5: Influence on the process of hydrolytic hydrogenation of cellulose by the type of high-pressure reactor.

Reactor volume, cm^3	Cellulose conversion, %	Selectivity for sorbitol, %
30	71.3	36.0
50	64.0	43.5
100	62.3	41.2
150	58.3	42.3

205 °C, 60 bar H_2, 3% Ru/HPS MN 270, 60 min, Ru/cellulose ratio 0.042/1(mmol/g).

Based on the experimental data obtained, a reaction scheme for glucose hydrogenolysis was proposed, shown in Figure 1.

https://doi.org/10.5593/sgem2024/4.1/s17.21

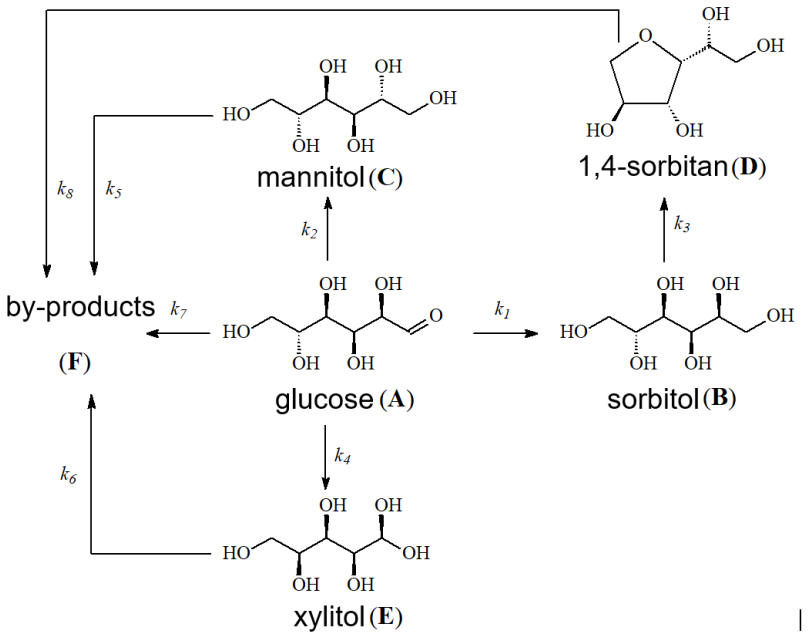


Figure 1: Scheme of hydrogenation/hydrogenolysis of glucose in the presence of a 3 % Ru/HPS MN270 catalyst.

To generalize the experimental data obtained at different values of the load on the catalyst, a transition was made to dimensionless concentrations of the substrate and product using the relationship: $X_i = C_i/C_0$, where C_i is the current concentration of the product, mol/l; C_0 - current glucose concentration, mol/l. Then the mathematical description of the experimental data can be presented in the form of a system of differential equations:

$$(dX_A/d\theta) = -k_1[A] - k_2[A] - k_4[A] - k_7[A]$$
$$(dX_B/d\theta) = k_1[A] - k_3[B]$$
$$(dX_C/d\theta) = k_2[A] - k_5[C]$$
$$(dX_D/d\theta) = k_3[B] - k_8[D]$$
$$(dX_E/d\theta) = k_4[A] - k_6[E]$$
$$(dX_F/d\theta) = k_5[C] + k_6[E] + k_7[A] + k_8[D],$$

where $(dX_i/d\theta)$ is the reaction rate at a unit initial glucose concentration C_o = 1 mol/l and a unit catalyst concentration C_k = 1 mol/l. The inverse problem was solved using the explicit integral method. From several possible options for systems of differential equations, a mathematical model was selected that most adequately described the experimentally obtained data (Figure 2).

The calculated values of the model parameters are given in Table 6.

Table 6: Results of solving the inverse problem for the kinetic model of glucose hydrogenation/hydrogenolysis on the 3% Ru/HPS MN270 catalyst.

Parameter	Value	Parameter	Value
k_1	$6.90 \cdot 10^{-4}$	k_5	$9.75 \cdot 10^{-5}$
k_2	$6.23 \cdot 10^{-5}$	k_6	$1.38 \cdot 10^{-4}$
k_3	$1.11 \cdot 10^{-4}$	k_7	$2.90 \cdot 10^{-4}$
k_4	$8.36 \cdot 10^{-5}$	k_8	$1.29 \cdot 10^{-3}$
The average deviation of experimental data from the calculation: $2.20 \cdot 10^{-2}$.			

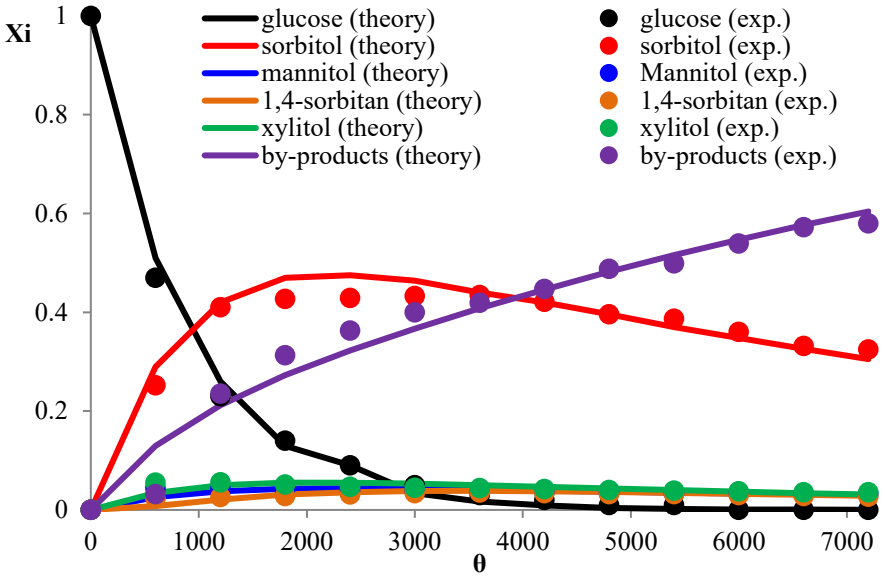


Figure 2: Dependence X ~ θ for the hydrogenation/hydrogenolysis of glucose on the 3 % Ru/HPS MN270 catalyst.

CONCLUSION

During the study, the reaction conditions for the hydrolytic hydrogenation of microcrystalline cellulose in a superheated water environment in the presence of a Ru-containing catalyst based on hypercrosslinked polystyrene – 3 % Ru/HPS MN270 were optimized. As a result, under optimal conditions (205 °C, 60 min, 60 hydrogen pressure 60 bar and a ratio of 0.042/1 mmol ruthenium in the catalyst per 1 g of cellulose), the sorbitol selectivity was 43.5% with a conversion of the original cellulose of 64%. The resulting catalysate, in addition to sorbitol, contains percentage amounts of mannitol, xylitol and other valuable polyols, while the total amount of by-products is minimal. Based on the experimental data obtained, a mathematical model was proposed that formally describes the kinetics of the hydrogenation/hydrogenolysis reaction of glucose under the optimal conditions indicated above. Calculated values of the parameters of a mathematical model that adequately describe the experimental data were obtained. The obtained research results can be used as a basis for developing new and improving existing technologies for processing plant raw materials into valuable products for chemical synthesis and biofuel production.

ACKNOWLEDGEMENTS

Russian Science Foundation, grant 23-79-00009.

REFERENCES

[1] Werpy T., Peterson G., Top Value Added Chemicals from Biomass Volume I – Results of Screening for Potential Candidates from Sugars and Synthesis Gas, National Renewable Energy Laboratory: Golden, CO, USA, 2004, pp 1-76.

https://doi.org/10.5593/sgem2024/4.1/s17.21

[2] Ahmed M.J., Hameed B.H., Hydrogenation of glucose and fructose into hexitols over heterogeneous catalysts: A review. J. Taiwan Inst. Chem. E., Taiwan, vol. 96, pp 341-352, 2019.

[3] Newman A.W., Vitez I.M., Mueller R.L., Kiesnowski C.C., Findlay W.P., Rodriguez C., Davidovich M., McGeorge G., Sorbitol. In Analytical Profiles of Drug Substances and Excipients, USA, vol. 26, pp 459-502, 1999.

[4] Chen M., Wang Y., Lu J., Du J., Tao Y., Cheng Y., Li Q., Wang H., Combinatorial pretreatments of reed straw using liquid hot water and lactic acid for fermentable sugar production. Fuel, vol. 331, p 125916, 2023.

[5] Zhang Y., Zhang G., Chen T., Efficient one-pot conversion of cellulose to sorbitol over Ni-based carbon. Fuel, vol. 339, p 127447, 2023.

[6] Rinaldi R., Catalytic Hydrogenation for Biomass Valorization. RSC Publishing: Cambridge, Great Britain, 2014, p 310.

[7] Li Y., Liao Y., Cao X., Wang T., Ma L., Long J., Liu Q., Xua Y. Advances in hexitol and ethylene glycol production by one-pot hydrolytic hydrogenation and hydrogenolysis of cellulose. Biomass and Bioenergy, vol. 74, pp 148-161, 2015.

[8] Ribeiro L.S., Delgado J.J., Órfão J.J.M., Pereira M.F.R. Direct conversion of cellulose to sorbitol over ruthenium catalysts: Influence of the support. Catalysis Today, vol. 279, issue 2, pp 244-251, 2017.

[9] Wang H., Lv, J., Zhu X., Liu X., Han J., Ge Q. Efficient Hydrolytic Hydrogenation of Cellulose on Mesoporous HZSM-5 Supported Ru Catalysts. Topics in Catalysis, vol. 58, issue 10-11, pp 623-632, 2015.

[10] Liang G., He L., Cheng H., Zhang C., Li X., Fujita Sh., Zhang B., Arai M., Zhao F., ZSM-5-supported multiply-twinned nickel particles: Formation, surface properties, and high catalytic performance in hydrolytic hydrogenation of cellulose. Journal of Catalysis, vol. 325, pp 79-86, 2015.

[11] Zhang B., Li X., Wu Q., Zhang C., Yu Y., Lan M., Wei X., Ying Z., Liu T., Liang G., Zhao F. Synthesis of Ni/mesoporous ZSM-5 for direct catalytic conversion of cellulose to hexitols: modulating the pore structure and acidic sites via a nanocrystalline cellulose template. Green Chem., vol. 18, pp 3315-3323, 2016.

[12] Adsuar-García M.D., Flores-Lasluisa J.X., Azar F.Z., Román-Martínez M.C. Carbon-Black-Supported Ru Catalysts for the Valorization of Cellulose through Hydrolytic Hydrogenation. Catalysts, vol. 8, pp 572-586, 2018.

[13] Ribeiro L.S., Delgado J.J., Órfão J.J.M., Pereira M.F.R. Carbon supported Ru-Ni bimetallic catalysts for the enhanced one-pot conversion of cellulose to sorbitol. Applied Catalysis B, Environmental, vol. 217, pp 265-274, 2017.

[14] Dar B.A., Khalid S., Wani T.A., Mir M.A., Farooqui M. Ceria-Based Mixed Oxide Supported CuO: An Efficient Heterogeneous Catalyst for Conversion of Cellulose to Sorbitol. Green and Sustainable Chemistry, vol. 5, pp 15-24, 2015.

[15] Matveeva, V.G., Sulman, E.M., Manaenkov, O.V., Filatova, A.E., Kislitza, O.V., Sidorov, A.I., Doluda, V.Yu., Sulman, M.G., Rebrov, E.V. Hydrolytic hydrogenation of cellulose in subcritical water with the use of the Ru-containing polymeric catalysts. Catalysis Today, vol. 280, pp 45-50, 2017.

PHOSPHATE REMOVAL ON BIOCHAR

Drd. Popescu Mihaela Alexandra[1]
Prof. Dr. Elena-Emilia Sirbu[1,2]
Asst. Prof. Dr. Catalina Calin[1]
Asst. Prof. Dr.Cristina Popa[1]
Dr. Cristina Emanuela Enascuta[2]
[1]Faculty of Petroleum Refining and Petrochemistry Petroleum-Gas University of Ploiesti, **Romania**
[2] National Institute for Research & Development in Chemistry and Petrochemistry, ICECHIM, Bucharest, **Romania**

ABSTRACT

Biochar can be used as an alternative and efficient adsorbent for organic and inorganic pollutants. Therefore, based on previous study in which, a biochar loaded with mixed metal oxides of iron, tin or titanium catalysts results as a by-product of levulinic esters synthesis from biomass carbohydrates, this paper aim was to test this residue as biochar for the retention of phosphate from water samples. The obtained adsorbents based on Fe_2O_3-SnO_2 and Fe_2O_3-La_2O_3-TiO_2 were characterized by FT-IR and TGA analyses. The effects of adsorbent dosage, initial concentrations of phosphate, and adsorption time were investigated. The results showed that each synthetized adsorbent was able to remove phosphate from aqueous samples with efficiency above 80%. The experimental data obtained were used to estimate the equilibrium adsorption capacity for the two adsorbents applying three machine learning methods. The results obtained were in good agreement with the experimental data indicating that Support Vector Machine has a good potential in the prediction of B-Fe_2O_3-SnO_2 and artificial neural network model is the best for Fe_2O_3-La_2O_3-TiO_2 to predict adsorption capacity..

Keywords: biochar, phosphate, catalyst

INTRODUCTION

Rapid increase of population, climatic change, and variation in standard of living led to the development of new agricultural practices for massive food production [1]. Although phosphorus is an essential element for the growth of animals and plants. However, the massive use of phosphate fertilizers has raised environmental problems. For instance, high phosphorus content in water is an important cause of the eutrophication, as it can determinate algae bloom when its concentration reaches 0.2 mg/L [2]. The reduction of human-induced P input is the key to counteract eutrophication in polluted water bodies. Consequently, it is becoming essential to explore effective technologies to eliminate phosphorus from storm water runoff prior to its discharge into urban surface water [3].

Significant efforts have been made by scientists worldwide to find ways to lower the phosphate concentration in wastewater. Several techniques such as crystallization, membrane separation, chemical precipitation biological [4], however, the high cost of operation associated with these technologies limits their usage. In contrast to more expensive techniques, adsorption is an affordable and efficient method, with a high ease

https://doi.org/10.5593/sgem2024/4.1/s17.22

of operation and minimal generation of byproducts during operation; moreover, it has been widely used to remove phosphate from water, especially at low concentrations [5].

Several types of adsorbents have been proposed for phosphate removal in recent decades, such as activated carbons [6, 7], biochar, and synthetic beads [8]. The modification of biochars with metal compounds, such as Fe, Mg, Al, and La, can change their physical and chemical properties, and thus, improve their phosphorus adsorption capacity. The removal rate of phosphorus by biochar is lower than 10%, but after biochar modification with MgO or $FeCl_3$ the removal rate can be increased to 74.6% and 85% [2,9]. Additionally, the metal oxides generated after pyrolysis are uniformly distributed on the surface of the biochars, which produces a complexation reaction with phosphorus and improved the adsorption capacity of phosphorus [2]. Therefore, based on previous study [10] in which, a biochar loaded with mixed metal oxides of iron, tin or titanium catalysts results as a by-product of levulinic esters synthesis from biomass carbohydrates, this paper aim was to test this catalytic waste as biochar for the retention of phosphate from water samples.

MATERIALS AND METHODS

Preparation of adsorbents

Biochar based on Fe_2O_3-SnO_2 (B-Fe_2O_3-SnO_2) absorbent was obtained in two steps. In the first step the mixed oxide of Fe_2O_3-SnO_2 was prepared by co-precipitation method of 1 to 1 molar ratio $FeCl_3$ to $SnCl_2$), followed by testing as catalyst for levulinate esters synthesis from fructose using a 600 mL Parr batch autoclave reactor. After the reaction is finished, the catalyst is removed by filtration and washed with water to remove unreacted fructose from the adsorbent pores. The synthesis of Fe_2O_3-La_2O_3-TiO_2 was described in a previous paper [10].

Phosphate adsorption experiments

In order to test the adsorption efficiency of the phosphate anion as well as the photocatalytic decomposition activity of the Fe_2O_3-La_2O_3-TiO_2 adsorbent on glyphosate, a glyphosate solution of 90 ppm was subjected to photocatalytic degradation, so that after the total decomposition of the glyphosate the maximum concentration of phosphate would be approximately 50 ppm. Preliminary studies have shown that the time required for the total degradation of glyphosate to the phosphate anion is around 80 hours of sunlight irradiation. Phosphate stock solution of 500 ppm was prepared by dissolving 1.8849 g of Na_2HPO_4 in 1000 mL of distilled water and diluted to desired concentrations of 20, 30, 40 and 50 ppm. The influence of temperature, contact time, adsorbent mass and phosphate concentration was investigated by adding various biochar mass to 50 mL phosphate solutions in an Erlenmeyer glass. The adsorption experiments were carried out in an orbital shaker TOU-59N at 150 rpm at controlled temperature. After shaking, the adsorbent was separated by filtration and the residual phosphate concentration was measured by spectrophotometric using molybdenum blue method [11].

The equilibrium adsorption capacity of the biochar was calculated based on the formula:

$$Qe = (Co-Ce)*V/m \quad (1)$$

where Qe is the amount of the phosphate adsorbed by adsorbent at equilibrium (mg/g), C0 and Ce are the initial and equilibrium concentrations of the phosphate (mg/L), V is the solution volume (L) and m is the adsorbent mass (g).

Adsorbent characterisation

The presence of functional groups on adsorbent surface was evaluated by Shimadzu FT-IR TRACER-100, Kyoto, Japan spectrometer. Thermogravimetric analysis (TGA) was performed using the TGA 2 STAR SYSTEM from METTLER TOLEDO with a heating rate of 10 ºC/min in the range of 25 to 550 ºC and 20 mL/h nitrogen.

RESULTS

Characterisation of adsorbents

The presence of biochar on the surface of Fe_2O_3-SnO_2 absorbent was highlighted by the identification of characteristic absorption bands of biomass (fig.1) attributed to bond vibrations of -CH_2 and -CH_3 groups (2918 and 2872 cm^{-1}), aliphatic C-O-C and alcohol C-OH (1375 and 1025 cm^{-1}) [12]. The broad bands at 3304 and 1635 cm^{-1} are assigned to OH stretching vibrations. Peaks common to Fe-O and Fe-OH bonds were observed for both adsorbents at 2358 cm^{-1} (goethite ($Fe_2O_3 \cdot H_2O$)),418 cm^{-1}(Fe-OH) and 520 cm^{-1} (Fe-O) [13]. These findings agree with the thermogravimetric analysis. For example, the TGA of B-Fe_2O_3-SnO_2 exhibit 4 weight loss stages. First stage, between 40-120 ºC, which is also recorded for Fe_2O_3-La_2O_3-TiO_2 is caused by water loss, the second and third (120-390 ºC) are caused by biomass decomposition, meanwhile the last in the range 420-460 ºC is which is also commune with Fe_2O_3-La_2O_3-TiO_2 is determined by the formation of the mixed oxide.

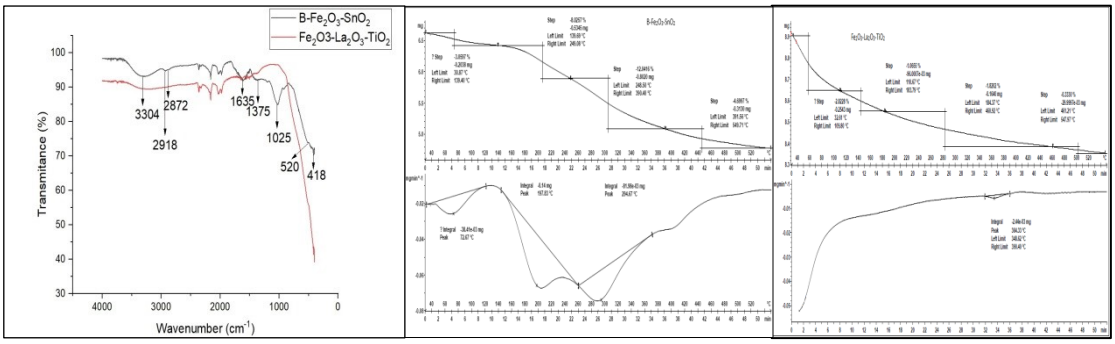


Fig.1 Characterisation of adsorbents

Phosphate adsorption

The experimental data presented in table 1 indicate that both adsorbents have the same behaviour in the phosphate adsorption process, which is significantly influenced by the reaction parameters. For example, for both adsorbents, a long contact time leads to an increase of Qe from 66.3% for 1 h to 92.21 % after 2.5 h for B-Fe_2O_3-SnO_2 and from 52.47 to 88.65 %, respectively for Fe_2O_3-La_2O_3-TiO_2. After this period, the adsorption process reaches equilibrium, and significant changes in the Qe value are no longer recorded. Another parameter that influences the adsorption process is the phosphate concentration. An increase in Qe is observed as the phosphate concentration increases from 20 ppm to 30 ppm, after which the Qe value decreases slightly, due to the limited ability to retain the phosphate anion by the active centres on the surface of the adsorbent. On the other hand, as the adsorbent mass increases, the Qe values also increases. This behaviour can be attributed to the increase in adsorption sites on the biochar surface that could be contacted with phosphate.

https://doi.org/10.5593/sgem2024/4.1/s17.22

Table 1. The experimental data of phosphate adsorption

Entry	Time reaction (h)	Phosphate (ppm)	Mass (g)	Temperature (°C)	Qe (%)
Adsorbent - B-Fe_2O_3-SnO_2					
1	1	30	0,4	35	66,3
2	2	30	0,4	35	84,87
3	2,5	30	0,4	35	92,21
4	3	30	0,4	35	91,85
5	4,0	30	0,4	35	91,53
6	2,5	20	0,4	35	87,52
7	2,5	30	0,4	35	92,21
8	2,5	40	0,4	35	88,46
9	2,5	50	0,4	35	86,12
10	2,5	30	0,1	35	53,1
11	2,5	30	0,2	35	79,33
12	2,5	30	0,3	35	89,25
13	2,5	30	0,4	35	92,21
14	2,5	30	0,4	25	69,14
15	2,5	30	0,4	35	92,21
16	2,5	30	0,4	40	90,11
Adsorbent - Fe_2O_3-La_2O_3-TiO_2					
1	1	30	0,3	40	52,47
2	2	30	0,3	40	71,19
3	2,5	30	0,3	40	88,65
4	3	30	0,3	40	88,15
5	4,0	30	0,3	40	85,78
6	2,5	20	0,3	40	55,31
7	2,5	30	0,3	40	88,65
8	2,5	40	0,3	40	86,2
9	2,5	50	0,3	40	85,59
10	2,5	30	0,1	40	33,3
11	2,5	30	0,2	40	67,89
12	2,5	30	0,3	40	88,65
13	2,5	30	0,4	40	89,01
14	2,5	30	0,3	25	77,36
15	2,5	30	0,3	35	80,96
16	2,5	30	0,3	40	88,65

DISCUSSION

The experimental data obtained was used to estimate the Qe using machine learning (ML) techniques. The predicted Qe for B-Fe_2O_3-SnO_2 and Fe_2O_3-La_2O_3-TiO_2, was regression learning Toolbox from MATLAB@. The methods used to predict are Support Vector Machine (SVM), exponential Gaussian regression (EGR), and artificial neural network (ANN). The steps to implement this method are selecting data,

choosing the learning method, training the model, and analyzing the performance of the model. Support Vector Machine (SVM) is a supervised ML used to predict models for linearly separable data sets and linearly inseparable data sets. The algorithm is supposed to separate the data with hyperplane and determine the maximum margin with relation [14,15]

$$margin = \arg min\, d(x) = \arg \min \frac{|x \cdot w + b|}{\sqrt{\sum_{i=1}^{d} w_i^2}} \quad (1)$$

In this equation *d* is the distance between the hyperplane, *x* the vector point, *w* is weight and b constant

Figure 2 presents the comparison between output data and input data for Qe for B-Fe_2O_3-SnO_2 and Fe_2O_3-La_2O_3-TiO_2, using SVM algorithm.

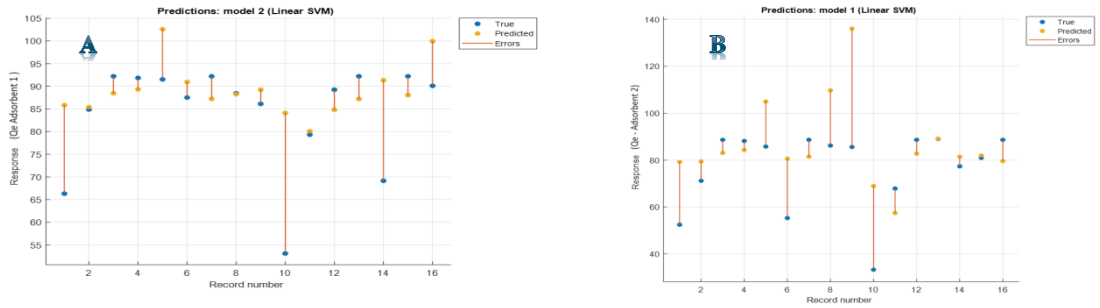


Fig. 2. A) Comparison between Qe_exp and $Qe_{_pred}$ using SVM for B-Fe_2O_3-SnO_2 and B) Comparison between Qe_exp and $Qe_{_pred}$ using SVM for Fe_2O_3-La_2O_3-TiO_2.

Exponential Gaussian regression is a machine learning algorithm that combines linear regression with exponential regression [16]. The relationship between input data and output data is

$$y = e^{ax+b} + \varepsilon \quad (2)$$

Where *x*i is the input data, *y* the output data, *a and b* coefficient of linear regression, ε error. Figure 3 presents the comparison between output data and input data for Qe for B-Fe_2O_3-SnO_2, respectively Fe_2O_3-La_2O_3-TiO_2, using EGR algorithm.

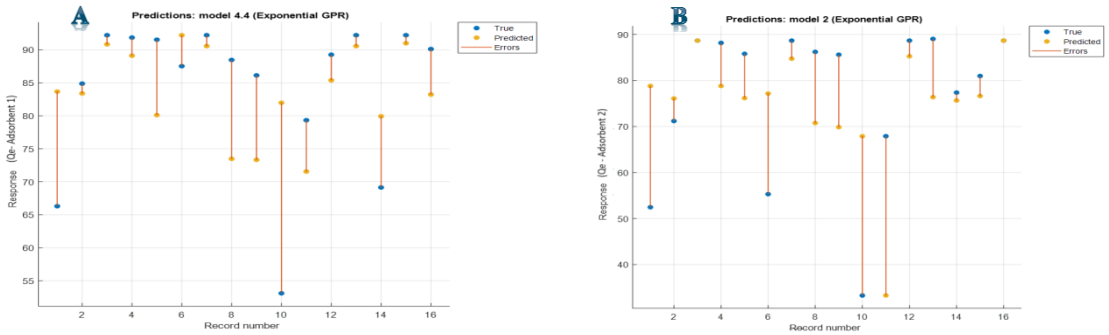


Fig. 3. A) Comparison between Qe_exp and $Qe_{_pred}$ using EGR for B-Fe_2O_3-SnO_2; B) Comparison between Qe_exp and $Qe_{_pred}$ using EGR for Fe_2O_3-La_2O_3-TiO_2.

The artificial neural network is a machine learning inspired by the structure and function of the human brain [17]. The model developed using ANNs is a black box described by mathematical equations that calculate the output variables depending on

https://doi.org/10.5593/sgem2024/4.1/s17.22

the input variables. The structure of the neural network is an input layer, hidden layers, and output layer.

For adsorbent B-Fe_2O_3-SnO_2, the artificial neural network's hidden layers contain 10 neurons and the activation function is the exponential linear, and for adsorbent Fe_2O_3-La_2O_3-TiO_2 hidden layers contain 12 neurons and the activation function is the exponential linear.

Figure 4 presents the comparison between output data and input data for Qe for B-Fe_2O_3-SnO_2 and Fe_2O_3-La_2O_3-TiO_2, using ANN.

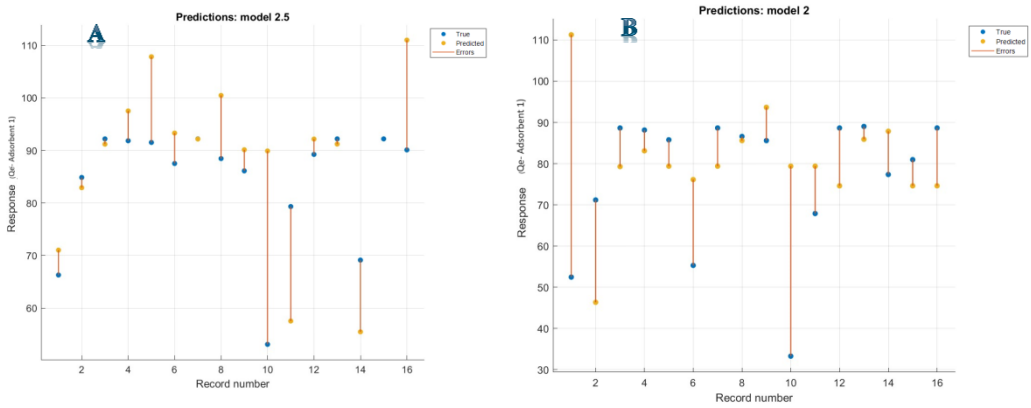


Fig. 4. A) Comparison between Qe_exp and Qe_{pred} using ANN for B-Fe_2O_3-SnO_2; B) Comparison between Qe_exp and Qe_{pred} using ANN for Fe_2O_3-La_2O_3-TiO_2.

The evaluation of the efficiency of each algorithm was done using specific evolution metrics described by Root mean square error (RMSE), R squared error (R^2), mean squared error (MSE) and median absolute error (MAE). The equations of the used performance criteria are presented in the paper [18]. Table 2 presents the evolution metrics for three algorithms. Bases on data from table 2 for B-Fe_2O_3-SnO_2 is recommend to use model obtain with SVM, and from Fe_2O_3-La_2O_3-TiO_2 the ANN model.

Table 2. The evolution metrics for the three algorithms

	SVM		EGR		ANN	
	B-Fe_2O_3-SnO_2	Fe_2O_3-La_2O_3-TiO_2	B-Fe_2O_3-SnO_2	Fe_2O_3-La_2O_3-TiO_2	B-Fe_2O_3-SnO_2	Fe_2O_3-La_2O_3-TiO_2
RMSE	11.69	20.166	0.99	16.7	10.84	21.83
R^2	0.06	-0.38	0.17	0.06	0.16	-0.65
MSE	136.67	406	120	278	117	476.39
MAE	7.91	14.78	8.10	12.4	7.31	15.57

CONCLUSION

This study presents the synthesis and testing of two adsorbent based on Fe_2O_3-SnO_2 and Fe_2O_3-La_2O_3-TiO_2. The influence of reaction parameters such as adsorbent dosage, initial concentrations of phosphate, and adsorption time was investigated. The results showed that both adsorbents were able to remove phosphate from aqueous samples with efficiency of 92.21 % for B-Fe_2O_3-SnO_2 and 88.65 % for Fe_2O_3-La_2O_3-TiO_2 respectively. The experimental data obtained were used to estimate the adsorption

capacity applying three machine learning methods: Support Vector Machine (SVM), exponential Gaussian regression (EGR) and artificial neural networks (ANN). A comparison of the data obtained with the three methods showed that the artificial neural network (ANN) is more suitable to estimate de Fe_2O_3-La_2O_3-TiO_2, because the median absolute error is much lower (7.31) in this case compared with other methods. For B-Fe_2O_3-SnO_2 the SVM method is better than the other two methods because the median absolute error is much lower (14.78). The results obtained were in good agreement with the experimental data.

ACKNOWLEDGEMENTS

The authors thankfully acknowledge the Petroleum-Gas University of Ploiesti, Romania for the financial support, project GO-GICS number 11059/08.06.2023–for the Fe_2O_3-SnO_2 biochar experimental data;

This work was carried out through the PN 23.06 Core Program—ChemNewDeal within the National Plan for Research, Development, and Innovation 2022–2027, developed with the support of the Ministry of Research, Innovation, and Digitization, project no. PN 23.06.01.01 (AQUAMAT)-for the Fe_2O_3-La_2O_3-TiO_2 photocatalyst experimental data.

REFERENCES

[1]Dhanuskodi K.V., Kannan P., Thomas N.J. I. Edison, Senthilkumar A., Biochar from green waste for phosphate removal with subsequent disposal, Waste Management, Volume 68, pp 752-759 2017.

[2]Wang H., Dai J., Chen H., et al., Adsorption of phosphate by Mg/Fe-doped wheat straw biochars optimized using response surface methodology: Mechanisms and application in domestic sewage, Environmental Engineering Research.;28(2),pp 210602, 2023.

[3]Z. Zhong , G. Yu , W. Mo , C. Zhang , et al., Enhanced phosphate sequestration by Fe(iii) modified biochar derived from coconut shell, *RSC Adv.*, **9** , pp. 10425-10436, 2019.

[4]Sun, E., Zhang, Y., Xiao, Q. *et al.* Formable porous biochar loaded with La-Fe(hydr)oxides/montmorillonite for efficient removal of phosphorus in wastewater: process and mechanisms. *Biochar* **4**, 53, (2022

[5]dos Reis GS, Thue PS, Cazacliu BG, *et al.*, Effect of concrete carbonation on phosphate removal through adsorption process and its potential application as fertilizer, . J Clean Prod., 256, pp. 120416, 2020.

[6]Bondarev, A., Popovici, D.R., Călin, C., et al., Black Tea Waste as Green Adsorbent for Nitrate Removal from Aqueous Solutions, Materials, 16(12), pp. 4285, 2023.

[7]Popovici, D., Dusescu, C., Neagu, M., Removal of phenol from aqueous solutions on activated carbon obtained from coffee grounds, Revista de Chimie, 2016, 67(4), pp. 751–756.

[8]Kang J-K, Seo E-J, Lee C-G, Park S-J., Fe-loaded biochar obtained from food waste for enhanced phosphate adsorption and its adsorption mechanism study via

https://doi.org/10.5593/sgem2024/4.1/s17.22

spectroscopic and experimental approach. J. Env. Chem. Eng. 9(4), pp. 105751, 2021.

[9]Liu JW, Jiang JG, Aihemaiti A., Removal of phosphate from aqueous solution using MgO-modified magnetic biochar derived from anaerobic digestion residue., J. Environ. Manage., 250, pp. 109438, 2019.

[10] Oprescu, E.-E., Enascuta C.-E., Doukeh, R., Calin, C., Lavric, V., Characterizing and using a new bi-functional catalyst to sustainably synthesize methyl levulinate from biomass carbohydrates, Renewable Energy, 176, pp. 651-662, 2021.

[11] S. Pradhan, M.R. Pokhrel, Spectrophotometric determination of phosphate in sugarcane juice, fertilizer, detergent and water samples by molybdenum blue method, Scientific World, 11, pp. 58-62, 2013.

[12] P.A. Trazzi, J.J. Leahy, M.H.B. Hayes, W. Kwapinski, Adsorption and desorption of phosphate on biochars, J. Environ. Chem. Eng., 4, pp. 37-46, 2016.

[13] Yang Q.; Wang X.; Luo W.; et al., Effectiveness and mechanisms of phosphate adsorption on iron-modified biochars derived from waste activated sludge. Bioresour. Technol., 247, pp. 537–544. 2018.

[14] Burges C., "A tutorial on support vector machines for pattern recognition", In "Data Mining and Knowledge Discovery". Kluwer Academic Publishers, Boston, 1998, (Volume 2).

[15] Nello Cristianini and John Shawe-Taylor, "An Introduction to Support Vector Machines and Other Kernel-based Learning Methods", Cambridge University Press, 2000.

[16] Williams, C.K.I.: Prediction with Gaussian processes: From linear regression to linear prediction and beyond. In Jordan, M.I., ed.: Learning in Graphical Models. Kluwer Academic, pp. 599–621, 1998.

[17] S. Sinsomboonthon, Performance Comparison of New Adjusted Min-Max with Decimal Scaling and Statistical Column Normalization Methods for Artificial Neural Network Classification, International Journal of Mathematics and Mathematical Sciences, 6, pp. 2-11, 2022.

[18] R. R. Reza, B. Mohammadreza, S. M. Sajadi, M. Pirmoradian, M. R.Renani , Sh. Baghaei, S. Salahshour, Prediction of the thermal behavior of multi-walled carbon nanotubes-CuO-CeO2 (20-40-40)/water hybrid nanofluid using different types of regressors and evolutionary algorithms for designing the best artificial neural network modeling, Alexandria Engineering Journal, 84, pp. 184–203, 2023.

PHOTOVOLTAIC SYSTEM FOR POWERING A REMOTE ACTUATION SYSTEM

PhD. Eng. Radu Rădoi[1]

PhD. Stud. Eng. Liliana Dumitrescu[1]

PhD. Stud. Eng. Bogdan Tudor[1]

Eng. Andrei Benescu[1]

PhD. Stud. Eng. Robert Blejan[1]

[1] Hydraulics and Pneumatics Research Institute INOE 2000 – IHP Bucharest**, Romania**

ABSTRACT

In isolated areas without access to the grid where it is necessary to operate certain equipment, such as the operation of a valve in a mining area or some gates on a irrigation canals, an installation with fotovoltaic supply can be used. Considering the intermittent operation regime of the driven equipment, a solar-powered drive installation can be designed, and by storing the energy in a battery, operation can be ensured during the night as well. Thus, the PV power system must be sized (PV peak power, battery and inverter capacities) so as to support the power of a compact hydraulic power pack and accessory equipment. In order not to be damaged by the weather conditions, the equipment must be housed in a water-resistant enclosure The system must also be equipped with an energy management unit and remote control (GSM or LoRa Gateway). The article presents the realization of such a system and the tests carried out to monitor the production and consumption of electricity during several operating cycles.

Keywords: photovoltaic power system, hydraulic, remote drive, actuation system

INTRODUCTION

The need to operate some equipment from the mining field, irrigation, gas pipelines, etc., installed in isolated locations, can be a problem due to the lack of an electricity network. There are actuation systems with electric actuators, but sometimes it is necessary to use systems with higher power density. Even more so in the case of difficult conditions at the location of the driven equipment, an electrohydraulic system has the advantage of greater reliability. The extension of an electrical network to the targeted location can be unprofitable from the point of view of resource consumption. If the equipment does not require continuous operation at high power, an optimal solution is to use a renewable energy source of the photovoltaic type. This requires, in addition to the electrohydraulic actuation equipment, the installation of a photovoltaic energy capture system. The photovoltaic system includes solar panels, mppt charger, mppt charger control equipment, an electric energy storage battery and battery monitoring equipment. Since the hydraulic drive group uses a single-phase electric motor at 230 Vac, an inverter is also used. A GSM module or a low-power wireless I/O module can be used for remote control of the actuation system. The most important parameter that can be monitored remotely is the one that indicates the battery state of charge (SOC) Table 1.

https://doi.org/10.5593/sgem2024/4.1/s17.23

Table 1 State of charge for Lead Acid-AGM-GEL (at rest)

SOC	Battery voltage	SOC	Battery voltage
100%	12.73	50%	12.10
90%	12.62	40%	11.96
80%	12.50	30%	11.81
70%	12.37	20%	11.66
60%	12.24	10%	11.51

A number of authors have carried out works in the field of solar energy supply or actuation systems for houses or some equipment. Thus McChesney drew up a report on solar electric power for instruments at remote sites [1]. B. Abdullah et al. investigated the design and economically analyzed a 3.3 kW PV system for a villa in Duhok [2]. Gutierrez J. et al. made a photovoltaic system for powering a pump with an AC motor [3]. Aganah K. et al. carried out a review of plug-and-play off-grid solar power supply systems and proposed an architecture for an off-grid PV power supply system [4]. Redekar A. et al. analyzed the functionality of electric actuators in renewable energy systems. The paper analyzed the types of actuators (linear, rotary, spherical) associated with renewable applications, their functioning, their motion type, present use, advantages, disadvantages, and operational problems [5]. Lakhotia R. designed and developed an economical waste compactor with solar power [6]. Ahsan S. et al. designed a PV power supply system useful for houses located in an area where the availability of a power grid is rare or for rural areas in India. A cost analysis was also carried out for a 1kW photovoltaic system based on actual performance in the Indian scenario [7].

There are also companies in the world that have developed installations powered by photovoltaic energy. Thus in fig. 1 it can be seen a waste compactor and a baler made by Sun Built™ company from the USA [11,12]. Solar compactors are useful for a wide variety of uses. A solar compactor can compact up to 20 bins per day in an ecological way. These compactors do not require an electrician to connect the equipment to an electrical network, they only run on highly-efficient solar power.

There are also portable solar compactors that can be placed or moved in various locations. These are very useful when organizing events with a large audience when large amounts of waste are collected.

Solar powered hydraulic units are essential for operating equipment from remote locations, which work in difficult conditions, such as controlling valves in the field of oil extraction. The solar modules are sized based on the required watt-hours and the peak sun hours per day at the location.

This article presents the realization of an electrohydraulic actuation system powered by a 600 W photovoltaic system. Laboratory experiments were carried out to demonstrate the technical feasibility of such an actuation system.



(a) (b)

Fig. 1 Compactor (a) and baler (b) powered by solar energy products of the company Sun Built™

MATERIALS AND METHODS

When designing a PV system, a series of criteria must be taken into account, for example: the required electrical power, the installation location in an area without shading, the mounting solution for the panels, equipment specifications, monitoring and maintenance requirement [8,9]. The electrical scheme of the developed system (figure 2) includes two photovoltaic panels each with a peak power of 300 W, a solar charger MPPT 100/50, which allows a voltage of the solar panels of 100 V and a maximum current of 50 A. Thus if necessary, the number of photovoltaic panels can be supplemented with other panels connected in series or parallel. The solar panels are connected to the PV charger by means of 2 DC fuses installed in a solar PV double fuse holder, in derivation being connected an overvoltage protection device. In order to see the status and be able to setup the MPPT charge controller, an MPPT Control module from the company Victron Energy was also included in the scheme. To store electricity from PV panels a 12V / 220 Ah lead battery is used. A 2 kW / 230 V inverter is used to power the AC electric motor of the pumping group. The inverter can be on-grid or off-grid depending on the application, residential or remote location. A shunt was installed on the DC circuit between the solar charger, battery and inverter, an accessory of a battery monitor type BMV-702 also from Victron Energy. The remaining battery capacity is influenced by the ampere-hours used, the discharge current, temperature, and the battery's age. Complex software algorithms are required to account for all these factors. Besides the basic display options like voltage, current, and ampere-hours consumed, the BMV-702 also shows state of charge, time remaining, and power consumption in watts. It includes an additional input to measure the voltage of a second battery, temperature, or midpoint voltage, along with corresponding alarm and relay settings. A single faulty cell or battery can ruin a large and costly battery bank. When batteries are connected in series, by measuring the midpoint voltage with this device can be generated a timely warning to take the necessary measures. This can also be prevented by installing a battery balancer for batteries connected in series.

https://doi.org/10.5593/sgem2024/4.1/s17.23

The AC output of the inverter is connected to the electric motor of the pumping group by means of a circuit breaker and a soft starter. The soft starter was included in the scheme in order not to overload the inverter when starting the electric motor (inrush current). In order to start the system from a remote location, by means of a remote control, a contactor was inserted into the electric circuit of the hydraulic group. The electric motor used to drive the hydraulic pump is of AC type with the characteristics of 230 V / 1500 W.

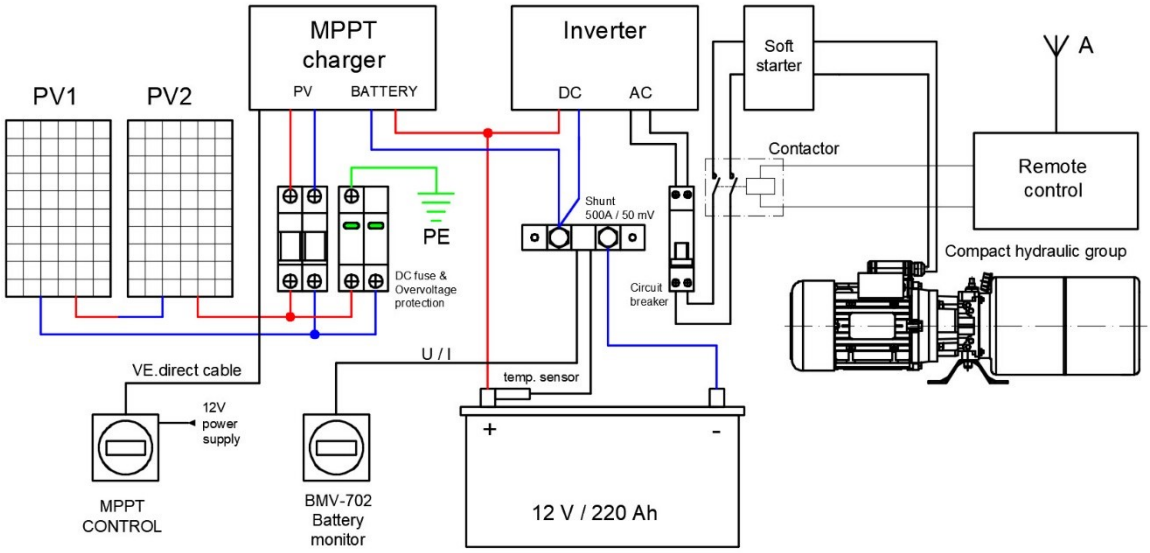


Fig. 2 – Electric sheme of the system

The hydraulic diagram of the hydraulic power generation system for driving hydraulic actuators for the control of some equipment can be found in figure 3. The diagram contains a compact hydraulic group that includes a gear pump, electric motor, suction filter, relief valve and check valve. To simulate the operating conditions (load), a restrictor check valve and a manometer were installed by means of hydraulic hoses.

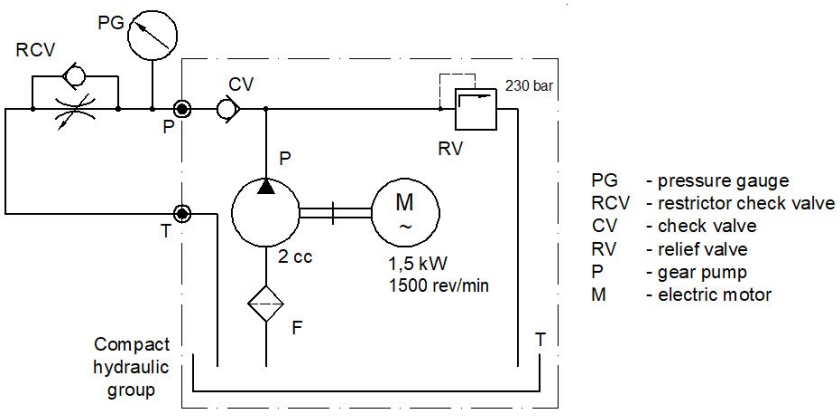


Fig. 3 Schematic of the hydraulic power source with PV supply

Figure 4 shows the box with the electrical components of the PV power supply system. In the box were installed the solar charger, the fuses, the shunt for monitoring the energy produced and consumed, the soft starter, the displays for MPPT control and for monitoring the battery, as well as terminals for connecting the cables.

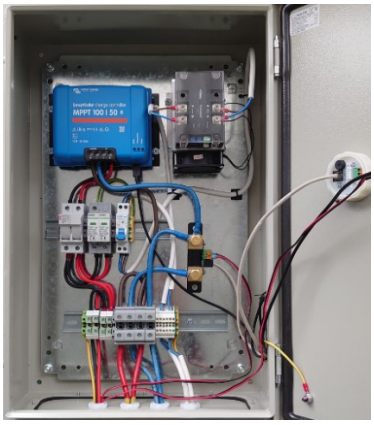


Fig. 4 The box with the electrical components



Fig. 5 The system during tests in the laboratory

Figure 5 shows the system during laboratory tests.

For the tests, a pressure of 200 bar was adjusted with the restrictor valve and the pump flow rate being ~ 3 l/min, a pump drive power of 1176 W is obtained using formula (1). The inverter can provide this power from the battery and/or from the photovoltaic panels.

$$P_{dr} = \frac{p \cdot Q}{600 \cdot \eta_t} \quad (1)$$

where
P_{dr} – pump drive power [kW]
p – pressure [bar]
Q – flow [l/min]
η_t - total efficiency (0,85)

The recording of the electricity production and consumption parameters of the photovoltaic system can be done with a GX equipment from Victron Energy that allows the data to be saved in the VRM portal, from where they can be downloaded.

RESULTS

The first test carried out consisted in monitoring the production of solar energy during one day in June. Figure 6 shows the evolution of the power supplied by the solar panels during an entire day.

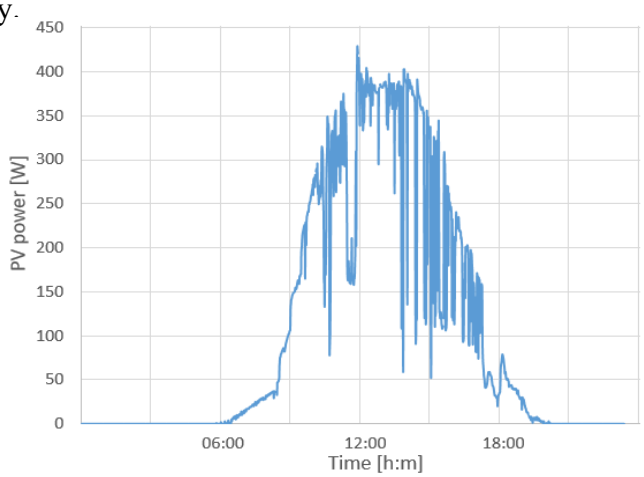


Fig. 6 The evolution of the power provided by solar panels during a day

https://doi.org/10.5593/sgem2024/4.1/s17.23

Figure 7 shows the evolution of the voltage and current supplied by the solar panels during the same day.

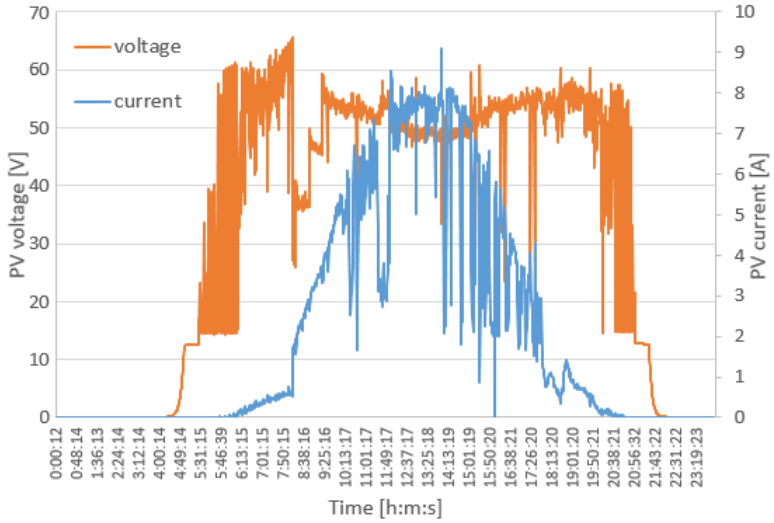


Fig. 7 The evolution of the voltage and the current provided by the 2 solar panels during a day

The second test consisted of following the operation of the pump in a time interval with the realization of some load steps by raising the pressure with the help of the restrictor valve, observing the evolution of the power supplied by the inverter. On this occasion, a heating of the electric motor was observed during periods without high load.

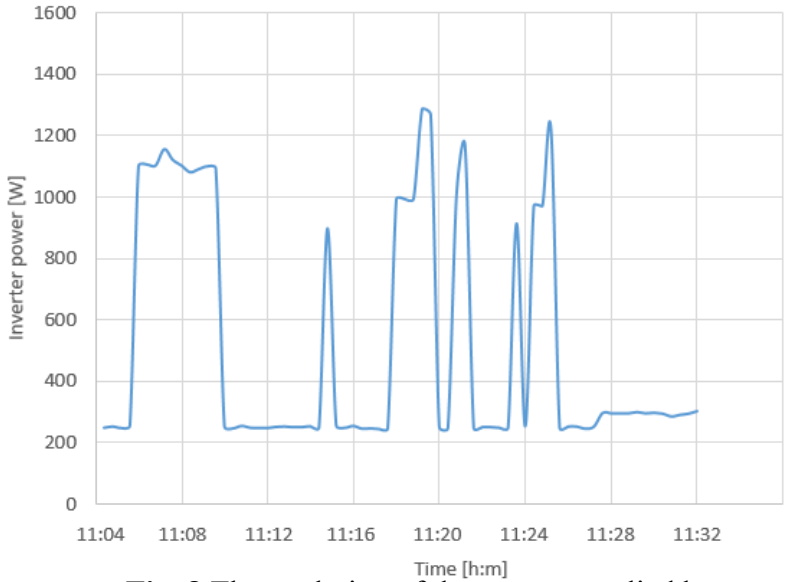


Fig. 8 The evolution of the power supplied by the inverter during the tests performed

DISCUSSION

The heating of the electric motor observed is due to the influence of the harmonics from the inverter which causes the reduction of the efficiency of the induction motor [10]. If in practice it is found that the losses are high and affect the operation of the system, it is possible to opt for the version of compact hydraulic group with DC motor powered

directly from the battery, giving up the inverter, or the AC motor must be paired with a pure sine wave inverter.

CONCLUSION

The practical implementation and testing of the system demonstrated that a compact hydraulic group with a photovoltaic energy source can be used for various drives, the only limitation being related to the total duration of operation, which must be from time to time with short operating periods. Considering that there can be cloudy seasons that can last for days in a row, the battery capacity must have a reserve for such periods.

Examples of locally produced solar photovoltaic energy in areas without access to the electrical grid include: irrigation systems powered by solar pumps, hydraulic actuation systems for irrigation canal gates, and hydraulic drives for knife gate valves in the mining industry.

The utilization of electrical energy derived from solar power directly aids in reducing harmful pollution, particularly when it substitutes energy that would otherwise be generated by burning fuels (e.g. in hybrid mobile machines). In remote areas, electricity from solar energy is often the sole solution to support human activities.

When using compact hydraulic groups at 230 Vac with photovoltaic power, care must be taken to use a pure sine wave inverter to avoid losses in the motor due to harmonics.

ACKNOWLEDGEMENTS

This paper has been funded by the Romanian Ministry of Research and Innovation under NUCLEU Programme, Financial Agreement no. 11N/2023, Ad 5/2024, Project code PN 23-05.02-02, Project title "Frontier research regarding the creation of innovative methods, technologies, products and services used in solving global problems and increasing knowledge-based competitiveness", Phase 22 "Research on the realization of a photovoltaic powered hydraulic power units".

REFERENCES

[1] McChesney P.J., Solar electric power for instruments at remote sites, Open-File Report, U.S. Geological Survey, 2000, doi: 10.3133/ofr00128

[2] Abdullah, B.S., Ameen Y. Off-Grid Photovoltaic System for a Villa at AVRO City in Duhok. Al-Rafidain Engineering Journal (AREJ). 28. 14-23, 2023, https://doi.org/10.33899/rengj.2022.134729.1188.

[3] Gutierrez J., Merino G., Lara D., Salazar L., Hydraulic assessment of a photovoltaic system driving a conventional AC surface electric pump, Sustainable Energy Technologies and Assessments, Volume 45, 2021,

https://doi.org/10.1016/j.seta.2021.101060.

[4] Aganah K., Chukwuma J., Ndoye M., A Review of Off-Grid Plug-and-Play Solar Power Systems: Toward a New "I Better Pass My Neighbour" Generator. *2019 IEEE PES/IAS PowerAfrica*, 182–186, 2019

https://doi.org/10.1109/PowerAfrica.2019.8928727

https://doi.org/10.5593/sgem2024/4.1/s17.23

[5] Redekar A., Deb D., Ozana S., Functionality Analysis of Electric Actuators in Renewable Energy Systems—A Review. *Sensors* **2022**, *22*, 4273.

https://doi.org/10.3390/s22114273

[6] Lakhotia R., Fazal A., Yadav A., Bhattacharjee, A., Design and Development of an Economical and Reliable Solar-Powered Trash Compactor. In: Bose, M., Modi, A. (eds) Proceedings of the 7th International Conference on Advances in Energy Research, 1265-1273, 2021, https://doi.org/10.1007/978-981-15-5955-6_121

[7] Ahsan S., Javed K., Rana A.S., Zeeshan M., Design and cost analysis of 1kW photovoltaic system based on actual performance in Indian scenario. Perspectives in Science Journal, Volume 8, 2016, https://doi.org/10.1016/j.pisc.2016.06.044.

[8] Rehman, A., Iqbal M. T., Design and Control of an Off-Grid Solar System for a Rural House in Pakistan. 0786-0790, 2020,

http://dx.doi.org/10.1109/IEMCON51383.2020.9284867

[9] Ali, Waqas & Farooq, Haroon & Rehman, Atta & Awais, Qasim & Jamil, Mohsin & Noman, Ali. (2018). Design Considerations of Stand-Alone Solar Photovoltaic Systems. https://doi.org/10.1109/ICECUBE.2018.8610970.

[10] Benhaddadi M., Khaldi R., Benghanem M., Experimental study of heating in induction motor fed by PWM inverter, IEEE Instrumentation and Measurement Technology Conference Sensing, Processing, Networking. IMTC Proceedings, Ottawa, ON, Canada, 1997, pp. 335-338 vol.1, https://doi.org/10.1109/IMTC.1997.603967.

[11] https://www.hydrolecinc.com/sun-built

[12] https://www.pde.uk.com/our-products/solar-powered-compactors/

REDUCING CEMENT INDUSTRY EMISSIONS: SYNTHETIC GAS FROM CARBON DIOXIDE AND GREEN HYDROGEN

Assoc. Prof. Dr. David Bolonio[1,2]
Assist. Prof. Dr. Isabel Amez[1,2]
Assist. Prof. Dr Blanca Castells[1,2]
Assist. Prof. David León[1,2]
Assist. Prof. Enrique García Franco[1,2]
[1] Department of Energy and Fuels, E.T.S. Ingenieros de Minas y Energía, Universidad Politécnica de Madrid, **Spain**
[2] TECMINERGY, Technical University of Madrid, Spain, C/Eric Kandel, 1 (TECNOGETAFE), Parque Científico y Tecnológico de la UPM, **Spain**

ABSTRACT

The actual climate crisis is forcing the development of new energy sources that mitigate the negative effects of the climate change. Because of that, the use of fossil fuels is expected to be significantly reduced in the coming decades. In this scenario, the production of renewable fuels that reduce the greenhouse gas emissions (GHG) is one of the main world challenges. The present study focuses on synthetic gas production using carbon dioxide from the cement industry, and green hydrogen, simulating the process using Aspen to address the technical and economic viability of the synthetic gas production. Advanced techniques such as the calcium looping and oxycombustion were used to efficiently capture CO_2 and generate a renewable fuel with a reduced carbon footprint. Moreover, the integration into the existing infrastructure in Spain optimizes the operational efficiency of the project. A detailed technical-economic analysis was carried out to evaluate the feasibility and associated costs, as well as a sustainability analysis that includes all the production steps from the CO_2 capture to the use of synthetic gas, with the aim of quantifying the reductions in GHG. The versatility and adaptability of this research allows adjustments according to market demand and external conditions. Because of that, this research is expected to contribute significantly to sustainable development by providing an innovative solution for carbon capture and clean energy generation.

Keywords: CO_2 capture, synthetic gas, calcium looping, oxycombustion

INTRODUCTION

Renewable methane is seen as an alternative to meet some of the decarbonization targets and offers a promising option for long-term energy storage with significant importance for the industrial, energy and transport sectors. This renewable fuel is particularly attractive because it can be produced from anthropogenic carbon dioxide and hydrogen within a circular economy framework. The cement industry is a major contributor to anthropogenic CO_2, accounting for 5.7% of global CO_2 emissions [1]. In the cement manufacturing process, roughly 60% of the CO_2 emissions are released from the

https://doi.org/10.5593/sgem2024/4.1/s17.24

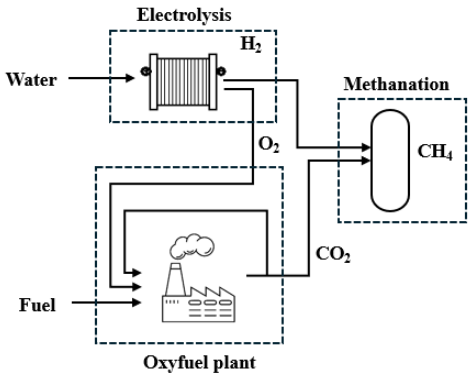
decomposition of $CaCO_3$ to CaO which is used as an intermediate material for clinker production. Globally, clinker production reaches around 4000 Mt/year. For instance, in Spain, clinker production amounted 15.35 Mt by 2022. Considering a clinker emission factor of 0.51 t CO_2/t clinker, the local clinker production represents 7.83 Mt of CO_2 emissions [2],[3]. This amount highlighted a considerable potential for further valorization in the case that these emissions can be effectively captured and stored.

There are three main technologies for the capture and sequestration of CO_2, precombustion, postcombustion and oxycombustion. In precombustion, the fuel undergoes gasification to produce syngas, followed by the transformation of CO into CO_2 through the water gas shift reaction. The resulting hydrogen-rich gas is then fired in the cement kiln after CO_2 capture [4]. Postcombustion of CO_2 involves the separation of CO_2 from flue gas using adsorption or absorption cycles. Oxycombustion, on the other hand, relies on burning fuel in a purified oxygen-rich stream instead of ambient air, resulting in nitrogen-free flue gas. Oxygen is typically obtained from an air separation unit (ASU), although new processes are exploring the use of oxygen derived from water electrolysis [4].

Among the various capture systems, calcium looping (CaL) combined with oxyfuel combustion appears to be particularly promising. Growing concerns about CO_2 emissions have accelerated the development of CaL technology, which has reached a Technology Readiness Level (TRL) of 6-7. In the calcium looping process, flue gas is passed through a carbonator at 650°C, where a stream of CaO captures CO_2 to form $CaCO_3$. The resulting stream from the carbonator is then directed to a calciner, where the $CaCO_3$ is decomposed to regenerate CaO. The energy required for this process is provided by fuel combustion using oxygen and recycled flue gas at 900°C. As a result, the flue gas is primarily composed of water vapour and CO_2.

Once a purified stream of CO_2 stream is obtained, it undergoes hydrogenation using green H_2 produced from water electrolysis in a Power-to-Gas (PtG) process, yielding synthetic methane (CH_4). Fig. 1 presents a scheme of the PtG concept. Typically, the primary energy source for this process is a surplus of renewable energy. Proton Exchange Membrane (PEM) electrolyzers offer certain advantages over alkaline electrolysis in terms of dynamic operation. As early as 1980, a combination of seawater electrolysis and CO_2 methanation was proposed as an alternative to mitigate global warming, but its feasibility for sustainable energy production is still being evaluated [5].

Following the PtG concept several demonstration plants have been recently constructed. The most representative is the Audi e-gas plant in Wertle, Germany. This facility operates with a (6MW) alkaline electrolyser to produce hydrogen, as well as synthetic methane to injection into the gas grid [5]. The specifications for injecting methane-rich gas are slightly different for each country, but for the injection of gas into the Spanish grid, the following specifications apply (%mol): CH_4 > 90; O_2 < 0.3; CO_2 < 2; H_2 0-5; HHV kWh/m^3 (10.26 - 13.26) [6]. To achieve these requirements, it is crucial to ensure a high yield of methane (CH_4). Based on the stoichiometry of the reaction, a minimum yield of 97.83% mol CH_4/mol CO_2 is necessary to obtain gas suitable for direct injection into the grid.



$$H_2O(l) \rightarrow H_2(g) + \frac{1}{2}O_2(g) \quad (1)$$

$$H_2(g) + CO_2(g) \leftrightarrow CH_4(g) + 2H_2O(g) \quad (2)$$

Fig. 1. Scheme of Power to gas technology.

Methanation Process

Methane is produced by the Sabatier reaction according to equation (2). Typically, this reaction is carried out by Ru-TiO_2 or Ru/γ-Al_2O_3 catalytic reactors and is highly exothermic releasing approximately 164 kJ/mol of energy, which results in an adiabatic temperature rise [5]. Therefore, the temperature must still be maintained in the range of 200 to 500°C to ensure optimal kinetics and prevent catalyst damage or deactivation. [7]. Catalyst deactivation can occur due to physical fouling, poisoning, or loss of active area with trace elements such as sulfur (>1 ppm) being particularly detrimental. Therefore, effective flue gas cleaning and high-quality feedstocks are essential prior to methanation [5].

To control the temperature many reactor configurations has been evaluated [5]. A typical configuration uses two adiabatic beds with recycling unconverted gas into the first reactor to dilute the feed and control the adiabatic temperature [7]. In thermodynamic equilibrium, methane formation is favored by high pressures, whereas high temperatures tend to limit methane formation [5]. Considering these technical requirements, a common approach involves two adiabatic beds and recycling unconverted gas into the first reactor to dilute the feed and regulate the adiabatic temperature [8].

The Sabatier process is typically operated stoichiometrically at a CO_2:H_2 ratio of 1:4 and a pressure of 10 atm [8]. Increased pressure enhances reaction rates, peak temperatures, and methane yield. [9]. To model the reaction kinetics a pseudo homogeneous model is usually employed. This model was developed by [10] and is presented in eq. (3)

$$r_{CO_2} = \frac{k}{1 + \alpha P H_2 O}\left[P_{CO_2}^n P_{H_2}^{4n} - P_{CH_4}^n P_{H_2O}^{2n}/K_p^n\right] \quad (3)$$

Where k is an Arrhenius type constant ($k = Ae^{-Ea/RT}$), the preexponential factor $A =$ 94.5 mol CO_2/g cat·ata^{5n}·s, and the activation energy $Ea = 75.3\ kJ/mol$. The parameter $\alpha = 0.91$ considers the inhibition effect of water, $n = 0.152$ is the reaction order and K_p is the equilibrium constant [10]. The kinetic expression is based on partial pressures P_i of each component. The catalyst has a bulk density of 0.75 g/cm^3 and a bed porosity of 0.4.

https://doi.org/10.5593/sgem2024/4.1/s17.24

This work aims to analyze, in the first step, the methanation process involving electrolysis and calcium looping with oxycombustion to evaluate the techno-economic feasibility of the process and the potential positive environmental effects in terms of reducing CO_2 emissions. Various kinetic parameters were analyzed to produce a methane-rich gas that meets the technical requirements for direct injection into the gas grid. Additionally, based on the results of this research, efforts must be made to effectively integrate CO_2 capture technologies into existing cement plants or new plant configurations. This integration is crucial for mitigating greenhouse gas emissions and advancing energy sustainability within the industry.

MATERIALS AND METHODS

Kinetic Modelling

The first step of this study is to model the methanation plant using CO_2 and H_2 as feedstocks. To establish the capacity of the methanation plant, a clinker production rate of 31.4 kg/s was assumed, which is representative of clinker production in a city like Sagunto-Valencia.

The reaction kinetics were modelled in the software Aspen Plus using the kinetic rate presented in eq. (3). The reactor type is adiabatic, and the reaction class is Langmuir Hinshelwood Watson (LHHW) with partial pressure as the basis for reaction rate. K_{eq} is evaluated from the thermodynamics through Van't Hoff equation as is presented in eq. (6).

Several assumptions are considered in the kinetic modelling: Firstly, the pressure drop across the reactor bed is considered negligible. Additionally, ideal gas behaviour and steady-state conditions are assumed to be attained. Furthermore, it is assumed that gas concentrations are uniform in all reactor phases and there are no radial concentration or temperature gradients, and finally it is assumed that there is no catalyst deactivation. [9].

In the process a stream rich in CO_2 is mixed stoichiometrically with H_2. The mixture is compressed to 10 atm and preheated to 200°C before entering the first adiabatic fixed bed reactor. The outlet stream from the reactor is cooled to 25°C and is split to remove the water formed during the reaction. Due to the heat of reaction part of the dry stream is recycled back to the reactor to control the adiabatic temperature and enhance the conversion and yield to methane. Subsequently, the mixture passes through a second reactor where almost complete conversion is achieved, and the water is removed following the same process to obtain a methane-rich gas that is directly injectable into the natural gas grid. A schematic of the process is presented in Fig. 2.

To study the most representative kinetic parameters the process yield (Y) is calculated to consider the effect of recirculation in the global conversion of the reactor.

Additionally, the energy balance in the adiabatic reactor is calculated using the heat capacity of the feed per mol of CO_2 and $\Delta H_{rxn}(T)$ as is presented in eq (5).

$$Y = \frac{N x_{CO\,2,x}}{F x_{CO\,2,F}} x_f \quad (4)$$

$$X_{eq} = \frac{\sum \Theta_i \widehat{C_{pl}} (T - T_o)}{-\Delta H_{rxn}(T)} \quad (5)$$

$$\ln K_{eq} = 2.693 - \frac{2989.954}{T} + 0.0695 \cdot lnT - 4.737 \cdot 10^{-5} T \quad (6)$$

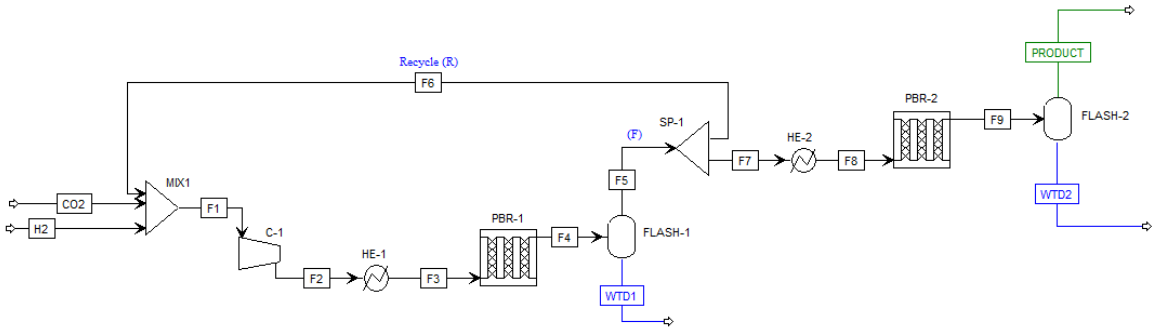


Fig. 2. Outline of the Aspen simulation.

RESULTS

The main results obtained for the simulation of CO_2 methanation using two catalytic reactors are presented in

Table **1**.

Table 1. Aspen simulation results

Process conditions			
F CO_2 (kmol/s) F H_2 (kmol/s)		0.3643 1.457	
Parameter	Units	Adiabatic reactor (1)	Adiabatic reactor (2)
Temperature	(°C)	200 – 500	200 – 368.0
Mass of catalyst	(t)	32.061	6.221
R/F	mol/mol	0.866	0
Y	mol/mol	0.924	0.979
X	mol/mol	0.618	0.721
x_{CH4}	mol CH_4/mol	0.594	0.900
HHV	(kWh/m^3)	8.662	10.260

* Y: methane yield, *X*: conversion of methane, x_{CH4}: molar fraction of methane and R/F: recirculation ratio

In addition, a sensitivity analysis was carried out based on yield and conversion of methane, which is presented in Fig. 3. Also, the equilibrium conversion and the energy

https://doi.org/10.5593/sgem2024/4.1/s17.24

balance line are presented in Fig. 4. to identify the number of reactors needed to achieve a minimum yield of 0.975.

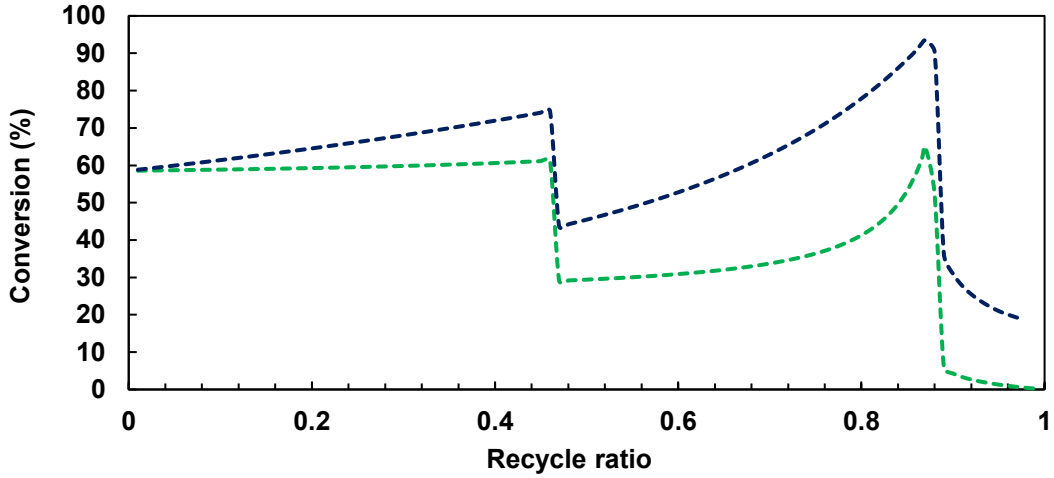


Fig. 3. Sensitive analysis of recycle ratio in the conversion of CO_2. (--) Sensitivity analysis of the methane yield (Y) and (--) Sensitivity analysis of the methane conversion (X).

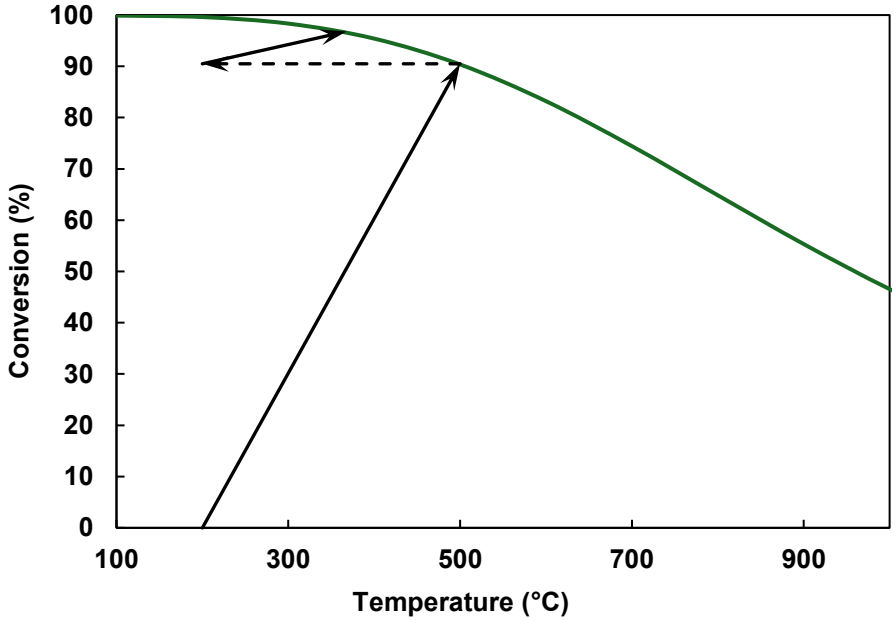


Fig. 4. Equilibrium conversion of adiabatic methanation with recycle to the reactor. (—) Energy balance of the reactor and (—) Chemical equilibrium.

DISCUSSION

The modelling was done assuming that the operating temperature of the catalyst is not exceeded (200 - 500 °C), therefore the maximum temperature that is possible to attain is 500 °C. This temperature is reached by adjusting the amount of catalyst in each catalytic bed.

In the base case, setting an inlet temperature of 200°C and a recirculation ratio (R/F) equal to zero, an adiabatic outlet temperature of 863 °C and a conversion of 58.5% is achieved. According to the stoichiometry a minimum conversion $x_f = 0.978$ is necessary to meet the gas grid specification (CH_4 > 90 %mol). Since without recirculation it is difficult to control the adiabatic temperature and several reactors in series would be required to achieve the necessary quality, the same reaction system is evaluated but with dry gas recirculation at the inlet of the first reactor. The temperature control of the first reactor is the most critical because it is here where the highest reaction rates are achieved in terms of chemical equilibrium.

Fig. 3 presents a sensitivity analysis of the recirculation ratio R/F in the reactor. In the figure, ratios below 0.46 do not meet the methane quality specification using a set of 2 reactors. However, for relations R/F > 0.47 the recirculation ratio favors the overall conversion and the yield to methane. The optimum recycle ratio is close to 0.87. This is the most favourable case using a series of two reactors, however recycling a large part of the output stream from the first reactor can lead to additional compression costs and oversizing of equipment, so in some cases it is more convenient to use three reactors to achieve the same conversion values. In this sense low recirculation ratios reduces the conversion and high recirculation ratios increase the yield as well as the size of the reactors. The optimal process will depend on the best trade-off between size of the reactors that involves the catalyst costs and the complexity of the system [8].

The equilibrium conversion and energy balance of the set of reactors are presented in Fig. 4. Through this figure it is possible to see how the recycling rate raises the slope of the energy balance which allows to reach a higher conversion. Also, water removal plays an important role in shifting the chemical equilibrium in the reactors and reducing the inhibitory effects. Additionally, the figure shows schematically the number of reactors required to achieve a conversion of 0.978 keeping the reactor temperature below 500°C.

In the optimal point R/F=0.866, X_f= 0.618, and $Y_{1,CH4}$=0.924. In the second reactor the remained CO_2 that is converted to CH_4 reached a X_f=0.979. Previous works studying the syn gas methanation have found that a R/F > 0.66 is required to meet the methane content to grid injection. Indeed, in the case of syn gas a relation of R/F < 0.66 is unfeasible because the second reactor achieves the chemical equilibrium in lower value than the technical specification [9].

CONCLUSION

The study models a methanation plant utilizing CO_2 and H_2 as feedstocks using a pseudo homogeneous kinetic model. Through detailed kinetic modelling and sensitivity analyses, key parameters such as recirculation ratio (R/F) are evaluated to optimize conversion efficiency. Using the kinetic model, an optimum reflux ratio of 0.866 was obtained, giving an overall conversion of 0.979. The results underscore the critical role of temperature control because it limits the conversion and the trade-off between reactor size and system complexity in achieving the desired conversion levels. These findings highlighted the importance of continued efforts to advance technologies that mitigate greenhouse gas emissions and promote energy sustainability on a global scale.

https://doi.org/10.5593/sgem2024/4.1/s17.24

ACKNOWLEDGEMENTS

This project has received funding from IV Convocatoria Catedra Empresa Fundación Cepsa de Energía y Medio Ambiente de la Escuela de Minas y Energía (UPM). – Proyecto OTT CAT200600041P. We thank Laura Najera for her technical support.

REFERENCES

[1] E. Moioli, R. Mutschler, and A. Züttel, "Renewable energy storage via CO_2 and H_2 conversion to methane and methanol: Assessment for small scale applications," *Renewable and Sustainable Energy Reviews*, vol. 107, pp. 497–506, 2019, doi: https://doi.org/10.1016/j.rser.2019.03.022.

[2] Ministerio de Industria y Turismo, "Estadística cemento correspondiente al mes de marzo," Madrid, España, 2024.

[3] O. of A. and R. U.S. Environmental Protection Agency, "Technical Support Document for Process Emissions from Cement: Proposed Rule for Mandatory Reporting of Greenhouse Gases," 2009.

[4] B. Arias, M. Alonso, and C. Abanades, "CO_2 Capture by Calcium Looping at Relevant Conditions for Cement Plants: Experimental Testing in a 30 kWth Pilot Plant," *Ind Eng Chem Res*, vol. 56, no. 10, pp. 2634–2640, Mar. 2017, doi: 10.1021/acs.iecr.6b04617.

[5] S. Rönsch *et al.*, "Review on methanation – From fundamentals to current projects," *Fuel*, vol. 166, pp. 276–296, 2016, doi: https://doi.org/10.1016/j.fuel.2015.10.111.

[6] Ministerio para la Transición Ecológica, "Resolución de 8 de octubre de 2018, de la Dirección General de Política Energética y Minas, por la que se modifican las normas de gestión técnica del sistema NGTS-06, NGTS-07 y los protocolos de detalle PD-01 y PD-02," 2018.

[7] F. Gutiérrez-Martín and L. M. Rodríguez-Antón, "Power-to-SNG technologies by hydrogenation of CO2 and biomass resources: A comparative chemical engineering process analysis," *Int J Hydrogen Energy*, vol. 44, no. 25, pp. 12544–12553, 2019, doi: https://doi.org/10.1016/j.ijhydene.2018.09.168.

[8] F. Gutiérrez-Martín, L. M. Rodríguez-Antón, and M. Legrand, "Renewable power-to-gas by direct catalytic methanation of biogas," *Renew Energy*, vol. 162, pp. 948–959, 2020, doi: https://doi.org/10.1016/j.renene.2020.08.090.

[9] F. Gutiérrez-Martín, L. M. Rodríguez-Antón, and M. Legrand, "Renewable power-to-gas by direct catalytic methanation of biogas," *Renew Energy*, vol. 162, pp. 948–959, 2020, doi: https://doi.org/10.1016/j.renene.2020.08.090.

[10] L. Falbo, M. Martinelli, C. G. Visconti, L. Lietti, C. Bassano, and P. Deiana, "Kinetics of CO_2 methanation on a Ru-based catalyst at process conditions relevant for Power-to-Gas applications," *Appl Catal B*, vol. 225, pp. 354–363, 2018, doi: https://doi.org/10.1016/j.apcatb.2017.11.066

ROUGHNESS EFFECT ON A FULL-SCALE GENERAL CARGO VESSEL TOTAL RESISTENCE AND EFFECTIVE POWER

PhD. Andreea Mandru[1]

Prof. Dr. Liliana Rusu[2]

Assoc Prof. Dr. Florin Pacuraru[1]

[1] "Dunarea de Jos" University of Galati, Faculty of Naval Architecture, Department of Naval Architecture, **Romania**
[2] "Dunarea de Jos" University of Galati, Faculty of Engineering, Department of Mechanical Engineering, **Romania**

ABSTRACT

The roughness of a ship's hull can have a significant impact on the environment, primarily through its effect on the ship's fuel consumption and, consequently, carbon emissions. The resistance a ship encounters as it moves through the water can be broadly categorized into two main types: frictional resistance and wave-making resistance. Hull roughness increases frictional resistance, also known as skin friction resistance. This resistence component is a major aspect of the total resistance of a merchant ship, leading to increased power and fuel consumption. The present study aims to systematically analyze the effect of hull roughness on ship resistance components based on Computational Fluid Dynamics (CFD) simulations of the full-scale general cargo vessel REGAL. To investigate the impact of roughness on the characteristics of the flow around the ship hull, the ISIS-CFD solver implemented in the Fidelity Fine Marine code provided CADENCE was employed. This solver is based on the Reynolds-Averaged Navier-Stokes (RANS) equations with a Volume of Fluid (VOF) approach. In order to ensure the accuracy of the results, grid convergence tests and comparisons with different results available have been performed. Four roughness conditions were simulated at a speed of 14 knots. The study of hull roughness and its effect on total resistance showed that, depending on the condition of the hull, resistance can rise by as much as 51.3% when small calcareous fouling or weed build up on the ship's hull

Keywords: roughness, full-scale, CFD, RANS, VOF

INTRODUCTION

Optimizing a vessel's performance to reduce ship resistance is a continuous challenge for naval architects. Ship resistance directly affects fuel efficiency, costs, and environmental footprint. As the need for efficiency grows, ship designers, operators, and researchers seek innovative solutions to minimize resistance and improve performance. Achieving this requires a deep understanding of resistance factors, including surface roughness on full-scale ships.

The main source of drag for some types of hulls is frictional drag, which can reach up to 90% of the total drag even if the hull is hydraulically smooth and clean [1]. Lackenby [2] reported an early review of the previous research in this area. Later, many studies

https://doi.org/10.5593/sgem2024/4.1/s17.25

have aimed to understand how coating roughness influences frictional drag [3-5]. The application of the CFD approach, based on the roughness functions model within the wall function, has expanded for ship hydrodynamics problems.

Song et al. used RANS CFD simulations for different geometries (flat plate, submarine, and two ships) at full scale Reynolds numbers using the k-omega SST eddy-viscosity model with different sand-grain roughness heights. They also compared the CFD results with empirical correlations for converting average roughness height to sand-grain roughness height [6]. Recent validations of the CFD approach for modelling roughness effect on ship resistance using a modified turbulence models with a wall function condition that accounts for different types of surface roughness have been reported by Eca et al. [7], and Song et al. [8].

The Present study investigates the effect of hull roughness on ship resistance components and on flow characteristics of a full-scale general cargo vessel, using CFD simulation. Fidelity Fine Marine code, provided by CADENCE, based on the RANS-VOF solver, has been used to evaluate the flow field around the hull at its service speed of 14 knots. Four different roughness conditions were considered for this investigation. Additionally, the simulation results for the case of smooth hull were compared to the data provided by LR in 2015 in the workshop proceeding.

MATERIALS AND METHODS

The general cargo vessel REGAL served as test case for this study. It was also the ship investigated in the first Lloyd's Register (LR) workshop dedicated to full-scale CFD analysis in 2016 (Workshop on Ship Scale Hydrodynamic Computer Simulation). Figure 1 illustrates the REGAL geometry, and Table 1 presents its main dimensions [9].



Figure 1. REGAL geometry

Table 1. Ship's main dimensions

Main Particulars	Symbol	Value	Units
Length over all	L_{oa}	149.9	m
Length between perpendiculars	L_{pp}	138.0	m
Breadth moulded	B	23.0	m
Depth to main deck	D	12.1	m
Draught max	T_{max}	8.5	m
Wetted surface area	S_W	3727	m^2

In order to evaluate the roughness effect on ship resistence in calm water and implicit on effective power several test cases were considered (Table 2). Three distinct sets of simulations were performed to investigate five different hull roughness conditions at a speed of 14 knots. The values for the equivalent sand-grain roughness height, H_r, correspond to those ones presented by Schultz [4]. The initial set of computations, REGAL_FS, were conducted for the full-scale vessel in conditions of free surface, sinkage, and trim. The second set of computations, REGAL_DB, was performed in double body condition, which means that only the wetted surface of the ship hull is considered, with no free-surface, sinkage, or trim. For this test case, the hull roughness

was also taken into considerations. The last set of computations, REGAL_FP, was performed for the equivalent flat plate of the full-scale general cargo, in double body conditions for all the hull roughness considered.

Table 2. Test cases

Simulation Type	Condition	Notation	H_r [μm]	Description of condition
Full-scale ship resistance	Resistance conditions	REGAL_FS	smooth	Hydraulically smooth surface
	Double body conditions	REGAL_DB	30 μm	Typical as applied AF coating
			100 μm	Deteriorated coating or light slime
			300 μm	Heavy slime
Flat plate resistance	Double body conditions	REGAL_FP	1000 μm	Small calcareous fouling or weed

The simulations were conducted employing the commercial software ISIS-CFD solver from Fidelity Fine Marine. The solver utilizes the finite volume method for spatial discretization of the governing equations. Specifically, it solves the incompressible steady Reynolds-Averaged Navier-Stokes (RANS) equations in a global approach, as outlined in [10]. The discretization scheme employs a second-order upwind scheme for the convective terms and a central difference scheme for the diffusion terms. The discretization and solutions of additional transport equations for modelled variables in turbulent flows follow the same principle [11].

Integration of turbulence is achieved using the k-ω SST model with wall function formulation and a wall roughness model. This model incorporates components from established two-equation models as presented by Menter [12-14]. Roughness is implemented into the k-ω SST model through the wall function formulation, which incorporates the equivalent sand grain roughness. Dirling's correlation [15] defines the link between the mean roughness height and the sand grain roughness.

A Rhie & Chow SIMPLE-like method ensures pressure-velocity coupling. At each time step, velocity updates are obtained from the momentum equations, and pressure is computed through transformation of the mass conservation constraints into pressure equations [16]. The Volume of Fluid (VOF) method with a high-resolution interface scheme captures the free surface based on a multi-phase flow approach. The conservation equations are utilized for each volume fraction to simulate incompressible and non-miscible flow, as outlined in [17].

Three computational domains were generated for each set of simulations. The domains are fully rectangular and are defined in such a way to take advantage of the symmetry of the hull. The dimensions and the boundary conditions of the computational domains were established according to ITTC recommendations [18]. Thereby, the domain size extends from $1.5L_{pp}$ at the upstream to $3L_{pp}$ at the downstream, while in the lateral side extends to $2L_{pp}$ with respect to the symmetry plane. The bottom is located at $1.5L_{pp}$ and the top at $1L_{pp}$ in respect to the undisturbed free surface. Regarding the boundary conditions, the symmetry plane has been defined as mirror, the inlet, outlet, and side boundaries have been set as far field, while the top and bottom of the computational domain have been set as prescribed pressure. For the hull surface, the wall-function condition has been adopted and for the deck, the slip condition.

For the second set of simulations, performed in double-body condition, the dimensions of the computational domain are the same, except that there is no top boundary and the free surface is replaced by a symmetry plane defined as mirror. Since there is no deck

https://doi.org/10.5593/sgem2024/4.1/s17.25

for, a wall-function condition has been adopted on the hull surface. In the case of flat plate configuration, the Regal hull has been replaced with a flat plate with a length equal with the length between perpendiculars and with the same wetted surface area. About the flat plate breadth, is insignificantly small.

An unstructured hexahedral computational grid has been generated by using the HEXPRESS™ automatic grid generator. Details of the near-hull grid for each test case are shown in Figure 2. For all test cases, additional refinement had been applied on the fore and aft part of the geometry in question. The same surface and curve refinement has been applied for the Regal hull both for first test case and for second test case. For the first test case a sector refinement has been used to define a more refined mesh in the region where ship waves system develops. Moreover, an analytical weighting mesh deformation approach has been employed, ensuring that both trim and sinkage were solved during the computations. For the other two test cases to define a finer mesh around the geometry has been used a box refinement that covers the entire computational domain.

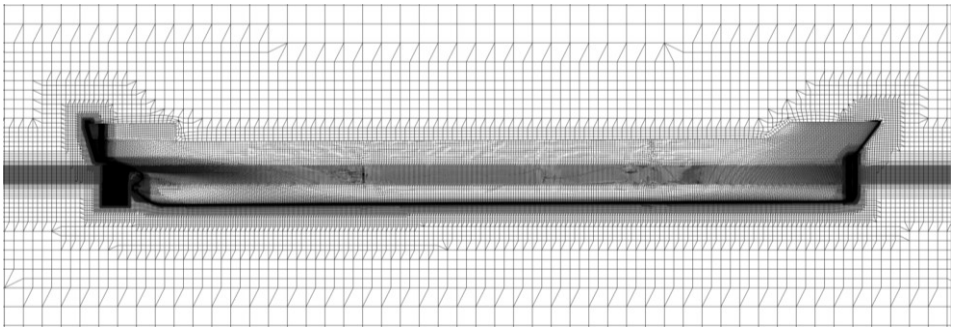


Fig. 2. Mesh generated around simulated geometry

RESULTS AND DISCUSSION

The total resistance (R_T) is mainly composed of frictional resistance (R_F), due to shear stress on the hull surface, and residuary resistance (R_R), due to pressure related drag, which consists also of two components, the wave resistance (R_W) and viscous pressure resistance (R_{PV}). In order to determine each component, the following assumptions were made as presented in Figure 3: the total resistance, R_T, was considered equal with the total resistance computed through the first set of simulations, REGAL_FS, the frictional resistance was considered equal with the total resistance computed through the third set of simulations, REGAL_FP, and the viscous pressure resistance was determined by the difference between the total resistance computed through second set of simulation, REGAL_DB, and third set, REGAL_FP.

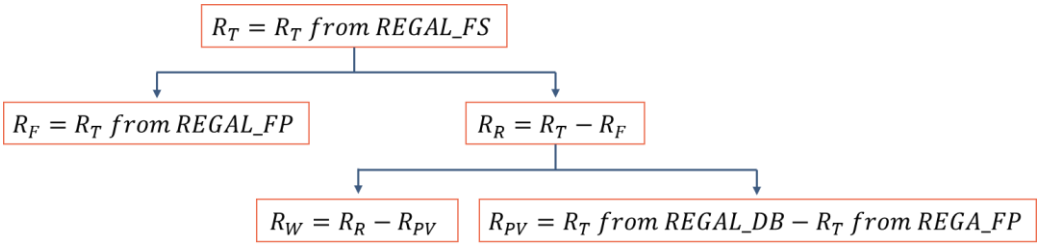


Fig. 3. Total hull resistance components

In Table 3 is presented the relative difference in ship total resistance and its components compared with the smooth hull for each equivalent sand grain roughness height

analyzed. The results show a minimal increase (3.39%) in total resistance for a typical antifouling (AF) coating (30 μm). However, with coating deterioration or light slime (100 μm) on the hull surface, the increase in total resistance becomes significant and continues to rise with more severe fouling conditions, as observed in [4]. For a scenario with calcareous fouling or weed (1000 μm), the total resistance is 51.24% higher compared to the hydraulically smooth hull. This translates to a significant increase in effective power required to maintain the desired speed. Since resistance increases with roughness, a higher effective power would be needed to maintain speed, leading to increased fuel consumption and reduced efficiency. Among the resistance components, those most dependent on the Reynolds number, such as frictional resistance and viscous resistance, exhibit the largest increases with severe fouling.

Table 3. Relative total resistance and total resistance components difference

H_r [μm]	R_T [%]	R_F [%]	R_R [%]	R_{PV} [%]	R_W [%]
0	-	-	-	-	-
30	3.39	2.22	5.03	15.92	2.12
100	13.95	16.76	10.03	32.70	3.98
300	30.72	38.56	19.81	70.00	6.41
1000	51.24	65.47	31.42	113.80	9.43

Comparisons of wave elevation between the smooth hull condition and heavy slime, respectively small calcareous fouling or weed are illustrated in Figure 4. Analysis of the free-surface topology reveals that roughness effects appear to dampen the wave amplitudes, particularly in the wake region. This observation aligns with findings reported in [4] and [19]. The decrease in wave amplitude can likely be attributed to the influence of viscosity on the wave system.

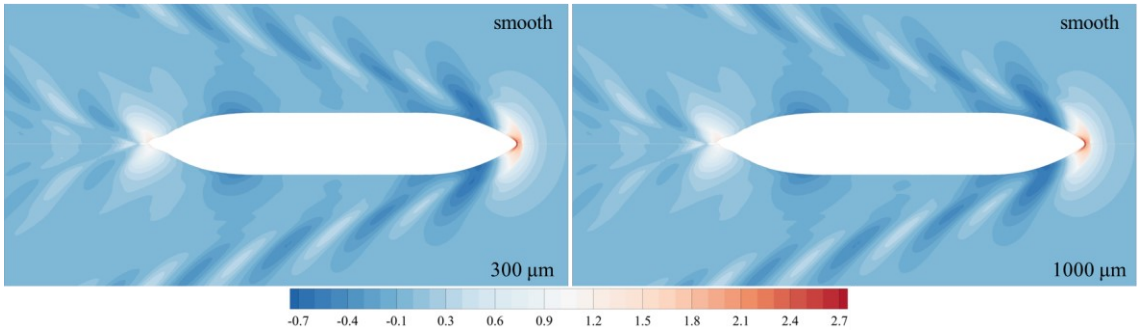


Fig. 4. Wave elevation [m] – top view

The axial velocity and the turbulent kinetic energy plotted comparatively in cross section at the midship for smooth hull condition and heavy slime, respectively small calcareous fouling condition are represented in Figure 5 and 6. While the turbulent kinetic energy increases with the respect of surface roughness, the axial velocity decreases. This drop in axial velocity can be attributed to the heightened turbulence caused by the surface roughness. The increase in the turbulent kinetic energy, can explain the increase in turbulence, which is associated with an increase in turbulence stress and wall shear stress [4]. These forces act near the hull, slowing down the flow and resulting in the observed decrease in axial velocity. It is worth to mention that the surface roughness leads to the development of a thicker turbulent boundary layer and

https://doi.org/10.5593/sgem2024/4.1/s17.25

reduced flow velocities near the hull's surface. Also, the decrease in velocity profile near the hull due to surface roughness leads to an increase in frictional resistance.

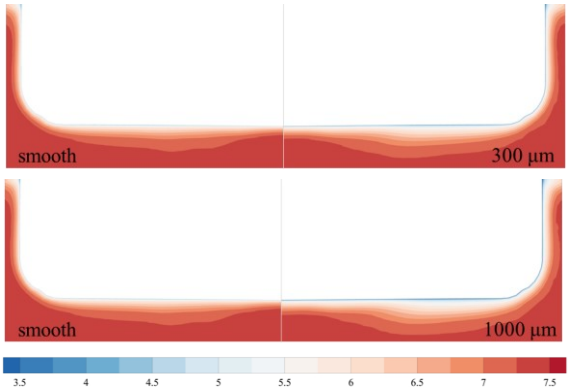


Fig. 5. Axial velocity [m/s] midship section

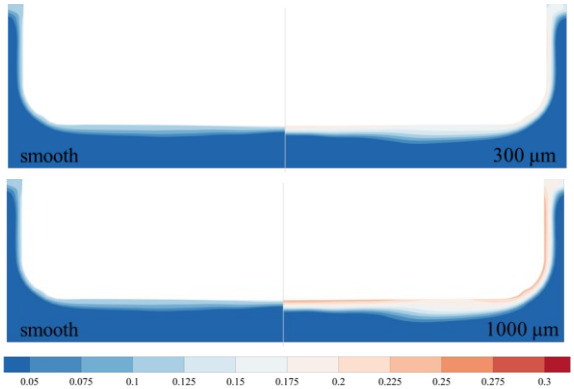


Fig. 6. Turbulent kinetic energy [J/kg] midship section

In Figures 7 and 8 is depicted the comparison for hydrodynamic pressure at the stern and for the axial velocity in the propeller plane between the smooth hull condition and the four roughness conditions considered in this investigation. The roughness on the ship's hull has an impact on the hydrodynamic pressure, resulting in a smaller pressure magnitude at the stern of the ship. The smaller pressure at the stern in the rough case can be due to the increased viscous pressure resistance [19] and also can affect the axial velocity in the propeller plane.

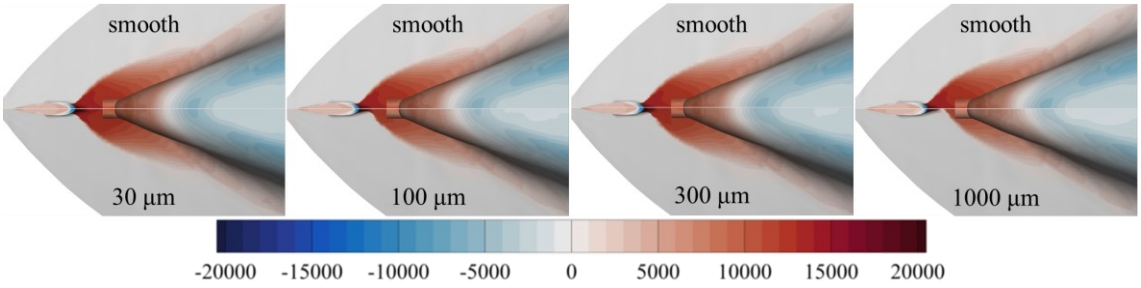


Fig. 7. Hydrodynamic pressure [Pa] – stern view

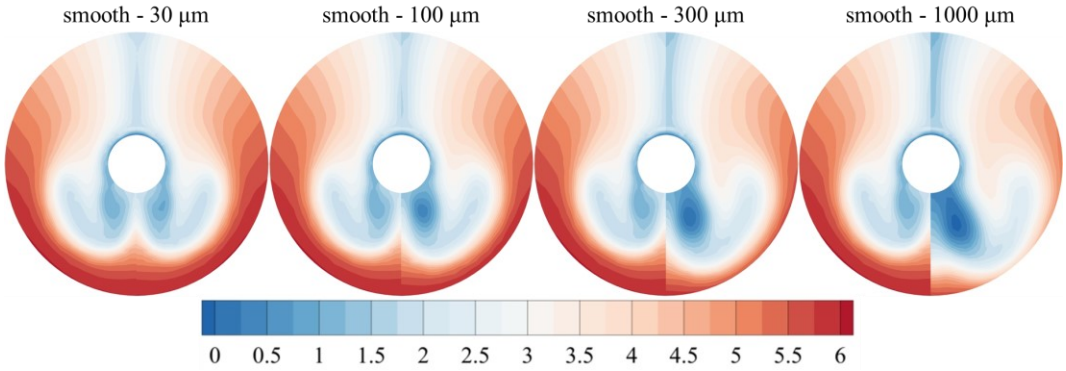


Fig. 8. Axial velocity [m/s] – propeller plane

CONCLUSION

In order to investigate the effect of hull roughness on the ship total resistance and on the flow around the hull, a systematic study has been performed based on RANS-VOF simulations. Four hull roughness conditions at design speeds have been analysed.

When comparing the smooth hull condition to the severe fouling condition (1000 μm), the total resistance increased total resistance by more than 51%. This results in to a significant increase in effective power required to maintain speed, as effective power directly reflects the energy used to overcome resistance. The most significant impact was observed on the frictional and viscous resistance, which are dependent on the Reynolds number. Analysing the wave topology at the stern of the vessel, it appears that the presence of roughness has a dampening effect on wave amplitudes, potentially due to the influence of viscosity. The decrease in stern pressure observed with roughness might be attributed to increased viscous pressure resistance, which could have an impact on propeller performance.

Maintaining a smooth hull is essential for achieving optimal performance and fuel efficiency, as it directly affects the total resistance, wave patterns, and flow characteristics. A smooth hull minimizes effective power requirements, leading to reduced fuel consumption and environmental impact.

REFERENCES

[1] Kempf, G., On the effect of roughness on the resistance of ships, Trans INA, vol. 79, pp. 109 – 119, 1937.

[2] Lackenby, H., Resistance of ships, with special reference to skin friction and hull surface condition, Proceeding of the Institution of Mechanical Engineering, vol. 176, pp. 981 – 1014, 1962.

[3] Townsin, R., Dey, S., The correlation of roughness drag with surface characteristics, Proceedings of the RINA International Workshop on Marine Roughness and Drag, Spinger Netherlands, Dordrecht, pp. 181-191, 1990.

[4] Schultz, M. P., Effects of coating roughness and biofouling on ship resistance and powering, Biofouling, vol. 23/issue 5, pp. 331-341, 2007.

[5] Ünal, U. O., Correlation of frictional drag and roughness length scale for transitionally and fully rough turbulent boundary layers. Journal of Ocean Engineering, vol. 107, pp. 283–298, 2015.

[6] Song, B., Demirel, Y. K., Atlar, M., Incecik, A., Validation of the CFD approach for modelling roughness effect on ship resistance, Journal of Ocean Engineering, vol. 200, paper 107029, 2020.

[7] Eça, L., Starke, A. R., Kerkvliet, M., Raven, H. C., On the contribution of roughness effects to the scaling of ship resistance. Journal of Ocean Engineering and Marine Energy, vol. 8/issue 4, pp. 539-551, 2022.

[8] Song, S., Dai, S., Demirel, Y.K., Atlar, M., Day, S., Turan, O., Experimental and theoretical study of the effect of hull roughness on ship resistance, Journal of Ship Research, vol. 65/issue 1, pp. 62–71, 2021.

https://doi.org/10.5593/sgem2024/4.1/s17.25

[9] Lloyd's Register, Proceeding Workshop on Ship Scale Hydrodynamic Computer Simulation, Southampton, UK, 2016

[10] Guilmineau, E., Deng, G. B., Leroyer, A., Queutey, P., Visonneau, M., Wackers, J., Influence of the turbulence closures for the wake prediction of a marine propeller Proc. of the 4th International Symposium on Marine Propulsors, 2015.

[11] Duvigneau, R., Visonneau, M., Deng, G. B., On the role played by turbulence closures in hull shape optimization at model and full-scale, Journal of Marine Science and Technology, vol. 8/issue 1, pp. 1–25, 2003.

[12] Menter, F. R., Influence of freestream values on k-omega turbulence model predictions, AIAA Journal, vol. 30/issue 6, pp. 1657-1659, 1992

[13] Menter, F. R., Zonal two-equation k-omega turbulence models for aerodynamic flows, 23rd Fluid Dynamics Conference, 1993.

[14] Menter, F. R., Two-equation eddy viscosity turbulence models for engineering applications, AIAA Journal, vol. 32, pp. 1299–1310, 1994.

[15] Dirling, J. R., A Method for Computing Rough Wall Heat Transfer Rates on Re-Entry Nosetips, 8th Thermophysics Conference, 1973.

[16] Visomneau, M., Deng G. B., Guilmineau, E., Queutey, P., Wackers, J., Local and global assessment of the flow around the Japanese bulk carrier with and without energy saving devices at model and full scale, Proceeding of the 31st Symposium of Naval Hydrodynamics, 2016.

[17] Queutey, P., Visonneau, M., An interface capturing method for free-surface hydrodynamic flows, Computers & Fluids, vol. 36/issue 9, pp. 1481–1510, 2007.

[18] International Towing Tank Conference, Practical Guidelines for Ship CFD Applications, 7.5-03-02-03, 2014

[19] Demirel, Y. K., Turan, O., Incecik, A., Predicting the effect of biofouling on ship resistance using CFD, Journal of Applied Ocean Reserch, vol. 62, pp. 100-118, 2017.

SAWDUST LIQUIEFACTION OVER SCHUNGITE-BASED CATALYST

Assoc. Prof. Dr. Antonina A. Stepacheva
Assoc. Prof. Dr. Mariia E. Markova
Assoc. Prof. Dr. Oleg V. Manaenkov
Assoc. Prof. Dr. Elena I. Shimanskaya
Prof. Dr. Valentina G. Matveeva
Tver State Technical University, **Russia**

ABSTRACT

The deep processing of lignocellulose feedstock (including waste from the woodworking industry, agriculture, and agro-industry) allowing the high-added value products to be obtained is one of the key scientific problems. Lignocellulose biomass is a potential feedstock for the production of heat, electricity, fuel, chemicals, and other bioderived products. The liquefaction is considered to be one of the most promising ways to convert lignocellulose biomass into liquid fuels. During the liquefaction, lignocellulose biomass can be efficiently converted into important base compounds, such as furfural, 5-hydroxymethylfurfural, levulinic acid and its esters, γ-pentylactone, alkyl glycosides, and phenols. The search of effective catalysts for liquefaction is the main task for the development of the technology for obtaining liquid fuels from biomass.

In this work, the liquefaction of the wood waste in the presence of a heterogeneous catalyst was studied. The novel Ni-containing catalyst supported on the natural carbonaceous material was used in this work. The influence of the reaction parameters on the biomass conversion, and product yield was estimated. The effect of the solvent, reaction temperature, hydrogen pressure, and preliminary treatment of biomass was analysed. It was shown that the developed catalyst allows the feedstock conversion to be about 90 wt. % for the non-hydrolysed sawdust. The preliminary hydrolysis of the feedstock increased the conversion up to 95 wt. %. The composition of the liquid products were presented by the products of the hydrolysis of cellulose, hemicelluloses, and lignin, as well as the polyols, 5-hydroxymethylfurfural, aromatics, and cyclic compounds.

Keywords: sawdust, liquefaction, bio-oil, catalyst, schungite

INTRODUCTION

Biomass liquefaction is one of the thermochemical methods allowing the liquid products to be obtained. The liquefaction process is generally carried out at moderate temperatures and relatively low pressure. The product yield is mainly influenced by the composition of biomass, the catalyst, and the solvent as well as the presence of hydrogen in the reaction mixture [1]. Several types of liquefaction are usually used.

For the reductive liquefaction, a gaseous hydrogen is used. Traditional metallic catalysts are widely used for catalytic hydrogenation of biomass (Ni, Pd). The most active catalyst for the reductive liquefaction is considered to be Ni. Besides, homogeneous catalysts (iron chlorides, sodium molybdate, etc.) can be effectively used for the

https://doi.org/10.5593/sgem2024/4.1/s17.26

liquefaction of wood and its components. The reductive liquefaction of wood biomass is carried out in a temperature range of 250-350 °C at an initial hydrogen pressure of 1.6-10 MPa. In this method, the water-soluble organic compounds and gaseous products (primarily CO and CO_2) are formed [2].

The use of hydrogen in liquefaction leads to an increase in the process cost, thus, the liquefaction of biomass in the presence of CO was developed. The studies of the biomass liquefaction by CO in water solutions at 250-400 °C showed that water played the role of hydrogen donor for the hydrogenation of the polysaccharide hydrolysis products. The development of CO-assisted liquefaction processes showed that the optimal operation temperature in that case was found to be 300-350 °C. At lower temperatures, the conversion of the feedstock was low and the liquefaction products had the form of bitumen-like material with melting temperature of 100 °C. The higher temperatures in liquefaction led to water vaporization and a significant increase in the process pressure. The effective catalysts for CO-assisted liquefaction were found to be carbonates and formates of alkali metals, iron and cobalt nitrates, etc. [3].

Depolymerization of wood biomass can be carried out in the presence of organic solvents being hydrogen donors. This process allows bio-oil, water-soluble organics, and gaseous products to be obtained. In the liquefaction process, a hydrogen donor solvent undergoes the dehydrogenation. Such solvents as light alcohols, tetraline, formic acid, and phenols are used. Ethanol and propanol were found to be the most effective solvents for liquefaction of biomass. The process is carried out in a temperature range of 200-350 °C at an autogenic pressure. Feedstock conversion varies from 60 to 95 % depending on the type of biomass. Products of liquefaction can be divided into gasoline-, gasoil, and naphtha-like fractions. Pd, Ni, Zn-Cr, and Fe-Zn-Cr are used as liquefaction catalysts. Acid catalysts (i.e. phenol, methane sulfoacid, etc.) can be used to increase the rate of the polysaccharides hydrolysis [4-7].

In this work, the liquefaction of the wood sawdust was studied in the presence of a Ni-containing catalyst supported on the natural carbonaceous mineral – schungite. The effect of the solvent, biomass pretreatment, and process conditions on the composition and yield of products was studied.

MATERIALS AND METHODS

Catalyst Synthesis Procedure

Schungite dust – a natural carbon-containing material – was purchased from Zazhogino field, Karelia Republic, Russia. The material was used as a catalyst support. For the catalyst preparation, 1 g of schungite, 0.1 g of sodium bicarbonate, and a calculated amount of nickel nitrate hexahydrate (5 wt. % of Ni) were suspended in 15 mL of distilled water. The suspension was placed into the stainless-steel batch reactor Parr 4307 (Parr Instrument, USA) equipped with a mechanical stirrer. The reactor was sealed, purged with nitrogen 3 times, and heated up to 200 °C under a hydrogen pressure of 4.0 MPa. The mixture was kept under the synthesis conditions for 15 min. Then, the mixture was cooled down to room temperature, filtered, and washed with 10 mL of distilled water to remove carbonate and nitrate ions. The synthesized catalyst was dried at 100±5 °C overnight and then reduced in a glass tube at 300 ± 5 °C with a hydrogen flow (flow rate 30 mL/min) for 3 h.

Liquefaction Procedure

The pinewood sawdust was purchased from the harvesting company of Tver region, Russia. The feedstock used was characterized as follows: moisture content – 7.0 wt. %, ash content – 3.6 wt. %, cellulose – 53.1 wt. %, hemicelluloses – 7.9 wt. %, lignin – 25.4 wt. %, extractives – 6.3 wt. %. The sawdust was milled, and the fraction with the particle size less than 0.25 mm was used. The liquefaction of the sawdust was carried out in a six-cell Parr Series 5000 Multiple Reactor System (Parr Instrument, USA) with a cell volume of 50 mL. 1 g of the sawdust, 0.1 g of the catalyst, and 30 mL of the solvent were placed in the reactor cell. The reactor was sealed, purged with nitrogen, and heated up to the reaction temperature. Hydrogen was used for the reduction and hydrogenolysis of the feedstock. The hydrogen pressure was set after the rector heating.

The sampling was carried out during the reaction, and the final sample was taken after the reactor cooling. The liquid phase was analysed using gas chromatograph GC-2010 and mass-spectrometer GCMS-QP2010S (SHIMADZU, Japan) equipped with chromatographic column HP-1MS with 30 m length, 0.25 mm diameter, and 0.25 μm film thickness. The column temperature program was set as follows: initial temperature of 120 °C was maintained for 5 min then the column was heated up to 250 °C at the rate of 5 °C/min and maintained at 250 °C for 5 min. Helium (volumetric velocity of 20.8 cm3/s, the pressure of 253.5 kPa) was used as a gas carrier. The injector temperature was 280 °C, the ion source temperature was 260 °C; the interface temperature – 280 °C. For the quantitative estimation, the calibration for pure reactants and main products was carried out.

RESULTS AND DISCUSSIONS

The synthesized catalyst was characterized by low-temperature nitrogen physisorption, transmission electron microscopy, elemental analysis, and X-ray photoelectron spectroscopy. The results of the catalyst characterisation are summarized in Table 1.

Table 1. Schungite-based catalyst characterisation

Parameter	Schungite	Ni/Schungite
S_{BET}, m^2/g	22.2	36.5
V_{pore}, cm^3/g	0.05	0.06
Pore size, nm	5.2	9.3
Ni concentration, wt. %	-	4.8
Ni particle size, nm	-	2.4
Ni form	-	NiO

Schungite was found to be a microporous material with a quite low surface area. When the Ni was supported on the schungite by the precipitation in hydrothermal conditions, an increase in surface area by 2 times was observed. This can be explained by the partial leaching of alkali and alkali-earth metal oxides from the support. Moreover, silicon and aluminum oxides contained in the schungite tend to undergo recrystallization during the treatment in subcritical water. In our previous works it was shown that an increase in the surface area of the support during the hydrothermal treatment was mainly connected with the leaching of components from the material [8]. Meanwhile, the proposed method of catalyst synthesis allows the catalytic system with high carbon content, fine distribution of the active phase, and the catalyst acidity of 750 μmol/g to be obtained.
The liquefaction process was carried out for both hydrolysed and non-hydrolysed sawdust. The preliminary hydrolysis was carried out at 170 °C in the presence of 2 wt. % aqueous solution of sulfuric acid for 3 h.

https://doi.org/10.5593/sgem2024/4.1/s17.26

First, a solvent that will ensure maximum conversion of the feedstock into liquid products was selected. The effect of water, ethanol, methanol, and isopropanol was studied. The lowest conversion was noted when using water, which, along with the acidic support of the catalyst, mainly provided the hydrolysis of cellulose and hemicellulose contained in sawdust. This is seen in a decrease in the conversion in the case of hydrolyzed feedstock (Table 2).

Table 2. Solvent influence on the conversion of pinewood sawdust (catalyst Ni/Schungite, temperature 260 °C, hydrogen pressure 4 MPa, process duration 1 h)

Solvent	Conversion, wt. %	
	Hydrolysed sawdust	Non-hydrolysed sawdust
Water	35	52
Methanol	78	56
Ethanol	62	45
Isopropanol (IPA)	68	51
Water-IPA (15 % IPA)	41	56
Water-IPA (30 % IPA)	54	62
Water-IPA (45 % IPA)	69	71
Water-IPA (60 % IPA)	82	77
Water-IPA (75 % IPA)	78	71

When using alcohols, the conversion increases in the raw "ethanol-isopropanol-methanol". This can be explained by an increase in the solvent's H-donating ability. The highest conversion was obtained using methanol for both hydrolyzed and non-hydrolyzed sawdust. However, the composition of the products showed a low concentration of compounds formed during the hydrolytic reductive conversion of cellulose and hemicelluloses. Therefore, to increase the degree of conversion of the feedstock, a study was performed in an aqueous-alcohol (water-isopropanol) mixture. The latter was chosen based on its lower toxicity compared to methanol. The study showed that an increase in alcohol concentration led to an increase in sawdust conversion and passed through a maximum of 60 wt. %. At the same time, both polysaccharide monomers and lignin monomers were observed in the products (Table 3).

Table 3. Composition of products of pinewood sawdust liquefaction (catalyst Ni/Schungite, temperature 260 °C, hydrogen pressure 4 MPa, process duration 1 h, solvent water-IPA (60 % IPA))

	Yield, wt. %	
	Hydrolysed sawdust	Non-hydrolysed sawdust
Hexoses	9.6	10.3
Pentoses	3.2	4.8
C_5-C_6 polyols	8.2	12.1
C_2-C_4 polyols	6.8	5.7
5-HMF	1.7	1.3
Phenols	22.3	17.4
Aromatic hydrocarbons	17.2	13.6
Cyclic hydrocarbons	5.3	2.2

The influence of process conditions on the conversion of hydrolysed and non-hydrolysed pinewood sawdust in the liquefaction in the presence of a schungite-based catalyst was studied. The results obtained are summarized in Table 4.

Table 4. Influence of the biomass liquefaction conditions (catalyst Ni/Schungite, process duration 1 h, solvent water-IPA (60 % IPA))

	Hydrolysed sawdust			Non-hydrolysed sawdust		
	X, %	η_m,%	η_h,%	X, %	η_m,%	η_h,%
Temperature, °C						
260	87	45.1	39.2	82	42.5	34.9
270	91	43.9	44.8	86	41.2	42.3
280	95	40.7	51.8	90	39.6	48.5
290	86	36.9	47.6	80	34.2	44.8
300	71	28.4	41.7	69	25.4	34.1
Hydrogen pressure, MPa						
4	87	45.1	39.2	82	42.5	34.9
5	90	42.1	43.2	83	40.7	38.6
6	94	40.7	52.4	84	39.4	42.9
Feedstock/catalyst ratio, g/g						
10	87	45.1	39.2	82	42.5	34.9
20	80	42.2	35.1	76	40.3	32.5
30	68	39.4	27.6	64	38.1	23.2

X – conversion, η_m – monomer yield (saccharides and phenols), η_h – yield of monomer conversion products (polyols, hydrocarbons, etc.)

Studies on the influence of process conditions showed that an increase in temperature had a positive effect on biomass conversion and the yield of valuable products (Table 4). However, with an increase in temperature above 280 °C, sintering and charring of the heterogeneous phase were observed. This led to an increase in the yield of biochar and a decrease in the yield of liquid components. An increase in the partial pressure of hydrogen did not lead to a significant increase in the conversion of non-hydrolysed sawdust, however, it increased the conversion of hydrolysed feedstock. In addition, it was noted that with increasing hydrogen pressure, the content of hydrogenation/hydrogenolysis/deoxygenation products of polysaccharides and lignin

https://doi.org/10.5593/sgem2024/4.1/s17.26

monomers increased. For hydrolysed feedstock with an increased lignin content, an increase in pressure, on the contrary, led to an increase in the conversion, as well as for experiments with pure lignin [9]. At the same time, deoxygenation processes were accelerated and the yield of aromatic and cyclic hydrocarbons increased. When varying the catalyst-feedstock ratio, it was noted that the conversion of the feedstock decreased with increasing the catalyst loading. At the same time, the processes of monomer transformation were inhibited.

CONCLUSION

The study of the liquefaction of pinewood sawdust using a nickel-containing catalyst supported on a natural carbonaceous mineral, schungite, demonstrated the effectiveness of this method. The influence of various parameters such as solvent, biomass pretreatment, and process conditions were studied. This allowed the optimal parameters for obtaining high-quality products to be determined. Water-isopropanol mixture containing 60 vol. % alcohol was found to be the most effective solvent for liquefaction. The optimal process conditions were determined as follows: temperature 280 °C, hydrogen pressure 4 MPa, feedstock/catalyst ratio 10:1 g/g. The chosen conditions allowed 90 wt. % of non-hydrolysed and 95 wt. % of hydrolysed sawdust to be converted into the liquid containing both products of the biomass component hydrolysis and the monomer hydrogenation/hydrogenolysis/deoxygenation products. The schungite-based catalyst was found to be promising for the liquefaction of lignocellulosic biomass.

ACKNOWLEDGEMENTS

The work is financially supported by the Russian Science Foundation (grant 22-79-10096).

REFERENCES

[1] Arlete T., Ozkan S., Ribeiro A.P., Cristino A.F., dos Santos R.G., Thermochemical liquefaction of biomass with ionic liquids: Exploring a sustainable pathway for a cleaner bio-oils production, Journal of Cleaner Production, vol. 434, p 140114, 2024.

[2] Usman M., Cheng S., Boonyubol S., Cross J.S., From biomass to biocrude: Innovations in hydrothermal liquefaction and upgrading, Energy Conversion and Management, vol. 302, pp 118093, 2024.

[3] Shahbeik H., Shariat Panahi H.K., Dehhaghi M., Guillemin G.J., Fallahi A., Hosseinzadeh-Bandbafha H., Amiri H., Rehan M., Raikwar D., Latine H., Pandalone B., Khoshnevisan B., Sonne C., Vaccaro L., Nizami A.-S., Gupta V.J., Lam S.S., Pan J., Lique R., Sels B., Peng W., Tabatabaei M., Aghbashlo M., Biomass to biofuels using hydrothermal liquefaction: A comprehensive review, Renewable and Sustainable Energy Rewiews, vol. 189, part B, pp 113976, 2024.

[4] Ocal B., Recepoglu Y.K., Yuksel A., Thermal liquefaction of olive tree pruning waste into bio-oil in water and ethanol with NaOH catalyst, Journal of the Energy Institute, vol. 113, pp 101533, 2024.

[5] Jiang W., Kumar A., Adamopoulos S., Liquefaction of lignocellulosic materials and its applications in wood adhesives - A review, Inductrial Crops and Products, vol. 124, pp 325-342, 2018.

[6] Song L., Jiang Y., Zhang Z., Ouyang Y., Insight into mechanism of hydrogen-supplied liquefaction of lignocellulose over varied catalysts, Biomass and Bioenergy, vol. 184, pp 107208, 2024.

[7] Wu Y., Wang H., Li H., Han X., Zhang M., Sun Y., Fan X., Zeng Y., Xu C.C., Xu X., Applications of catalysts in thermochemical conversion of biomass (pyrolysis, hydrothermal liquefaction and gasification): A critical review. Renewable Energy, vol. 196, pp 462-481, 2022.

[8] Stepacheva A.A., Markova M.E., Schipanskaya E.O., Matveeva V.G., Sulman M.G., Highly Effective Schungite-Based Catalyst for Deoxygenation of Biomass Components, Chemical Engineering Transactions, vol. 88, pp 283-288, 2021.

[9] Stepacheva A.A., Manaenkov O.V., Markova M.E., Sidorov A.I., Bykov A.V., Sulman M.G., Kiwi-Minsker L., Lignin Hydrogenolysis over Bimetallic Ni–Ru Nanoparticles Supported on SiO_2@HPS, Catalysts, vol. 13, pp 856, 2023.

https://doi.org/10.5593/sgem2024/4.1/s17.26

STUDY OF CHANGES IN HYDROGEN CONCENTRATION IN SOIL GAS SAMPLES

Paulina Kopera[1]
Anna Twaróg[2]
Henryk Sechman[3]

[1]AGH University of Krakow, Faculty of Geology, Geophysics and Environmental Protection, Department of Energy Resources, **Poland**

[2]AGH University of Krakow, Faculty of Geology, Geophysics and Environmental Protection, Department of Energy Resources, **Poland**

[3]AGH University of Krakow, Faculty of Geology, Geophysics and Environmental Protection, Department of Energy Resources, **Poland**

ABSTRACT

Hydrogen can originate from various geological processes and its ability to migrate to near-surface layers makes soil gas analysis crucial for identifying subsurface accumulations. Current methods using portable analysers are often insufficient for precise determination, highlighting the need for gas chromatography in controlled laboratory settings. Hydrogen's high mobility and chemical reactivity make it difficult to maintain stable soil gas samples from collection to analysis. To address this challenge, an experiment was conducted to assess the impact of storage time and conditions on hydrogen concentrations in field-collected soil gas samples.

The study involved the preparation of four mixtures of hydrogen with synthetic air. Obtained hydrogen concentrations were: 47.5 ppm (M1), 93.2 ppm (M2), 15477.9 ppm (M3), 2105.6 ppm(M4). Samples were stored in glass bottles with saturated NaCl solution and in Tedlar bags at room temperature and refrigerated conditions. Hydrogen concentrations was measured on the day the test material was prepared (t0), two weeks later (t1), one month later (t2) and two months after t0 (t3) using an Agilent 7820A gas chromatograph.

The findings demonstrated that glass bottles at room temperature provided the most stable environment, with minimal concentration variation. Refrigerated samples showed increased variability, likely due to temperature-dependent solubility changes. Tedlar bags exhibited rapid hydrogen loss, attributed to the material's permeability. For accurate hydrogen determination, glass containers at room temperature are recommended, with optimal analysis occurring within two weeks (and a month a most) of sample collection. During this period, hydrogen concentrations undergo minimal changes, which are within the analytical error of the instrument.

Keywords: natural hydrogen, hydrogen concentration, soil gas sampling, storage stability

https://doi.org/10.5593/sgem2024/4.1/s17.27

INTRODUCTION

Growing awareness of global environmental challenges and the need for energy transformation mean that hydrogen is gaining importance as a key element of future energy systems. Its potential as a clean energy carrier capable of reducing greenhouse gas emissions stimulates both research and investment in hydrogen technologies. This gas is generated under a variety of conditions and can come from a variety of sources including volcanic activity, geothermal systems, evaporate deposits, coal-bed methane or oil and gas fields [1]. Due to the ability of hydrogen to migrate to near-surface layers, the analysis of soil gas composition is an essential element in identifying anomalies that may indicate its accumulation in deeper layers of geological formations. The search for natural hydrogen deposits is currently underway in many countries around the world including the USA, Australia, Brazil and France [2].

Many publications present ways to determine hydrogen concentrations in soil gas using portable analysers [e.g., 3, 4]. These devices enable quick analysis directly in the field, however, in the context of searching for potential hydrogen deposits, it is necessary to use more precise methods, such as gas chromatography. Laboratory conditions minimize the risk of external interferences, such as changes in temperature, pressure or humidity. Chromatography analysis also allows detection of low gas concentrations, often below detection thresholds offered by portable analysers [5].

Hydrogen has high mobility and chemical reactivity, which poses a challenge to researchers in maintaining the stability of soil gas samples from collection to analysis [6]. With this in mind, an experiment was performed to analyse the influence of time and storage conditions of field-collected soil gas on changes in hydrogen concentrations. The conducted research will help strengthen the methodological foundation of surface geochemical surveys, which serve as one of the first exploration methods for potential sites of natural hydrogen accumulation.

MATERIALS AND METHODS

Mixtures preparation

Based on previous information on the concentrations of hydrogen present in the soil gas [e.g., 7, 8], four mixtures (M_1, M_2, M_3, M_4) representing different concentrations of hydrogen were made. After mixing the hydrogen with synthetic air in tedlar bags, molecular composition analyses were performed using gas chromatographs, confirming the obtained concentrations. The hydrogen concentrations of the obtained mixtures were, respectively: 47.5 ppm (M_1), 93.2 ppm (M_2), 15477.9 ppm (M_3), 2105.6 ppm (M_4). Each mixture was then injected using a gas-tight syringe tipped with a needle into two 125-ml glass bottles, initially filled with saturated NaCl solution. While the gas was injected into the bottle, excess brine flowed out through the second (injection) needle until the pressures within the container equalized. Such filling is free of atmospheric gases, eliminating the risk of contaminating the sample. The small amount of brine remaining in the bottle further ensures that the rubber stopper is sealed during storage and transport of samples to the laboratory in the upside down position . The methodology used is analogous to that used for soil gas sampling in the search for hydrocarbon accumulations, using a patented methodology and probe [more in 9, 10].

Thus, two sets of glass containers were prepared with the same samples, one of which was stored in a refrigerator at 8.5˚C and the other at room temperature of about 23˚C.

The unused portion of the gas remained in tedlar bags. Only in the case of the M_2 mixture, due to the smaller volume of prepared gases, no larger volumes of gas remained in the tedlar bag after pumping. In addition, during the pumping of this mixture into one of the glass bottles, the sample was aerated. This resulted in the determination of lower initial (t_0) hydrogen concentrations in this series of tests compared to those determined in the same mixture stored at room temperature.

Concentration analyses were performed: i) on the day the test material was prepared (t_0), ii) two weeks later (t_1), iii) one month later (t_2) and iv) two months after t_0 (t_3). Both samples from glass bottles and the remaining gas mixture stored in tedlar bags were measured.

Chromatography analysis

Hydrogen concentration determinations were performed on a 7820A dual-channel gas chromatograph from Agilent Technologies with a TCD detector. After the bottle containing the gas sample was connected to a 1 ml dispensing loop, brine of 10 ml was injected into the bottle. This pushed the gas into the dispensing loop. From the samples in the tedlar bags, 10 ml of gas was collected through a Push Lock Valve (PLV) using a gas-tight syringe, and then applied directly to the loop. Each sample was analysed twice.

The gas chromatograph used a column with a temperature program: 35°C for the first 3 min, then 35-120°C with an increase of 40°C/min, ending at 120°C for 3 min. The detection threshold of the TCD detector for hydrogen was 1 ppm, and the analytical accuracy was 2% of the measured value. The assay value was the average of two measurements. The measurement error was calculated for the measured hydrogen concentrations (Table 1). This parameter was expressed as the percentage change in the concentration of the gas being determined compared to its concentration at time t_0.

RESULTS AND DISCUSSION

The study clearly proves that the type of container and method of sample storage significantly affects the reliability of hydrogen determination. In the case of samples stored in glass bottles at room temperature, the concentration variations were the smallest, as evidenced by the calculated errors (Table 1). Only in the case of the M_3 mixture, in which the hydrogen concentration was the highest among the samples analysed, the measurement error was greater than the analytical accuracy of the chromatograph (±2%) after time t_2. For the second highest concentration, determined in the M_4 mixture, the error was exceeded after time t_3.

Samples stored in the fridge had larger measurement errors, indicating greater variability in hydrogen concentrations under these conditions. The observed differences in the stability of hydrogen concentration as a function of storage temperature may be due to Henry's law, which states that at a given temperature, the solubility of a gas in a liquid is proportional to the pressure of that gas over the liquid. Changes in temperature affect the equilibrium constant determined by this law, which implies that at lower temperatures and constant pressure, the solubility of the gas in the liquid increases [11]. Thus, it can be assumed that storing samples under cooler conditions leads to selective absorption of hydrogen by the brine, and thus a decrease in its concentration in the tested gas.

https://doi.org/10.5593/sgem2024/4.1/s17.27

Table 1. Average concentrations of hydrogen and helium depending on the time and storage conditions of the samples

Sample no.	T_0	T_1		T_2		T_3	
	average	average	error	average	error	average	error
bottle with brine (room temp.)							
M_1	49.7	50.0	-0.60	49.6	0.30	49.8	-0.20
M_2	99.3	99.0	0.35	100.3	-0.96	98.9	0.55
M_3	15666.4	15722.8	-0.36	15283.7	2.44	15055.9	3.90
M_4	2137.8	2143.8	-0.28	2124.2	0.63	2074.3	2.97
bottle with brine (fridge temp.)							
M_1	50.3	49.7	1.29	49.3	2.09	49.0	2.68
M_2	86.0	84.6	1.69	87.6	-1.86	97.4	-13.26
M_3	15761.4	15322.6	2.78	15094.7	4.23	14624	7.22
M_4	2131.9	2109.	1.07	1958.3	8.14	1817.6	14.75
tedlar bag (room temp.)							
M_1	47.5	23.7	50.1	11.9	74.9	3.3	93.1
M_2	93.2	-	-	-	-	-	-
M_3	15477.9	1913.4	87.6	165.4	98.9	0	100.0
M_4	2105.6	608.9	71.1	160.3	92,4	9.0	99,6

The most dynamic changes in concentrations were observed in samples stored in tedlar bags (Fig. 1), where hydrogen concentrations dropped already two weeks after sample preparation. Tedlar bags, made of polyvinylidene fluoride (PVDF), despite their good chemical resistance and popularity for storing gaseous samples, do not provide the same tightness as glass for fine substances [12]. Hydrogen has a unique ability to diffuse through most materials, including polymers, which may explain the rapid loss of its concentration in samples stored in tedlar bags.

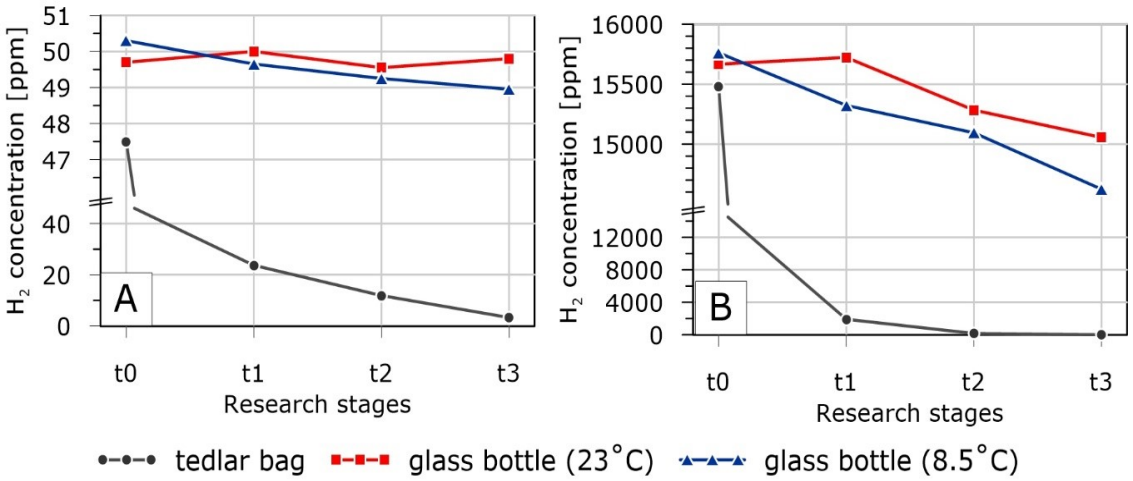


Fig. 1. Changes in hydrogen concentrations depending on time for the M_1 (A) and M_3 (B) mixture

CONCLUSION

The experiment showed that samples stored in glass bottles, turned upside down with a small amount of brine remaining sealing the cap in which punctures were previously made (when filling the sample with gas), have the greatest stability in determining hydrogen concentrations. It seems reasonable to store these samples under room temperature conditions (identical to the temperature at which they are dispensed into the chromatograph). This method of storage minimizes the risk of unwanted proces that may change the amount of gas in the sample. Glass bottles sealed with brine provide a better barier to hydrogen compared to tedlar bags, limiting its loss and protecting against external contaminants.

The results of the study also show that the optimal time to analyse the collected material is two weeks after collection (and a month at most). During this period, hydrogen concentrations undergo minimal changes, which are within the analytical error of the instrument. Longer storage of samples may lead to a gradual decrease in hydrogen concentrations. It is recommended that hydrogen samples collected for detailed laboratory testing take into account the above analyses, which will significantly improve their precision and reliability.

ACKNOWLEDGEMENTS

The research project was supported by program "Excellence initiative – research university" IDUB for the AGH University of Krakow (project number 6237).

REFERENCES

[1] Tian Q. N., Yao S. Q., Shao M. J., Zhang W. and Wang H. H., Origin, discovery, exploration and development status and prospect of global natural hydrogen under the background of “carbon neutrality”, China Geology, vol. 5/issue 4, pp 722-733, 2022. https://doi.org/10.31035/cg2022046.

[2] Carrillo Ramirez A., Gonzalez Penagos F., Rodriguez G., Moretti I., Natural H_2 Emissions in Colombian Ophiolites: First Findings, Geosciences, vol. 13/issue 12:358, pp 1-17, 2023. https://doi.org/10.3390/geosciences13120358.

https://doi.org/10.5593/sgem2024/4.1/s17.27

[3] Frery E., Langhi L., Maison M. and Moretti I., Natural hydrogen seeps identified in the north perth basin, western Australia, International Journal of Hydrogen Energy, vol. 46/issue 61, pp 31158-31173, 2021. https://doi.org/10.1016/j.ijhydene.2021.07.023.

[4] Pasquet G., Idriss A. M., Ronjon-Magand L., Ranchou-Peyruse M., Guignard M., Duttine M., Ranchou_Peyruse A. and Moretti I., Natural hydrogen potential and basaltic alteration in the Asal–Ghoubbet rift, Republic of Djibouti, BSGF-Earth Sciences Bulletin, vol. 194/issue 1:9, pp 1-24, 2023. https://doi.org/10.1051/bsgf/2023004.

[5] Prinzhofer A., Rigollet C., Lefeuvre N., Françolin J. and de Miranda P. E. V., Maricá (Brazil), the new natural hydrogen play which changes the paradigm of hydrogen exploration, International Journal of Hydrogen Energy, vol. 62, pp 91-98, 2024. https://doi.org/10.1016/j.ijhydene.2024.02.263.

[6] Tarkowski R., Underground hydrogen storage: Characteristics and prospects, Renewable and Sustainable Energy Reviews, vol. 105, pp 86-94, 2019. https://doi.org/10.1016/j.rser.2019.01.051.

[7] Moretti I., Prinzhofer A., Françolin J., Pacheco C., Rosanne M., Rupin F. and Mertens J., Long-term monitoring of natural hydrogen superficial emissions in a brazilian cratonic environment. Sporadic large pulses versus daily periodic emissions, International Journal of Hydrogen Energy, vol. 46/issue 5, pp 3615-3628, 2021. https://doi.org/10.1016/j.ijhydene.2020.11.026.

[8] Etiope G., Massive release of natural hydrogen from a geological seep (Chimaera, Turkey): Gas advection as a proxy of subsurface gas migration and pressurised accumulations, International Journal of Hydrogen Energy, vol. 4/issue 25, pp 9172-9184, 2023. https://doi.org/10.1016/j.ijhydene.2022.12.025.

[9] Dzieniewicz M. and Sechman H., Zestaw do ręcznego pobierania próbek gazowych z warstw przypowierzchnio-wych [Method of and set for manually sampling gas from superficial layers of soil]. Patent PL 184080 B1, Urząd Patentowy Rzeczypospolitej Polskiej, 2002. http://patenty.bg.agh.edu.pl/pelneteksty/PL184080B1.pdf.

[10] Sechman H., Detailed analysis of gaseous components in soil gases around petroleum wells-An effective tool for evaluation of their integrity, Applied Geochemistry, vol. 142/issue 105346, 2022. https://doi.org/10.1016/j.apgeochem.2022.105346.

[11] Bazarkina E. F., Chou I. M., Goncharov A. F. and Akinfiev N. N., The behavior of H_2 in aqueous fluids under high temperature and pressure, Elements: An International Magazine of Mineralogy, Geochemistry, and Petrology, vol. 16/issue 1, pp 33-38, 2020. https://doi.org/10.2138/gselements.16.1.33.

[12] Han F., Zhong H., Li T., Wang Y., Liu F., Storage stability of volatile organic compounds from petrochemical plant of china in different sample bags, Journal of analytical methods in chemistry, vol. 2020/issue 1:9842569. https://doi.org/10.1155/2020/9842569.

THERMOELECTRIC PERFORMANCE OF $Na_2B_4O_7$-DOPED AND GRAPHENE-DISPERSED $Bi_2Sr_2Co_2O_y$ COMPOSITES

Vakhtang Zhghamadze[1]
Dr. Nikoloz Margiani[1]
Prof. Dr. Masatoshi Takeda[2]
Iamze Kvartskhava[1]
Dr. Giorgi Mumladze[1]

[1] Georgian Technical University, **Georgia**

[2] Nagaoka University of Technology, **Japan**

ABSTRACT

Renewable energy technologies are becoming increasingly important with the world's growing energy needs and environmental deterioration. In this context, thermoelectric materials capable of converting waste heat directly into electric power are at the forefront of extensive studies. The layered cobaltites have great potential for use in thermoelectric generators due to their environmental friendliness, good thermal and chemical stability, and relatively low cost of raw materials. Improving the thermoelectric properties of cobaltites using appropriate dopants and additives can increase their application potential. In this paper, we studied the impact of $Na_2B_4O_7$-doping and addition of graphene on the thermoelectric performance of $Bi_2Sr_2Co_2O_y$ cobaltite. Reference and $Na_2B_4O_7$-doped $Bi_2Sr_2Co_2O_y$ composites embedded with 0.8 wt. % graphene were prepared by the solid-state reaction route. The phase evolution and microstructure of the final products were studied by X-ray diffraction analysis (XRD) and scanning electron microscopy (SEM) techniques. Temperature dependences of electrical resistivity, Seebeck coefficient, and thermal conductivity were measured and values of power factor (*PF*) and figure of merit (*ZT*) were calculated. It was found that the doping with $Na_2B_4O_7$ and graphene dispersion enhanced the *PF* and *ZT* values by about 83 % and 20 %, respectively, compared with the reference $Bi_2Sr_2Co_2O_y$.

Keywords: thermoelectricity, $Bi_2Sr_2Co_2O_y$, doping, power factor, figure of merit

INTRODUCTION

Considering the growing demand for energy consumption and the fast-changing climate, we must use our energy sources more efficiently. Up to 70 % of the total energy generated by the resources mankind uses is currently being wasted as heat, which raises global environmental issues. Thermoelectricity is a green renewable energy technology that can be used to directly convert some of this wasted heat into profitable electricity via the Seebeck effect. The efficiency of thermoelectric materials is characterized by the dimensionless figure of merit $ZT = S^2T/\rho k$, where *S*, *T*, ρ, and κ are Seebeck coefficient, absolute temperature, resistivity, and thermal conductivity, respectively [1]. Thus, the higher the *ZT*, the larger the conversion efficiency, implying that a high performance

https://doi.org/10.5593/sgem2024/4.1/s17.28

thermoelectric material is characterized by a large S, and low values of ρ and k [1]. The electrical part of ZT expression (S^2/ρ), called power factor, PF, is also used to determine the thermoelectric performance of materials when thermal conductivity measurements are not possible to make [2]. State-of-the-art thermoelectric materials with promising heat-to-electricity conversion efficiency must not only possess high performance but also be stable at high temperatures and be composed of nontoxic and low-cost elements, which is a major criteria of today's global ecological challenge. The discoveries of *p*-type layered $NaCo_2O_4$, $Ca_3Co_4O_9$ and $Bi_2M_2Co_2O_x$ (M = Ca, Sr or Ba) thermoelectric cobaltites [3-6] gave rise to enormous interest of research groups all over the world. The cobaltite materials are advantageous, exhibiting many attractive characteristics, such as high chemical and thermal robustness, inexpensiveness, and environmentally friendly application in the air. Nevertheless, due to their relatively low performance when compared with the conventional intermetallic thermoelectric materials, the practical use of cobaltites still remains a problem [7]. Adjusting carrier concentration and introducing phonon scattering centers via element substitution (doping) and nano-additive dispersion are promising strategies to enhance the functional properties of thermoelectric materials [8]. Over the past decade, graphene/ceramic nanocomposites have stimulated worldwide scientific and technological interest, because graphene can dramatically alter the electrical and thermal transport properties and broaden applications of ceramic materials, including energy conversion technology [9–10]. Since 2015, research on oxide thermoelectric families, chalcogenides, and skutterudites has confirmed that the presence of graphene nano-inclusions could result in increased electrical conductivity and/or decreased lattice thermal conductivity (because of the stronger interfacial phonon scattering at point defects and grain boundaries) [11-13]. As a result, ZT of nanocomposites will be markedly enhanced. Our preliminary, albeit encouraging, results showed that adding 0.70 wt. % graphene enhanced the power factor in graphene/$Bi_2Sr_2Co_{1.8}O_y$ nanocomposite by about 40 % compared to pristine compound [14]. In this work, the dual impact of $Na_2B_4O_7$ doping and graphene dispersion on the phase formation, microstructure, electrical and thermal transport properties of $Bi_2Sr_2Co_2O_y$ system was studied. The results of the transport measurements were used to determine the PF and ZT values.

MATERIALS AND METHODS

Reference and $Na_2B_4O_7$-doped graphene/$Bi_2Sr_2Co_2O_y$ nanocomposites with 0.8 wt. % graphene as additive were prepared by solid-state reaction method from reagent-grade powders of bismuth oxide (Bi_2O_3), strontium carbonate ($SrCO_3$), cobalt (II, III) oxide (Co_3O_4), borax ($Na_2B_4O_7$), and graphene nanopowder (www.graphene-supermarket.com, purity: 99.2 %, average flake thickness: 12 nm (30–50 monolayers), average particle (lateral) size: ~ 4.5 μm). Precursor powders of Bi_2O_3, $SrCO_3$, Co_3O_4, and $Na_2B_4O_7$ were weighed according to the compositions: $Bi_2Sr_{2-x}[Na_2B_4O_7]_{x/2}Co_2O_y$ (x = 0, 0.02, 0.05, 0.08, 0.12) and $Bi_{2-x}[Na_2B_4O_7]_{x/2}Sr_2Co_2O_y$ (x = 0.05). The mixtures of these powders were homogenized in a planetary ball mill "Fritsch Pulverisette 7 Premium line" for 1 h at a rotating speed of 150 rpm. After homogenization, the powders were calcined at 1053÷1078 K for 22 h with intermediate grindings in an agate mortar. Calcined powders were mixed with 0.8 wt. % of graphene, homogenized in a planetary ball mill, then pressed into pellets at a hydrostatic pressure of 220 MPa. Finally, the pellets were sintered at 1083 K in air for 20 h, then cooled to room temperature in the furnace. The phase formation and microstructure of the prepared materials were examined using X-ray

diffraction (XRD, Dron–3M diffractometer, CuKα–radiation) and scanning electron microscopy (SEM, VEGA TS5130MM) techniques. The Seebeck coefficient and resistivity as a function of temperature were measured simultaneously in the range from 300 to 923 K using a homemade setup fitted with a KEITHLEY DMM6500 multimeter. Electrical transport measurements were performed on bar-shaped samples with dimensions of approximately 13×7×2 mm^3. Thermal conductivity was measured between 300 and 573 K using the "Hot Disk TPS 500 thermal constants analyser" coupled with a TPS temperature platform. Finally, the *PF* and *ZT* values were calculated to assess the thermoelectric performance of the prepared materials.

RESULTS

Fig. 1 illustrates the XRD patterns of the prepared samples.

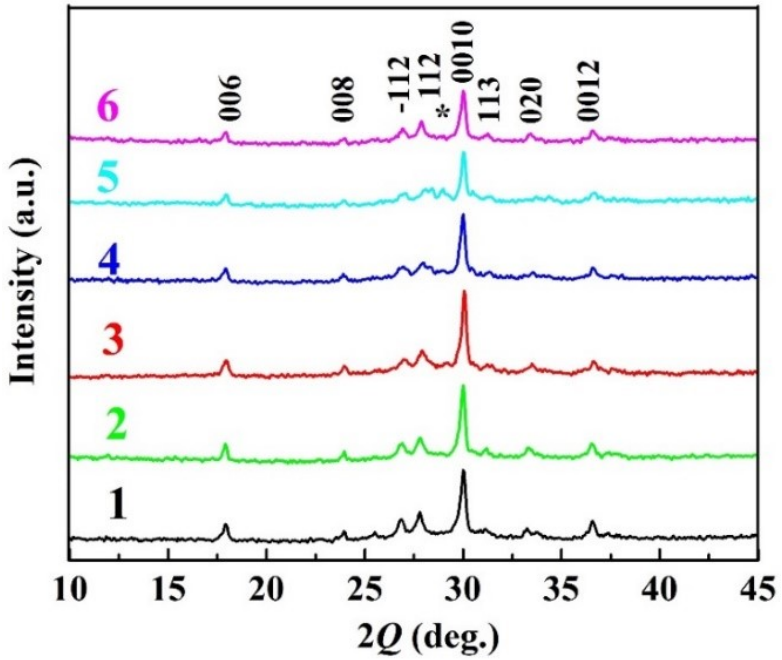


Fig. 1. XRD patterns of reference (1), $Bi_2Sr_{2-x}[Na_2B_4O_7]_{x/2}Co_2O_y$ + 0.8 wt. % graphene: (2) – x = 0.02, (3) – x = 0.05, (4) – x = 0.08, (5) – x = 0.12, and $Bi_{2-x}[Na_2B_4O_7]_{x/2}Sr_2Co_2O_y$ + 0.8 wt. % graphene: (6) – x = 0.05. * denotes a secondary phase.

https://doi.org/10.5593/sgem2024/4.1/s17.28

SEM images of the surface morphology of samples are presented in Fig. 2.

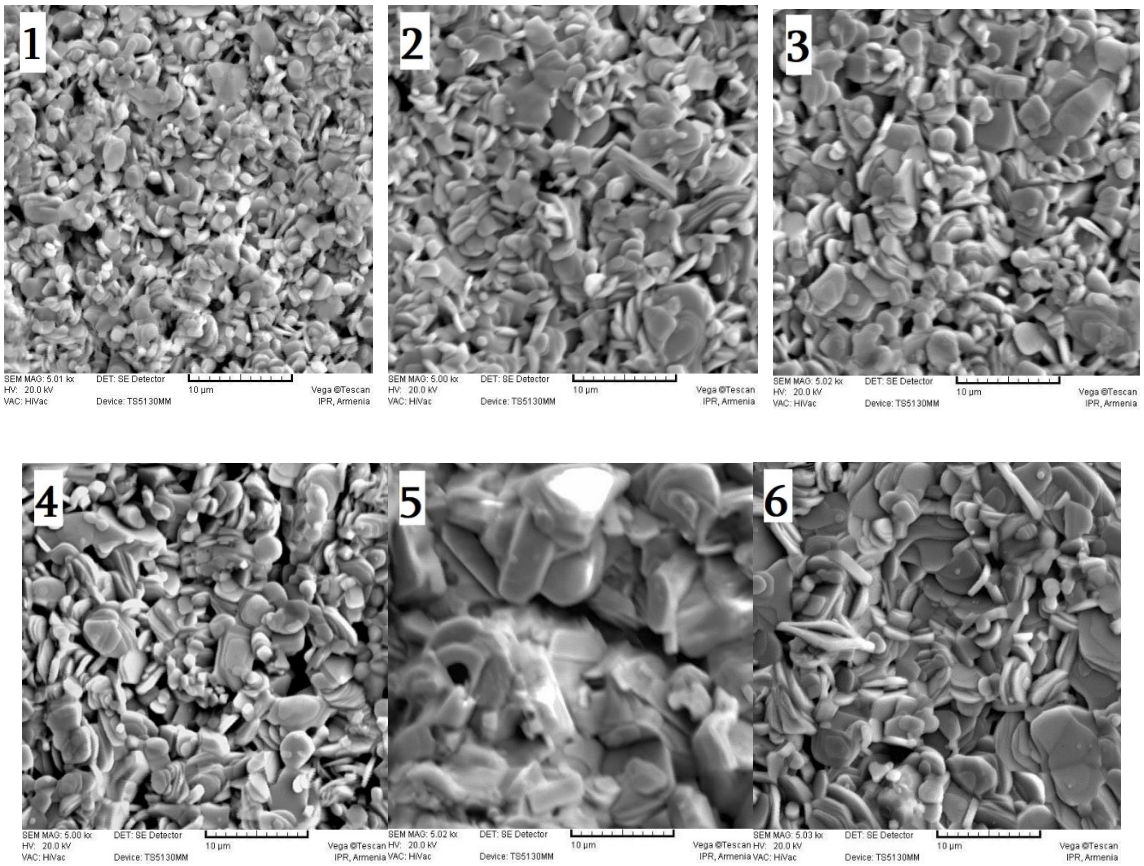


Fig. 2. Surface SEM micrographs of reference (1), $Bi_2Sr_{2-x}[Na_2B_4O_7]_{x/2}Co_2O_y$ + 0.8 wt. % graphene: (2) – x = 0.02, (3) – x = 0.05, (4) – x = 0.08, (5) – x = 0.12, and $Bi_{2-x}[Na_2B_4O_7]_{x/2}Sr_2Co_2O_y$ + 0.8 wt. % graphene: (6) – x = 0.05.

Temperature dependence of resistivity (a) and Seebeck coefficient (b) is shown in Fig. 3.

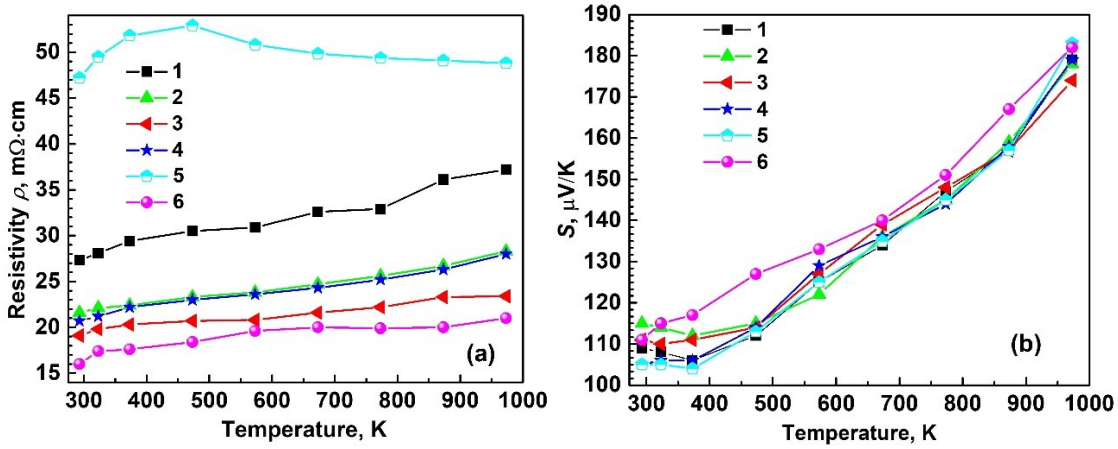


Fig. 3. Temperature dependence of resistivity (a) and Seebeck coefficient (b) of reference (1), $Bi_2Sr_{2-x}[Na_2B_4O_7]_{x/2}Co_2O_y$ + 0.8 wt. % graphene: (2) – x = 0.02, (3) – x = 0.05, (4) – x = 0.08, (5) – x = 0.12, and $Bi_{2-x}[Na_2B_4O_7]_{x/2}Sr_2Co_2O_y$ + 0.8 wt. % graphene: (6) – x = 0.05.

Fig. 4 displays the temperature dependence of thermal conductivity of prepared samples.

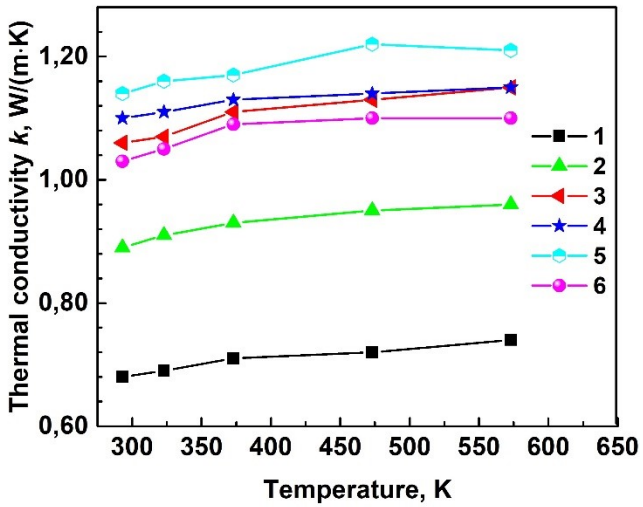


Fig. 4. Temperature dependence of thermal conductivity of reference (1), $Bi_2Sr_{2-x}[Na_2B_4O_7]_{x/2}Co_2O_y$ + 0.8 wt. % graphene: (2) – x = 0.02, (3) – x = 0.05, (4) – x = 0.08, (5) x = 0.12, and $Bi_{2-x}[Na_2B_4O_7]_{x/2}Sr_2Co_2O_y$ + 0.8 wt. % graphene: (6) – x = 0.05.

Based on the electrical and thermal transport measurement results, we have calculated the *PF* and *ZT* values, which are plotted in Fig. 5.

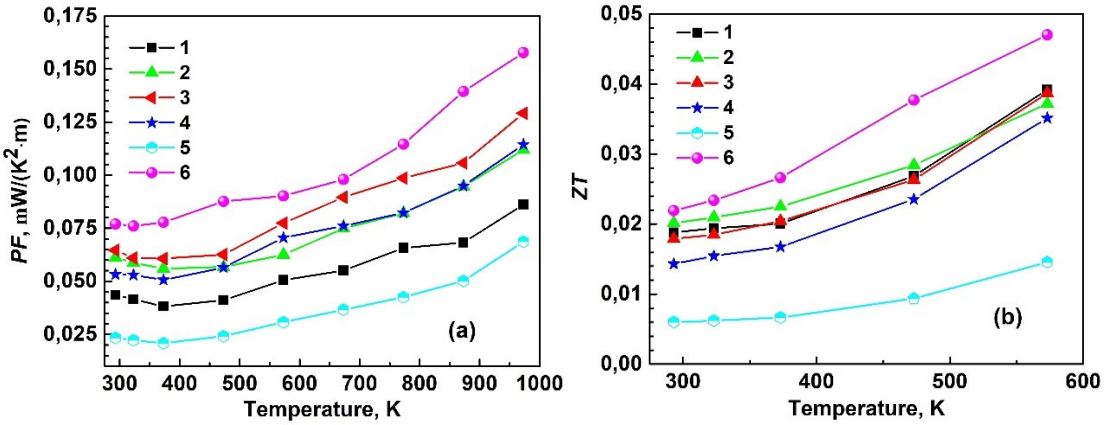


Fig. 5. Temperature dependence of power factor (a) and figure of merit (b) of reference (1), $Bi_2Sr_{2-x}[Na_2B_4O_7]_{x/2}Co_2O_y$ + 0.8 wt. % graphene: (2) – x = 0.02, (3) – x = 0.05, (4) – x = 0.08, (5) – x = 0.12, and $Bi_{2-x}[Na_2B_4O_7]_{x/2}Sr_2Co_2O_y$ + 0.8 wt. % graphene: (6) – x = 0.05.

DISCUSSION

The XRD observations are consistent with prior reports on $Bi_2Sr_2Co_2O_y$ monoclinic structure [7]. The low-intensity peak at 29 º for the largest amount of $Na_2B_4O_7$ dopant (x = 0.12) could be attributed to the cobalt-free secondary phase [7]. The Archimedes method was used to calculate density by taking four iterative measurements for each composite, with 6.81 g/cm^3 as the theoretical value [15]. Substituting $Na_2B_4O_7$ for SrO in the range of x = 0.02÷0.12 and adding graphene into the $Bi_2Sr_2Co_2O_y$ matrix results in a gradual increase in density from 74.30 % of the theoretical value for the reference sample

https://doi.org/10.5593/sgem2024/4.1/s17.28

to 86.64 % for the doped one with x = 0.12. The density of the sample with x = 0.12 rises due to larger grain sizes. However, substituting $Na_2B_4O_7$ for Bi_2O_3 with x = 0.05 results in a slightly lower apparent density of 82.10 %. Plate-like grains grow slightly in average size from 1.8 μm for the reference $Bi_2Sr_2Co_2O_y$ to 2.0÷2.2 μm for x = 0.02÷0.08. With further rise of doping level to x = 0.12, the average grain size increases significantly to 5.2 μm. Except for the sample with x = 0.12, the resistivity of prepared samples increases approximately linearly with temperature, like that in metallic conductors. A heavily $Na_2B_4O_7$-doped sample (x = 0.12) exhibited metallic dependence up to 473 K before changing to semiconducting at higher temperatures. The considerable increase in resistivity of this sample compared to other compositions could be caused by the formation of insulating layers at grain boundaries, which are unfavorable to electrical conductivity between grains [16]. $Na_2B_4O_7$-doped (x = 0.02÷0.08) graphene/$Bi_2Sr_2Co_2O_y$ composites possess much lower values of ρ compared to the reference sample. This experimental result could be explained by the partial substitution of Na^{1+} for Bi^{3+} and Sr^{2+} in the insulating rock-salt-type layer. Such aliovalent doping promotes the oxidation of Co^{3+} to Co^{4+} in the conducting layer, resulting in an increase in charge carrier concentration and, hence, enhancing electron transport [7]. Moreover, increasing the density and average grain size of doped samples (x = 0.02÷0.08) compared to the reference one also contributes to decreased resistivity. $Na_2B_4O_7$ serves as a sintering aid and provides densification of material due to the formation of the liquid phase [7]. The temperature dependence of the Seebeck coefficient reflects positive values for all samples over the whole measurement temperature range of 293 to 973 K, confirming *p*-type electrical conductivity. The over-doped sample, with highest level of substitution of $Na_2B_4O_7$ for SrO (x = 0.12), and the sample with partial substitution of $Na_2B_4O_7$ for Bi_2O_3 (x = 0.05) exhibit slightly higher S values of 182-183 μV/K among the studied ones. Doped composites possessed higher thermal conductivity than the reference sample. However, the enhanced electrical conductivity governs the values of power factor and figure of merit over the raised thermal conductivity. The maximum *PF* and *ZT* values achieved in $Na_2B_4O_7$-doped graphene/$Bi_2Sr_2Co_2O_y$ composites are higher by about 83 % and 20 %, respectively, compared with the reference $Bi_2Sr_2Co_2O_y$.

CONCLUSION

This work examined the combined impact of $Na_2B_4O_7$-doping and dispersion of graphene nano-inclusions on the phase composition, microstructure, and thermoelectric characteristics of $Bi_2Sr_2Co_2O_y$ ceramics. Graphene/$Bi_2Sr_2Co_2O_y$ composites with $Na_2B_4O_7$ partial substitution for Bi_2O_3 and SrO, embedded with 0.8 wt. % graphene nano-inclusions were synthesized by the solid-state reaction method. A suitable content of $Na_2B_4O_7$-dopant optimized both the carrier concentration and density of the final products. This resulted in a significant decrease in resistivity, while Seebeck coefficients were close to each other. Thermal conductivity is raised in $Na_2B_4O_7$-doped graphene/$Bi_2Sr_2Co_2O_y$ composites. Despite this, the impact of resistivity decreasing is stronger than that of thermal conductivity increasing, and it is a decisive determinant in the thermoelectric performance of prepared samples. Overall, the best resulting $Na_2B_4O_7$-doped graphene/$Bi_2Sr_2Co_2O_y$ composite showed 1.84 and 1.20-fold enhancement of power factor and figure of merit, respectively, over the reference $Bi_2Sr_2Co_2O_y$. Therefore, it was shown that the combination of $Na_2B_4O_7$-doping and graphene dispersion can effectively improve the thermoelectric performance of $Bi_2Sr_2Co_2O_y$.

ACKNOWLEDGEMENTS

This work was supported by the Shota Rustaveli National Science Foundation of Georgia (SRNSFG) [grant number AR-22-470, Borates-containing graphene/ceramic thermoelectric composites — a step toward commercialization].

The authors would like to thank Dr. Armen Kuzanyan and Dr. Georgi Badalyan from the Institute for Physical Research, Ashtarak, Armenia for the SEM measurements.

REFERENCES

[1] Koumoto K., Funahashi R., Guilmeau E., Miyazaki Y., Weidenkaff A., Wang Y., Chunlei Wan C., Thermoelectric ceramics for energy harvesting, J. Am. Ceram. Soc., vol. 96/ issue 1, pp 1–23, 2013. https://doi.org/10.1111/jace.12076.

[2] Sotelo A., Rasekh Sh., Torres M. A., Madre M. A., Diez J. C., Preparation of high performance $Bi_2Sr_2Co_{1.8}O_x$ thermoelectric materials from nanosized precursors, Advances in Applied Ceramics, vol. 116/issue 7, pp 383-391, 2017. https://doi.org/10.1080/17436753.2017.1339491.

[3] Terasaki I., Sasago Y., Uchinokura K., Large thermoelectric power in $NaCo_2O_4$ single crystals, Phys. Rev. B, vol. 56/issue 22, pp R12685–R12687, 1997. https://doi.org/10.1103/PhysRevB.56.R12685.

[4] Funahashi R, Matsubara I., Ikuta H., Takeuchi T., Mizutani U., Sodeoka S., An oxide single crystal with high thermoelectric performance in air, Jpn. J. Appl. Phys, vol. 39/issue11B, pp L1127–L1129, 2000. DOI 10.1143/JJAP.39.L1127.

[5] Masset C., Michel C., Maignan A., Hervieu M., Toulemonde O., Studer F., B. Raveau B., Hejtmanek J., Misfit-layered cobaltite with an anisotropic giant magnetoresistance: $Ca_3Co_4O_9$, Phys. Rev. B, vol. 62/issue 1, pp 166–175, 2000, https://doi.org/10.1103/PhysRevB.62.166.

[6] Funahashi R., Matsubara I., Sodeoka S., Thermoelectric Properties of $Bi_2Sr_2Co_2O_x$ polycrystalline materials, Appl. Phys. Lett, vol. 76/issue 17, pp. 2385–2387, 2000. https://doi.org/10.1063/1.126354.

[7] Karakaya G. Çetin., Özçelik B., Torres M. A., Madre M. A., Sotelo A., Effects of K substitution on thermoelectric and magnetic properties of $Bi_2Sr_2Co_2O_y$ ceramic, Journal of Materials Science: Materials in Electronics, vol. 28/issue 17, pp 12652–12659, 2017. https://doi.org/10.1007/s10854-017-7090-4.

[8] He Q., Yang D., Xia S., Song H., Ultra-low thermal conductivity and improved thermoelectric performance in La_2O_3-dispersed $Bi_2Sr_2Co_2O_y$ ceramics, Materials Science and Engineering: B, vol. 299, article # 116976, 2024. https://doi.org/10.1016/j.mseb.2023.116976.

[9] Porwal H., Grasso S., Reece M. J., Review of graphene–ceramic matrix composites, Advances in Applied Ceramics, vol. 112/issue 8, pp 443-454, 2013. DOI: 10.1179/174367613X13764308970581.

[10] Huang Y., Wan C., Controllable fabrication and multifunctional applications of graphene/ceramic composites, J. Adv. Ceram., vol. 9/issue 3, pp 271–291, 2020. DOI: https://doi.org/10.1007/s40145-020-0376-7.

https://doi.org/10.5593/sgem2024/4.1/s17.28

[11] Okhay O., Tkach A., Impact of Graphene or Reduced Graphene Oxide on Performance of Thermoelectric Composites. C – Journal of Carbon Research, vol. 7, article # 37, 2021. DOI: https://doi.org/10.3390/c7020037.

[12] Daichakomphu N., Sakdanuphab R., Harnwunggmoung A., Pinitsoontorn S., Sakulkalavek A., Achieving thermoelectric improvement through the addition of a small amount of graphene to $CuAlO_2$ synthesized by solid-state reaction, Journal of Alloys and Compounds, vol. 753, pp 630-635, 2018. DOI: 10.1016/j.jallcom.2018.04.276.

[13] Koçyiğit S., Aytimur A., Uslu I., Temperature dependent Seebeck coefficient and thermal conductivity properties of graphene undoped and doped Ca-Pr-Co oxide thermoelectric nanocomposites, J. Vac. Sci. Technol. A vol. 37/issue 6, 061201, 2019. https://doi.org/10.1116/1.5121253.

[14] Margiani N., Zhghamadze V., Mumladze G., Kvartskhava I., Adamia Z., Klyndyuk A., Kuzanyan A., Impact of Graphene Addition on the Microstructure and Thermoelectric Properties of $Bi_2Sr_2Co_{1.8}O_y$ Ceramics, Bulletin of the Georgian National Academy of Sciences, vol. 16/issue 1, pp 17-24. 2022, DOI: http://science.org.ge/bnas/t16-n1/03_Margiani_Physics.pdf.

[15] Rubešová K., Hlásek T., Jakeš V., Huber Š., Hejtmánek J., Sedmidubský D., Effect of a powder compaction process on the thermoelectric properties of $Bi_2Sr_2Co_{1.8}O_x$ ceramics, Journal of the European Ceramic Society, vol. 35/issue 2, pp 525-531, 2015. DOI: 10.1016/j.jeurceramsoc.2014.08.037.

[16] Tanaka Y., Fujii T., Nakanishi M., Kusano Y., Hashimoto H., Ikeda Y., Takada J., Systematic study on synthesis and structural, electrical transport and magnetic properties of Pb-substituted Bi–Ca–Co–O misfit-layer cobaltites, Solid State Communications, vol. 141/issue 3, pp 122-126, 2007 https://doi.org/10.1016/j.ssc.2006.10.015.

USING A HEAT PUMP TO COVER PEAK HEAT LOADS IN HARSH CLIMATES

Prof. Dr. Sergey Shcheklein[1]

Prof. Dr. Vladimir. Velkin[1]

Assoc. Prof. PhD Andrey Matveev[1]

Assoc. Prof. PhD Igor Koshkin[2]

Sergey Pushkarev[2]

[1] Ural Federal University named after the first President of Russia B.N. Yeltsin, **Russia**

[2] NJSC "Kostanay Regional University named after A. Baitursynov", **Kazakhstan**

ABSTRACT

Most modern heat pump installations can only generate a maximum temperature of 50-55°C. This temperature potential is not sufficient to integrate them with existing convective and radiator-based space heating systems in severe climates.

This paper discusses the findings from an experimental study evaluating the efficiency of a fan coil-based air heating system.

Using a peaking boiler fueled by natural gas from the main supply has been shown to be the most cost-effective method for generating thermal energy with peak-load heating systems.

For consumers without access to the main gas supply, a heat pump system that heats the room air by extracting heat from the ground through a well system is significantly more efficient than any other heating system options available.

One significant drawback of this system is its substantial upfront capital expenditures, which are significantly higher – more than 5 times – than those of all other viable alternatives.

These technical solutions become viable (with a payback period of less than 10 years) when energy prices rise significantly, by more than an order of magnitude.

Keywords: climate, heat pump, fan coil, electrical energy consumption.

INTRODUCTION

Most regions of the Russian Federation have harsh climatic conditions as indicated by the number of heating degree days (HDD), an integral measure of the total heating requirements based on temperature variations inside and outside a building over a specific period. Figure 1 compares the values of this indicator for a number of regions in Russia and other countries [1, 2].

This comparison can help quantify the energy consumption of the people living in a given territory. For example, energy consumption for Germany is 2-2.5 times less than that of most of the Russian territory.

https://doi.org/10.5593/sgem2024/4.1/s17.29

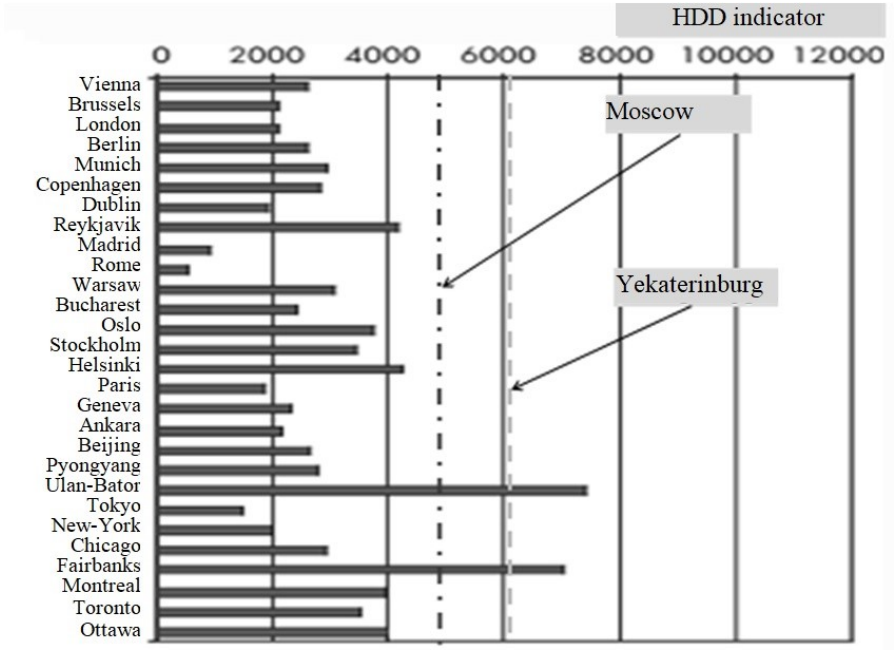


Figure 1. Heating degree days (HDD) for various regions in Russia and globally during the heating season.

However, even in Russia, due to seasonal and daily temperature fluctuations heating systems can lower their base power by utilizing peaking heat sources to supplement thermal energy during colder periods.

In urban environments, this problem is solved by using backup (peaking) heat sources at thermal power stations and boiler houses. Special redundancy conditions arise in buildings equipped with autonomous heat supply systems in suburban and rural areas. In most cases, supplemental heat supply during peak demand periods is provided by expensive electric heating systems.

It is well-established that the efficiency of using electrical energy for heat supply can be significantly enhanced by using, for example, ground source heat pumps [3-5].

The temperature at depth relative to the surface temperature does not vary in response to solar energy. In regions with significant temperature fluctuations, such as Russia and Kazakhstan, the temperature at depths greater than 20 meters remains constant at an average of 7-8 °C. During the summer, when the air temperature rises to an average of 20-25 °C, the soil temperature at a depth of 80 meters remains almost constant at 7 °C. This stability makes the ground a reliable source of energy that can be utilized year-round (for both heating and cooling systems).

This paper presents an experimental study on the feasibility and efficiency of a peak-load heat supply system utilizing a heat pump with a heat collector probe placed deep underground. The study is based on data collected on the environmental and soil temperature characteristics.

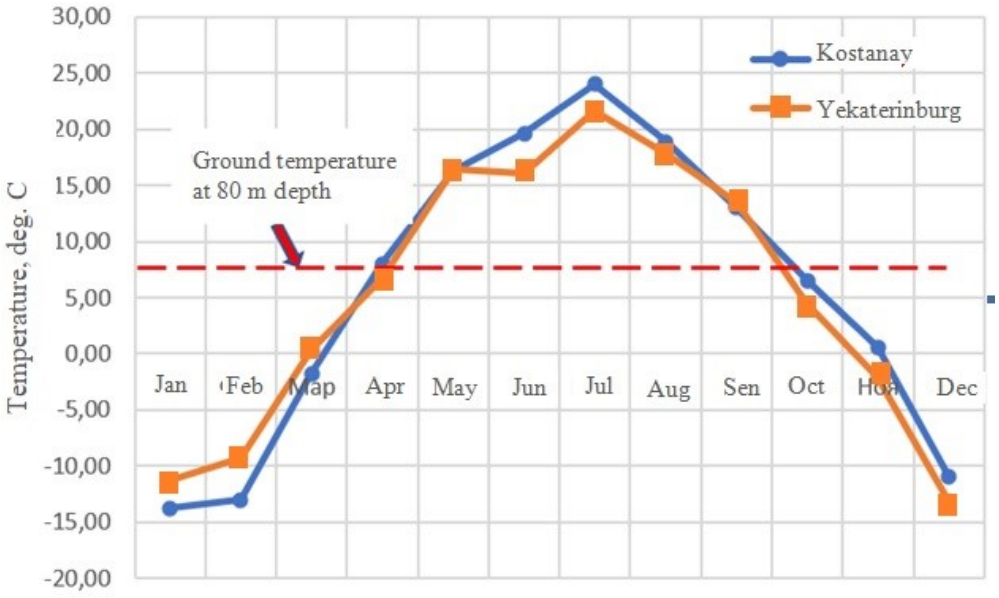


Figure 2. Annual variations in air and ground temperatures in Kostanay (Kazakhstan) and Yekaterinburg (Russia).

However, modern heat pump installations, which actually consume significantly less electrical energy to generate heat, have limitations in terms of heat potential. Most modern heat pump installations can only generate a maximum temperature of 50-55°C. This temperature potential may not be sufficient to integrate them with existing convective and radiator-based space heating systems in severe climates.

There are two primary approaches for integrating heat pumps into peaking space heating systems:
- heat supply through a floor heating system with liquid coolant;
- heat supply through an air heating system.

The purpose of this study is to experimentally evaluate the energy efficiency of a peak-load air heating system that integrates a heat pump and a fan coil-based system in regions with harsh climatic conditions.

EXPERIMENTAL SETUP LAYOUT AND EXPERIMENTAL PROCEDURE

This paper discusses the findings from an experimental study evaluating the efficiency of a fan coil-based air heating system. Figures 3 and 4 depict the system's general appearance and schematic diagram.

https://doi.org/10.5593/sgem2024/4.1/s17.29



Figure 3. General appearance of the experimental setup.

1- Heat pump VaillantVWS-63/2; 2-Storage tank Drazice OKS-250 NTTR; 3- Fan coil pump Grundfos.

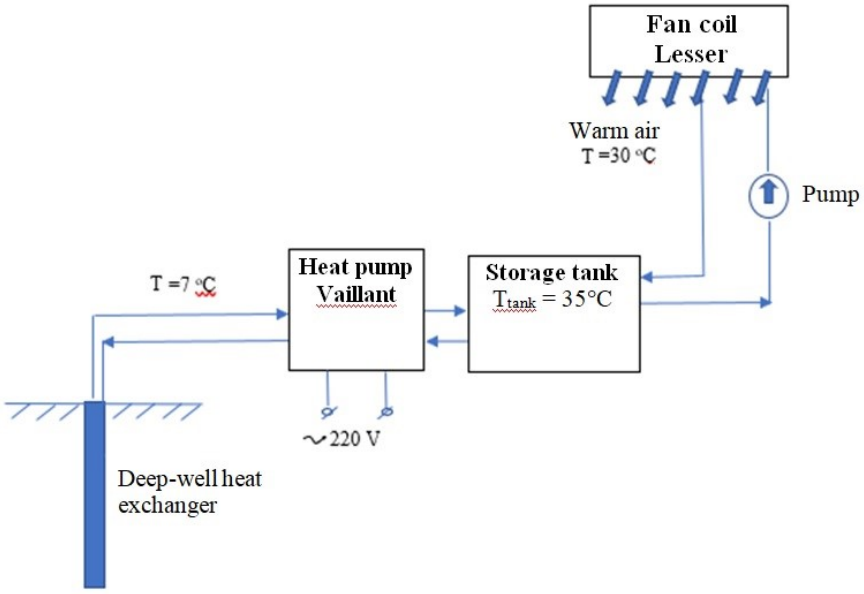


Figure 4. Schematic diagram of a heat supply system using ground heat, heat pump, and a fan coil.

In most populated areas of Russia, the soil at depths exceeding 20 meters maintains a constant year-round temperature between 6-8 °C. This study employed a deep-well heat exchanger situated at a depth of 80 meters, ensuring a consistent temperature of at least 7°C at the well outlet throughout the year. The heat exchanger's surface area was sufficient to extract at least 5 kW of thermal energy from the ground.

The energy carrier entered the heat pump intake, where the compression thermodynamic cycle produced heat of higher temperature potential (up to 55 °C) [6]. The heat was transferred to a storage tank containing water where its heating temperature was limited to a maximum of 35°C.

Heat was extracted from the storage tank using an intermediate coolant circulated by a pump, which was then fed into the fan coil heat exchanger. From there, the heated air generated in the fan coil was then distributed to the room by a fan [7].

A control system regulated the periodic activation of all circuit elements based on the air temperature setting at the outlet of their corresponding fan coil (from 20 to 30 °C). In this manner, the circuit elements were not in continuous operation but were instead activated by the signal of the set air temperature, delivering 3.8 kW of thermal energy to the room.

The built-in information module of the Vaillant VWS-63/2 heat pump was used to record and store data on two key temperatures: the temperature of the coolant flowing from the bore-hole heat collector to the heat pump's inlet, and that of the intermediate coolant entering the heat storage tank. The system's performance was monitored using an Arduino-based controller, which recorded the following parameters: temperatures and flow rates of the heat transfer circuit to the fan coil heat exchanger; temperatures and flow rates of the air being heated in the fan coil; and electrical power consumption of each system component: the drives of the heat pump, intermediate circuit pump, fan coil air fan, as well as monitoring and control system.

FINDINGS OF THE EXPERIMENTAL STUDY

Experimental data in Figure 5 illustrates the electrical energy consumption of the heat pump compressor, fan coil pumps and fan, and control system throughout the daily cycle

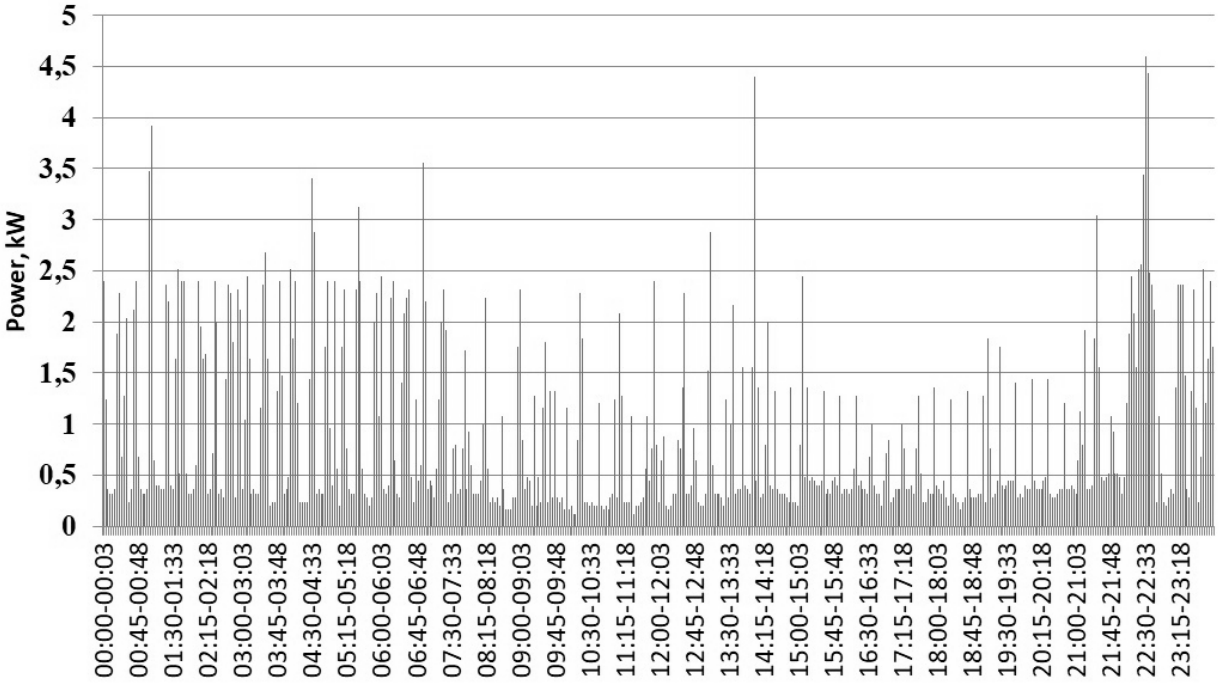


Figure 5. Electrical energy consumption of the heat pump compressor, fan coil pumps and fan, and control system throughout the daily cycle.

Figure 6 shows distribution diagram of consumed electrical power throughout the daily cycle.

https://doi.org/10.5593/sgem2024/4.1/s17.29

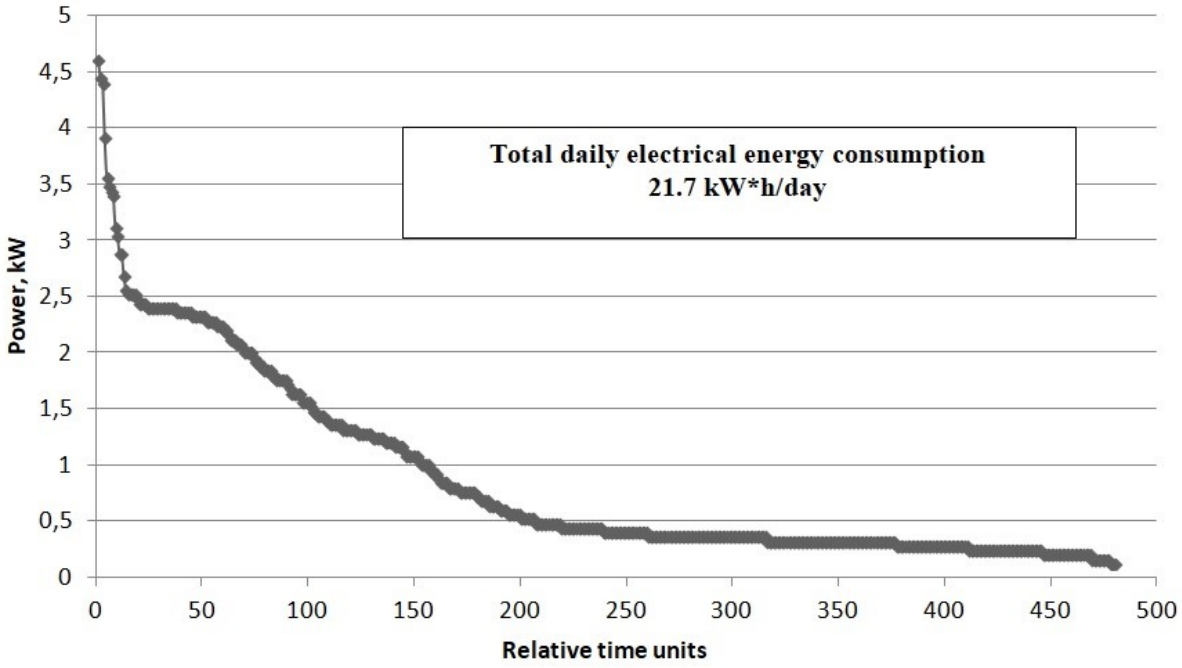


Figure 6. Distribution diagram of consumed electrical power throughout the daily cycle.

The total daily electrical energy consumption of 21.7 kWh/day is obtained by integrating the area under the curve in Figure 5.

When utilized directly, the electrical energy consumption required to generate an equivalent amount of heat (as with the use of electric convectors for direct air heating) would be

$$E_{daily} = P*\tau = 3.8*24 = 91.2 \text{ kW*h}.$$

Where: P is the electric power of the convector, kW,

τ is the period of operation during the day cycle, h.

The thermal utilization factor of electrical energy when using a heat pump in this scenario will be:

$$TUF = E_{daily} / E_{hp} = 91.2/21.7 = 4.2.$$

Where: E_{daily} is electrical energy consumption of an electric convector, kWh,

E_{hp} - electrical energy consumption of a system with a heat pump, kWh.

COMPARISON OF THE ECONOMICS OF PEAK-LOAD HEATING SYSTEMS

The table 1 presents a comparison of economic indicators across different peaking space heating systems operating in the Russian Federation's climate [8].

Table 1. Daily cost of generating the same amount of thermal energy (3.8 kW).

System type	Utility type	Unit	Tariff	Amount, RUR
System with a heat pump	electricity	RUR/kWh	3.61	78
Electric convectors for direct air heating	electricity	RUR/kWh	3.61	329
Peaking liquid-fuel boiler	diesel	RUR/L	60	390
Peaking mains gas boiler	gas	RUR/cu.m.	5.76	48
Peaking boiler fueled by liquefied natural gas (LNG)	liquefied natural gas	RUR/L	34	224

CONCLUSION

1. For regions with sharply continental climates, common in much of Russian Federation and the Republic of Kazakhstan, heat pump systems are particularly well-suited for heating room air using a borehole system that extracts heat from the ground.

2. Using a peaking boiler fueled by natural gas from the main supply is the most cost-effective method for generating thermal energy with peak-load heating systems.

3. For consumers without access to the main gas supply, a heat pump system that heats the room air by extracting heat from the ground through a well system is significantly more efficient than any other heating system options available.

4. One significant drawback of this system is its substantial upfront capital expenditures, which are significantly higher – more than five times – than those of all other viable alternatives.

5. The results obtained show possible directions for further improvement of the energy and economic efficiency of the use of heat pump equipment for the conditions of the Russian Federation and the Republic of Kazakhstan: identification of thermally active areas of the territory (deposits of warm soil zones), reducing the cost of manufacturing and delivery of heat pump equipment through the development of national production with a corresponding reduction in manufacturing costs, tax, transport and customs costs.

ACKNOWLEDGEMENTS

This work was supported by the Ural Federal University (UrFU, Yekaterinburg, Russia) within the framework of the “Priority-2030” program (grant number FEUZ-2022-0031).

https://doi.org/10.5593/sgem2024/4.1/s17.29

REFERENCES

[1] Construction norms and rules of the Russian Federation. Building clim atology. Reference books for SNiP 23-01-99, Russia, 2006, ISBN 5-88111-201-6.

[2] Khromov S.P., Petrosyants M.A., Meteorology and climatology Russia, pp 582, 2006.

[3] Antipov Yu.A., Shkarin K.V., Shatalova I.I., Egorov S.A., Matyakubova N.U. Influence of temperatures of a low-potential heat source and consumer on the efficiency of a heat pump, Bulletin of the Peoples' Friendship University of Russia, Russia, series: Engineering Research, vol. 20, № 1, pp 14-19, 2019 .

[4] Kurtz-Orecka K., Tuchowski W. Combined heat pumpdistrict heating network energy source, E3S Web of Conferences, Poland, 2018.

[5] Wołoszyn J., Gołaś A. Coefficient of Performance Stabilisation in Ground Source Heat Pump Systems, Journal of Sustainable Development of Energy, Water and Environment Systems, Poland, № 5 (4), pp. 645—656, 2017.

[6] Vaillantgeotherm Installation Guide, web source: www.manualslib.com/manual/1250891/Vaillant-Geotherm

[7] Wall-mounted fan coil units Lessar. Installation and operation instructions, web source: www.c-o-k.ru/library/instructions/brands

[8] Resolution No. 248-PK of the Regional Energy Commission of the Sverdlovsk Region dated December 27, 2021 “On the establishment of electricity tariffs for the population and equivalent categories of consumers in the Sverdlovsk Region for 2022”, Russia, 2021.

SECTION RECYCLING

AIR CONVERSION OF PYROLYSIS PRODUCTS OF HYDROCARBON RAW MATERIALS INTO SYNTHESIS GAS (H_2+CO) FOR THE PRODUCTION OF ELECTRICAL ENERGY USING SOLID OXIDE FUEL CELLS

Prof. Dr. Sergey Shcheklein[1]

Prof. Dr. Alexey Dubinin[1]

Assoc. Prof. PhD Andrey Matveev[1,2]

Vyacheslav Filippenkov[2]

[1]Ural Federal University named after the First President of Russia B.N. Yeltsin, **Russia**

[2]NPP Dinamika LLC, **Russia**

ABSTRACT

The paper presents a medium-temperature modular pyrolysis plant generating electricity from syngas (SG) produced by air conversion of pyrolysis liquid and fed into the electrochemical generator (ECG) battery. Electric output of the plant and district water heater is 100 kW and 126 kW, respectively. The main power characteristics of the plant are determined by physicochemical modeling and energy budgeting methods. Specific consumption of pyrolysis liquid to produce electricity and heat is shown as 108 g/kW·h (169 gsf/(kW·h)) and 30 kg/GJ (197 kgsf/Gcal), respectively. Fuel utilization factor is 46.4%.

Specific consumption of natural and standard fuels with this plant is slightly higher than that of the power plants running on hydrocarbon natural fuels yet, at the same time, far below that of standalone diesel-electric plants. The paper provides recommendations on how to use pyrolysis liquid to generate electrical and thermal energy using a SOFC-based high-temperature fuel cell.

Keywords: pyrolysis, electrochemical generator, air, COP, power.

INTRODUCTION

The process of hydrocarbon feedstock pyrolysis normally produces three streams of energy carriers, namely, pyrolysis gas, pyrolysis liquid, and solid carbon residue, all in different states of aggregation. The yield of various fractions and their chemical composition depend on the type of feedstock and the thermodynamic parameters of the pyrolysis process, which may vary widely among different types of feed stocks.

The use of catalysts [1 - 4] and microwave or plasma-chemical uniform heating systems to heat the entire volume of feedstock [5 - 11] may significantly change the parameters and efficiency of pyrolysis. Different pyrolysis technologies can provide a preferential yield of either gas or liquid product [2].

https://doi.org/10.5593/sgem2024/4.1/s18.31

Pyrolysis of wood at 400 °C is described in [3]. The yield of pyrolysis products is as follows: carbon 37%, gas 17%, and liquids 46% of dry wood weight. Most common plastics decompose at 350°C [4]. At 500 °C, they decompose with no solid residue. Plastics are melted until decomposed. Rubber products start to decompose at 280 °C. The yield of waste pyrolysis at 400 °C is 12% gas, 61% liquid, and 27% pyrolysis residue, as demonstrated in [5]. The heat value of pyrolysis products is 31 MJ per kg of pyrolysis products. A plant producing methane from car tire pyrolysis is described in [6]. The heat value of syngas is 9,385 kJ/m³. The plant has the COP of 55%. In [7], fractured and dried household waste is subjected to pyrolysis at 450 °C for one hour. Pyrolysis gas is fed into a high-temperature furnace. Ash particles are removed in the form of liquid slag. Combustion products are cooled to 600 °C and then fed into a waste heat boiler. Water vapor at 4 MPa and 400 °C enters the steam turbine. Turbine generator produces 3 MW of electricity. Exhaust gases are removed at 170°C. The ash is returned to the furnace, where it is melted and then removed in liquid form. The plant can process 70 thousand MT of household waste per year. Diagrams of an SMW combustion process with liquid slag removal capable of producing electricity and supplying heat to a residential area are discussed in [8]; new SMW recycling technologies, including catalytic and plasma-chemical methods, are described in [9, 10].

Various hydrogen production methods for use in electrochemical generators are studied in [15, 16]. Calculated analysis of power and heat generation in solid oxide fuel electric generators fueled by products of steam gasification of coal mined from the Borodinsky deposit are described in [17]. The prospects of producing heat and electricity by SMW combustion are discussed in [11 - 18]. Applicability of a Rankine cycle-based steam turbine for using both carbon and liquid pyrolysis fractions as fuel (in the form of paste-like fuel composition) is discussed in [13].

This paper examines a more efficient utilization of liquid pyrolysis products by their conversion into syngas for direct production of electrical energy in an electrochemical generator [12 - 14]. Schematic diagram of the pyrolysis method used to process hydrocarbon-containing waste is shown in Fig. 1.

Structurally, the modular plant is manufactured in the form of an inclined rotary drum equipped with a feedstock charger and separate extraction points for pyrolysis gas, pyrolysis liquid, and solid carbon residue. General view of the plant is shown in Fig. 2.

Pyrolysis gas used to maintain the required pyrolysis temperature ensures high energy efficiency of the plant, while the loading and unloading devices and drum rotation are powered by utilizing 10% of the energy produced by SOFC.

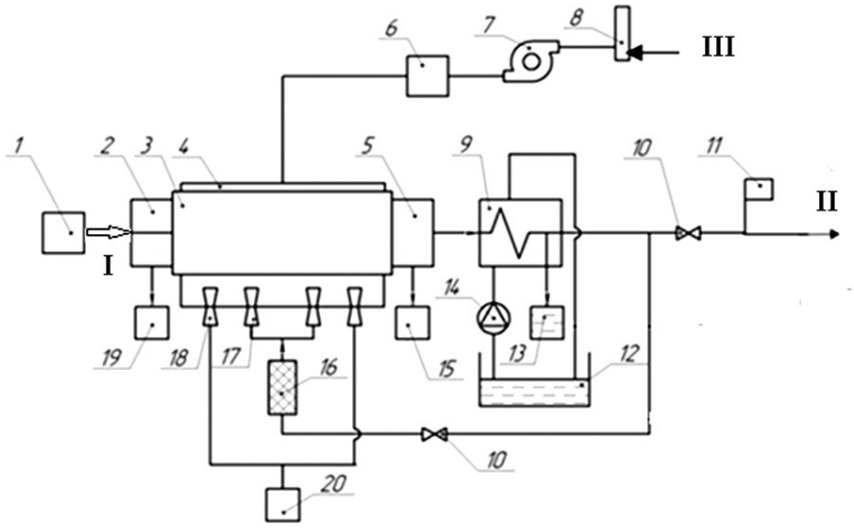


Figure 1. Schematic diagram of a pyrolysis plant for hydrocarbon-containing waste management.
1 – feedstock to be processed, 2 – feedstock loading and extraction of metal, glass, rocks, etc.; 3 – rotating reactor drum; 4 – reactor drum housing; 5 – activated carbon extractor; 6 – wet scrubber; 7 – smoke exhaust; 8 – stack flue; 9 – condensation unit; 10 – shut-off valves; 11 – safety valve; 12 – cooling tank; 13 –pyrolysis liquid storage reservoir, 14 – circulation pump; 15 – activated carbon collector; 16 – gas filter; 17 – gas burner; 18 –fuel oil burner; 19 – collector for metal, glass, rocks, etc.; 20 –fuel storage reservoir.
I –feedstock charging; II – pyrolysis liquid entering evaporator; III - complete oxidation products exiting waste heat boiler.



Figure 2. Pyrolysis plant for hydrocarbon-containing waste management.

https://doi.org/10.5593/sgem2024/4.1/s18.31

MODELING PHYSICAL AND CHEMICAL PROCESSES IN A CIRCUIT DIAGRAM BASED ON A CATALYTIC BURNER FOR AIR CONVERSION OF PYROLYSIS LIQUID AND AN ELECTROCHEMICAL GENERATOR

The circuit diagram of the process whereby pyrolysis liquid is converted into syngas through air conversion in a catalytic burner to power the electrochemical generator is shown in Fig. 3. Pyrolysis liquid enters the waste heat boiler (WHB) where itis evaporated and fed into the catalytic burner in vapor form. The air heated in the waste heat boiler is also supplied into the burner. At the air flow rateα of 0.379, liquid is converted into syngas. After that, syngas is cooled to 800°C with the air supplied to the cathodic channel, and enters the anodic channel. In the anode, hydrogen is partially oxidized by oxygen from the air fed into the cathodic channel. Products from the anodic channel and oxygen-depleted air from the cathodic channel enter the waste heat boiler. In the boiler, hydrogen is oxidized fully and carbon monoxide is oxidized. The heat from oxidation is utilized to heat the primary air and evaporate the pyrolysis liquid. After that, combustion products from the waste heat boiler enter district water heater to heat the delivery water used for heating, ventilation, and hot water supply to heat consumers. After the district water heater, the products of complete oxidation (combustion) are discharged into the stack flue at 120 °C.

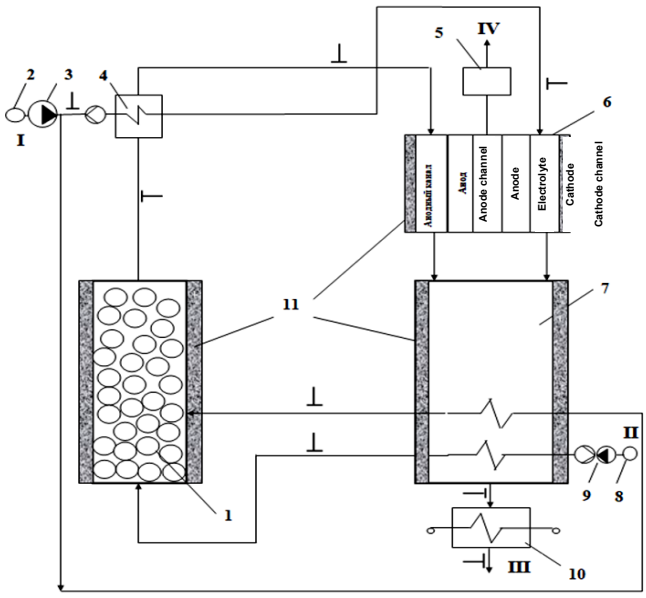


Fig.3. Circuit diagram of a combined heat and power plant based on a catalytic burner and a stack of solid oxide fuel cells (SOFC).
1- catalytic burner; 2- air duct; 3-air blower; 4- recuperator unit; 5- inverter with an electrical load; 6- SOFC stack; 7- waste heat boiler; 8- fuel collector; 9- fuel pump; 10- district water heater; 11- thermal insulation.
I - air inlet; II - pyrolysis liquid inlet; III – full oxidation products outlet; IV – electrical energy output.

The core of syngas production is the catalytic burner 1 filled with coarse aluminum-nickel catalyst KSN-2. Vaporized pyrolysis liquid from the waste heat boiler 7 and oxidizer (air) heated in the waste heat boiler are fed into the burner at a flow rate of less than 1. After exiting the burner, syngas passes through the cooler 4 and then goes into

the anodic channel of the SOFC stack. A part of the air from the air blower 3 that passes through cooler 4 heats up and enters the cathodic channel of the SOFC stack. Electricity delivered to the consumer is passed through inverter 5.

Products from the anodic channel containing carbon monoxide, insufficiently oxidized hydrogen and oxygen-depleted air from the cathodic channel are fed into the waste heat boiler 7 where CO and residual H_2 are completely oxidized.

The heat released during oxidation is utilized for pyrolysis liquid evaporation and heating of air. The output not utilized for BOP needs in the waste heat boiler is supplied to the district water heater 11 where it heats up the water for the hot water supply system.

MODELING PROCESSES IN A CATALYTIC BURNER

The minimum air flow coefficient at which ash can no longer be thermodynamically formed during air conversion of the pyrolysis liquid $–C_nH_m$ (where n = 3, m = 4. l = 0) [19].

Molecular mass μ = 40 kg/mol

$$\alpha_c = \frac{n - l}{2n + 0.5m - l}, \quad (1)$$

where l = 0, the number of oxygen atoms in a molecule of liquid.

Air flow coefficient $\alpha > \alpha_c = 0.375$ ($\alpha = 0.379$). Syngas is produced in the reaction volume of the catalytic burner at air flow coefficient of 0.379 according to the stoichiometric equation for incomplete combustion of a liquid:

$$C_3H_4 + 1.5(O_2 + 3.76N_2) = 3CO + 2H_2 + 5.64N_2. \quad (2)$$

The resulting syngas has the following composition: CO – 28.1; H_2 – 18.8; N_2 – 53.1 (%vol).

Complete combustion of the pyrolysis liquid at air flow coefficient α = 1 can be described by the stoichiometric equation:

$$C_3H_4 + 4(O_2 + 3.76N_2) = 3CO_2 + 2H_2O + 15.04N_2. \quad (3)$$

Therefore, the air flow coefficient in equation (2):

$$\alpha = \frac{1,5}{4} = 0.379.$$

Reaction heat (2) [20,21] of syngas formation:

$$\Delta H = \frac{3\Delta H_{CO} - \Delta H_{C_3H_4}}{\mu_{C_3H_4}} = \frac{3 \cdot (-110.59) - 185.7}{40 \cdot 10^{-3}} = -12,930$$

– kJ/kg liquid; per 1 kg of syngas

$$\Delta H^* = \frac{-12,930 \cdot 40}{245.9} = -2,103 \text{ kJ/kg},$$

where 245.9 is the syngas mass in equation (2). The reaction is exothermic.

https://doi.org/10.5593/sgem2024/4.1/s18.31

Heat of reaction (3) per 1 kg of liquid:

$$Q_{\text{н}}^{\text{p}} = \frac{3\Delta H_{\text{CO}_2} + 2\Delta H_{\text{H}_2\text{O}} - \Delta H_{\text{C}_3\text{H}_4}}{\mu} = \frac{3 \cdot (-393.8) + 2 \cdot (-242.02) - 185.7}{40 \cdot 10^{-3}} = \\ = 46 \cdot 10^3 \frac{\text{kJ}}{\text{kg}},$$

where ΔH_{i} is the heat of substance formation [21], kJ/kmol.

The heat of syngas combustion can be defined by equation:

$$3\text{CO} + 2\text{H}_2 + 5.64\text{N}_2 + 2.5(\text{O}_2 + 3.76\text{N}_2) = 3\text{CO}_2 + 2\text{H}_2\text{O} + 15.04\text{N}_2. \quad (4)$$

$$q_{ch} = \frac{3\Delta H_{\text{CO}_2} + 2\Delta H_{\text{H}_2\text{O}} - \Delta H_{\text{CO}}}{3\mu_{\text{CO}} + 2\mu_{\text{H}_2\text{O}} + 5.64\mu_{\text{N}_2}} = \frac{3 \cdot (-393.8) + 2 \cdot (-242.02) - 3 \cdot (-110.59)}{3 \cdot 28 + 2 \cdot 2 - 5.64 \cdot 28} = \\ = -5{,}420 \frac{\text{kJ}}{\text{kg of syngas}}.$$

By preliminary calculations, the required flow rate of syngas with the heat value of q_x = 5,420 kJ/kg for an electrochemical generator with the electric output of Q_{el} = 100 kW shall be:

$$B_{sg} = \frac{Q_{el}}{q_{ch} \cdot \eta^*}, \frac{\text{kg}}{\text{s}}, \quad (5)$$

where COP of the SOFC stack η^* = 0.285 (28.5%) is preliminarily set to the value specified in [22].

To produce B_{sg}, the flow of pyrolysis liquid to be fed into the burner shall be (from eq. (2))

$$G_{pl} = \frac{B_{sg} \cdot \mu_{\text{C}_3\text{H}_4}}{3\mu_{\text{CO}} + 2\mu_{\text{H}_2} + 5.64\mu_{\text{N}_2}}, \text{kg/s} \quad (6)$$

and that of primary air shall be:

$$G_{a1} = \frac{G_{pl} \cdot 1.5\left(\mu_{\text{O}_2} + 3.76\mu_{\text{N}_2}\right)}{\mu_{\text{C}_3\text{H}_4}}, \frac{\text{kg}}{\text{s}}. \quad (7)$$

HEAT BALANCE EQUATION FOR A CATALYTIC BURNER

$$\Delta H^*(1 - q_3 - q_5) + q_{vpl} + q_{a1} = C_{sg} \cdot t \quad (8)$$

On the left-hand side of equation (8) is the amount of heat received from incomplete combustion of the pyrolysis liquid by equation (2), including losses due to radiation q_5 = 0.3 and incomplete combustion q_3= 0.005, from the primary air heated in the waste heat boiler q_{a1} and vapor q_{vpl} of the pyrolysis liquid.

Heat introduced into the burner by primary air heated to t_1 = 380 °C.

$$q_{a1} = \frac{C_{в1} \cdot t_1 \cdot 1.5\left(\mu_{O_2} + 3.76\mu_{N_2}\right)}{3\mu_{CO} + 2\mu_{H_2} + 5.64\mu_{N_2}}. \quad (9)$$

Heat introduced by the pyrolysis liquid vapor heated to

$$q_{vpl} = \frac{C_{п} \cdot \mu_{C_3H_4} \cdot t_1}{3\mu_{CO} + 2\mu_{H_2} + 5.64\mu_{N_2}}, \quad (10)$$

where $C_{в1}$= 1.056 and C_{pl}= 1.52 $\frac{\text{kJ}}{\text{kg} \cdot \text{K}}$ arethe true specific heat capacity of the air and pyrolysis liquid vapor, respectively. True specific isobaric heat capacity of syngas C_{sg}= 1.49 $\frac{\text{kJ}}{\text{K} \cdot \text{kg syngas}}$.

The temperature of the products of incomplete pyrolysis liquid combustion can be determined from the heat balance equation

$$t = \frac{\Delta H^*(1 - q_3 - q_5) + q_{a1} + q_{vpl}}{C_{sg}}. \quad (11)$$

Chemical COP of the catalytic burner

$$\eta_{ch} = \frac{B_{sg} \cdot q_{ch}}{G_{pl} \cdot Q_l^w} \quad (12)$$

PHYSICAL-CHEMICAL PROCESSES IN THE ECG BATTERY

Syngas cooled in the heat exchanger 4 (see Fig. 3) to t_3 = 800 °C enters the anodic channel, while the air heated in the heat exchanger 4 to t_2 = 620 °C is fed to the cathodic channel.

According to [22], the contribution to EMF of the CO oxidation reaction occurring within the SOFC anode is less than 1% of that of the hydrogen oxidation, therefore, it can be neglected in calculations, and only hydrogen is oxidized in the SOFC anode.

Water gas reaction $CO + H_2O \rightarrow CO_2 + H_2$cannot donate H_2 as it only occurs in the presence of an iron-chromium catalyst, which is absent in the anode [23].

In the anode of a SOFC stack, the hydrogen from syngas is oxidized by the oxygen coming from the cathode through the electrolyte, as described by the stoichiometric equation under the assumption that all hydrogen is oxidized

$$3CO + 2H_2 + 5.64N_2 + O_2 = 3CO + 2H_2O + 5.64N_2\,. \quad (13)$$

Exothermic effect of reaction (13) at standard parameters:

$$\Delta H^{**} = \frac{2\Delta H_{H_2O}}{3\mu_{CO} + 2\mu_{H_2} + 5.64\mu_{N_2}} = \frac{2 \cdot (-242.02 \cdot 10^3)}{245.9} == -1{,}968 \frac{\text{kJ}}{\text{kg syngas}}.$$

The temperature of hydrogen oxidation products in the anode has been determined experimentally [24]

https://doi.org/10.5593/sgem2024/4.1/s18.31

$$T_3^* = 783 + 273 = 1{,}056\ \text{K}\,. \tag{14}$$

Gibbs free energy [25] measured at 1,056 K $-\Delta G^*_{1{,}056\ \text{K}} = 190 \cdot 10^3\ \frac{\text{kJ}}{\text{kmol water}}$.

Change in Gibbs free energy in kJ/kg of syngas:

$$\Delta G^*_{1{,}056\ \text{K}} \cdot \frac{2}{245.9} = \frac{2 \cdot 190 \cdot 10^3}{245.9} = 1{,}545, \tag{15}$$

where 2 is the number of kilomoles before H_2 in equation (4), 245.9 is the mass of syngas in equation (4). Fuel cells usually operate under isobaric-isothermal conditions [25], and electrical power equals the product of change in Gibbs free energy G^*kJ/kg of syngas and the syngas flow rate B_{sg} kg/s.

$$Q_{el} = \Delta G^*_{1056\text{K}} \cdot B_{sg}, \text{kW}. \tag{16}$$

On the other hand, electrical power is given by:

$$Q_{el} = B_{sg} \cdot q_{ch} \cdot \eta, \text{kW}. \tag{17}$$

By equating expressions (16) and (17), we refine the previously assumed COP value of the SOFC stack.

$$\eta = \frac{\Delta G^*_{1{,}056\text{K}}}{q_{ch}}\,. \tag{18}$$

The value of η is compared to [22, 26].

HEAT LOSS DUE TO EXHAUST GASES FROM THE WASTE HEAT BOILER

The power supplied to WHB from the SOFC stack

$$Q_{inp} = B_{sg} \cdot q_{ch} - Q_{el}, \text{kW}.$$

In view of incomplete combustion losses q_3 = 0.005 and heat leakage through thermal insulation q_5 = 0.3 in the waste heat boiler, the available power is:

$(1 - q_3 - q_5)\big(B_{sg} \cdot q_{esg} - Q_{el}\big)$kW.

Primary air $B_{sg} \cdot q_{a1}$and pyrolysis liquid $B_{sg} \cdot q_{pl}$take power away from WHB.

WHB power output

$$Q_{\text{yx}} = (1 - q_3 - q_5)\big(B_{sg} \cdot q_{esg} - Q_{el}\big) - \big(q_{a1} + q_{pl}\big)B_{sg}, \text{kW}. \tag{19}$$

The specific true heat capacity of the flue gases from WHB can be determined from equation (3) using the rules described in [27]. C_{out}= 1.09 $\frac{\text{kJ}}{\text{K} \cdot \text{kg}}$. The flow of complete combustion products on exit from WHB (from equation 3).

$$G_{out} = \frac{G_{pl} \cdot \left(3\mu_{CO_2} + 2\mu_{H_2O} + 15.04\mu_{N_2}\right)}{\mu_{C_3H_4}}. \quad (20)$$

Temperature of the flue gases from the WHB,

$$t_{out} = \frac{Q_{out}}{G_{out} \cdot c_{out}}, \quad (21)$$

District water heater output, kW

$$Q_{wh} = G_{out} \cdot C_{out} \cdot (t_{out} - t^*_{out}), \quad (22)$$

where t^*_{out} is the temperature of gases vented into the stack flue, set to 120°C. Natural fuel (pyrolysis liquid) utilization factor

$$K_f = \frac{Q_{el}+Q_{wh}}{G_{pl} \cdot Q_l^w}. \quad (23)$$

Specific consumption of the pyrolysis liquid for electrical energy production, kg/kWh

$$b_{el} = \frac{3{,}600}{Q_l^w \cdot \eta_{ch}}. \quad (24)$$

Specific consumption of natural fuel (pyrolysis liquid) for thermal energy production, kg/GJ

$$b_f = \frac{10^6}{Q_l^w \cdot \eta_{ch}} \quad (25)$$

Specific electricity production in the heat-end mode operation, kWh/GJ

$$W_h = \frac{Q_{el} \cdot 10^6}{Q_{wh} \cdot 3{,}600} \quad (26)$$

Table 1 - Material balance of the plant

	Inflows:	WHB outflows:
Air at the input	G_{al} = 0.1445 kg/s	G_{out}= 0.15503 kg/s
Pyrolysis liquid at the input	G_{pl} = 10.53 · 10^{-3}kg/s	
Total:	0.15503 kg/s	0.15503 kg/s

https://doi.org/10.5593/sgem2024/4.1/s18.31

Table 2 - Heat balance of the power plant

Input power	Output power
$Q_{\text{вх}} = G_{pl} \cdot Q_l^w =$ $= 487.14$ kW	Electric power $Q_{el} = 100$ kW
	Power losses in the catalytic burner $Q_{cb} = Q_{in}(1 - \eta_{\text{ch}}) = 134{,}5$ kW
	District water heater output $Q_{wh} = 126$ kW
	Flue gas output downstream of the district water heater $Q_{out}^* = G_{out} \cdot C_{out} \cdot t_{out}^* = 20.3$ kW
	Power losses in WHB $Q_{WHB} = (q_3 + q_5)\left(B_{sg} \cdot q_{ch} - Q_{el}\right) = 76.5$ kW
	Power losses in the SOFC stack $(q_3 + q_5)\left(B_{sg} \cdot q_{ch}\right) = 28$ kW
	Total 485 kW

Specific flow rates of the standard fuel are compared with the reported data [28 – 30] (see Table 3).

Table 3 - Comparative estimate of specific fuel flow rates for various power plants

Information source	b_{el}, g s.f./kW·h
Natural gas CHP plant [28]	163
Cogeneration diesel-electric plant [29, 30]	250
Rankine cycle TPP fueled with pyrolysis products [31]	474
SOFC CHP plant fueled with pyrolysis products (this paper)	169

As can be seen from Table 1, in terms of specific consumption of standard fuel for heat and power generation, a SOFC-based combined heat and power plant fueled with pyrolysis liquid is second only to a thermal power plant running on natural gas.

SPECIFIC FUEL CONSUMPTION IS SIGNIFICANTLY LOWER THAN THAT OF THE DIESEL GENERATOR PLANTS OF THE SAME CAPACITY AND STEAM TURBINE THERMAL POWER PLANTS RUNNING ON PYROLYSIS PRODUCTS

All calculations for the rated operation mode of a power plant fueled with pyrolysis liquid and equipped with electrochemical generators on solid oxide fuel cells are summarized in Table 4.

Table 4 – Calculations for the rated operating mode of a power plant fueled with pyrolysis liquid.

Characteristic	Symbol	Unit	Equation	Result
Air flow coefficient	α_c	m^3/m^3	1	0.375
Syngas flow rate	B_{sg}	kg/s	5	$64.74 \cdot 10^{-3}$
Pyrolysis liquid flow	G_{pl}	kg/s	6	$10.53 \cdot 10^{-3}$
Primary air flow	G_{a1}	kg/s	7	$54.2 \cdot 10^{-3}$
Heat introduced by primary air	q_{a1}	kJ/kg	9	336
Heat introduced by liquid vapor	q_{vpl}	kJ/kg	10	93.9
Temperature of combustion products	t	°C	11	1269
Burner COP	η_{ch}	–	12	0.724
SOFC stack COP	η	–	18	0.285
Power of gases on exit from WHB	Q_{out}	kW	19	146.5
Flow of combustion products on exit from WHB	G_{out}	kg/s	20	0.1553
Temperature of gases on exit from WHB	t_{out}	°C	21	867
District water heater output	Q_{wh}	kW	22	126
Fuel utilization factor	K_f	–	23	0.464
Specific consumption of pyrolysis liquid for power generation	b_{el}	g/kW·h	24	108
Specific consumption of pyrolysis liquid for heat generation	b_h	kg/GJ	25	30
Heat-end mode electricity production	W_h	kW·h/GJ	26	220

CONCLUSION

1. The concept of using pyrolysis liquid to generate electrical and thermal energy in SOFC-based power plants equipped with electrochemical generators has been demonstrated. The plant and district water heater have electrical output of 100 kW and 126 kW, respectively.

2. Syngas is produced by air conversion of the pyrolysis liquid with the air flow coefficient set to 0.379, which is higher than the minimum at which ash formation is possible. The heat of syngas combustion is 5420 kJ per kg of syngas.

3. Material and heat balances have been drawn up, from which specific flow rates of natural and standard fuels has been obtained:

- for electricity generation 169 gs.f./(kWh);
- for heat generation 197 kg s.f./Gcal;
- specific electricity production in the heat-end mode operation 220 kWh/Gcal;
- fuel (liquid) utilization rate 46.4%.

4. The specific indicators turned out to be slightly inferior when compared to the same indicators at thermal power plants running on hydrocarbon fuels, with the exception of specific electricity production in the heat-end mode operation.

5. Specific indicators of the SOFC when compared to cogeneration diesel-electric plants and Rankine cycle-based steam turbine thermal power plants fueled with pyrolysis

https://doi.org/10.5593/sgem2024/4.1/s18.31

products have demonstrated a significant advantage of the proposed technology for generating electrical and thermal energy at the power plants equipped with high-temperature electrochemical generators based on SOFC.

ACKNOWLEDGMENTS

Ural Federal University development program under the program “Priority-2030”.
Grant number FEUZ-2022-0031

REFERENCES

[1] Snowdon R, Friedt W., European biodiesel can be sustainable, Nature, Germany, 490 (37), 2012.

[2] Yu Z, Wang Y, Jiang L, Dai L, Liu Y, Ruan R, et al., Microwave-assisted catalytic pyrolysis of Chinese tallow kernel oil for aromatic production in a downdraft, Journal of Analytical and Applied Pyrolysis, China, vol. 133, pp. 16-21, 2018.

[3] Y Wang, Q Wu, Sh Yang, et al., Pyrolysis coupled with microwave-absorbent of soapstock for bio-oil in a downdraft reactor, Energy Conversion and Management, USA, vol. 185, pp. 11-20, 2019.

[4] Yu Z, Wang Y, Jiang L, Dai L, Liu Y, Ruan R, et al. Conversion of woody oil into bio- oil in a downdraft reactor using a novel silicon carbide foam supported MCM41 composite catalyst, Great Britain, RSC Adv; 9:19729–39. 2019.

[5] Wang F, Xu J, Jiang J, Liu P, Li F, Ye J, et al. Hydrotreatment of vegetable oil for green dieselover activated carbon supported molybdenum carbide catalyst. China. Fuel, vol. 216, pp. 738-746, 2018.

[6] Lam SS, Wan Mahari WA, Jusoh A, Chong CT, Lee CL, Chase HA. Pyrolysis using microwave absorbents as reaction bed: An improved approach to transform used frying oil into biofuel product with desirable properties. Malaysia. J Cleaner Prod;147. 2017.

[7] Xu L, Cheng J-H, Liu P, Wang Q, Xu Z-X, Liu Q, et al. Production of bio-fuel oil from pyrolysis of plant acidified oil. China. Renewable Energy; 130:910–9. 2019.

[8] Wiggers VR, Beims RF, Ender L. Renewable Hydrocarbons from Triglyceride’s Thermal Cracking. Frontiers in Bioenergy and Biofuels, Brazil, 2017.

[9] Zakera A, Chen Z, Wang X, Zhang Q. Microwave-assisted pyrolysis of sewage sludge: A review. Fuel Process Technol; Canada, 187:84–104. 2019

[10] Wang X, Morrison W, Du Z. Biomass temperature profile development and its implications under the microwave-assisted pyrolysis condition. ApEn 2012;99: 386–92. China, 2012.

[11] Zhang Y, Chen P, Liu S, Peng P, Min M, Cheng Y, et al. Effects of feedstock characteristics on microwave-assisted pyrolysis – A review. Bioresour Technol. China, 2017.

[12] Shpilrain E.E., Malyshenko S.P., Kuleshov G.G. Introduction to hydrogen energy. Russia. Moscow: Energoatomizdat. 1984.

[13] Pilar Lisbona, Luis M., Romeo Enhanced. Coal gasification heated by unmixed combustion integreated with an hybrid system of SOFC/GT // International Journal of Hydrogen Energy. Spain. Volume 33, p. 5755-5764, Issue 20, October 2008.

[14] Promes E.J., Woudstra T., Schoenmakers L., Oldenbroek V., Thallam Thattai A., Aravind P.V. Thermodynamic evaluation and experimental validation of 253 MW Integrated Coal Gasification Combined Cycle power plant in Buggenum, Netherlands // Applied Energy, Volume 155, p. 181-1941, October 2015.

[15] Solodova N. L. , Cherkasova E. I., Salakhov I.I., Tutubalina V. P. Hydrogen – the energy carrier and the reagent. The technology of its receipt. Problems of energy. Russia. V. 19. № 11-12. p. 39-50. 2017.

[16] Filimonova AA., Chichirov AA., Chichirova ND., Filimonov AG., Pechenkin AV. Prospects for the development of hydrogen power engineering in Tatarstan. Problems of energy. Russia. v. 22 № 6, p. 79-91. 2020.

[17] Dubinin A.M., Shcheklein S.E. Coal mini CHP plants on the basis of a gas generator and electrochemical generator. International Scientific Journal for Alternative Energy and Ecology (ISJAEE), Russia, № 7-9 (219-221) p. 60-74. 2017.

[18] Baskakov A.P. Prospects of incineration of municipal solid waste in Russia to generate heat and electricity, Teploenergetika, Russia. N4 pp. 21-29. 2014

[19] Baskakov A.P. Heating and cooling of metals in a fluidized bed. Russia. Moscow: Metallurgiya. 272 p. 1974.

[20] Karapetiants Kh M. In: Karapetiants Kh M, editor. Chemical thermodynamics; Russia. Moscow: Chemistry. 1975.

[21] Karapetiants Kh M. Basic thermodynamic constants of inorganic and organic substances/Karapetiants Kh M., M. L. Karapetiants//M.: Chemistry, Russia, 470 p. 1968.

[22] Korovin NA. Fuel cells and electrochemical installations. In:Korovin NA, editor. Russia. Moscow: MPEI publishing house; p.145. 2005

[23] Baskakov A.P., Dubinin A.M., Tuponogov V.G. On the mechanism of steam gasification of coal // Industrial energy. Russia, №4. S. 40-42. 2008.

[24] Muntz VA. Study of characteristics of a 5 kW power plant on solid oxide fuel cells with steam reforming of natural gas. In: Muntz VA, Volkova YuV, Plotnikov NS, Dubinin AM, Tuponogov VG, Chernyshov VA, editors. Thermal power engineering. Russia. N11; p. 15-20. 2015.

[25] Baskakov AP. Physical and chemical bases of thermal processes. In: Baskakov AP, Volkova YuV, editors. Teplotechnik; Russia. p. 173. 2013.

[26] Zhao Yingru, Sadhu Khan Juma, Lanzini Andrea, Brandon Nigel, Shah Nilay. Optimal integration stratigies for a syngasfuelled SOFC and gas turbine hybrid // Journal of Power Sources, England, Volume 196, Issue 22, p. 9516-9527. 15 November 2011.

[27] Korolev V.N., Tolmachev E.M. Technical thermodynamics: Textbook / V.N. Korolev, E.M. Tolmachev. Russia. Ekaterinburg: USTU-UPI. 180 p. 2001.

https://doi.org/10.5593/sgem2024/4.1/s18.31

[28] Yakovlev B.V. Improving the efficiency of heating and heat supply systems / B.V. Yakovlev - M.: Heat supply news. Russia, 448 p. 2008.

[29] A.M.Leonov, B.V.Yakovlev, Handbook of heat power engineering of electric plants. Publisher Belarus. 1974.

[30] Bazhenov M.I., Bogorodsky A.S., Sazanov B.V., Yurenev.V.N.; Ed. Sokolov E.Ya. Industrial ther-mal power plants: a textbook for universities / – 2nd ed., Rev.-M: Energiia, Russia, 296 p. 1979.

[31] Matveev A.V., Shcheklein S.E., Dubinin A.M., Mohammed A. Qasim, Filippenkov V.A. Electricity production from hydrocarbon pyrolysis products// International scientific journal Alternative energy and ecology. Russia, № 4 (409) p. 94-103. 2023.

ANALYSIS OF THE EFFECTIVENESS OF VARIOUS TYPES OF BLEACHING EARTHS FOR PARAFFIN REFINING ON THE EXAMPLE OF THE TERRA TRADE COMPANY

Engr. Jan Udaliszczew[1]

[1]AGH University of Krakow, **Poland**

ABSTRACT

Modern industrial production of paraffin and other hydrocarbon-based products, such as mineral oils or waxes, is extremely closely related to the process of raw material purification. One of the key stages of this process is paraffin filtration, which aims to remove impurities and undesirable substances that may affect the quality and properties of the final product. Filter earth plays an irreplaceable role in the paraffin filtration process. The paper presents the main aspects related to soil for paraffin filtration, including its physical and chemical properties, production processes and use in industry. The aim of the work is to analyse the effectiveness of types of filter soil in terms of the quality of the finished raw material and to present other methods of paraffin purification. This work provides a comprehensive look at paraffin filtration soil and provides the necessary knowledge to understand its key role in the production process.

Keywords: hydrocarbons, paraffin, bleaching earths, refining, wax

INTRODUCTION

Global trends shape numerous aspects of our daily lives, with recycling and upcycling being pivotal among them. As the world moves towards more sustainable practices, industries across the board are seeking innovative ways to reuse and repurpose recyclable resources. One such resource is paraffin wax, a material familiar to many of us in the form of candles.

Paraffin wax is derived from petroleum and has a variety of applications beyond candle making, including in cosmetics, pharmaceuticals, and food industries. However, to meet the quality standards required for these diverse applications, the wax often needs to undergo a refining process to remove impurities and enhance its properties. This process typically involves the use of bleaching earths, which play a crucial role in decolorizing and purifying the wax.

The aim of this paper is to analyze different types of bleaching earths utilized in the paraffin refining process by Terra Trade. By evaluating these bleaching agents, we strive to determine which ones yield the most colorless and pure paraffin wax. The study involves performing rigorous laboratory tests using various types of filter earths, along with the addition of activated carbon, following the standard procedures established in the company's laboratory. These tests will provide insights into the effectiveness of different bleaching earths, ultimately guiding the selection of the most efficient materials for producing high-quality paraffin wax.

https://doi.org/10.5593/sgem2024/4.1/s18.32

In summary, this research not only aims to improve the paraffin refining process but also contributes to the broader effort of promoting sustainable practices through effective recycling and upcycling of industrial materials.

MATERIALS AND METHODS

The research programme included a controlled paraffin refining process carried out in the company's laboratory using the company's methodology. It involves staining a colourless paraffin sample into two separate colours – green and red – using 0.1% of pigments used in the candle industry. Six types of sorbents were applied to separate beakers and adsorption refining was carried out, bleaching was repeated until the starting raw material was obtained, or refining was stopped if the adsorbent was found to be ineffective. Finished samples were labelled by number of iterations and type of bleaching earth.

The paper analysed the effectiveness of selected five different types of bleaching earths from different suppliers from all over the world:

Palmax – The Netherlands; Galleon V2G — India; M200 — Mexico; E200 — Spain; D2 — Spain.

Table 1 shows the chemical compositions of bleaching earths determined on the basis of spectroscopic analysis.

Table 1. Chemical composition of bleaching earths obtained by spectroscopic method. [1]

Chemical compound [%]	Bleaching earths				
	Palmax	M200	E200	D2	Galleon V2G
SiO_2	59,94	64,8	53,7	53,4	58,26
Al_2O_3	9,18	13,0	4,0	4,5	8,30
Fe_2O_3	6,74	4,6	1,4	1,6	9,85
CaO	7,15	1,5	0,6	0,8	5,34
MgO	7,24	3,5	26,2	30,8	1,27
Na_2O	0,19	0,9	0,1	0,2	0,33
K_2O	0,99	2,8	0,8	1,0	0,65
SO_4	2,57	–	–	–	–
TiO_2	–	–	–	–	2,73
SO_3	–	–	–	–	2,75

The colour compatibility of the refinied samples with the base (output paraffin) is presented by using GIMP computer program in the form of hexadecimal RGB (red, green, blue) notation used in HTML coding and in colour determination using the colour picker tool to retrieve a specific colour from a picture. The samples were compared to determine the optimal optical refining bleaching earth from those used.

The next step is to contaminate paraffin with a mixture of 50% paraffin and 50% palm wax and 0.1% green dye and a second sample of 0.1% red dye. Such a study was proposed to give a real context to the samples refined by the company, since the waste that the company obtains from the producers has fillers such as animal lard, palm wax or soy wax, which significantly reduces the adsorption efficiency of the earth and coal. The sorbents used are refining earth, which gave the best results, and activated carbon. The mixtures were doped with sorbents in an amount sufficient to obtain the transparent raw material obtained in the previous test. A mixture of sorbents with a ratio of 4% bleaching earth and 2% activated carbon was also used, the proportions of which were taken from a paper from the same field of study [2].

The final stage of the laboratory research programme was to carry out refining using the results of previous analyses and implement them in subsequent studies from production with a color difficult to refine to white color.

The analysis of bleaching earths composition was performed based on analysis provided by the company in order to select a group of chemical components that best adsorb dyes in paraffin and paraffin compositions.

The sequence of actions to obtain the refining of paraffin in the laboratory has been described below.

1. First, a multiple of 100 g of white paraffin should be poured on each type of bleaching earth or activated carbon. Transfer the measured quantity to be tested in a 1000 cm3 beaker. The beaker prepared in this way should be placed on a hob or put in an industrial dryer to melt the raw material.

2. Measure with an analytical weight of 0.5% (total mass of melted paraffin) the dye of the appropriate colour, pour the dye into a beaker and stir with a baguette for faster diffusion.

3. After complete melting, pour 100 g of coloured paraffin into beakers using a precision scale – place the beaker on the scale, weigh the scale and pour the contents of a large beaker in compliance with health and safety regulations. The prepared beakers should be signed with the name of the sorbent.

4. Samples waiting for their refining turn are deposited in an industrial dryer to prevent solidification.

5. 1 % of the appropriate sorbent should be measured on the analytical balance, in these tests it was 1 g of earth and coal during the first refining.

6. The prepared sorbent is added to a properly signed beaker.

7. Place the beaker on a stirrer with the hot plate set to the appropriate power to achieve a temperature in the beaker between 125°C and 130°C, place the metal mixing capsule in the beaker and turn on the rotation at 400 rpm. The mixing and heating process should last 30 minutes, so set the clock for this time.

8. After 30 minutes, remove the beaker from the mixer and pour the contents through the coffee filter into the next beaker to separate the refined paraffin from the earth or coal. We put the beaker in the industrial dryer for the time of filtration.

9. After filtration, 20 g of the sample should be poured onto the lid of the can to preserve the optical parameters of the refining.

https://doi.org/10.5593/sgem2024/4.1/s18.32

10. Repeat steps from step 4 until a satisfactory result is obtained or further testing is discontinued due to lack of visual effects of refining.

RESULTS

For green dye, the refining process had to be repeated three times to obtain a paraffin close to the primary colour, whereas for red dye the refining process had to be repeated twice. The results of the studies are shown in Figure 1 and 2.

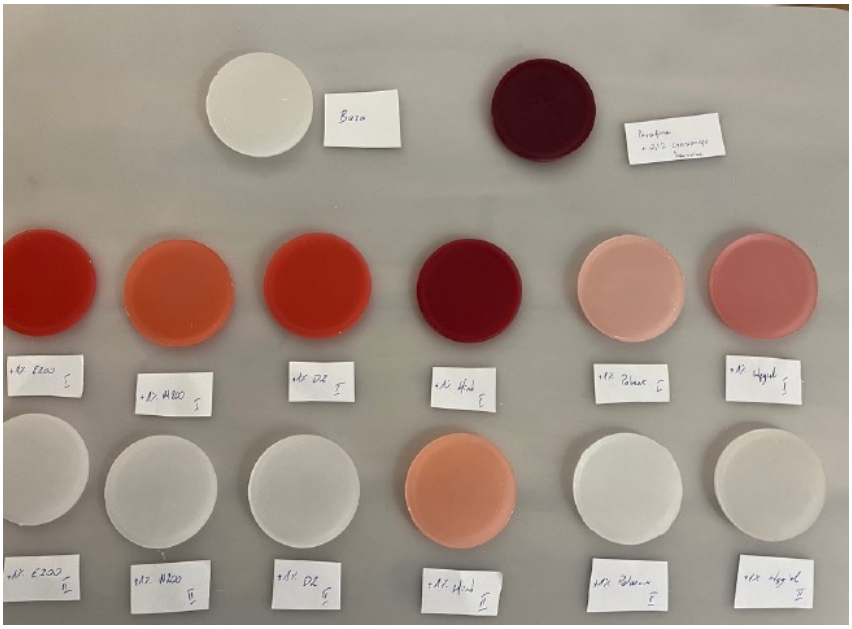


Figure 1. Process of refining red dye.

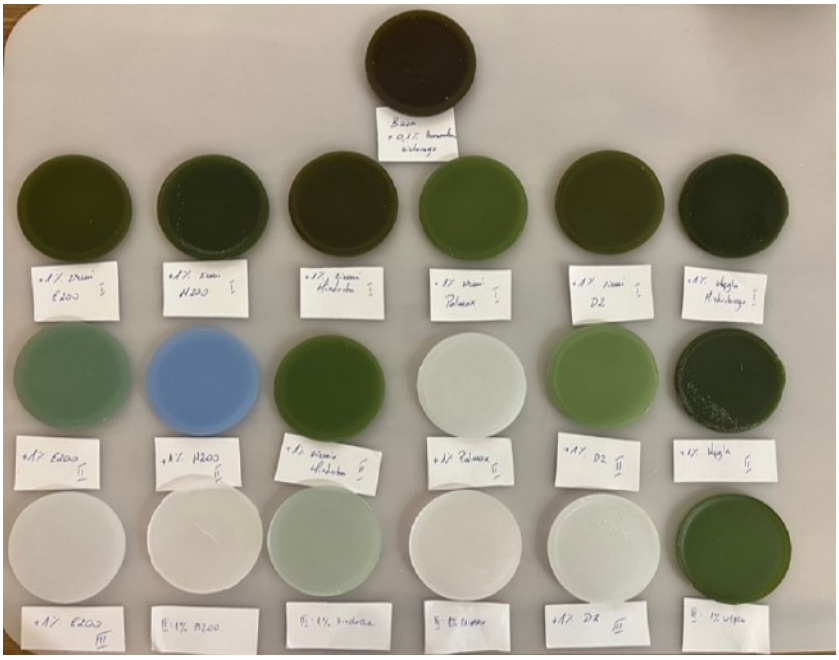


Figure 2. Process of refining green dye.

Colors have been transferred using color-picker tool to GIMP to obtain the color in HTML notation. Results have been presented in tables 2 and 3 shown below.

Table 2. Refining results of red dye using HTML code

	Base			Base + dye		
	#D6D2C1			#380D14		
	Sorbent					
	E200	M200	Galleon V2G	Palmax	D2	Active Carbon
Iteration I	#8E0E15	#9C3C32	#520005	#BA8989	#981A26	#9F5A57
Iteration II	#A69E91	#BCB7AC	#AF6C50	#D3CCC4	#C8C2B6	#C7C1B6

Table 3. Refining results of green dye using HTML code

Base, Base + dye	#D6D2C1			#2A1F17		
Sorbent	E200	M200	Galleon V2G	Palmax	D2	Active Carbon
Iteration I	#2E310B	#242B14	#29280D	#424B20	#343411	#272A16
Iteration II	#58674A	#5A7494	#344118	#BABBA8	#5C6C3B	#2B321A
Iteration III	#C9BDAD	#D8CEBF	#949983	#E0D8CF	#D1D0C5	#435125

The next step in the conducted research, was to mix clear white paraffin wax with palm wax, and dye that solution with appropriate dye. Results of that experiment are presented in table 4 and 5.

Table 4. Refining results of palm wax + red dye using HTML code

Base	#DAD7C1		
Base + red dye	#6F0011		
Used sorbent	2% Active Carbon	2% Bleaching Earth	4% Bleaching Earth + 2% Active Carbon
Result	#B1907D	#7E0F1E	#C1B8A9

https://doi.org/10.5593/sgem2024/4.1/s18.32

Table 5. Refining results of palm wax + green dye using HTML code

Base	#DAD7C1		
Base + green dye	#4B481A		
Used sorbent	3% Active Carbon	3% Bleaching Earth	4% Bleaching Earth + 2% Active Carbon
Result	#3F4C18	#3F4D1B	#BDC4BA

DISCUSSION

In the process of refining red dye, Palmax and D2 earth gave the best result, activated carbo left a darker glaze, E200 and M200 earths also did worked in bleaching paraffin, leaving a light pink glow. Galleon V2G Earth did not bleach the sample satisfactorily and further refining was discontinued. The refining process has been completed after two stages, as the results achieved are satisfactory to the company (Figure 1). The most effective earths in green dye refining were Palmax and M200. The D2 and E200 earths left a slight green glow, while the Galleon V2G earths left a visible glow of the output dye. The activated carbon did not give satisfactory results and the tests were discontinued after three refining cycles.

The introduction of palm waxes into the paraffin refining process may have negative effects both in terms of technology and quality. It is assumed that Palmax earth will be used, which showed the best effect in green and red dye, and the sorbent weight will correspond to the quantity used in the previous test, which gave the desired effect of refining. 3 g of earths and carbon will be used for the refining of green dye and 2 g of earth and carbon for red dye. A ratio of 4 g of soil and 2 g of carbon was also tested sourced from literature [2].

CONCLUSION

By analysing the colors obtained during the refining process using the GIMP computer program, results were obtained indicating that the codes most similar to the code of the base sample #D6D2C1 are:

–in the red dye refining process (as appropriate):

•#D3CCC4 – PALMAX,

•#C8C2B6 – D2,

–in the process of refining the green dye:

•#D8CEBF – M200,

•#E0D8CF – PALMAX.

The results were obtained based on the analysis of minimizing the difference of individual colors of the RGB spectrum from the initial sample. It should be mentioned that the initial color of parafiin wax isn't pure white since paraffin is obtainted from refining slack waxes, that have a yellow or brown color. [3] The analyzed variables in the process of refining sorbents were their usage specification presented in Table 1. Laboratory factors that could affect the results of the tests, such as mixing time, process temperature, paraffin and sorbent quantities, were eliminated by following the test programme with particular care. The results between different earth types in the study of the refining of the two dyes did not differ from each other. Palmax, D2, E200 and M200 gave similar and satisfactory refining results. Galleon V2G did not give as effective effect as other sorbents analyzed, because only on the fourth relapse produced transparent paraffin. From the examination of these chemical samples, it can be concluded that the substances present only in Galleon earth (2.73% titanium dioxide and 2.75% sulphur (VI) oxide), representing more than 5% of the total composition, are not actively involved in the refining of the dyes tested.

Palmax earth in the purification of green dye already at the second relapse allowed to achieve a satisfactory effect, almost stripping the sample of color, while in the study of red dye at the first refining already achieved a very good effect, thus gaining an advantage over other types of earths, it was evaluated as the leader of this study.

All soils consist of nearly 55% silicon oxide, which is certainly the main factor giving them the properties of paraffin dye purification, whereas this compound is present in very approximate proportions in each of the earths, which allows to draw the conclusion that it is not the main compound determining the quality of refining. However, the earths that gave the expected result consist of more magnesium oxide than Galleon V2G earths, which leads to the conclusion that the advantage of this compound gives a better effect during refining. While continuing to investigate the differences in chemical composition, attention should be paid to further compounds present at a higher concentration in Palmax earth compared to other earths and giving a satisfactory result. These are iron (III) oxide and calcium oxide, which most likely contributes to the final refining effect. The remaining compounds are present in proportions that do not give conclusive results in the assay.

The study used one of the most popular paraffin fillers – palm wax, which in color and properties is similar to the raw material it is supposed to imitate, while it worsens the characteristics of burning, hardness and, most importantly, refining. The aim of this study was to determine to what extent palm wax compromises the refining process. It was noted that when a mixture of 50% paraffin and 50% palm wax was used, the amount of sorbents initially sufficient to completely purify the paraffin gave a negligible effect for the green dye and a moderate result for the red dye and the use of activated carbon.

Studies on the use of palm wax additives in the refining process have shown that such additives may introduce some difficulties in the refining process. The results obtained indicate that the presence of palm wax may lead to the formation of new chemical bonds in the mixture, which are characterized by specific physicochemical properties. These properties make palm wax removal in the refining process more complicated and time-consuming. Analyzing these results, it can be concluded that further study of the impact of palm wax and other types of additives (such as soy waxes or animal fats) on the refining process is necessary to understand the exact mechanisms that occur during the refining

https://doi.org/10.5593/sgem2024/4.1/s18.32

process. In addition, there is a need to develop new refining strategies and technologies that can effectively deal with the challenges associated with the presence of these types of additives.

ACKNOWLEDGEMENTS

I would like to express my sincere gratitude to Dr. Eng. Mariusz Niekurzak, supervisor of the Scientific Circle Production Manager. Thank you for your help with the work and substantive support.

I would also like to thank the management and employees of Terra Trade sp. z o.o. for the opportunity to conduct research, provide documents and information, and provide scientific and technological support. Thank you for your knowledge and professional mentoring approach to research.

REFERENCES

[1] Materials obtained from the laboratory of „Terra Trade" sp. z o. o. [unpublished material].

[2] Antosz A., Ptak S., Badania możliwości powtórnego wykorzystania surowców odpadowych powstających w trakcie produkcji świec, Nafta-Gaz, Poland, vol. 10, pp. 760–775, 2022.

[3] *Kirk-Othmer Encyclopedia of Chemical Technology*, Vol. 28, Wiley John and Sons, New York 2007.

DETERMINATION OF THE PRODUCT DEVELOPMENT DIRECTIONS FOR THE FERTILIZER PRODUCTS MADE FROM PIG FATTENING AND SLAUGHTERING BY-PRODUCTS

Dr. Anita Csiba[1]
Dr. Arpad Ferencz[1]
[1] University of Szeged Faculty of Agriculture, **Hungary**

ABSTRACT

Nowadays The storage of pig slurry has been an unsolved problem for a long time in Hungary, therefore the appropriate processing technology is a very important question in order we can produce from the pig fattening and slaughtering by-products the best possible quality of final product. The determined goals of the product development can be achieved in two ways. The first possible method for it preserving the nutrients in the slurry and the another way adding fertilizers or other valuable materials, that improve the soil. At the end of the industrial research project, we can develop a new technology. There are all the liquid manure can be processed in the pig farms with this new technology, which has the most important result to produce a final product with rich nutrient content and with low emission. The fermented manure can be supplement with second category slaughterhouse by-products or even nitrogen, phosphorus and potassium fertilizers. The active ingredients for completing, like different fertilizers or different slaughterhouse by-products specialize the fermented manure product for successfully use as fertilizer of the different plant species. Maybe the most important part of product development activity is the market research and use of the collected data with a consumer questionnaire to identify the directions of product development.

Keywords: pig fattening and slaughterhouse by-product processing, product development, recycling

INTRODUCTION

Even though agriculture today represents only a small share of the economies of developed countries, including that of the European Union, public intervention has recently been stepped up, with agro-rural policies that have added other dimensions in support of the traditional function of primary activity, namely the production of foodstuffs, including sustainable development, the fight against climate change, spatial and landscape planning, diversification and vitality of the rural economy, public health, product quality, and the production of energy and biomaterials. Support for public assets or non-commercial aspects of agriculture – in other words, those not rewarded by the market – has thus become a key strand of today's agricultural and rural policies, including the CAP. [1]

The CAP defines the conditions that will allow farmers to fulfil their functions in society in for example about the environmentally sustainable farming. Farmers have a double challenge – to produce food whilst simultaneously protecting nature and

https://doi.org/10.5593/sgem2024/4.1/s18.33

safeguarding biodiversity. Using natural resources prudently is essential for our food production and for our quality of life – today, tomorrow and for future generations. [2]

The Commission supported EU countries throughout the preparation of their CAP Strategic Plan so that:

EU countries take full advantage of the CAP 2023-27 and its instruments to support their farmers in the transition towards increased sustainability in our food systems.

Each CAP Strategic Plan includes an intervention strategy explaining how each EU country will use CAP instruments to achieve the CAP objectives, in keeping with the Green Deal ambitions. [3]

The ten key objectives

For the period 2023-27, the common agricultural policy (CAP) is built around ten key objectives. Focused on social, environmental and economic goals, these objectives are the basis upon which EU countries designed their CAP Strategic Plans. [4]

The objectives are:

- to ensure a fair income for farmers;
- to increase competitiveness;
- to improve the position of farmers in the food chain;
- climate change action;
- environmental care;
- to preserve landscapes and biodiversity;
- to support generational renewal;
- vibrant rural areas;
- to protect food and health quality;
- fostering knowledge and innovation. [4]

Green Deal

Climate change and environmental degradation are an existential threat to Europe and the world. To overcome these challenges, the European Green Deal will transform the EU into a modern, resource-efficient and competitive economy, ensuring:

- no net emissions of greenhouse gases by 2050
- economic growth decoupled from resource use
- no person and no place left behind. [5]

The European Commission has adopted a set of proposals to make the EU's climate, energy, transport and taxation policies fit for reducing net greenhouse gas emissions by at least 55% by 2030, compared to 1990 levels. [5]

Farm to Fork Strategy

The European Green Deal sets out how to make Europe the first climate-neutral continent by 2050. It maps a new, sustainable and inclusive growth strategy to boost the economy, improve people's health and quality of life, care for nature, and leave no one behind. The Farm to Fork Strategy is at the heart of the Green Deal. It addresses

comprehensively the challenges of sustainable food systems and recognizes the inextricable links between healthy people, healthy societies and a healthy planet. [6]

Biodiversity Strategy for 2030

The EU's biodiversity strategy for 2030 is a comprehensive, ambitious and long-term plan to protect nature and reverse the degradation of ecosystems. The strategy aims to put Europe's biodiversity on a path to recovery by 2030, and contains specific actions and commitments. A core part of the European Green Deal. [7]

MATERIALS AND METHODS

Fermented pig slurry production

The first processing step of the pig slurry before the fermentation is the separation. We have to reduce the moisture content of the pig slurry under 65%.

Pig slurry separation

The separation is the first step in slurry management. It is the starting point for further effective manure processing. After separation into solid and liquid media, there are many purposeful possibilities for further processing. Today, valuable bedding material or compost is produced from the separated solid matter. The liquid manure, in turn, ensures safe growth on the cropland in every vegetation phase. This replaces chemical fertilizer and saves money, protects the environment and promotes animal health. [8]



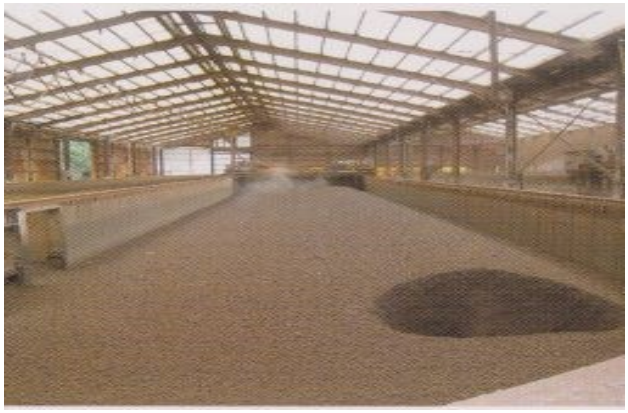
Picture 1: FAN PSS 3.2-780 Slurry separator [9]

Hosoya fermentation system

The fermentation system F1 (Phase-1 system) has a structure in which the rotary blade rotates through the fermentation tank. The rotary blade crushes poultry manure on the right half (side A) and stirs it, turns to the left side (B side), turns to the left while stirring the left half, moves to the end, moves to the right side, continues to rotate. At this point (point C), 30 to 80% of the chicken manure that was issued and about 35% moisture is dropped to the floor and the remaining 20 to 70% is moved to (point D).

https://doi.org/10.5593/sgem2024/4.1/s18.33

Fresh poultry manure (moisture 60 to 78%) will be added by heavy machine (D point) so that the depth is 1 m (or the depth of the tank is 1.3 m by the specification). Raw poultry manure is mixed with return manure of about 35% moisture, the moisture content reaches about 60%, and a large amount of actinomycete acts immediately to cause hard fermentation and its temperature becomes about 70 ° C. This severe high-temperature fermentation finishes only on the right side (A side) and after shifting to the left side (B side), the poultry manure is gently fermented and aged (point C), pulled out, the first fermentation process is over and the second fermentation It is transferred to the tank. The stirrer is agitated very gently by a pair of special rotary blades with a diameter of 1.28 m (special specification is 1.56 m) and 0.65 m. [12]



Picture 2: HOSOYA manure fermentation system [10]

Secondary fermentation box

The semi-ripened poultry manure delivered from under the floor of the phase-1 system tank is left to stand in one of the secondary pahse-2 fermentation sedimentary layers partitioned into 5 to 6, and fermentation is continued. Poultry manure is sequentially transferred to the next tank every 3 days, and the turnover is done at this time. Thus in four compartments 3 days X 5 cells = 15 days, that is, about 15 days, it becomes fermented poultry manure with a moisture amount of about 20%. [12]



Picture 3: Hosoya fermented manure drying system [11]

Organic fertilizer (Poultry manure fermented fertilizer)

Organic fertilizer made by poultry manure fermentation / drying system of Hosoya is an excellent organic fertilizer containing many effective chemical ingredients suitable for growing plants. It can be classified into several kinds according to the size of the grain, and it can be used according to each purpose such as vegetables, fruit trees, golf course etc. In addition, Hosoya's organic fertilizer is a fertilizer that is easy to handle without odor of the product owing to the agglomeration phenomenon of actinomycetes, the product is granular and easy to spread fertilizer, and it is manufactured by the process of high temperature fermentation. [12]

The market research product development

In our industrial research project, we would like to produce different organic fertilizer products for different costumers, but they have very different needs. In this part of our industrial research we are looking for the answer what are the needs of the costumers for which they are willing to pay more money. The most important aim that the products must be sold in good price, therefore we make market research in our industrial research project for the product development and we would like to introduce the results of this part of our research project in this study. In the market research activity, we examined also the individual and professional costumers needs. Our goal was the information collection in the market of individual and professional consumers. Our method was a filling of the customer questionnaire forms with the individual and professional customers. We made filled the customer questionnaire forms with 100 people. Our market research project also examined the consumers habits of individual and professional costumers. We would like to know their individual and professional preferences. Finally, we can say, that we have got useful information from these market research and we can use it for product development and the planning for successful marketing strategy for these products.

RESULTS

The database of the customer questionnaire fillers

A total of 100 people filled out the Google questionnaires used for the questionnaire survey. 90% of those who filled out the questionnaires are engaged in agricultural activities in field crop production, horticultural production, or viticulture, ornamental plant cultivation, herb cultivation. The size of the land of the infill farmers ranges from 0.38 hectares to 950 hectares. In terms of sectors, 85% are engaged in arable crop production, 12% in horticultural production, and 2% in viticulture.

Results of the consumer questionnaire survey

76% of respondents are satisfied with the currently used products, while 24% are not, but 71% of respondents would be willing to try other fertilizer or organic fertilizer products.

The 69% of the farmers use artificial fertilizers, 67% of them use organic fertilizers, 35% of them use leaf fertilizers, and 23% of them use vegetable compost. The

https://doi.org/10.5593/sgem2024/4.1/s18.33

respondents could give more than one answer, as it is conceivable that several products/by-products are used for soil fertilizers.

Table 1: Which fertilizers use the respondent farmers?

Which fertilizers use the respondent farmers*	
Artifical fertilizers	**69%**
Organic fertilizers	**67%**
Leaf fertilizers	**35%**
Vegetable compost	**23%**

* The respondents could give more than one answer, as it is conceivable that several products/by-products are used for soil fertilizers.

45% would try fermented organic manure, 34% would try plant and animal origin compost and 21% would try a products, that contains organic and artificial fertilizers mixture. Respondents could select several products here as well.

Table 2: Which other fertilizers would be trying the respondent farmers?

Which other fertilizers would be trying the respondent farmers? *	
Fermented organic manure	**45 %**
Plant and animal origin compost mixture	**34 %**
Organic and artifical fertilizers mixture	**21 %**

* The respondents could give more than one answer, as it is conceivable that several products/by-products are used for soil fertilizers.

The main aspects of choosing fertilizer products are the price and value rate, the quality of the products and the special properties.

Table 3: How many % extra price would pay the participant customers of the market research for the better qualities soil organic fertilizer products with extra added materials?

How many % extra price would pay the participant customers of the market research for the better qualities organic soil fertilizer products with extra added materials?	
Customers who would not pay more extra price	**28%**
Customers who would pay 10% extra price	**3%**
Customers who would pay 20% extra	**29%**
Customers who would pay 30% extra price	**15%**
Customers who would pay 40% extra price	**13%**
Customers who would pay 50% extra price	**12 %**
Customers who would pay 100% extra price	**0%**

Table 4: The most important characteristic of the organic soil fertilizers according to the participant customers opinion in the market research

The most important characteristic of the organic soil fertilizers according to the participant customers opinion in the market research	
Higher organic material content	**61 %**
Retard effects organic soil fertilizers with organic bound nutrients	**33 %**
Higher level processed products	**27 %**
Organic soil fertilizers, that can be used for different needs of different cultivated plant species	**24%**

The customers could give more answer for this question. The 61 % of the farmers would use organic soil fertilizer products with higher organic material content. The 33% of the respondents would like to use products with organic bond nutrients, because these fertilizers have a retard effects. The 27% of the farmers would use higher level processed products and the 24% of the filler farmers would like to try organic soil fertilizers, that can be used for different needs of different cultivated plant species.

CONCLUSION

Nowadays the majority of customers are conscious customers. It is also clear from the processed data of the questionnaire, that the consumers are regularly informed about the organic soil fertilizers. The main sources of information are found on internet. It is important for the majority of customers who filled the questionnaire form the using the excellent qualities and effective organic soil fertilizers. According the customers the most important parameter of the organic soil fertilizer the high organic material content. The retard effects organic soil fertilizers with organic bound nutrients as important characteristics are on the second place and the third most important of the important parameter of the list is the high-level processing. The fourth most important thing, that the developed organic soil fertilizer could be used for different needs of different cultivated plant species. These are encouraging facts for the product development, that a significant proportion of respondents would be willing to pay more for these higher quality products with these added characteristics, that were listed.

REFERENCES

[1] https://www.europarl.europa.eu/factsheets/en/sheet/103/a-kozos-agrarpolitika-kap-es-a-szerzodes

[1] https://www.europarl.europa.eu/factsheets/en/sheet/103/the-common-agricultural-policy-CAP-and-the-treaty

https://doi.org/10.5593/sgem2024/4.1/s18.33

[2] https://agriculture.ec.europa.eu/common-agricultural-policy/cap-overview/cap-glance_hu#title

[3] https://agriculture.ec.europa.eu/cap-my-country/cap-strategic-plans_en

[4]https://agriculture.ec.europa.eu/common-agricultural-policy/cap-overview/cap-2023-27/key-policy-objectives-cap-2023-27_hu

[5]https://commission.europa.eu/strategy-and-policy/priorities-2019-2024/european-green-deal_hu

[6]https://eur-lex.europa.eu/resource.html?uri=cellar:ea0f9f73-9ab2-11ea-9d2d-01aa75ed71a1.0001.02/DOC1&format=PDF

[7] https://environment.ec.europa.eu/strategy/biodiversity-strategy-2030_hu?etrans=hu

[8] https://www.bauer-at.com/en/product/slurry-technology/separators/

[9] https://www.fan-separator.de/en/product/separators-pss/separator-pss-1-2-and-3-2/

[10] https://hevesgep.hu/en/termek/hosoya-fertilizer-machine/#gallery-4

[11] https://hevesgep.hu/en/termek/hosoya-fertilizer-machine/#gallery-8

[12]http://www.khosoya.co.jp/en/file/pdf/Hosoy%20Poultry%20Manure%20Fermentation%20System%20ver200602.pdf

EXPERIENCES WITH THE USE OF CUPOLA FURNACE SLAG IN CONSTRUCTION INDUSTRY

Ing. Patrik Fedorko [1]

prof. Ing. Alena Pribulova, CSc.[1]

Assoc. Prof. Ing. Jozef Petrik, PhD[1]

Ing. Peter Blasko, PhD[1]

Assoc. Prof. Ing. Peter Futas, PhD[1]

[1] Technical University of Kosice - **Slovak Republic**

ABSTRACT

Gray cast iron is still the most used material for the production of castings. It can be made in several ways, but the most efficient and economical way to make gray cast iron is in a cupola furnace. A by-product in its production is slag, which arises from impurities that may be present in the charge, from coke, which is used as fuel for the cupola furnace and part of it also passes into the slag, from the lining of the cupola furnace as well as from oxides formed during of the smelting process, sulfides and phosphides. The amount of slag from the cupola furnace represents 5-10% of the weight of the produced metal. Gray cast iron can be melted in a hot-air or cold-air cupola furnace, and the slag can be cooled on the air to form lump slag, or it can be water-cooled to form granular slag. In the article, the authors dealt with the treatment of slag and its use in the preparation of concrete. In the first series of experiments, slag was used as a substitute for sand in concrete, being added in different amounts and the properties of the concrete were tested after 28 days, 3 months, 6 months and after a year. In the second series of experiments, it was ground to the grain size of cement and was added as a substitute for cement in concrete. The quality of the raw concrete was monitored by the cone test and the quality of the hardened concrete by measuring the compressive strength and hardness. However, the achieved results did not meet our expectations and were the worst compared to other metallurgical slags.

Keywords: cupola furnace, slag, concrete, cement replacement, aggregate replacement

INTRODUCTION

The construction industry's pursuit of innovative materials and methodologies supports ongoing efforts to improve durability, sustainability, and economic viability. This effort is increasingly focused on the reuse of industrial by-products to limit the amount of incoming waste and reduce the need for raw material extraction [1]. Gray cast iron maintains a dominant position in casting due to its universal properties and cost-effectiveness, with many countries utilizing cupola furnaces for its production (according to Modern Casting magazine, in 2021, 102 million metric tons of castings were produced, of which 48.8 million metric tons were gray cast iron) [2]. When melting cast iron in cupola furnaces, slag is produced, which is a mixture of impurities from the raw materials, by-products of coke combustion, and remnants from the furnace

https://doi.org/10.5593/sgem2024/4.1/s18.34

lining. Gray cast iron can be melted in a hot air or cold air cupola furnace, and the slag can be air-cooled to form lumpy slag (which requires crushing and milling before use) or water-cooled to form granulated slag. Slag typically makes up 5-10% of the weight of the produced metal and is a significant but underutilized material that has been relegated to waste status in the past. There are various industries where cupola furnace slag is used very successfully alone or with other waste material. Very good results with its use were achieved in glassmaking, in the synthesis of zeolite, in production of ceramic foams and as a source of phosphoric fertilizers. However, the most frequently discussed sector of its use is construction [3, 4].

In our work, we have explored the possibility of integrating this slag into concrete production, an area where it is little used despite its promising properties. A very important property that affects the use of slag in the construction industry is its hydraulicity [5, 6]. This term is used in connection with materials capable of reacting with water (e.g., cement). The hydraulicity of the slag is influenced by its chemical and mineralogical composition, alkalinity, and the amount of vitreous phase. Authors [7] have indicated that the hydraulicity of cupola slag increases with increasing levels of CaO, Al_2O_3, MgO, and decreases with increasing SiO_2 content. An important parameter that affects the reactivity of slag in concrete is its fineness. Finely grounded slag creates a firmer phase than coarsely grounded slag. Given the hydraulicity of the slag, it is feasible to use it in concrete production. Slag from the cupola furnace should help not only in the setting and hardening of concrete but also contribute to resistance against environmental degradation [8]. The hydraulicity of the slag can be optimized by appropriate processing, such as grounding, which increases the surface area and reactivity with water. In the concrete industry, granulated slag from the cupola furnace can be used in two ways: as a partial replacement for aggregate and as a partial replacement for cement. The crucial factor is the proportion of slag in concrete formulas, which requires careful optimization to ensure the desired properties of the concrete, such as workability, compressive strength, flexural strength, and durability. Studies [8, 9, 10] have shown that concrete made using slag from the cupola furnace, whether replacing aggregate or cement, can exhibit improved properties such as compressive strength and durability, making it an attractive option for sustainable construction practices. The use of this slag in concrete mixtures has the potential to reduce the demand for cement and aggregate while allowing the utilization of a by-product from the foundry industry, offering environmental benefits such as reduced CO_2 emissions and protection of natural resources.

MATERIALS AND METHODS

In the study, experimental work was conducted to explore the possibilities of replacing aggregate and cement with slag from cupola furnaces. The main objective was to assess the impact of substituting cement and aggregate on the physical and mechanical properties of concrete. Granulated slag from cupola furnaces, a by-product of the production of various grades of gray cast iron, was used as the primary material.



Fig. 1 Granulated slag from cupola furnace

Cupola furnace slag is characterized by its unique composition, primarily high in SiO_2, followed by CaO and Al_2O_3. The chemical composition of the slag (Tab. 1) directly

depends on the melting technology and the composition of the input materials. The chemical composition of the slag has a direct impact on its viscosity, as well as on the rate of crystallization during cooling, which in turn affects the porosity, size, and character of the crystals in the solidified slag. These characteristics are crucial for the potential use of slag in various applications. The pH of slags from cupola furnaces can vary from acidic to slightly alkaline, indicating their diverse properties.



Fig. 2 Aggregate (building quartz sand)

In the experimental usage, slag from cupola furnaces was tested in three different granularities: in its unmodified, natural form, as coarse grounded slag, and as fine grounded slag. The detailed granulometric composition of the slag in these forms is illustrated in Figure 3. In the first phase of the study, the slag from the cupola furnace was used in the production of concrete mixes as a replacement for aggregate, while in the second phase, the slag replaced cement. For the aggregate replacement, slag was used in its unground, natural state and as finely grounded slag. The replaced aggregate was commonly used construction quartz sand (Fig. 2), whose chemical composition is shown in Table 1. As can be seen in Figure 3, the granulometric composition of the unground slag and the aggregate is very similar; in both cases, the proportion above 1.4 mm represents approximately 30% of the total weight. In addition to this similarity, in the case of slag from the cupola furnace, SiO_2 is the dominant component. These factors suggest that unground cupola slag represents a potentially suitable aggregate replacement. Other components of the concrete mix included:

- Portland blast-furnace slag cement (I45,5R), which amounted to 16.2% of the total mix weight (excluding water weight). This amount was determined according to the class of concrete produced, C20/25, as described by the standard STN EN 206.
- A plasticizing additive (MC powerFlow 2695).
- Water. The volume of water was adjusted to achieve the desired consistency and ease of processing. The correct consistency of the mix was verified by a slump test in accordance with the standard STN EN 12350-2.

Tab. 1 Chemical composition of cupola furnace (CF) slag and aggregate in %

	Fe	FeO	Fe_2O_3	SiO_2	CaO	MgO	Al_2O_3	MnO	Na_2O
CF slag	2.6	2.44	1.12	45.27	24.08	5.85	9.95	0.50	-
Aggregate	-	-	0.79	89.54	0.21	-	5.21	-	1.12

Granulated (ungrounded) slag gradually replaced aggregate in amounts ranging from 5% to 100%. Concrete samples were made in metal molds (cube and prism shapes), where they hardened for 24 hours. After hardening, the samples were removed from the molds and placed in a water container for 7 days. After 28 days from creation, the samples were subjected to tests for compressive strength and flexural strength.

https://doi.org/10.5593/sgem2024/4.1/s18.34

In the next phase of the experiment, the aggregate was replaced with finely ground slag, but based on findings from the first phase, it was determined that the replacement of aggregate with slag would only be carried out in the range from 5% to 40%. The samples were prepared, treated, and tested in the same way as in the first phase. Coarsely ground slag from the cupola furnace differed in its granulometry from the aggregate, leading to an increase in the proportion of fine particles at the expense of coarser ones. This shift in granular composition caused increased water consumption in the fresh concrete to maintain workability and consistency. It is well known that increasing the amount of water can negatively affect the strength properties of hardened concrete. In the study [8], authors found that slag has a higher water absorption capacity than the aggregate typically used.

Cement in the concrete mixtures was replaced with coarsely and finely ground slag obtained from the cupola furnace. The substitution of cement with slag was carried out in the range from 10 to 100%. However, it is important to note that samples where the cement replacement with slag exceeded 60% showed high brittleness and insufficient strength, leading to their disintegration during regular handling. The preparation and treatment process of these samples was consistent with the methodology described in previous sections. Attention was primarily focused on monitoring the effect of substitution on the compressive strength of concrete, which was critically affected by the amount of slag used.

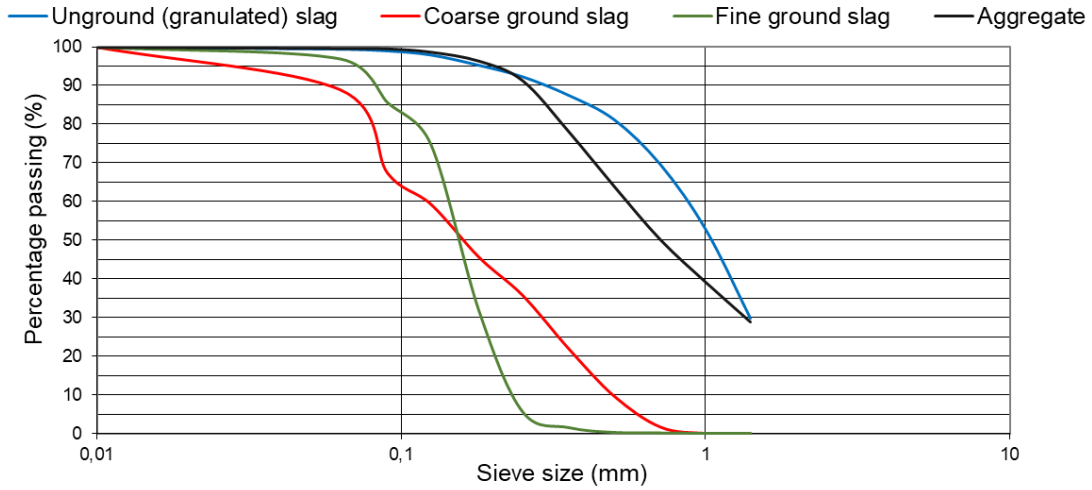


Fig. 3 Sieve analysis of materials used

RESULTS AND DISCUSSION

A detailed analysis of the impact of substituting traditional aggregate with granulated cupola slag, used in its natural (granulated) state, on the properties of concrete after hardening has revealed significant changes in its mechanical properties. According to the graph (Fig. 4), which illustrates the results of our measurements in detail, it is evident that directly replacing just 5% of the aggregate with slag significantly affects both the compressive strength and the flexural strength. This decrease in strength is considerable, yet it is remarkable that further increasing the slag content beyond 5% does not significantly reduce the mechanical characteristics of the concrete, even in the case of complete aggregate replacement. This phenomenon indicates a possible limit to the influence of the slag used on the mechanical properties of the concrete, which opens

the way for further investigation of the optimum amount of slag to maintain the desired properties of the concrete.

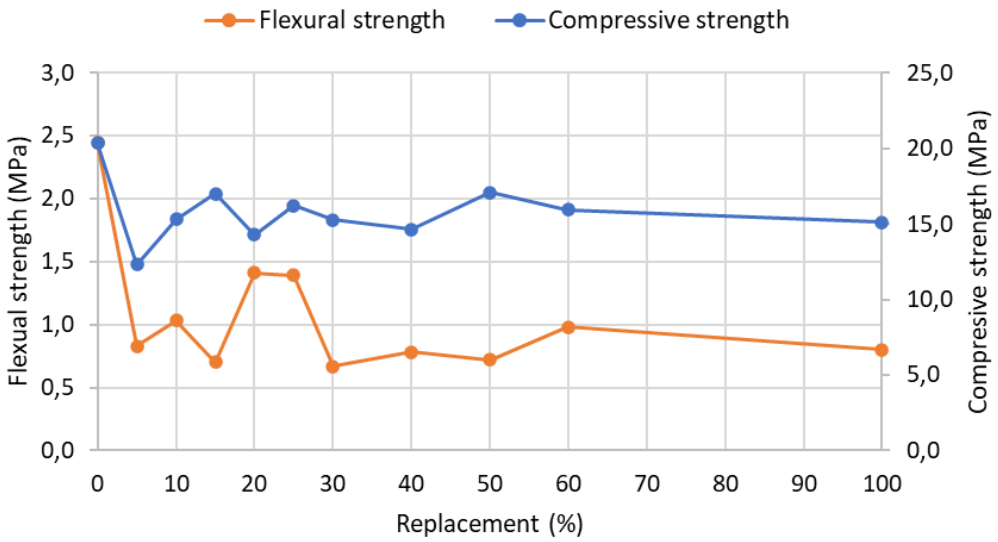


Fig. 4 The impact of substituting aggregate with granulated (unprocessed) cupola furnace slag on compressive strength and flexural strength

The integration of fine ground blast furnace slag into the concrete production process could be a key contribution to achieving sustainability in concrete practices. Experimental results show that fine ground slag has a similar effect on the flexural strength of concrete as slag used in its natural state. Findings indicate that there was no significant difference in flexural strength between the two types of slag (Fig. 5). Both slag variants exhibited similar behavior, suggesting that the granulometric composition of finely milled and granulated slag, when replacing aggregate, does not have a significant impact on the flexural properties of concrete. On the other hand, compressive strength test results revealed interesting differences. After substituting traditional aggregate with fine ground slag, there was a significant increase in compressive strength, reaching up to 35 MPa, which represents a 40% improvement compared to the reference sample without slag. This considerable increase in compressive strength can be attributed to the activation of the hydraulic properties of the slag, which were described at the beginning of the article. However, when exceeding a 25% slag content in the concrete mixture, a reverse trend was observed, where compressive strength began to decrease. This phenomenon points to potential limitations at higher slag concentrations and the need for further research to optimize its proportion in the mix. The negative effects on flexural strength, found when using blast furnace slag as an aggregate replacement, indicate potential challenges in applications where high flexural strength is important. This finding is critical for constructors and engineers, as it highlights the need to thoroughly assess the suitability of the material depending on the required mechanical properties of concrete structures.

https://doi.org/10.5593/sgem2024/4.1/s18.34

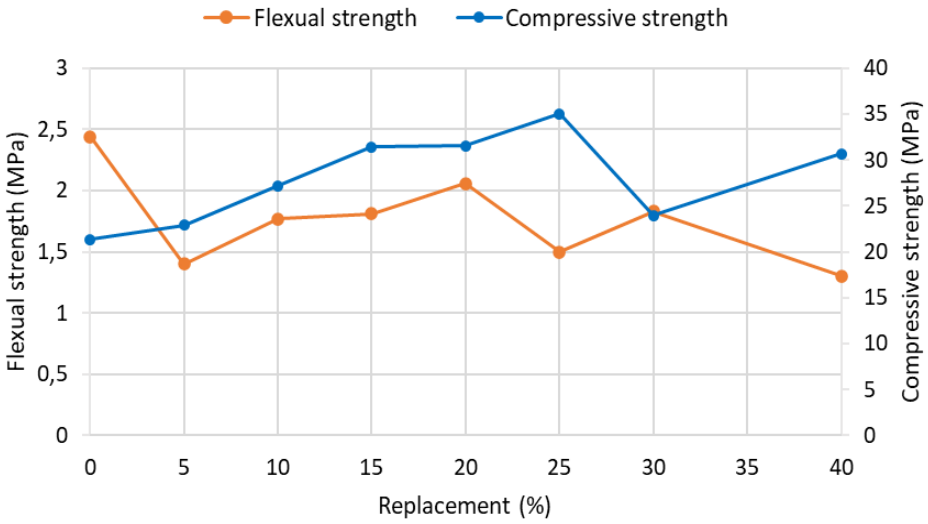


Fig. 5 The impact of substituting aggregate with fine grounded cupola furnace slag on compressive strength and flexural strength.

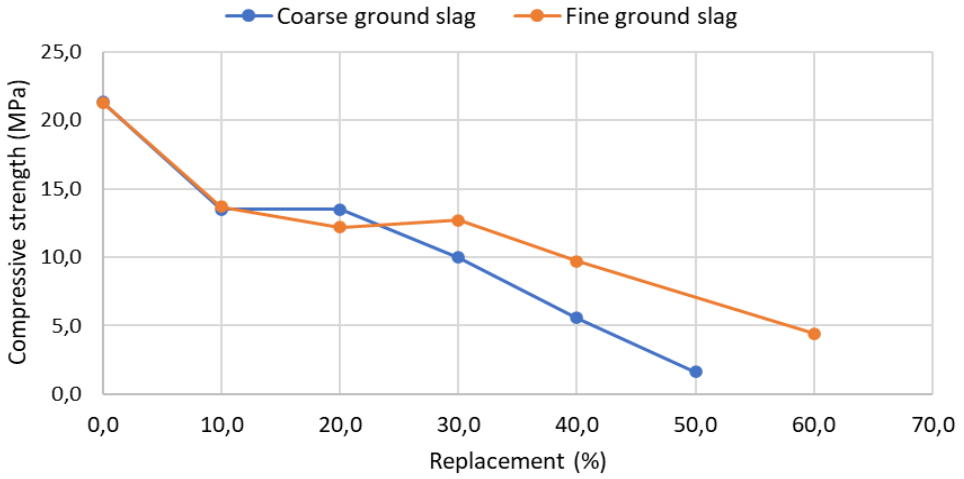


Fig. 6 The impact of replacing cement with ground cupola furnace slag of various granulometric compositions on the compressive strength of concrete.

Replacing cement with slag from blast furnaces was motivated by the need to reduce the environmental impact of cement production. Despite the positive environmental reasons, however, the results revealed significant negative effects on the quality and properties of the hardened concrete. It is important to note that even with the fine grounding of blast furnace slag, its granulometric composition significantly differed from the granulometry of commonly used Portland cement. This difference was a result of the limitations of our grounding, which under the given conditions did not allow achieving a granularity identical to that of cement. This fact contributes to the understanding of the observed differences in compressive strength and emphasizes the need for a more detailed examination of the granulometric characteristics of alternative materials in the context of their impact on the mechanical properties of concrete. Figure 6 illustrates the impact of substituting cement with slag on concrete strength. It is evident that the compressive strength decreases proportionally with the increase in the

proportion of slag replacing cement, regardless of its granulometric composition and degree of fineness of grounding. This trend confirms that the granularity and grounding of the slag have a secondary significance compared to the actual volume of replaced cement in the mix. As a result of these observations, it can be stated that although grounding of slag can achieve certain improvements in its reactivity, the volumetric proportion of slag in the concrete mix plays a critical role in the resulting compressive strength. These findings are essential for engineers and designers of concrete mixtures, as they underline the importance of carefully designing mixtures using slag as an alternative to cement.

CONCLUSION

Our studies suggest that slag from blast furnaces can be a valuable material for more environmentally sustainable construction practices. The conclusion of our study highlights the significant impact of using blast furnace slag as a replacement for traditional aggregate or cement in concrete mixes. Findings indicate that slag substitution can, in some cases, increase the compressive strength of concrete. In other cases, such as replacing aggregate with granulated slag or replacing cement with milled slag, there is a decrease in the strength properties of hardened concrete even at minimal slag proportions.

The research also suggests that fine milling of the slag can improve its reactive properties, although our milling process did not achieve a granulometric composition comparable to standard Portland cement. This fact is key to understanding how the granulometric differences of the used materials affect the final properties of concrete. In conclusion, further research should include studies focused on detailed examination of different ways of modifying slag and their impact on concrete properties. Optimal use of blast furnace slag could contribute to the development of more sustainable concrete mixes, which would simultaneously improve material properties and reduce the need for traditional raw materials.

ACKNOWLEDGEMENTS

This work was supported by the Scientific Grant Agency of The Ministry of Education of the Slovak republic No. VEGA 1/0002/22 and APVV-22-0580

REFERENCES

[1] Chakravarty, S., Haldar, P., Nandi, T., & Sutradhar, G. (2021). Cupola Slag Reutilization for Sustainable Waste Management: Review and Economic Analysis. International Journal of Environmental Science and Technology, 20(1), 1169–1184. doi:10.1007/s13762-021-03574-x

[2] Modern Casting January 2023 Page 34. Modern Casting [Online]. 10 January 2023. Available online: https://www.qgdigitalpublishing.com/publication/?m=55001&i=778043&p=36&ver=html5 (accessed on 4 March 2024).

[3] Sikder, R., Chakravarty, S., Haldar,P., Nandi,T., Sutradhar,G. (2023). Scope for cupola slag reuse in construction: a sustainable green solution. International Jornal of Environmental Science and Technology 20:7019-7028. doi.org/10.1007/s13762-022-04257-x

https://doi.org/10.5593/sgem2024/4.1/s18.34

[4] Raja, R., Kumar,S. (2023). Cupola slag as a green concrete – making material and its performance characteristics – A review. Renewable and Sustainable energy Reviews, Vol.185, 113573

[5] Vlcek,J., Svrcinova,R., Burda,J., Topinkova,M., Klarova,M., Ovcarcikova,D., Jancar,D., Velicka,M.(2016). Hydraulic properties of ladle slags. Metalurgija (55) 3, 399 – 402.

[6] Thakur,K.K., Rahman, A., Shafeeq,M.M., Mondal,D.P. (2022). Effect of cupola furnace slag addition on the characteristics of ordinary Portland cement blocks. Journal of Sustainable Metallurgy, 8:1606-1616. doi.org/10.1007/s40831-022-00586-w

[7] Pribulova, A., Baricova, D., Futas, P., Pokusova, M., & Eperjesi, S. (2019). Cupola Furnace Slag: Its origin, properties and utilization. International Journal of Metalcasting, 13(3), 627–640. doi:10.1007/s40962-019-00314-3

[8] Alabi, S. A., & Mahachi, J. (2022). Performance of concrete made from cupola furnace slag and recycled concrete aggregate. Materials Today: Proceedings, 62. doi:10.1016/j.matpr.2022.02.095

[9] Waseem, S. A., Thakur, N., Islam, S. U., Kumar, M., & Saini, J. S. (2021). Cupola slag as partial replacement of fine aggregate in concrete – an experimental study. Journal of Building Engineering, 44, 103343. doi:10.1016/j.jobe.2021.103343

[10] Sikder, R., Chakravarty, S., Haldar, P., Nandi, T., Mandal, S., & Sutradhar, G. (2023). Cupola slag as partial replacement of coarse aggregate in concrete. Materials Today: Proceedings. doi:10.1016/j.matpr.2023.03.190Title of the paper, International Scientific Event, Country, vol. 3, pp 185-193, 2000.

FACTORS INFLUENCING SELECTIVE WASTE COLLECTION

M Sc, Eng. Jakub Tytko[1]

Prof. Dr, D.Sc. Eng. Mohamed Alwaeli[1]

Silesian University of Technology, **Poland**

ABSTRACT

Waste management is a current and future challenge due to the increasing volume of waste. The amount of waste generated directly correlates with production and consumption patterns. The current level of natural resource utilization exceeds the Earth's capacity for replenishment. Therefore, humanity must take action to mitigate the consequences of rampant natural resource consumption. One way to achieve this goal is to increase the level of waste recycling. However, the amount of waste actually recycled is significantly lower than the theoretical processing capacity. Understanding human behavior is essential for improving efficiency and developing an integrated and effective recycling strategy.

The growing number of products sold poses a challenge. The challenge is growing number of products sold. Consequently, we reach a point where not only the technical aspects of collection and recycling are important, but the sociological aspect also proves essential for understanding the complexity of the problem. Demographic changes, such as the increase in single-person households, also affect the amount of waste generated. Factors such as social policy, the provision of additional benefits and subsidies, income growth, and lifestyle changes are also influencing factors affecting waste generation patterns, and these changes are noticeable. The quantity of municipal waste generated depends not only on population size but also on consumption patterns and economic prosperity. Other factors influencing the type and quantity of waste generated include the type of area (urban, rural), population density, type of housing (single-family, multi-family), number of tourists, existence of public facilities, and the type, size, and number of advertising, industrial, and service facilities. Pandemics and natural disasters occur suddenly and always have a measurable impact on waste management.

Keywords: waste management, selective collection, recycling behavior, socioeconomic factors, community participation

INTRODUCTION

Waste management is emerging as one of the most pressing challenges of the 21st century, exacerbated by rapid urbanization, industrial growth, and increasing consumption patterns. The surge in waste production has outpaced the development of effective management systems, leading to significant environmental, economic, and social concerns. At the heart of these challenges lies the critical issue of selective waste collection and recycling, processes that are not only reliant on technological advancements but are profoundly influenced by human behavior and societal engagement.

https://doi.org/10.5593/sgem2024/4.1/s18.35

Effective waste management systems hinge on the active participation of communities, particularly in the initial stages of waste sorting at the source. As the demand for high-quality secondary raw materials grows, the importance of reducing contamination through proper waste segregation becomes paramount. However, the success of such systems is not solely dependent on the availability of advanced infrastructure or stringent regulations. It is equally contingent on the willingness and motivation of individuals to engage in these practices. Understanding what drives or deters people from participating in selective waste collection is crucial for improving recycling rates and ensuring the sustainability of waste management systems.

Socio-economic factors, such as income levels, education, and lifestyle, play a significant role in shaping waste management behaviors. Additionally, psychological elements, including individual attitudes, perceptions of convenience, and moral and social norms, are critical in determining how and to what extent people engage in recycling activities. For instance, the perception of convenience—whether it be the proximity of recycling facilities, the frequency of waste collection, or the ease of sorting materials—can greatly influence an individual's likelihood to participate in waste sorting. Moreover, the level of trust in local authorities and the perceived fairness and transparency of waste management policies can either encourage or discourage public cooperation.

Beyond individual behaviors, broader social dynamics also come into play. Cultural factors, community norms, and collective attitudes toward environmental responsibility can either foster a culture of recycling or contribute to its neglect. In collectivist societies, for example, social norms and peer influence may significantly impact waste management practices, with individuals more likely to engage in recycling if it is perceived as a community norm. Conversely, in more individualistic cultures, personal ethics and a sense of moral responsibility may play a more dominant role.

This article delves into these complex and multifaceted factors, examining how they intersect to influence waste management outcomes. By exploring the interplay between socio-economic conditions, psychological motivations, and infrastructural elements, the discussion aims to shed light on the importance of designing waste management systems that are not only technically efficient but also socially inclusive and responsive to the needs and behaviors of the communities they serve. The goal is to provide a comprehensive understanding of the factors that drive effective waste management and to offer insights into how these systems can be optimized to enhance participation, increase recycling rates, and ultimately contribute to a more sustainable and environmentally conscious society.

RELATED WORK

Experiences show that active participation of society in waste management systems is a crucial element of selective waste collection. As the requirements for the quality of secondary raw materials become increasingly stringent, the involvement of residents in selective collection of secondary raw materials from households at the source is crucial for reducing pollution. This is also essential for improving the overall efficiency of recycling and enabling maximum recovery of high-quality useful materials [1]. Residents and their behaviors are the key links in increasing recycling rates [2].

Experiences also indicate that effective selective collection systems depend on how well society participates in them [3]. Important factors for the success of community participation in selective collection include socio-economic factors as well as the perception of practical, health, and environmental benefits. Additionally, the availability of effective infrastructure enabling residents to sort materials near households is certainly a key component of any recycling program that motivates residents to use such infrastructure [4]. Human recycling behaviors also vary depending on the location; for example, the level of waste sorting at workplaces is noticeably lower than at residential areas [5]. However, the availability of effective infrastructure is crucial for the overall success and effectiveness of selective collection, and consequently, waste recycling [6].

In addition to technical and organizational actions, the level of collection largely depends on residents' interest in participating in segregation and sorting of secondary raw materials. Therefore, it is necessary to consider how to influence residents' awareness and motivate them to cooperate. Developing a system that caters to individuals of different ages, genders, places of residence, and belonging to different social strata is essential. To achieve this, it is necessary to understand the "barriers" that discourage or prevent society from participating in selective collection and how they can be overcome. Understanding the reasons why society does not participate in selective collection is undoubtedly the first step toward promoting actions related to selective collection of secondary raw materials. The next step is to attempt to categorize barriers into different types based on an understanding of behaviors related to selective collection and what influences them [4].

In the process of creating and improving effective selective collection systems, understanding the underlying social factors influencing societal behavior is commonly underestimated but of great importance. The Value-Belief-Norm (VBN) theory defines environmental behavior as behavior relevant to the environment and suggests that values influence pro-environmental behaviors through environmental beliefs and personal standards - moral norms [7]. Social factors are defined as any influences that affect individual or group behavior [8].

Many studies on social environmental behaviors generally rely on the Theory of Planned Behavior (TPB) and examine the extent to which there are important connections between four fundamental variables: attitude, motivation, knowledge, and behavior. The basic premise is that behavior is an implication of knowledge and understanding, combined with attitude [9]. Additionally, personal ethics are a significant factor influencing the promotion of residents' behaviors in participating in waste sorting [10]. Many scholars argue that values, the goals people pursue in life, influence or guide preferences and behaviors. It is widely believed that values mainly influence behavior indirectly, through beliefs, attitudes, and norms. The VBN theory specifies three types of value orientations that determine pro-environmental behaviors, namely: egoistic, altruistic, and biospheric. Individuals with strong egoistic values will particularly value and consider the consequences for their personal benefits. In contrast, individuals with strong altruistic values will focus more on the consequences for other people. Finally, people with strong biospheric values will focus on the consequences for nature and the environment [7].

Jackson [11] states that there are two theoretical research methods on societal environmental behavior:

https://doi.org/10.5593/sgem2024/4.1/s18.35

- the method based on environmental sociology, which starts from the interaction between micro-individuals and socio-environmental systems and assumes that individual behavioral intentions are determined by the process and state of socio-technological development,

- the method based on environmental psychology, which mainly concerns the influence of irrational factors on individual behavior.

One of the most important factors increasing household waste sorting behaviors is convenience [12]. The more the system corresponds to local conditions, the more efficient it is. However, the perception of convenience depends on the individual who wants to participate in the sorting system. To personalize the system, it is necessary to combine the project action plan with a deeper understanding of the characteristics of the system users [1]. Incidentally, perceived effort, especially the time factor, is also associated with convenience [8]. Although some may not consider external factors (referred to as situational-contextual, technological, or organizational) as socio-psychological, since they are related to infrastructure and service provision, they are significant in behavioral contexts. They seem to influence internal factors [13]. In fact, the lack of necessary infrastructure may be one of the most important barriers for households to participate in selective collection activities [14]. Even small changes increasing convenience can significantly affect behavior. Factors that could potentially affect convenience include:

- short distance and strategic location of secondary raw material collection points,
- appropriate storage space in households,
- optimal collection frequency,
- clean collection points,
- location of containers and easy access, while keeping them clean and well-marked [1].

Negative behavioral features may also result from aspects of design schemes that lead to inconvenience. Social norms are one of the variables that determine the level of convenience perceived by individuals and also have a significant impact on behaviors related to selective collection, especially in collectivist cultures. Another factor is moral norms, which motivate behaviors and intentions related to sorting household secondary raw materials. Compared to social norms, which are enforced by explicit approval or disapproval from others, moral norms have a direct impact on residents' behaviors [8]. People can develop a sense of moral responsibility for sorting secondary raw materials if they are aware of the negative consequences of not sorting them or if they have a need to comply with the law. Residents will sort secondary raw materials if they feel personally responsible for it [8]. An amoral norm means that individuals sanction themselves, while a social norm is enforced by explicit approval or disapproval from others. However, in practice, making a clear empirical distinction between these two types of norms may be difficult, especially since all social influences are assigned to internalized standards (norms). In other words, moral norms are activated by social interactions. Another factor influencing behavior and willingness to sort waste is environmental concern.

Another driver of behaviors related to selective collection is society's trust in local authorities. Residents with good relationships with local authorities are more open to

selective collection requirements and demonstrate better results. Activities that take place daily under similar conditions (habits) can also influence behavior. Transforming residents' habits to automatically sort waste into different containers from using one bin requires strong internal motivation, influenced by attitudes and social norms [15].

Additionally, economic factors and legal regulations are external elements that strongly influence societal behaviors related to selective collection and can also affect moral norms. Besides psychological and economic factors, attitudes are also influenced by a wider socio-demographic range, such as education level, age, financial stability, type of housing, unemployment, gender, as well as cultural aspects. Therefore, the system should be tailored to the characteristics of target social groups.

The diversity of factors influencing societal behaviors makes it worthwhile to acquire specialized knowledge [15]. To change behavior in a way that serves both individuals and society, it is necessary to combine environmental sciences, economics, social psychology, and ecology. Non-governmental organizations, social groups, scientists specializing in applying behavior change theories in the secondary raw materials sector, behavioral analysis teams consisting of psychologists and economists, and specially trained environmental and secondary raw materials consultants can be involved in this process.

DISCUSSION

Sociological factors appear to be very complex (figure 1) and multifaceted. At the same time, humans, as significant elements of waste management, have a considerable influence on waste collection, which ultimately affects the quantity and quality of secondary raw materials. The impact of participants' behavior, as it greatly affects the

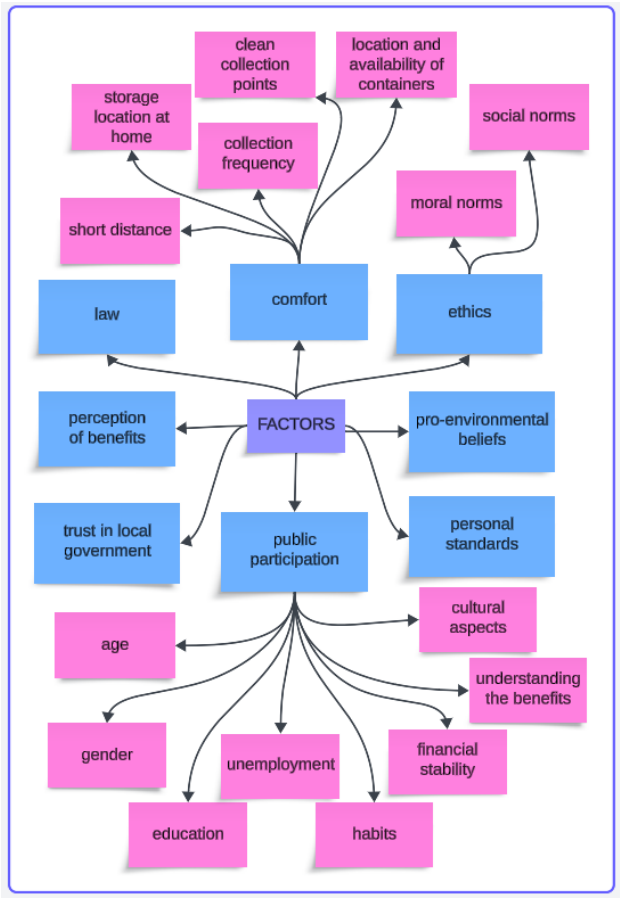


Figure 1 Factors influencing selective waste collection

https://doi.org/10.5593/sgem2024/4.1/s18.35

final outcome of recycling systems, should be a key consideration during the design of waste management systems, including collection, recovery, and processing systems. Even the best technically designed system will not be effective without the willingness and engagement of participants. Observing existing waste management systems and their implementations, one may have the impression that many of the factors mentioned in the text are overlooked. However, long-term observations allow us to notice positive changes towards a system that recognizes the significant role of humans. Increasing awareness of the existence of factors and their relationships will contribute to the creation of a user-oriented system, which will result in greater people's involvement and, consequently, increased efficiency of the entire system.

CONCLUSION

Based on the above text, it can be concluded that understanding the various social, psychological, economic, and regulatory factors influencing societal behavior is crucial for the development and improvement of effective selective collection systems. The Value-Belief-Norm Theory (VBN) highlights the importance of values, beliefs, and moral norms in shaping pro-environmental behaviors, while the Theory of Planned Behavior (TPB) emphasizes the role of attitudes, motivation, knowledge, and behavior. Convenience, trust in local authorities, social norms, moral norms, concern for the environment, economic factors, and legal regulations are identified as key drivers of behavior related to waste sorting. Personalizing collection systems to local conditions and user characteristics, as well as addressing perceived effort and convenience, can significantly influence participation in selective collection activities. Furthermore, the engagement of various stakeholders, including NGOs, social groups, scientists, and consultants, is essential for implementing behavior change strategies that benefit both individuals and society.

ACKNOWLEDGEMENTS

The work was supported in part by the doctorate project no. DWD/6/0513/2022 (RJO15/SDW/006-54).

REFERENCES

[1] Varotto A., Spagnolli A., Psychological strategies to promote household recycling. A systematic review with meta-analysis of validated field interventions., Journal of Environmental Psychology, vol. 51, 2017, pp 168-188;

[2] Perrin D., Barton, J., Issues associated with transforming household attitudes and opinions into materials recovery: a review of two kerbside recycling schemes, Resources, Conservation and Recycling, vol. 33/Issue 6, pp 61-74, 2001.

[3] Thomas C., Public understanding and its effect on recycling performance in Hampshire and Milton Keynes, Resources, Conservation and Recycling, vol. 32/issue 3-4, pp 259-274, 2001.

[4] Alwaeli N.A., Recykling w ujęciu gospodarki o obiegu zamkniętym : rola, bariery, stymulowanie, Politechnika Śląska, Poland, 2022.

[5] Brito J.S., Chaves B. R., de Sousa G.F., de Souza Vale J. G., de Miranda M. E. M., Mariano A. M., Factors influencing waste sorting for Selective Collection in a Brazilian monetary institution, Procedia Computer Science, vol. 214, pp 1121-1127, 2022.

[6] Parrot L., Sotamenou J., Dia B. K. Municipal solid waste management in Africa: Strategies and livelihoods in Yaoundé, Cameroon, Waste Management, vol. 29/issue 2, pp 986-995, 2009.

[7] Hiratsuka J., Perlaviciute G., Steg L., Testing VBN theory in Japan: Relationships between values, beliefs, norms, and acceptability and expected effects of a car pricing policy, Transportation Research Part F: Traffic Psychology and Behaviour, pp 74-83, 2018.

[8] Miafodzyeva S., Brandt N., Recycling behaviour of householders: synthesizing determinants via a meta-analysis. Waste and Biomass Valorization, vol. 3, pp 221-235, 2013.

[9] Lizina S., Van Dael M., Van Passel S., Battery pack recycling: Behaviour change interventions derived from an integrative theory of planned behaviour study, Resources, Conservation and Recycling, vol. 122, pp 66-82, 2017.

[10] Nguyen T.T.P., Zhu D., Le N.P., Factors influencing waste separation intention of residential households in a developing country: Evidence from Hanoi, Vietnam, Habitat International, vol. 48, pp 169-176, 2015.

[11] Jackson T., Name2 S. T., Motivating sustainable consumption: A review of evidence on consumer behaviour and behavioural change, University of Surrey Guildford, Surrey 2005.

[12] Bernstad A., Household food waste separation behavior and the importance of convenience, Waste Management, vol. 34/issue 7, pp 1317-1323, 2014.

[13] Tonglet M., Phillips P. S., Read A.D., Using the Theory of Planned Behaviour to investigate the determinants of recycling behaviour: a case study from Brixworth, UK, Resources, Conservation and Recycling, vol. 41/issue 3, pp 191-214, 2004.

[14] Timlett R.E., Williams I.D., The impact of transient populations on recycling behaviour in a densely populated urban environment, Resources, Conservation and Recycling, vol. 53/issue 9, pp 498-506, 2009.

[15] Li C.J. Huang Y.Y., Harder M.K., Incentives for food waste diversion: Exploration of a long term successful Chinese city residential scheme, Journal of Cleaner Production, vol. 156, pp 491-499, 2017.

https://doi.org/10.5593/sgem2024/4.1/s18.35

HIGH STRENGTH ZOLOGYPSUM COMPOSITE

Prof. Dr. Victoria Petropavlovskaya

Assoc. Prof. Dr. Kirill Petropavlovskii

Mr. Petr Kalyaskin

Assoc. Prof. Dr. Tatiana Novichenkova

Prof. Dr. Mikhail Sulman

Tver State Technical University, **Russia**

ABSTRACT

Gypsum composites are promising building materials, but they have disadvantages such as low strength and water resistance. To improve these properties, a self-reinforcement method can be used, where the gypsum matrix is reinforced with crystals other than gypsum. One type of such crystals is ettringite. To obtain a self-reinforced gypsum composite, it is necessary to maintain a high pH environment and sufficient ions to form ettringite. In this work high-calcium fly ash, which is a waste product of coal combustion and contains about 50% CaO and 20% SiO_2, is used. This ash has a problem with late hydration, which negatively affects the final strength of the composite. Therefore, aluminosilicate component of bottom ash and microsilica are added to the composite. This allows to maintain high pH of the medium necessary for ettringite formation. High-calcium fly ashes stored in ash dumps represent an ecological problem for many regions of the country. One of the ways to realise these ashes is their use in construction composites based on gypsum binder. In this work the possibility of obtaining self-reinforced gypsum composite of high strength with the use of high-calcium fly ash, aluminosilicate component and microsilica has been investigated. The purpose of this work is to study the effect of the addition of the aluminosilicate component of bottom ash and microsilica on the strength of a self-reinforced gypsum composite.

Keywords: self-reinforced gypsum, composite, high-calcium fly ash, ettringite.

INTRODUCTION

The use of gypsum compositions has a long tradition dating back thousands of years. Gypsum has a number of advantages: low cost, simple production, relative distribution, fast setting, fire resistance, etc.. However, with the advent and spread of hydraulic binders in the first half of the 19th century, gypsum becomes less popular [1]. The disadvantages of gypsum, which are primarily low strength, water resistance and creep, do not allow its full use as a construction material. One of the approaches to solving this problem is, according to the theory of multilevel reinforcement, the use, first of all, of self-microreinforcement or self-reinforcement [2]. Self-reinforcement is the reinforcement of the microlevel of the material by artificial or synthesized crystals in the process of hydration, which reinforce and modify the binder matrix. For gypsum, effective formulations using ettringite as a synthesizable crystal have already been obtained. For this purpose, aluminum sulfate and lime are added to the gypsum solution.

https://doi.org/10.5593/sgem2024/4.1/s18.36

Both in Russia and in most developed countries the utilization of fly ash and, in particular, high-calcium fly ash is an extremely urgent problem. Thermal power plants and combined heat and power plants operating on lignite and hard coal as a result of their operation leave a large amount of chemically active ash. The remaining unutilized ash is dumped or stored in ash dumps, which leads to land degradation [3] and also poses a great potential threat to human life and health [4]. Additional economic burden associated with the development and maintenance of disposal sites falls on the coal plant, which also increases the cost of production. At the same time, fly ashes have a great potential for recycling as they contain glassy aluminosilicate phase [5], while high calcium fly ashes also contain a large amount of free lime CaO, which can replace the usual chemically pure lime obtained by decarbonization of limestone $CaCO_3$, which will also reduce energy costs. Thus, today ash is already used as an additive in wastewater treatment [6], as well as in a number of construction materials [6], [7]

In Russia some of the largest volumes of high-calcium fly ash come from Berezovskaya GRES. The ash from this power plant, produced by burning charcoal, has a high amount of free lime (up to 30%), which has a high potential for application. However, the hydration of ash does not occur at the same time, part of calcium oxide hydrates already after the formation of binder structure, due to which many materials with it are destroyed from the inside by CaOH late hydration [8]. One of the suggested ways to solve this problem is the use of pozzolanic additives [9], which could bind the excess lime, thus strengthening the composite structure.

Various types of microsilica can be used as pozzolanic additives as well as aluminosilicate spheres derived from slag and ash [10], [11]. The aluminosilicate component in early terms can reduce the strength of the composite [12], which does not allow to evaluate the quality of the effect of pozzolanic additives up to 28 days. In works [12], [13] it is shown that the use of aluminosilicate microspheres changes the structure of mineral binder compositions based on gypsum.

It should also be noted that the moisture content of the composite has a great influence on the rate of reactions. If there is a lack of moisture, the processes of ettringite synthesis and pozzolanic reactions can be slowed down or disrupted altogether. Thus, this study is devoted to the possibility of using pozzolanic additives in self-reinforced gypsum composites under different conditions.

MATERIALS

High-strength gypsum G-16 Samaragips together with hyperplasticizer PC-1021 Eurochem was chosen as gypsum binder. Berezovskaya fly ash - high-calcium fly ash was selected as fly ash, chemical composition of which is given in Table 1.

Table 1. Chemical composition of high calcium ash from the Beryozovsky lignite deposit.

SiO_2, %	Al_2O_3, %	Fe_2O_3, %	TiO_2, %	CaO, %		MgO, %	SO_3, %	R_2O, %
				all	free			
11.30-42.78	5.10-10,10	8.00-24.20	0.33-0.65	26.34-54.00	2.00–21.70	4.85-9.10	1.43-10.00	0.87-1.98

As pozzolanic additives were chosen microsilica (MS) as well as aluminosilicate component of Kashirskaya ash (ACKA). Their chemical compositions are given in Tables 2. Hereinafter samples with addition of microsilica will be designated as MS

samples and with aluminosilicate component of Kashira ash as ACKA samples. For mixing the mixture was used aluminum sulfate solution and distilled water.

Table 2. Chemical composition of pozzolanic additives.

Oxide	Na_2O	MgO	Al_2O_3	SiO_2	K_2O	CaO	TiO_2	MnO	Fe_2O_3	P_2O_5	SO_3	C
	Content, %											
MS	-	1.01	0.68	92	-	-	-	-	-	-	-	-
ACKA	0.6	1.6	21.5	57.8	2.1	2.3	0.9	0.1	4.6	0.4	0.1	3.2

In all investigated compositions the amount of gypsum, fly ash, hyperplasticizer, as well as the mass of dry part were chosen as unchangeable. Thus, relative to the weight of the dry part the weight of each component was: for gypsum - 79%, plasticizer - 1%, fly ash together with pozzolanic additive - 20%.

The studied formulations differed in the ratio m(pozzolanic additive)/m(Fly ash), which was assumed for both MS and ACKA formulations to be 0; 0.25; 0.66; 1.55; 4, respectively. Thus, 2 series of formulations of 5 points each were investigated, in which 0 point is common.

METHODS

Fabrication. When preparing the mixture, gypsum, ash and pozzolanic additive were first mixed until the ash and additive were evenly distributed in the volume of gypsum, then a one-normal solution of aluminum sulfate and a saturated solution of lime were mixed. Hyperplasticizer was added to the resulting solution and then mixed until it was completely dissolved. The last step was the gradual addition of the dry portion to the mortar with constant manual stirring. 2x2x2x2 cm cube specimens were selected as the specimens for strength testing. After preparing the mixtures according to the above methodology, they were poured into standard steel molds. After the moment of the end of setting, the specimens were taken out of the molds and stored.

Sample storage. All samples were divided into 3 main groups. The samples of the first group were stored in open, normal conditions. The samples of the second group were placed in a desiccator containing a desiccant and further sealed with an airtight lid. The samples of the third group were placed in a desiccator filled with water so that the samples did not come in contact with water (Table 3).

Testing. Before testing, the specimens were taken out of their storages, dried to constant mass in a desiccator. The geometric parameters and mass of each specimen were then determined. After that, the cubes were tested by means of a hydraulic press in compression until complete destruction according to the standard methodology.

https://doi.org/10.5593/sgem2024/4.1/s18.36

Table 3. Relative humidity of samples

Additive type	Conditions of curing	m (pozzolanic additive)/m (Fly ash)				
		0	0.25	0.66	1.5	4
MS	Dry	-	0.03	0.07	0.69	0.7
	Humid	-	0.06	0.02	0.11	0.1
	Normal	-	0.98	0.79	0.56	0.8
ACKA	Dry	-	0.06	0.11	0.55	0.01
	Humid	-	0.12	0.03	0.08	0.01
	Normal	-	0.9	1.2	1.44	0.79
No additive	Dry	0.09	-	-	-	-
	Humid	0.47	-	-	-	-
	Normal	1.37	-	-	-	-

RESULTS

During the experiments, results were obtained for the relative moisture content of the samples, their compressive strength and density (Figure 1, Figure 2) and specific compressive strength (Figure 3, Figure 4).

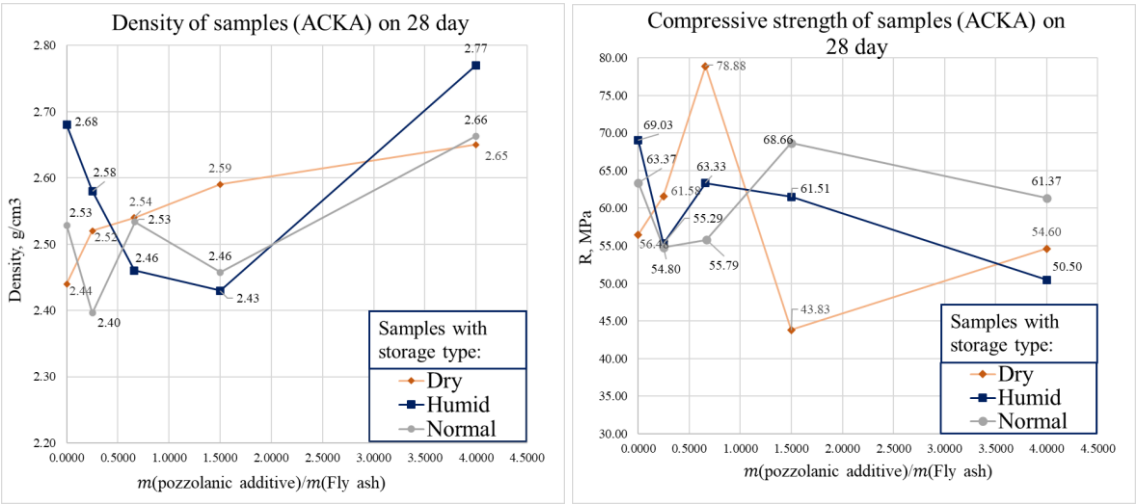


Figure 1. Density and strength of composites using aluminosilicate component of Kashira ash on 28 day.

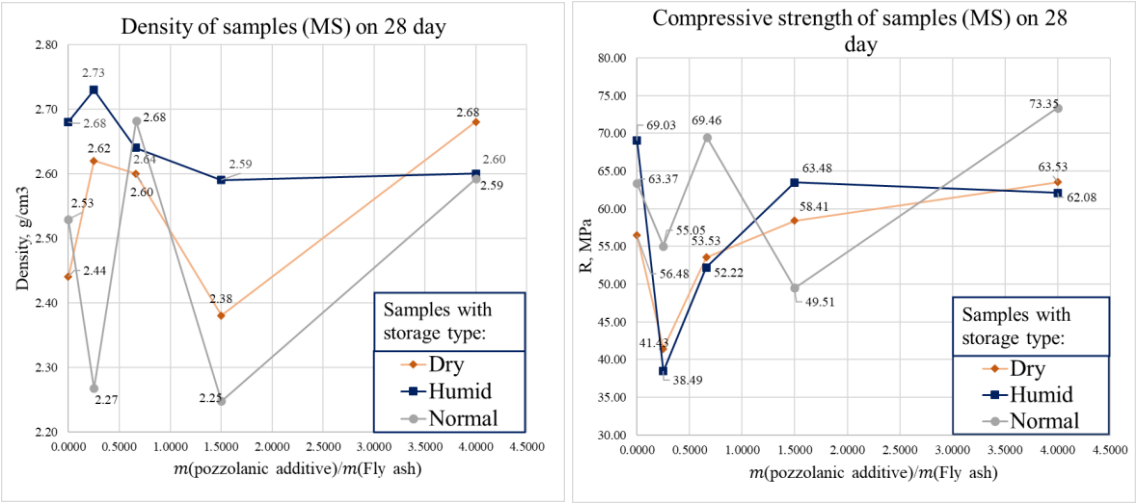


Figure 2. Density and strength of composites using microsilica on 28 day.

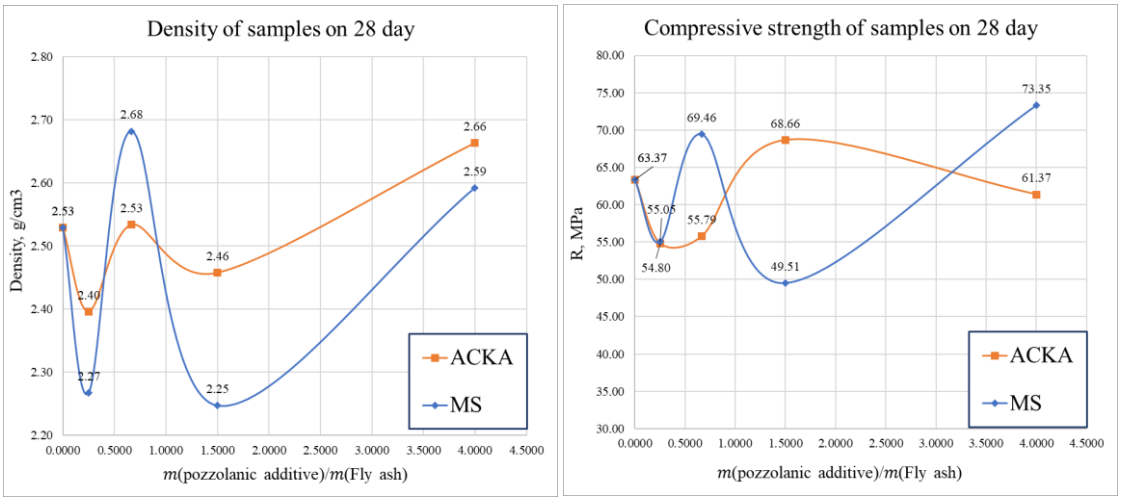


Figure 3. Comparison of density and strength of composites with different pozzolanic additives.

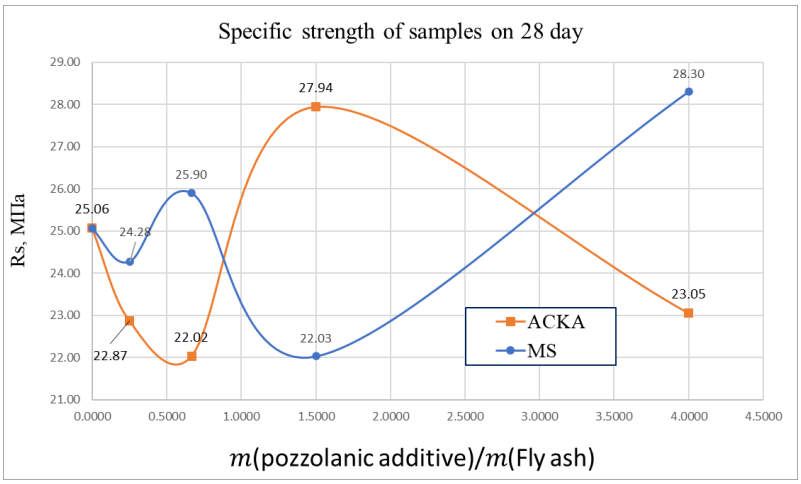


Figure 4. Comparison of specific strength of composites with different pozzolanic additives.

https://doi.org/10.5593/sgem2024/4.1/s18.36

DISCUSSION

The obtained data indicate the presence of both expected and unexpected results.

On the one hand, it can be said that the proposed compositions showed high compressive strength and are promising for further investigation to implement the results. When comparing the strength and density of the composites at 28 days obtained with the addition of ACKA and MS it can be said about the more «compressed» function of MS. This is quite understandable, since it is assumed that microsilica contains a greater number of particles of amorphous phase, which are more active in the reaction, providing a pozzolanic effect. At the same time, the composite using aluminosilicate component of hydrous fly ash showed high values of relative strength.

At the same time, the data obtained considering different ways of ageing the specimens are extremely ambiguous. All samples contain traces of late hydration of Berezovskaya fly ash, which indicates that the pozzolanic effect was insufficient to completely bind excess $Ca(OH)_2$. At the same time relative humidity of samples stored in all types of conditions was extremely low, and did not exceed a few percent.

CONCLUSION

The study investigated the possibility of using the pozzolanic effect on self-reinforced gypsum composites. According to the research results, it was found that:

1) The use of pozzolanic additives in given intervals does not disturb the process of ettringite formation, which results in increased strength relative to the strength of gypsum stone.

2) All composites, regardless of storage conditions have extremely low relative humidity, which can be explained by the extremely high density of the structure of the self-reinforced stone. This result is quite important, since no studies have been conducted to find the equilibrium moisture content of self-reinforced gypsum composites. This low relative humidity of such composites may indicate that the water resistance problem of gypsum, and consequently creep, has been partially overcome.

3) Since composites stored in dry conditions also showed the presence of late hydrated lime, it can be said that the moisture contained in the mixture at the time of setting of gypsum dough is sufficient for late hydration of particles of Berezovskaya fly ash.

4) The humidity at which the composites are stored has a significant influence on the strength and density of the material, and this dependence is not linear, at which the best conditions would be the most humid or on the contrary the driest.

The most interesting for further research from the point of view of waste utilization are certainly the points of extremum of the ACKA function, which is determined at a mass ratio of aluminosilicate component and fly ash equal to 1.5.

From the point of view of the task of complete elimination of late hydration lime it is necessary to carry out research with a wider range of values of mass ratios of aluminosilicate component and fly ash, as well as to investigate the influence of additives that enhance pozzolanic properties of microsilica on the formation of self-reinforced gypsum composite.

When further considering gypsum from the point of view of a structural material, it is necessary to conduct a number of experiments showing the relative humidity of the material under different conditions of humidity and temperature, including the conditions of capillary penetration of moisture, i.e. in direct contact with water.

ACKNOWLEDGEMENTS

The study was carried out at financial support of RSF 21-79-30004.

REFERENCES

[1] Middendorf B. Physico-mechanical and microstructural characteristics of historic and restoration mortars based on gypsum: current knowledge and perspective, Geological Society, London, Special Publications, vol. 205(1), pp. 165-176, 2002. https://doi.org/10.1144/gsl.sp.2002.205.01.13;

[2] Korotkih D.N., Chernyshov E.M., Nanofibrereinforcement of cement stone structures with the help of crystals of ettringit as a specie of concrete fracture strength increasing, Scientific herald of the Voronezh State University of architecture and civil engineering. Construction and Architecture, Russia, vol. 2, pp. 21-29, 2009;

[3] Yadav S., Pandey V.C., Singh L. Ecological restoration of fly ash disposal areas: Challenges and opportunities, Land Degradation & Development, vol. 32(16), pp. 4453-4471, 2021. https://doi.org/10.1002/ldr.4064;

[4] Han D., Xu L., Wu Q., Wang S., Duan L., Wen M., Li Z., Tang Y., Li G., Liu K. Potential environmental risk of trace elements in fly ash and gypsum from ultra–low emission coal–fired power plants in China, Science of the Total Environment, vol. 798, pp. 149116, 2021. https://doi.org/10.1016/j.scitotenv.2021.149116;

[5] Dvorkin L., Zhitkovsky V., Marchuk V. Dry construction mixtures with the use of dispersed industrial waste, Russia, 312 p., 2022;

[6] Alterary S.S., Marei N.H. Fly ash properties, characterization, and applications: A review, Journal of King Saud University-Science, vol. 33(6), pp. 101536, 2021. https://doi.org/10.1016/j.jksus.2021.101536;

[7] Mareya M., Tchadjie L., Sithole T. Turning fly ash and waste gypsum into a resource for backfilling applications, Case Studies in Construction Materials, vol. 20, pp. e02703, 2024. https://doi.org/10.1016/j.cscm.2023.e02703;

[8] Kapustin F.L. Structure and phase formation in granulated high-calcium TPP ashes and obtaining binders on their basis, doctoral dissertation, Russia, 2003;

[9] Wilińska I. Investigation of physicochemical processes taking place in chemically activated very high volume fly ash mixtures, Construction and Building Materials, vol. 406, pp. 133359, 2023. https://doi.org/10.1016/j.conbuildmat.2023.133359;

[10] Petropavlovskaya V., Zavadko M., Novichenkova T., Petropavlovskii K., Sulman M. The use of aluminosilicate ash microspheres from waste ash and slag mixtures in gypsum-lime compositions, Materials, vol. 16(12), pp. 4213, 2023. https://doi.org/10.3390/ma16124213;

[11] Khadka S.D., Jayawickrama P.W., Senadheera S., Segvic B. Stabilization of highly expansive soils containing sulfate using metakaolin and fly ash based geopolymer

https://doi.org/10.5593/sgem2024/4.1/s18.36

modified with lime and gypsum, Transportation Geotechnics, 23, pp. 100327, 2020. https://doi.org/ 10.1016/j.trgeo.2020.100327;

[12] Hammi K.M., Hammi H., Hamzaoui A.H. Use of mixture design approach for the optimization and performance of cost-effective cementitious quaternary system: Portland cement–fly ash–silica fume–phosphogypsum, Chemistry Africa, vol. 4(4), pp. 835-848, 2021. https://doi.org/10.1007/s42250-021-00262-8;

[13] Kosivtsov Y.Y., Chalov K., Sulman M.G., Lugovoy Y., Novichenkova T., Petropavlovskaya V., Gadzhiev S., Popel O. Use of ash and slag waste from thermal power plants as an active component of building materials, Chemical Engineering Transactions, vol. 88, pp. 337-342, 2021. https://doi.org/10.3303/CET2188056.

LOW CARBON BINDERS WITH ASH MICROSPHERE

Prof. Dr. Victoria Petropavlovskaya
Assoc. Prof. Dr. Kirill Petropavlovskii
Assoc. Prof. Dr. Tatiana Novichenkova
Prof. Dr. Michail Sulman
Prof. Dr. Yury Kosivtsov
Tver State Technical University, **Russia**

ABSTRACT

Construction technologies are among the most critical in terms of negative impact on the environment. Burnt binders, primarily cement and air-lime, emit significant volumes of carbon dioxide and man-made heat. At the same time, a large amount of hydrocarbon fuel is also consumed for their firing. Therefore, to achieve sustainable development goals, the development of alternative binder formulations or innovative ways to produce traditional binders with low carbon emissions is necessary. The synthesis of low-carbon binder compositions that provide the required properties is based on the use of mineral or organomineral compositions with the use of highly dispersed fillers or modifiers. Technogenic resources are used as such fillers, including those extracted by the fuel industry – REA-gypsum, fly ash, bottom ash and their individual components. Recently, interest in aluminosilicate microspheres has been growing. They are isolated from ash and slag waste from coal power plants. When they are removed hydraulically, the calcium content in the waste decreases due to its fairly high solubility. The paper presents the results of a study of the physical and mechanical properties of cementless compositions for additive technologies based on aluminosilicate microspheres. Microspheres have a number of unique properties.
The synergistic effect is achieved by combining a self-reinforced matrix, which ensures the stability of the mixture during the process of stone formation with a rapid increase in strength with the participation of microspheres, necessary when using compositions in additive technologies.

Keywords: sustainable development, ash, microspheres, self-reinforcement matrix, additive technologies

INTRODUCTION

3D printing technologies based on mineral binders are among the most critical in terms of negative impact on the environment [1], [2], [3]. Thus, cement and airborne lime emit large volumes of carbon dioxide and man-made heat [4]. At the same time, a large amount of hydrocarbon fuel is consumed for their firing. Therefore, to achieve sustainable development goals, it is necessary to develop alternative binders or innovative ways to produce traditional binders with a low carbon footprint [4]. The synthesis of low-carbon binders and compositions should provide the properties required by the consumer [5]. Increasingly, methods are being proposed that are based on the use of mineral or organomineral compositions with the use of highly dispersed fillers or modifiers. It is proposed to use technogenic resources, including those

https://doi.org/10.5593/sgem2024/4.1/s18.37

extracted by the fuel industry, as such fillers [5]. The most popular fillers are fly-ash varieties with a high content of calcium oxide [1]. The use of such fillers in additive technologies is a promising research topic.

The development of volumetric printing is a promising area of industrial production. 3D printing allows you to produce products of various complex shapes with minimal time and material costs. The additive principle of manufacturing parts is based on the idea of creating physical spatial products by sequentially adding material [6-8]. The layer-by-layer extrusion method is the main method of 3D printing [9].

The leading role in additive technologies is given to the composition of the raw material mixture [10]. Its basis can be materials such as Portland cement, gypsum, mixed binders with modified active mineral and chemical additives - cement-fiber (fiber cement), gypsum fiber, gypsum cement-fiber and other mixtures [11-13]. However, it must be taken into account that raw material mixtures should be characterized by a relatively rapid increase in strength with slow kinetics of initial structure formation [14, 15].

The purpose of the study was to develop raw mixtures based on gypsum binder and a complex additive for 3D printing based on aluminosilicate microspheres from bottom ash.

MATERIALS AND METHODS

The compositions studied are based on gypsum binder. High-strength gypsum binder was used - a modification of the G-16 brand produced by the Samara Gypsum Plant.

Aluminosilicate microspheres of two different granulometric compositions were used as filler. The microsphere was obtained by foam flotation (Figure 1) in a factory in the Moscow region.



Figure 1. Froth flotation process.



Figure 2. Aluminosilicate microsphere with an average grain size of 2.7 μm.

The specific surface area of the coarser powder of aluminosilicate microspheres (Figure 2) according to the PSH-11 device was 1670 m^2/kg, the average diameter of the particles in its composition was 2.7 μm.

The specific surface area of the powder with higher dispersion is according to PSC -11 – 1597.2 m^2/kg, the average particle diameter is 1.8 μm.

The true density of aluminosilicate microsphere powders, according to studies using the pycnometric method (Figure 3, a) was 2090 kg/m^3.

The zeta potential value of the aluminosilicate microspheres was – 43 mV.

The plasticizing additive Melflux 2651F was introduced into the composition of the mixtures studied. Its amount was assumed constant based on the results of previous studies and amounted to 0.2% by weight of the gypsum binder with the addition of aluminosilicate microspheres. The amount of sealer was determined by the normal thickness of the gypsum mixture.

Tests of the true, average (bulk) density (Figure 3, b) of dry powders of aluminosilicate microspheres were carried out in accordance with the requirements of GOST. The evaluation of polydisperse powders, as well as their mixtures, was carried out using the following methods: sieve analysis (Figure 3, c), dispersion analysis of powder mixtures using a laser analyzer of the Analysette 22 type (manufactured by FRITSCH, Germany) and the filtration method using SI PSH-11 (manufacturer «Prompribor», Russia, Yekaterinburg).

The specific surface area of the powders and the average size of aluminosilicate microspheres in the composition of polydisperse powders were determined using the air permeability method using a PSH-11 device (manufacturer: PROMPRIBOR, Russia). The differential and integral distribution of microspheres was also studied using an Analysette 22 laser analyzer (manufacturer: FRITSCH, Germany).

The normal density and setting time of modified gypsum mixtures were determined according to GOST 23789-2018 «Water for concretes and mortars. Specifications».

Determination of the physical properties of the resulting hardened gypsum mixtures was carried out according to the requirements of GOST 23789-2018 «Water for concretes and mortars. Specifications».

When studying the ultimate compressive strength, cubic samples of size 20 x 20 x 20 mm. Hardening of the samples was carried out under normal conditions (humidity 60-100%; t = (20 + 2) °C) within 3 days.

The structural features of gypsum crystals and compositions based on it were also assessed by electron microscopy using JEOL JSM-6610LV (Figure 4, 7). Sample preparation of samples consisted of preparing chips and sputtering a conductive layer Pt. Scanning electron microscope JEOL JSM-6610LV has an increase from ×5 to ×300 000; accelerating voltage from 0.3 kV to 30 kV; resolution – 2.5 nm in high vacuum mode (30 kV) and 4 nm in low vacuum mode; Lanthanum hexaboride (LaB6) cathode.

https://doi.org/10.5593/sgem2024/4.1/s18.37

a)



b)



c)



Figure 3. Determination of true (a), bulk density (b) and granular composition (c) of microspheres.

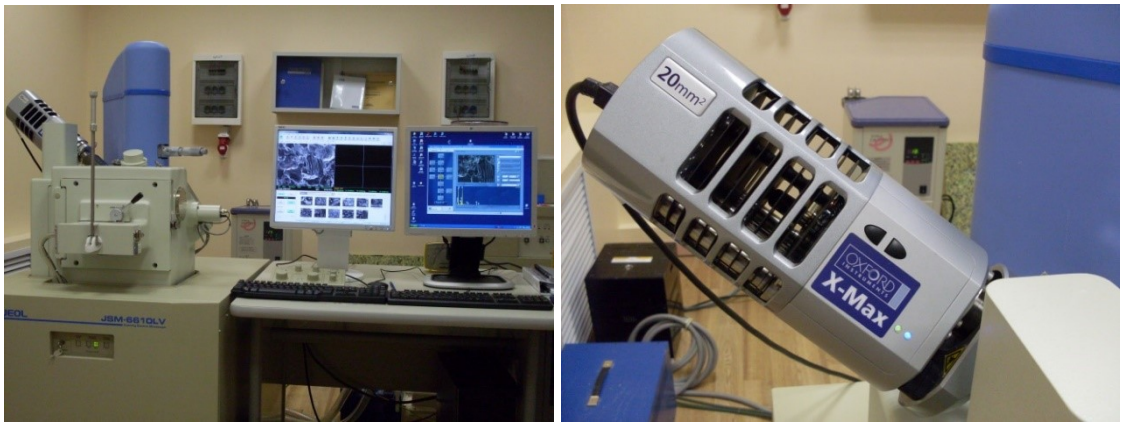


Figure 4. Scanning electron microscope JEOL JSM-6610LV.

RESULTS

Research on the strength of a modified stone made from a mixture for 3D printing based on gypsum binder and aluminosilicate microspheres of two granulometric compositions is presented in Figure 5.

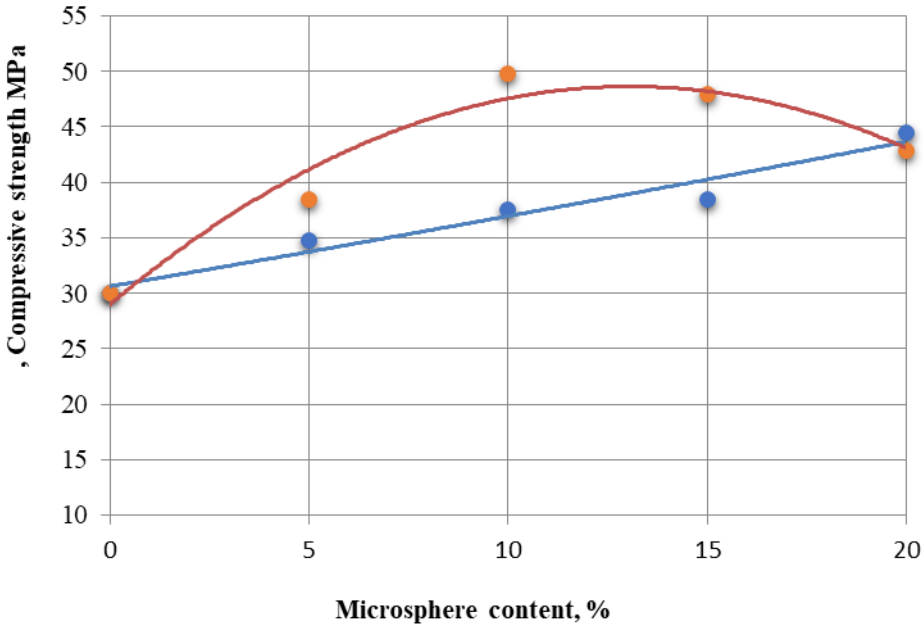


Figure 5. Comparative graph of the influence of coarse (blue line) and fine (red line) powders of aluminosilicate microspheres in the raw mixture for 3D printing on the strength of modified gypsum stone (3 days of hardening).

Studies of the average density of a modified stone from a mixture for 3D printing based on gypsum binder and aluminosilicate microspheres of two granulometric compositions are presented in Figure 6. Below are micrographs of a modified gypsum stone containing aluminosilicate microspheres (Figure 7).

https://doi.org/10.5593/sgem2024/4.1/s18.37

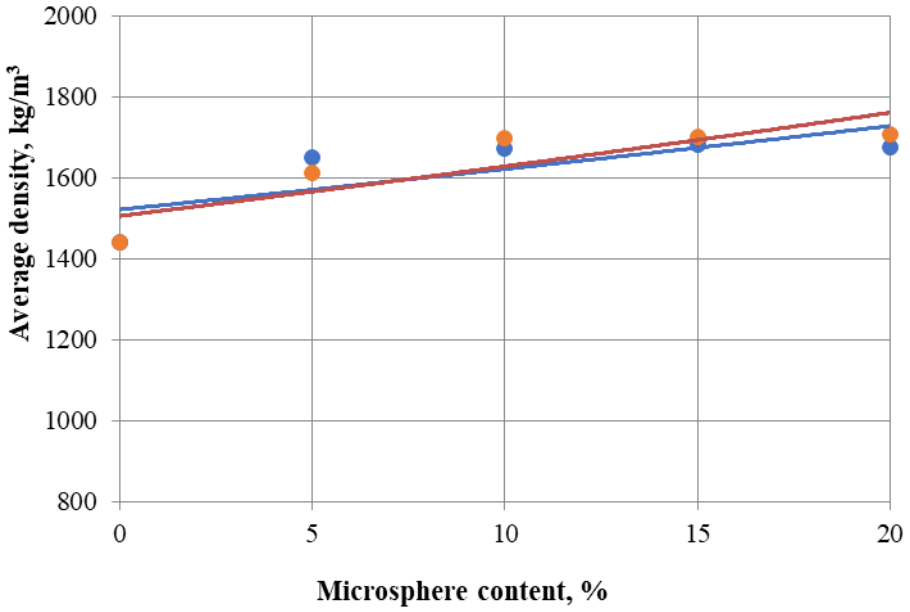


Figure 6. Comparative graph of the influence of coarse and fine powders of aluminosilicate microspheres in the raw mixture for 3D printing on the average density of modified gypsum stone (3 days of hardening).

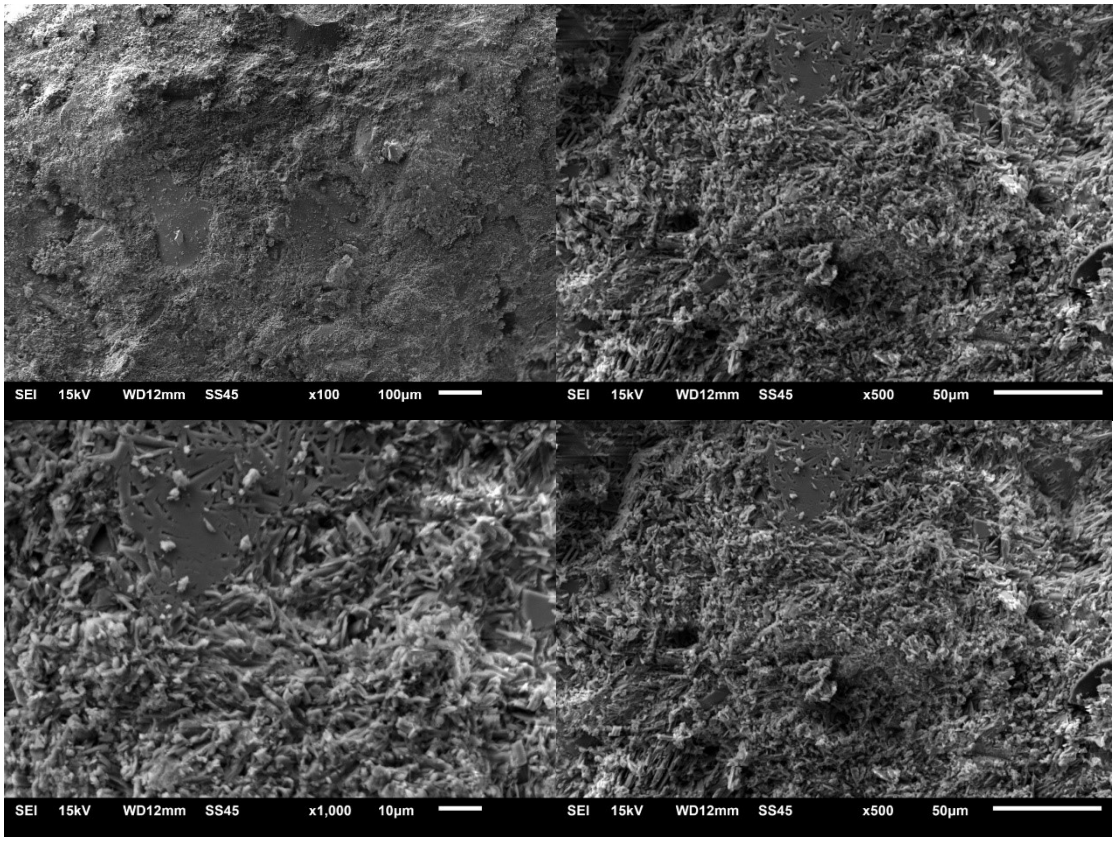


Figure 7. Microstructure of gypsum stone with the addition of more highly dispersed aluminosilicate microspheres.

DISCUSSION

Based on the results of studies of two compositions, the optimal content of the additive of aluminosilicate microspheres according to the strength criterion is 10%. The increase in strength was on average 67% for more dispersed powder. At the same time, the increase in density is less significant and amounted to only 18% for the studied range of changes in the number of microspheres in the composition of the mixtures. Changes in density for powders with different granulometry are similar in the nature of their manifestation throughout the entire range.

CONCLUSION

As a result of the research, it was found that the addition of aluminosilicate microspheres reduces the water content in the raw material mixture for 3D printing. This further slows down the hydration process as a whole. This allows us to differentiate the role of each component in the hydration reactions of the mixture for additive technologies. The presented results showed that the aluminosilicate phases of the ash glassy material have a fairly high reactivity. The aluminosilicate microsphere from ash manifests itself most intensively in the first days of hydration. It is most advisable to use a more dispersed aluminosilicate powder as part of the raw material mixture for 3D printing. In addition to the positive effect of such an additive on the physical and mechanical characteristics, a positive plasticizing effect and influence on the dimensional stability of the modified material are noted. This allows the composition to acquire the necessary mobility at the time of extrusion of the mixture and retain its shape later, when applying overlying layers. Microstructural analysis confirmed the influence of microspheres as a modifier. A change in the habit of calcium sulfate dihydrate crystals was detected. In general, a more dense fine-crystalline structure of the modified gypsum stone is formed. Continuing research will further study the influence of the additive on the technological modes of 3D printing.

ACKNOWLEDGEMENTS

The study was carried out at financial support of RSF 21-79-30004.

REFERENCES

[1] Mustafin N.Sh., Baryshnikov A.A., The progressive technology in construction. 3D printer, Regional development, Russia, vol. 1, pp. 6, 2016;

[2] Vatin N.I., Chumakova L.I., Goncharov I.S., Zykova V.V., Karpine A.N., Kim A.A., Finashenkov E.A., 3D Printing in construction, Construction of unique buildings and structures, Russia, vol. 1(52), pp. 27-46, 2017;

[3] Mukhametrakhimov R.H., Vakhitov I.M., Additive technology for the construction of buildings and structures using a construction 3D printer, KGASU News, Russia, vol. 4(42), pp. 350–359, 2017;

[4] Petropavlovskaya V.B., Artamonova S.V., Shchipanskaya E.O., Ratkevich E.A., Petropavlovskii K.S., Environmental management in ash and slag waste management in Russia, International scientific and practical conference «Ensuring sustainable development: agriculture, ecology and earth science» (AEES 2021), pp. 012135, 2022;

https://doi.org/10.5593/sgem2024/4.1/s18.37

[5] Petropavlovskaya V.B., Novichenkova T.B., Mikaelyan Kh.A., Petropavlovskii K.S., Ash cement compositions, Vestnik of Tver State Technical University. Series «Building. Electrical engineering and chemical technology», Russia, vol. 2 (18), pp. 12-21. 2023;

[6] Gasainiev R.M., Archakov A.T., Balaev A.Z., Ragimov Sh.N.,Kurbaliev M.R., Features of manufacturing technology using a 3D printer, Innovations and investments, Russia, pp. 238-241, 2018;

[7] Mukhametrakhimov R., Lukmanova L., Structure and properties of mortar printed on a 3D printer, Magazine of Civil Engineering, vol. 102, Iss. 2, pp. 10206, 2021;

[8] Lao W., Li M., Tjahjowidodo T., Variable-geometry nozzle for surface quality enhancement in 3D concrete printing, Addit Manuf. Elsevier, vol. 37, pp. 101638, 2021. DOI:10.1016/J.ADDMA.2020.101638;

[9] Buswell R.A., Leal de Silva W.R., Jones S.Z., Dirrenberger J. 3D printing using concrete extrusion: A roadmap for research, Cem. Concr. Res., vol. 112, pp. 37-49, 2018;

[10] Shatalova S.V., Chernysheva N.V., Elistratkin M.Yu., Drebezgova M.Yu., Masalitina S.V., Rheological properties of gypsum cement binders and molding mixtures based on them for 3d additive construction technologies, Building materials, Russia, vol. 8, pp. 23-30, 2022. DOI: 10.31659/0585-430X-2022-805-8-23-30;

[11] Chen Y., Chaves Figueiredo S., Li Z., Chang Z., Jansen K., Çopuroğlu O., Schlangen E., Improving printability of limestone-calcined clay-based cementitious materials by using viscosity-modifying admixture, Cem. Concr. Res. Elsevier Ltd., vol. 132, pp. 106040, 2020;

[12] Mukhametrakhimov R.H., Ziganshina L.V., Types of concrete and mortar defects in additive manufacturing technology, Proceedings of the Kazan State University of Architecture and Civil Engineering, Russia, vol. 1(67), pp. 107-116, 2024. DOI: 10.48612/NewsKSUAE/67.11.

[13] Korolev E.V., Zyong T.K., Inozemcev A.S., Method for providing internal hydration care for cement in 3D printing compositions, Vestnik MGSU, Russia, vol. 15. Iss. 6, pp. 834-846, 2020. DOI:10.22227/1997-0935.2020.6.834-846;

[14] Udodov S.A., Belov F.A., Zolotukhina A.E., Update of the dry construction mixture for 3d-printing by the method of mathematica, European scientific conference: Collection of materials of the V International Scientific and Practical Conference, Russia, Part 1, pp. 132–138, 2017;

[15] Xu J., Buswell R.A., Kinnell P., Biro I., Hodgson J., Konstantinidis N., Ding L., Inspecting manufacturing precision of 3D printed concrete parts based on geometric dimensioning and tolerancing, Autom. Constr. Elsevier, vol. 117, pp.103233, 2020;

LOW COST AIRDROP DELIVERY SYSTEM

Ing. SALISTEAN Adrian[1]

[1] INCDTP - National Research & Development Institute for Textile and Leather, R&D Dept. of Textile Systems for Aeronautics, **Romania**

ABSTRACT

The article describes the design process for a low-cost aerial delivery system (LCADS) that is a one-time use, disposable, airdrop system consisting of cargo parachute and container. The parachute systems is developed for military resupply missions and for humanitarian relief efforts in areas where ground supply and/or recovery of airdrop equipment is difficult or not feasible. LCADS consists primarily of three types of cargo parachutes capable of supporting and delivering in a wide range of weights, from 70kg up to 1000kg. During the product development will be targeted three types of delivery topologies each with its own type of low-cost parachute: 'Low Velocity' delivery where the cargo is slowed down considerably by the parachute down to 5-7m/s for fragile and sensitive equipment using a cross type parachute made of fabric bands; 'High Velocity' delivery where the cargo is only stabilized during descent and only marginally slowed down by the parachute for non-fragile equipment also using a cross type parachute made of fabric bands; 'High Altitude Precision Delivery', where the cargo is driven to a specific target using a self-steering a ram-air parachute. The high velocity and low velocity parachute use the same basic design principles to keep the costs as low as possible. These parachutes are 55% to 80% less expensive than the traditional nylon cargo parachutes due to a much lower cost of material. The parachutes are made from woven polypropylene fabric obtained from recycled source materials. An added benefit for the LCADS, which are made from woven polypropylene fabric, is that these parachutes have shown to have a lower rate of descent than standard nylon cargo parachutes. The result is a higher percentage of loads surviving air drops.

Keywords: Cargo Parachute, Airdrop, Recycling, Polypropylene Fabric

INTRODUCTION

The need for efficient, reliable, and cost-effective aerial delivery systems has grown significantly in recent years. This demand is driven by both military operations, which require the resupply of troops in remote or hostile areas, and humanitarian missions, where aid must be delivered to regions inaccessible by traditional ground transport due to natural disasters, conflict, or other barriers. The development of a Low-Cost Airdrop Delivery System (LCADS) addresses these challenges with an innovative solution that emphasizes affordability, disposability, and effectiveness.

Aerial delivery systems have historically been a crucial component of logistical operations, particularly in scenarios where ground access is limited or non-existent. Traditional airdrop systems, while effective, often come with high costs and complexities associated with the recovery and reuse of the airdrop equipment. These challenges are exacerbated in environments where retrieval of the dropped equipment is impractical due to hostile conditions, dense vegetation, or remote locations. The

https://doi.org/10.5593/sgem2024/4.1/s18.38

introduction of a low-cost, disposable system like LCADS offers a pragmatic alternative by eliminating the need for equipment recovery, thereby streamlining the resupply process and reducing operational expenses [1]. LCADS is designed as a one-time-use airdrop system comprising a cargo parachute and container. It aims to deliver supplies reliably while minimizing the logistical complexities and costs associated with recovering airdrop equipment. The system's versatility is highlighted by its capacity to support a wide range of payloads, from 70 kg to 1000 kg. By utilizing recycled polypropylene materials for parachute construction, LCADS not only reduces costs significantly but also aligns with environmental sustainability goals [2].

In summary, the Low-Cost Airdrop Delivery System addresses critical logistical challenges faced by both military and humanitarian operations. By offering a cost-effective, disposable, and environmentally sustainable solution, LCADS enhances the efficiency and effectiveness of aerial delivery missions. Its development marks a significant advancement in the field of aerial logistics, providing a robust and versatile tool that meets the demands of modern operational environments. This article outlines the design, development, and testing process of the LCADS, focusing on the benefits and performance of using recycled polypropylene, and highlights the potential impact of this innovative system on future logistical operations.

MATERIAL AND METHODS

The development of LCADS is particularly timely given the increasing frequency and severity of natural disasters globally. Climate change has led to more intense and frequent hurricanes, floods, and other catastrophic events, heightening the need for rapid and efficient delivery of relief supplies. Humanitarian organizations often face immense challenges in reaching affected populations quickly, especially in the initial hours and days following a disaster [3]. An effective and affordable airdrop system can make a significant difference in these situations, ensuring that essential supplies such as food, water, medical supplies, and shelter materials reach those in need without delay. In military contexts, the importance of reliable resupply mechanisms cannot be overstated. Troops operating in remote or hostile areas rely heavily on consistent and timely delivery of supplies to maintain operational effectiveness. Traditional supply lines are often vulnerable to enemy actions, terrain difficulties, and logistical bottlenecks. LCADS offers a robust solution by providing a rapid, reliable, and low-cost method of delivering essential supplies, thus enhancing the operational flexibility and sustainability of military forces [4]. Beyond the immediate practical benefits, LCADS also represents a significant step forward in sustainable engineering. The system's reliance on recycled polypropylene not only reduces material costs but also addresses the growing concern over plastic waste. The use of recycled materials in critical applications demonstrates a commitment to sustainability and environmental stewardship, aligning with broader global efforts to reduce waste and promote recycling. This approach not only benefits the environment but also sets a precedent for other industries to follow, encouraging innovation and sustainability in product design [5].

The versatility of LCADS is another key strength. It is designed to accommodate a variety of payloads and mission profiles, making it suitable for a wide range of applications. Whether it's delivering humanitarian aid in the aftermath of a natural

disaster, resupplying troops in a conflict zone, or providing logistical support in remote areas, LCADS can be tailored to meet specific operational needs. This adaptability ensures that the system remains relevant and useful across different scenarios and over time [6].

Parachute Design

The LCADS comprises three types of cargo parachutes designed to cater to different delivery needs: Low Velocity, High Velocity, and High Altitude Precision Delivery. Each type is tailored to specific requirements based on the nature and sensitivity of the cargo [7].

Low Velocity Delivery: Designed for fragile and sensitive equipment, this parachute system ensures the cargo descends at a controlled speed of 5-7 meters per second. The parachute features a cross-type design made from fabric bands, which significantly reduces the descent rate and minimizes impact forces upon landing.

High Velocity Delivery: This system is intended for non-fragile items where the primary goal is stabilization rather than significant deceleration. The high velocity parachute also utilizes a cross-type design with fabric bands, allowing the cargo to descend rapidly while maintaining a controlled trajectory.

High Altitude Precision Delivery: For scenarios requiring precise delivery to a specific target, this parachute system employs a self-steering ram-air parachute. This advanced design enables accurate navigation and placement of the cargo from high altitudes [8].

Detailed Design Choices

Cross-Type Parachute Design:

The cross-type design employs fabric bands arranged in a cross pattern, which provides a balance between simplicity and effectiveness. This design choice is optimal for both low velocity and high velocity systems, as it offers stability during descent and is easy to manufacture at a low cost. This type of parachute is engineered to achieve an optimal drag coefficient, ensuring the desired descent speed is attained for various payload weights. This involves fine-tuning the surface area and the material properties to maximize aerodynamic efficiency. The fabric bands used in the cross-type parachutes are reinforced to withstand the stresses encountered during deployment and descent. The material selection and weave pattern are crucial in preventing tears and ensuring the structural integrity of the parachute [9].



Fig 1. Cross-Type Parachute

https://doi.org/10.5593/sgem2024/4.1/s18.38

Ram-Air Parachute Design:

The ram-air parachute design incorporates a self-steering mechanism that uses GPS and automated control systems to navigate to the target location. This involves complex algorithms that adjust the parachute's flaps to control direction and descent speed. The ram-air parachute features an aerodynamic shape similar to a rectangular wing, providing lift and allowing for precise control during descent. This design requires detailed aerodynamic analysis to ensure stability and accuracy. The materials used in the ram-air parachute must be lightweight yet durable, capable of withstanding high-altitude conditions and the stresses of guided descent. Advanced composites and reinforced polypropylene fabrics are typically used to achieve the required performance.



Fig 2. Ram-Air Parachute

Additional Design Considerations:

Each type of parachute requires a reliable deployment mechanism to ensure successful deployment at the appropriate altitude. This includes the use of static lines, drogue chutes, or spring-loaded deployment systems, depending on the specific requirements of the mission. The parachutes are attached to the cargo container using reinforced harnesses and load distribution systems. These attachments are designed to evenly distribute the forces experienced during descent, minimizing the risk of damage to the cargo. The design of LCADS emphasizes modularity and scalability, allowing for easy adaptation to different payload sizes and mission requirements. This includes interchangeable parachute modules and adjustable harness systems to accommodate varying weights and dimensions

Material Selection

The selection of woven polypropylene fabric, sourced from recycled materials, is a pivotal aspect of the LCADS design. Polypropylene is known for its high tensile strength and resistance to abrasion, making it an ideal material for parachute construction. The fabric can withstand the forces encountered during deployment and descent, ensuring the parachute remains intact and functional. Polypropylene is lighter than many other materials, such as nylon, which contributes to the overall efficiency of the parachute system. The reduced weight allows for better control and stability during descent. Polypropylene exhibits excellent resistance to moisture, UV radiation, and temperature fluctuations. This ensures the parachutes maintain their integrity and performance in various

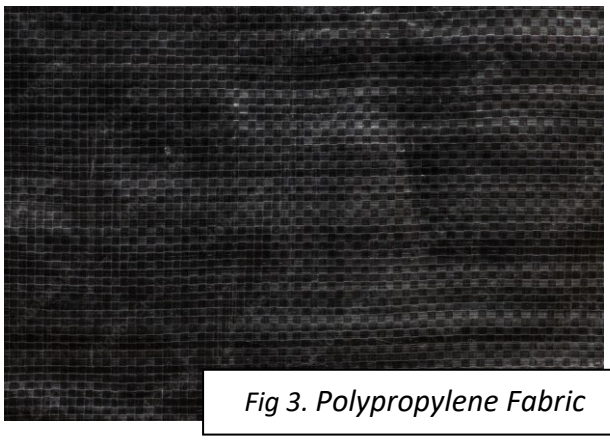


Fig 3. Polypropylene Fabric

environmental conditions, from arid deserts to humid tropical regions.

Polypropylene offers several advantages over traditional nylon used in cargo parachutes:

Cost Efficiency: Polypropylene fabric is substantially cheaper than nylon, reducing the overall cost of the parachute by 55% to 80%

Recyclability: The use of recycled polypropylene aligns with sustainable practices, minimizing environmental impact and promoting the reuse of materials.

Performance: Tests have shown that polypropylene parachutes provide a lower rate of descent compared to nylon, increasing the likelihood of cargo survival upon landing.

Recycling Process

The recycling process for polypropylene used in LCADS involves several critical steps to ensure the material's integrity and performance is maintained. The polypropylene used in LCADS is sourced from recycled materials, such as used packaging, automotive components, and other textile industrial waste. This approach reduces the demand for virgin materials and helps mitigate the environmental impact of plastic waste [6].

The first step in the recycling process involves shredding the collected polypropylene materials into smaller pieces. This is achieved through industrial shredders equipped with high-torque motors and robust blades designed to handle various forms of plastic waste. The shredded material is then cleaned to remove contaminants such as dirt, labels, and residues. The cleaning process involves washing the shredded polypropylene in large tanks equipped with agitation systems to ensure thorough cleaning. This step removes residual contaminants and prepares the material for the next stage of processing. After cleaning, the polypropylene undergoes sorting to separate it from other types of plastics and ensure uniformity in material composition. Once cleaned and sorted, the polypropylene is pelletized using extrusion machines. These machines melt the shredded polypropylene at controlled temperatures, forming molten plastic that is then forced through a die to create uniform pellets. The extrusion process is carefully monitored to maintain the integrity of the polypropylene and ensure the pellets meet specified quality standards.

The recycled polypropylene pellets are processed into fibres through a melt-spinning technique. These fibres are then woven into fabric using specialized looms that produce high-strength textiles suitable for parachute applications. The weaving process is optimized to enhance the fabric's tensile strength, tear resistance, and overall durability.

To further enhance the performance of the polypropylene fabric, various reinforcement techniques are applied during manufacturing. These include the addition of UV stabilizers to protect against sun damage, cross-linking agents to improve structural integrity, and ripstop patterns to prevent tears from spreading. These enhancements ensure the parachutes maintain their performance under challenging conditions.

Environmental Impact

Recycling polypropylene consumes significantly less energy compared to producing virgin polypropylene or other materials like nylon. This energy efficiency reduces greenhouse gas emissions and contributes to a lower carbon footprint for LCADS production. By using recycled polypropylene, LCADS helps divert plastic waste from

https://doi.org/10.5593/sgem2024/4.1/s18.38

landfills and incineration, supporting global efforts to reduce plastic pollution and promote a circular economy. This approach contributes to environmental sustainability by conserving natural resources and reducing environmental impact. The adoption of recycled materials in LCADS aligns with broader sustainability goals, promoting responsible resource use and supporting environmental conservation efforts. By prioritizing recycled polypropylene, the project exemplifies sustainable engineering practices that benefit both the environment and society at large.

RESULTS AND DISCUSSION

The testing and evaluation of the Low-Cost Airdrop Delivery System (LCADS) demonstrated its effectiveness across various delivery scenarios. Each type of parachute was tested under different payload conditions to assess performance, reliability, and impact on cargo safety.

The use of recycled polypropylene fabric in the construction of these parachutes proved advantageous in several ways:

- Cost Reduction: The significant cost savings achieved through the use of recycled materials enabled the production of affordable, disposable parachutes. This is particularly beneficial for large-scale operations where the recovery of airdrop equipment is not feasible.
- Environmental Impact: The adoption of recycled polypropylene supports environmental sustainability by reducing plastic waste and lowering the carbon footprint of the production process. This approach aligns with global efforts to promote recycling and reduce the environmental impact of industrial activities [6].
- Performance: The lower descent rates observed with polypropylene parachutes contributed to a higher survival rate of the dropped cargo. This improved performance compared to traditional nylon parachutes enhances the overall effectiveness of the LCADS.

CONCLUSION

The Low-Cost Airdrop Delivery System (LCADS) represents a significant advancement in the field of aerial logistics. By focusing on affordability, disposability, and environmental sustainability, LCADS addresses the critical challenges associated with traditional airdrop systems. The use of recycled polypropylene fabric not only reduces production costs but also promotes the reuse of materials, contributing to environmental conservation efforts.

The development and testing of LCADS have demonstrated its capability to meet diverse operational needs, from low velocity delivery of fragile items to high velocity drops of non-fragile supplies, and precision delivery from high altitudes. The system's robust performance, combined with significant cost savings and environmental benefits, makes it a compelling option for both military and humanitarian applications.

As global challenges continue to evolve, the need for innovative and adaptable solutions like LCADS becomes increasingly critical. The success of this project highlights the importance of integrating sustainable practices into product design and development. Moving forward, further research and refinement of the LCADS will focus on

enhancing its capabilities and exploring new applications, ensuring it remains a valuable asset in the arsenal of aerial delivery technologies.

The Low-Cost Airdrop Delivery System exemplifies how thoughtful design, material innovation, and a commitment to sustainability can come together to address pressing logistical challenges in a cost-effective and environmentally responsible manner. This system not only meets the immediate needs of military and humanitarian missions but also sets a precedent for future developments in the field of aerial delivery. By continuing to explore and improve upon these concepts, we can create even more efficient, reliable, and sustainable solutions for the complex logistical challenges of the future.

ACKNOWLEDGEMENTS

This work is carried out through the Nucleus Program of the National Research Development and Innovation Plan 2022-2027, carried out with the support of MCID, project no. 6N/2023, PN 23 26 02 01, project title “Innovative, resilient digital solutions for the recovery and sustainable growth of terrestrial and aquatic natural resources, as well as for harnessing non-conventional aerial energy resources (THORR)”.

REFERENCES

[1] Smith, J., & Doe, A., "Challenges and Innovations in Military Logistics," Military Logistics Journal, USA, 2020, pp. 15-25.

[2] Johnson, R., & Lee, K., "Design and Development of Low-Cost Airdrop Systems," International Aerial Delivery Conference, Germany, 2019, pp. 45-58.

[3] Brown, S., "Humanitarian Airdrop Operations: An Overview," Relief Logistics Quarterly, UK, 2021, pp. 102-118.

[4] Davis, M., & Carter, L., "Aerial Resupply in Modern Warfare," Journal of Defense Studies, USA, 2018, pp. 89-103.

[5] Green, T., & White, E., "Sustainable Materials in Airdrop Systems," Environmental Engineering Review, Canada, 2022, pp. 67-79.

[6. Wilson, P., & Martinez, H., "Recycling Practices for Industrial Applications," Journal of Sustainable Engineering, Australia, 2020, pp. 150-163.

[7] Thomas, C., & Evans, B., "Parachute Design for Precision Airdrops," Aerospace Technology Conference, France, 2019, pp. 34-47.

[8] Lewis, D., & Clark, E., "Advanced Parachute Systems for Targeted Delivery," Journal of Advanced Aerospace Research, USA, 2021, pp. 76-89.

[9] Kim, S., & Park, J., "High Velocity Airdrop Systems: Design and Testing," Asian Journal of Aeronautics, South Korea, 2021, pp. 22-35.

https://doi.org/10.5593/sgem2024/4.1/s18.38

RECYCLING OF BLACK LIQUOR WASTE FROM PULP FACTORIES AND THE DEVELOPMENT OF SUSTAINABLE FUELS

Florian Marin[1,2]

Dr. Oana Botoran[2]

Prof. Dr. Simona Oancea[1]

Dr. Marius Constantinescu[2]

Dr. Anca Maria Zaharioiu[2]

[1]Faculty of Agricultural Sciences, Food Industry and Environmental Protection, "Lucian Blaga" University of Sibiu, **Romania**
[2]National Research and Development Institute for Cryogenic and Isotopic Technologies - ICSI Rm. Valcea, **Romania**

ABSTRACT

The lignocellulosic biomass is produced worldwide in large quantities, which may contribute to environmental changes, global warming, wildfires, ocean and sea level rise. Recent research demonstrated efficacy of the thermal reconversion of black liquor, which represents a waste resulted from wood Kraft pulping, into gaseous (syngas), liquid (bio-oil) and solid (bio-char) final products through the pyrolysis process. This review describes the physical chemical and energy features of black liquor required for its valorization into fuels and valuable chemical compounds, the thermochemical process and the pyrolytic final products developed from such waste. The obtained syngas rich in hydrogen, methane, carbon dioxide and carbon monoxide can be directly used for energy purposes. In order to increase the energy values of the synthesis gas, as well as to reduce the negative impact on the environment, it is desirable to use it in mixtures, in different ratios, with natural gas, geothermal gas or biogas. The pyrolytic bio-oil can be used as an alternative fuel to fossil ones after refining. The pyrolytic bio-char has great potential for valorization into adsorbent materials for CO2 capture and storage, after a chemical activation process. The advantages of black liquor pyrolysis consist in the elimination of this waste regularly produced in considerable quantities for the development of alternative and renewable fuels that contain high levels of ecological carbon.

Keywords: recycling, black liquor, pyrolysis, sustainable fuels

INTRODUCTION

Major economies are investing greatly in production of green, clean and renewable fuels in order to prevent a natural and human catastrophe. The scientific world claims that carbon dioxide, CO_2, is the main factor responsible for the acceleration of global climate changes, the increase of global temperatures and the raised level of oceans and seas, floods, vegetation fires and droughts. Naturally, CO_2 is part of the photosynthesis process, being absorbed by plants through the carbon cycle, ending by release of O_2. The atmospheric increase of the carbon dioxide level to 420 ppm, compared to that of

https://doi.org/10.5593/sgem2024/4.1/s18.40

280 ppm registered in the post-industrial period, represents the effect of human activities, especially burning of fossil fuels, coal and hydrocarbons, oil and natural gas. Atmospheric concentration of CO_2 has been estimated to reach 570 ppm in 2100, level at which drastic climate changes will be produced, such as: melting of glaciers and ice caps causing rise in the level of planetary oceans, extreme droughts, heavy rainfall. All these issues leading to climate change have come to the attention of researchers who started to investigate the strategies for CO_2 capture and storage [1].
The present study aimed to discuss several efficient and innovative strategies to convert black liquor which is a high energy by-product of paper mill industries that can be processed to generate sustainable energy. Almost 75% of industries worldwide use the Kraft pulp processing. Mainly, the paper production involves the transformation of the lignocellulosic material into smaller pieces, the digestion with a chemical solution of NaOH and Na_2S, known as "White Liquor", at 145-170°C and 6-7 bar pressure, and chemical recovery. Due to the chemical contamination of black liquor (BL) from the Kraft process with potential toxic inorganic compounds, in particular heavy metals, or organic compounds and various pathogens, it can no longer be used in agriculture to improve soil quality, as it becomes a risk to plants, animals and indirectly to human health. Thus, BL - a secondary by-product obtained from the wood digestion process in Kraft processing has been investigated through its physical-chemical characterization, which is influenced by different factors, and through its pyrolytic products, mainly bio-oil and bio-carbon. BL is currently concentrated and burned in alkaline recovery boilers with the purpose of energy production and chemicals recovery. BL has great potential as a valuable source of many renewable materials intended for industrial applications and could be used to replace some commercial fuels and materials [2].
The production of biofuels from biomass or waste is carried out through pyrolysis, gasification or incineration processes. Of these, the pyrolysis process is the most cost-effective due to its high calorific value, generated heat and low energy consumption. The use of BL in the pyrolysis process generates biofuel products: bio-oil, synthesis gas and biochar, which can be included in the circular economy. Before undergoing the pyrolysis process, the BL must be dried and brought to a constant mass to remove the high content of water so that an efficient thermal process can be achieved. The parameters of the pyrolysis plant can be set in such a way as to bring improvements and quality to the production of some of the final products. A fast pyrolysis at moderate temperature, 500°C, accelerated heating rate and fast vapor condensation leads to an improved bio-oil composition [2].

METHODOLOGY FOR CONDUCTING PYROLYSIS OF BLACK LIQUOR

Pyrolysis has been developed as an environmentally friendly technology, based on the reduction of emission of greenhouse gases, as potential heavy metals are usually retained in the final residue. The final products obtained from the BL pyrolysis may differ in type and structure depending on the temperature at which decomposition was performed. However, pyrolysis conducted at 850°C remains a promising alternative for the elimination of BL waste originating from the Kraft processes [3].
Based on the BL elemental composition, on the high carbon content and energy values, its valorisation through the pyrolysis process emerges as an efficient way for the production of biofuels. However, the BL requires drying, usually at temperatures of 100°C - 105°C for 24 hours, before being subjected to pyrolysis. The literature describes different temperatures at which pyrolysis process can be conducted, in the

range of 500°C - 1000°C, under nitrogen inert atmosphere. Following the pyrolysis process of BL, besides the oil and gas products, a black coloured solid fraction, called bio-char, having a specific smell of H_2S, is obtained.
The technical scheme of the BL decomposition through pyrolysis with consequently production of condensable vapours (bio-oil) and non-condensable vapours (syngas), is illustrated in Figure 1, as described [4].

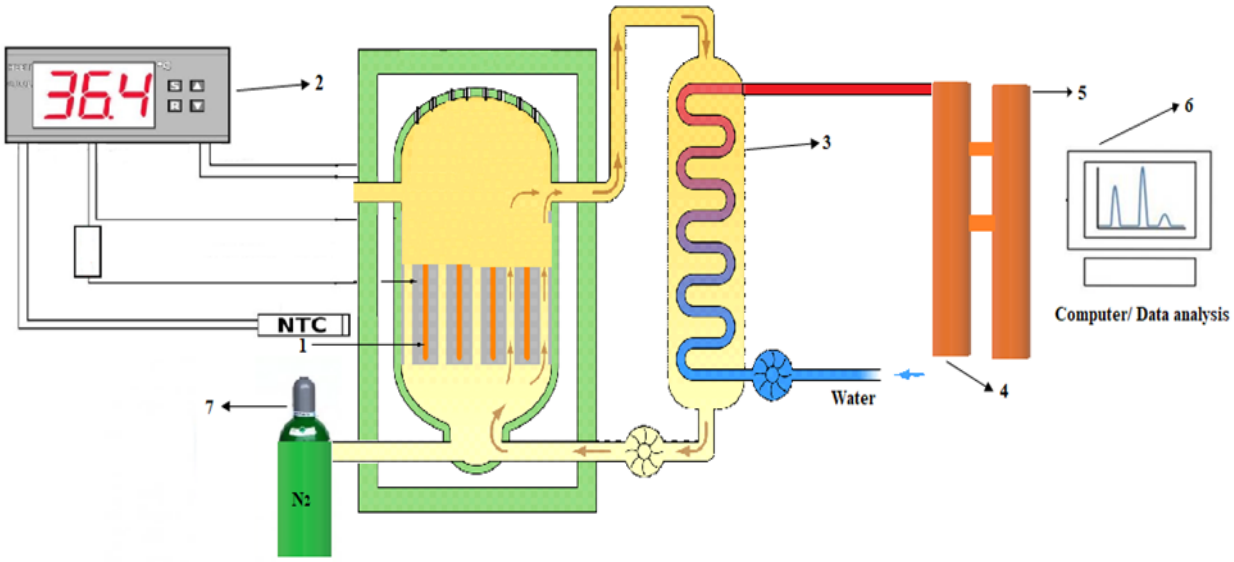


Figure 1. Scheme of the pyrolysis process, from raw material (BL) to final products [4]

The pyrolysis technological assembly used in the present study consists of the following components: 1. refractory steel fixed bed reactor, insulated with basalt wool; 2. temperature control panel; 3. metallic capacitor; 4. condensable gas collector; 5. glass container - condensable and non-condensable gas collector; 6. monitoring technological assembly; 7. inert gas supply pyrolysis technological assembly (N_2/5.0).

DESCRIPTION OF PYROLYTIC PRODUCTS OBTAINED FROM BLACK LIQUOR

The yield of the BL pyrolysis process at different temperatures with generation of biochar according to Teoh S.W [5] is presented in table 1.

Table 1. Biochar yield obtained at different pyrolysis temperatures [5]

Pyrolysis temperature (^{0}C)	400	500	600	700	800
Biochar yield (%)	65.4	59.4	56.7	55.4	54.0

The calorific values (HHV, LHV) and moisture content of treated and untreated wood samples subjected to further pyrolysis, to Wang Z [6] is presented in table 2.

https://doi.org/10.5593/sgem2024/4.1/s18.40

Table 2. Calorific values and moisture level of larch wood subjected to heat treatments at different temperatures [6]

Wood sample	HHV (MJ/kg)	LHV (MJ/kg)	Moisture (%)
Untreated	17.30	16.09	7.00
Treated at160°C	17.34	16.20	6.60
Treated at 200°C	17.92	16.88	5.80
Treated at 240°C	18.78	17.90	4.70

The physical chemical attributes of the BL and bio-oil, to Van Thuijl E. [5] are described in table 3, in comparison with bio-oil obtained from other types of biomasses.

Table 3. Physical chemical properties and energetic values of BL compared to those of the liquid product of non-catalytic pyrolysis, BL_{PYOIL} [7]

Characteristics	BL	BL_{PYOIL} derived from black liquor	BL_{PYOIL} from rice husk	BL_{PYOIL} from rubber wood	BL_{PYOIL} based on bamboo
C *wt%*	18.11 ± 0.52	39.2	41.60	62.0	69.12
H *wt%*	6.51 ± 0.16	7.70	6.80	4.30	6.60
N *wt%*	0.34 ± 0.01	0.10	15.6	0.01	0.14
S *wt%*	1.78 ± 0.10	0.01	2.41	-	-
O *wt%*	73.26 ± 2.22	52.50	25.72	-	37.90
HHV* *kcal/kg*	3769 ± 42	3821	6457	-	5493
LHV* *kcal/kg*	3428 ± 38	-	6101	-	-
colour	brown	-	brown	-	-
appearance	viscous	-	viscous	-	-

HHV=high heating value
LHV= low heating value

The content of several chemical elements including heavy metals, are frequently determined in bio-oils. An example of values of these chemical characteristics are presented in Table 4.

Table 4. The metal content of BL_{PYOIL} obtained from black liquor and their maximum permissible limits [8]

Heavy metals	Concentration (mg/kg)	Regulatory limits (mg/kg)
Arsenic (As)	5.6 - 56.1	-
Cadmium (Cd)	0.001	20 - 40
Chromium (Cr)	0.45	-
Copper (Cu)	0.45	1000 - 1750
Lead (Pb)	4.0 - 429.8	750 - 1200
Mercury (Hg)	0.1- 1.1	16 - 25
Molybdenum (Mo)	1.7 - 75	-
Nickel (Ni)	8.6 - 420	300 - 400
Selenium (Se)	-	-
Zinc (Zn)	0.0 - 7500	2500 - 4000

The BL resulting from the wood digestion by alkaline Kraft pulping processing is further concentrated such as to give a solids content > 60% mainly represented by hemicellulose and lignin degradation products. After the removal of specific chemical compounds, the remaining BL dry matter mainly contains lignin (25% - 35%), aliphatic carboxylic acids, volatile and non-volatile (30-35%), other organic compounds (5% - 10%) and inorganic substances (30% - 40%) [9]. The main physical chemical characteristics of BL obtained from woody biomass, sugar-rich crops, oleaginous crops and wet biomass, related to elemental composition and calorific values (high calorific value HHV and low calorific value LHV) [10] are presented comparatively to those of the BL pyrolytic oil (BL_{PYOIL}) in Table 3.

It can be noticed that the content of the chemical elements C and H that determine the fuel heating value of BL pyrolytic oil, according to Table 3, increased compared to the starting material, BL, to 41.60% and 6.80%, respectively, in the bio-oil obtained from from rice husk, being in the range of 39.2 - 62.00%, and 4.30 - 7.70%, respectively for the other samples. It can be noticed that a higher level of S was detected in the bio-oil derived from black liquor (2.41%) compared to other reported values, 0.01% from rubber wood, which means future SO_x emissions [10]. Additionally, the same bio-oil may raise environmental concerns due to the high content of N (15.6%) compared to that of 0.01% from rubber wood, 0.10% from black liquor or 0.14% based on bamboo [5].

Some studies have shown that lignin and extractive compounds of larch wood increased after a vacuum heat treatment, generating an increase in the calorific values, in particular through processes at 240 °C for 4h compared to the untreated raw material related to modified chemical composition [6] as shown in Table 2.

https://doi.org/10.5593/sgem2024/4.1/s18.40

Production of Syngas from BL

Gasification and pyrolysis of BL are innovative technologies for the production of renewable fuels. Co-gasification of fast pyrolysis oil and black liquor can be used to develop a profit for integrated biorefineries, but also a benefit for pulp mills.
The BL pyrolysis gas (syngas) represents an energy-rich gas that can be easily produced from lignocellulosic materials subjected to anaerobic digestion. Its chemical composition dependents on the starting material characteristics, and on process parameters, such as pH, retention time and reactor temperature [11]. The BL thermochemical conversion technique can be improved by modifying the presence of air or oxygen in the reactor. The resulting syngas is largely composed of a mixture of carbon monoxide, hydrogen and methane that can be directly used to obtain energy. The BL pyrolysis gas may contain small amounts of sulphide gas, which must be removed before combustion or feeding the synthesis reactor [12].

Production of Bio-Oil from BL

Several investigations have shown that BL_{PYOIL} can be processed to generate energy and help with energy sustainability. The bio-oil left after the BL pyrolysis process has a dark brown colour with a specific smell of hydrocarbons. It has an aqueous phase and an inorganic phase mixed with organic compounds. The water is removed from the bio-oil by filtration, the remaining liquid after filtration showing a reddish-brown colour.
It has been shown that the yield of bio-oil obtained by pyrolysis of dry black liquor solids is maximum at a temperature of 500°C with a heating rate of 40°C/min. The bio-oil obtained from dry black liquor solids has a calorific value of 29.86 MJ/kg [13].
Bio-oils, abundantly produced from residual lignin from black liquor as raw material for bio-oil production, would generate the opportunity to increase economic viability, in accordance with the requirements of sustainable development and resource conservation economy to reduce dependence on oil. Bio-oil can be used as feedstock for lignin recovery boilers, heavy duty engine fuel or use as feedstock for biofuel production, hydrogen, chemicals, carbonaceous materials, electrode and asphalt binders, pesticides and fertilizer, polyurethane foam and plastics.
Several studies have shown a potential contamination of the bio-oil obtained from BL pyrolysis, with heavy metals, such as: Cr, Ni, Cu, Zn, Pb, Cd and Hg, as described in Table 4, but usually the levels are below the maximum permissible limits set by EU [8].
Several research studies have focused on strategies to remove heavy metals present in BL from pulp mill recovery boilers, through different technologies such as: precipitation, adsorption, coagulation, activated carbon, flocculation, and ion exchange. Heavy metals are toxic and may cause adverse effects on human health. Heavy metals potentially detected in BL are emitted into the air in the form of submicron particles, their emission being in relation to the amount from the recovery boiler, the volatilization of the metals in the boiler, and the efficiency of the electrostatic precipitator to remove the metals [14].

Production of Bio-char from BL

BL is a promising material for the production of bio-char due to its high content of lignin and energetic elements that help hydrothermal carbonization.
The BL pyrolysis process generates a residue, the so-called bio-carbon (bio-char) in the proportion of C~35%. The yield of biochar obtained at different intervals of pyrolysis temperature is presented in Table 1. The increase in pyrolysis temperature conducted to

a decrease of the yield of biochar. The biochar yield decreased from 65.4% to 54.0% when the pyrolysis temperature varies from 400°C to 800°C. The biochar yields are relatively higher (>50%) than those obtained from biochar from biomass such as rice husk, palm fibre and wheat straw (< 40%) [5]. This pyrolytic solid residue may be used in acidic agricultural soils for loosening or for the total reduction of CO_2 based on the use of biochar as adsorbent material, to achieve zero emissions. It has been estimated that the production of 373 million tons per year of biochar derived from wood waste could capture about 500 million tons of CO_2 per year [15].
BL can be also valorised as starting material for recovery/production of other valuable chemical products (organic acids, inorganic salts) thus being part of the circular economy.

CONCLUSIONS

The present study showed that there is a great potential to produce alternative biofuels using technologies such as pyrolysis, for the production of electricity, from the wastes generated from kraft pulp mills. The results of this study open discussions about transforming the black liquor to an alternative biofuel in an expensive fossil fuel economic scenario.
Pyrolysis of black liquor generated valuable end products such as syngas, bio-oil and bio-char. The synthesis gas obtained from the pyrolysis process is rich in methane, hydrogen, carbon dioxide and carbon monoxide and can be used for energy purposes. The bio-oil after the refining process can be used for the production of biofuels for the automotive industry. Additionally, the bio-oil represents a valuable raw material for obtaining high-value chemical compounds, such as aromatic compounds and organic compounds, esters and acids. The bio-char resulting from the pyrolysis process has a great potential for agriculture applications or as adsorbent materials for the capture and storage of CO_2, after a chemical activation process.
The advantages of black liquor pyrolysis consist in the elimination by valorisation of waste produced regularly in considerable quantities from the pulp mill industry and the development of alternative and renewable fuels that contain high levels of ecological carbon.

ACKNOWLEDGEMENTS

The authors acknowledge the support from the Ministry of Research, Innovation and Digitization through the NUCLEU Program (financing contract no. 20N/2023, Project PN 23 15 04 02/2023-2026), titled “Capitalizing on laboratory experiments in the development of biofuel production technologies from agro-industrial waste”.

REFERENCES

[1] Liu Z., Deng Z., Davis S.J., Giron C., Ciais P., Monitoring Global Carbon Emissions in 2021, Nature Reviews Earth & Environment, vol. 3, pp 217–219, 2022.

[2] Al-Kaabi Z., Pradhan R.R., Thevathasan N., Chiang Y.W., Gordon A., Dutta A., Potential Value Added Applications of Black Liquor Generated at Paper Manufacturing Industry Using Recycled Fibers. Journal of Cleaner Production, vol. 149, pp 156–163, 2017.

https://doi.org/10.5593/sgem2024/4.1/s18.40

[3] Zhao Y., Zhang H., Zong P., Zhou H., Tian Y., Evaluation of Pyrolysis Characteristics and Product Distribution of Black Liquor Using Py-GC/MS and down Tube Reactor: Comparison with Lignin, Fuel, vol. 292, pp 120286, 2021.

[4] Carlsson P., Marklund M., Wiinikka H., Gebart R., Comparison and Validation of Gas Phase Reaction Schemes for Black Liquor Gasification Modeling, Energy Technology Centre, 2014.

[5] Teoh S.W., Yoon L.W., Wong W.Y., Low J.H., Application of Black Liquor Derived Carbonaceous Compound as Fuel in Direct Carbon Fuel Cell, International Journal of Integrated Engineering, vol. 14, pp 146–156, 2022.

[6] Wang Z., Yang X., Sun B., Chai Y., Liu J., Cao J., Effect of Vacuum Heat Treatment on the Chemical Composition of Larch Wood, Bioresources, vol. 11, pp 5743–5750, 2016.

[7] Van Thuijl E., Roos C.J., Beurskens L.W.M., An overview of biofuel technologies, markets and policies in Europe, ECN-C--03-008, Netherlands, 2003.

[8] Alvarez J., Amutio M., Lopez G., Barbarias I., Bilbao J., Olazar M., Sewage Sludge Valorization by Flash Pyrolysis in a Conical Spouted Bed Reactor, Chemical Engineering Journal, vol. 273, pp 173–183, 2015.

[9] Kevlich N.S., Shofner M.L., Nair S., Membranes for Kraft Black Liquor Concentration and Chemical Recovery, Current Progress Challenges and Opportunities, vol. 52, pp 1070-1094, 2017.

[10] Möllersten K., Yan J., Westermark M., Potential and Cost-Effectiveness of CO_2 Reductions through Energy Measures in Swedish Pulp and Paper Mills, Energy, vol. 28, pp 691–710, 2003.

[11] Cerón-Vivas A., Cáceres K.T., Rincón A., Cajigas Á.A., Cerón-Vivas A., Cáceres, K.T., Rincón A., Cajigas Á.A., Influence of PH and the C/N Ratio on the Biogas Production of Wastewater, Revista Facultad de Ingeniería Universidad de Antioquia, vol. 92, pp 88-95, 2019.

[12] Pola L., Collado S., Oulego P., Díaz M., Kraft Black Liquor as a Renewable Source of Value-Added Chemicals. Scopus, vol. 448, 137728, 2022.

[13] Chutia S., Narzari R., Bordoloi N., Saikia R., Gogoi L., Sut D., Bhuyan N., Kataki R., Pyrolysis of Dried Black Liquor Solids and Characterization of the Bio-Char and Bio-Oil. Materials Today Proceedings, vol. 5, pp 23193–23202, 2018.

[14] Nurmesniemi H., Pöykiö R., Perämäki P., Kuokkanen T., The Use of a Sequential Leaching Procedure for Heavy Metal Fractionation in Green Liquor Dregs from a Causticizing Process at a Pulp Mill, Chemosphere, vol. 61, pp 1475–1484, 2005.

[15] Bae Y.J., Ryu C., Jeon J.K., Park J., Suh D.J., Suh Y.W., Chang D., Park Y.K., The Characteristics of Bio-Oil Produced from the Pyrolysis of Three Marine Macroalgae. Bioresource Technologies, vol. 102, pp 3512–3520, 2011.

THE EFFECT OF THE AMOUNT OF BINDER ON THE PROPERTIES OF BRIQUETTES PREPARED FROM FOUNDRY DUST

Prof. Ing. Alena Pribulová, CSc.[1]

Assoc. Prof. Ing. Peter Futáš, PhD[1]

Ing. Patrik Fedorko [1]

Prof. Ing. Marcela Pokusova, PhD[2]

Assoc. Prof. Ing. Maria Mihalikova, PhD[1]

[1] Technical University of Košice - **Slovak Republic**
[2] Slovak University of Technology in Bratislava – **Slovak Republic**

ABSTRACT

Briquetting is the pressing of dusty materials into pieces of the same shape and size. Briquetting can be done without a binder or with the addition of a binder to the briquetting mixture. Briquettes can have any shape, but the most common is the shape of a cylinder. The briquettes must be strong enough to eliminate the possibility of damage during transport and must be strong enough even at high temperatures. The briquettes have a regular shape, have the same weight, are more durable and easier to transport. They are ecologically safe and it is possible to use carbon filling in briquettes to activate the process in metallurgical furnaces. Among the most important properties of briquettes are compressive strength and resistance to abrasion when falling. The briquettes were prepared from 4 types of dust from different parts of the foundry process. Dust from blasting castings cast into bentonite molding compounds was used. It is the dust caught in the catch box under the cyclone of the separator (B). The second dust (B_{mp}) was separated magnetic component of dust B. Dust (GF) captured in the collection reservoirs from the filter devices from the pendulum grinders. Dust (BF) from blasting castings cast in furan mixtures. Dust (G/B_{mp}) was a mixture of dust G and B_{mp} in a 2:1 ratio, and dust (G/BF) was a mixture of dusts G + BF in a 2:1 mass ratio. Bentonite and molasses were used as binders. The best properties were obtained from briquettes prepared from dust from grinding castings (G) and from a mixture of dust from grinding castings with dust from blasting castings cast into furan molds (G/BF)

Keywords: briquettes, foundry dust, molasses, bentonite, Shattered resistance.

INTRODUCTION

The production and processing of metals is associated with a large amount of different types of waste [1, 2]. One type of these wastes are dusts and sludges that arise as a result of melting processes or during the molding, casting and cleaning of castings. Dust from smelting processes is most often collected on filters, washing machines or in Venturi scrubbers. Dust particles produced during the finishing operations of castings (grinding and blasting) remain in the grinding mills or are trapped and captured on filters.

Slovak foundries pay very little attention to the modification of foundry dust into a form that is not harmful and suitable for transport and that does not pollute the environment,

https://doi.org/10.5593/sgem2024/4.1/s18.41

but above all enables its further metallurgical processing. The dust that is collected in Slovak foundries is deposited in a landfill and has a very negative impact on the environment and on the contamination of groundwater. The technology of processing dust waste in metallurgical processes with blowing into the melting unit is not very widespread in Slovakia due to the lack of technical equipment [3]. The majority of dusty waste cannot be processed directly in metallurgical aggregates and therefore it is necessary to compact this material. One of the dust compaction technologies is briquetting [4, 5].

Briquetting is a cold joining method that involves pressing mixtures of fine particles into rollers. In order to achieve additional strength, the briquettes can be fired afterwards. This technique is generally more expensive than other agglomeration techniques due to equipment wear and energy consumption.

The briquetting process transforms the briquetted material with a low bulk density into briquettes with a high density [6 - 8]. The choice of binder and additives depends on the quality and price of the briquettes.

The binders used in the briquetting process can be divided into inorganic and organic binders. The most used binder is bentonite, water glass, molasses and starch. Cement and cementitious materials - Portland cement is a well-known cement binder and consists mainly of CaO and SiO2.

The most important properties of briquettes are: moisture content, bulk density, shattered index, shattered resistance, resistance to water penetration and compression strength [9,10].

The aim of the experiments presented in this paper was to modify the dusts that are created in the foundry process into a form that will allow their re-metallurgical processing in the foundry and the use of their metal component. Briquetting of the dust was chosen as the treatment process, and the briquettes can be further used as a charge in the furnace unit, either in a cupola furnace or in an electric induction furnace. 2 types were chosen as binders for the preparation of briquettes: the cheapest binder – bentonite and relatively expensive organic molasses (the choice of binder was based on previous experiments).

MATERIALS AND METHODS

The following types of dust were used for the production of briquettes:

1. Dust from the blasting of cast iron castings cast into a molding mixture with bentonite, captured under cyclones (***B***). *(B – blasting).*
2. Magnetic (mp) proportion of dust from blasting castings (***Bmp***).
3. Dust from the grinding of cast iron castings, which were cast into a molding mixture with bentonite, collected in catch tanks from filtration devices (**G**) - grinding.
4. Dust from the blasting of cast iron castings cast into molds from furan molding compounds, captured in the cassette separator (**BF**-blasting, furan).
5. Dust (**G/B$_{mp}$**) was a mixture of dust from grinding castings (G) with a magnetic portion from blasting castings in a ratio of 2:1.
6. Dust (**G/BF**) was a 2:1 mixture of casting grinding dust and casting blasting dust cast into furan molding compounds.

In tab. 1 is the chemical composition of the dusts used in the experiments. Figures 1-4 show the grain morphology of individual dusts and their granulometric composition.

Tab. 1 Chemical composition of dusts used in experiments in %

	Fe	FeO/Fe_2O_3*	Fe_m	SiO_2	P	S	SiC	Mn	C
B	58.64	21.27	39.32	24.71	0.09	0.155	-	0.37	5.67
B_{mp}	74.34	26.58	49.37	9.01	0.06	0.156	-	0.46	3.31
G	88.58	0.72/0.48*	87.91	8.84	0.06	0.104	1.01	0.58	3.38
BF	24.29	4.02	12.17	51.24	-	-	-	0.43	5.41

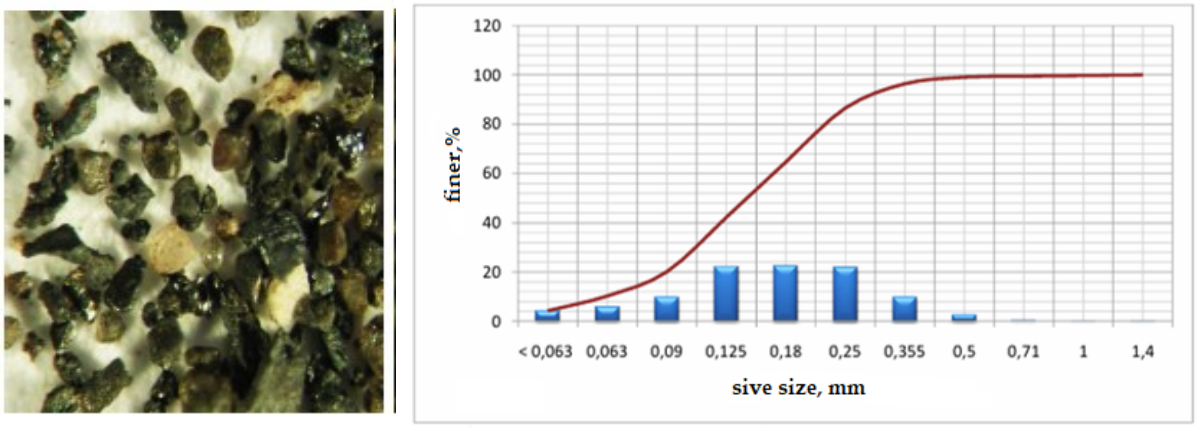


Fig.1 Dust from blasting castings (**B**) – magnification 5x and its granulometric composition

Chemical analyzes of the dust were done in the accredited chemical laboratory of USSteel Košice, the granulometric composition was done on a sieving device of the company LPzE-2e Multiserw, briquettes were produced using a manual briquette press at a pressure of 10 MPa. 300 g of the mixed mixture was used to prepare one briquette. The briquettes were tested for compressive strength and disintegration. The compressive strength test was carried out on a WPM Leipzig type blasting machine. The drop resistance test consisted of dropping briquettes from a height of 1.5 m onto a metal pad. Each briquette was dropped 3 times, and the briquette was weighed after each fall.

Shattered index. The durability of the briquettes was determined in accordance with the Shattered index described by Sengar [9]. This involved dropping the briquette samples repeatedly from a specific height of 1,5 m onto a solid base. The fraction of the briquette retained was used as an index of briquette breakability. The percentage weight loss of briquettes was expresed as a percentage of the initial mass of the material remaining on the solid base, while the shatter resistance was obtained by subtracting the

https://doi.org/10.5593/sgem2024/4.1/s18.41

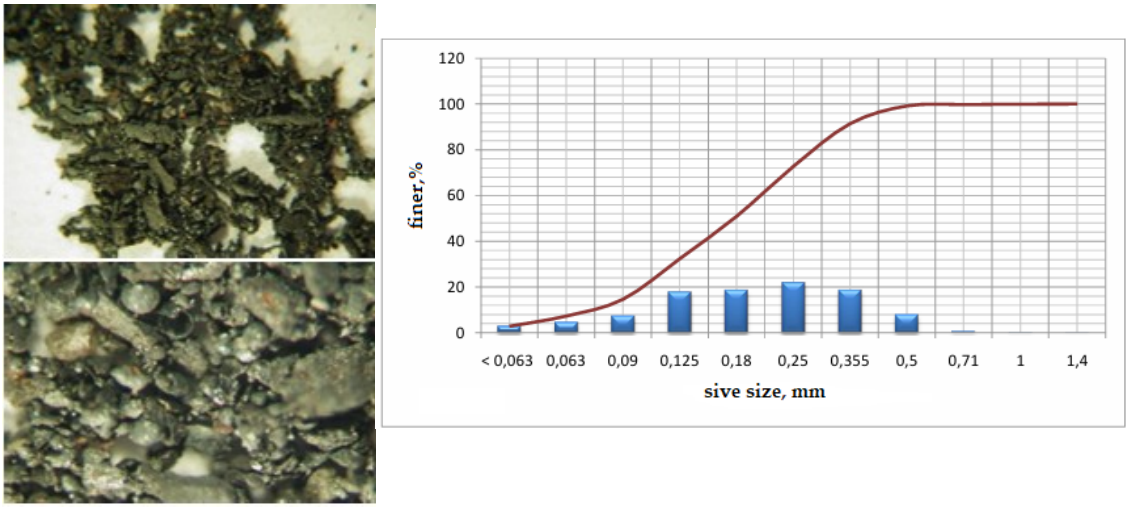


Fig. 2 Morphology of the grains of the magnetic part of the dust from the blasting of castings cast into bentonite molding mixtures (**B_{mp}**) (magnification 1.5, 5x) and its granulometric composition

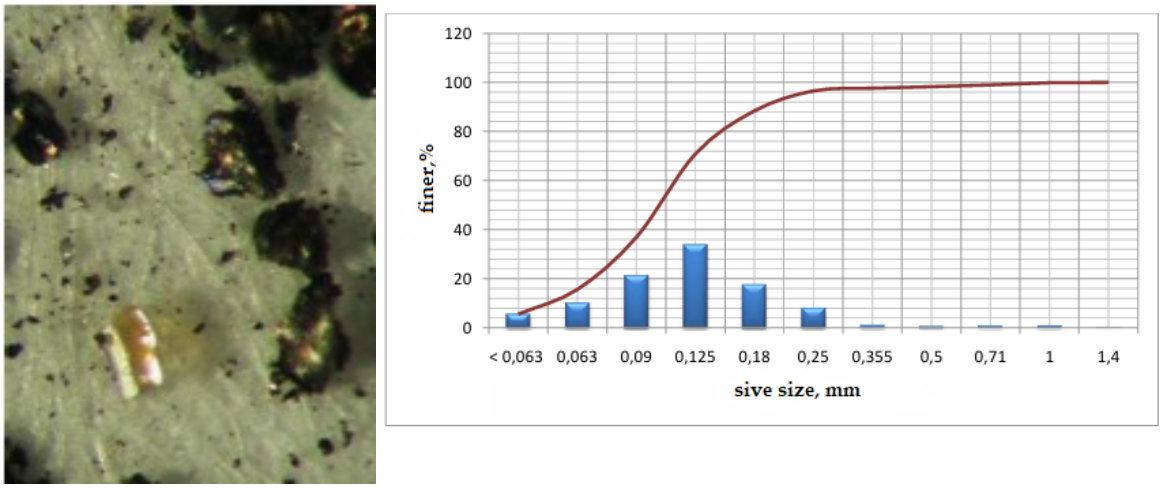


Fig.3 Dust from the grinding **G** (magnification 12x) and its granulometric composition

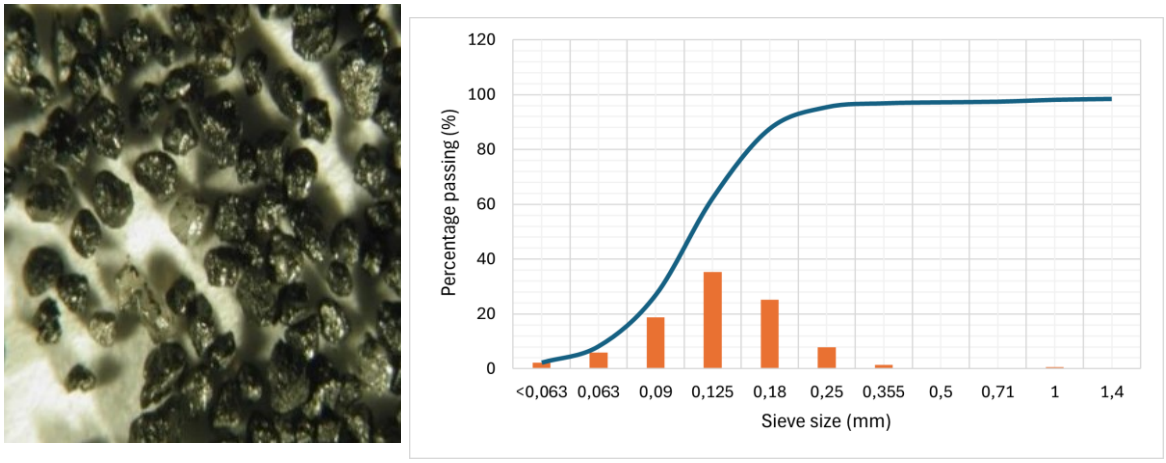


Fig.4 Dust from the blasting cast into molds from furan molding compounds **BF** (magnification 5x) and its granulometric composition

percentage weight loss from 100.

$$\% WL = \frac{wB - wA}{wB} \times 100\% \quad (1)$$

wB – initial weight before shatter, g
wA – weight of shattering, g
WL – weight loss – Shattered index, %
$SH_R = 100 - W_L$
SH_R *– Shattered resistance, %*

RESULTS AND DISCUSSION

a) Briquetting of dust from grinding castings.

Bentonite was added to the dust from the grinding of castings in the amount of 0; 2.5; 3; 5; 6; 8; 10% and molasses in the amount of 2, 4, 6, 8, 10%, the total weight of the mixture per briquette was 300 g, the amount of added water in the case of using bentonite was 30 ml, for molasses it was half of 15 ml, which represents 10% and 5% of the weight of the briquette. Table 2 shows the composition of the briquetting mixture, compressive strength, shattered index after the first (WL_1) and third fall (WL3) of the briquette and shattered resistance (SH_R)

Tab.2 Composition of briquetting mixtures and properties of briquettes from grinding dust (G)

	Bentonite (B/ Molasses (M) %	compressive strength,MPa	W_{L1} %	W_{L3} %	SH_R %
G_{B0}	0	4.3	100	the briquette fell apart	0
$G_{B2,5}$	2.5	9.3	100	the briquette fell apart	0
G_{B3}	3	10.22	20	the briquette fell apart	0
G_{B5}	5	10.47	1.57	5	95
G_{B6}	6	12.51	0.1	1.53	98.47
G_{B8}	8	14	0.1	1.13	98.87
G_{B10}	10	16.4	0	1.05	98.95
G_{M2}	2	24.6	0.2	0.2	99.98
G_{M4}	4	31.6	0.1	0.27	99.73
G_{M8}	8	20.04	0	0.55	99.45
G_{M10}	10	16.8	0.1	1.72	98.28

b) Briquetting of dust from castings blasting (B)

Bentonite in the amount of 2,4,6,8 and 10% and molasses in the amount of 2,4,5,6,8 and 10% was added to the dust from the blasting of the castings. Water was added similarly to the previous case. Table 3 shows the composition of the briquetting mixture, compressive strength, shattered index after the first (WL1) and third fall (WL3) of the briquette and shattered resistance (SHR). Increasing the bentonite content increased the strength of the briquettes, but the briquettes with 2.4 and 6% bentonite disintegrated after the first drop. When adding molasses, the strength increased from 12.2 MPa to

https://doi.org/10.5593/sgem2024/4.1/s18.41

16.4 MPa. With a molasses content of 2 and 4%, the briquettes fell apart after the first drop, with another increase in the molasses content, the shattered resistance increased to 98.95%

Tab.3 Composition of briquetting mixtures and properties of briquettes from dust from castings blasting

	Bentonite (B/ Molasses (M),%	compressive strength,MPa	W_{L1} %	W_{L3} %	SH_R %
B_{B2}	2	3.8	100	the briquette fell apart	0
B_{B4}	4	5.3	100	the briquette fell apart	0
B_{B6}	6	6.1	20	the briquette fell apart	0
B_{B8}	8	8.3	1.57	5	95
B_{B10}	10	8.7	0.1	1.53	98.47
B_{M2}	2	12.2	100	the briquette fell apart	0
B_{M4}	4	13.2	100	the briquette fell apart	0
B_{M5}	5	14	0.3	2.1	97.9
B_{M6}	6	14.9	0.1	2.05	97.95
B_{M8}	8	15.4	0.12	1.8	98.2
B_{M10}	10	16.4	0	1.05	98.95

*c) Briquettes from the magnetic part of the dust from the blasting of castings cast into bentonite mixtures (**B_{mp}**)*

Briquettes were prepared from a mixture of dust and bentonite in the proportions used in the previous two cases and from dust and molasses (2, 4, 5 and 10% molasses). Briquettes with bentonite reached strength from 4.3 (2% bentonite) to 10.22 MPa (10%), but they all shattered after the first drop. When using molasses, the strength increased from 5 MPa to 12.51 MPa at 10% molasses. At 5% molasses, the briquette was shattered after the second drop, and only at 10% molasses was a Shattered resistance of 98.87% achieved.

*d) Briquetting of dust from blasting castings cast into furan mixtures (**BF**)*

Dust from blasting castings cast into furan mixtures was mixed with bentonite and molasses similarly to other cases. When bentonite was used, the compressive strength of the briquettes increased from 5.3 to 8.1 MPa, but all the briquettes disintegrated after the first drop. In the case of molasses, the strength ranged from 14 to 17 MPa. Resistance to breakage was from 95 to 99.64%.

*e) Briquetting of dust **G/B_{mp}** (dust from grinding and magnetic part dust from blasting 2:1)*

Dust G/Bmp was mixed with both bentonite and molasses. The strength of briquettes with bentonite ranged from 3 to 7.3 MPa, but all briquettes broke after the first or second fall. When using molasses as a binder, the minimum strength was 7.9 MPa at 10% molasses and 11 MPa at 2%. Shattered resistance gradually decreased from 48.28% at 4% molasses to a value of 0.1% at 10% molasses.

f) Briquetting of G/BF dust (dust from grinding and dust from blasting of castings cast into furan molding compounds - ratio 2:1

When bentonite was used, compressive strengths from 3 to 9 MPa were achieved at 10% bentonite, and the briquettes disintegrated after the second drop. The results using molasses as a binder are shown in tab. 4

Tab.4 Composition of briquetting mixtures and properties of briquettes from dust G/BF

	Molasses (M),%	compressive strength,MPa	$W_{L1,}$ %	$W_{L3,}$ %	SH_R %
G/BF_{M2}	2	16.5	100	the briquette fell apart	0
G/BF_{M4}	4	20.3	1	2.1	97.9
G/BF_{M6}	6	21.5	0,43	1.58	98.42
G/BF_{M8}	8	24.2	0,11	1,03	98,97
G/BF_{M10}	10	25.1	0	0.05	98,95

CONCLUSION

Dust briquetting is one of the methods that enables the reuse of foundry dust in the foundry process. Six dust samples were used in the experiments, four of which were dust generated during finishing operations in the foundry and two were a mixture of these dusts. Bentonite and molasses were used as binders. The 2 most important properties of the briquettes were evaluated: compressive strength and shattered resistance. By increasing the bentonite content, the strength of the briquettes also increased in all dusts, bentonite fulfilled its role in the case of Shattered resistance only when using sanding dust (more than 5% bentonite) and dust from blasting castings when using at least 8% bentonite. In other cases, the briquettes were broken (measurements took place after 7 days from the preparation of the briquettes). Molasses is a very good binder both in the case of compressive strength and in the case of measuring Shattered resistance for all used powders and their mixtures. The best compressive strengths were achieved with briquettes prepared from dust from grinding castings. This may be due to the shape of the dust grains, which look more like "slices" of metal and contain the smallest amount of silicon, and at the same time 60% of the grains are smaller than 0.125 mm. When using molasses, it was found that increasing its amount in the mixture leads to a decrease in the strength of the briquettes and a decrease in the shattered index. A 2% share of molasses as a binder is completely sufficient. Very good results were also achieved in the briquetting of dust from grinding and dust from blasting of castings cast into furan molds (G/BF). This dust, on the other hand, has the highest SIO2 content compared to sanding dust and thus also the largest proportion of rounded grains, which probably complement well with the uneven sanding dust grains.

ACKNOWLEDGEMENTS

This work was supported by the Scientific Grant Agency of The Ministry of Education of the Slovak republic No. VEGA 1/0002/22 and APVV-22-0580

https://doi.org/10.5593/sgem2024/4.1/s18.41

REFERENCES

[1] Danko,R., Jezierski,J., Holtzer,M.,Physical and chemical characteristics of after-reclamation dust from used sand moulds, Arabian Journal of Geosciences, 9(2), 153, **2016**, pp. 1 –8.

[2] Jursová S., 2010. Metallurgical waste and possibilities of its processing. Proceedings of 19th International Conference on Metallurgy and Materials, Metal **2010**. Ostrava, Czech Republic, 115- 120.

[3] Danko,R., Holtzer,M., Danko,J., Investigations of physicochemical properties of dusts generated in mechanical reclamation process of spent moulding sands with alkaline resins, China Foundry, Vol.11, Issue 2, **2014**, pp. 132 – 138.

[4] Socalici,A., Heput,T., Ardelean,E., Ardelean,M., Ferrous waste processing by pelletizing, briquetting and mechanically mixed, International Journal of Energy and Environment, Vol.5, Issue 4, **2011**, pp.532 – 540

[5] Pustejovska,P., Brozova,S., Jursova,S., An ecological perspective the use of metallurgical waste, International Multidisciplinary Scientific GeoConference Surveying Geology and Mining Ecology Management, SGEM, Albena, Vol.1, Issue 5, **2014,** pp.11 – 14.

[6] Magdziarz,A., Kuznia,M., Bembenek,M., Gara,P., Hryniewicz,M., Briquetting of EAF dust for its utilization in metallurgical process, Chemical and Process Engineering, Vol.36, Issue 2, pp,**2015**, 263 – 271.

[7] Zhao, H.; Zhou, F.; Ma, C.; Wei, Z.; Long,W., Bonding mechanism and process characteristics of special polymers applied in Pelletizing Binders. Coatings **2022**, 12, 1618. https://doi.org/10.3390/coatings12111618

[8] Kotta,A.B., Patra,A., Kumar,M., Karak,S.K., Effect of molasses binder on the physical and mechanical properties of iron ore pellets, International Journal of Minerals, Metallurgy and Materials, Volume 26, Number 1, January 2019, Page 41, https://doi.org/10.1007/s12613-019-1708-x

[9] Sengar,S.H., Mohod,A,G., Khandetod, Y.P., Patil,S.S., Chendake,A.D., Performance of briquetting machine for briquette fuel, International journal of Energy Engineering, Vol.2, Issue 1, **2012**, pp. 28 – 3

[10] Ambrisko,L., Marasova,D.: Studies of mechanical properties of the cover layers of rubber conveyor belts, Przemysl Chemiczny, **2022,** 101 (3) , pp.205-209

THE POTENTIAL COMPLEXING IMPACT OF SOME ORGANIC COMPOUNDS' AMINE AND CARBOXYL GROUPS ON TRANSITION METALS

PhD(c).E Adelina Haskaj[1]
PhD(c). Prof.Dr.Musaj Pacarizi[2]
Prof.Dr.Sonja Lepitkova[3]
Berat Sinan[4], PhD(c)
Bahri Sinani[4] .PhD(c)
Elida Dreshaj[1]

[1]Alma Mater Europaea Campus College "REZONANCA", Prishtinë, **Kosovo**
[2]University of Prishtina, Faculty of Mathematical-Natural Sciences, Prishtinë, **Kosovo**
[3]University of Štip" Goce Delčev"- Štip,**North Macedonia**
[4]University of Mitrovica, Faculty of Geo-Science, Mitrovicë, **Kosovo**
[5]Mitrovica Municipality, Mitrovicë, **Kosovo**

ABSTRACT

Environmental water chemistry is substantially aided by modern electrochemical research. Sensitive voltammetric techniques are much more useful for metal species in natural waters, where complexation with organic molecules predominates. Many environmental electrochemists are still interested in determining the stability constants of metal ion complexes with various ionic species found in natural waterways. The aim of this work is to investigate the possible influence of complexation of amine and carboxyl groups of some organic molecules (with EDTA, NTA and aniline, using differential pulse polarography). The Differential Pulsed Polarography (DPP) is experimental technique that consist on three-electrode electrochemical cell of: working electrode (SMDE "Static Mercury Drop Electrode"), reference electrode (Ag/AgCl electrode) and auxiliary electrode (graphite electrode). In our research we have followed the polarographic waves of metal ions (Me^{n+}), in constant concentration ($C=1x10^{-4}$ mol/dm^3) titrating in perchlorate solution with complexing agents: aniline, NTA and EDTA, in concentrations from C $1x10^{-5}$ to $1x0^{-3}$ $mol.dm^{-3}$, at two pH values (pH = 4 and pH = 6). To prove the competition of organic ligands in the complexion of metal ions (Me^{n+}) we have prepared solutions by completely complexing the metal ions with aniline and then we have gradually added the strongest complexing agents NTA and EDTA.

Keywords: complexation, stability constants , EDTA, NTA

INTRODUCTION

Nickel in nature has ten times more than cobalt. It is mainly found in the form of silicates such as Garnier, [(Ni, Mg)6Si4O10 (OH) 8], but today nickel is mostly obtained from sulfurores, of which the most important is pentlandite (Ni, Fe) S8 (Filipoviq et al., 1997)[6].

https://doi.org/10.5593/sgem2024/4.1/s18.42

Nickel (Zhou et al., 2020)[1], and its compounds are less toxic, except for nickel carbonyl ifinhaled (it inhales the lungs and can even cause death due to the formation of the lung endemic) (Kabata-Pendias et al., 2007)[12]. Frank Nestle from the University of Zurich in Switzerland, has found that one and two euro coins had 240 to 320 times greater amount of nickel than allowed by EU regulation (Neste, F et al.,2002)[7]. In some cases, concentrations up to 1000 μg / l have been detected in the case of the first water leak from the channel if the water has remained for a long time (Pendias et al 2010)[11].Cobalt is a rare element in the earth's crust. In the soil, the mass share of cobalt is $1x10^{-3}$% cobalt (Yildiz. Y, 2017)[19]. Chromium is a rare element in the earth's crust (0.03% mass fraction). Its main ore is chromite, $FeCr_2O_4$, which is actually a complex oxide FeO x Cr_2O_3 with a spinel structure (Krishnamoorthy et al., 2012)[8]. Chromium is also a very toxic element, it has harmful effects on the kidneys, liver, and respiratory organs with a hemorrhagic effect, while exposure to Cr^{6+} can cause dermatitis. In addition to occupational dermatitis, chromium production workers may suffer from ulceration and damage to the nasal septum (Ferner D., 2001)[4]. The amount of chromium in water depends mainly on the activity of the industry (ILO., 1999)[9]. These metals can form complex compounds with different ligands such as EDTA, NTA, and aniline. Carboxylic acids are compounds that in their molecule possess the carboxyl group composed of the carbonyl group and if the hydroxyl group of the carboxylic group is replaced by

those substituents, the carboxylic acid derivatives are obtained (Lajqi. A., 1998)[14]. The word "complex" was first used by Alfred Werner in 1893 for compounds treated with coordinate bonds. According to him, complex compounds contain at least one complex ion, which consists of a central metal atom bonded (coordinated) to a certain number of atoms or group of atoms (ligands) (Kamberi. B., 1996)[13].

The constant or the formation constant of the complex expresses the stability (stability) of the complex and the greater its value the more stable the complex is and vice versa [18]. The metal ion can be complexed with other ligands, so it can be partof other complexes, also the free ligand can complex ions of other metals, in a word, along with the main complex, other complexes are formed (Bacaj. M., 2002)[2].Experimental measurements proved that EDTA and NTA form very stable complexes with heavy metal ions, which appear at much more negative reduction potentials compared to the reduction of the metal ions investigated: Ni (II), Co (II), and Cr (III). While aniline forms labile complexes and does not appear as separate polarographic waves but coexists with metal ion waves. From the experimental data, by measuring thechange in the reduction potential of metal ions, and metal complexes with organic ligands, we calculated the stability constants of complexes formed, and our results are very close to values from the literature. The complexation of metal ions is greater in solutions with pH=6, compared to pH=4, as the result of the influence of H^+ions.

METHODS AND METHODOLOGY OF THIS RESEARCH

Polarography is a special technique of voltammetric methods (volt ammeter). Voltammetry summarizes a set of electroanalytical methods based on the study of current-potential intensity dependence for a polarized electrode in the solution underanalysis. The term "polarography" is commonly referred to as the voltammetric technique, in which a dripping mercury electrode is used as the polarizing electrode (Çullaj, A., (2004)[3]. Its

application in analytical chemistry, ie in chemical analysis is ofspecial importance. Polarographic analysis has been expanded and perfected as a multidisciplinary technique since its discovery (Filipovic, I., 1978)[5].

Differential Pulsed Polarography (DPP) was used as an experimental technique during our research. A three-electrode electrochemical cell consisting of a working electrode (SMDE "Static Mercury Drop Electrode"), a reference electrode (Ag/AgCl electrode), and an auxiliary electrode (graphite electrode) was used. During polarographic measurements, the potential was swept from E = 0.2 mV to E = -2000 mV versus the comparative electrode, at a scan rate of 12 mV/s, and the dropping time of the mercury droplet was 1s. The pH value of the solutiwaswere measured before polarographic measurements.

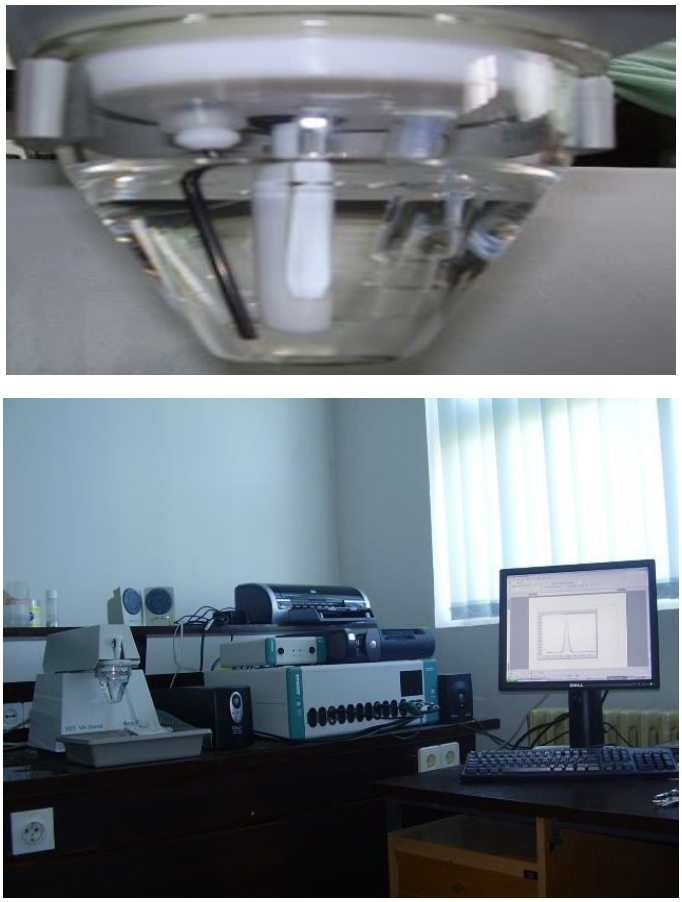


Figure 1. Autolab PGSTAT12 Potentiostat/Galvanostat with MultiModeElectrode 663 VAStand Metrohm.

RESULTS AND DISCUSSION

In this paper are presented the experimental results obtained from polarographic research of the complexation of Ni (II), Co (II), and Cr (III) ions with NTA, EDTA, and aniline in thepresence of perchlorates as the base electrolyte.

In our research, we have transmitted the polarographic waves of free metal ions Ni (II) ionic, Co (II) ionic, and Cr (III) ionic and complexed them in solutions of organic ligands

https://doi.org/10.5593/sgem2024/4.1/s18.42

(NTA, EDTA, and aniline), in two different values of pH (at pH = 4 and pH = 6). Measurements were made after stabilizing the solutions for 24 hours. Measurements were followed by the pulsed differential polarography (DPP) technique. Samples were placed in the electrolytic cell after measuring the pH value. The solution was deaerated for 5 minutes at a pressure of 1 bar of nitrogen and at the same time mixed a with Teflonmixer at 1500 rpm. During the measure, elements the potential was transmitted from 0.0V to -1.8 V to the comparative electrode Ag / AgCl. The mercury dropping time was 1s, the scanning speed was 12 mV / s, and the mercury droplet size was kept constant at 0.4 mm2.In our research we followed the polarographic waves of metal ions (Men^{+}) with unchanged concentration (C = $1•10^{-4}$ mol / dm^3) titrating in perchlorate solution with complex means (Ligande): aniline, NTA and EDTA with concentrations of C = $1•10^{-5}$ to $1•10^{-3}$ $mol.dm^{-3}$, at two pH values (pH = 4 and pH = 6). To prove the competition of organicligands in the complexion of metal ions (Men +) we have prepared solutions by completely complexing the metal ions with aniline and then we have gradually added the strongest complexing agents NTA and EDTA.

$$E_{1/2} = E^0 - \frac{RT}{nF} \ln K_C - \frac{pRT}{nF} \ln [X]$$

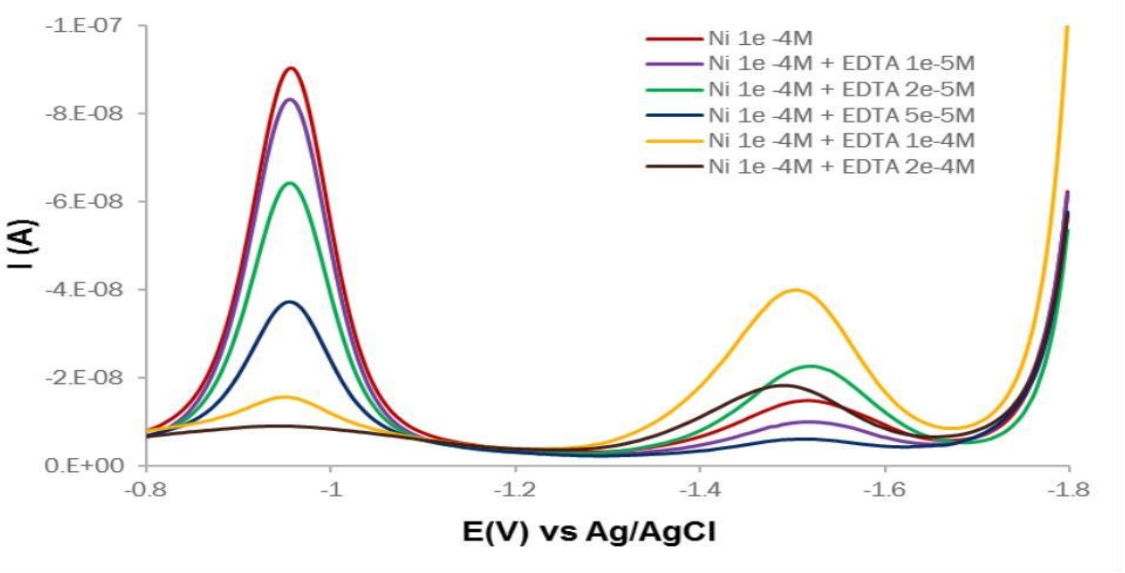


Figure 2. DP voltammograms of titration Ni^{2+},C=1x10^{-4} M with EDTA in perchloratesC=0.1 M, pH=4.

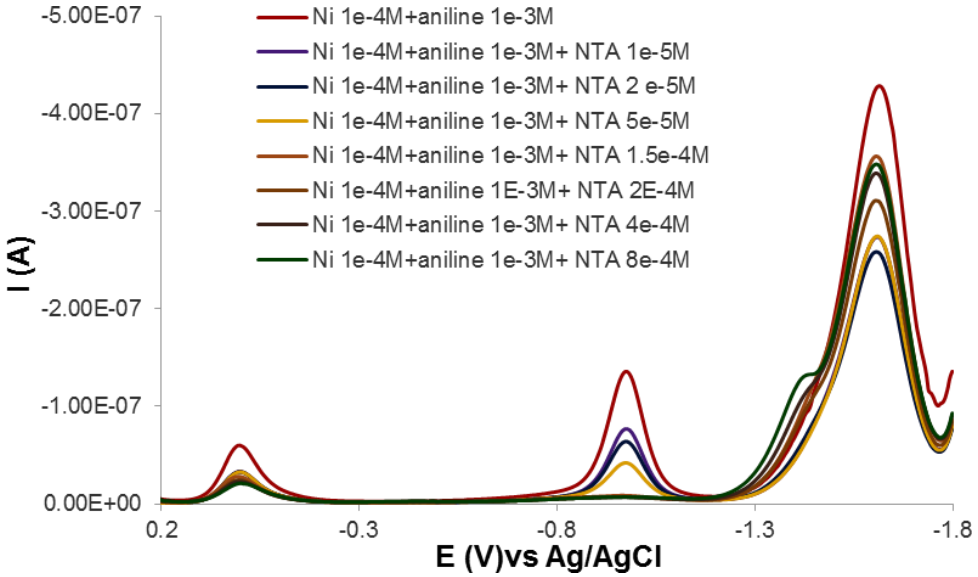


Figure 3. DP voltammograms of titration Ni^{2+}, C=1x10^{-4} M with NTA in aniline, pH=4.

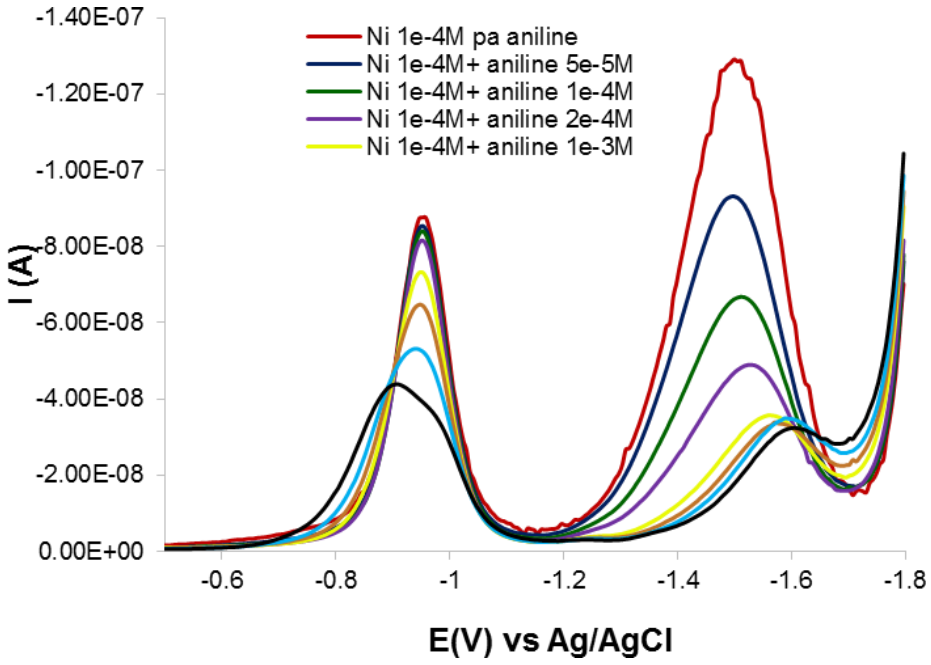


Figure 4. DP voltammograms of titration Ni^{2+}, C=1x10^{-4} M with aniline.

https://doi.org/10.5593/sgem2024/4.1/s18.42

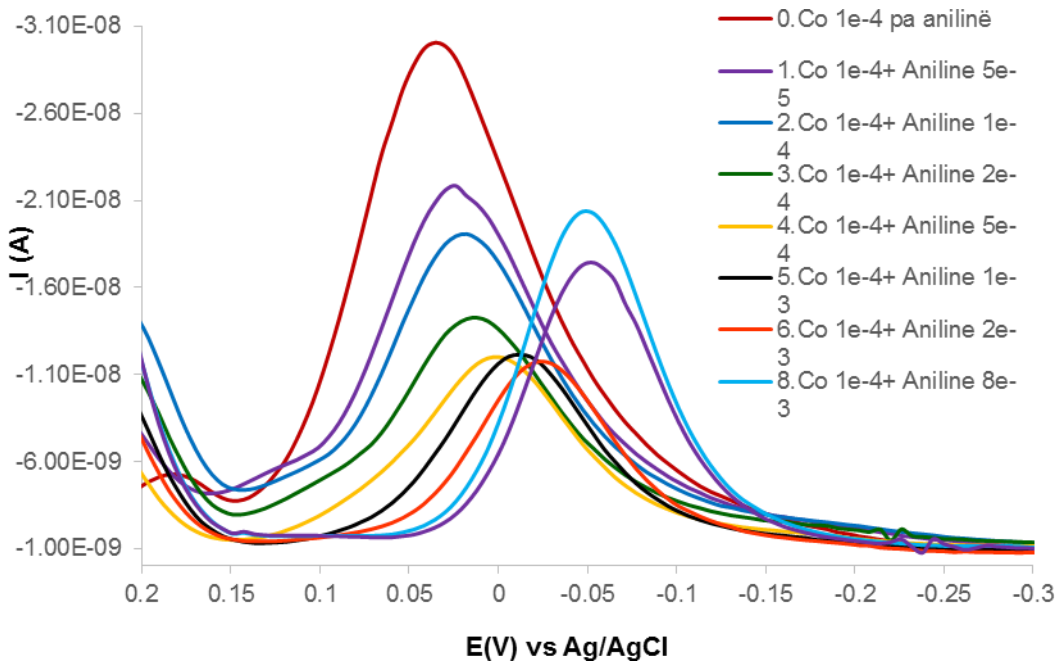


Figure 5. DP voltammograms of titration Co^{2+},C=1x10^{-4} M with aniline, pH=4.

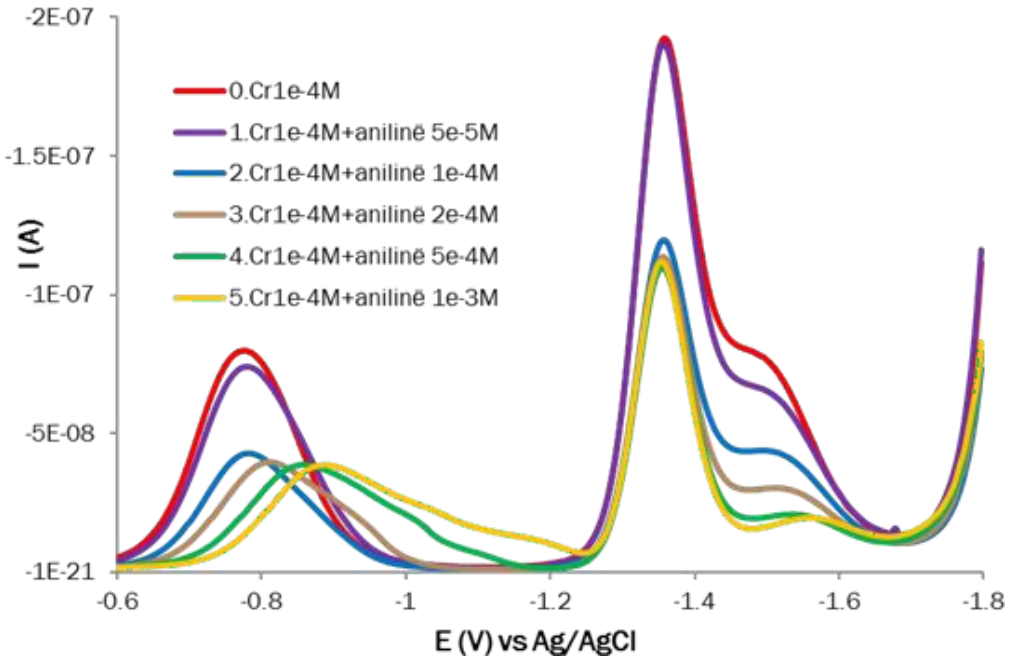


Figure 6. DP voltammograms of titration Cr^{3+}, C=1x10^{-4} M with aniline.

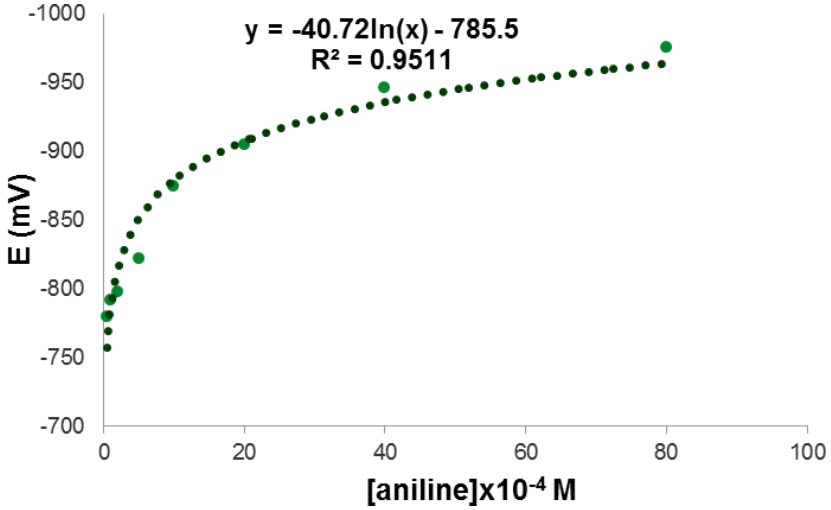


Figure 7. Correlation between reduction potential of Cr^{3+} by aniline concentration.

CONCLUSIONS AND RECOMMENDATION

During experimental dates, we proved that organic ligand EDTA is the strong complexing agent and with the investigation, metals forms very strong complexes Ni(II)EDTA, Co(II)EDTA, and Cr(III)EDTA. With increasing aniline concentration we observe deviations of the reduction potential from -1510 mV to -1600 mV, as a resultof the formation of Ni (II) (aniline) x complexes. Similarly, many authors use the reduction potential reduction to calculate the stability constants of complexes. (Paçarizi, M., 2007; Omanovic, D., 2006)[16-17]; Paçarizi M., 2008)[18]. Based on the presentation of two polarographic waves even when we have not added NTA complex ligand at all as well as from the literature (Jia l., 2019)[10], we are convincedthat the reduction of Cr (III) to Cr (0) ions occurs in two ways different. Organic ligand NTA is a weaker complexing agent than EDTA, but stronger than anilineand this is proved from experimental dates and also from literature (Martell A., 1998)[15]. Our conclusions we have derived by measuring the intensities of the currents of polarographic waves of Me^{n+} ions, when we titrated with the different organic ligands in the same concentrations and the metal ions are the most complexed of the same mostly metal ions are complexed (the reduced of currents intensity) in the presence of EDTA, then in presence of NTA but with the addition of aniline we don't show decrease of the intensity of the current but only changing the reduction potential of metal ions. Based on experimental data such as the difference reduction potential and reduction ofthe intensity of the current, we conclude that Cr(III) forms more stable complexes with the ch of ligands used, than Ni(II) and Co(II) form less stable complexes. In the perchlorate solutions in pH=4, complexation was less than in the pH=6, and thisis because the H^{+} ion is a Lewis acid and makes competition with the Me^{n+} ion in the connection with organic ligand (Lewis base).

REFERENCES

[1] Zhou.J., Yongzhi.Y., Ma.Y.,(2020), Assembling Nickel Oxide Nanoparticles into Porous Polyhedra: Highly Active Electrocatalysts for Alkaline Water Oxidation https://doi.org/10.1002/slct.202002414.

https://doi.org/10.5593/sgem2024/4.1/s18.42

[2] Bacaj, M., (2002). Kimia analitike 1-Bazat teorike, Fakulteti i Shkencave Matematiko-Natyrore, Universiteti i Prishtinës, Prishtinë.

[3] Çullaj, A., (2004). Metoda instrumentale të analizës kimike, Shtëpia Botuese e Librit Universitar, Tiranë, 111-119.

[4] Ferner, D.J., (2001), Toxicity of heavy metals, eMed. J, Vol. 2, No. 5.

[5] Filipovic, I., Sabiencelo, P., (1978) Laboratorijski Prirucnik, I Dio – Knjiga druga, 2 izdanje, Tehnicka knjiga, Zagreb.

[6] Filipoviq. I., Lipanoviq,S., (1997): General and inorganic chemistry; Vol. 2, 1202-1204, Textbook.

[7] Frank O Neste , Hannes Speidel, Markus O Speidel, (2002), Metallurgy: high nickel release from 1- and 2-euro coins, Sep 12;419(6903):132, https://doi.org/10.1038/419132a.

[8] G.Krishnamoorthy, S.Sadulla, P.K.Sehgal, Asit BaranMandal, (2012), Green chemistry approaches to leather tanning process for making chrome-free leather by unnatural amino acids, Volumes 215–216, 15 May, Pages 173-182. https://doi.org/10.1016/j.jhazmat.2012.02.046.

[9] International Occupational Safety and Health Information Centre. Metals. (1999). In Basics of Chemical Safety, Chapter 7. Geneva: International Labour Organization.

[10] Jia, Lixin, Xingwang Pei, and Fei Yang. (2019). "Electrolysis-Assisted Mn(II)/Sulfite Process for Organic Contaminant Degradation at Near-Neutral pH" *Water* 11, no. 8: 1608. https://doi.org/10.3390/w11081608.

[11] Kabata Pendias, A. and Mukherjee, A.B. (2007) Trace Elements from Soil to Human,Springer-Verlag,Berlin,23.61-62 http://dx.doi.org/10.1007/978-3-540-32714-1.

[12] Kabata-Pendias, A., Pendias, H., (2001). Trace Elements in Soils and Plants, 27-28. https://doi.org/10.1201/b10158.

[13] Kamberi, B., (1996). Universiteti i Prishtinës, Prishtinë.

[14] Lajçi, A., Kalaj.V., (1998). Kimia (për studentët e mjekësisë, stomatologjisë, dhe biologjisë), Fakulteti i Shkencave Matematiko-Natyrore, Prishtinë, pp 345-346, Textbook.

[15] Martell, A., Smith, R., (1998) *Critically selected stability constants of metal complexes database (Vers. 5.0)*, Texas A. & M. University, College Station, TX.

[16] Omanovic, D., (2006). Determination of Stability Constants of Labile Metal Complexes; Croatica Chemica Acta, 79 (1), pp.67-76 https://www.researchgate.net/publication/285722948_Pseudopolarography_of_trace_metals_Part_III_Determination_of_stability_constants_of_labile_metal_compl exes.

[17] Paçarizi M., Shehdula M., Lajçi A., Faiku F., (2008). *Kompleksimi i joneve Pb(II) me acidin nitrilotreacetik në prani të acideve karboksilike*; AKTET e Takimit Ndërkombëtar,Vjetor,IASH, 1(2),pp. 121-127. https://docplayer.net/65498198-Bashkeveprimi-i-joneve-pb-ii-me-ligande-organike.html.

[18] Paçarizi, M., (2007). Disertacion i doktoratës, Universiteti i Prishtinës, Fakulteti i Shkencave Matematiko-Natyrore, Prishtinë.(1988). Kimia analitike-Bazat teorike, Libri Universitar, Tiranë.

[19] Yasemin Yildiz (2017), General aspects of the cobalt chemistry.

THERMAL DECOMPOSITION OF WOOD WASTE. THERMOGRAVIMETRIC ANALYSIS

Assoc. Prof. Dr. Antonina A. Stepacheva
Assoc. Prof. Dr. Yury V. Lugovoy
Prof. Dr. Vladimir P. Molchanov
Prof. Dr. Yury Yu. Kosivtsov
Prof. Dr. Mikhail G. Sulman
Tver State Technical University, **Russia**

ABSTRACT

Wood processing is a prospective way to minimize the waste of forestry and woodworking industries. Nowadays, different methods are used for wood waste processing: combustion, pyrolysis, liquefaction, torrefaction, carbonization, etc. These methods are applied for the obtaining of valuable chemicals, combustible gases, and biochar. Despite the thermochemical methods (pyrolysis, carbonization, torrefaction) being considered to be the most efficient methods for waste utilization, systematic studies are required for the proper technology development. Thermogravimetric analysis is one of the major methods used to study the thermal decomposition of biomass. The thermogravimetric data collection for the different types of biomass waste is an important task. It is known that the rates, mechanisms as well as product yields of biomass thermal decomposition strongly depend on the type of feedstock, the vegetation area and conditions, and on the part of the plants.

In this work, the thermal decomposition of wood waste was studied in a temperature range of 25-1000 °C by a thermogravimetric analysis. For types of wood waste were studied: pine and birch sawdust, and pine and birch bark.

Keywords: sawdust, wood bark, thermogravimetry, decomposition, biomass waste conversion

INTRODUCTION

The use of biomass for energy production is considered to be one of the perspective ways to substitute fossil fuels and energy sources. The biomass of wood is the richest available feedstock for energy production. The wood biomass mainly consists of three biopolymers: cellulose, hemicelluloses, and lignin. The biomass components are widely used for obtaining platform chemicals (e.g., ethanol, furfural, 5-hydroxymethyl furane, levulinic acid, phenols. etc.), liquid fuels (bio-oil), gases (syn-gas, light hydrocarbons), and biochar [1]. For these purposes, pure wood biomass or its fractions are used. On the other side, the wood waste forming during the harvesting is a promising feedstock allowing the biofuel production cost to be decreased. More than 200 million tons of wood waste is formed annually [2, 3]. Among them, over 70 million tons is practically not used. Large areas used for wood waste storage are tended to the soil contamination and fire danger. Thus, the conversion of wood waste is of great interest.

https://doi.org/10.5593/sgem2024/4.1/s18.43

Among the methods used for the conversion of biomass to energy and fuels, the thermochemical methods are considered to be the most effective [4]. Pyrolysis, gasification, torrefaction, and liquefaction are widely applied for producing gaseous, liquid, and solid fuel from biomass. For the proper development of conversion methods, as well as for the creation of technologies based on these methods, systematic studies are needed. Thermogravimetric analysis is one of the key steps for such investigations. This method allows the main information about thermal decomposition and degradation of the feedstock to be obtained. Despite, a large number of thermogravimetric studies available for different types of wood, there is lack of data on the thermal decomposition of wood waste including sawdust, roots, bark, brushwood, etc.

This paper is focused on the thermogravimetric studies of pine and birch wood waste. Two types of waste (sawdust and bark) were used for the studies. The analysis of the volatile products obtained during the thermal decomposition was carried out. The kinetic parameters of the decomposition of the wood waste were obtained based on the thermogravimetric analysis.

MATERIALS AND METHODS

Wood Waste Composition

The wood waste (pine and birch sawdust and bark) was purchased from the harvesting company of Tver region, Russia. The feedstock was dried at 90±5 °C for 12 h and milled until the mesh of 0.25 mm. The elemental composition, fractional composition, humidity, and ash content were estimated. The humidity and ash content were analysed according to the standard procedure [5]. The elemental composition was studied using CHNS-O EMA502 analyser (VELP Scientifica, Italy). The content of extractives was estimated using the Soxhlet extraction apparatus according to [6]. Analysis of cellulose, hemicelluloses, and lignin content was carried out according to RU2534067 [7] and EA005492 Patents [8]. The composition and properties of the wood waste are presented in Table 1.

Thermogravimetric Analysis Procedure

For thermogravimetric analysis, the samples were milled, and a fraction with a particle size of < 0.25 mm was taken. The thermogravimetric analysis of the samples was carried out using NETZSCH TG IRIS 209 F1 thermogravimetric analyser. The samples were placed in corundum crucibles and heated at a constant rate (10 °C/min) in an inert argon atmosphere in the temperature range of 50-1000 °C.

The mass spectrometric study of volatile products of thermal decomposition was carried out using Aelos CSM 403 P mass spectrometric attachment to a NETZSCH TG IRIS thermal analyser. The volatiles were analysed in the mass range of 1-300 amu in the indicated temperature diapason.

For the kinetic study, the differential scanning calorimetry analysis of the wood waste samples was performed using NETZSCH DSC Q200 instrument in the temperature range of 50-600 °C at a heating rate of 10 °C/min in argon.

Table 1. Composition of the feedstock

Parameter	Sawdust		Bark	
	pinewood	birch	pinewood	birch
Humidity, wt. %	7.0	5.2	2.2	2.3
Ash content, wt. %	3.6	1.4	2.7	3.6
Cellulose, wt. %	53.1	39.5	50.3	42.7
Hemicelluloses, wt. %	7.9	17.9	8.3	19.1
Lignin, wt. %	25.4	31.1	28.1	27.2
Extractives, wt. %	6.3	4.9	8.4	5.1
C, wt. %	48.8	50.2	50.4	50.9
H, wt. %	6.1	6.0	5.9	5.8
N, wt. %	0.1	0.6	0.3	0.7
O, wt. %	44.6	42.2	43.4	42.6

RESULTS AND DISCUSSION

To estimate the temperatures for the thermal decomposition of the biomass components, the thermogravimetric analysis was carried out for individual components – cellulose, lignin, and hemicelluloses (Fig. 1).

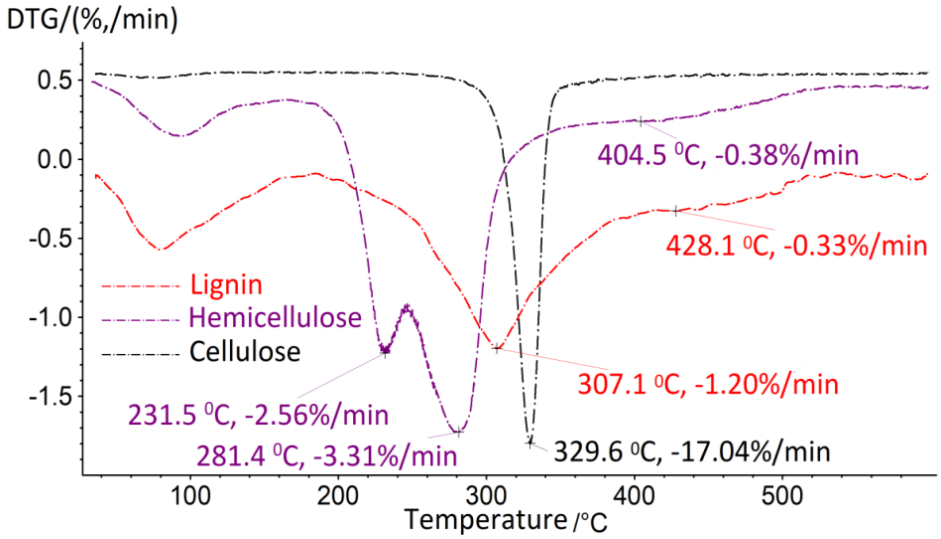


Figure 1. DTG curves of pure biomass components in a temperature range of 35-600 °C

The differential thermogravimetric (DTG) curve shows a peak at ca. 80 °C for all substances studied. The peak corresponds to the vaporisation of water adsorbed by the compounds. For cellulose, one narrow peak with the maximum at 329 °C can be observed indicating the degradation of glycoside bonds and decomposition of cellulose. The DTG curve of hemicelluloses shows the presence of three peaks with the maximum at 231, 281, and 404 °C. The intensive decomposition of hemicellulose starts at ca. 200 °C and ends at 310-320 °C. This temperature range indicates the breaking of β-1→2-, β-1→3-, β-1→4, and β-1→6-bonds of polysaccharide. The last wide peak in the DTG curve for hemicellulose corresponds to the decomposition of mono- and oligosaccharides as well as the dehydration of the decomposition products. For lignin, a

https://doi.org/10.5593/sgem2024/4.1/s18.43

wide peak from 200 to 500 °C is observed. This temperature range corresponds to the breaking of β-O-4, β-1, and β-5 bonds.

Thermogravimetric Analysis of Sawdust

The results of the thermogravimetric analysis of birch and pinewood sawdust are presented in Fig. 2. The TG curves show that the weights of the residues of the thermal decomposition are close for both sawdust studied (Fig. 2a). This can be explained by the similar properties and compositions of the feedstock. However, the DTG curves have differences in a temperature range of 200-400 °C due to the difference in the component concentrations, a.i. the different content of hemicelluloses and cellulose (Fig. 2b). For the pinewood sawdust, the concentration of lignin and hemicelluloses was found to be less than those for the birch sawdust (see Table 1).

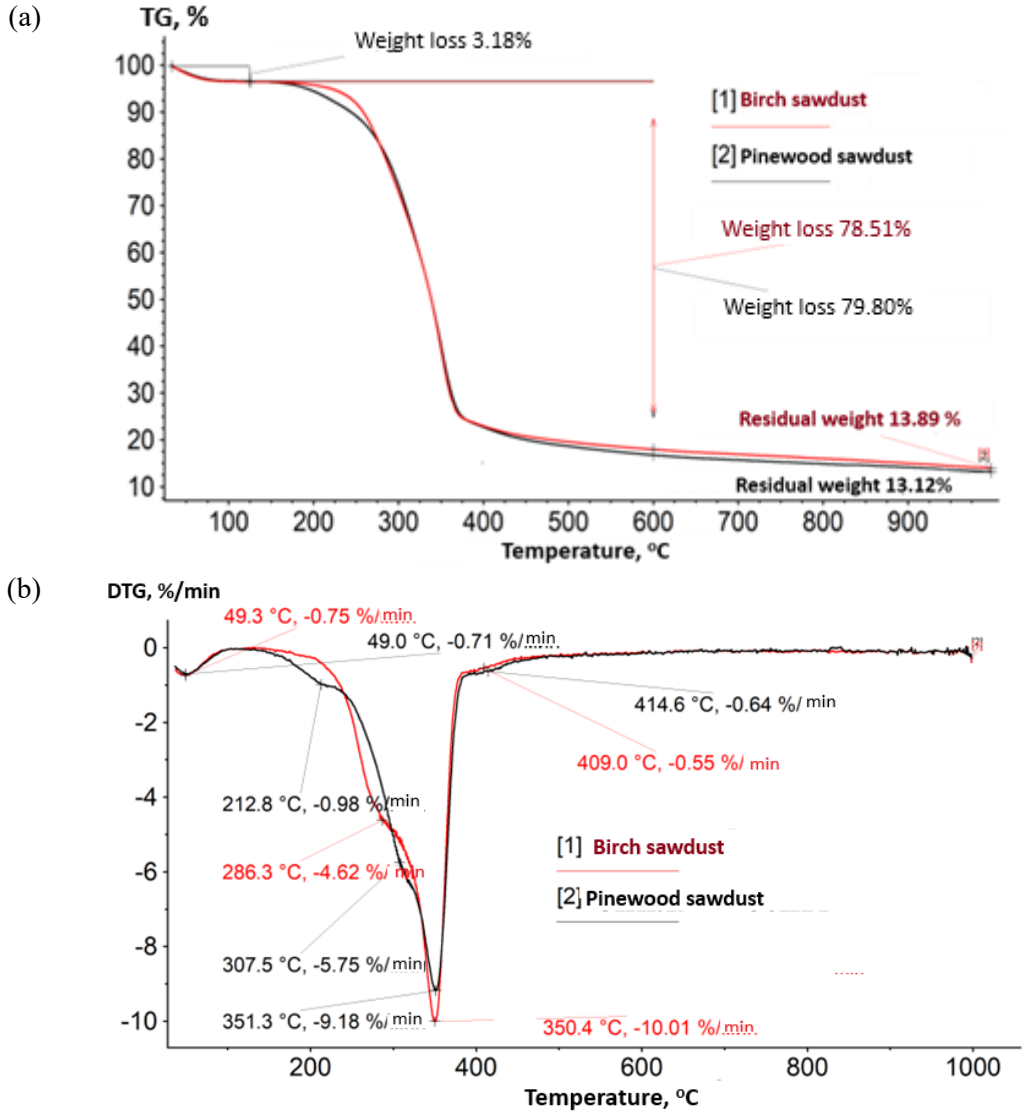


Figure 2. TG (a) and DTG (b) curves for birch and pinewood sawdust in a temperature range of 35-1000 °C

The kinetics of the thermal decomposition of sawdust was studied in a temperature range of 175-600 °C at different heating rates of the feedstock: 10, 25, and 50 °C/min. The analysis of the data was carried out using the Ozava-Flinn-Wall method. The kinetic parameters of the decomposition of birch and pinewood sawdust are presented in Table 2. The activation energy for the thermal decomposition of birch sawdust was found to be 8.9-15.1 kJ/mol higher than that for the pinewood sawdust. This indicates the lower thermal stability of the pinewood sawdust in the studied temperature range.

Table 2. Kinetic parameters of thermal decomposition of sawdust

Sawdust type	Model-independent methods		Linear kinetics method
	ASTM E698	ASTM E1641	
Birch			
E_a, kJ/mol	141.1±7.3	123.6±9.0	128.2
A_{exp}	$9.9 \cdot 10^{-1}$	$9.0 \cdot 10^{-1}$	$9.3 \cdot 10^{-1}$
Reaction order	-	-	2.53
Pinewood			
E_a, kJ/mol	126.0±5.7	76.3±17.4	119.3
A_{exp}	$9.9 \cdot 10^{-1}$	$4.4 \cdot 10^{-1}$	$8.4 \cdot 10^{-1}$
Reaction order	-	-	2.31

Thermogravimetric Analysis of Bark

The results of thermogravimetric analysis of birch and pinewood bark are presented in Fig. 3. The TG and DTG curves for both types of bark are similar to each other. Four main peaks corresponding to water evaporation (ca. 86-89 °C), hemicelluloses (300-320 °C), cellulose (ca. 470 °C), and lignin (ca. 315 °C, 415-420 °C) decomposition can be observed. The residuals seem to be about 30 wt. %. This value is higher than that for the sawdust. It can be explained by the higher ash and carbon content in the feedstock (see Table 1). For the pinewood bark, the peaks of maximum weight loss shifted to the higher temperatures. Thus, the higher temperature stability of the pinewood bark can be proposed.

The higher temperature stability of the pinewood bark was confirmed by analyzing the kinetics of thermal decomposition. The activation energy for the thermal decomposition of bark was found to be 11-25 kJ/mol higher for birch and 63-76 kJ/mol higher for pinewood in comparison with the respective sawdust. Higher thermal stability can be related to the higher hardness of the feedstock, its morphology as well as the differences in the biomass component concentrations.

https://doi.org/10.5593/sgem2024/4.1/s18.43

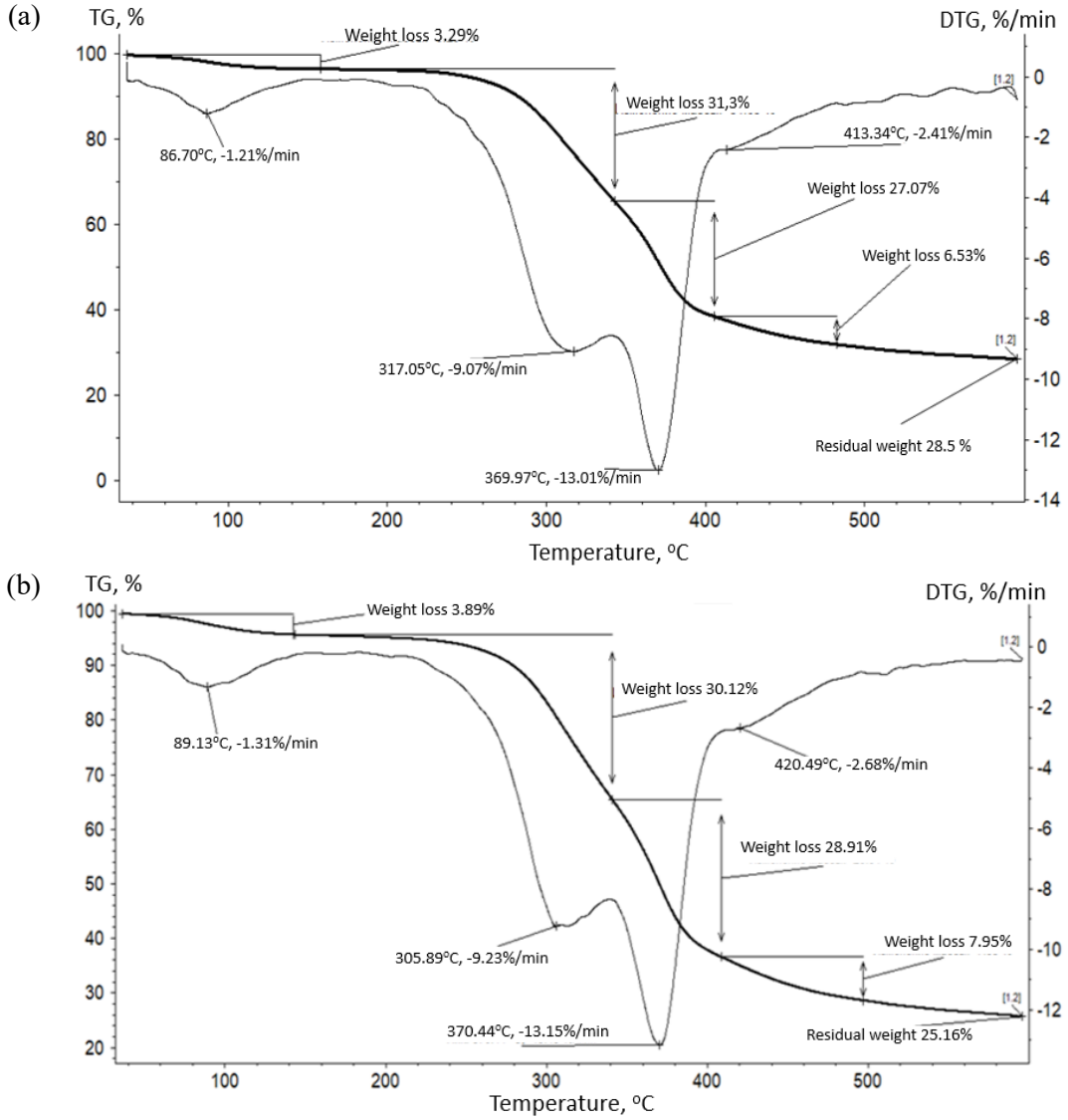


Figure 3. TG and DTG curves for birch (a) and pinewood (b) bark in a temperature range of 35-600 °C

Table 3. Kinetic parameters of thermal decomposition of bark

Sawdust type	Model-independent methods		Linear kinetics method
	ASTM E698	ASTM E1641	
Birch			
E_a, kJ/mol	146.0±8,4	134.2±8.0	137.6
A_{exp}	$9.2 \cdot 10^{-1}$	$8.6 \cdot 10^{-1}$	$8.5 \cdot 10^{-1}$
Reaction order	-	-	2.61
Pinewood			
E_a, kJ/mol	152.3±9,2	143.4±7.2	148.6
A_{exp}	$8.7 \cdot 10^{-1}$	$5.7 \cdot 10^{-1}$	$7.9 \cdot 10^{-1}$
Reaction order	-	-	2.74

Volatile Analysis

In this work, the analysis of the volatile products of biomass waste thermal decomposition was studied using the mass-spectrometry method. The results of the analysis for pinewood sawdust and bark are presented in Fig. 4. The volatile products of thermal decomposition of different types of waste are similar. The molecular weight of the products varies from 2 to 100 a.e.m. The low-weight products can be hydrogen, water, CO, CO_2, light alkanes, and olefins. Higher molecular weight products can be related to furfural, acetic acid, phenols, and phenolic compounds, as well as tars. It should be noted that the higher intensity of the mass-spectra signals was observed in a temperature range of 200-400 °C which corresponds to the higher weight loss of the feedstock according to TG data.

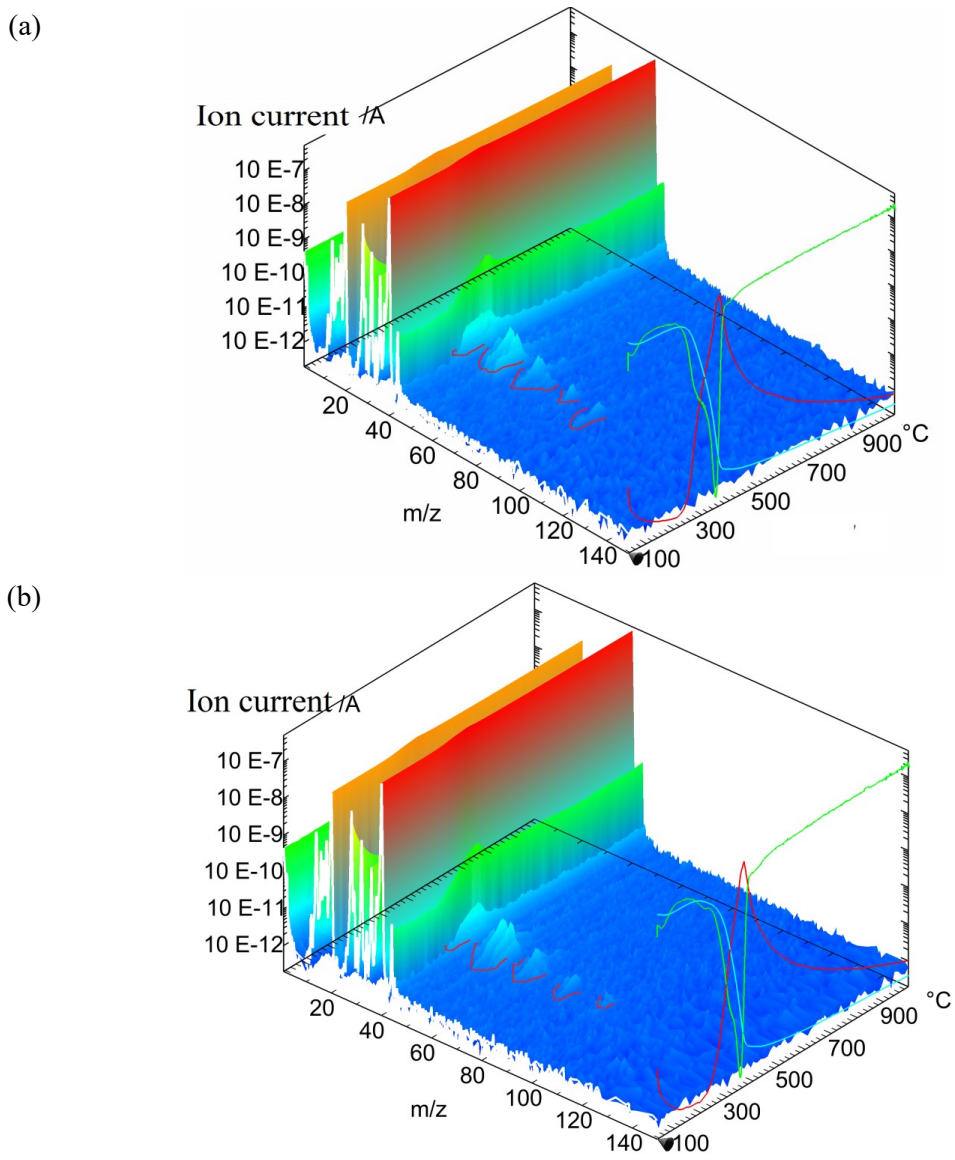


Figure 4. Molecular-weight distribution of volatiles obtained by thermal decomposition of pinewood sawdust (a) and bark (b)

https://doi.org/10.5593/sgem2024/4.1/s18.43

CONCLUSION

This work was carried out in the framework of the project devoted to the complex processing of wood waste to produce energy and materials. In the paper, the results of thermogravimetric analysis of pinewood and birch types of waste (sawdust and bark) are presented. The analysis was carried out to estimate the composition and properties of waste, and to study the kinetics of thermal decomposition of the feedstock. The results of the study can be used for the development of novel technologies for wood waste conversion into valuable products as well as for the improvement of the effectiveness of the use of renewable sources.

ACKNOWLEDGEMENTS

The work is financially supported by the Russian Science Foundation (grant 22-79-10096).

REFERENCES

[1] Elliott D.C., Hart T.R., Catalytic hydroprocessing of chemical models for bio-oil, Energy & Fuels, vol. 23, pp 631−637, 2008.

[2] Gryazkin A.V., Beliaev V.V., Beliaeva N.V., Kovalev N.V., Shakhov A.G., The logging waste as an inexhaustible resource for alternative energy, Thermal Science, vol. 21/issue 2, pp 1135-1142, 2017.

[3] Medvedev S.O., Mokhirev A.P., Chernikova A.V., Features of implementation of technology for integrated processing of logging waste, Bulletin of Altay Academy of Economics and Low, vol. 9/issue 2, pp 283-288, 2020.

[4] Pang S., Advances in thermochemical conversion of woody biomass to energy, fuels and chemicals, Biotechnology Advances, vol. 37, pp 589-597, 2019.

[5] National standard GOST R 56888-2016. Wood Fuel. Determination of ash content by standard method. 8 p. 2017.

[6] Ostroukhova L.A., Fedorova T.E., Onuchina N.A., Levchuk A.A., Babkin V.A., Study of the content of extractives in wood, roots, and bark of Siberia coniferous trees: Larix Sibirica L., Pinus Sylvestris L., Abies Sibirica L., Picea Obovata L., Pinus Sibirica Du Tour, Chemistry of plant materials, vol. 4, pp 185-195, 2018 (in Russian).

[7] Patt R., Kreipl A. Method of obtaining cellulose from lignocellulose-containing biomass. Patent RU2534067. Date of publication 27.11.2014. Bull. 33, 25 p.

[8] Kettenbach G., Stein A., Method for separating hemicelluloses from a biomass containing hemicelluloses. Patent EA005492B1. Date of publication 24.02.2005. 12 p.

UTILIZATION OF ASH FROM THE COMBUSTION OF KUZNETSK AND EKIBASTUZ COALS

Dr. Leonid Delitsyn[1]
Prof. Dr. Mikhail Sulman[2]
Dr. Ruslan Kulumbegov[1]
Prof. Dr. Oleg Popel[1]
Dr. Alexander Sidorov[2]
[1]Joint Institute for High Temperatures of the Russian Academy of Sciences, **Russia**
[2]Tver State Technical University, **Russia**

ABSTRACT

One of the promising areas of utilization of solid technogenic waste from energy generation is their processing to produce alumina, the production of which is accompanied by the formation of by-products that can be used to produce belite sludge ($2CaO•SiO_2$). The basic schemes of purification of the initial ash from carbon and iron oxides are proposed. Using the example of ash from coal burning in the Ekibastuz basin, the possibility of obtaining two grades of belite sludge is shown. Up to 1.5-1.8 tons of belite sludge can be obtained per ton of recycled ash (depending on its quality), which can be used in cement production. The article presents the results of experimental studies aimed at developing a technology for producing belite sludge from high-alumina ash from coal-fired power plants. The influence of various technological parameters on the process of obtaining the target product has been studied. A solution of sodium silicate with the extraction of 28% silica into it was obtained by the method of alkaline desilination of ash. The possibility of obtaining a white, high-quality belite sludge suitable for the production of white cement by treating a solution of sodium silicate with calcium oxide is shown. At the second stage, during the processing of alumina concentrate, gray belite sludge was obtained suitable for use in the construction industry.

Keywords: ash, alumina, belite sludge.

INTRODUCTION

The coal of the Kuznetsk and Ekibastuz basins occupy a significant share in the coal power industry of Russia. The ashes formed during the combustion of these coals in thermal power plants are characterized by a low content of calcium and magnesium oxides, a high content of silicon oxide and belong to acidic ash. Nevertheless, the chemical composition of the ash from these basins varies (Table 1) and, accordingly, different methods of their processing are required. A distinctive property of the chemical composition of the ash of Ekibastuz coal is the high content of Al_2O_3 and SiO_2, which in total range from 85 to 90%. The rest of the components (Fe_2O_3, CaO, MgO, Na_2O, K_2O, TiO_2, P_2O_5, MnO, S, etc.) account for 10-15%. Ash is also characterized by a low (less than 1%) content of sodium, potassium, calcium, magnesium and sulfur oxides. It also has a low content of iron oxides (4 - 8%) and unburned coal particles (3 – 5%), “underburning". Nevertheless, it is necessary to take

https://doi.org/10.5593/sgem2024/4.1/s18.44

into account these components, because in the process of ash enrichment and its further chemical and metallurgical processing into alumina, belite sludge and other products, they can accumulate at different stages of the technological process and affect the quality of the final products (for example, alumina).

Table 1. Nain components of coal ash from the Kuznetsk (K) and Ekibastuz (E) basins

Components	Statistical parameters							
	X, % by weight.		S, % by weight.		V, % relative		N	
	K	E	K	E	K	E	K	E
SiO_2	53.37	57.75	6.65	2.24	12	3.7	19	34
Al_2O_3	21.75	28.4	2.88	1.99	13	7.1	19	34
Fe_2O_3	7.98	4.8	1.64	2.03	21	33.7	19	34
CaO	5.96	0.95	2.45	0.37	41	39.4	19	34
MgO	2.04	0.48	0.56	0.22	27	45.8	19	34
Na_2O+K_2O	3.27	0.87	0.86	0.1	26	12.8	17	34
TiO_2	0.94	1.05	0.14	0.17	15	13.9	18	34
P_2O_5	0.77	0.59	0.42	0.13	55	26.5	19	31
SO_3	3.16	0.11	1.37	0.50	43	71.4	19	32
C	14.0	5.0	3.75	1.2	26	24	16	24

(X, % - the arithmetic mean content, S, % - the mean square deviation, V, % coefficient of variation, N – number of analyses)

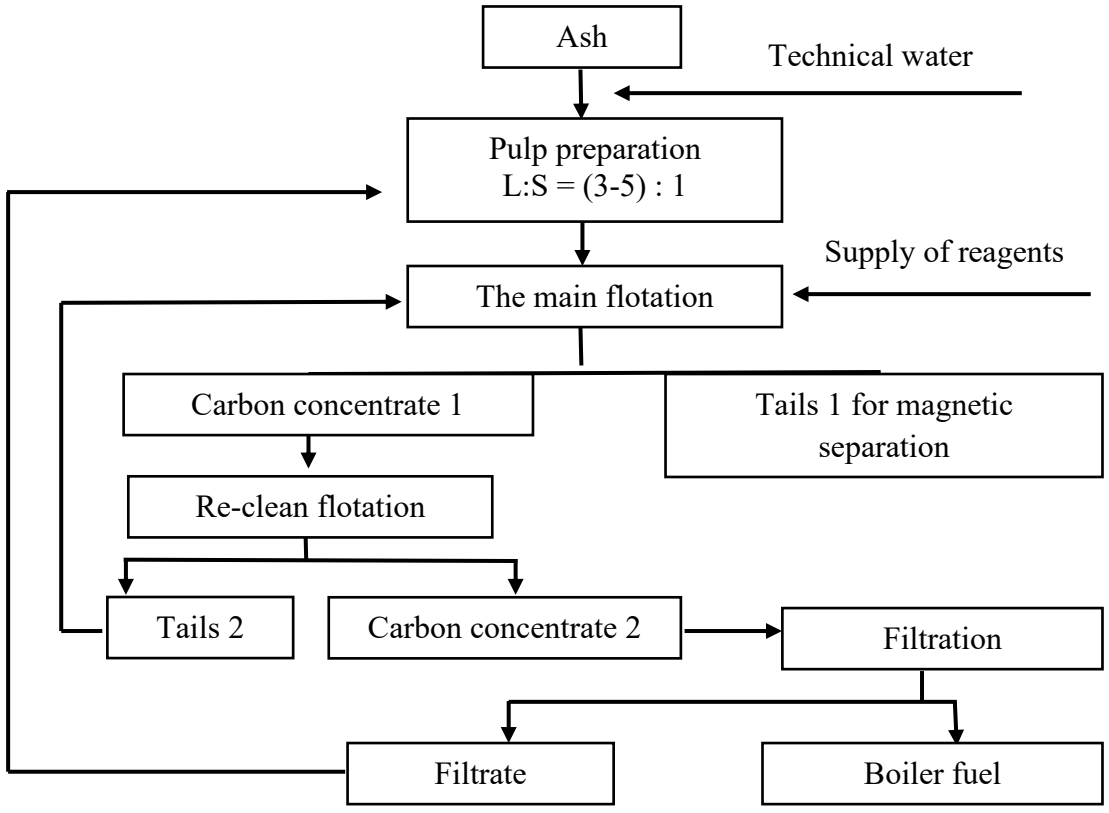


Figure 1. Basic technological scheme for the production of carbon concentrate from ash

Unlike other coal basins, the ash composition of Ekibastuz coal is stable. First of all, this applies to the content of SiO_2 and Al_2O_3. The mean square deviation for these components was about 2%, and the coefficient of variation was 3.7 and 7.1%, respectively. The same applies to other components, even with a low value of their arithmetic mean. The main mineral phases in the ash of the Ekibastuz coal thermal power plant are mullite (17%), quartz (4%) and glass phase (70%), in smaller quantities – magnetite (4%, hematite, α-cristobalite, burnt clay substance; FeO, sillimanite, anhydrite, ferruginous cordierite are noted as possible phases [1]. Unlike the Ekibastuz basin, the ash of the Kuznetsk basin is characterized by a complex phase composition. It contains an amorphous substance, quartz, glaucophane, magnetite, wustite, hematite and an admixture of mullite. The X-ray amorphous substance gives two halos in the spectrum: one in the region of Bregg angles 8-14º, the other in the area 19-32º. Presumably, it can be assumed that the first halo belongs to glaucophane, the second to X–ray amorphous cristoballite [2]. Despite the differences in the chemical composition of the ash of the Ekibastuz and Kuznetsk basins, the first stages of their processing are identical: the separation of carbon and magnetite concentrates (Fig. 1, 2).

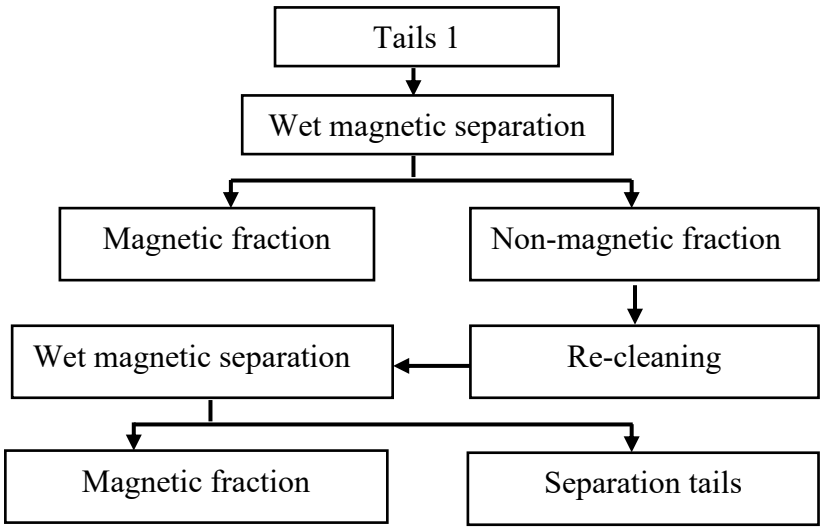


Figure 2. Schematic diagram of the separation of the magnetic fraction

The carbon concentrate obtained as a result of ash flotation it is a powdery black material with a carbon content of 60-65% [3]. Flotation tails (aluminosilicate product) are a light gray powdery material containing 2-4% carbon. As a result of magnetic separation of flotation tailings, a magnetite concentrate with an iron oxide content of 50-55% is released, which can be used in ferrous metallurgy to produce cast iron. The aluminosilicate product purified from carbon and iron oxides, depending on its source, is directed: in the case of coal ash from the Kuznetsk basin to the production of building materials [4,5]; in the case of coal ash from the Ekibastuz basin to the production of alumina [6,7]. Recently, a large number of works have been published on the production of geopolymer materials for construction purposes from fly ash [8,9]. The production of porous thermal insulation materials is also considered [10]. In the process of obtaining alumina from ash, it is also possible to obtain a belite sludge, which is a bicalcium silicate ($2CaO•SiO_2$), which is formed during the production of alumina from bauxite and nepheline. Currently, the main areas of processing of belite sludge include the production of Portland cement, adsorbents, bricks, glass and ceramic products, materials

https://doi.org/10.5593/sgem2024/4.1/s18.44

used in road construction and agriculture. Cement production accounts for about 7% of global greenhouse gas emissions into the atmosphere. Thus, the use of solid industrial waste generated during coal combustion in cement production makes it possible to solve some environmental problems [11]. In this regard, the ashes of the Ural thermal power plants burning the coals of the Ekibastuz basin turn out to be a promising object for the production of belite sludge.

The purpose of the work is to study the regularities of technological parameters for the production of belite sludge from coal ash in the Ekibastuz basin. The results of the study can be used to isolate high-quality belite sludge in the development of a method for obtaining alumina from ash of a similar composition.

MATERIALS AND METHODS

For the experiments, the following were used: ash from the coal burning of the Ekibastuz basin; NaOH – pure; Na_2CO_3 – pure; $CaCO_3$ - chemically pure; $Ca(OH)_2$ was prepared by mixing calcium oxide with water; CaO – chemically pure.

The ash was classified into fractions on laboratory sieving U1-ERL-10 Class >0.315 mm are tailings. The fraction < 0.315 mm (85 – 82%) is the working fraction for research. Ash was cleaned from carbon in a flotation machine 237 FL-A, with a chamber volume of 1.7 liters. Ash loading was 0.5 kg, the duration of the main flotation was 5-10 minutes. Vacuum gasoil and kerosene were used as collectors. The flotation agent oxalum T–66 is used as foamers. Carbon–free ash (residual content; carbon - 2%,) in an amount of 300 g, to remove part of SiO_2, was dissolved in 750 ml of 20% NaOH solution with constant stirring in a Stegler MB-6 top-drive agitator (500 rpm) for 180-360 minutes at a temperature of 20-100 °C in fluoroplastic cups. The resulting pulp was filtered on a single-stage vacuum pump VE-160. The alumina concentrate was washed with distilled water to a neutral pH, dried at t = 105 °C to a constant weight. The dried alumina concentrate was mixed with Na_2CO_3 and $CaCO_3$ and sintered at t = 1200-1250 °C. The resulting sinter was leached with water at t = 75 ° C. The heat treatment of the charge was carried out in a muffle furnace "INCANDESCENT" model PL-514 in an air atmosphere. The concentration of major oxides and some trace elements in the samples was determined by X-ray spectral fluorescence analysis (XRF), Axios mAX model No. DY5530 manufactured by PANalytical. The phase composition was determined by X-ray method on a DRON-2 diffractometer, CuKa radiation, phase identification was carried out on the basis of the Pcpdfwin-ICPDS database.

RESULTS

The solubility of the ash depends on the concentration of the NaOH solution and temperature. Up to a temperature of 70 °C, the SiO_2 contained in the ash is dissolved in alkaline solutions in small amounts. In a solution containing 100 g/dm^3 NaOH at 70 °C, the solubility was 5.5%, at 80 °C – 9.2%, at 90 °C – 13.0%, at 100 °C the solubility of ash was 17.3%. In a solution containing 200 g / dm^3 NaOH, at 80 ºC the solubility of SiO2 was – 23.4%, at 90 ºC it reaches 24.9% and at 100 ºC – 25.0 - 27.0%. With a solution content of 200 g/dm^3 NaOH, the solubility of ash reaches its highest value. A further increase in the NaOH concentration to 335 and 415 g/dm^3 does not increase the solubility of SiO_2. Saturation of the alkaline SiO_2 solution occurs after 120 minutes, a further increase in the duration does not lead to an increase in the solubility of SiO_2. As

a result of dissolution of ash in 20% NaOH solution at 90-100 ° C, a solution of sodium silicate and an insoluble aluminosilicate residue of partially desilicated ash are formed according to the reaction:

$$\text{Ash} + 2\text{NaOH} \rightarrow \text{Na}_2\text{SiO}_3 + \text{H}_2\text{O} + \text{aluminosilicate product} \quad (1)$$

At this stage, about 25-28% SiO_2 is extracted from the ash and an insoluble ash residue is formed. The composition and properties of the insoluble residue differ radically from the initial ash (Table 2). Essentially, the insoluble residue is an alumina concentrate, which becomes a raw material for the production of alumina and belite sludge suitable for the production of Portland cement.

Table 2. Chemical composition of the main components in alumina concentrate

Material	Main components							μSi
	SiO_2	Al_2O_3	Fe_2O_3	Na_2O	CaO	MgO	TiO_2	
Alumina concentrate	39.5	38.0	4.65	7.38	2.26	0.87	1.36	0.96
Initial ash	57.75	28.4	4.8	0.37	0.95	0.48	1.05	0.49

μSi - Al_2O_3/ SiO_2 mass ratio

Belite sludge was obtained by adding an excess amount of $Ca(OH)_2$ (10% of stoichiometry) to a Na_2SiO_3 solution and after two hours of stirring at a temperature of 75-80 °C, belite sludge formed in the form of a pulp ($2CaO•SiO_2 • 2H_2O$) according to the reaction:

$$\text{Na}_2\text{SiO}_3 + 2\text{Ca(OH)}_2 + \text{H}_2\text{O} \rightarrow 2\text{CaO}•\text{SiO}_2 • 2\text{H}_2\text{O} + 2\text{NaOH} \quad (2)$$

The conversion of Na_2SiO_3 at a 10% excess of $Ca(OH)_2$ is 94-96%. Since belite sludge is obtained from a sodium silicate solution, it contains a small amount of impurities (Table 3). The belite sludge dried at 105 °C is a finely dispersed weakly crystallized hydrated white material. Using the XRF method, it was established that after calcination at a temperature of 1000 °C it is β – $2CaO•SiO_2$ and is practically no different from the mineral belite and can be used in the production of white cement.

Table 3. Chemical composition of the main components of the belite sludge

Sample	Heat treatmen, ºC	Concentration, wt. %							Molar ratio CaO:SiO_2
		SiO_2	CaO	Al_2O_3	Fe_2O_3	Na_2O	K_2O	MgO	
Belite sludge	105	21.8	41.0	0.78	0.12	1.13	0.04	0.10	2.02
	1000	32.5	57.3	1.30	0.17	-	-	-	1.90

The alumina concentrate obtained at the first stage of the process as a result of desiliconization of ash was further processed using sintering technology. For this purpose, a mixture of alumina concentrate, sodium carbonate and calcium carbonate was sintered at 1200-1250 ºC for 40-50 minutes, and kept at this temperature for 30-45 minutes. The result is a cake consisting of sodium aluminate and dicalcium silicate. When leaching with water at t = 75 °C, almost all sodium aluminate goes into solution, the insoluble residue is dicalcium silicate with impurities. In contrast to the white belite sludge obtained at the first stage, it is characterized by a gray color due to impurities of oxides of aluminum, iron, magnesium, etc. The content of components in it is, wt.%:

https://doi.org/10.5593/sgem2024/4.1/s18.44

CaO 60-61, SiO_2 22.4, Fe_2O_3 4.4, Al_2O_3 до 11.O, CaO : SiO_2 = 2.9-3.0. The process of obtaining belite sludge by the sintering method is described within the framework of the CaO – SiO_2 – Al_2O_3 phase equilibrium diagram. The topology of the CaO – SiO_2 – Al_2O_3 diagram (Fig. 3) indicates that during ash processing there is no need to achieve complete extraction of alumina from it, as is done during bauxite processing. Since the composition of Portland cement contains aluminate phases, the residual content of Al_2O_3 in the belite sludge can be 5-10%.

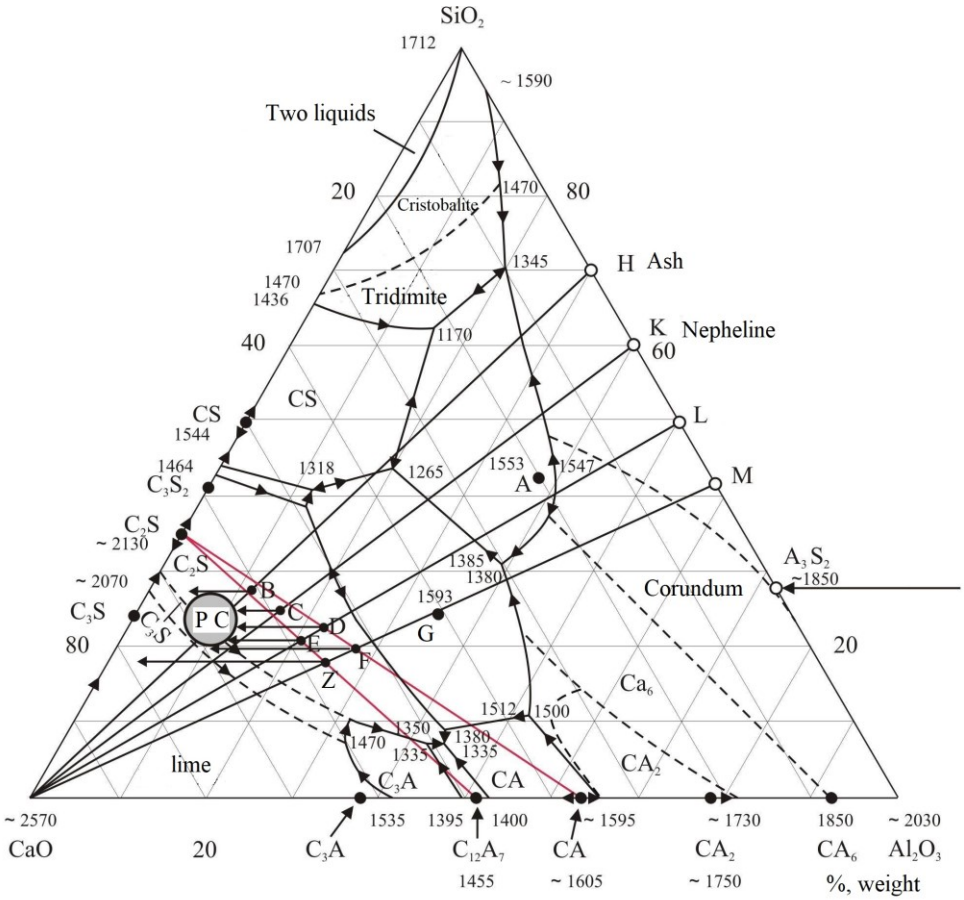


Figure 3. Diagram CaO – SiO_2 – Al_2O_3: H – composition of the initial ash; K – composition of nepheline concentrate; L – composition of alumina concentrate after chemical enrichment of ash; M – composition of calcined alumina concentrate at 1000 ° C after its chemical enrichment; point A – anorthite; point G – gelenite; PC – portland cement field; C_2S – bicalcium silicate; $C_{12}A_7$ – calcium aluminate (12 CaO•7Al_2O_3); CA – calcium aluminate (CaO•Al_2O_3); B, C, D, E, F, Z – points corresponding to different charge compositions

The principal part of ash processing using sintering technology is the calculation of the composition of the charge and the production of sinters. This part of the technology is insufficiently covered in the scientific and technical literature and is discussed below. The remaining technological operations (leaching, etc.) are known and there is no need to consider them in detail.

In Fig. 3 on the side face of the SiO_2 - Al_2O_3 diagram CaO - SiO_2 - Al_2O_3 shows 4 points: H - the initial composition of the ash, K - the composition of the nepheline concentrate, L - the composition of the alumina concentrate and M - the composition of the alumina concentrate obtained after processing the ash calcined at 1000 °C 20% NaOH solution. Points H, K, L and M are connected by rays to the top of CaO. The diagram shows a field corresponding to the composition of Portland cement (PC). When sintering the initial ash (point H), with limestone (CaO – H ray), a lime-alumina sinter corresponding to point B is obtained. After leaching, calcareous-calcium sludge remains from the alumina sinter, which does not enter the field of Portland cement. When using alumina concentrate obtained after chemical enrichment of ash (point L), then when sintering it with limestone, there are two options for calculating the charge. The first one, indicated in Fig. 3 by point D, and the second, indicated by point E. According to the first and second variants, after alumina leaching, the sinter compositions (points D, E) fall directly into the Portland cement field (ray movement from points D and E towards the PC). Moreover, the crystallization of the cakes begins with the formation of C_2S, then gehlenite is added to them, and crystallization in the eutectic C_2S + CA + $C_{12}A_7$ ends.

CONCLUSION

A basic technological scheme for the preparation of ash for its further processing into alumina and belite sludge is proposed. Which consists of decarbonization, by flotation, and de-ironing by wet magnetic separation. By X-ray phase analysis, it was found that calcined at 1000 °C, the belite sludge turns into a well crystallized β - Ca_2SiO_4. It is shown that 2 grades of belite sludge can be obtained from the ash of the Ekibastuz basin coals. The white belite sludge obtained at the first stage contains practically no impurities and can be used in the production of white cement. A larger-scale product in the proposed technological chain is gray belite sludge containing impurities of aluminum, iron, magnesium oxides, etc. components that meet the requirements of Portland cement production. Thus, coal ash from the Ekibastuz basin is a major source for the production of alumina and belite sludge, which are widely used in the construction industry. The presence on the territory of the Chelyabinsk region of a number of large deposits of flux limestones (Turgoyakskoye, Cheremshanskoye, Agapovskoye), limestones for the cement industry (Varninskoye, Uvelskoye, Sheninskoye) and a number of others (Churovskoye, Fedorovskoye) opens up prospects for the industrial implementation of the technology in question.

ACKNOWLEDGEMENTS

The work was carried out with the financial support of the Russian Science Foundation, grant №. 21-79-30004

REFERENCES

[1] Vdovenko M.I. The mineral part of energy coals (physico-chemical research) / Nauka Publishing House of the Kazakh SSR, Alma–Ata. 256 p. 1973.

[2] Borg I.Y. Optical properties and cell parameters in the glaucophane - riebekite series // Contributions to Mineral and Petrology. Germany. V. 15, pp 67-92. 1967

https://doi.org/10.5593/sgem2024/4.1/s18.44

[3] Delitsyn L. M., Ryabov Yu. V., Kulumbegov R. V. [et al.]. The influence of flotation reagents on the extraction of carbon from the ash of coal-fired thermal power plants // Ecology and Industry of Russia. Russia. Vol. 26. No. 2, pp. 14-19. 2022.

[4] Zaravelisa F., Theodorakisa N., Triantafylloua A., Stivanakis V. Fly ash of Megalopolis and ferroalumina in the production of building materials // Materials Today: Proceedings. Greece. V. 5, pp 27434–27440. 2018

[5] Onaizi Ali M., Waiching Tang, Mugahed Amran, Yanju Liu, Umer Sajjad, Mohammad Alhassan. Towards increased adoption of furnace bottom ash as sustainable building materials: Characterization, standardization, and applications // Journal of Building Engineering. Australia. V. 82, 108274. 2024.

[6] Delitsyn L. M, Kulumbegov R. V., Popel' O. S., Sul'man M. G. Obtaining Alumina from the Ash of Coal-Fired Power Plants // Thermal Engineering. Russia. Vol. 69, No. 12, pp. 933–941. 2022

[7] Chunbin Guo, Jingjing Zou, Shuhua Ma, Jianlin Yang, Kehan Wang. Alumina Extraction from Coal Fly Ash via Low-Temperature Potassium Bisulfate Calcination // Minerals. China. 9(10). 585 2019.

[8] Babaev D.D., Petropavlovskaya V.B., Novichenkova T.B., Petropavlovski K.S., Zavadko M.Yu. synthesis of geopolymer compositions based on alkaline man-made products of fuel stations // Bulletin of the Tver State Technical University. Series: Construction. Electrical engineering and chemical technologies. Russia. No. 4 (20), pp. 83-90. 2023.

[9] Naghizadeh A., Tchadjie L.N., Ekolu S.O., Welman-Purchase M. Circular production of recycled binder from fly ash-based geopolymer concrete // Construction and Building Materials. South Africa. V.415. 135098. 2024

[10] A.S. Kosarev, V.A. Smoliy, A.V. Skorikov. Assessment of the possibility of using ash and slag wastes of heat power engineering in the production of granular porous aggregate for concrete and heat-insulating filling material // Izvestiya vuzov. Severo-kavkazskiy region. Russia. No 4, pp-111-117. 2018

[11] Ch. Guo, L. Zhao, J. Yang, K. Wang, J. Zou. A novel perspective process for alumina extraction from coal fly ash via potassium pyrosulfate calcination activation method // Journal of Cleaner Production. China. V. 271. Article No. 122703. 2020.

VALORIFICATION OF PRUNUS CERASIFERA FRUITS (PULP, PEEL, WHOLE FRUIT) FOR YOGURT PRODUCTION

PhD. Mădălina Moga[1]

Dr. Mihaela Tița[2]

Dr. Adelina Constantinescu[2]

Dr. Ovidiu Tița[2]

[1] Doctoral School of "Lucian Blaga" University of Sibiu, **Romania**

[2] Faculty of Agriculture Science, Food Industry and Environmental Protection,"Lucian Blaga" University of Sibiu, **Romania**

ABSTRACT

Sustainable food production is growing along with consumer demands to find healthy products. The management and minimization of food by-products and the recovery of products with low economic value represent both a trend and a current necessity for the food industry. Prunus cerasifera is a species of plum native to Southeast Europe and Western Asia. It is also called Cherry Plum and Myrobolan Plum. It is cultivated mainly as an ornamental plant with several varieties differing in leaf and bud color and secondarily for fruit production. The fruits have a limited use, most often they are used in the production of brandy and certain areas, in the production of jam. The present study addresses the use of cherry plum (peel, pulp, and peel+pulp) in producing cherry plum yogurt. The obtained products were analyzed from a physico-chemical point of view, and for the sensory analysis, a non-numerical method based on several criteria of multipersonal agreement was used. The yogurt was also analyzed from a sensory point of view using a 5-point hedonic scale. The results show a better resistance of the yogurts for the water retention capacity and syneresis, but also good acceptability of the yogurts with cherry plum additions in terms of sensory analysis, taste, and fruity smell.

Keywords: prunus cerasifera, cherry plum, myrobolan plum, yogurt

INTRODUCTION

Prunus Cerasifera is a species of plum known by the common names cherry plum and myrobalan plum. It is native to Southeast Europe and Western Asia, and is naturalized in the British Isles[4] and scattered locations in North America. It is one of the first European trees to flower in spring, often around mid-February. [1]

Prunus Cerasifera is not picky about the soil, preferring fertile, well-drained soils. Prunus Cerasifera grows well on Clay, Loamy, Sandy, and Calcareous soils (rich in carbonates). Frost and drought-resistant species. Most of the time, the cork oak is used in agriculture as a rootstock for the varieties of plum, almond, peach, nectarine, apricot, etc. [2]
The corks are currently used to obtain jam and for the production of plum brandy, but unfortunately, a huge part of the production of corks ends up unutilized. Although they

https://doi.org/10.5593/sgem2024/4.1/s18.45

are quite widespread, being a tree that does not need special conditions for development, there are currently few studies on cork oaks.

Their composition in bioactive substances is 1.34 to 6.11 g/kg total phenolic content, the peel has 1.93 to 19.86 g/kg peel anthocyanins, and the antioxidant power is 11.20 to 44, 83 mole Trolox equivalent/g FW. [3]

The results of another study showed that the total content of polyphenols, flavonoids, phenolic acid, and flavanols in the extracted polyphenols were 439.17, 186.37, 168.27, and 68.86 mg/g, respectively. Therefore, the total polyphenol content of Prunus Cerasifera is relatively high, and the main components are flavonoids, The corresponding DPPH free radical scavenging rate was 97.42%, and the antioxidant activities measured using FRAP and ABTS methods were 4, 36 mmol/mL and 0.48 mmol/mL Trolox, respectively. [4]

Also, a study shows the potential of applying Prunus Cerasifera in developing anti-inflammatory drugs that prevent inflammatory diseases by inhibiting the secretion of pro-inflammatory cytokines, NF-kappa B, MAPK pathway, and inflammasome activation. [5]

The present study proposes the development of some acidic dairy products, such as yogurt, with the addition of yellow powder fruits of Prunus Cerasifera (pulp+peel - the whole fruit, peel, pulp) to obtain some dairy products with improved characteristics that promote health, but and to valorize the fruits of Prunus Cerasifera - products with low economic value.

MATERIALS AND METHODS

Materials

The yellow fruits of Prunus Cerasifera were harvested from Mureș County, Romania. They were washed, the seeds were removed, and one part was dried, and the other part was separated into anatomical parts by drying the peel and pulp of the fruits separately. A fruit and vegetable dryer was used for drying, and the temperature used for drying was 60 ^{o}C. After drying, the fruits were crushed using a coffee grinder.

Cow's milk was procured from a local producer. The starter culture was purchased from Chr. Hansen Holding A/S.

Preparation of yogurt samples

Table 1. Yogurt Sample Description

Sample code	Sample description				
	Cow milk	Starter culture	Yellow Prunus Cerasifera dried fruits		
			Peels+pulp	Peels	Pulp
CSY	100 %	0.2 %	-	-	-
YCP 1%/ 3%/ 5%	100 %	0.2 %	1%/ 3%/ 5%	-	-
YCPP 1%/ 3%/ 5%	100 %	0.2 %	-	1%/ 3%/ 5%	-
YCPC 1%/ 3%/ 5%	100 %	0.2%	-	-	1%/ 3%/ 5%

The milk purchased from a local producer was pasteurized at a temperature of 90-95 ^{o}C for 20 minutes. The milk was then cooled to 42-45^{o}C and inoculated with 0.2% (w/v) yogurt starter culture. The cork powders were added to the inoculated milk according to

the indications in Table 1, then the samples were placed in 200 mL glass beakers and were introduced to thermosetting at 42 ºC for 4 hours. After fermentation, the yogurt samples were cooled and then refrigerated for the entire analysis period.

Methods of analysis

Sensory analysis

To perform the sensory analysis, a non-numerical multi-criteria multi-personal agreement method was described by Fadhil and collaborators**.** [6]

The observed characteristics were consistency, color, stickiness, taste, and odor. Table 2 shows the evaluation scale used, and it also shows the level of importance of the criteria based on the scale.

Next, a matrix of evaluation criteria was formulated based on the opinion of the evaluators and the chosen alternative. The determination of the negation of the level of importance of the criteria was done using the formula (1):

$$Neg\ (W_k) = \ (W_{q\,-\,k\,+\,1}\,) \tag{1}$$

Where: Neg (W_k) – score negation of criteria k; k – index; q – scale amount;

For the approval process based on criteria, the formula (2) was used:

$$V_{ij} = \min\,[\,Neg\ (W_{ak}) \vee V_{ij}\ (a_k)] \tag{2}$$

Where: V_{ij} – the score of alternative i by person j; V_{ij} (a_k) – the score of alternative i by person j on criteria k; k – 1, 2, …., m;

Determining the score using the formula (3):

$$Q_k = \ Int\,[\,1\ +\ (k * \frac{q-1}{r})] \tag{3}$$

Where: Q_k – the score k; Int – integer; R – the number of assessors;

Aggregation process for a person (assessor) using the formula (4):

$$V_i = \ f(\,V_i\,)\max\,[\ Q_j \wedge b_j\,] \tag{4}$$

Where: V_i – the total value for alternative I; Q_j – score j; J – 1, 2, …, *m;* b_j – order from the biggest alternative score i from alternative score j.

Table 2 Linguistic Assessment Scale and Criteria importance level

Linguistic Assessment Scale			**Criteria importance level**		
Scale	**Description**	**Abbreviation**	**Scale**	**Description**	**Abbreviation**
1	Like very much	LV	1	Very high	LV
2	Like moderately	LM	2	High	LM
3	Like Slightly	LS	3	I neither like nor dislike	NT
4	I neither like nor dislike	NT	4	Low	DM
5	Dislike slightly	DS	5	Very low	DV
6	Dislike moderately	DM			
7	Dislike very much	DV			

https://doi.org/10.5593/sgem2024/4.1/s18.45

Sensory analysis using a 5-point hedonic scale

A group of 5 tasters were invited to taste the 10 yogurt samples and rate each sample with a score from 1 to 5 (1= not felt, 5= felt very much). The evaluated attributes were adapted according to Tugba Aktar [7] and others [8] [9]: fruity taste, sourness, consistency, aftertaste, general acceptance.

Physicochemical analysis

Titratable acidity: The acidity of a certain volume of the sample prepared for analysis is neutralized by titration with 0.1 n sodium hydroxide solution, in the presence of phenolphthalein as an indicator. [10]

Water holding capacity (WHC): A quantity of 5 g of yogurt was centrifuged at 4500 x g for 30 min at 10°C. The resulting supernatant was discarded and the expelled precipitate was collected and weighed.). [11] [12] WHC was calculated using the equation:

$$WHC(\%) = \left(1 - \frac{W_1}{W_{2)}}\right) * 100 \quad (5)$$

Where: W_1= whey mass after centrifugation; W_2= quantity of yogurt analyzed;

Syneresis degree drainage method: 8 g of yogurt was placed on filter paper (260 μm). The amount of whey drained was measured after 2 hours at 10°C. [13]

Degree of syneresis centrifugation method: After mixing, 10 cm^3 of yogurt was placed in a calibrated test tube and centrifuged for 10 minutes at 1500 × g. The volume of released whey was measured. [14]

Syneresis expressed in % was calculated using the following formula:

$$Sy, \% = \frac{Volum\ zer}{Volum\ de\ iaurt} * 100 \quad (6)$$

Statistical analysis

Yogurt samples were stored at refrigerated temperatures for 14 days and analyzed on the first, seventh, and fourteenth days. On each day of storage, 3 determinations were made for each sample. Minitab Software [15] was used to perform statistical analysis. The results obtained for the mean of triplicates ± standard deviation were plotted, and the bar represents the standard deviation.

RESULTS

Sensory analyses

Determining alternatives

First, the calculation of the negation of the importance level of the criteria was carried out using the formula (1). The results of the calculation of the denial of the criteria are presented in Table 3. The opinions of the tasters obtained are presented in Table 4.

Table 3 Negating the importance level of the criteria

The importance level of the criteria		Negating the importance level of the criteria	
Criterion 1 =	Very high	Criterion 1 =	Very low
Criterion 2 =	High	Criterion 2 =	Low
Criterion 3 =	I neither like nor dislike	Criterion 3 =	I neither like nor dislike
Criterion 4 =	Low	Criterion 4 =	High
Criterion 5 =	Very low	Criterion 5 =	Very high

Table 4 The sensory assessment for each person

Persons	Alternative	Evaluation criteria														
		Consistency			Stickiness			Color			Taste			Odor		
		Day 1	Day 7	Day 14	Day 1	Day 7	Day 14	Day 1	Day 7	Day 14	Day 1	Day 7	Day 14	Day 1	Day 7	Day 14
P1	A1	NT	LS	LS	NT	NT	NT	NT	NT	NT	LS	LS	LM	LM	LM	LM
	A2	LS	LM	LM	LM	LM	LV	LM	LV	LV	LV	LV	LV	LV	LV	LV
	A3	LM	LV	LV	LM	LM	LM	LM	LV	LV	LV	LV	LV	LV	LV	LV
	A4	LM	LV	LV	LV	LV	LV	LS	LS	LM	LS	LM	LM	LM	LV	LV
	A5	LM	LM	LV	LM	LM	LM	LV	LV	LV	LM	LV	LV	LV	LV	LV
	A6	LV	LV	LV	LM	LV	LV	LM	LV	LV	LV	LV	LV	LV	LV	LV
	A7	LV	LV	LV	LM	LV	LV	LS	LS	LM	LS	LM	LS	LM	LM	LM
	A8	LS	LS	LS	LM	LM	LS	LM	LM	LM	LM	LV	LV	LV	LV	LV
	A9	LS	LM	LM	LM	LM	LM	LM	LV	LV	LM	LM	LV	LV	LV	LV
	A10	LM	LV	LV	LM	LV	LV	LV	LV	LV	LV	LV	LV	LV	LV	LV
P2	A1	NT	NT	NT	NT	NT	LS	NT	NT	NT	LS	LS	LS	LM	LM	LV
	A2	LM	LM	LM	LM	LV	LV	LM	LM	LM	LS	LV	LV	LV	LV	LV
	A3	LV	LV	LV	LM	LV	LV	LM	LV	LV	LV	LV	LV	LV	LV	LV
	A4	LV	LV	LV	LV	LV	LV	LS	LM	LM	LM	LM	LM	LV	LV	LV
	A5	LM	LV	LV	LM	LM	LV	LM	LV	LV	LV	LV	LV	LV	LV	LV
	A6	LV	LV	LV	LV	LV	LV	LV	LV	LV	LV	LV	LV	LV	LV	LV
	A7	LV	LV	LV	LV	LV	LV	LS	LS	LM	LS	LS	LS	LM	LM	LV
	A8	LS	LS	LS	LM	LM	LS	LV	LV	LM	LM	LV	LV	LV	LV	LV
	A9	LS	LS	LM	LM	LM	LM	LM	LV	LV	LV	LV	LV	LV	LV	LV
	A10	LM	LV	LV	LV	LV	LV	LM	LV	LV	LM	LV	LV	LV	LV	LV
P3	A1	LS	NT	NT	NT	NT	LS	NT	NT	NT	LS	LS	LM	LM	LM	LM
	A2	LM	LM	LS	LM	LV	LV	LV	LV	LV	LV	LV	LV	LV	LV	LV
	A3	LV	LV	LV	LV	LV	LV	LV	LV	LV	LV	LV	LV	LV	LV	LV
	A4	LM	LV	LV	LM	LV	LV	LS	LM	LM	LM	LM	LM	LV	LV	LV
	A5	LM	LV	LV	LM	LV	LV	LS	LM	LM	LM	LV	LV	LV	LV	LV
	A6	LV	LV	LV	LM	LV	LV	LM	LV	LV	LM	LV	LV	LV	LV	LV
	A7	LM	LV	LV	LM	LV	LV	LS	LM	LM	LS	LM	LM	LM	LM	LV
	A8	LS	LS	LS	LM	LM	LS	LV	LM	LM	LM	LV	LV	LV	LV	LV
	A9	LS	LM	LM	LV	LM	LM	LV	LV	LV	LV	LV	LV	LV	LV	LV
	A10	LM	LV	LV	LV	LV	LV	LV	LV	LV	LV	LV	LV	LV	LV	LV
P4	A1	NT	NT	DS	NT	LS	LS	NT	NT	NT	LM	LM	LM	LM	LM	LS
	A2	LV	LV	LV	LM	LM	LM	LM	LM	LV	LM	LV	LV	LM	LV	LV
	A3	LM	LV	LV	LM	LV	LV	LM	LV	LV	LV	LV	LV	LV	LV	LV
	A4	LM	LV	LV	LM	LV	LV	LS	LS	LS	LS	LS	LM	LM	LM	LV
	A5	LM	LM	LV	LV	LV	LV	LV	LV	LV	LV	LV	LV	LV	LV	LV
	A6	LV	LV	LV	LV	LV	LV	LV	LV	LV	LV	LV	LV	LV	LV	LV
	A7	LM	LV	LV	LV	LV	LV	LM	LM	LM	LM	LM	LM	LM	LM	LM
	A8	LS	LS	LS	LM	LM	LS	LV	LV	LM	LM	LM	LV	LV	LV	LV
	A9	LS	LM	LM	LV	LM	LM	LV	LV	LV	LM	LM	LV	LV	LV	LV
	A10	LM	LV	LV	LM	LM	LV	LM	LV	LV	LM	LV	LV	LV	LV	LV
P5	A1	DS	NT	DS	NT	LS	LS	NT	NT	NT	LS	LS	LM	LM	LM	LS
	A2	LM	LV	LV	LM	LV	LV	LV	LV	LV	LV	LV	LV	LM	LV	LV
	A3	LV	LV	LV	LV	LV	LV	LM	LV	LV	LM	LV	LV	LV	LV	LV
	A4	LV	LV	LV	LV	LV	LV	LS	LS	LM	LS	LM	LM	LM	LV	LV
	A5	LM	LV	LV	LM	LM	LM	LM	LV	LV	LM	LV	LV	LV	LV	LV
	A6	LV	LV	LV	LV	LV	LV	LV	LV	LV	LV	LV	LV	LV	LV	LV
	A7	LV	LV	LV	LV	LV	LV	LS	LS	LM	LS	LS	LM	LM	LV	LV
	A8	LS	LS	LS	LM	LM	LS	LV	LM	LM	LV	LV	LV	LV	LV	LV
	A9	LS	LM	LM	LV	LM	LM	LM	LV	LV	LV	LV	LV	LV	LV	LV
	A10	LM	LV	LV	LM	LV	LV	LM	LV	LV	LV	LV	LV	LM	LV	LV

Where: A1= CSY; A2= YCP 1%; A3= YCP 3%; A4= YCP 5%; A5= YCPP 1%; A6= YCPP 3%; A7= YCPP 5%; A8= YCPC 1%; A9= YCPC 3%; A10= YCPC 5%

https://doi.org/10.5593/sgem2024/4.1/s18.45

Determination of criteria

The approval criteria for each alternative were calculated using formula (2), so the obtained results are illustrated in table 5 for each alternative.

Table 5 The approval criteria for each alternative

Day of storage	A1	A2	A3	A4	A5	A6	A7	A8	A9	A10
Day 1	NT, NT, NT, NT, DS	LM, LM, LM, LM, LM	LM, LM, LV, LM, LM	LS, LS, LS, LS, LS	LM, LM, LS, LM, LM	LM, LV, LM, LV, LV	LS, LS, LM, LM, LS	LS, LS, LS, LS, LS	LS, LS, LS, LS, LS	LM, LM, LM, LM, LM
Day 7	NT, NT, NT, NT, NT	LM, LM, LM, LM, LV	LM, LV, LV, LV, LV	LS, LM, LM, LS, LS	LM, LM, LM, LM, LM	LV, LV, LV, LV, LV	LS, LS, LM, LM, LS	LS, LS, LS, LS, LS	LM, LS, LM, LM, LM	LM, LV, LV, LV, LM, LV
Day 14	NT, NT, NT, DS, DS	LM, LS, LM, LM, LV	LM, LV, LV, LV, LV	LM, LM, LM, LS, LM	LM, LV, LM, LV, LM	LV, LV, LV, LV, LV	LM, LM, LM, LM, LM	LS, LS, LS, LS, LS	LM, LM, LM, LM, LM	LV, LV, LV, LV, LV

Determination of tasters

Before calculating the approval process of a taster, we used formula (3) to determine the value weights. The value weights for Q1, Q2, Q3, Q4, Q5 are DM, NT, LM, LV, LV.

To determine the approval process of the tasters, we used formula 4.

Table 6 The person aggregation for each alternative

Day of storage	A1	A2	A3	A4	A5	A6	A7	A8	A9	A10
Day 1	NT	LM	LM	LS	LM	LM	LS	LS	LS	LM
Day 7	NT	LM	LV	LS	LM	LV	LS	LS	LM	LV
Day 14	NT	LM	LV	LM	LM	LV	LM	LS	LM	LV

From Table 6 it can be seen that the most appreciated samples were the sample with 3% cherry plum dried fruit, the sample with 3% cherry plum peel powder, and the sample with 5% cherry plum pulp powder. All 3 samples were obtained „like moderately" on the first day of analysis and „like very much" on days 7 and 14. The control sample obtained a neutral score (neither like nor dislike).

Sensory analysis using a 5-point hedonic scale

As can be seen from figure 1, the strongest fruity taste was felt in the samples with the addition of 5% of the three powders, also these samples were evaluated as the most consistent. The sour taste was felt the strongest in the control sample, followed by the YCPC 1% sample and the YCPP 3% and 5% samples.

The aftertaste was evaluated with average values for all samples, slightly higher than those for the control sample.

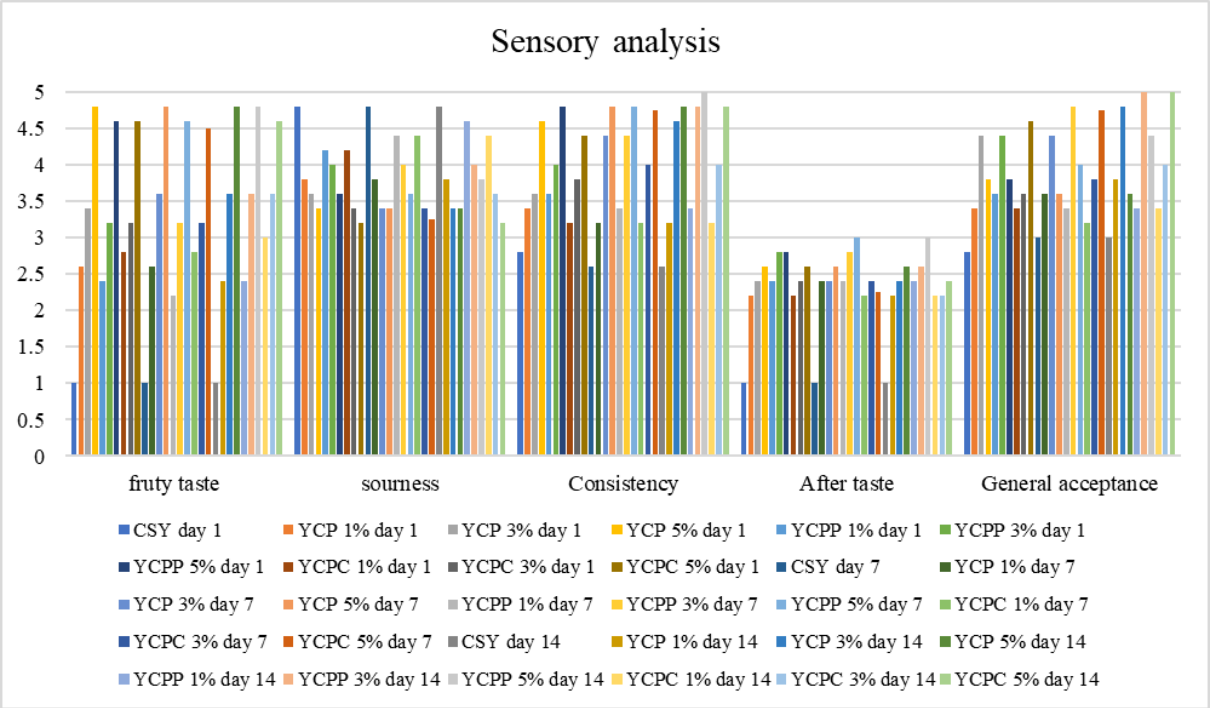


Figure 1 Sensory Analysis of the sample

The overall acceptability of the samples was rated higher for samples with 3% yellow cherry plum peel powder, 3% yellow cherry plum powder, and 5% yellow cherry pulp powder.

Physicochemical analysis

Titratable acidity

As can be seen from Figure 2, the acidity of the yogurt samples increases during the storage period. This is due to the accumulation of lactic acid through the action of lactic acid bacteria on the lactose in the milk, with fermentation continuing slowly throughout this period.

The samples with 3 and 5% yellow cherry plums obtained the highest results, and the samples with the addition of yellow cherry plum pulp obtained the lowest results.

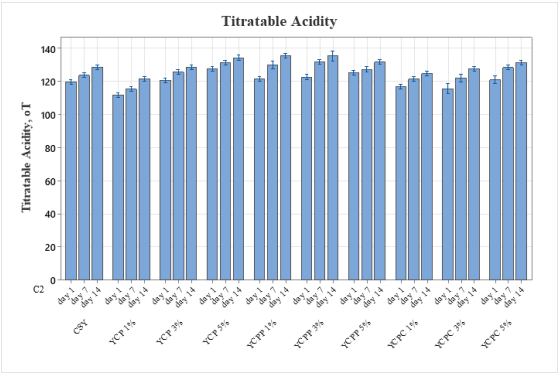


Figure 2 Evolution of Titratable Acidity during the storage time

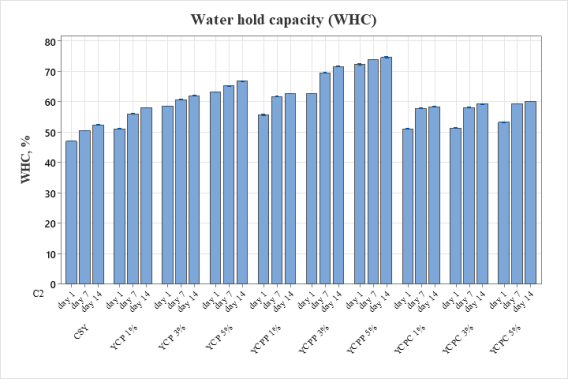


Figure 3 Evolution of WHC during the storage time

https://doi.org/10.5593/sgem2024/4.1/s18.45

Water hold capacity (WHC)

As can be seen from Figure 3, the samples with the addition of yellow cherry plum powder obtained better results, and this could be because the dry substance interacts with the water in the product and the water in the product can have an effect on hydration on these products and the explosion of the water in the coagulum mass is thus prevented.

WHC increases during storage, and this is due to the hydration of cork particles and the binding of water by them.

The best values were obtained by the samples with the addition of yellow cherry plums peel, followed by the samples with the addition of whole cherry plums, respectively by the samples with the addition of cherry plums pulp. The amount of powder added directly proportionally influenced the WHC for its category.

Determination of the degree of syneresis

Whey removal is an undesirable indicator in yogurt because it negatively influences consumer perception.

As can be seen from Figure 4 where the syneresis obtained by centrifuging a sample amount is represented, the best values for syneresis were obtained for the samples with the addition of 3 and 5% of yellow corkscrew powder, the control sample being the most prone to syneresis. This may be due to the increase in dry matter content in the yogurt samples which has the effect of strengthening and stabilizing the mass of the clot.

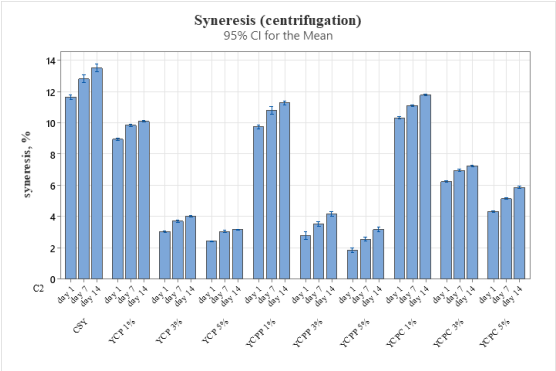


Figure 4 Evolution of Syneresis by centrifugation during the storage time

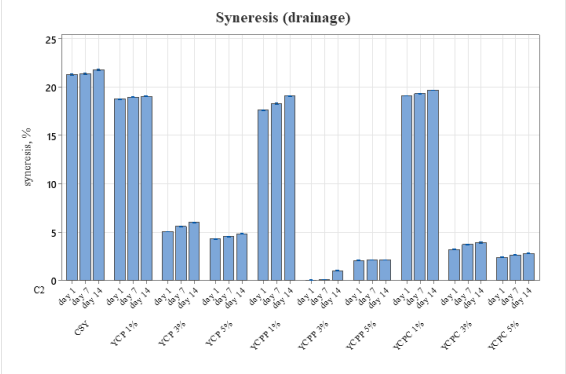


Figure 5 Evolution of Syneresis by drainage during the storage time

As can be seen from Figure 5, in the case of all 3 types of yogurt samples, an improvement can be observed when cherry plum powder (cherry plum, cherry plum peel, and cherry plum pulp) was added 1% to the yogurts. A greater improvement is seen between 1% and 3% addition, with syneresis decreasing by up to 4 percent for cherry plum pulp yogurt, 6 percent for cherry plum yogurt, and 7 percent for cherry plum peel yogurt. Continuous syneresis decreased when the powder percentage was increased to 5% for all 3 powder types.

Regarding the evolution of syneresis during the storage period, an increase in syneresis can be observed for all types of samples.

CONCLUSION

Yellow cherry plum powders improve the sensory characteristics of the yogurts, giving the yogurts a fruity flavor specific to these fruits, also improving the consistency.

Applying the non-numerical statistical method for sensory analysis, we can conclude that the most appreciated yogurt samples were the yogurt sample with 3% addition of yellow cherry plum powder, the sample with 3% addition of yellow cherry plum peel powder, and the sample with 5% yellow cherry plum peel.

Incorporating the powders into the yogurt leads to an increase in the acidity of the samples.

Regarding syneresis and water retention capacity, which are important indicators for yogurt quality, these powders led to better results directly proportional to the increase in the powder content in the product.

ACKNOWLEDGEMENTS

We sincerely thank the Research Center in Biotechnology and Food Engineering (C.C.B.I.A.) and the Lucian Blaga University of Sibiu for their support throughout the research period.

REFERENCES

[1] wikipedia, "Prunus cerasifera," 2024. [Online]. Available: https://en.wikipedia.org/wiki/Prunus_cerasifera. [Accessed 2024].

[2] horticultorul.ro, "Corcodus, Mirobolan (Prunus Cerasifera)," 2023. [Online]. Available: https://www.horticultorul.ro/pomi-fructiferi/corcodus-mirobolan-prunus-cerasifera/.

[3] Y. Wang, X. Chen, Y. Zhang, and X. Chen, "Antioxidant activities and major anthocyanins of Myrobalan plum (Prunus cerasifera Ehrh.)," *J Food Sci,* vol. 74, no. 4, pp. 88-93, 2012.

[4] Z. Jiaojiao, T. Wushouer, H. Weiwei and L. Yonhong, "Antioxidant Activities of Prunus cerasifera Polyphenols and Their Protective Effects on the Livers of Obese Mice," *Modern Food Science and Technology,* vol. 38, no. 10, pp. 40-46, 2022.

[5] X. Duan, J. Li, J. Cui, H. Wen, X. Xin and H. Aisa, "A network pharmacology strategy combined with in vitro experiments to investigate the potential anti-inflammatory mechanism of Prunus cerasifera Ehrhart.," *J Food Biochem.,* vol. 46, no. 6, p. 14396, 2022.

[6] R. Fadhil, R. Agustina and R. Hayati, "Sensory Assessment of Sauerkraut Using a Non-Numeric Approach Based on Multi-Criteria and Multi-Person Aggregation," *Bull. Transilv.,* vol. 13, pp. 112-118, 2020.

[7] A. Tugba, "Physicochemical and sensory characterization of different yogurt production methods," *International Dairy Science,* vol. 125, p. 105245, 2022.

[8] E. Foegeding and M. Drake, "Invited review: Sensory and mechanical properties of cheese texture," *Journal of Dairy Science,* vol. 90, pp. 1611-1624, 2007.

[9] M. Meilgaard, G. Civille and B. Carr, Sensory evaluation techniques (3rd ed.), Taylor & Francis , 2007.

[10] M. Tița, Handbook of Quality Analysis and Control in the Dairy Industry („ Manual de analiză și control calității în industria laptelui"), Sibiu, Romania: "Lucian Blaga" University Publishing House, 2002.

[11] M. Barkallah, M. Dammak, I. Louati, F. Hentati, B. Hadrich, T. Mechichi and M. Ayadi, "Effect of Spirulina platensis fortification on physicochemical, textural, antioxidant and

https://doi.org/10.5593/sgem2024/4.1/s18.45

sensory properties of yogurt during fermentation and storage," *LWT -Food Science and Technology,* vol. 84, pp. 323-330, 2017.

[12] F. Harte, L. Luedeck, B. Swanson and G. Barbosa-Ca´novas, "Low-Fat Set Yogurt Made from Milk Subjected to Combinations of High Hydrostatic Pressure and Thermal Processing," *Journal of Dairy Science,* vol. 86, p. 1074–1082, 2003.

[13] F. Dannenberg and H. Kessler, "Effect of denaturation of β-lactoglobulin on texture properties of set-style nonfat yogurt," *Syneresis. Milchwissenschaft,* vol. 43, no. 10, pp. 632-635, 1988.

[14] A. Pluta, A. Kazimierczak and D. Wąsowska, "Influence of selected hydrocolloids on quality of yoghurt „Wpływ wybranych hydrokoloidów na jakość jogurtu ”," *Food Industry „Przemysł Spożywczy”,* vol. 3, pp. 41-43, 1999.

[15] Minitab, "Minitab," 2023. [Online]. Available: https://www.minitab.com/en-us/.

SECTION

AIR POLLUTION AND CLIMATE CHANGE

AEROSOL FORMATION DURING THE HANDLING OF BEECH-PLASTIC PELLETS

Ing. Nikola Čajová Kantová, PhD.[1]

Ing. Alexander Čaja, PhD.[2]

prof. Ing. Radovan Nosek, PhD.[2]

Ing. Alexander Backa[2]

[1] Research Centre, University of Žilina, **Slovakia**
[2] Department of Power Engineering, Faculty of Mechanical Engineering, University of Žilina, **Slovakia**

ABSTRACT

Plastic waste pollution represents extensive threats to ecosystems and human health. A lot of plastic waste enters the ocean or ends on landfills, where it threatens the ecosystem. Therefore, it is crucial to find methods for its effective disposal or reuse. A significant amount of plastic can be found in personal protective equipment used to protect against viral infections and transmission, for example during the COVID-19 pandemic. This article focuses on the utilization of plastic waste by mixing it with beech sawdust and subsequently producing pellets. The pellets serve as a fuel, and aerosols were measured during their loading into a pellet hopper by an optical particle sizer in the range from 0.3 μm to 10 μm. The most commonly measured property of aerosols is just mass concentration which was observed. A previous study showed that the pellet combustion process did not influence aerosol formation in the laboratory with an automatic pellet boiler and retort burner. This study found that the total measured aerosol concentration increased by up to 72.6% during their handling in the hopper compared to the total aerosol concentration before the handling. However, the produced pellets represent a promising way to utilize plastic waste as an additive to wood pellets.

Keywords: plastic waste, pollution, aerosols, combustion, pellets

INTRODUCTION

Plastic waste generated from medical equipment, also waste produced in connection with COVID-19, presents a significant challenge due to its potential to be contaminated with infectious materials. This necessitates meticulous disposal protocols to safeguard against disease transmission. Beyond the immediate healthcare concern, plastic waste pollution poses a multifaceted threat to ecosystems and human health. One direct pathway of human health detriments is exposure to plastic-derived chemicals, which can occur through both food chain contamination and direct contact. The ramifications of plastic pollution extend beyond health, encompassing significant economic and societal consequences. Clean-up efforts incur substantial costs, while potential damage to tourism and the depletion of natural resources pose further challenges. A comprehensive approach is paramount to mitigating plastic pollution. This multifaceted strategy should encompass the reduction of plastic usage, the implementation of improved waste

https://doi.org/10.5593/sgem2024/4.1/s19.46

management practices, and the development and adoption of sustainable alternatives [1,2,3].

Liu et al. (2015) posited that the selection of an optimal treatment technology for COVID-19 medical waste treatment is a highly complex process, encompassing economic, technical, environmental, and social considerations [4]. Currently, high-temperature incineration has emerged as a prevalent treatment method for these materials. Furthermore, several disinfection treatments, including gas sterilisation, chemical disinfection, microwave treatment, thermal inactivation, irradiation, and autoclaving, have been employed to neutralise COVID-19 medical waste for subsequent processing [5]. The objective of research of Yousef et al. (2022) was to develop a novel thermochemical strategy for the extraction of butane from the vast quantity of discarded COVID-19 masks. The experiments were conducted with 3-ply face masks over ZSM-5 zeolite with different ratios using thermogravimetry at different heating conditions. Consequently, the catalytic pyrolysis strategy over ZSM-5 zeolite can be employed effectively to dispose of contaminated masks and to convert them into butanol, a compound that can be used as a liquid fuel and lubricant [6]. Purnomo et al. (2021) conducted a review of thermochemical processes, including incineration, torrefaction, pyrolysis, and gasification, in relation to their applicability to medical waste generated by the coronavirus (COVID-19). Additionally, the mechanical treatment of medical waste into sanitized refuse-derived fuel was discussed as a preliminary stage before thermochemical conversion. In terms of material flexibility, incineration is practically applicable for all types of COVID-19 medical waste. However, it has the highest potential to emit the largest amount of CO_2 and other harmful gases. Furthermore, gasification and pyrolysis are considered promising in terms of energy conversion efficiency and environmental impacts. On the other hand, carbonization faces several technical problems following thermal degradation due to insufficient operating temperature [7].

The aim of this article is energy utilization of COVID-19 medical waste by its adding to beech sawdust and the production of pellets for combustion purposes. The energy assessment of COVID-19 medical waste as a potential fuel [8] and health risks connected with energy disposal of pandemic waste [9] were investigated in previous works. Another previous study also showed that the pellet combustion process did not influence aerosol formation in the laboratory with an automatic pellet boiler and retort burner [10]. This study deals with the pellet handling in the hopper. The most commonly measured property of aerosols, and important for health and environmental effects, is mass concentration. In this work, mass concentration was measured by an optical particle sizer (OPS) in the laboratory before and during the loading of produced pellets into a pellet hopper. Pellets consisting of beech sawdust and plastic waste from FFP2 masks were chosen as fuel.

MATERIALS AND METHODS

The detailed parameters of used materials are stated in Table 1. The main material was beech sawdust as waste from beech wood cutting. The added materials were FFP2 masks with the 5% content and 10% content. These masks were prepared by crushing and mixing devices into small pieces useable in the pellet process. The particle size of beech sawdust was from 0.01 to 3 mm. Input material was compressed by small pellet press with a power of 7.5 kW. Pellets were produced under the same conditions and

they had approximately the same diameter of 6 mm. Further they were stored at the temperature of 20 °C and relative humidity from 40% to 50% for seven days. Produced pellets are shown in Figure 1.

Table 1 The detailed parameters of pellet samples

Sample	Weight Proportion Beech Sawdust [%]	Weight Proportion FFP2 masks [%]	Carbon [%]	Hydrogen [%]	Nitrogen [%]	Sulphur [%]	Pellet moisture [%]	Ash in dry sample [%]	Lower calorific value [MJ/kg]
Beech 100	100	0	45.90	6.93	0.00	0.05	5.25	1.60	16.86
Beech 95	95	5	48.87	6.64		0.01	4.78	1.00	18.15
Beech 90	90	10	50.97	7.04		0.05	4.60	1.10	19.78

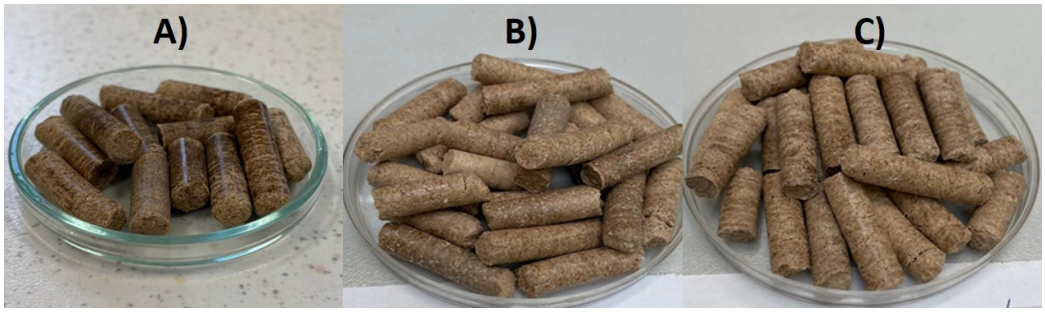


Figure 1 Pellet samples: A) Beech 100; B) Beech 95; C) Beech 90

Pellets were burned in an automatic boiler for pellet combustion with a heat power of 18 kW. First were combusted Beech 100, and then samples Beech 95 and Beech 90. Aerosols were measured during their loading into a pellet hopper by an optical particle sizer in the range from 0.3 µm to 10 µm. Each measurement was conducted as a series of ten one-minute intervals. The resulting values of mass concentration represent the mean of these series.

RESULTS

The results are processed into graphs showing the mean diameter of each range and the mean values of the measured mass concentrations. The results of measuring the aerosol mass concentration before filling the pellet hopper are shown in Figure 2. The highest mass concentration was measured with an average value of 78.97 µg/m^3 for the range 8.031-10.0 µm. The total mass concentration was 198.67 µg/m^3.

https://doi.org/10.5593/sgem2024/4.1/s19.46

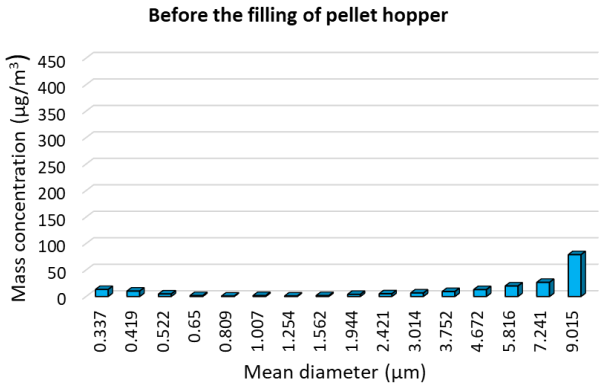


Figure 2 Aerosol mass concentration before the filling of pellet hopper

The results of the measurement of the aerosol mass concentration during the filling of the pellet hopper with Beech 100 as fuel are shown in Figure 3. The highest mass concentration was measured with an average value of 443.89 µg/m^3 for the range 8.031-10.0 µm. The total mass concentration was 724.63 µg/m^3.

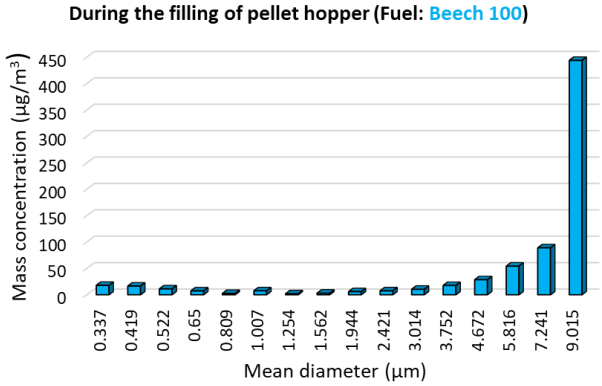


Figure 3 Aerosol mass concentration during the filling of pellet hopper with Beech 100

The results of the measurement of the aerosol mass concentration during the filling of the pellet hopper with Beech 95 as fuel are shown in Figure 4. The highest mass concentration was measured with an average value of 402.18 µg/m^3 for the range 8.031-10.0 µm. The total mass concentration was 621.36 µg/m^3.

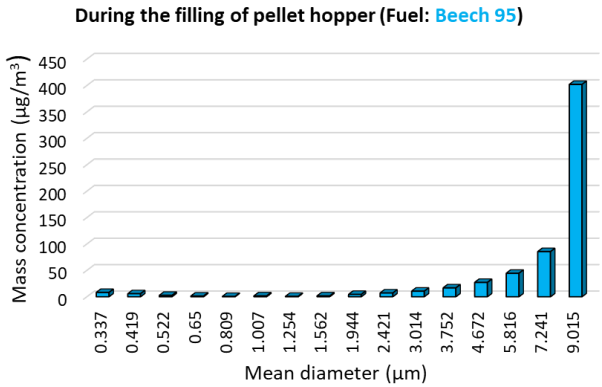


Figure 4 Aerosol mass concentration during the filling of pellet hopper with Beech 95

The results of the measurement of the aerosol mass concentration during the filling of the pellet hopper with Beech 90 as fuel are shown in Figure 5. The highest mass concentration was measured with an average value of 274.70 µg/m^3 for the range 8.031-10.0 µm. The total mass concentration was 406.12 µg/m^3.

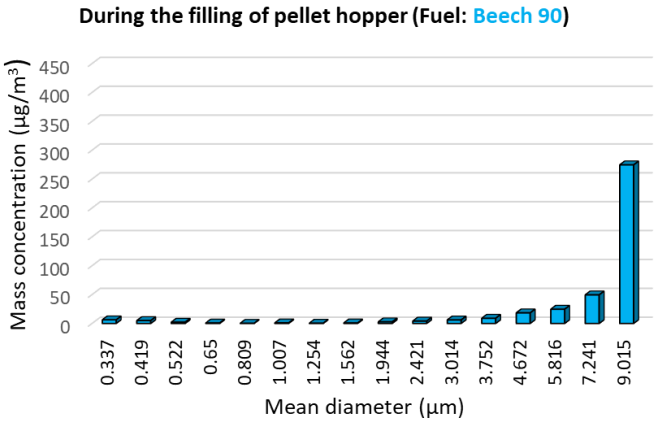


Figure 5 Aerosol mass concentration during the filling of pellet hopper with Beech 90

DISCUSSION

The total mass concentration was 198.67 µg/m^3 prior to the filling of the pellet hopper. The concentration increased by up to 72.6% during the handling of sample Beech 100 in the hopper in comparison to the total aerosol concentration prior to the handling. The total mass concentration was found to be higher, at approximately 68%, during the handling of sample Beech 95 in the hopper compared to the total aerosol concentration before the handling. The handling of sample Beech 90 resulted in the lowest concentration increase, at 51.1%, in comparison to the total aerosol concentration before the handling. Aerosols are commonly measured by an optical particle sizer. For instance, Pal et al. (2020) measured atmospheric aerosols by Scanning Mobility Particle Sizer (SMPS) and Optical Particle Sizer (OPS) [11]. The SMPS is capable of measuring aerosols in the range of 10 nm to 400 nm, while the OPS is able to measure aerosols in the range of 0.3 µm to 10 µm.

CONCLUSION

This article focuses on the utilization of plastic waste by mixing it with beech sawdust and subsequently producing pellets compressing by a small pellet press. The pellets serve as a fuel in an automatic pellet boiler. Aerosols were measured during their loading into a pellet hopper by an optical particle sizer in the range from 0.3 µm to 10 µm. The most commonly measured property of aerosols is just mass concentration which was observed.

A previous study showed that the pellet combustion process did not influence aerosol formation in the laboratory with an automatic pellet boiler and retort burner. This study found that the total measured aerosol concentration increased by up to 72.6% during their handling in the hopper compared to the total aerosol concentration before the handling. However, beech sawdust contains lower lignin content than spruce sawdust in general, which could cause lower pellet durability and consistency. This would

https://doi.org/10.5593/sgem2024/4.1/s19.46

consequently cause more aerosols in the air when feeding beech pellets compared to spruce pellets.

As Żukowski et al. stated, incineration of polymers leads to waste reduction of more than 90% [12]. The produced pellets represent a promising way to utilize plastic waste as an additive to wood pellets. Based on these and previous research results, it can be concluded that FFP2 masks can be added to wood sawdust and compressed into pellets used as fuel, provided that FFP2 masks would be used only as an additive and the main material would be wood sawdust; materials prepared to the pelletization process would be processed in an appropriate form; appropriate combustion conditions would be used.

ACKNOWLEDGEMENT

This publication has been produced with the support of VEGA No. 1/0150/22: Energy utilization of produced waste in connection with the COVID-19 pandemic through pellets as an alternative fuel.

REFERENCES

[1] Ganguly, R.K., Chakraborty, S.K.: Integrated approach in municipal solid waste management in COVID-19 pandemic: perspectives of a developing country like India in a global scenario. Case Studies in Chemical and Environmental Engineering, 3 (2021), Article 100087.

[2] Ganguly, R.K., Chakraborty, S.K.: Plastic waste management during and post Covid19 pandemic: Challenges and strategies towards circular economy. Heliyon, Volume 10, Issue 4, 29 February 2024, e25613.

[3] Tausova, M., Mihalikova, E., Culkova, K., Stehlikova, B., Taus, P., Kudelas, D., Strba, L., Domaracka, L., Analysis of Municipal Waste Development and Management in Self-Governing Regions of Slovakia, Sustainability, 12/14, 5818, 2020.

[4] Liu, H.-.C., You, J.-.X., Lu, C., Chen Y.-.Z.: Evaluating health-care waste treatment technologies using a hybrid multi-criteria decision making model. Renew. Sustain. Energy Rev., 41 (2015), pp. 932-942, 10.1016/j.rser.2014.08.061.

[5] Sharma, H.B., Vanapalli, K.R., Cheela, V.R.S., Ranjan, V.P., Jaglan, A.K., Dubey, B. et al.: Challenges, opportunities, and innovations for effective solid waste management during and post COVID-19 pandemic Resour. Conserv. Recycl., 162 (2020), Article 105052, 10.1016/j.resconrec.2020.105052.

[6] Yousef, S., Eimontas, J., Striūgas, N., Abdelnaby, M. A.: A new strategy for butanol extraction from COVID-19 mask using catalytic pyrolysis process over ZSM-5 zeolite catalyst and its kinetic behavior, Thermochimica Acta, Volume 711, 2022, 179198, ISSN 0040-6031, https://doi.org/10.1016/j.tca.2022.179198.

[7] Purnomo, C. W, Kurniawan, W., Aziz, M.: Technological review on thermochemical conversion of COVID-19-related medical wastes, Resources, Conservation and Recycling, Volume 167, 2021, 105429, ISSN 0921-3449, https://doi.org/10.1016/j.resconrec.2021.105429.

[8] Čajová Kantová, N., Cibula, R., Szlek, A., Čaja, A., Nosek, R., Belany, P.: The energy assessment of COVID-19 medical waste as a potential fuel, Energy Reports, Volume 9, 2023, Pages 4995-5003, ISSN 2352-4847,

https://doi.org/10.1016/j.egyr.2023.04.018.

[9] Čajová Kantová, N., Cibula, R., Holubčík, M., Ďurčanský, P.: Health risks connected with energy disposal of pandemic waste, Heliyon, Volume 10, Issue 3,
2024, e25139, ISSN 2405-8440, https://doi.org/10.1016/j.heliyon.2024.e25139.

[10] Čajová Kantová, N., Čaja, A., Hrabovský, P.: Aerosol Measurements Before and During Combustion of Various Pellets from Spruce Sawdust and Face Masks FFP2, MATEC Web Conf., 369 (2022) 02005, DOI: https://doi.org/10.1051/matecconf/202236902005.

[11] Pal, D., Dastoor, A., Ariya, P. A. (2020). Aerosols in an urban cold climate: Physical and chemical characteristics of nanoparticles. Urban Climate, 34 (2020) 100713. https://doi.org/10.1016/j.uclim.2020.100713

[12] Zukowski, W., Jankowski, D., Baron, J., Wrona, J., 2021. Combustion dynamics of polymer wastes in a bubbling fluidized bed. Journal of Cleaner Production, 320, 128807. https://doi.org/10.1016/j.jclepro.2021.128807.

https://doi.org/10.5593/sgem2024/4.1/s19.46

AGRICULTURE AS A DRIVER FOR CLIMATE CHANGE

Lecturer Dr. Carmen Simona Dumitrescu[1]

Prof. Dr. Sorin Mihai Stanciu[1]

Lecturer Dr. Raul Pașcalău[2]

Assoc. Prof. Dr. Cosmin Sălășan[1,3]

[1] University of Life Sciences "King Mihai I" from Timișoara, Faculty of Management and Rural Tourism, **Romania**

[2] University of Life Sciences "King Mihai I" from Timișoara, Faculty of Agriculture, **Romania**

[3] Escuela de Agronomía, Facultad de Ciencias Agrarias y Forestales, Universidad Católica del Maule, **Chile**

ABSTRACT

If a few years ago climate change was a new and fanciful concept and not everyone was aware of its entire action range, today we are witnessing increasingly pronounced climate change. At the European Union level are many political initiatives in order to mitigate the climate change so the next generations to have the same changes to a good environment. All the efforts must be put into shifting the development to a more sustainable one. There are different drivers that interfere with the climate. Among energy, transport, industrial processes, waste, land use, we also find agriculture as a driver for climate change. In agriculture the livestock, the utilized agricultural area, the type of farms depending on the input level, the consumption of inorganic fertilizers influences the climate, either through green gas emissions, water and air pollution, desertification etc. So, we could say that there are many aspects of agriculture that influence climate change. In the work, a brief screening of the aspects of agriculture that have a negative impact on the environment at the level of the European Union was carried out.

Keywords: agriculture, climate, change, impact

INTRODUCTION

Climate change is one of the greatest threats to human health in the 21st century. Global surface temperatures are rising and the frequency and intensity of extreme weather events, such as heatwaves, droughts, floods and storms, are expected to increase in the upcoming decades [11,15] In 2019, the European Green Deal was presented at the European Union level, a new strategy aimed at making the European economy more sustainable by combating climate and environmental changes and turning these threats into opportunities. Through the European Green Deal, the European Union has committed to become neutral in terms of environmental impact by 2050 [4]. On November 4, 2016, the Paris Agreement on climate change entered into force on the territory of the European Union. The purpose of this agreement is to facilitate concerted action at Union level to slow the rise in global temperatures and keep the rise to less than 2°C compared to pre-industrial levels, while limiting the rise to 1.5° C [9]. The EU

https://doi.org/10.5593/sgem2024/4.1/s19.47

and national governments have set clear objectives to guide European environmental policy until 2020 and have defined a vision for the period 2020-2050, supporting them with a series of research programs, norms and funding possibilities [3]. Within the European Union, the activity of environmental protection and combating climate change is very well organized through the existing institutional structures. Thus, the inventories of GHG emissions from each member state are collected at the European level by the agency responsible for the environment acting on behalf of the European Commission, and in particular the Directorate General for Climate Action, facilitating the realization of the union's inventory of GHG emissions. Agriculture contributes to climate change through greenhouse gases emissions (GHGs) that trap heat in the atmosphere [1,5]. In particular, agricultural sector generates direct GHGs emissions through (i) nitrous oxide emissions from soils, (ii) applications of fertilizers, (iii) dejections from grazing animals, (iv) methane production by ruminant animals, and indirect GHGs emissions due to land-use changes, including land clearing and deforestation [8,12,14]. Due to its direct contribution to global GHG emissions, agriculture can also serve as an important climate change mitigation strategy [2,7,13], both by reducing GHG emissions to the atmosphere, and by sequestering atmospheric carbon into plant biomass and soil, though the role of some soil carbon sequestration practices for climate mitigation has been questioned [2,10].

MATERIALS AND METHODS

The methodological approach involves a combination of research methods. The collection of primary data is carried out by main methods: searching for data in the online environment, documentation by studying European Union reports, studying European and national regulations regarding the chosen topic. The processing of information uses either descriptive method, consisting in the simple sorting of the information obtained and the use of statistical analysis methods and the graphic presentation of the data subject to research. It used descriptive and exploratory research, using data collection methods such as observation and analysis of documents, comparative study. The methodology served by the purpose is one that complies with the requirements of the content, combining the following techniques and methods: documentation, documentary analysis, including documentation, statistical methods (synthesis, graphic presentation of observed processes and phenomena, classification, static and dynamic comparative analysis, etc.). Through information sources, there can be mentioned various articles, in particular regulations and reports of the European Commission, the Directorate for Agriculture and Rural Development, statistics etc.

RESULTS

In the last three decades, the GHG emissions of the European Union have followed a downward trend (figure 1). Thus, in 2021, the total GHG emissions were about 3.5 billion tons of CO2 compared to 4.9 billion tons in 1990, which represents a decrease of 1.4 bilion tons, or 29% [6]. Net GHG emissions (including land use, land-use change and

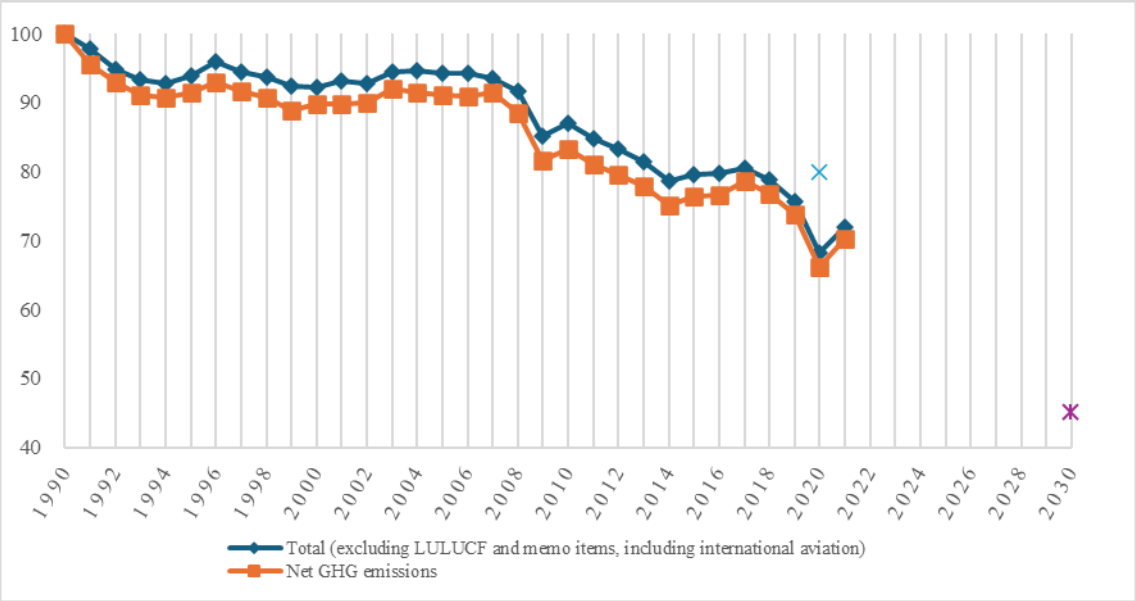


Figure 1 Evolution of GHG emissions in European Union, 1990=100%

forestry), i.e. taking into account net removals, amounted to 3.3 billion tons in 2021, compared to 4.7 billion tons in 1990.

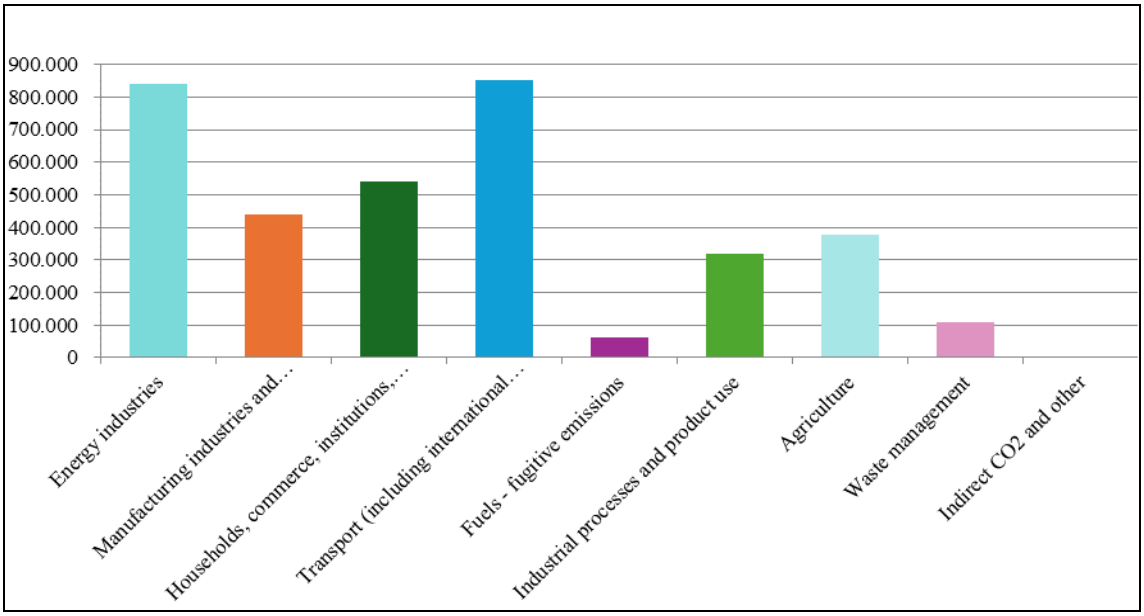


Figure 2 GHG emissions in activity sectors in 2021, thousand tons

Analysing GHG emissions by activity sector, the transport and the energy industry occupy the first places in terms of greenhouse gas emissions, being the main drivers for climate change. In 2021, agriculture ranked 5th in terms of GHG with around 11%.

The main activities from agriculture can be separated as drivers for climate change are enteric fermentation, more precisely the fermentation of feed, manure, agricultural soils, fertilisers etc.

https://doi.org/10.5593/sgem2024/4.1/s19.47

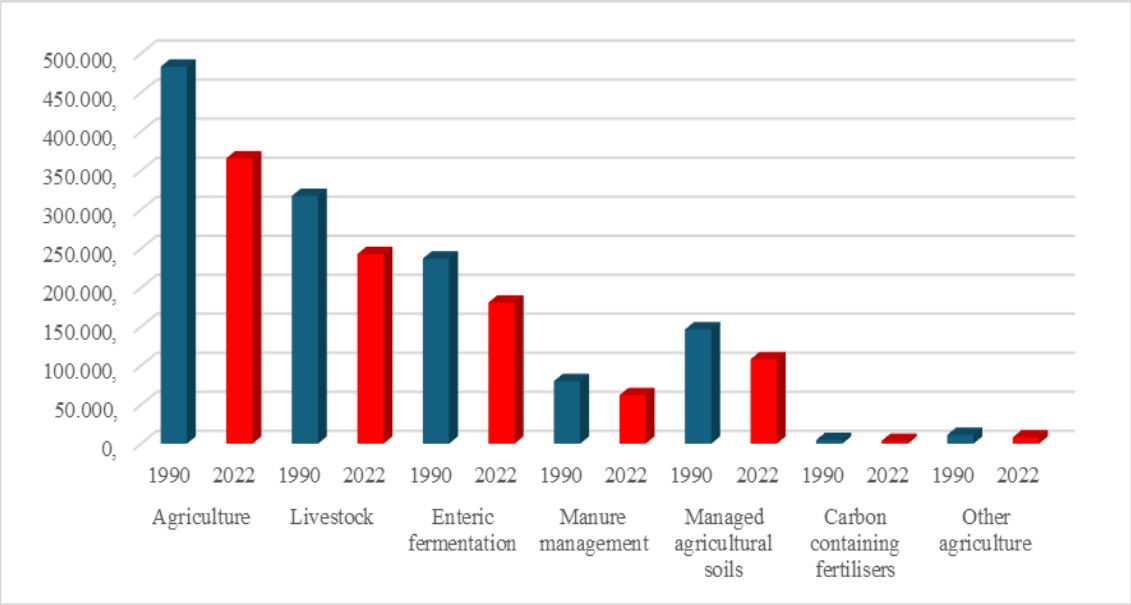


Figure 3 Evolution of GHG emissions from agriculture 1990-2022, thousand tons

The efforts of European Union materialised through its policies and support measures, had led to the decrease of GHG emissions in 2022 with almost 25% comparing to 1990 levels.

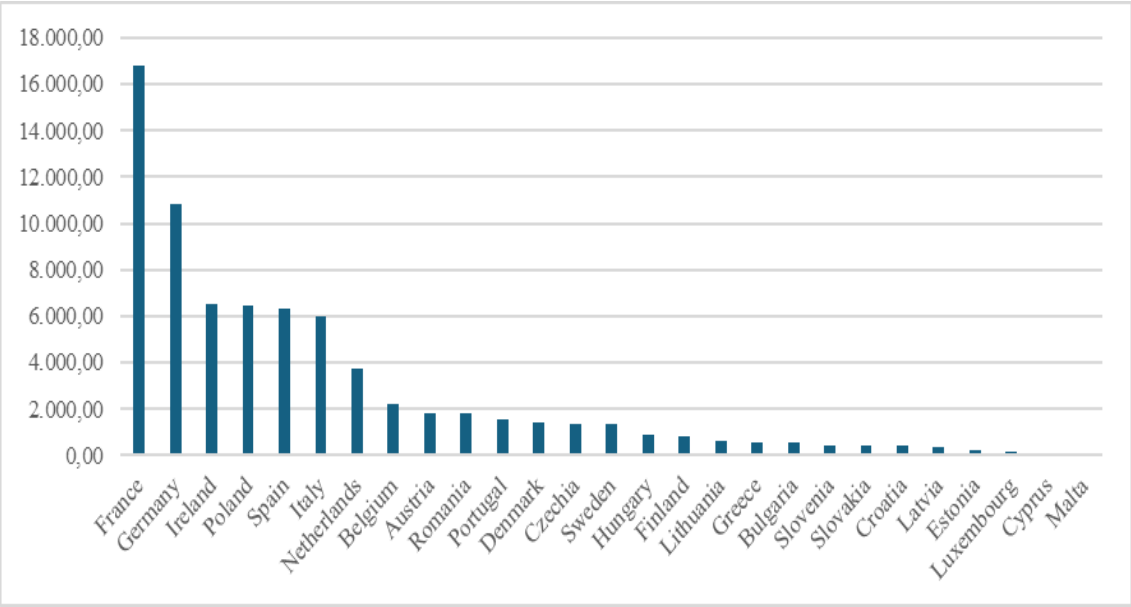


Figure 4 Bovine population, 2021, thousand heads

The digestive systems of cattle are responsible for highest part of the GHG emissions resulting from enteric fermentation. In European Union, France has the largest number of bovine populations, followed by Germany. But in order to have a clear image of the importance of bovine populations in agriculture, there must be specified the share of main livestock types. In 2021, the bovine population represented 49.98%, horses, asses, mules and hinnies 2.08%, swine, domestic species 24.84%, sheep 6.39%, goats 1.62%, poultry 15.09. The animal population must be put in relation with the agricultural area of the country to calculate the livestock density index. According to data provided by

statistics, the highest index in 2020 corresponds to Netherlands, 3,45, closely followed by Malta, 3,27 and then Belgium 2,68.

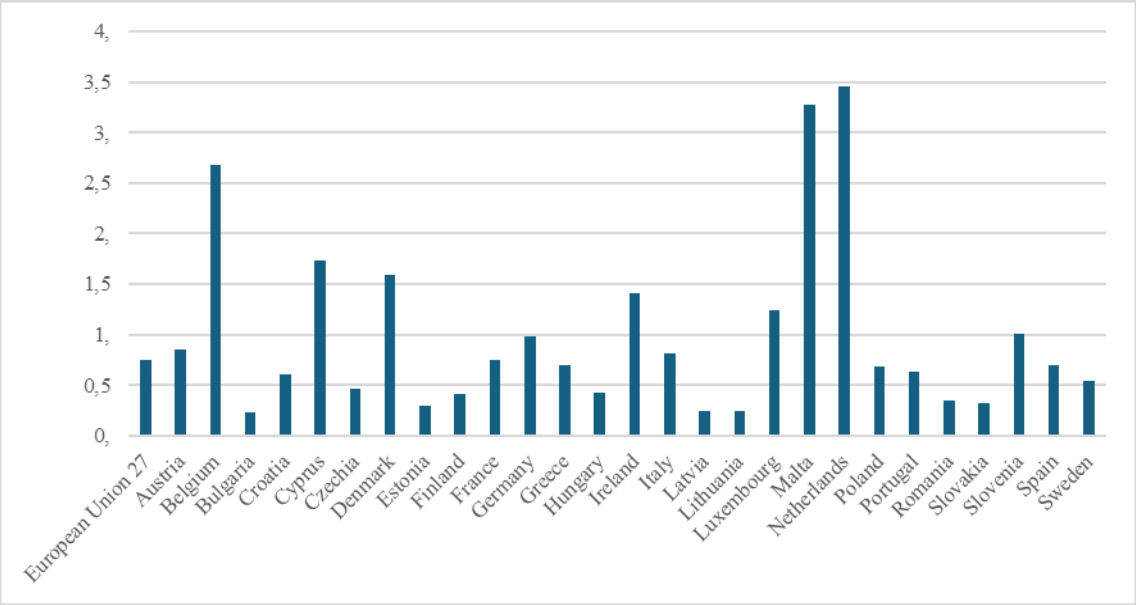


Figure 5 Livestock density index

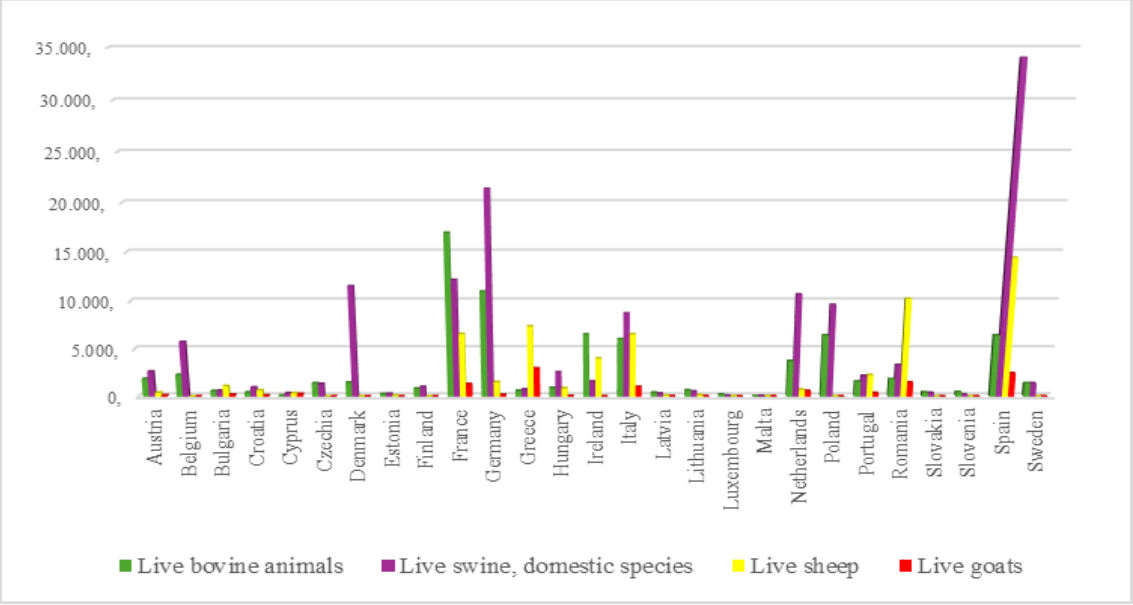


Figure 6 Animal populations, thousand heads

Spain has the largest animal population in European Union, having the largest swine population. On the second place, is France with less than 20,000 thousand heads, and then Germany with almost 34,000 thousand heads. But they have also the largest utilised agricultural areas.

https://doi.org/10.5593/sgem2024/4.1/s19.47

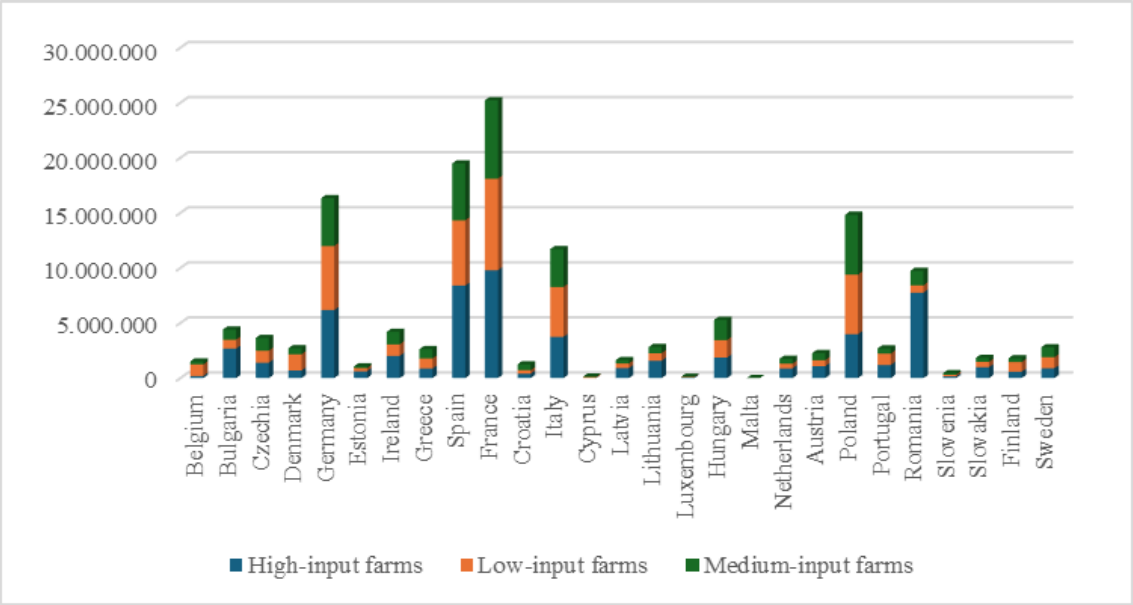


Figure 7 Utilised agricultural area, hectares

When referring to utilized agricultural area, Spain is overtaken by France, which has the largest utilized agricultural area, followed by Germany, Poland, Italy. But it is also very important to stratify the agricultural area used according to the type of farm, more precisely the level of inputs used at that level.

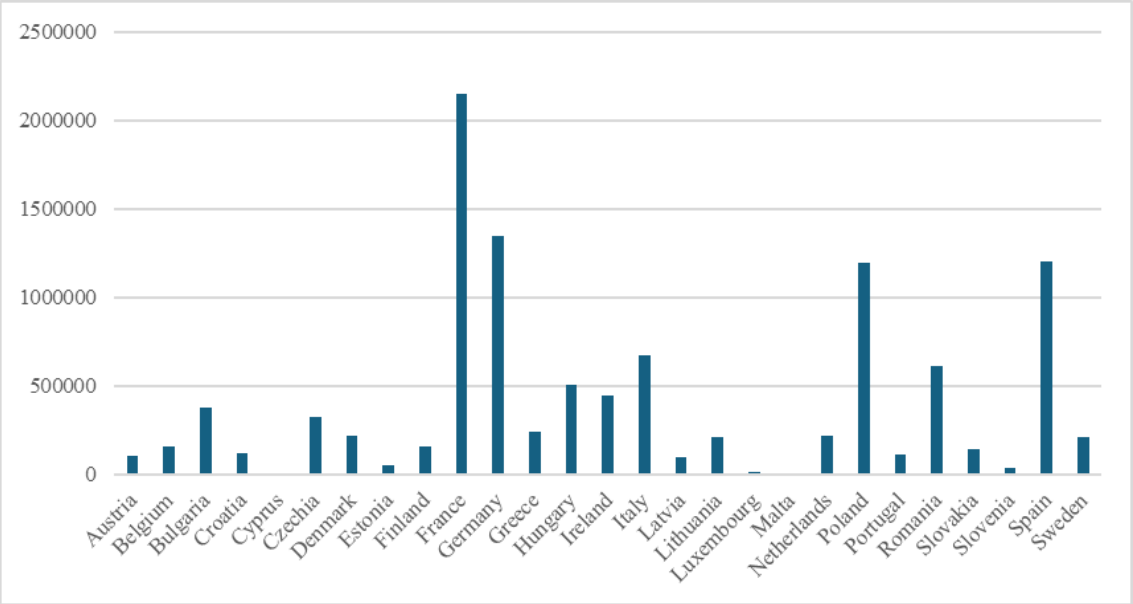


Figure 8 Consumption of inorganic fertilizers, tons

Inorganic fertilizers used in agriculture are also a driver of climate change. The consumption of inorganic fertilizers is directly related to the agricultural systems adopted, to the degree of agricultural intensity. In 2021, France was the highest consumer for inorganic fertilisers, followed by Germany, Spain, Poland.

DISCUSSION

In the European Union, GHG emissions have decreased as a result of the policies and measures adopted, the recorded values being below the target set for 2020. But the target for 2030 is much more ambitious and requires sustained efforts to achieve it. If the Covid pandemic, through the measures that were imposed in all European states, contributed to the significant reduction of GHG emissions, this reduction is due mainly to other sectors, not to agriculture. The decrease in GHG emissions from agriculture is mainly due to the adoption of less polluting technologies, but the decrease in the livestock also have an important contribution, leading to a decrease in GHG emissions from 317.459 thousand tons in 1990 to 243018 thousand tons in 2022. A major part of GHG emissions generated by livestock are due to enteric fermentation. The enteric fermentation and managed agricultural soils are the main two contributors to decrease the GHG emissions. In France the number of cattle decreased by about 20% between 1990-2021, while in Germany the decrease was much more drastic, over 40%. Almost half of livestock is 2021 is represented by bovine population and so can be explained the high percentage of GHG due to enteric fermentation. Livestock density index is another indicator for agriculture action as a climate change driver, but the low value in countries with high bovine population can be determined by the large utilised agricultural areas, or the rest of livestock from that country. The degree of intensity of agriculture determines, through the amount of inputs used, a different degree of GHG emissions. France has the largest agricultural area and about 38% is under high-input farms, fact supported by the consumption of inorganic fertilisers.

CONCLUSION

Climate change and environmental degradation are threats to the European Union and the entire planet. Climate change caused by human activities is considered a major threat to society mainly due to its wide impact on all aspects of life, whether we refer to nature, economy, health or well-being of people. Climate change is wide-ranging and is considered an issue of common concern, requiring action for a global response to limit and combat the risks and impacts of climate change. Through the adopted policies and European mechanisms, sets of measures have been adopted to contribute to the reduction of pollution and the achievement of sustainable development objectives. The European Union has succeeded in reducing its GHG emissions beyond the values agreed by the Kyoto Protocol. The efforts of each state to reduce GHG emissions from agriculture must be placed in the political and economic context of that country, taking into account measures for carbon sequestration, encouragement and support for farmers in adopting less polluting technologies or measures to encourage more responsible consumption. Unlike the other economic sectors that act as a driver for climate change, agriculture also stands out for its dual potential – on the one hand, it acts as a driver of climate change, and on the other hand, by sequestering carbon, it acts to combat climate change. The combined action of policy maker, farmer and consumer is needed for the decrease of GHG emissions and mitigating climate change through agriculture.

ACKNOWLEDGEMENTS

This paper is published from the own research funds of the University of Life Sciences "King Mihai I" from Timisoara.

https://doi.org/10.5593/sgem2024/4.1/s19.47

REFERENCES

[1]. Agovino Massimiliano, Casaccia Mariaconcetta, Ciommi Mariateresa, Ferrara Maria, Marchesa Katia, Agriculture, climate change and sustainability: The case of EU-28, Ecological Indicators Volume 105, pp 525-543, 2019

[2]. Anwar, M. R., Liu, D. L., Macadam, I., & Kelly, G, Adapting agriculture to climate change: A review. Theoretical and Applied Climatology, 113(1), pp 225–245, 2013

[3]. Climate change https://europa.eu/climate-pact/about/climate-change_ro

[4]. Communication from the Commission to the European Parliament, the European Council, the Council, the European Economic and Social Committee and the Committee of the Regions the European Green Deal, COM/2019/640 final, available online https://eur-lex.europa.eu/legal-content/EN/TXT/?uri=COM%3A2019%3A640%3AFIN

[5]. Delmas R., Serça D.,Jambert C., Global inventory of NOx sources, Nutrients Cycling in Agroecosystems, Volume 48, pp 51–60, 1997

[6]. Eurostat, https://ec.europa.eu/eurostat/databrowser/view/NRG

[7]. Greenhouse gas emission statistics - air emissions accounts, Statistics Explained, https://ec.europa.eu/eurostat/statistics-explained/SEPDF/cache/30599.pdf

[8]. Mark Howden S., Jean-François Soussana, Francesco N. Tubiello, Holger Meinke - Adapting agriculture to climate change, Proceedings of the National Academy of Sciences, vol 140, issue 50, 2007

[9]. OECD, Better policies to improve the environmental performance of the agriculture sector, available online https://www.oecd.org/agriculture/topics/agriculture-and-the-environment/

[10]. Powlson D.S., Stirling C.M., Jat M.L., Gerard B.G., Palm C.A, Sanchez P.A., Cassman K.G., Limited potential of no-till agriculture for climate change mitigation, Nature Climate Change, 4, pp. 678-683, 2014

[11]. Rocha, J., Oliveira, S., Viana, C. M., & Ribeiro, A. I., Chapter 8—Climate change and its impacts on health, environment and economy. In J. C. Prata, A. I. Ribeiro, & T. Rocha-Santos (Eds.), One Health, Academic Press, pp. 253–279, 2022

[12]. Smith CS, McDonald GT, Assessing the sustainability of agriculture at the planning stage, Journal of Environmental Management Volume 52, Issue 1, pp 15-37, January 1998

[13]. Smith P., Haberl H., Popp A., Erb K.-H., Lauk C., Harper R., Tubiello F., de Siqueira Pinto A., Jafari M., Sohi S., Masera O., Böttcher H., Berndes G., Bustamante M., Ahammad H., Clark H., Dong H.M., Elsiddig E.A., Mbow C., Ravindranath N.H., Rice C.W., Robledo Abad C, Romanovskaya A., Sperling F., Herrero M., House J.I., Rose S., How much land based greenhouse gas mitigation can be achieved without compromising food security and environmental goals? GCB Bioenergy, 19, pp. 2285-2302, 2013

[14]. Smith P., Martino D., Cai Z., Gwary D., Janzen H., Kumar P., McCarl B., Ogle S., O'Mara F., Rice C., Scholes B., Sirotenko O, Howden M., McAllister T., Pan G., Romanenkov V., Schneider V., Towprayoon S., Wattenbach M., Smith J., Greenhouse gas mitigation in agriculture, Philos. Trans. R. Soc. B Biol. Sci., 1492, pp. 789-813, 2008

[15]. Tilman David, Cassman G. Kenneth, Matson A. Pamela, Naylor Rosamond, Polasky Stephen, Agricultural sustainability and intensive production practices, Nature 418, pp 671-677, 2002

AIRBORN MICROORGANISMS IN HOT POINT AND GREEN AREAS AT DIFEERENT HIGHT OF GROUND AIR

Asen Peshev
Assist. Prof. Dr. Bilyana Grigorova-Pesheva
Assist. Prof. Dr. Georgi Kadinov
University of Forestry, Faculty of Forestry, Department of Silviculture, **Bulgaria**

ABSTRACT

Air pollution is a major problem related to human health and the protection and quality of the environment. Increasingly emphasis is placed on the problems associated with fine dust particles, without paying enough attention to the potential problems associated with the increase of microorganisms in the ground air layer. The present pilot study aims to establish the dynamics in the number of microorganisms at different height in the ground air. Six hot spots and six green zones were analyzed at a distance from the earth's surface - 0.5 m, 1 m and 1.5 m, respectively. An “open air” method was used. Samples were taken simultaneously at all points. Basic meteorological parameters were recorded - air temperature, air humidity, wind direction and speed, solar radiation. The amounts of bacteria, microscopic fungi and actinomycetes were recorded. The total microbial number for each of the points per 1 cubic meter of air was calculated. The data show a different scatter of the total number of microorganisms depending on the height. The number of airborne microorganisms is higher in hot spots. Certain differences in the dominant microbial groups were reported depending on the altitude and area considered. The data suggest a direct link, with increased levels of the airborne microbial community and vehicular traffic intensity in hotspots.

Keywords: microorganisms, airborne microorganisms, particular matter

INTRODUCTION

Air pollution is a major problem related to human health and the protection and quality of the environment. Increasingly emphasis is placed on the problems associated with fine dust particles, without paying enough attention to the potential problems associated with the increase of microorganisms in the ground outdoor air. Microorganisms enter the air carried on dust particles, through the separation of soil particles from agricultural and construction activities, through pollution generated by road transport and many others. As point out [1].] once entered in the air, microorganisms can be carried over great distances by the air flow. Microorganisms in the air are often defined as bioaerosols [2], although according to [3] this concept is not entirely correct, considering that bioaerosols also include parts of microorganisms as well as plant pollen. Most of the studies such as those of [4], [5] focus on the long-distance transport of airborne microorganisms and their potential risk to human health. There are not enough studies on the stratification and concentration of microorganisms in the ground air of urban areas. In addition, the dynamics in the amount and type of microorganisms in green urban areas, compared to hotspots, is not well studied. Several studies have indicated specificity in the redistribution of the dominant microbial community in

https://doi.org/10.5593/sgem2024/4.1/s19.48

different urban areas [6]. Other studies focus on the influence of climatic factors on the concentration of microorganisms in the air [7], [8]. There are some studies which point out that the number of airborne microorganisms sharply decreases at high altitude, given the inhospitable conditions for them - UV light, low temperatures, etc..[9] However, there are few studies that consider the amount and dominant group of microorganisms in ground air in Bulgarian urban areas.
The main goal of the present pilot study is to determine the dynamics in the number of microorganisms at different heights in the ground air, in different urban parts of the territory of the city of Sofia (hot spots and green zones)

MATERIALS AND METHODS

For the purposes of the present study, six points in a busy urban area - hotspots and six points in nearby park areas - have been selected. The sampling locations are as follows:

- Sample PP1.1: Ring mall, 214 Okolovrasten pat bul. – hot spot
- Sample PP1.2: Mountain Vitosha – green area
- Sample PP2.1: 15 Andrey Lyapchev bul. – hot spot
- Sample PP2.2: Vartopo park – green area
- Sample PP3.1: Crossroad of 8 Dekemvri St. and Rosario St. - hot zone
- Sample PP3.2: Studentski Grad Park – green area
- Sample PP4.1: 38 Rodopski izvor str. – hot spot
- Sample PP4.2: Park Slavia – green area
- Sample PP5.1: 131 Evlogii I Hristo Georgievi bul
- Sample PP5.2: Military Park – green area
- Sample PP6.1: Crossroad Orlov most – hot spot
- Sample PP6.2: park Borisova Gradina – green area

We used the "Open air" technique as outlined by Nustorova and Malcheva (2020). This technique is based on natural settling of microbial cells due to gravitational forces. It is founded on the principle that within a span of 5 minutes, 10 liters of air traverse through an area of 100 cm^2, i.e. the microorganisms contained in 10 liters of air settle. Conversion to a volume of $1m^3$ of air was conducted for each sample. Petri dishes containing specific selective nutrient agar media appropriate for the targeted microorganisms were employed in the experiment. Each measurement was performed in three replicates, the average value was calculated and presented. The samples were collected during the spring season of 2024. All samples were collected at the same time in all locations at 0.5 m, 1 m and 1.5 above the ground. Samples were collected after precipitation day, because according to [10], after a rainy period, the number of microorganisms in the air increases due to the higher humidity. Basic meteorological parameters are reported - air temperature, air humidity, wind direction and speed, solar radiation. The amounts of bacteria, microscopic fungi and actinomycetes were recorded. The total microbial number (TMN) for each of the points per $1m^3$ of air was calculated. Statistical processing of the collected data was performed using StatSoft Statistica 12 program.

RESULTS

The reported average air temperature is 10.4 °C, relative air humidity- 89%, atmospheric pressure 1006.4 millibars and wind speed 4 m/s from the northwest. The amounts of the main microbiological groups – bacteria, actinomycetes and microscopic

fungi – were determined. The results of the conducted microbiological analyzes are presented in Table 1. The data are recalculated relative to 1 m^3 of air and are presented in column-forming units per 1 m^3 of air.

Table 1 Main microbial parameters

	Hight	TMN	Bacteria	Actinomycetes	Fungi
PP1.1	0.5 m	16.31 ± 7.25	11.34 ± 5.66	2.80 ± 3.13	2.17 ± 1.12
	1 m	7.39 ± 4.10	5.61 ± 3.47	1.15 ± 0.77	0.64 ± 0.48
	1.5 m	15.67 ± 7.27	12.36 ± 4.75	2.17 ± 7.12	1.15 ± 0.81
PP1.2	0.5 m	9.55 ± 7.25	5.48 ± 5.66	2.17 ± 3.13	1.91 ± 1.12
	1 m	5.10 ± 4.10	3.44 ± 3.47	0.64 ± 0.77	1.02 ± 0.48
	1.5 m	14.01 ± 7.25	10.45 ± 4.75	2.42 ± 7.12	1.15 ± 0.81
PP2.1	0.5 m	20.64 ± 7.25	15.29 ± 5.66	3.69 ± 3.13	1.66 ± 1.12
	1 m	10.70 ± 4.10	8.15 ± 3.47	1.78 ± 0.77	0.76 ± 0.48
	1.5 m	12.99 ± 7.25	9.81 ± 4.75	2.04 ± 7.12	1.15 ± 0.81
PP2.2	0.5 m	5.48 ± 7.25	3.44 ± 5.66	0.64 ± 3.13	1.40 ± 1.12
	1 m	3.57 ± 4.10	2.17 ± 3.47	0.38 ± 0.77	1.02 ± 0.48
	1.5 m	5.22 ± 7.25	3.18 ± 4.75	0.51 ± 7.12	1.53 ± 0.81
PP3.1	0.5 m	9.55 ± 7.25	7.90 ± 5.66	1.02 ± 3.13	0.64 ± 1.12
	1 m	10.83 ± 4.10	6.88 ± 3.47	2.80 ± 0.77	1.15 ± 0.48
	1.5 m	8.41 ± 7.25	2.93 ± 4.75	4.97 ± 7.12	0.51 ± 0.81
PP3.2	0.5 m	8.66 ± 7.25	6.88 ± 5.66	0.89 ± 3.13	0.89 ± 1.12
	1 m	8.66 ± 4.10	6.11 ± 3.47	1.40 ± 0.77	1.15 ± 0.48
	1.5 m	9.55 ± 7.25	6.11 ± 4.75	2.42 ± 7.12	1.02 ± 0.81
PP4.1	0.5 m	14.90 ± 7.25	2.42 ± 5.66	11.85 ± 3.13	0.64 ± 1.12
	1 m	1.15 ± 4.10	0.13 ± 3.47	1.02 ± 0.77	0.00 ± 0.48
	1.5 m	26.50 ± 7.25	0.25 ± 4.75	26.24 ± 7.12	0.00 ± 0.81
PP4.2	0.5 m	8.66 ± 7.25	3.44 ± 5.66	4.08 ± 3.13	1.15 ± 1.12
	1 m	5.73 ± 4.10	2.17 ± 3.47	2.17 ± 0.77	1.40 ± 0.48
	1.5 m	10.45 ± 7.25	1.53 ± 4.75	5.99 ± 7.12	2.93 ± 0.81
PP5.1	0.5 m	1.53 ± 7.25	0.64 ± 5.66	0.89 ± 3.13	0.00 ± 1.12
	1 m	1.91 ± 4.10	0.76 ± 3.47	1.02 ± 0.77	0.13 ± 0.48
	1.5 m	2.17 ± 7.25	1.15 ± 4.75	0.89 ± 7.12	0.13 ± 0.81
PP5.2	0.5 m	1.27 ± 7.25	0.51 ± 5.66	0.64 ± 3.13	0.13 ± 1.12

https://doi.org/10.5593/sgem2024/4.1/s19.48

	1 m	0.89 ± 4.10	0.38 ± 3.47	0.25 ± 0.77	0.25 ± 0.48
	1.5 m	1.02 ± 7.25	0.38 ± 4.75	0.51 ± 7.12	0.13 ± 0.81
PP6.1	0.5 m	25.10 ± 7.25	18.47 ± 5.66	2.55 ± 3.13	4.08 ± 1.12
	1 m	12.48 ± 4.10	10.96 ± 3.47	1.15 ± 0.77	0.38 ± 0.48
	1.5 m	16.31 ± 7.25	12.36 ± 4.75	2.80 ± 7.12	1.15 ± 0.81
PP6.2	0.5 m	7.26 ± 7.25	5.73 ± 5.66	1.02 ± 3.13	0.51 ± 1.12
	1 m	2.04 ± 4.10	1.53 ± 3.47	0.38 ± 0.77	0.13 ± 0.48
	1.5 m	3.18 ± 7.25	2.17 ± 4.75	0.64 ± 7.12	0.38 ± 0.81

A comparison was made of the reported total number of airborne microorganisms for all samples (Figure 1).
The obtained results show higher levels of microbial load in the lowest studied layer - 0.5. Samples prevail, where the amounts of microorganisms in urban hot areas are many times higher than those reported in green park areas.

The number of the main microbiological groups (bacteria, actinomycetes and microscopic fungi) was reported for the individual sample areas - urban hot spots and green areas, at different heights - 0.5 m, 1 m and 1.5 m (Figure 2).

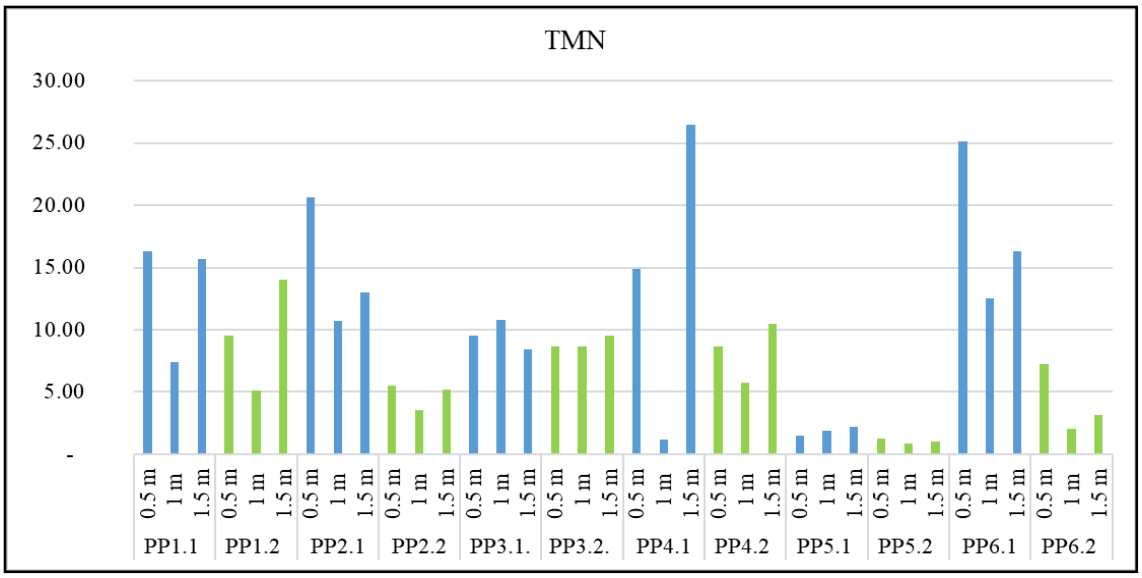


Figure 1. TMN of the surveyed points, in height – 0.5, 1.0 и 1.5 m

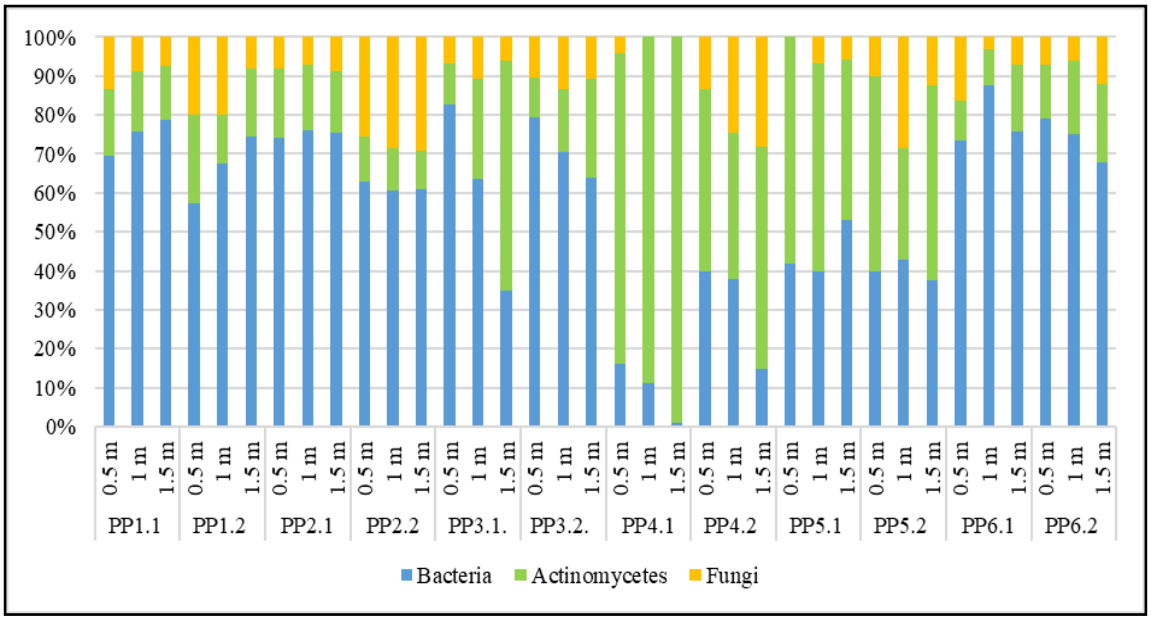


Figure 2. Percentage participation of individual microbiological groups compared to TMN

DISCUSSION

The results of the performed statistical processing of the data show the greatest dispersion of the data in the actinomycete group at a height of 1.5, relative to the standard deviation. A large standard deviation is also shown by the results for the group of bacteria at all studied heights. With the least movement around the average value is the group of microscopic fungi. These results show the dynamics in the distribution and number of airborne microorganisms. The results show a clear trend of least dispersion of the amount of microorganisms studied at a height of 1 meter for all the studied groups. The height of 1 meter appears to be transitional between the underlying ground air and the more dynamic air at 1.5 m. Our data show that at this height the dynamics in the number of microorganisms in the individual points is lower, compared to the other investigated heights.

Our study, similar to that of [6], showed higher microbial load in intensive urban hotspots, relative to park areas (Fig. 1), regardless of height. An exception to this trend is group 4 of the investigated points. With this group again at a height of 0.5 and 1.5 higher amounts of microorganisms are observed in the hot spots, but for a height of 1 m we have the opposite trend. In zone 4.1 at a height of 1 meter, the amount of reported microorganisms is 5 times lower compared to park zone 4.2. These data are very specific and suggest local environmental parameters that influenced the distribution of microorganisms at the studied altitudes. However, it should be noted that RR 4.1 is in the interior of the neighborhood, without intense car traffic, while Park Slavia (RR4.1) is surrounded by heavily congested boulevards.

The present pilot study demonstrates the significant influence that vegetation has on the distribution and concentration of airborne microorganisms. Vegetation, especially in the active spring leafing season, captures a large part of the widespread dust particles in the air, which are carriers of microbial cells [11]. A number of studies emphasize the influence of vegetation, its quantity and foliage on the abundance of airborne

https://doi.org/10.5593/sgem2024/4.1/s19.48

microorganisms, including the reduction of the quantities of pathogenic species [12]. Moreover, in their study [13] demonstrated that vegetation specificity influences the distribution of airborne microbial communities. Hot spots in the lowest studied layer (0.5 m) stand out with the highest microbial load. The large amount of microorganisms at this height is related to the constant lifting of dust particles, which as indicated in their studies by [3] are condensation nuclei for the attachment of MO. These data show the danger to human health, especially for children in strollers, because the standard height at which babies are placed is about 55-65 cm, i.e. at this height we have a large amount of not only microbial cells, but also dust particles. The data from the remaining two heights are of interest. Predominantly the sample areas in hot zones, where the reported total microbial number at 1.5 height has higher values compared to 1 m (PP1, PP2, PP4 and PP6). These results are explained by the transitivity of the considered height. Unlike the lower 0.5 layer, in which microorganisms are generated from the earth's surface, the 1-meter test zone is transient. It does not contain a large number of microorganisms, because the adsorbed microbial cells on heavier material particles fall to the ground, and the lighter ones are suspended in the higher layer - 1.5.

Car traffic needs to be given serious attention as a potential spreader of airborne microorganisms. In their study, [14] highlighted the increased levels of microorganisms in intersection hotspots. The extent of the influence of car traffic is clearly evident when we look at hotspots 5.1 and 6.1, which are located no more than 300 meters apart. Hot spot 5.1 is located at a less busy intersection where there are no traffic jams, while hot spot 6.1 represents one of the busiest intersections in the territory of the city of Sofia. The height difference of 0.5 meters is more than 16 times. This shows the strong influence of car traffic on the distribution and concentration of microorganisms at this height, not only due to the gases released by the cars, but also due to the dust raised by the car movement.

When looking at results for the percentage participation of individual microbial groups, there is no clear trend for a predominant microbial group (Figure 2). The percentage of microscopic fungi increases in park areas relative to hotspots. In other studies, the opposite trend was observed [15]. The data for sample areas 4.1 and 4.2 are highly specific, in which the group of actinomycetes is dominant, while microscopic fungi are absent in the urban area at heights 1 and 1.5. These data show the specificity of airborne microorganisms and the need for a deeper study of their concentration, distribution and percentage participation of individual groups.

CONCLUSION

The main goal of the present pilot study was to determine the dynamics in the amount of microorganisms at different heights in the ground air in different urban parts (hot spots and green zones) of the territory of the city of Sofia. The generated results show a higher microbial load in hot spots compared to green zones. This imposes the thesis about the active influence of vegetation to minimize the number of microorganisms suspended in the air. The height most saturated with microorganisms is 0.5, followed by 1.5, regardless of the area considered. Intense car traffic increases the number of microorganisms in the air many times, regardless of the height. When analyzing two of the hot spots located close to each other, a large difference in the total microbial count was observed. In PP6.1 compared to PP5.1, the levels of micro-organisms are more than sixteen times higher, which is related to increased automobile traffic in PP6.1, respectively with the greater amount of dust particles in the air.

Data on the distribution of microbial groups do not show a trend in the dominant group. The group of microscopic fungi has a higher percentage participation in park areas than in hotspots. The present study is of a pilot nature. The generated results will serve as a future basis for in-depth analyzes of the ground microflora at different height.

ACKNOWLEDGEMENTS

This research work was carried out with the support of Research Fund of Ministry of Education and Science in Bulgaria, project №: КП-06-Н74/5 „Relationships between the amount of fine particulate matter and airborne microorganisms in "hot spots", park areas, urban background areas and control forest areas''

REFERENCES

[1] Obasola Ezekiel Fagade, Adeniyi Adewale Ogunjobi, Moses Akindele Abiala, Olutayo Israel Falodun, Chapter 3 - Fate and transport of microorganisms in the air, In Developments in Applied Microbiology and Biotechnology, Aeromicrobiology, Academic Press, 2023, Pages 39-58, ISBN 9780323961226, https://doi.org/10.1016/B978-0-323-96122-6.00006-2.).

[2] Kim, K., Kabir, Eh. & Jahan, Sh., Airborne bioaerosols and their impact on human health. J Environ Sci (China), 67:23-35, 2018, DOI: 10.1016/j.jes.2017.08.027.

[3] Chen, X., Kumari, D. & Achal, V., A Review on Airborne Microbes: The Characteristics of Sources, Pathogenicity and Geography. Atmosphere, 11(9), 919, 2020, DOI: https://doi.org/10.3390/atmos11090919.

[4] Penner, J., Andreae, M., Annegarn, H., Barrie, L., Feichter, J., Hegg, D., Jayaraman, A., Leaitch, R., Murphy, D., Nganga, J. & Pitari, G., Aerosols, their Direct and Indirect Effects-Chapter 5, 300, 2020, Cambridge Uk, Cambridge University Press.

[5] Xu, C., Ewi, M., Chen, J., Zhu, Chao, Li, J., Lv, G., Xu, X., Zheng, L., Sui, G., Li, W., Chen, B., Wang, W., Zhang, Q., Ding, A. & Mellouki, A. (2017). Fungi diversity in PM2. 5 and PM1 at the summit of Mt. Tai: abundance, size distribution, and seasonal variation. Atmos. Chem. POhys, 17, 11247-11260, DOI:https://doi.org/10.5194/acp-17-11247-2017.

[6] Mhuireach, G., Johnson, B., Altrichter, A., Ladau, J., Meadow, J., Pollard, K. & Green, J., Urban greenness influences airborne bacterial community composition. Science of Total Environment, 571, 680-687, 2016, DOI: https://doi.org/10.1016/j.scitotenv.2016.07.037.

[7] Cao, C., Jiang, W., Wang, B., Fang, J., Lang, J., Tian, G., Jiang, J. & Zhu, T., Inhalable microorganisms in Beijing's PM2.5 and PM10 pollutants during a severe smog event. Environ. Sci Technol., 48, 1499–1507, 2014.

[8] Fang, Z., Guo, W., Zhang, J. & Lou, X., Influence of Heat Events on the Composition of Airborne Bacterial Communities in Urban Ecosystems. International Journal of Environment Research and Public Health, 15, 2295, 2018, DOI: I10.3390/ijerph15102295.

https://doi.org/10.5593/sgem2024/4.1/s19.48

[9] Tanaka, D., Sato, K., Goto, M., Fujiyoshi, S., Maruyama, F., Takato, Sh., Shimada, T., Sakatoku, A., Aoki, K., Nakamura, Sh., Airborne Microbial Communities at High-Altitude and Suburban Sites in Toyama, Japan Suggest a New Perspective for Bioprospecting, Front. Bioeng. Biotechnol., 2019, Sec. Bioprocess Engineering, Volume 7, 2019 | https://doi.org/10.3389/fbioe.2019.00012

[10] Jones M. & Harrison, M., The effects of meteorological factors on atmospheric bioaerosol concentrations – a review. Science of the Total Environment, 326(1):151–180, 2004.

[11] Azis, A., Lee, K., Park, B., Park, H., Park, K., Choi, I. & Chang, I., Comparative study of the airborne microbial communities and their functional composition in fine particulate matter (PM2.5) under non-extreme and extreme PM2.5 conditions. Atmospheric Environment, 194, 82-89, 2017.

[12] Li, H., Wu, Zh., Yang, X., An, X., Ren, Y. & Su, J., Urban greenness and plant species are key factors in shaping air microbiomes and reducing airborne pathogens. Environment International, Volume 153, 106539, 2021, https://doi.org/10.1016/j.envint.2021.106539

[13] Lymperopoulou, S., Adams, I. & Lindow, E., Contribution of vegetation to the microbial composition of nearby outdoor air. Appl. Environ. Microbiol. 82, 3822–3833, 2016.

[14] Amarasekara, R., Vithanage, M., Samaraweera, P., Goonetilleke, A. & Magana-Arachchi, D., Effect of traffic congestion and vegetation on airborne bacteria in a city of a developing country, Quality, Atmosphere & Health, 14:1103–1116, 2021, https://doi.org/10.1007/s11869-021-01001-1).

[15] Korneykova, M.V.; Soshina, A.S.; Novikov, A.I.; Ivashchenko, K.V.; Sazonova, O.I.; Slukovskaya, M.V.; Shirokaya, A.A.; Vasenev, V.I.; Vetrova, A.A.; Gavrichkova, O. Microscopic Fungi in Big Cities: Biodiversity, Source, and Relation to Pollution by Potentially Toxic Metals, Atmosphere 12, 1471, 2021.

ASSESSMENT OF HEAVY METAL POLLUTION IN SNOW SAMPLES COLLECTED AT VARIOUS DISTANCES FROM ROAD SECTIONS: CASE STUDY JELGAVA

PhD Kristine Valujeva[1]

PhD Candidate Jovita Pilecka-Ulcugaceva[1]

Mg.sc.ing. Sindija Liepa[1]

Dr.geogr. Oskars Purmalis[2]

Assoc. Prof. Ph.D Inga Grinfelde[1]

[1] Latvia University of Life Sciences and Technologies, **Latvia**
[2] University of Latvia, **Latvia**

ABSTRACT

The increasing flow of traffic passing through cities on a daily basis, especially those cities that have a difficult situation with bypass, raises concerns about the air quality in sections of the transport corridors, as well as in the city as a whole. Heavy metal pollution is a serious environmental concern, especially in urban and suburban areas where vehicle emissions contribute to air and soil pollution. The aim of the study is to assess the extent of heavy metal contamination in snow samples collected at different distances from roads in different areas of the city. Snow samples were collected from different distances (1 m; 50 m, 100 m) from the roadway to analyze the spatial distribution of heavy metals such as chromium (Cr), copper (Cu), lead (Pb), zinc (Zn). Heavy metal concentrations were measured using the analytical method - inductively coupled plasma atomic emission spectroscopy. The results revealed different levels of heavy metal pollution, with higher concentrations observed closer to the roadway compared to further away from the roadway. The maximum concentrations of chromium (15.4 µg/l), copper (63.6 µg/l), lead (19.5 µg/l) and zinc (419.2 µg/l) were observed at a distance of 1 m from the roadway. This spatial analysis provides valuable insight into the impact of vehicle emissions on heavy metal pollution and highlights the importance of mitigation measures to improve air quality and reduce environmental risks in urban environments.

Keywords: car transport, city, air pollution, transport corridors, ICP-OES

INTRODUCTION

The contamination of heavy metals poses a significant environmental concern, particularly in urban and suburban regions, where vehicle emissions are a major contributor to both air and soil pollution [1]. The increasing volume of daily traffic passing through urban centres, particularly those with challenging bypass infrastructures, raises concerns regarding air quality along transportation corridors and within urban environments overall [2]; [3].

Snow has a notable capacity to accumulate diverse contaminants from the atmosphere. As it melts, pollutants once trapped within it are released into the environment through

https://doi.org/10.5593/sgem2024/4.1/s19.49

several mechanisms. These mechanisms involve transferring into the soil in regions where snow accumulated during the cold period, contributing to runoff as the melting progresses, and some pollutants being emitted back into the atmosphere through evaporation [4]. In urbanized areas, this presents a potential risk of adverse effects not only on the immediate surroundings near roadways but also on surface and groundwater reservoirs during the spring snowmelt, particularly due to expected stormwater runoff [5]; [6].

This study analyses the spatial distribution of heavy metals such as chromium (Cr), copper (Cu), lead (Pb), zinc (Zn) in snow samples collected near roads with varying traffic intensities in Jelgava city. Additionally, the study aims to assess the impact of vehicle emissions on heavy metal pollution and to provide mitigation measures to improve air quality in urban environments.

MATERIALS AND METHODS

Jelgava, located in central Latvia in Northern Europe, is the fourth largest city in the country, covering 60.3 km² with 2.72 km² of water, 1.62 km² of parks and green spaces, and 12.64 km² of forests. Its strategic location leads to heavy cargo transportation and well-developed, accessible services used by both local and international companies. Situated 42 km from Riga, Jelgava benefits from important goods and passenger links to the capital, where many businesses and administrative operations are concentrated. This results in a steady traffic flow, increasing pollutant emissions near roadways.

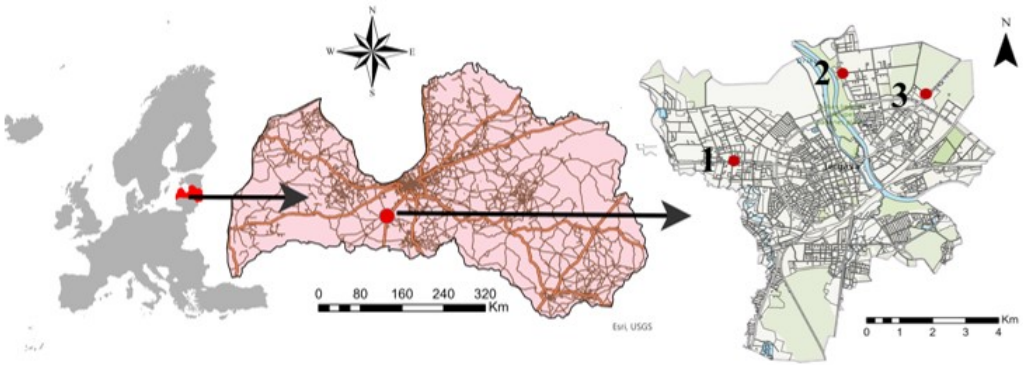


Figure 1. Snow sampling site in the city of Jelgava

The conditions during sampling were an air temperature of -4.7 ^{0}C, relative humidity of 82.5%, and a precipitation level of 0.1 mm. In the previous days (January 1 to January 8, 2019), the average air temperature was -2.95 ^{0}C, with a total precipitation of 16 mm and an average relative humidity of 88.5%. During the winter of 2018/2019 in Latvia, the average air temperature was -1.4 ^{0}C. The total precipitation for this winter was 116.0 mm. In January 2019, Latvia experienced an average air temperature of -4 ^{0}C. The total precipitation for January was 46.5 mm. During the first ten days of January, the average air temperature was -3.6 ^{0}C, with a maximum temperature of +6.4 ^{0}C. Precipitation during this period totaled 17.2 mm.

Snow samples were collected on January 9, 2019, at three points (see Figure 1near roads with varying traffic intensities in Jelgava city at distances of 1 m, 50 m and 100 m from the roadway additionally the reference (R) snow samples were taken in natural territory

[7]. The snow samples were taken, the average snow layer thickness was 9.6 cm. In the previous days of January, the average snow layer thickness was 5.6 cm.

To determine the contamination of pollutants in snow samples, concentrations of chromium (Cr), copper (Cu), lead (Pb), and zinc (Zn) were analyzed using an ICP-OES spectroscopy device (iCap 7000). A detailed description of the device and methodology can be found in Pilecka et al. (2018) and Grinfelde et al. (2021) [6]; [7].

Descriptive statistics, correlation analysis, ANOVA, and the Kruskal-Wallis test were conducted on the heavy metal concentration data.

RESULTS

Table 1 presents a statistical summary of the concentrations of heavy metals in the snow samples. Cr has the lowest average value at 2.977 µg/l, whereas Zn has the highest average value at 94.269 µg/l. The median values for all four metals are lower than the average values, indicating the presence of some extreme values in the samples. This is further evidenced by the analysis of the maximum values for each metal, with Zn reaching 419.2 µg/l and Cr reaching 15.40 µg/l.

Table 1. Descriptive statistics.

Variables		Cr, µg/l	Cu, µg /l	Pb, µg /l	Zn, µg /l
N	Valid	18	18	18	18
	Missing	0	0	0	0
Mean		2.977	19.869	6.091	94.269
Std. Error of Mean		0.946	3.652	1.277	28.173
Median		1.415	13.830	3.498	31.782
Std. Deviation		4.014	15.494	5.420	119.528
Variance		16.113	240.051	29.372	14286.934
Minimum		0.400	5.800	2.200	21.100
Maximum		15.400	64.600	19.500	419.200
Percentiles	25	0.542	8.589	2.710	25.362
	50	1.415	13.830	3.498	31.782
	75	3.106	28.799	7.593	112.146

Given that the data are not normally distributed, Spearman's correlation coefficient was utilized for analysis. All heavy metals, except for Cu and Cr, exhibit a positive correlation with each other (Table 2), suggesting a common pollution source. Conversely, all heavy metals show a negative correlation with distance from the road edge (p-value < 0.05). As the distance from the road increases, the concentrations of pollutants decrease.

Table 2. Correlation between concentrations of heavy metals and distance from road.

Factors	Cr, µg/l	Cu, µg /l	Pb, µg /l	Zn, µg /l	Distance, m
Cr	1	0.447	**0.796****	**0.796****	**-0.643****
Cu	0.447	1	**0.717****	**0.804****	**-0.643****
Pb	**0.796****	**0.717****	1	**0.816****	**-0.695****
Zn	**0.796****	**0.804****	**0.816****	1	**-0.682****
Distance	**-0.643****	**-0.643****	**-0.695****	**-0.682****	1

*Correlation is significant at the 0.05 level

**Correlation is significant at the 0.01 level

https://doi.org/10.5593/sgem2024/4.1/s19.49

In the ANOVA analysis, where distance from the road and location were used as variables, distance was found to be a statistically significant factor (p-value < 0.01) affecting the concentrations of all heavy metals in the snow.

Table 3. ANOVA results of distance from road.

ANOVA		Sum of Squares	df	Mean Square	F	Sig.
Cr, µg /l	Between Groups	132.222	2	66.111	6.998	0.007
	Within Groups	141.698	15	9.447		
	Total	273.920	17			
Cu, µg/l	Between Groups	2380.368	2	1190.184	10.499	0.001
	Within Groups	1700.493	15	113.366		
	Total	4080.862	17			
Pb, µg/l	Between Groups	291.735	2	145.868	10.540	0.001
	Within Groups	207.583	15	13.839		
	Total	499.318	17			
Zn, µg/l	Between Groups	147031.443	2	73515.722	11.505	0.001
	Within Groups	95846.437	15	6389.762		
	Total	242877.881	17			

Additionally, the Kruskal-Wallis test was performed to compare the concentrations of heavy metals at sampled points in the city with the reference (R) to determine their correspondence to the natural background levels. The results indicate statistically significant differences between groups for all heavy metals (p-value < 0.01).

Table 4. Summary of Kruskal-Wallis test by distance and reference.

Kruskal-Wallis test				
	Cu	Pb	Zn	Cr
K (Observed value)	10.187	10.187	11.415	8.994
K (Critical value)	5.991	5.991	5.991	5.991
DF	2	2	2	2
p-value (Two-tailed)	0.006	0.006	0.003	0.011
alpha	0.05	0.05	0.05	0.05

Multiple pairwise comparisons conducted using the Steel-Dwass-Critchlow-Fligner procedure for all heavy metals reveal that at distances of 50 m and 100 m from the road, the concentration of heavy metals in snow aligns with that of the natural environment.

Table 5. Multiple pairwise comparisons using the Steel-Dwass-Critchlow-Fligner procedure.

	p-values:								
	Cr|1	**Cr|50**	**Cr|100**	**Cr|R**		**Cu|1**	**Cu|50**	**Cu|100**	**Cu|R**
Cr|1	**1.00**	**0.05**	**0.05**	**0.02**	**Cu|1**	**1.00**	**0.02**	**0.05**	**0.02**
Cr|50	**0.05**	**1.00**	1.00	0.77	**Cu|50**	**0.02**	**1.00**	1.00	0.77
Cr|100	**0.05**	1.00	**1.00**	0.22	**Cu|100**	**0.05**	1.00	**1.00**	0.92
Cr|R	**0.02**	0.77	0.22	**1.00**	**Cu |R**	**0.02**	0.77	0.92	**1.00**

	p-values:								
	Zn| 1	Zn| 50	Zn| 100	Zn| R		Pb|1	Pb|50	Pb|100	Pb|R
Zn | 1	**1.00**	**0.02**	**0.02**	**0.02**	Pb | 1	**1.00**	**0.05**	**0.02**	**0.02**
Zn | 50	**0.02**	**1.00**	0.99	0.85	Pb | 50	**0.05**	**1.00**	1.00	0.58
Zn | 100	**0.02**	0.99	**1.00**	1.00	Pb | 100	**0.02**	1.00	**1.00**	0.38
Zn | R	**0.02**	0.85	1.00	**1.00**	Pb | R	**0.02**	0.58	0.38	**1.00**

DISCUSSION

Several studies have shown that the concentration of heavy metals in snow decreases with increasing distance from roads. For instance, Adamiec et al. (2016) observed elevated levels of heavy metals such as Pb, Zn, and copper (Cu) in snow samples collected near major roads [8]. Similarly, our findings reveal significantly higher concentrations of Cr (15.4 µg/l), Cu (63.6 µg/l), Pb (19.5 µg/l), and Zn (419.2 µg/l) within 1 meter of roadways compared to distances of 50m and 100m from the road.

Studies consistently identify vehicle emissions as a primary source of heavy metal pollution in urban environments. Faiz et al. (2009) and Elgammal et al. (2014) highlight that metals such as Cr, Cu, and Zn originate from tire wear, brake linings, and exhaust gases. Our study corroborates these findings, as higher concentrations of these metals have been observed near roads. This observation underscores the enduring and widespread impact of vehicle-related pollution [9]; [10].

CONCLUSION

This study has clarified several critical aspects concerning the distribution and sources of heavy metal contamination, specifically focusing on Cr, Cu, Pb, and Zn. The findings indicate a close correlation between these heavy metals across all monitoring points, strongly suggesting a common source of contamination. This pattern is indicative of anthropogenic activities, likely linked to transport pollution sources.

Furthermore, the analysis of heavy metal concentrations in relation to their proximity to roadways has revealed a statistically significant gradient. Heavy metal pollution is significantly higher near the roadside, emphasizing the influence of vehicle emissions and road degradation on environmental contamination. However, as the distance from the roadside increases to 50 meters and 100 meters, the concentration levels of these metals diminish and align with those found in natural, uncontaminated environments.

https://doi.org/10.5593/sgem2024/4.1/s19.49

These insights are pivotal for developing targeted environmental management strategies and mitigation measures. Addressing the root sources of contamination, particularly those related to transportation, is essential for reducing the heavy metal load in urban transport corridors. Moreover, the observed decline in metal concentrations with increased distance from roads highlights the potential efficacy of buffer zones and green belts in mitigating roadside pollution.

REFERENCES

[1] Gupta, V. (2020). Vehicle-Generated Heavy Metal Pollution in an Urban Environment and Its Distribution into Various Environmental Components. In: Shukla, V., Kumar, N. (eds) Environmental Concerns and Sustainable Development. Springer, Singapore.

[2] Abhijith K.V., Kumar P., Gallagher J., McNabola A., Baldauf R., Pilla F., Broderick B., Di Sabatino S., Pulvirenti B., Air pollution abatement performances of green infrastructure in open road and built-up street canyon environments – A review, Atmospheric Environment, vol. 162, pp 71-86, 2017.

[3] Roy S., Gupta S. K., Prakash J., Habib G., Kumar P. A global perspective of the current state of heavy metal contamination in road dust, Environmental Science and Pollution Research International., vol. 29, pp 33230-33251, 2022.

[4] Bućko M.S., Magiera T., Johanson B., Petrovský E., Pesonen L.J., Identification of magnetic particulates in road dust accumulated on roadside snow using magnetic, geochemical and micro-morphological analyses, Journal Environ. Pollut., vol. 159, pp. 1266-1276, 2011.

[5] Sillanpää N., Koivusalo H., Catchment-scale evaluation of pollution potential of urban snow at two residential catchments in southern Finland. Journal Water Sci. Technol., vol. 68, pp. 2164-2170, 2013.

[6] Pilecka J., Grinfelde I., Valujeva K., Straupe I., Purmalis O., The temporal and spatial analysis of transport impact on trace elements in snow samples, 18th International Multidisciplinary Scientific Geoconference, SGEM 2018; Albena; Bulgaria; 2 July 2018 through 8 July 2018, vol. 18, Issue 4.2, Pages 671-677, 2018.

[7] Grinfelde I., Pilecka-Ulcugaceva J., Bertins M., Viksna A., Rudovica V., Liepa S., Burlakovs J., Dataset of trace elements concentrations in snow samples collected in Jelgava City (Latvia) in December 2020, Data in Brief, vol. 38., 2021.

[8] Adamiec E., Jarosz-Krzemińska E., Wieszała R., Heavy metals from non-exhaust vehicle emissions in urban and motorway road dusts. Environmental Monitoring and Assessment, vol. 188, 2016.

[9] Faiz Y., Tufail M., Javed M. T., Chaudhry M. M., Siddique N., Road dust pollution of Cd, Cu, Ni, Pb and Zn along Islamabad Expressway, Pakistan, Microchemical Journal, vol. 92/issue 2, pp 186-192, 2009.

[10] Elgammal M., Ali R.R., Samra R. A., Assessing Heavy Metal Pollution in Soils of Damietta Governorate, Egypt, International Conference on Advances in Agricultural, Biological & Environmental Sciences (AABES-2014), 2014

BIOMONITORING OF HEAVY METALS IN THE CITY OF JELGAVA, LATVIA USING LICHEN, *XANTHORIA PARIETINA*

PhD Candidate Jovita Pilecka-Ulcugaceva[1]

PhD Candidate Anda Bakute[1]

Dr.geogr. Oskars Purmalis[2]

Bc.sc.ing. Kristaps Siltumens[1]

Assoc. Prof. Ph.D Inga Grinfelde[1]

[1] Latvia University of Life Sciences and Technologies, **Latvia**
[2] University of Latvia, **Latvia**

ABSTRACT

In urban environments, human health is increasingly affected by air quality, particularly air pollution with particulate matter (PM), which contains various toxic chemical elements. Car traffic is one of the main sources of air pollution in urban areas, which not only raises dust from roadways but also emits micro particles from diesel engines and tire wear containing heavy metals. The aim of the study is to evaluate the ability of the lichen species *Xanthoria parietina*, commonly found in Latvia, to biomonitor and bioaccumulate various heavy metals (As, Cd, Cu, Cr, Mn, Ni, Pb, Zn, V), and to use this lichen to determine the risk pollution zones in the city of Jelgava. In this study, the epiphytic lichen *Xanthoria parietina* was used as an air pollution biomonitor to assess long-term air pollution in Jelgava. Lichen samples of *Xanthoria parietina* were collected on February 14, 2017. In total, 60 samples were collected from 20 monitoring points, and 3 samples from one monitoring point outside the city center of Jelgava, approximately 7 km away. The lichen samples were analyzed using ICP-OES.
Analyzing the results, five pollution groups could be identified - the first group reflected parks, while the remaining groups indicated the influence of car traffic with various metal footprints. The average element content in the samples, in descending order, was Mn>Zn>Cu>Pb>Cr>V>Ni>As>Cd. Our results indicate that heavy metals come from vehicles and fossil fuel combustion processes, such as As (0.4 µg/l – 1.9 µg/l), Cr (2.1 µg/l – 13.8 µg/l), Cu (5.7 µg/l – 40.2 µg/l), Ni (1.1 µg/l – 6.8 µg/l) and V (0.9 µg/l – 10.0 µg/l).

Keywords: air pollution, heavy metals; ICP-OES; particulate matter; *Xanthoria parietina*

INTRODUCTION

Human daily activities have caused climate change, with its effects increasingly being observed globally. Air pollution is recognized as a significant issue; however, it is not merely a local problem. Air pollution is a global challenge requiring local solutions across different regions [1]. The impact of air pollution is most acutely felt in urban areas. In cities, air quality increasingly affects human health, particularly particulate matter (PM) pollution containing various toxic chemical elements [2]; [3]. The emission of multiple chemicals, gases, aerosols, and other pollutants into the air is caused by

https://doi.org/10.5593/sgem2024/4.1/s19.50

human activities, transportation, and industrial development [2]. Traffic is identified as one of the primary sources of urban air pollution, producing road dust and micro-particles containing heavy metals from diesel engines and tire wear. Biological monitoring is a reliable method based on the premise that environmental changes impact indicator organisms, which can serve as early warning signals for detecting environmental changes. Since the late 1960s, lichens have been extensively used worldwide to monitor atmospheric pollution in both local and regional studies. This is because lichens are widely distributed and depend on the atmosphere for nutrient intake [4]; [5]. In this study, the epiphytic lichen *Xanthoria parietina* was used as an air pollution biomonitor. *Xanthoria parietina*, commonly used in biomonitoring studies, is sensitive to atmospheric pollution and widely distributed [6]; [5]. Studies on the accumulation of heavy metals have shown that *Xanthoria parietina* can accumulate various heavy metals [7], including those associated with traffic pollution, such as lead (Pb), cadmium (Cd), and zinc (Zn). The concentrations of these metals in lichen tissues can provide valuable insights into the spatial distribution and intensity of pollution caused by vehicle emissions [8].

The aim of this study is to evaluate the ability of the lichen species *Xanthoria parietina*, commonly found in Latvia, to biomonitor and bioaccumulate various heavy metals (As, Cd, Cu, Cr, Mn, Ni, Pb, Zn, V), and to use this lichen to determine the risk pollution zones in the city of Jelgava.

MATERIALS AND METHODS

Jelgava (56°38′25″N 23°43′58″E) is situated in the central part of Latvia. The study was conducted within the administrative territory of Jelgava, which covers a total area of 60.56 km². The population of Jelgava was recorded as 57,053 in 2016, decreasing to 56,743 in 2017 [9]. Jelgava is traversed by a transport corridor from the city of Dobele, as a bypass is not available. Additionally, intensive traffic flows into the city from the south, where vehicles enter from Lithuania. Consequently, the city is exposed to vehicular emissions. Jelgava lacks distinct industrial zones; industrial areas often adjoin residential zones.

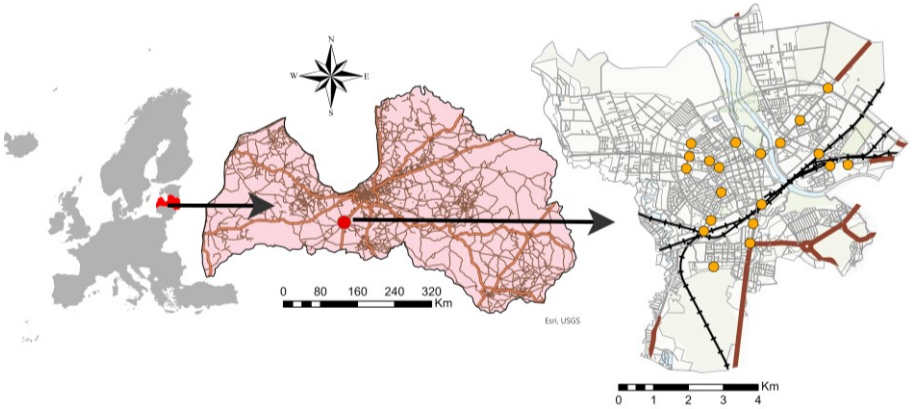


Figure 1. The geographical location of Jelgava and the placement of lichen sampling plots within the city of Jelgava.

The foliose lichen *Xanthoria parietina* was collected from the central part of Jelgava city on February 14, 2017. This species was selected due to its widespread occurrence

throughout Latvia. *Xanthoria parietina* is suitable for determining long-term pollution accumulation in lichens and is already utilized in biomonitoring studies [8]; [6].
Lichen samples were collected from 20 sampling plots (see Figure 2), with three replicates at each plot, located in areas of Jelgava city with the highest anthropogenic load. Sampling plots were chosen from various areas, including multi-story residential blocks, private house districts, industrial zones, and sections with heavy traffic, representing diverse anthropogenic influences. Reference samples were collected from a natural forest 7 km outside the city borders. The lichen *Xanthoria parietina* was gathered from the trunks of deciduous trees at approximately 1.3 to 1.5 meters above ground level. The lichen was collected by separating the thalli from the tree trunks using tweezers, and the samples were placed in absolutely clean glass containers. During the collection process, dust-free nitrile gloves were used (see Figure 3). After collection, the samples were transported to the laboratory [10].



Figure 2. The sampling locations for lichen (Xanthoria parietina) within the city of Jelgava



Figure 3. A sample of the lichen (*Xanthoria parietina*) collected from a tree trunk

To determine the chemical elements accumulated in the lichens, the sample was prepared according to the following sequence:

1. The lichens were dried, and after drying, they were weighed in 50 ml glass beakers to 0.3000 ± 0.0002 g using an analytical balance.
2. The sample was then added to 10 ml of concentrated HNO3 and 5 ml of concentrated H2O2 (both of which are high-quality reagents).
3. The samples were left for 12 hours. After 12 hours, the solutions were extracted by heating them in a block at a temperature of 160 °C.
4. After cooling the extract to a volume of 7.5 ml, the sample solutions were filtered and diluted to 20 ml with pure deionized water in polypropylene tubes.

Metal concentrations and chemical elements were measured using an ICP–OES spectrometer. This spectrometer is designed for the analysis of solid samples, which are dissolved and then analyzed (Labcompere). Chemical elements were identified in 60 lichen samples (*Xanthoria parietina*) from the city and three lichen samples (*Xanthoria parietina*) from a forest outside the city [10]; [11].

https://doi.org/10.5593/sgem2024/4.1/s19.50

RESULTS

In the study, the average content of various elements in the collected samples was analyzed. The average element content in the samples, in descending order, was Mn>Zn>Cu>Pb>Cr>V>Ni>As>Cd. These results indicate that the presence of heavy metals in the samples is primarily associated with anthropogenic activities, particularly vehicle emissions and fossil fuel combustion processes. The elevated levels of elements such as As (0.4 µg/l – 1.9 µg/l), Cr (2.1 µg/l – 13.8 µg/l), Cu (5.7 µg/l – 40.2 µg/l), Ni (1.1 µg/l – 6.8 µg/l), and V (0.9 µg/l – 10.0 µg/l) highlight the impact of industrial activities and vehicular pollution on air and environmental quality. Cluster analysis reveals four homogeneous groups and one outlier (see Figure 4).

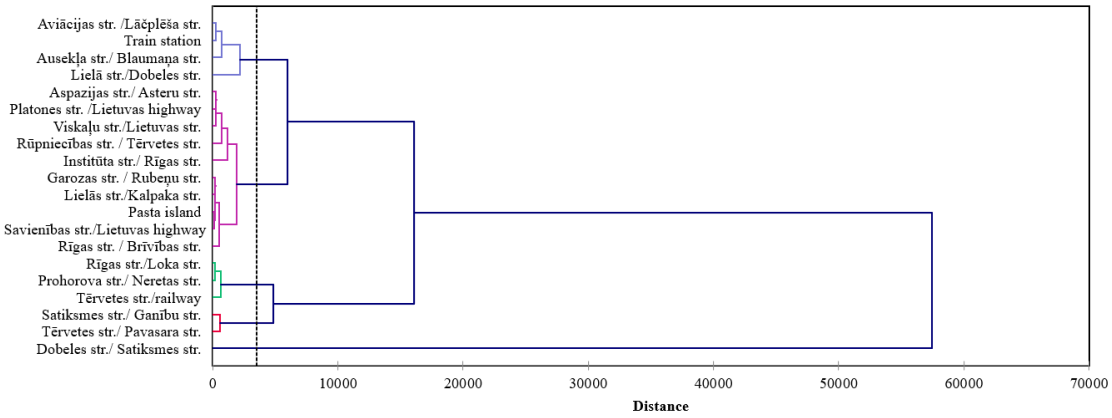


Figure 4. Dendrogram of the elemental clusters in *Xanthoria parietina*.

The first group comprises control and open public areas. The second group consists of transport corridors. The third group includes railway corridors. The fourth group encompasses private residential areas. The fifth group contains a single point, influenced by transport and industrial areas.

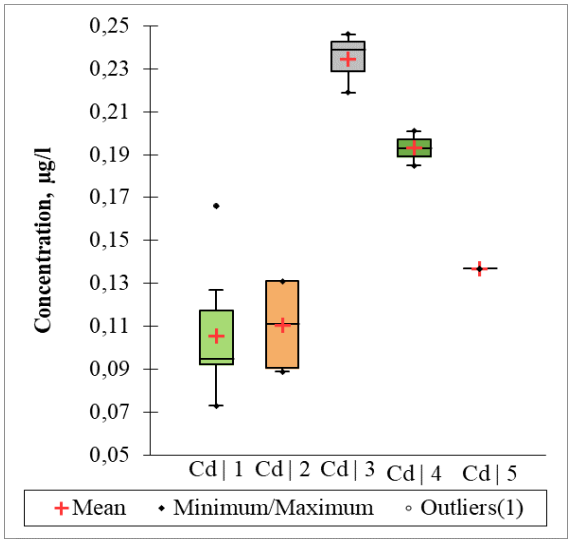


Figure 5. Cadmium (Cd) concentrations in the territory of Jelgava city

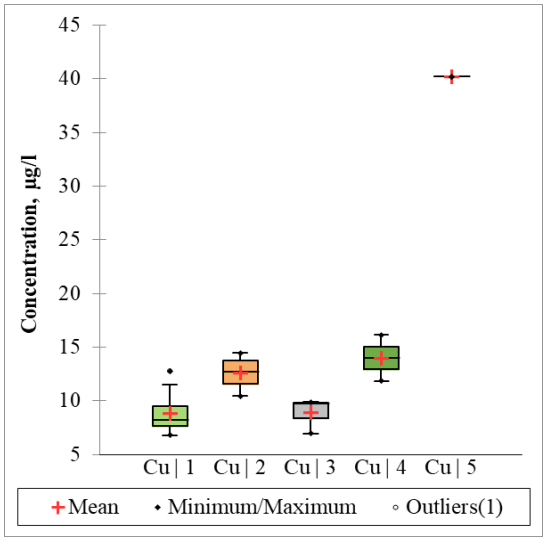


Figure 6. Copper (Cu) concentrations in the territory of Jelgava city

The highest cadmium values are found in the third and fourth clusters, corresponding to railway transport [12] and decentralized heating systems [13]. In parks and transport corridors, cadmium values are similar to control values, indicating minimal

anthropogenic impact on air quality. Copper concentrations significantly differ from the control in the 2nd, 4th, and 5th clusters. The abrasion of copper particles from vehicle engines has been identified in several studies [8]; [14]. The elevated copper content in private residential areas is associated with decentralized heating systems [13].

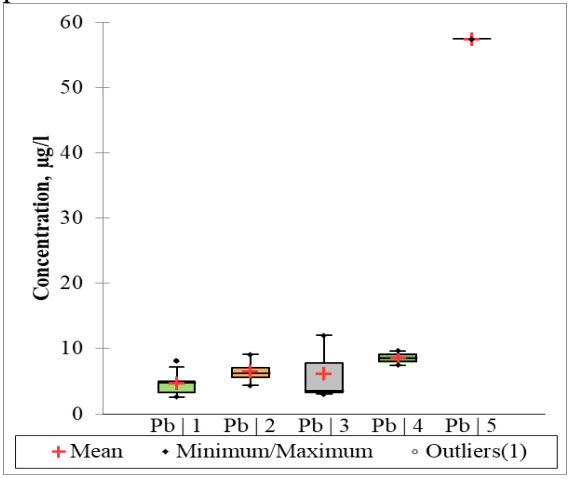


Figure 7. Lead (Pb) concentrations in the territory of Jelgava city

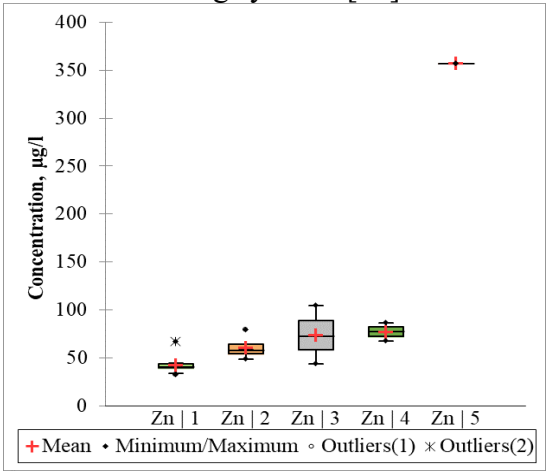


Figure 8. Zinc (Zn) concentrations in the territory of Jelgava city

The concentrations of lead and zinc in the fifth cluster exceed the average values of the other clusters by three times, which can be explained by the combined impact of transport and industrial pollution [15]; [8].

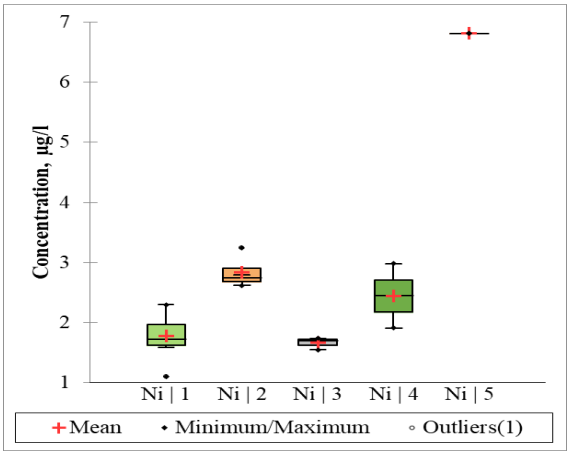


Figure 9. Nickel (Ni) concentrations in the territory of Jelgava city

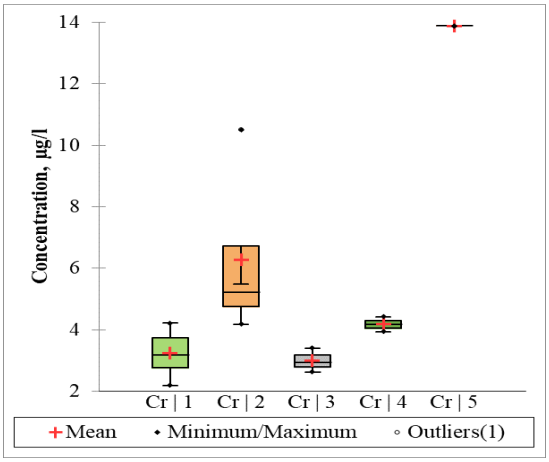


Figure 10. Chromium (Cr) concentrations in the territory of Jelgava city

Concentrations of nickel and chromium in the control cluster are significantly different from those in the transport, private residential areas, and complex pollution zones.

https://doi.org/10.5593/sgem2024/4.1/s19.50

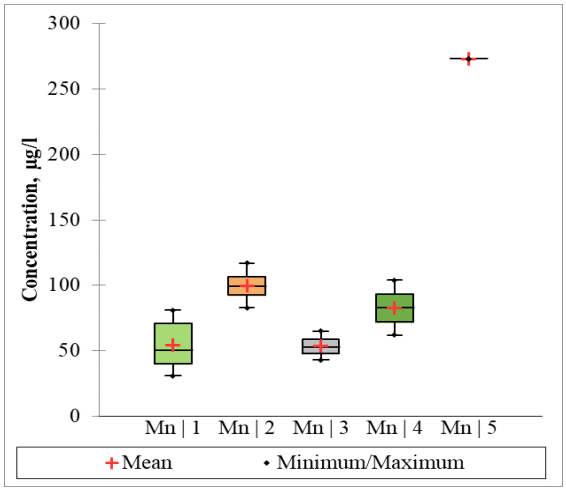


Figure 11. Manganese (Mn) concentrations in the territory of Jelgava city

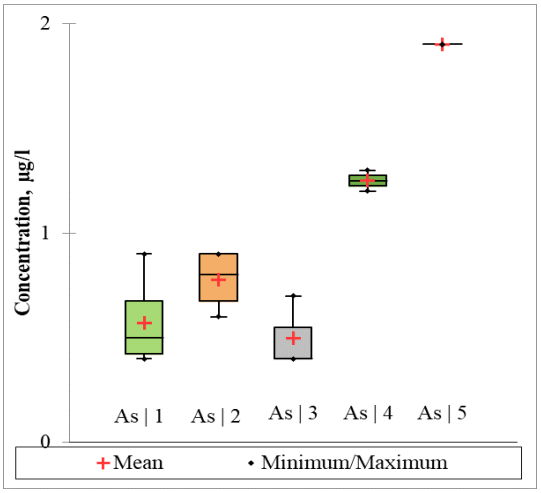


Figure 12. Arsenic (As) concentrations in the territory of Jelgava city

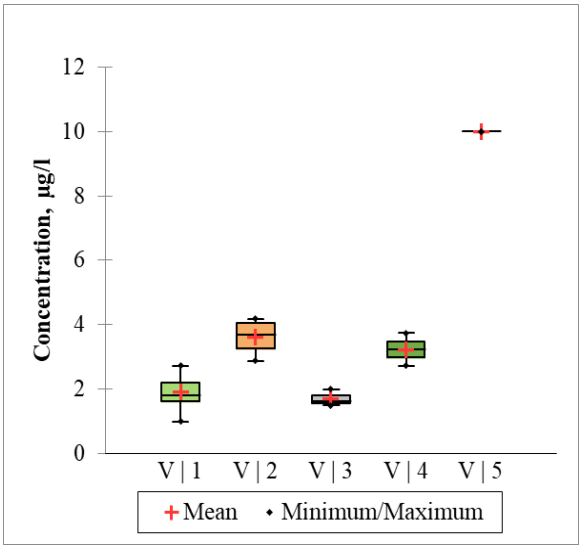


Figure 13. Vanadium (V) concentrations in the territory of Jelgava city

The concentrations of manganese, arsenic, and vanadium significantly differ from those in the control zone compared to those in the transport, private residential, and complex pollution zones.

DISCUSSION

The study by Jeanjean et al. (2022) revealed higher pollution levels of several metals (Cd, Cr, Co, Ni, and Pb) in the maritime sunburst lichen (*Xanthoria parietina*). A significant correlation was found between elevated blood lead levels and residents living close to the main industrial area [15]. In the study by Brunialti (2007), Cd, Cr, Ni, Pb, V, Cu, Zn, and Fe exhibited medium to high concentrations, indicating that vehicular traffic and industrial emissions are the primary pollutants in the study region. Similarly, in the study, high concentrations were observed near main roads and industrial areas [8]; [14]. Approximately 75% of atmospheric vanadium (V) can be attributed to human activities, particularly fossil fuel combustion, and its use as a

microstructure and gas content controller in copper alloys [16]. Also, the highest vanadium concentrations were found in the industrial area in the Jelgava study. The study by Brunialti and Frati (2007), which examined air quality in urban environments, identified the following metal concentrations: As, Cd (0.2±0.17 μg/g), Cu (9.04±4.05 μg/g), Cr (2.7±1 μg/g), Mn, Ni (3.05±2.83 μg/g), Pb (2.43±1.85 μg/g), Zn (47.8±26.9 μg/g), and V (1.81±0.89 μg/g) [8], indicating that lichens are good indicators of air quality. In a study conducted in the city of Pisa (Italy), the concentrations of various chemical elements were as follows: As (0.04-0.90), Cd (0.08-0.57), Cr (0.36-10.7), Ni (0.01-9.54), Pb (0.9-27.66), Zn (5.5-80.5), and V (0.32-4.02) μg/g dry wt [7].

CONCLUSION

Biomonitoring of lichens can be helpful in risk assessment for human health and a powerful tool in environmental planning to ensure long-term improvement of urban air quality.

Transport corridors contribute to air pollution with particles of aluminum, copper, vanadium, manganese, nickel, and chromium, primarily originating from internal combustion engines, tire wear, and the combustion of fuel products.

Open public areas help reduce air pollution in urban environments, where the concentrations of all metals correspond to natural environmental levels attributed to the rate of air exchange in these areas.

The most significant air pollution is caused by complex pollution sources, where industry combined with transport corridors significantly increases the amount of particulate matter (PM) containing heavy metals.

Long-term monitoring using *Xanthoria parietina* can reveal trends in pollution levels over time, allowing for the evaluation of the effectiveness of pollution control measures over time and the identification of emerging environmental threats.

REFERENCES

[1] Battista, G., de Lieto Vollaro R., Correlation between air pollution and weather data in urban areas: Assessment of the city of Rome (Italy) as spatially and temporally independent regarding pollutants, Atmospheric Environment, vol. 165, pp 240–247, 2017.

[2] Wahab M. I. A., Razak W. M. A. A., Sahani M., Khan M. F. Characteristics and health effect of heavy metals on non-exhaust road dusts in Kuala Lumpur, Science of the Total Environment, vol. 703, 135535, 2020.

[3] Li Z., Feng X., Li G., Bi X., Zhu J., Qin H., Dai Z., Liu J., Li Q., Sun G., Distributions, sources and pollution status of 17 trace metal/metalloids in the street dust of a heavily industrialized city of central China, Environmental Pollution, vol. 182, pp 408–416, 2013.

[4] Garty J., Biomonitoring atmospheric heavy metals with lichens: theory and application, Critical Reviews in Plant Sciences, vol. 20 (4), pp 309–371, 2001.

[5] Wolterbeek B., Biomonitoring of trace element air pollution: principles, possibilities and perspectives, Environmental Pollution, vol. 120/issue 1, pp 11–21, 2002.

https://doi.org/10.5593/sgem2024/4.1/s19.50

[6] Doğrul Demiray A., Yolcubal I., Akyol N. H., Çobanoğlu G., Biomonitoring of airborne metals using the Lichen Xanthoria parietina in Kocaeli Province, Turkey, Ecological Indicators, vol. 18, pp 632–643, 2012.

[7] Scerbo R., Ristori T., Possenti L., Lampugnani L., Barale R., Lichen (Xanthoria parietina) biomonitoring of trace element contamination and air quality assessment in Pisa Province Tuscany, Italy, Science of The Total Environment, vol. 286/issues1-3, pp 27-40, 2002.

[8] Brunialti G., Frati, L., Biomonitoring of nine elements by the lichen Xanthoria parietina in Adriatic Italy: A retrospective study over a 7-year time span, Science of The Total Environment, vol. 387, pp 289–300, 2007.

[9] Official statistics portal, Population by sex by main age groups in regions, republican cities, counties and 21 development centers at the beginning of the year – Territorial unit and Time period. Available at: https://data.stat.gov.lv/pxweb/lv/OSP_PUB/START/IRD010/table/tableViewLayout1/ (in Latvian). Last accessed 18.04.2024.

[10] Pilecka J., Grinfelde I., Valujeva K., Straupe I., Purmalis O., Heavy metal concentration and distribution of snow and Lichea samples in urban area: Case study of Jelgava, 17th International Multidisciplinary Scientific GeoConference, Bulgaria, vol. 17/issue 41, pp 459-466, 2017.

[11] Stankevica M., Grinfelde I., Bakute A., Pilecka-Ulcugaceva J., Purmalis O., Heavy metals air pollution in Jelgava city Latvia, 21st International Multidisciplinary Scientific GeoConference, Bulgaria, vol. 21, pp 75-84, 2021.

[12] Font A., Tremper A., H., Lin C., Priestman M., Marsh D., Woods M., Heal M., R., Green D., C., Air quality in enclosed railway stations: Quantifying the impact of diesel trains through deployment of multi-site measurement and random forest modelling, Environmental Pollution, vol. 262, 2020.

[13] Elihn K., Dalmijn J., Froment J., Håland A., Johansson J., H., Karlsson H., L., Martin J., W., Mikoviny T., Norman M., Piel F., Sadiktsis I., Schlesinger D., Silvergren S., Srikanth Vallabani N.V., Wisthaler A., Steimer S. S., Air quality impacts of a large waste fire in Stockholm, Sweden, Atmospheric Environment, vol. 315, 2023.

[14] Sun C., Luo Y., Li J., Urban traffic infrastructure investment and air pollution: Evidence from the 83 cities in China, Journal of Cleaner Production, vol.172, pp 488–496, 2018.

[15] Jeanjean M., Goix S., Dron J., Periot M., Austruy A., Douib K., Persoons R., Etienne M., Revenko G., Chamaret P., Influence of environmental and dietary exposures on metals accumulation among the residents of a major industrial harbour (Fos-sur-Mer, France), Journal of Trace Elements in Medicine and Biology, vol. 73, 127021, 2022.

[16] Irwin R.J., Van Mouwerik M., Stevens L., Seese M.D., Basham W., Environmental contaminants encyclopedia, Arsenic entry, Water resources divisions, water operations branch, Colorado, USA, 1997.

CHALLENGES AND RISKS FOR ROMANIAN FARMERS

Lecturer Dr. Carmen Simona Dumitrescu[1]

Lecturer Dr. Cosmina Simona Toader[1]

Assoc. Prof. Dr. Cosmin Sălășan[1,2]

[1] University of Life Sciences "King Mihai I" from Timișoara, Faculty of Management and Rural Tourism, **Romania**
[2] Escuela de Agronomía, Facultad de Ciencias Agrarias y Forestales, Universidad Católica del Maule, **Chile**

ABSTRACT

Despite other sectors, agriculture faces the direct influences of the environment and climate. Today climate change represents a challenge for farmers around the world, not only for Romanian ones. The paper deals with this problem and agriculture resilience. It brings to attention the important issue of resilience and the challenges for agriculture and for farmers, especially for small farmers. The research is based on questionnaires applied to farmers focusing on their perception of risks, adaptation options and barriers. There were used qualitative risk analysis tools as risk management matrix and Venn Diagram to underline the farmers perception. In our analysis, we also considered coupling the risks with the supporting measures applied at national level. In the paper we analyzed each risk item related to agriculture starting from irrigation and going till agroecology. The farmers have prioritized the risks, the main risk being the ones related to water and agroecology, and they appreciated the interconnections between some of them.

Keywords: agriculture, climate change, adapting

INTRODUCTION

The agricultural sector is now encountering a growing and increasingly complex array of risks. Climate change and water scarcity are expected to amplify the intensity and frequency of climate-related shocks [14], increasing uncertainties and exacerbating other risks. The farmers, in order to improve their position, must fight not only with the external factors of the environment, but also with many issues of the internal management of the enterprises. [9]. Farmers, by the nature of their activity, are subject to risks, having to make decisions whose outcome cannot always be predicted because there are many risks involved in the activity carried out by a farmer [13]. The concept of risk is expansive and is sometimes conflated with terms like harm, danger, threat, or uncertainty. Alternatively, some contend that risk pertains to an event or the probability of its outcome. Risk encompasses both the potential for benefit and the potential for loss [3,6]. Many authors have identified the risks involved in agricultural activity and grouped them in five large classes of risks: production, marketing, financial, institutional or legislative, and those related to the human resource involved [5,8,12]. A farmer may encounter various challenges, such as sudden weather changes, significant price drops at harvest time, labor shortages during critical periods, equipment breakdowns during essential tasks, and legislative changes affecting production,

https://doi.org/10.5593/sgem2024/4.1/s19.51

marketing, and human resources. Farmers vary in their willingness to accept risk, with some being more open to it than others. Their attitudes towards risk are often influenced by their financial capacity to handle minor gains or losses. Farmers' attitudes can be categorized as follows: risk-averse, those who strive to avoid risks; risk-takers, those who are open to riskier business opportunities; and risk-neutral, those who fall between the two extremes [7]. Numerous risks are now being intensified by global environmental, social, and economic changes, such as ongoing human population growth, limited arable land, land degradation, and climate change. [11] Farmers' risk perceptions vary due to their diverse socio-economic backgrounds, including factors such as age, education, culture, religion, farming practices, income, peer pressure, and community values. These differences lead to distinct economic behaviors and decision-making processes, particularly in response to risks. [1,2]. Agricultural risks have previously been categorized into several types: production risk, financial risk, institutional risks, market risk and human resource risks [4,5]. Risks arising from weather variability, natural hazards, pests and diseases are particularly harmful because of the sector's dependence on natural resources and climate conditions [10].

MATERIALS AND METHODS

The production risks include weather -related risks, natural disasters, biological and environmental risks. Crop and livestock performance relies on biological processes influenced by weather conditions, as well as pests and diseases. Low rainfall or drought can result in reduced yields, while hail or heavy rains can damage or destroy crops. Additionally, pest or disease outbreaks can lead to significant yield losses in both crops and livestock. Marketing risks cover the ones related to prices and costs. Individual farmers cannot control price changes. The price of farm products is influenced by the product's supply, demand, and production costs. The supply of a product is influenced by a combination of production decisions made by farmers collectively, as well as by weather and other factors affecting yields. Demand for a product is shaped by consumer preferences, income levels, the strength of the general economy, and the supply and price of competing products. The cost of production per unit depends on both input costs and yields, making it highly variable. Although input costs are generally less variable than output prices, the combination of yield variations and input costs makes the cost of production a significant source of risk. Financial risk arises when borrowing money to finance the farm business. This risk is driven by uncertainties about future interest rates, the lender's willingness and ability to continue providing funds when needed, and the farmer's capacity to generate the income required for loan repayment. Smallholder farmers who borrow at high interest rates may particularly struggle with debt repayments. Lower than expected prices, combined with low yields, can make debt repayment challenging and may even force the sale of the farm. Institutional risk involves unpredictable changes in services provided by institutions that support farming, including banks, cooperatives, marketing organizations, input dealers, and government extension services. This risk encompasses uncertainties in government policies affecting farming, such as price supports and subsidies. Farmers often face risks resulting from decisions made by policymakers and managers, which can significantly impact the farm business. Examples include subsidies, food quality regulations for export crops, rules for animal waste disposal, and levels of price or income support payments. Human risk pertains to risks to the farm business arising from illness, death, and the personal circumstances of the farm family. Accidents, illnesses, and deaths can

disrupt farm operations. Additionally, labor migration from rural areas often leads to labor shortages, and political and social unrest can further limit labor availability. Production, marketing, financial, institutional, and human risks are present on most farms and are often interconnected. Debt repayment depends on production levels and the prices received for sold produce. Financing production relies on the ability to borrow capital and the lender's capacity to provide it promptly. These various risks frequently need to be considered in conjunction with one another. The questionnaire was designed to gather information about the respondent, their farm business, and attitudes toward challenges and risks they face in their activity all year round. The area delimited for the study was limited to the western part of Romania, more precisely Timiș County. A number of 130 questionnaires were applied to farmers during a Field Days event held in the spring and attended by farmers, input suppliers, and processors. 124 questionnaires were validated and for easier data analysis they were entered into excel. The questionnaire included questions related to age, sex, training because they were considered important factors regarding the farmers' perception of the challenges they encounter in their activity but also their attitude towards risks. Items such as compliance with legislation, product compliance, pollution reduction, optimization of input supply and consumption, carbon sequestration, biodiversity maintenance were framed as challenges for farmers.

RESULTS

After applying and processing the data, 23.4% of the respondents were women, while 76.6% were men. The stratification of farmers by age group, there are only 2 farmers younger than 20 years. The percentage from the upper age group is larger than 9.6%.

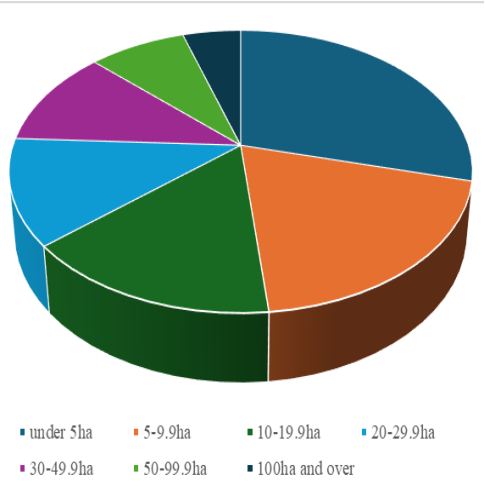


Figure 1. Farm dimenssions

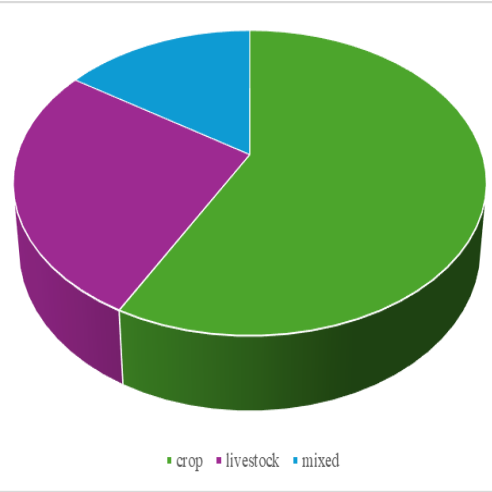


Figure 2. Farm type

The largest percentage of farmers belong to age group 50-59 years and together with the farmers over 60 years old they represent 50,8% from total. Most of the farmers who responded to the questionnaire have secondary education, 50.8%, while 42.7% have higher education and 6.4% have primary education.

https://doi.org/10.5593/sgem2024/4.1/s19.51

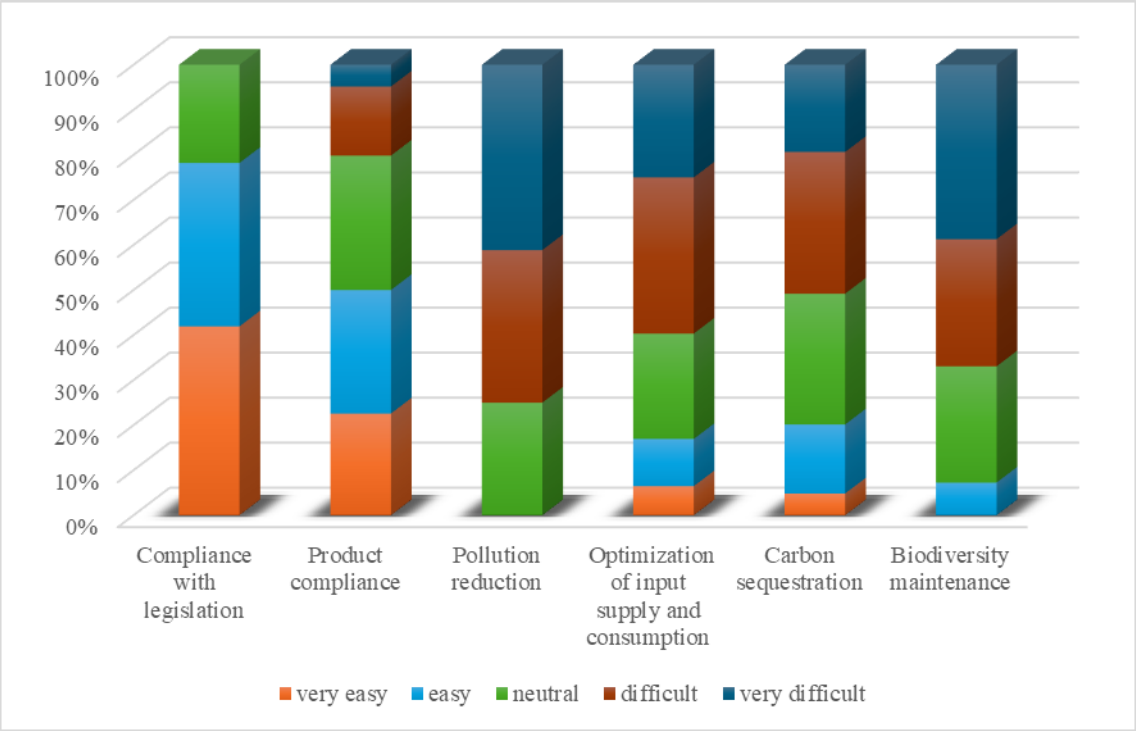


Figure 3. Challenges scaling

For risk classification, the risk matrix was used in which the severity of a risk and the frequency of its occurrence were quantified.

Table 1. Risks scores

	Risk matrix score (potential impact+likelihood occurred)								
Risks	**10**	**9**	**8**	**7**	**6**	**5**	**4**	**3**	**2**
Weather and climate	6	11	12	18	24	23	17	9	4
Natural disasters	0	0	0	23	28	35	38	0	0
Biological	15	21	22	19	16	14	8	6	3
Environmental risks	0	3	8	14	17	23	25	19	15
Prices	24	9	11	14	16	14	21	13	2
Costs	18	15	18	22	21	15	6	6	3
Access to market	12	21	25	18	18	16	12	2	0
Loans and interest rates	8	11	16	22	24	21	16	4	2
Policy changes	0	5	8	14	23	29	37	8	0
Price support, subsidies	14	22	28	26	21	6	4	3	0
Accidents	0	0	0	0	0	37	42	35	10
Illness	0	0	0	0	7	12	26	30	49
Labor force migration	0	0	0	19	28	36	38	3	0

DISCUSSION

From the total number of farmers, 87.1% of them affirmed that their farms are smaller than 50 hectares, while 41.9% of farms are vegetal farms, 19.4% are activating in husbandry and only 11,3% are mixed farms. The farmers appreciated the challenges they face in their activity using a Likert scale ranging from very easy to very difficult to face. The challenges raised by reducing pollution were considered difficult to achieve by 51 farmers.

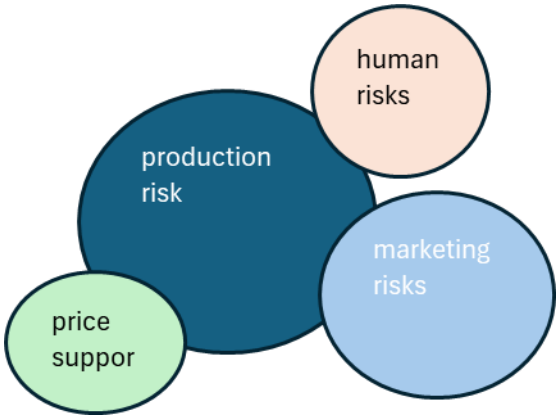


Figure 4: Venn diagram

Many farmers also consider the biodiversity preservation very challenging. The optimisation of input supply and consumption was referred as difficult by 43 farmers, while carbon sequestration was considered difficult only by 39 farmers. Product compliance is considered neutral by 37 farmers, while compliance with legislation is considered easy by 52 farmers. Risks related to weather and climate change received the maximum score from 6 farmers, who rated it with maximum score also in terms of frequency and severity, while natural disaster were appreciated by 38 farmers with 4 points. Only 22 farmers give 8 points to biological risks while the environmental ones were appreciated with 4 by 25 farmers.

CONCLUSION

The agricultural sector faces increasingly complex risks, with climate change and water scarcity expected to intensify climate-related shocks, heightening uncertainties and exacerbating other issues. Farmers must tackle both external environmental factors and internal management challenges. Due to their work's nature, farmers are inherently subject to risks and must make decisions with unpredictable outcomes. Risk includes both potential benefits and losses and is often confused with harm, danger, threat, or uncertainty. Farmers encounter challenges such as sudden weather changes, significant price drops at harvest, labor shortages, equipment breakdowns, and legislative changes affecting production, marketing, and human resources. Farmers' willingness to accept risk varies, influenced by their financial capacity to handle gains or losses, as they are risk-averse, risk-takers, or risk-neutral. Global environmental, social, and economic changes, like population growth, limited arable land, land degradation, and climate change, intensify risks. Farmers' risk perceptions differ based on socio-economic backgrounds, including age, education, culture, religion, farming practices, income, peer pressure, and community values, leading to distinct economic behaviors and decision-making processes.

https://doi.org/10.5593/sgem2024/4.1/s19.51

ACKNOWLEDGEMENTS

This paper is published from the own research funds of the University of Life Sciences "King Mihai I" from Timisoara.

REFERENCES

[1]. Ahsan, D.A. Farmers' motivations, risk perceptions and risk management strategies in a developing economy: Bangladesh experience. J. Risk Res. 14, pp.325–349. 2011. https://doi.org/10.1080/13669877.2010.541558

[2]. Bergfjord, O.J. Farming and risk attitude. Emir. J. Food Agric.25, pp 555–561, 2013, doi: 10.9755/ejfa.v25i7.13584

[3]. Girdžiūtė Laura, Risks in agriculture and opportunities of their integrated evaluation, Procedia - Social and Behavioral Sciences 62, pp 783 – 790, 2012

[4]. Hardaker, J.B.; Lien, G.; Anderson, J.R.; Hurine, R. Coping with Risk in Agriculture: Applied Decision Analysis, 3rd ed.; CAB International Publishing Company: Wallingford, UK, pp. 2-6, 2015

[5]. Harwood Joy, Heifner Richard, Keith Coble, Perry Janet, Somwaru Agapi – Managing Risk in Farming, Concepts, Research, and Analysis, An Economic Research Service Report, United States Department of Agriculture, pp 2-4, 1999

[6]. Jasanoff, SH., The Political Science of Risk Perception. Reliability Engineering and System Safety, 59, 91-99, 1998

[7]. Kahan David, Managing risk in farming, Farm management extension guide, Food and Agriculture Organization of the United Nations, Rome, 2008. https://www.fao.org/uploads/media/3-ManagingRiskInternLores.pdf

[8]. Komarek Adam M., De Pinto Alessandro, Smith Vincent H., A review of types of risks in agriculture: What we know and what we need to know, Agricultural Systems, Volume 178, 2020, 102738, ISSN 0308-521X, https://doi.org/10.1016/j.agsy.2019.102738. (https://www.sciencedirect.com/science/article/pii/S0308521X18312034)

[9]. Nadezda JANKELOVA 1 *, Dusan MASAR 2, Stefania MORICOVA, Risk factors in the agriculture sector, Agricultural Economics – Czech, 63, (6): pp 247–258, 2017, doi: 10.17221/212/2016-AGRICECON

[10]. OECD Meeting of Agriculture Ministers, Agricultural risk management for resilience, background note, 2022 https://www.oecd.org/agriculture/ministerial/documents/Agricultural%20Risk%20Management%20For%20Resilience.pdf

[11]. Sulewski, P.; Kloczko-Gajewska, A. Farmers' risk perception, risk aversion and strategies to cope with production risk: An empirical study from Poland. Stud. Agric. Econ., 116, pp 140–147, 2014

[12]. Thi Tam Duong, Tom Brewer, Jo Luck and Kerstin Zander, A Global Review of Farmers' Perceptions of Agricultural Risks and Risk Management Strategies, Agriculture, 9(1), 10; 2019, https://doi.org/10.3390/agriculture9010010

[13]. Ullah, R.; Shivakoti, G.P.; Zulfiqar, F.; Kamran, M.A. Farm risks and uncertainties: Sources, impacts and management. Outlook Agric., 45, pp 199–205, 2015

[14]. Wheeler, Tim & von Braun, Joachim, Climate Change Impacts on Global Food Security. Science (New York, N.Y.). pp 341, 2013, 508-13. 10.1126/science.1239402.

EVALUATING THE IMPACT OF AUTOMOBILE POLLUTION ON THE HEALTH OF THE ROMANIAN POPULATION THROUGH STATISTICAL METHODS

Assoc. Prof. Dr. Eng. Rus Madalina[1]

Assoc. Prof. Dr. Eng. Veresiu Silvia[1]

Prof. Dr. Eng. Mereuta Elena[1]

Assoc. Prof. Dr. Eng. Valentin Amortila[1]

PhD Eng. Balasoiu George[1]

[1]" Dunarea de Jos" University of Galati, **Romania**

ABSTRACT

This research aims to conduct a descriptive statistical analysis to identify the statistical correlation between categories of new and second-hand vehicles registered for circulation in Romania and various health conditions associated with atmospheric pollution.

Currently, a significant challenge for the global community lies in mitigating the impact of atmospheric pollution, considered a crucial factor both in terms of global climate change and its impact on public health. One major source of atmospheric pollution stems from emissions generated by internal combustion engines in the transportation sector. According to studies conducted by the European Environment Agency, approximately 70% of total greenhouse gas emissions originate from road transport, surpassing the European average in Romania due to the substantial number of second-hand vehicles registered and in circulation. Emissions resulting from petroleum-based fuels are associated with the onset of cardiovascular and respiratory system conditions.

Through this descriptive statistical analysis, grounded in the Pearson correlation coefficient, we aim to emphasize the existing relationship between the number of vehicles and the prevalence of respiratory and cardiovascular system conditions, etc., with the goal of drawing attention to the implications of auto pollution. To conduct this study, we utilized data available on the National Institute of Statistics (INSSE) portal, covering a 21-year interval from January 2000 to December 2021.

Keywords: Pearson coefficient, respiratory diseases, cardiovascular diseases, atmospheric pollution.

INTRODUCTION

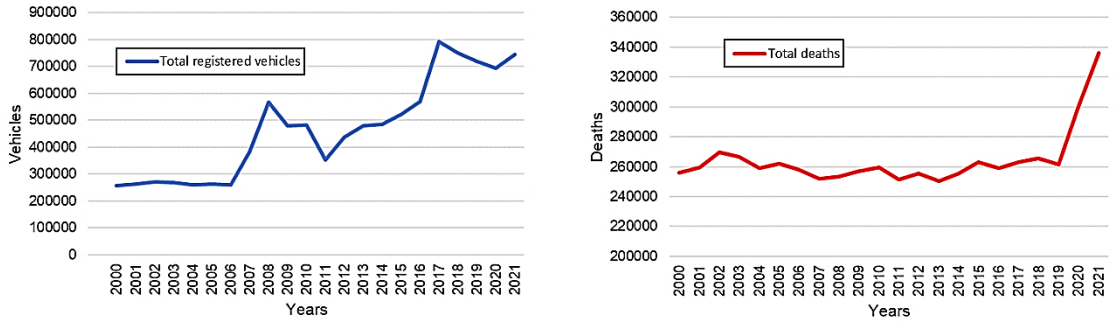
Car pollution in Europe is a significant problem in terms of its impact on public health and the environment. Motor vehicles contribute to air pollution through emissions of exhaust gases and fine particles, having the potential to adversely affect human health and amplify climate change. The European Union (EU) has implemented strict emission rules and standards for motor vehicles, particularly for diesel and petrol engine noxes and particulates, known as Euro standards, [1].

https://doi.org/10.5593/sgem2024/4.1/s19.52

These standards are adopted to reduce emission levels and improve air quality in all Member States. Many European cities have established low-emission zones (LEZs) or areas with traffic restrictions for more polluting vehicles, thus encouraging the use of public transport and less polluting vehicles or green alternatives such as bicycles and electric scooters, [2].
Car pollution is associated with various health conditions, including respiratory diseases, circulatory diseases, tumours, and other health problems. In addition, fine particles and other pollutants can impair air quality in urban and rural environments, [3].
In Romania, the approach to car pollution is similar to that in Europe, focusing on reducing emissions and improving air quality to protect public health and preserve the environment. Thus, the areas with the highest air pollution in Romania are determined by several factors, including traffic density, the level of industrialization, the use of fossil fuels and the age of vehicles. Studies suggest a correlation between the number of motor vehicles and the prevalence of respiratory and cardiovascular diseases, [4].
This paper analyses the influence of car registrations on the number of deaths in the four macro-regions of Romania in the period 2000-2021, especially regarding diseases associated with atmospheric pollution. The data used come from the National Institute of Statistics in Romania and are available to the public, [5].

MATERIALS AND METHODS

The assessment of the impact of the pollution generated by vehicles equipped with thermal engines started from the consultation of the statistical database provided by INSSE, collecting the car registration data of new and second-hand vehicles as well as deaths caused by diseases such as tumors, diseases of the circulatory or respiratory system on the four big regions in Romania.
In Romania, there is a variation in the registrations of new and second-hand vehicles, thus from the year 2000 when 70636 vehicles (motorcycles, cars, and buses) were registered, reaching a maximum of 320163 in 2007, because in year 2021 to reach a number of 128158 registrations, figure 1(a) Regarding deaths, there is an increase from 255820 in 2000 to 336063 in 2021, figure 1(b).



(a) (b)

Figure 1 The situation of vehicle registrations (a) and deaths (b) in Romania during the period 2000 - 2021

Reporting the deaths on the macro-regions in Romania and reporting to the main causes of death (tumours, diseases of the circulatory system, diseases of the respiratory system) a somewhat similar behavior of the phenomenon is observed in the four analysed regions, figure 2.

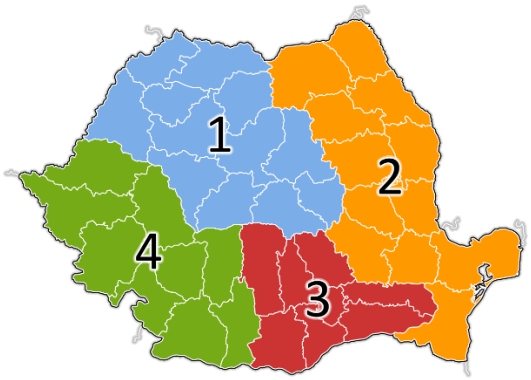


Figure 2 The localization of the four macroregions of Romania

These causes were analyzed because cars generate atmospheric pollutants such as nitrogen dioxide, carbon monoxide and fine particles, which can irritate the airways and aggravate conditions such as asthma, bronchitis and other respiratory problems, figure 3 In addition to the impact on the respiratory system, air pollution can also affect the cardiovascular system. Fine particles and other pollutants can enter the blood and cause inflammation, damage to blood vessels and increase the risk of cardiovascular diseases such as high blood pressure, atherosclerosis, and myocardial infarction.

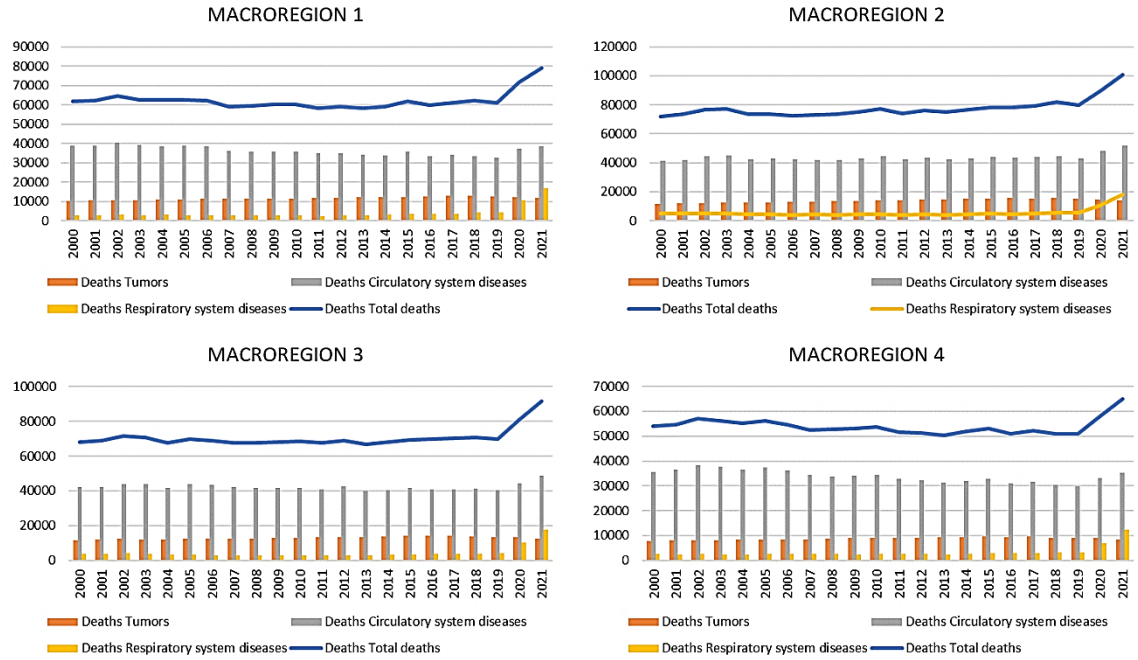


Figure 3 The situation of deaths by causes of diseases in the four macroregions of Romania during the period 2000 – 2021

Epidemiological studies have shown that in areas with heavy traffic and high pollution there is a significant association between high levels of pollution and increased prevalence of respiratory and cardiovascular diseases. Furthermore, reducing air pollution through measures such as promoting public transport, purchasing less polluting vehicles and improving infrastructure for cyclists and pedestrians can contribute to improving public health by reducing the incidence of these conditions, [6].

https://doi.org/10.5593/sgem2024/4.1/s19.52

To find a link between motor vehicle registrations and deaths from diseases associated with air pollution we used a statistical correlation method called the Pearson correlation. The Pearson correlation, also known as the Pearson correlation coefficient, or r, is a statistical measure of the linear relationship between two continuous variables. This measure provides information about how close the relationship is between two variables and in which direction this relationship lies. The Pearson correlation coefficient can vary between -1 and 1. A coefficient of +1 indicates a perfect positive correlation, meaning that the two variables increase together perfectly. A coefficient of -1 indicates a perfect negative correlation, meaning that the two variables vary in perfectly opposite directions. A coefficient of 0 indicates no linear correlation between the two variables. The intermediate values of the correlation can be appreciated from 0.2 to 0.2 as satisfactory, good, very good.

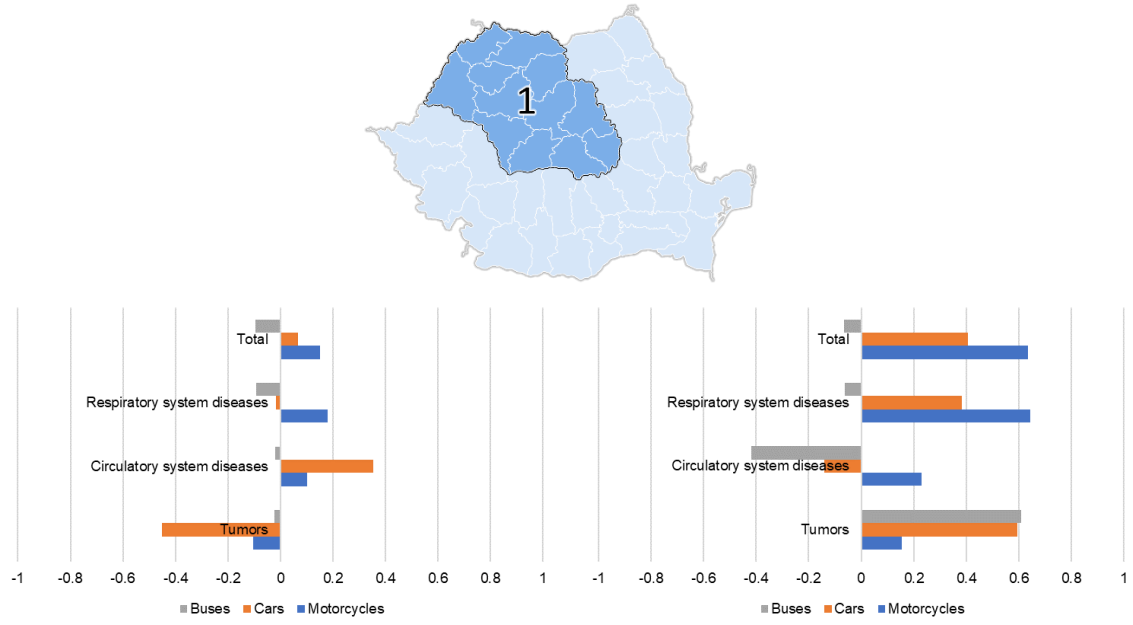
RESULTS AND DISCUSSION

The correlation analysis between air pollution-related disease deaths and motor vehicle registrations can be interpreted in a number of ways, depending on the context and the exact data used. In general, this analysis can explore the statistical relationship between the number of road deaths and the number of registered motor vehicles in a given time period and location. The interpretation of the Pearson correlation is based on the calculation of the coefficient "r" according to the table 1. The negative values follow the same interpretation only that the correlation is inverse, that is, while one variable increases the second variable decreases.

Table 1 Interpretation of Pearson coefficient (r) values

r ϵ [0; 0.2]	→	very weak, non-existent correlation
r ϵ [0.2; 0.4]	→	weak correlation
r ϵ [0.4; 0.6]	→	reasonable correlation
r ϵ [0.6; 0.8]	→	high correlation
r ϵ [0.8; 1]	→	very high correlation

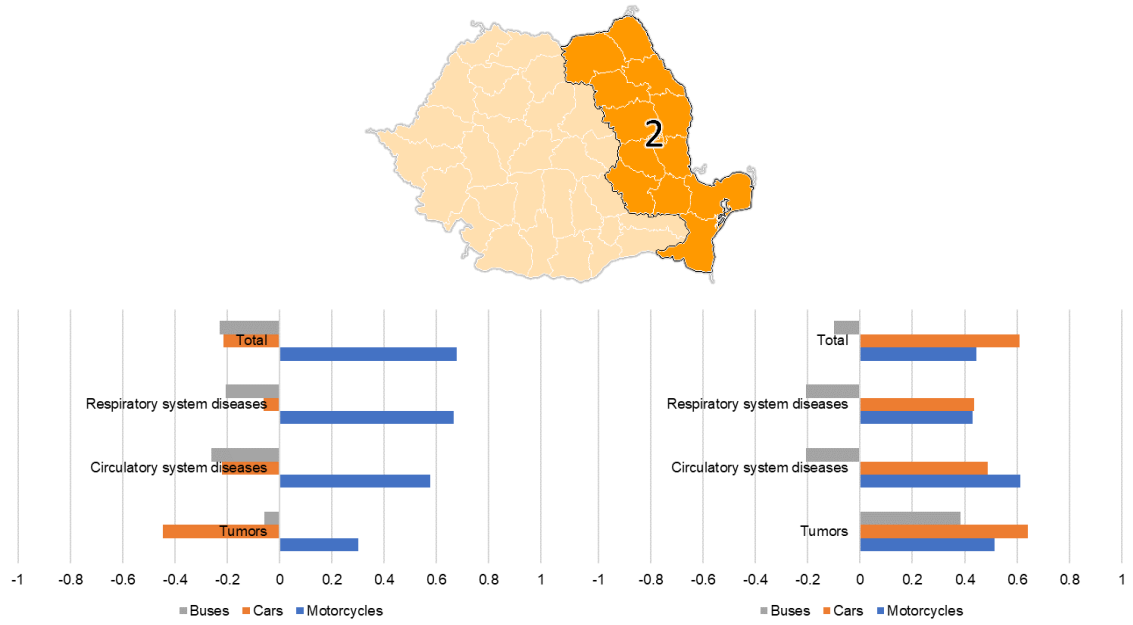
In macroregion 1, it is found that for newly registered vehicles, figure 4(a), the greatest influence on the onset of diseases of the circulatory system is cars, although the correlation index r=0.353, indicates a weak correlation (<0.4), thus not being able to conclude that there is a link between the two variables. In the case of second-hand vehicles registered in macroregion 1 of Romania, figure 4(b), it is found that buses and cars have a reasonable correlation in triggering tumors (r buses=0.608; r cars=0.594), and motorcycles show a high correlation in the case of deaths caused by respiratory diseases (0.644) and overall deaths in total (0.636).



(a) (b)

Figure 4 Pearson correlation analysis between newly registered (a) and used (b) vehicles in macroregion 1 with deaths from air pollution-related diseases

In macroregion 2, it is found that for newly registered vehicles, figure 5(a), motorcycles have the greatest influence on the outbreak of diseases. Thus, for deaths caused by diseases of the respiratory system, the correlation coefficient is 0.667, for deaths caused by diseases of the circulatory system, it is 0.577 and for the total of diseases causing death, it is 0.687. It can be said that new motorcycles, the figure 5(a) shows a causal link between their number and deaths.



(a) (b)

Figure 5 Pearson correlation analysis between newly registered (a) and used (b) vehicles in macroregion 2 with deaths from air pollution-related diseases

https://doi.org/10.5593/sgem2024/4.1/s19.52

In the case of second-hand vehicles registered between 2000 and 2021 in macroregion 2, it is found that both motorcycles and cars show a reasonably high correlation in the onset of circulatory, respiratory diseases and tumors, r > 0.4, the figure 5(b), being able to state that these vehicles from this region can be one of the main sources of death-generating pollution.

Macroregion 3 of Romania presents a reasonably high correlation in terms of newly motorcycle registrations and diseases causing death such as respiratory (r=0.593) and circulatory (r=0.639), figure 6(a). In this case it can be said that motorcycle exhaust gases can be one of the causes of deaths caused by circulatory and respiratory diseases. Also, a high correlation exists between motorcycles and the total number of diseases that cause death, (r=0.632). In the case of second-hand vehicles, only motorcycles and cars show a low correlation with circulatory and respiratory diseases, figure 6(b). Cars also show a low correlation with the occurrence of tumors that generated death (r=0.333).

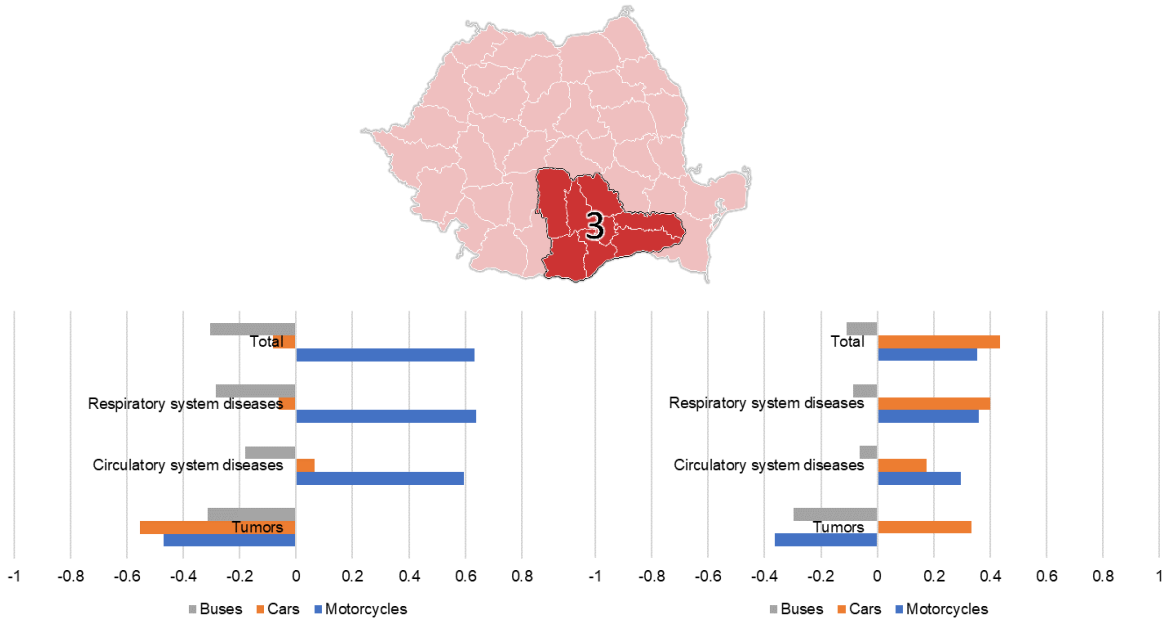
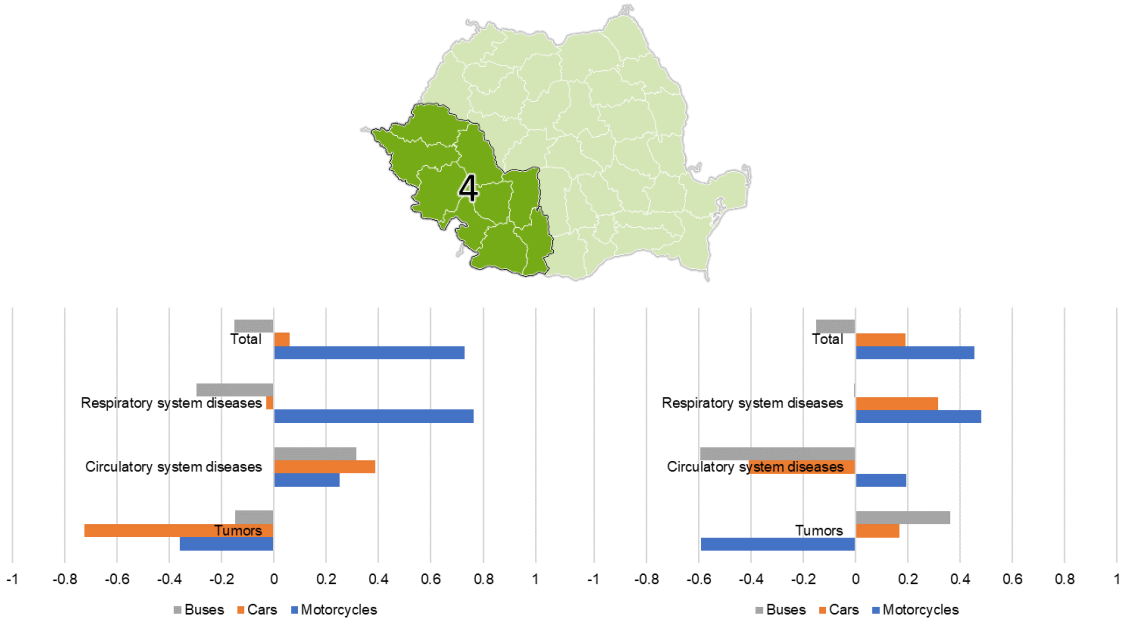


Figure 6 Pearson correlation analysis between newly registered (a) and used (b) vehicles in macroregion 3 with deaths from air pollution-related diseases

In macroregion 4 of Romania, a low correlation is found for newly registered motorcycles and newly registered cars with respect to circulatory diseases (r<4). But for the respiratory diseases that caused deaths and newly registered motorcycles, a high correlation is recorded, which can lead to the conclusion that the gases emitted by them can be one of the main sources of pollution that cause fatal respiratory diseases, figure 7(a). Motorcycles cases registered in macroregion 4 are characterized by a reasonable correlation (r>0.4) with respiratory diseases and the total number of diseases that caused deaths. The same moderate correlation is shown by buses in relation to diseases that cause incurable tumors, (r=0.361), figure 7(b).



(a) (b)

Figure 7 Pearson correlation analysis between newly registered (a) and used (b) vehicles in macroregion 4 with deaths from air pollution-related diseases

CONCLUSIONS

Air pollution caused by motor vehicles can contribute to and exacerbate several health conditions with fatal consequences. Respiratory diseases such as asthma, chronic bronchitis, and other chronic obstructive respiratory diseases (COPD) caused by fine particles and irritant gases emitted by motor vehicles can irritate the airways and cause inflammation, bronchial spasms, and difficulty breathing. Exposure to air pollution from motor vehicles can increase the risk of cardiovascular diseases such as high blood pressure, atherosclerosis, heart rhythm disorders and stroke. Air pollutants can contribute to inflammation of the cardiovascular system and damage to blood vessels. Some air pollutants emitted by motor vehicles are known carcinogens such as fine particles ($PM_{2.5}$) which are associated with an increased risk of lung cancer and other types of tumors.

The correlation analysis presented between vehicle registrations and diseases causing death in the Romanian macro-regions led to the following conclusions:

- In all four macro-regions it can be said that motorcycles influence the health level of the population and especially the occurrence of respiratory and circulatory diseases.
- New vehicles registered in these areas contribute less to the outbreak of diseases associated with atmospheric pollution.
- Second-hand vehicles present an increased risk compared to new ones in causing diseases of the circulatory or respiratory system.
- In macroregions 2, 3 and 4, the number of new motorcycles shows a strong connection with the number of deaths caused by respiratory diseases.
- In macroregions 1, 2 and 3, the moderate-high correlation with diseases that generate incurable tumors leads us to conclude that second-hand cars registered

https://doi.org/10.5593/sgem2024/4.1/s19.52

between 2000 and 2021 contribute significantly to the deaths associated with these diseases.

The interpretation of the Pearson correlation coefficient is important for understanding the relationship between two variables, motor vehicle registrations and disease causes of death. However, it is important to note that the Pearson correlation does not indicate a causal relationship between variables, but only a statistical relationship. Further investigations such as case studies or controlled experiments are needed to establish a causal relationship.

The reduction of health conditions associated with air pollution caused by motor vehicles involves a series of measures such as: reducing the number of old (second-hand) motor vehicles being registered, promoting public transport, supporting the purchase of new non-polluting motor vehicles by individuals and various companies to improve air quality. These measures can significantly contribute to protecting public health and improving air quality.

ACKNOWLEDGEMENTS

This scientific work was carried out within the Department of Mechanical Engineering at the Faculty of Engineering of "Dunarea de Jos" University in Galați and the Center for Interdisciplinary Research in Mechanical Engineering (CCIDIM).

REFERENCES

[1] P. Sicard, E. Agathokleous, A. De Marco, E. Paoletti, and V. Calatayud, “Urban population exposure to air pollution in Europe over the last decades,” *Environ. Sci. Eur.*, vol. 33, no. 1, pp. 1–12, Dec. 2021.

[2] “Air pollution and its impact on health in Europe: Why it matters and how the health sector can reduce its burden | Health at a Glance: Europe 2020 : State of Health in the EU Cycle | OECD iLibrary.” [Online]. Available: https://www.oecd-ilibrary.org/social-issues-migration-health/health-at-a-glance-europe-2020_5286cd4d-en. [Accessed: 24-Apr-2024].

[3] G. Năstase, A. Șerban, A. F. Năstase, G. Dragomir, and A. I. Brezeanu, “Air quality, primary air pollutants and ambient concentrations inventory for Romania,” *Atmos. Environ.*, vol. 184, pp. 292–303, Jul. 2018.

[4] C. Maftei, R. Muntean, and I. Poinareanu, “The Impact of Air Pollution on Pulmonary Diseases: A Case Study from Brasov County, Romania,” *Atmos. 2022, Vol. 13, Page 902*, vol. 13, no. 6, p. 902, Jun. 2022.

[5] “TEMPO Online.” [Online]. Available: http://statistici.insse.ro:8077/tempo-online/#/pages/tables/insse-table%5D. [Accessed: 24-Apr-2024].

[6] V. Amortila, E. Mereuta, D. Ganea, C. Humelnicu, and S. Ciortan, “Auto transportation-an important factor in polluation growth and in atmospheric changes,” in *International Multidisciplinary Scientific GeoConference Surveying Geology and Mining Ecology Management, SGEM*, 2018, vol. 18, no. 4.2, pp. 349–356.

FACTORS AFFECTING INDOOR AIR QUALITY IN KINDERGARTEN

Andrea Badurova, M. Sc.[1]

Petra Stiborova, M. Sc.[2]

Assoc. Prof. Dr. Iveta Skotnicova[3]

[1,2,3]VSB – Technical University of Ostrava, Faculty of Civil Engineering, **Czech Republic**

ABSTRACT

This article deals with the issue of the indoor environment in terms of optimal conditions of thermal comfort and the satisfactory quality of indoor air. A weekly measurement of the parameters of the indoor environment was carried out in the building of the day rehabilitation centre in order to verify the state of the indoor environment, to determine the processes that create the indoor environment and to define the factors that affect the resulting state of the indoor microclimate. One of the important factors is air quality, where the main factor that influences the indoor environment is the concentration of carbon dioxide, whose value affects the biological functions of the human organism. The analysis of the measured parameters found that the concentration of carbon dioxide in the monitored indoor space is not, as expected, the riskiest factor that may be the cause of dissatisfaction with the indoor microclimate.

Keywords: air quality, indoor environment, kindergarten, carbon dioxide, ventilation

INTRODUCTION

People spend most of their time in buildings, up to 90%. The quality of the indoor environment in buildings should therefore be one of the most important parameters in building design [1]. When measures to reduce the energy performance of buildings are implemented, the quality of the indoor environment should not be neglected. The quality of the indoor environment is influenced by the condition of the outdoor environment, but also comes from internal sources. The indoor air quality can be many times worse than the outdoor air quality. However, the state of the internal environment in buildings is not routinely monitored in most cases. It is important to measure and monitor the state of the indoor environment in buildings, and especially in buildings intended for the education of children and young people [2]. Children and pupils spend a large part of their day at school, and their organism is more sensitive to the influence of the surrounding environment. Inadequate ventilation of rooms with higher occupancy, such as nurseries and schools, can result in manifestations of health problems that disappear after leaving the area, such as fatigue, loss of concentration or headache, but can also cause higher morbidity. Therefore, in these buildings, an emphasis should be placed on compliance with CO_2 concentration limits as well as the optimal range of indoor air temperature and relative humidity [3].

https://doi.org/10.5593/sgem2024/4.1/s19.53

An optimal indoor microclimate is a prerequisite for the well-being and health of its inhabitants [4]. It is important to note that the concept of an optimal microclimate can be a very subjective assessment unless we are talking about it only in terms of standard requirements. Thermal comfort is closely related to an optimal microclimate. Thermal comfort in the indoor environment is one of the fundamental factors influencing the quality of the indoor environment quality and has a significant contribution to occupant satisfaction with the indoor environment. Thermal comfort means that thermal conditions are achieved where a person is neither too cold not too warm and therefore feels comfortable [5]. A person feels best in a climate with a temperature range of 20 to 22 °C and relative humidity range 40 to 60%. Climatic conditions outside this range are perceived by most people as uncomfortable. Temperature and humidity are essential factors that influence the optimal microclimate.

The basic prerequisite is the correct design of the thermal engineering properties of the building structures that enclose the interior space or the building under consideration and form the building envelope. Compliance with the building envelope level is part of the requirement for the energy performance of buildings. From the point of view of air temperature, it is also necessary that the heating system be designed in such a way that it reaches the design internal temperatures in the individual rooms in the winter and at the same time effective regulation is possible to prevent overheating.

In addition to the standard requirements for temperature, humidity, and ventilation, one of the main indicators of air quality is the concentration of CO_2, whose value informs about the quality of ventilation of the indoor space. It is expressed in ppm (parts-per-million) units. The ppm unit means the number of volumetric units of CO_2 in one million volumetric units of air [6]. In an outdoor environment, the CO_2 concentration is approximately 0.04%, that is, 400 ppm. In terms of hygiene standards, [7] provides as follows: "Residential rooms must have sufficient natural or mechanical ventilation and be adequately heated with the possibility of regulating the internal temperature. For ventilation of living rooms, a minimum amount of outdoor air exchange of 25 m^3/h per person or a minimum ventilation rate of 0.5 1/h shall be ensured during the stay of the persons. Carbon dioxide CO_2 shall be used as an indicator of the quality of the indoor environment and shall not exceed a concentration of 1500 ppm in the indoor air." In addition to CO_2, indoor air can also contain other pollutants such as formaldehyde, carbon monoxide, VOCs, radon, asbestos, dust particles, odors, and microorganisms. Proper ventilation of the building will of course ensure that the concentration of these substances is also reduced. The requirements for ventilation and parameters of microclimatic conditions that apply to the premises and operation of facilities and establishments for the education and training of children and adolescents are specified in [6]. The amount of fresh air supplied to classrooms must be at least 20 m^3/h per pupil.

Tab 1. Effect of CO_2 concentration (ppm) on the human body

Concentration CO_2 (ppm)	Evaluation and influence of CO_2 concentration
350-500	normal outdoor concentration high indoor levels
500 - 800	high level of healthy indoor environment
800 - 1000	acceptable level of healthy indoor environment
1000	**recommended value**
1000 - 1500	complaints of odours, feeling of heavy (foul) air, light fatigue
1500	**limit value - Decree No. 268/2009 Coll.**
1500 - 2500	decrease in concentration, fatigue
2500 - 5000	dullness, fatigue, possible health problems
> 5000	nausea, increased heart rate
> 15000	breathing difficulties
> 40000	possible loss of consciousness

MATERIALS & METHODS

The building selected for the analysis and experimental measurement of the state of the indoor environment was a day rehabilitation centre. It is a facility that provides comprehensive counselling and rehabilitation care for children with mobility disorders and delayed psychomotor development. It also provides the possibility for children to be there daily as part of pre-school attendance. A playroom and restroom visited by 10 children aged 3-6 years were selected for the measurement. Other adjacent spaces are the dining room, dressing room and hallways. The playroom is used for most active activities, the restroom is mainly used for resting after lunch. The dimensions of the playroom are 5.63 x 6.87 m and the dimensions of the restroom are 7.0 x 5.63 m. The height of both rooms is 2.6 m, see Fig.1.

https://doi.org/10.5593/sgem2024/4.1/s19.53

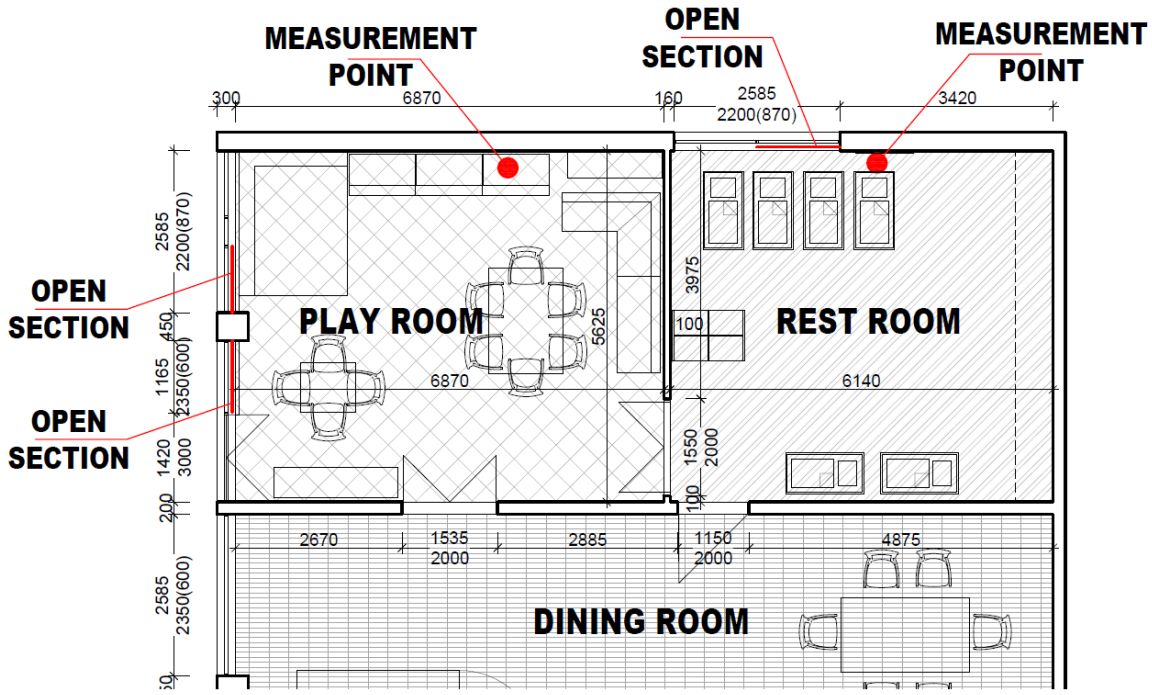


Fig. 1 Layout of the playroom and restroom

The operation of the day rehabilitation centre is from Monday to Friday between 6:30 a.m. and 3:30 p.m. The number of children present on a given day is affected by their sickness rate, which is high at this age due to their weakened immunity. Thermal-humidity sensors and CO_2 concentration sensors were placed in the playroom and in the restroom. The position of the sensors can be seen in Fig.1. The placement was chosen with respect to the spatial possibilities. It was not possible to place then in the centre of the room. The measured values were recorded every 15 minutes in dataloggers. The measurement took place over the course of a week in February 2024.

For the purpose of evaluating the development of the monitored parameters of the quality of the indoor environment of the monitored premises and possible negative effects on exceeding the required values, a detailed record of the activities in the measured rooms was kept throughout the measurement period. The children arrive at the day care centre between 6 and 8 a.m. Morning activities, such as a play time for the children and art activities, take place from 8:00 to 11:30 a.m. Afternoon activities take place from 2:00 to 3:15 p.m. At 9:00 - 9:30 a.m., a morning snack is served in the dining room, lunch is served from 11:30 a.m. to 12:00 p.m. and there is an afternoon snack at 1:30 - 2:00 p.m. The sleeping room is closed most of the day and is used for resting after lunch from 12:00 to 1:30 p.m. A concise list of these activities, which are almost always repeated every day, is given in Tab. 2.

Tab. 2 List of activities in the monitored rooms

Number of children (+staff)	Time	Type of activity
0-8 (+6)	6:00 – 8:00 a.m.	Arrival of children, free playtime
8 (+ 6)	8:00 – 9:00 a.m.	Joint ritual, free playtime
	9:00 – 9:30 a.m.	Snack (no children in the room)
	9:30 – 11:30 a.m.	Artistic activity, game
	11:30 a.m. – 12:00 p.m.	Lunch (no children in the room)
6	12:00 – 13:30 p.m.	Rest
0	13:30 – 14:00 p.m.	Snack (no children in the room)
0-8 (+ 6)	14:00 – 15:15 p.m.	Free playtime, departure of children

In addition to activities during the day, the frequency of ventilating the space was also recorded. Both of the rooms are directly ventilated using windows and there are panel radiators. Only natural ventilation is designed in the building. It is provided by plastic window openings realized in all the rooms used by people with the possibility of adjusting the opening casement to the open and tilting position. In the playroom there are also balcony doors, which are used only sporadically for ventilation. According to the records, the rooms used by people were ventilated almost constantly by means of the window openings in the window sections pursuant to Fig.1. Only on Monday at 10.00 - 10.30 a.m. and Thursday at 9.00 - 9.30 a.m. are the balcony doors used in addition to the ventilation windows. The size of the window casement, through which the ventilation is carried out in the restroom is 1.3 x 3.2 m. The playroom is ventilated with the help of two window casements, which can be only be opened only in a tilted position; the dimensions of the window openings are 1.0 x 0.5 m and 1.15 x 0.5 m. The size of the balcony doors is 1.42 x 3.0 m. Ventilation is only carried out during the centre's operating hours.

RESULTS

Based on the measurements made in two rooms designed for the children to stay in during the day in the day rehabilitation centre, the two following graphs were created. Fig.2 shows the progress of the carbon dioxide concentration during the week. Two levels are indicated in the graph, namely the recommended level of CO_2 concentration at 1000 ppm and the limit level of CO_2 concentration, which is 1500 ppm according to [7]. It is evident that this limit level was exceeded only once, otherwise the measured values were even below the recommended level most of the time. The measured values in the playroom, where the children spent more time, were higher than in the restroom. At the beginning of the day in the morning hours, the CO_2 concentration is the lowest and ranges between 500-600 ppm. A concentration of about 430 ppm was also measured in the morning hours in the outdoor environment of the building.

https://doi.org/10.5593/sgem2024/4.1/s19.53

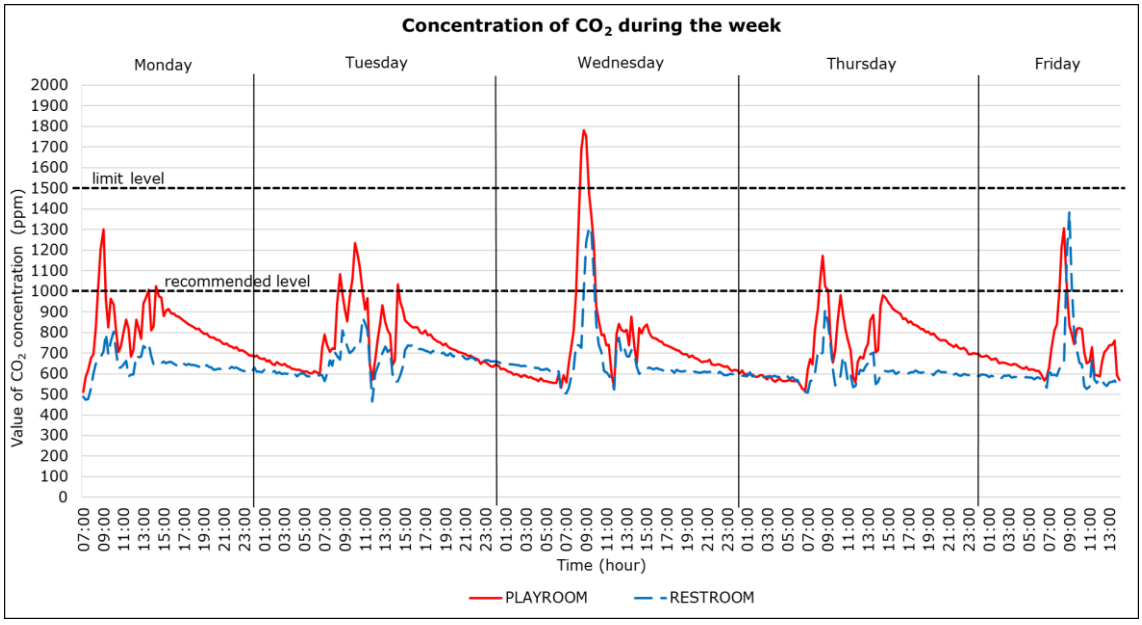


Fig. 2 Graph of concentration of CO_2 during the week

The measured values of the indoor air temperature and the relative air humidity, together with the outdoor air temperature, were plotted in the graph in Fig. 3. The temperature of the outside air was measured at a nearby weather station. The graph shows the areas of the optimal range of the indoor air temperature and relative humidity of the indoor air in terms of thermal comfort. The progress of the temperature of the internal air with slight fluctuations follows the upper limit of the optimum range, i.e. 22 °C. It is also apparent that the relative humidity values of the indoor air are below the lower limit of the optimal range, i.e. 40%. The measurements were carried out in February, when the outside air temperature ranged from -1.5 °C to +11.3 °C.

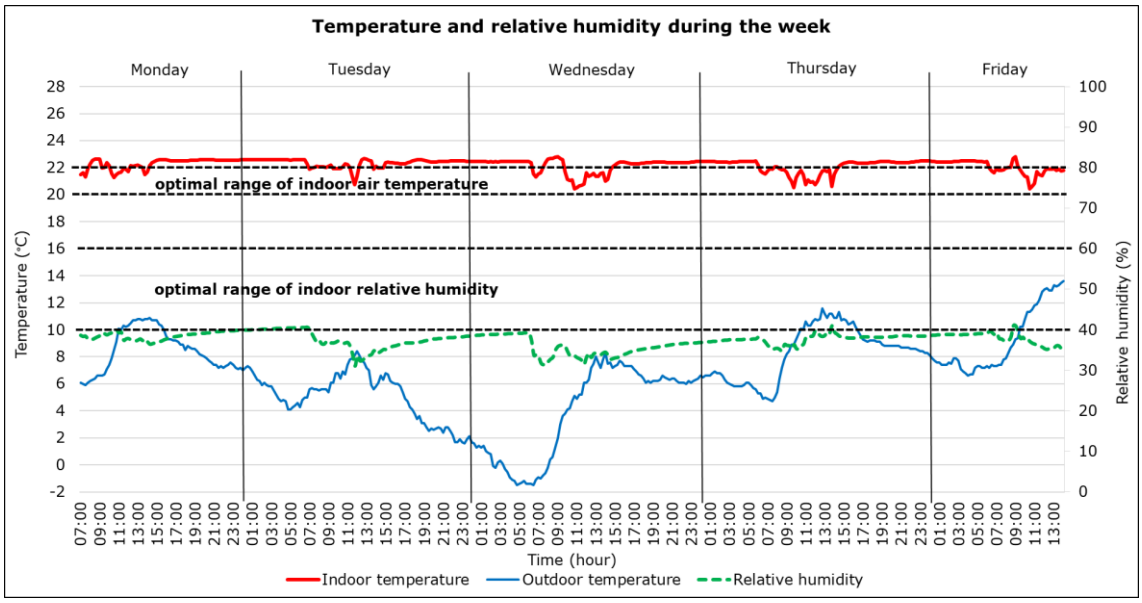


Fig. 3 Graph of temperature and relative humidity during the week

DISCUSSION

From the experimental measurement carried out in the day rehabilitation centre, it was found that the concentration of carbon dioxide as an indicator of the quality of the internal air is below the limit level. However, it is necessary to follow the ventilation regime, which significantly affects the CO_2 concentration level. The deviations that occurred in the middle and which can be seen in the graph in Fig. 2 were caused by the fact that the windows in the playroom were closed at the time from 8 to 10 a.m. At this time of day, all the children, as well as the staff, are already present in the area and regular rituals and other activities are taking place. In this case, the CO_2 concentration reached up to 1782 ppm. Ventilation using windows also affects the temperature of the air in the room, which was measured at a reasonable level. However, this type of ventilation can cause cold air currents near the window openings and thus local thermal discomfort. The measurements showed a low relative humidity of less than 40%. This low relative humidity can cause mucous membranes to dry out and cause respiratory problems.

CONCLUSION

From the experimental measurement carried out in the day rehabilitation centre, it was found that the concentration of carbon dioxide as an indicator of the quality of the internal air is below the limit level. However, it is necessary to follow the ventilation regime, which significantly affects the CO_2 concentration level. The deviations that occurred in the middle and which can be seen in the graph in Fig. 2 were caused by the fact that the windows in the playroom were closed at the time (from 8 to 10 a.m.). At this time of day, all the children, as well as the staff, are already present in the area and regular rituals and other activities are taking place. In this case, the CO_2 concentration reached up to 1782 ppm. Ventilation using windows also affects the temperature of the air in the room, which was measured at a reasonable level. However, this type of ventilation can cause cold air currents near the window openings and thus local thermal discomfort. The measurements showed a low relative humidity of less than 40%. This low relative humidity can cause mucous membranes to dry out and cause respiratory problems.

ACKNOWLEDGEMENTS

The work was supported by funds from the Student Grant Competition of VSB-TUO. The registration number of the project is SP2024/099.

REFERENCES

[1] Xiaoyi, Chen, Niu Runping, Liu Hua a Yu Kai. Analysis of the Importance of Fresh Air System to Indoor Environment of Green Building and Healthy Building. In: IOP Conference Series: Earth and Environmental Science, 2020, ISSN 1755-1307. DOI:10.1088/1755-1315/546/3/032021

[2] Stiborova P., Badurova A., Skotnicova I., Analysis of Indoor Air Quality in a Kindergarten, In: Slovak Journal of Civil Engineering, 2023, pp 1-8. ISSN 1338-3973. DOI:10.2478/sjce-2023-0007.

https://doi.org/10.5593/sgem2024/4.1/s19.53

[3] Skotnicova I., Rodkova C., Chudikova B., Stejskalova K., Analysis of indoor air quality and thermal environment in classrooms with different ventilation systems, In: Indoor Climate of Buildings – Proceedings of lecture, 2019.

[4] Coggins A. M., Wemken N., Mishra A. K., Sharkey M., Horgan L., and coll., Indoor air quality, thermal comfort and ventilation in deep energy retrofitted Irish dwellings. Building and Environment, 2022, ISSN 0360-132.

[5] Cihelka J., Vytápění, větrání a klimatizace, 1. Státní nakladatelství technické literatury, 1985. ISBN 04-201-85.

[6] Decree No. 410/2005 Coll., Decree on hygienic requirements for the premises and operation of facilities and establishments for the upbringing and education of children and adolescents, Czech Ministry of Health.

[7] Decree No. 20/2012 Coll., amending Decree No. 268/2009 Coll., on Technical Requirements for Buildings, Ministry for Regional Development of the Czech Republic.

IMPACT OF THE BUILT-UP AREA OF A CITY ON THE DIURNAL PATTERN OF TEMPERATURES DURING TROPICAL DAYS

Ing. Martin Minárik [1]
Dr. Vladimír Kišš [2]
Assoc. Prof. Dr. Martin Prčík [2]
Assoc. Prof. Dr. Ján Čimo [1]
Mgr. Maroš Turňa [3]

[1] Institute of Landscape Engineering/Slovak University of Agriculture in Nitra, **Slovakia**
[2] Institute of Law and Sustainable Development/Slovak University of Agriculture in Nitra, **Slovakia**
[3] Slovak Hydrometeorological Institute in Bratislava, **Slovakia**

ABSTRACT

Approximately 5% of the area of Slovakia is made up of built-up areas and courtyards. These represent land where buildings and courtyards, motorways, roads, local roads, railways, airports, and water structures are built. To compare the influence of the urbanized part of the country on the daily air temperature, the city of Nitra, located in the western part of Slovakia, was selected. Meteorological stations are in the territory of the city, from which air temperature data were obtained. For the comparison of the "non-urbanised" part, a meteorological station located in the experimental garden and a station located at the Nitra-Janikovce airport were selected. The summer months from 15 June to 15 September in 2021 and 2022 were selected for comparison. In both years, four periods of heat with temperatures above 30-degree Celzius lasting at least three days were recorded during this period. The onset of temperature after night-time cooling is about the same, but the station in the experimental garden has a delayed onset. Also, the maximum temperature at noon, even during the heat wave, did not reach the same value as at the other stations. The temperature drop arrives identically, but the temperatures in the city do not drop to the same level as the temperatures at the base stations in the evening. It is also interesting to compare the average temperature differences. For the most part, there are larger differences in temperatures between the stations in the city and the station in the experimental garden. The differences between the stations in the city and the station at the airport are noticeable, but not to that extent. Thus, our hypothesis is only partially confirmed. The built-up area affects the diurnal temperature course, especially when it cools down in the evening, but an area with a regularly mowed lawn does not have as much of a positive effect as the public thinks. From our comparison, the experimental garden comes out best, where all stages are represented, including trees and shrubs. These create a more suitable microclimate that better mitigates the effects of climate change.

Keywords: climate change, daily temperature trends, urbanization, tropical days

https://doi.org/10.5593/sgem2024/4.1/s19.54

INTRODUCTION

Today, all our activities are affected by the ongoing climate change. In most cases, this has negative impacts on nature, human activities and on humans themselves. Numerous studies have shown that since the beginning of the industrial revolution, human influence on the climate has increased considerably. The introduction of machinery into production, the increase in demand and the associated increase in production have led to a dramatic increase in the greenhouse gas content of the atmosphere. Their high concentration causes the trapping of reflected short-wave radiation. This trapping is reflected in an increase in average daily, monthly, and annual air temperatures. Increasing temperatures, together with the uneven distribution of precipitation throughout the year, lead to increased evapotranspiration. Logically, with increased evaporative intensity and inadequate rainfall, the likelihood of dry periods increases. Dry spells create stress for all components of the ecosystem, but especially for humans and fauna, but also for flora [1].

Approximately 5% of the area of Slovakia is made up of built-up areas and courtyards. These represent land where buildings and courtyards, motorways, roads, local roads, railways, airports, and water structures are built. Of these, urban and rural developments have the highest share. It is these that create heat islands in times of ongoing climate change. Buildings, roads, and paved surfaces accumulate heat, which is then gradually radiated to the surroundings. It is well known that settlement vegetation reduces these temperature extremes by creating a suitable microclimate through its processes. Also, shading by tree canopies prevents extreme overheating of building facades. The mitigation of temperature extremes in cities is currently receiving a great deal of attention. One mitigation measure is the introduction of green infrastructure in towns and cities [2]. The European Commission, in its Strategy to promote the use of green infrastructure, 'Green Infrastructure - Enhancing Europe's natural capital', defines green infrastructure as 'a strategically planned network of natural and semi-natural areas with other environmental features that are designed and managed to provide a wide range of ecosystem services. It includes green areas (green spaces) or blue areas if they are aquatic ecosystems [3].

MATERIALS AND METHODS

To compare the influence of the urbanized part of the country on the daily air temperature, the city of Nitra, located in the western part of Slovakia, was selected. In 2018, I.S.D.D plus s.r.o. installed 10 meteorological stations in the territory of the city. These record basic meteorological characteristics (temperature, humidity) and air quality (ozone content, PM2.5 and PM10 particulate matter). The data are available in a clear web application and are updated at 10-minute intervals. These stations were positioned by GPS as part of the field survey. Their location is shown in the map in Figure 2. We used five of them because others did not have completely data. These five stations are Hviezdoslavova ulica, Štefánikova trieda, Jesenského ulica, Dopravné ihrisko a Kmeťova ulica. Stations are shown on Figure 1.



Fig. 1: Meteorological stations (from left: Hviezdoslavova ul., Experimental garden, Nitra-Janikovce airport) (Kišš, 2024)

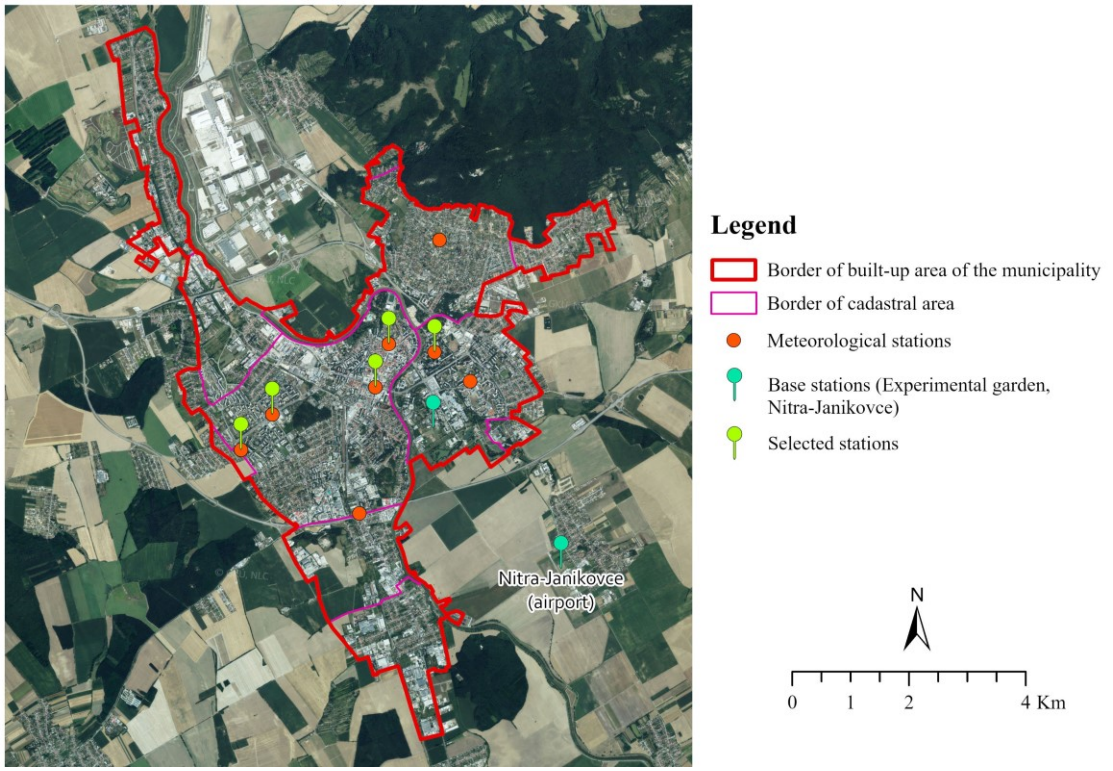


Fig 2: Position of meteorological stations in Nitra (Minárik, 2024)

Data from these stations were compared with two so-called baseline stations. One is in the experimental garden of the Slovak University of Agriculture in Nitra. Its surroundings are composed of herbaceous, shrub and tree vegetation. It is also located at a sufficient distance from the surrounding buildings so that they do not affect the measurements. The second base station is located at the Nitra-Janikovce airport. This is a rural type of airport designed for small aircraft. The surface of the runway is regularly mown grass.

For our comparison, we chose the period from 15 June to 15 September in the years 2021 and 2022. In these years, the data were complete at all stations. Further, we were interested in heat waves during these periods when the temperature reached at least 30 degrees Celzius and the heat wave lasted for at least 3 days.

According to these our specified criteria, we found four periods of hot weather in both years. To highlight the temperature extremes, we extended each period by two days before the onset of the heat and two days after the onset of the heat. It is at least clear to see the rise and fall of temperature extremes. For a more detailed description of the

https://doi.org/10.5593/sgem2024/4.1/s19.54

individual waveforms, we have chosen one period in each year. Specifically, these are the periods 16.6.2021 - 26.6.2021 and 24.6.2022 - 4.7.2022. Both selected heat periods are long enough to reliably depict the temperature progression in the built-up area during tropical days. Each comparison was shown in two graphs. One represents the daily temperature traces during the study period in hourly intervals. The other represents the average differences between a given station and the two baseline stations. Also, the daytime period lasting from 6:00 to 17:00 and the nighttime period lasting from 18:00 to 5:00 are considered separately.

RESULTS

When evaluating the results, we see a partial confirmation of our initial hypothesis. First, we take the selected heat period in 2021. Here we see that the onset of temperature is gradual (Figure 3 a_1 - e_1). The daily temperature traces coincide with small deviations in most of the observed stations. The temperature progression is mainly dependent on the environment in which a particular station is located. Most stations are in an area surrounded by buildings, paved areas, and roads. Station Dopravné ihrisko is in a courtyard, which is largely made up of green areas. Therefore, a difference can be seen in the daily temperature patterns. At the onset of the hot season here, we see that the temperature rises equally in the morning and morning hours at all observed locations. It reaches a maximum in the midday hours and then gradually decreases. In all graphs the temperature at the station Nitra-Janikovce has a similar pattern as the temperature at the stations in the city. The course of temperature in the experimental garden does not reach such a maximum as the other compared stations. Also, a difference can be seen in the evening when the temperature in the experimental garden decreases more than at the other compared stations. When we look at the average temperature differences (Figure 3 a_2 - e_2), we see that the largest differences are observed during the night interval compared to the experimental garden. In some cases, a higher difference is also recorded during the daytime interval. Compared to the Nitra-Janikovce station, the differences decrease during the hot season. Respectively, the diurnal differences are much lower than the nocturnal ones. The largest differences are recorded mainly during the day at the end of the heat period. This is true for the comparison with both base stations. When cooling down after a heat wave, the individual differences decrease.
Similarly, the 2022 heat season is similar (Figure 4 a_1 – e_1). It can also be seen from the comparison that the morning onset of extremes is similar, with a delayed onset for the experimental garden. Also, the stations in the city and at the Nitra-Janikovce airport reach higher maximum temperatures than the station in the experimental garden. In the evening, when the cooling occurs, the temperatures at the stations in the city do not drop to the same level as at the base stations. The night and day temperature differences are comparable to 2021 (Figure 4 a_2 – e_2). There are still higher differences in night temperatures compared to the station in the experimental garden. The highest differences in daytime temperatures are recorded before the end of the heat season. There are again higher differences in nighttime temperatures when compared to the experimental garden. However, for the Nitra-Janikovce station, these night temperature differences increase towards the end of the heat period. This is probably due to the gradual accumulation of heat by buildings and paved surfaces in the city. These surfaces cool down more slowly than the grassy surface of the airport runway.

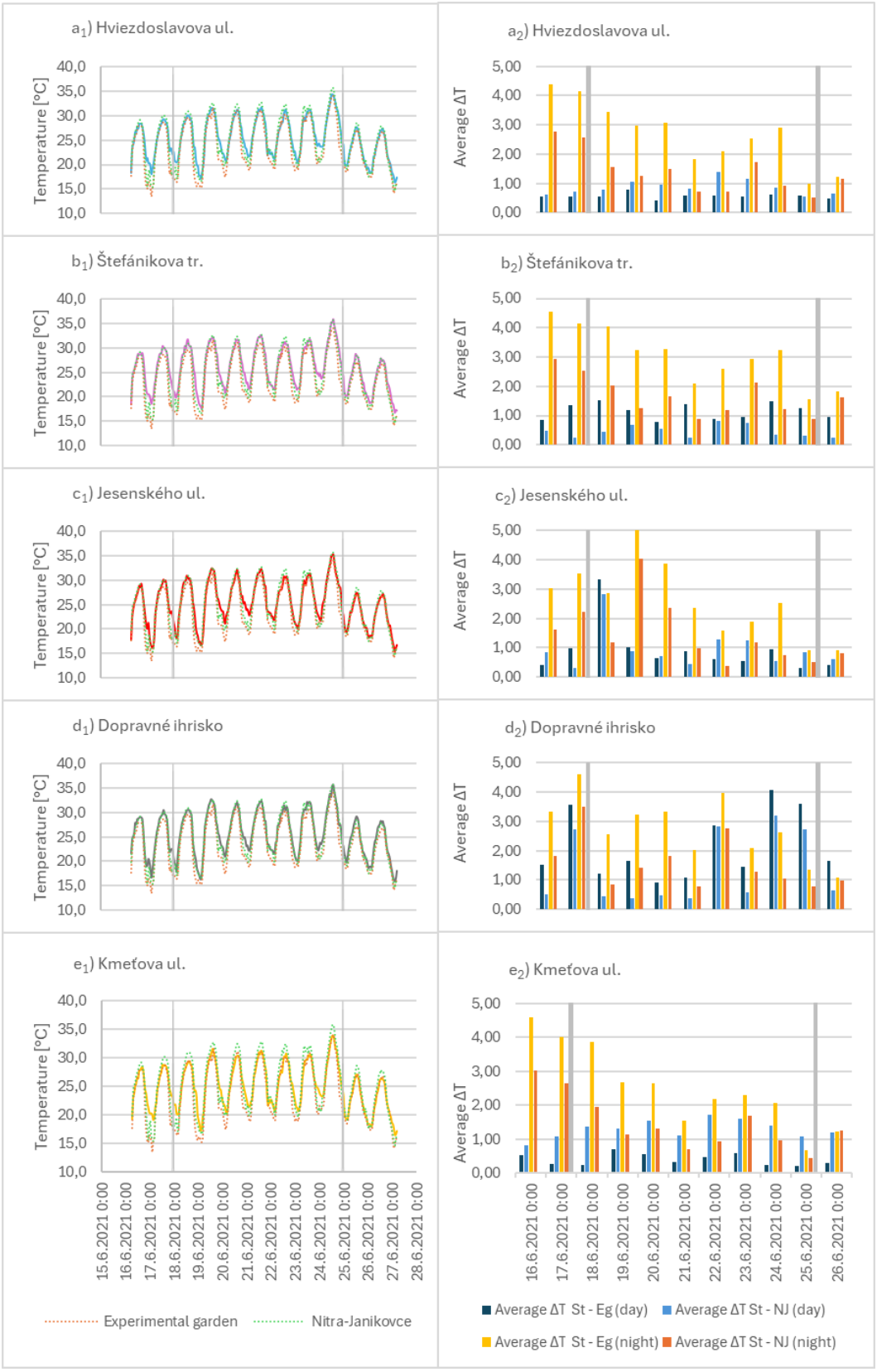


Fig. 3: Development of temperatures during heat wave in 2021
Average ΔT - average temperature difference; St – station; Eg – experimental garden; NJ – Nitra-Janikovce

https://doi.org/10.5593/sgem2024/4.1/s19.54

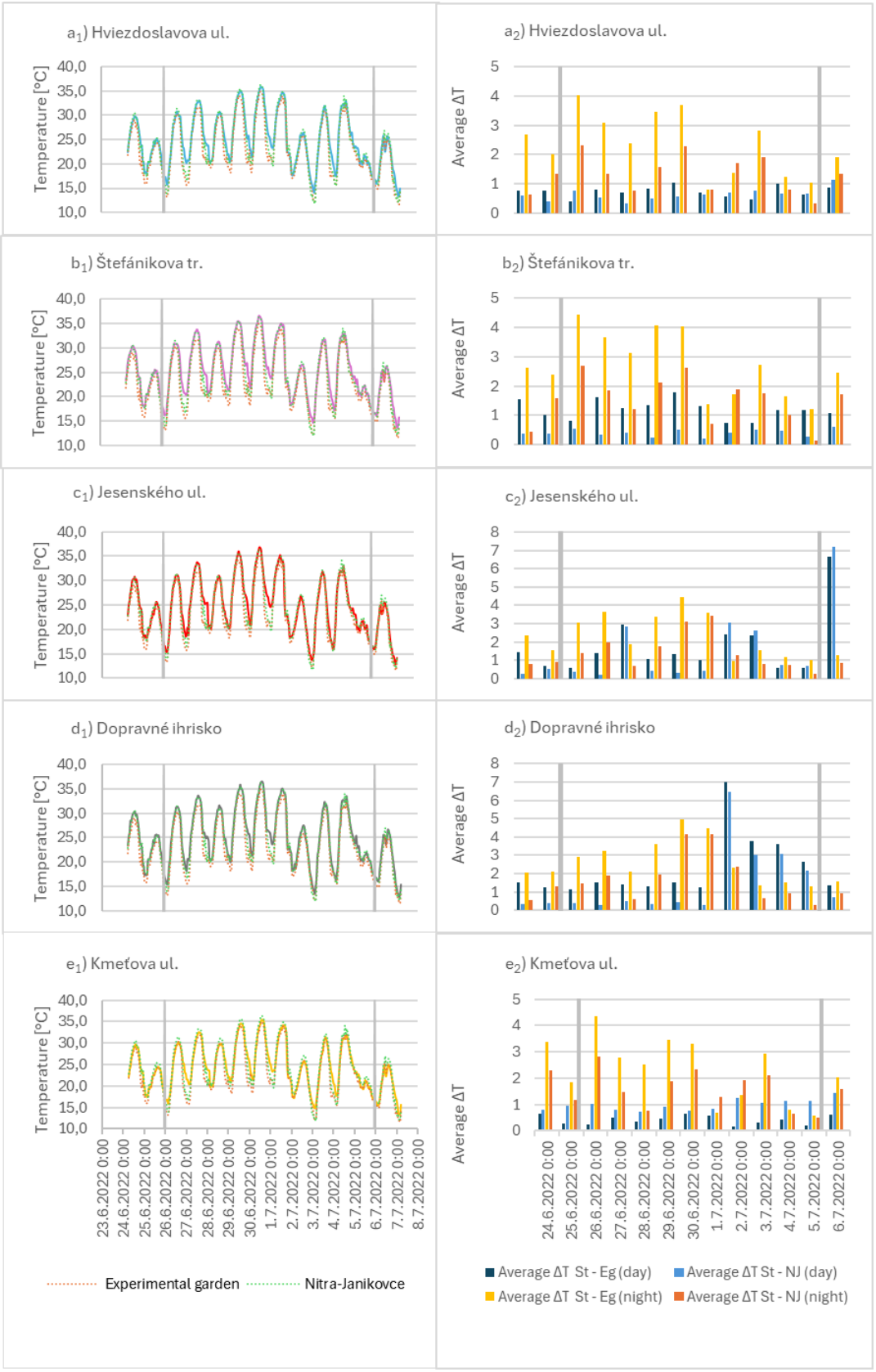


Fig. 4: Development of temperatures during heat wave in 2022

Average ΔT - average temperature difference; St – station; Eg – experimental garden; NJ – Nitra-Janikovce

DISCUSSION

Our results also support those of other studies conducted to determine the impact of built-up area on air temperature. Leeper, Ronald D. et at. (2019) conducted a study on the impact of cities on temperature in 2019. In their research, they measured temperature at certain distances from the city and found that the smallest differences in temperatures were measured at the stations closest to the city. The differences in measured temperatures also increased as the distance from the city increased. However, the largest differences were recorded in the evening, where the differences were approximately 1.0 degrees Celzius. As a result, even minor heat mitigation measures within 50 m of the city were able to reduce extreme temperature patterns [4].

Czarnecka, Kuchcik and Baranowski published a study in 2024 where they looked at urban temperature conditions as indicators of development. They examined the impact of temperature on different areas of life. Their results show that of all the characteristics studied, the biologically vital area has the greatest influence on temperature, which has the greatest influence on the thermal extremes in the city. Also, the height and density of buildings have a very significant influence. The problem is the formation of heat islands, which are most pronounced in the evening [5].

Hellings and Rienow (2021) carried out a study to investigate the pattern of temperatures in urbanised areas. The research was based on data from cities across Europe. Their results clearly show that the density of built-up areas has a direct influence on the formation of urban heat island. Their results also show that the built environment had on average higher temperatures than green areas. The difference was in some 4-6 degrees Celzius in some cases. Agricultural land close to cities showed similar values to the urban environment. A large effect according to the degree of built-up area, height of buildings and the proportion of green space, the composition of green areas and the morphology of the area [6].

CONCLUSION

At the outset, we set out a hypothesis for our work. This was that built-up areas with paved surfaces would have a greater influence on the diurnal pattern of temperatures. Paved areas and buildings accumulate more heat, which causes that in the evening it does not get so cold. We compared the stations in the city with two baseline stations, one in the experimental garden of the Slovak University of Agriculture in Nitra and the other at the rural airport Nitra-Janikovce. The comparison clearly shows that the effect of maintained grassland on the diurnal temperature pattern is not as significant as we thought. The temperature histories at the city and Nitra-Janikovce stations are similar. Comparatively higher differences in temperatures were recorded at the station in the experimental garden. Compared to the stations in the city, the night temperatures here were lower by an order of magnitude of 1.0 degrees Celzius. Here there is clear evidence that an environment composed of herbaceous, shrub and tree vegetation create more suitable conditions during periods of heat. This needs to be borne in mind when designing settlement vegetation to better help it fulfil its mitigation functions in the context of ongoing climate change, which is also associated with an increase in extreme heat events. Regularly mown lawns do not fulfil this required function to a sufficient extent.

https://doi.org/10.5593/sgem2024/4.1/s19.54

ACKNOWLEDGEMENT

This publication was supported by the Cultural and Educational Grant Agency no. Kega 026SPU-4/2023.

REFERENCES

[1] IPCC, 2022: Climate Change 2022: Impacts, Adaptation and Vulnerability. Contribution of Working Group II to the Sixth Assessment Report of the Intergovernmental Panel on Climate Change [H.-O. Pörtner, D.C. Roberts, M. Tignor, E.S. Poloczanska, K. Mintenbeck, A. Alegría, M. Craig, S. Langsdorf, S. Löschke, V. Möller, A. Okem, B. Rama (eds.)]. Cambridge University Press. Cambridge University Press, Cambridge, UK and New York, NY, USA, 3056 pp., doi:10.1017/9781009325844.

[2] Enviroportal, Využívanie územia, enviroportal.sk, Slovakia, 2023, https://www.enviroportal.sk/indicator/detail?id=161

[3] European Commission. (2013). Green Infrastructure - Enhancing Europe's Natural Capital. [Brochure]. Retrieved from https://ec.europa.eu/environment/nature/ecosystems/docs/green_infrastructure_brochure.pdf.

[4] Leeper, Ronal D. et al., Impact of Small-Scale Urban Encroachment on Air Temperature Observations, Journal of Applied Meteorology and Climatology, vol. 58/issue 6, pp 1369-1380, DOI10.1175/JAMC-D-19-0002.1

[5] Czarnecka K., Kuchcik M., Baranowski J., Spatial development indicators as a tool to determine thermal conditions in an urban environment, Sustainable Cities and Society, vol. 100, https://doi.org/10.1016/j.scs.2023.105014

[6] Helling A., Rienow A., Mapping Land Surface Temperature Developments in Functional Urban Areas across Europe, Application of Remote Sensing in Urban Climatology, 13(11), 2111, https://doi.org/10.3390/rs13112111

NEURAL NETWORK MODELING OF THERMAL ENGINES POWERED BY ALTERNATIVE FUELS FOR THE PURPOSE OF REDUCING ATMOSPHERIC POLLUTION

Assoc. Prof. Dr. Eng. Constantin Georgescu[1]

Assoc. Prof. Dr. Eng. Valentin Amortila[1]

Assoc. Prof. Dr. Eng. Cristian Muntenita[1]

[1] "Dunarea de Jos" University of Galati, **Romania**

ABSTRACT

This research investigates the increasing use of alternative fuels in internal combustion engines, a phenomenon that has experienced significant growth in recent decades due to the heightened interest in reducing atmospheric pollution. Although the pollution level associated with alternative fuels is generally lower compared to fossil fuels, it is essential to emphasize that the pollutant impact of alcohol-based fuels depends on various factors, such as engine technology, mixture composition, fuel quality, and usage patterns. Thus, this study analyzes the influence of the alcohol proportion in gasoline on engine performance and, consequently, atmospheric pollution through an innovative optimization method. This method is based on the use of a neural modeling computer application, EasyNN, which generated a series of neural models with 1, 2, or 3 hidden layers. The data were obtained through tests performed on a four-stroke single-cylinder engine with a capacity of 582 cm^3. Following the neural network modeling, it was concluded that the most advantageous combination is represented by an alternative fuel based on gasoline with a concentration of 6% methanol + 1.05% ethanol. In order to reduce the pollutant impact of vehicles, investigations in this field are ongoing, focusing on optimizing efficiency and reducing emissions associated with vehicles adopting alternative fuels.

Keywords: methanol, ethanol, atmospheric pollution, neural networks

INTRODUCTION

To mitigate the polluting impact of automobiles, the automotive industry and researchers are focusing on the development of more efficient propulsion technologies, including electric and hybrid vehicles. These technologies have the potential to significantly reduce greenhouse gas emissions and local pollution [1], [2], [3]. The promotion of a more efficient driving style and the advancement of emission reduction technologies at both the vehicle and infrastructure levels play a crucial role in combating air pollution.

The utilization of alternative fuels such as ethanol and methanol may be less polluting in some aspects, but they can still generate pollutant emissions under certain conditions. The combustion of alternative fuels, such as gasoline and alcohol blends (such as ethanol), can contribute to air pollution, albeit to a lesser extent than traditional fossil fuels [1]. It is imperative to consider a multitude of factors in this context.

https://doi.org/10.5593/sgem2024/4.1/s19.55

CO_2 Emissions: Ethanol and methanol are considered biofuels as they are derived from plants or other natural resources. When used in gasoline-alcohol blends, such as E10 (containing 10% ethanol), they can reduce carbon dioxide (CO_2) emissions compared to pure gasoline. However, the production and transportation of these biofuels can also generate CO_2 emissions.

Pollutant Emissions: The use of ethanol in gasoline blends can impact atmospheric pollutant emissions, such as carbon monoxide (CO) and volatile organic compounds (VOCs). The use of ethanol may lead to an increase in nitrogen oxide (NO_x) emissions, which can contribute to the formation of tropospheric ozone and photochemical smog, negatively impacting air quality.

Engine power, torque, and fuel consumption can significantly influence air pollution. Here's how these factors are linked to pollutant emissions:

Engine power is the ability of the engine to generate mechanical energy to propel the vehicle. High-powered engines may produce higher pollutant emissions compared to low-powered ones. High-powered engines, especially those with large natural aspiration, may require a richer fuel mixture to operate correctly at maximum power, leading to increased emissions of carbon monoxide (CO) and volatile organic compounds (VOCs). The power developed by an engine using ethanol or methanol depends on several factors such as engine design, compression ratio, propulsion system characteristics, and the exact composition of the fuel blend.

The energy value of a fuel is expressed in energy units, usually megajoules (MJ) or kilocalories (kcal) per unit of volume or mass. Approximate energy values for ethanol and methanol are as follows: ethanol has approximately 29 MJ/liter (megajoules per liter) or about 7.7 kcal/gram, while methanol has approximately 22 MJ/liter or about 5.56 kcal/gram. It is important to note that, although methanol has a lower energy value than ethanol, it can still be used to generate power. However, due to its toxicity, handling and using methanol require special precautions.

For both fuels, the engine's compression ratio plays a crucial role in efficiency and power development. Methanol, with a higher compression ratio, can benefit from certain advantages, but this depends on the specific engine design [4]. Ethanol is often used in gasoline engines, and generally, the compression ratios of ethanol-fueled engines are similar to those of gasoline-fueled engines. These ratios can generally range between 9:1 and 12:1, depending on the engine design and manufacturer requirements. Engines using methanol may have higher compression ratios than gasoline or ethanol. Compression ratios for methanol-fueled engines can range between 14:1 and 20:1, or even higher, depending on engine design and application.

Engine torque represents the engine's capacity to generate force to move the vehicle. The higher the engine torque, the easier the vehicle can accelerate and navigate diverse terrains. Using the appropriate engine torque can contribute to better vehicle efficiency, potentially reducing fuel consumption and associated emissions.

Fuel consumption is a measure of a vehicle's efficiency and the resources used to propel it over a certain distance. The lower the fuel consumption, the lower the emissions of CO_2 and other greenhouse gases. Fuel consumption can be influenced by various factors, including engine technology, vehicle weight, aerodynamics, driving style, and fuel quality [3], [5].

MATERIALS AND METHODS

Fuel consumption is influenced by several factors, among which the most important are engine power, torque (engine torque), and vehicle weight. A series of other factors, targeting the optimization of combustion processes (supercharging, computerized mixture control, etc.), can be considered by considering the engine displacement. Thus, at the same developed power, a supercharged engine with controlled mixture will have a smaller engine displacement than a traditional engine.

The use of alternative solutions for vehicle fuels has a direct impact on their performance. Both engine torque and the power developed by it, as well as fuel consumption, are influenced by the type/recipe of the fuel used. From this perspective, two issues arise:

- analysing the influence of fuel on vehicle performance.
- optimizing the fuel composition to achieve desired results.

Given that solving the aforementioned problems requires tests conducted on different compositions, under different conditions, which involves time and material consumption, the use of neural network modelling can be a solution to streamline the resolution of these issues.

The analysis was conducted on blends of conventional fuel (gasoline) in various proportions with methanol and/or ethanol. The required experimental data were sourced from [1], obtained through testing on a single-cylinder, four-stroke engine with a capacity of 582 cm^3. Utilizing artificial intelligence (AI) to assess the efficiency of fuels such as ethanol and methanol concerning engine power, torque, and consumption can be a useful and efficient approach. In contrast to the mentioned work, a detailed analysis was performed using artificial intelligence on the influence of the alcohol proportion in gasoline on engine torque and power, with an impact on fuel quantity and, consequently, fuel consumption. Additionally, an original optimization procedure was developed, based on the use of EasyNN software. This application is designed to handle multiple datasets while allowing users to customize functions as they see fit. EasyNN is an AI-based analysis software that employs algorithms and AI models to interpret and extract significant information from input data. It is a machine learning software package that we used for analysing the performance of engines with ethanol and methanol. An original optimization procedure was established based on the use of this software. EasyNN, a Python package, is designed to provide an easy-to-use neural network. The input data, presented in Table 1, represents fuel consumption at different speeds to achieve engine performance, power, and torque.

Table 1 The input data used for the neural network [1]

Engine Rotation [RPM]	Methanol [%]	Ethanol [%]	Engine Torque [Nm]	Engine Power [kW]	Fuel Consumption [g/kWh]
1250	0	0	31.5	4.12	368.6
1500	0.05	0	32	5.02	375.2
1750	0.1	0	33.5	6.14	337.3
2000	0.15	0	28.5	5.96	405.8
2250	0	0.05	26.5	6.24	434.2
2500	0	0.1	23.5	6.15	471.9
1000	0	0.15	30.5	3.19	401
1500	0.1	0.05	30	4.71	401.8
1750	0.05	0.1	30.5	5.58	371
2250	0.05	0.05	26.5	6.24	410.2

https://doi.org/10.5593/sgem2024/4.1/s19.55

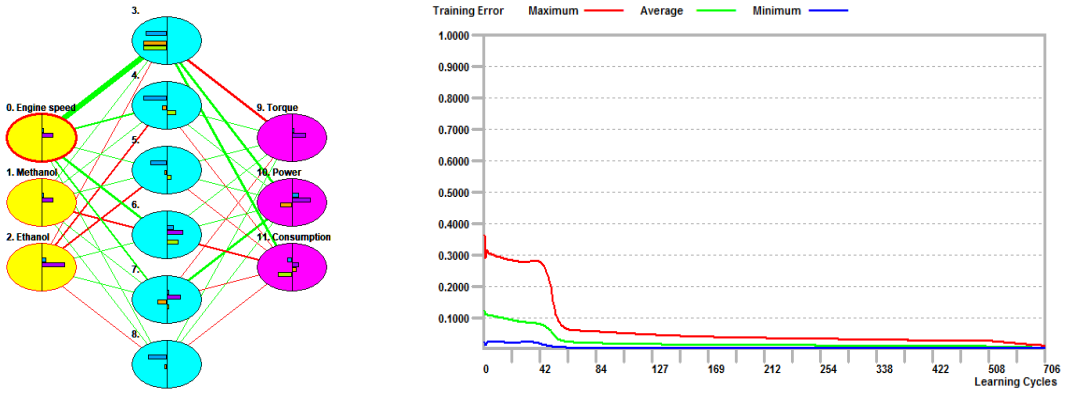
To use this software, it is necessary to gather relevant data for analysis, such as engine operating parameters, fuel composition, combustion efficiency, and others. This data will serve as a training set for machine learning models.

RESULTS

Machine Learning Model, Neural Network, is created to understand the relationships between various variables and engine performance. This model considers specific parameters for ethanol and methanol. Based on the collected data, the machine learning model is trained to understand the engine's behavior based on fuel composition and other variables. The chosen input data, according to Table 1, includes engine speed and the fuel mixture of gasoline with ethanol or methanol, while the output data consists of engine power, torque, and fuel consumption. Initially set parameters for running the neural model are learning rate of 0.9, momentum of 0.8, and maximum error during learning of 0.01%.

Considering that there is an optimal network structure for each analysed problem, multiple networks were tested with one, two, and three layers to determine the optimal architecture. The networks were then compared primarily in terms of sensitivity hierarchy and importance. These two parameters are crucial for assessing the correctness of a neural model. Sensitivity represents the quality of an input to induce major changes in outputs with minimal modifications. Classifying inputs by importance involves ranking them based on the sum of weights along the path connecting the respective input to the output. The second criterion for choosing the optimal network is related to the number of learning cycles; the fewer cycles, the faster, more efficient, and quicker the network learns. In the end, the structure that provides alignment between sensitivity order and input-output importance, with the smallest number of learning cycles, will be chosen [2].

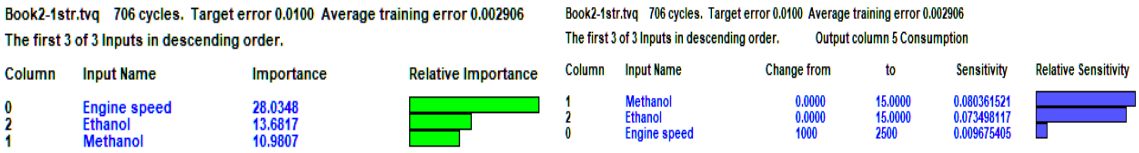
To obtain a model with a single hidden layer, the architecture generator was configured, resulting in the network depicted in Figure 1(a). Following the learning phase, the graph in Figure 1(b) illustrates the evolution of errors throughout the learning process. It is noteworthy that the number of cycles run until achieving the predetermined learning error is 706.



(a) (b)

Figure 1 The single hidden layer neural network model
(a) network architecture with a single hidden layer; (b) graph of the number of learning cycles

In Figures 2(a) and 2(b), the hierarchies of importance and sensitivity are presented, corresponding to the network with a single hidden layer.

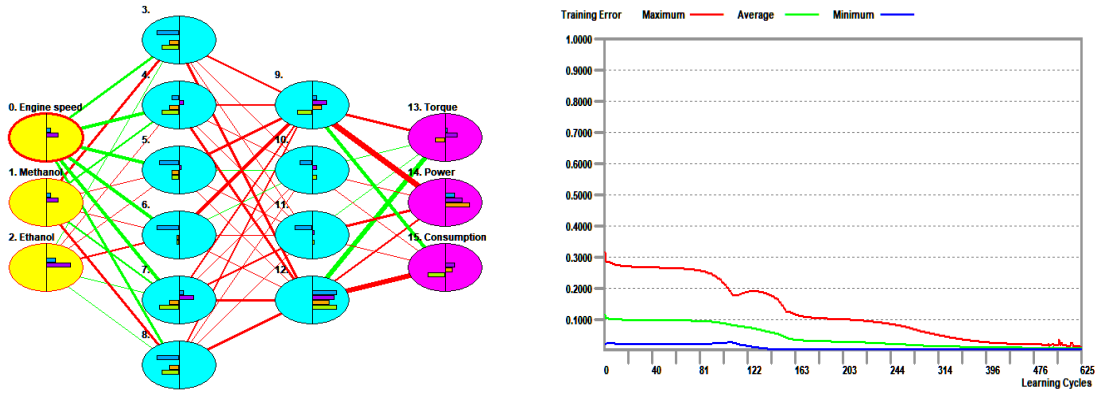


(a) (b)

Figure 2 The order of importance of the input data and its sensitivity to the output data in the single hidden layer model (a) importance (b) sensitivity

It can be observed in the above figures that there is a significant difference between the two hierarchies. Consequently, this model does not provide a sufficient degree of accuracy to be considered.

To obtain a two-layer model, the corresponding options are activated in the architecture generator, and the result is presented in Figure 3(a). The evolution of the learning error for this network is depicted in Figure 3(b).

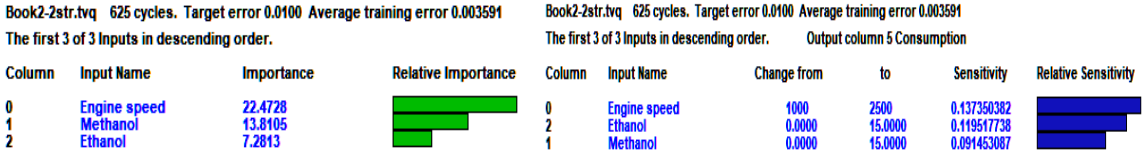


(a) (b)

Figure 3 The neural network model with two hidden layers
(a) network architecture with two hidden layers; (b) graph of the number of learning cycles

In Figure 3(b), it is observed that the number of learning cycles is smaller than that obtained in the case of the single-layer network, specifically 625 cycles. From this perspective, the two-layer network appears to be superior to the single-layer one, [6], [7], [8].

The order of sensitivity and importance of input data on output data is presented in Figures 4(a) and 4(b).



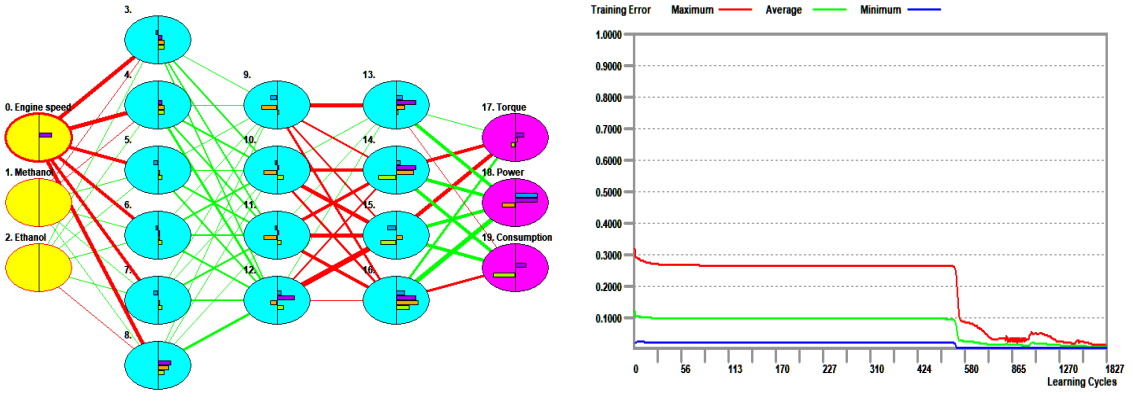
(a) (b)

Figure 4 The order of importance of the input data and its sensitivity to the output data in the hidden two-layer model (a) importance (b) sensitivity

https://doi.org/10.5593/sgem2024/4.1/s19.55

Analysing the above figures, a difference can be observed between the hierarchies of input importance and sensitivity. Consequently, this model does not provide an acceptable level of confidence.

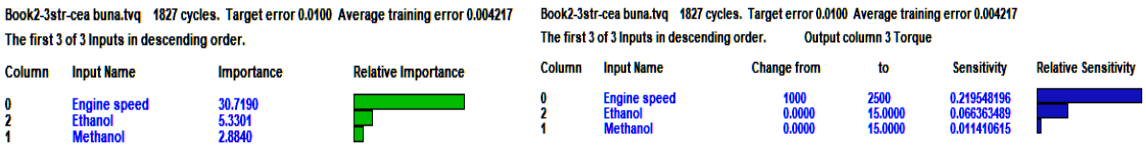
Obtaining a three-layer model is achieved by appropriately modifying the settings in the architecture generator, and the result is presented in Figure 5(a). The evolution of the learning error is depicted in Figure 5(b).



(a) (b)

Figure 5 Neural network model with three hidden layers
(a) network architecture with three hidden layers (b) graph of the number of learning cycles

It is noticeable in the above figure that the number of learning cycles is significantly higher (1827 cycles). This is explained by the elevated number of inter-neuronal connections due to the three hidden layers. Analysing the alignment of the two quality parameters in assessing network quality, namely, importance and sensitivity, a correlation between these parameters can be observed, Figure 6.



(a) (b)

Figure 6 The order of importance of the input data and its sensitivity to the output data in the three-hidden-layer model (a) importance (b) sensitivity

CONCLUSIONS

To conclude and determine the optimal architecture of the neural model for engine power, torque, and fuel consumption, it is necessary to compare the performance of the previously presented models. This involves assessing both the alignment between the hierarchies of sensitivity and the importance of input data on the output and the minimum number of learning cycles, along with the shape of the learning error variation curves. Table 2 provides a comparative presentation of the results obtained with various neural network architectures.

Following the analysis of the data presented in Table 2, aiming to optimize fuel efficiency, the neural network with three layers was chosen. The order of importance and sensitivity of input data coincides, even though the number of learning cycles is higher compared to the other two models.

Table 2 Comparative table of the three neural architectures

Neural network	Learning cycles	Relative importance	Relative sensitivity	Coincidence of importance and sensitivity hierarchies
One hidden layer	706	ES-E-M	E-ES-M	NO
Two hidden layers	625	ES-M-E	ES-E-M	NO
Three hidden layers	1827	ES-E-M	ES-E-M	YES

To establish the error level of the model, it is necessary to test it by comparing the delivered results with real ones for a set of known input data that were not used in the learning process. These were excluded from Table 1 specifically for this purpose. It is worth noting that a neural model cannot process input data outside the minimum or maximum limits of the input data used in training. Therefore, input datasets with extreme values (from Table 1) were used in training the network.

Table 3 presents the actual values of output parameters, the estimated values by the neural model, and the corresponding calculated errors.

Table 3 The actual values of the output parameters and the mean error

Inquiry	Engine Torque [Nm]		Engine Power [kW]		Fuel Consumption [g/kWh]		Mean error. [%]
	Actual	Estimate	Actual	Estimate	Actual	Estimate	
1	32	32.7665	5.02	5.7306	375.2	346.8789	3
2	26.5	24.5498	6.24	6.0119	434.2	453.3059	2.2
3	30	32.9960	4.71	5.9466	401.8	343.7290	7.2
4	26.5	25.0865	6.24	6.1272	410.2	444.3745	0.39
Mean error [%]							3.19

It can be observed in Table 3 that the average prediction error of the neural model is at an acceptable level, considering the limited amount of data used in training the network. To achieve a lower prediction error, the number of training datasets should be in the order of tens.

It is concluded that, once the optimal architecture for the neural model is established, it can be used for:

- analysing the influence of the operational regime (engine speed) and fuel recipe on output parameters, namely torque, power engine and consumption.
- optimizing the fuel recipe to achieve desired performance under imposed operating conditions.
- after model training, it has been used to analyse the future engine performance based on different fuels.
- the model can be optimized to suggest fuel blends that maximize efficiency.

ACKNOWLEDGEMENTS

This scientific work was carried out within the Internal Grant of the 2024 Department of Mechanical Engineering at the Faculty of Engineering of "Dunarea de Jos" University in Galati and the Centre for Interdisciplinary Research in Mechanical Engineering (CCIDIM).

https://doi.org/10.5593/sgem2024/4.1/s19.55

REFERENCES

[1] M.Kapusuz, H.Ozcan, J.A. Yamin, “Research of performance on a spark ignition engine fueled by alcohol-gasoline blends using artificial neural networks,” Applied Thermal Engineering 91 (2015)

[2] Tony Sandberg, “Heavy Truck Modeling for Fuel Consumption,” Simulation an Measurements, Linkoping Studies in Science and Technology Thesis No. 924, Division of Vehicular Systems, Department of Electrical Engineering, Linkoping University, S–581 83 Link¨oping, Sweden, http://www.vehicular.isy.liu.se/

[3] V. Amortila, “Controversy about car pollution: the electric vehicle or the classic vehicle?,” 19th SGEM Int. Multidiscip. Sci. GeoConference EXPO Proceedings19th, Energy Clean Technol., vol. 9, Dec. 2019.

[4] Z. Tian, X. Zhen, Y. Wang, D. Liu, and X. Li, “Comparative study on combustion and emission characteristics of methanol, ethanol and butanol fuel in TISI engine,” 2019.

[5] S. A. Shirazi, B. Abdollahipoor, B. Windom, K. F. Reardon, and T. D. Foust, “Effects of Blending C3-C4 Alcohols on Motor Gasoline Properties and Performance of Spark Ignition Engines: A Review,” 2019.

[6] J. Mueller, N. Kim, S. Lapointe, M. J. McNenly, M. Sjöberg, and R. Whitesides, “Optimization of fuel formulation using adaptive learning and artificial intelligence,” Artif. Intell. Data Driven Optim. Intern. Combust. Engines, pp. 27–45, Jan. 2022.

[7] Z. hao Ni, F. she Li, H. Wang, and H. Xiao, “Prediction of physical parameters of Jatropha biodiesel-ethanol dual fuel based on topological indices,” Appl. Energy, vol. 328, p. 120202, Dec. 2022.

[8] S.-H. Li et al., “Effects of Ethanol and Methanol on the Combustion Characteristics of Gasoline with the Revised Variation Disturbance Method,” vol. 7, 2022.

OPERATION CHARACTERISTICS OF A SMART MINI HYBRID HEAT PUMP USED FOR THE ENERGY ACCUMULATION

Ing. Alexander Čaja, PhD.[1]

Ing. Nikola Čajová Kantová, PhD.[2]

prof. RNDr. Milan Malcho, CSc.[1]

Ing. Patrik Nemec, PhD.[1]

[1]Department of Power Engineering, Faculty of Mechanical Engineering, University of Žilina, **Slovakia**
[2]Research Centre, University of Žilina, **Slovakia**

ABSTRACT

Heat pumps are important due to their efficiency and a target of climate neutrality. They also reduce the emissions of carbon dioxide. This article deals with the smart mini hybrid heat pump, which is planned to use for heat gain in summer, energy accumulation in the ground storage, and further consumption in winter. This heat pump can get heat from the surroundings or solar collectors. Heat pump water-water has been used in this article. Its input and output parameters were measured, a coefficient of performance (COP) was calculated and also a regression model was created based on the detected operation parameters. The main parameter affecting the operation characteristics of the used heat pump was the temperature of the energy source. The smart mini hybrid heat pump was tested at different temperatures of the heat source. The most suitable source temperature for this heat pump was around 14C with the recorded the highest COP value of 6.71. Based on the results, the smart mini hybrid heat pump can be used to accumulate heat into the accumulation layer and its subsequent removal for heating purposes. When using a combination with thermal solar panels, it is possible to replace the heat pump with a circulation pump in the summer mode. In the winter, it is possible to use photovoltaic panels to produce electricity that would drive the heat pump, which would have a positive effect on the overall energy and emission balance of facilities depending on the location of the building.

Keywords: Heat Pump, Energy Accumulation, Thermal Energy Storage, Coefficient of performance, Climate neutrality

INTRODUCTION

The energy can be obtained mainly in ways that use limited resources such as fossil fuels. In addition, the gaining energy from these sources is also accompanied by harmful side effects that impact human health. However, there are available energy sources, which are less energy-intensive, with a better impact on the environment, and in many cases are also characterized by greater user comfort. These are sources of low-potential heat from the environment. Low-potential heat can be converted into useful heat using heat pumps (HP) [1]. The heat thus obtained can be used, for example, to heat buildings. Low energy potential heat supply systems using the energy of the Sun,

https://doi.org/10.5593/sgem2024/4.1/s19.56

geothermal waters, and the environment represent a certain promising alternative compared to the limited resources of fossil fuels. Low potential heat presents heat below 150 °C. In addition to the widely available heat from solar radiation and geothermal energy, it also offers the possibility of using waste heat, which is generated as a by-product of industrial activity. However, the transformation of low-energy heat into other forms of energy is complicated. Heat pumps that convert low-potential heat to high-temperature heat or a low-temperature cooling outlet are so far the most efficient way to use low-potential heat [2].

Moreover, the European Commission has set a target in the reduction of carbon dioxide emissions by 90% for the building sector by the year 2050. HP presents an effective and environmental way to exploit renewable heat energy. When they are powered electrically, the amount of transferred heat can be three or four times larger than the electrical power consumed, which means that the value of a coefficient of performance (COP) can be 3 or 4 [3]. However, the declared COP corresponds to a certain outdoor temperature. Kazjonovs et al. dealt with a seasonal performance factor (SPF) of heat pump air-to-water [4].

The operation characteristics of a hybrid heat pump were observed in the work of Neubert et al. The authors applied the operation strategy in a field trial in a small unrenovated multifamily house built in 1964. Their results showed a decrease the direct fossil CO_2 emission by 61% [5]. Nakos et al. compared the performance of heat pumps with the older types. The results confirmed the better efficiency since the year 2004 but also the large spread in their performance [6].

The potential of autonomous groud-coupled heat pump was investigated in the work of Michopoulos et al. In general, the size of these systems depends on the building. The authors computed two model buildings' ground heat exchanger lengths for heating and cooling. Their results suggested that the autonomous systems may be deployed in regions with heating degree-days in the 800-950 K-day range [7]. Healy and Ugursal investigated the performance and economic feasibility of ground source heat pumps (GSHP). The results indicated that the GSHP systems are economically preferable to conventional systems. The system parameters can also have a significant effect on performance [8]. However, the long-time running of GSHP in the cooling dominated areas causes heat accumulation and the increasing the temperature under the ground. It results in the cooling performanceand other problems such as the change of thermal and microbial environment, or the organic carbon reserves in the soil. The scheme with a cooling tower in transitional seasons can be proposed for the hybrid GSHP system assisted with cooling tower [9].

This article deals with the smart mini hybrid heat pump, which is planned to use for heat gain in summer, energy accumulation in the ground storage, and further consumption in winter. This HP can get heat from the surroundings (air, water, ground) or solar collectors. Heat pump water-water has been used in this article. It is constructed for small constant amounts of heat energy, but with low electric energy consumption. Its input and output parameters were measured in this article. COP was calculated and a regression model was created based on the detected operation parameters.

Thermal energy storage (TES) systems can be utilized in numerous engineering applications including heat pumps via sensible [10], latent [11], and thermochemical heat storage [12]. TES integration to heat pumps can be achieved by techniques for

short and long term storage [13]. It can be a promising approach for effective and flexible usage of energy and ensuring demand side management. TES units can be integrated to either condenser or evaporator of the heat pumps [14]. Yıldız et al. dealt with the evaluation of thermal performance of a water-to-water heat pump system with a TES unit integration. Their results showed that the inclusion of phase change material can improve the heating time up and COP [14]. TES can be used also in air-source heat pumps, where they are more energy efficient and environment-friendly. However, operational costs are relatively higher, compared to conventional heat pump systems [15].

MATERIALS AND METHODS

The experimental measuring device consists of a circuit of a mini-hybrid heat pump with the working substance R140a and other circuits for heat exchange. The heat-carrying medium in the primary, secondary and tertiary circuits is water. Electrical energy enters the circuit of the heat pump with a value of approximately 380 W. However, this value also depends on the temperature of the heat source and the temperature of the heat consumer. Two circulation pumps ensure the flow of the heat-carrying medium in the water circuits. The connection of the individual components together with the heat pump is shown in Figure 1. Water circulation is divided into three sub-circuits: primary, secondary and tertiary. The secondary and tertiary circuits are connected to the water tank. The primary circuit represents the heat transfer system between the heat pump circuit and the tertiary circuit.

The evaporator takes heat energy from the primary circuit, which cools the water at the outlet of the evaporator, this cooled water subsequently flows back into the heat exchanger of the tertiary circuit. The need to use a tertiary circuit results only from the design of the heat pump constructed in this way. By using a separate exchanger, it is possible to take heat from various sources, either from the ground, from water, from the air, or by connecting thermal solar panels. The heat that was transferred to the refrigerant circuit in the evaporator increases its potential and is further transferred to the secondary circuit through the condenser. The water in the secondary circuit is heated in the condenser and its temperature drops at the outlet of the plate heat exchanger due to the transfer of heat to the water tank. The water in the reservoir is therefore a source of thermal energy and at the same time a heated medium of the experimental device.

a)

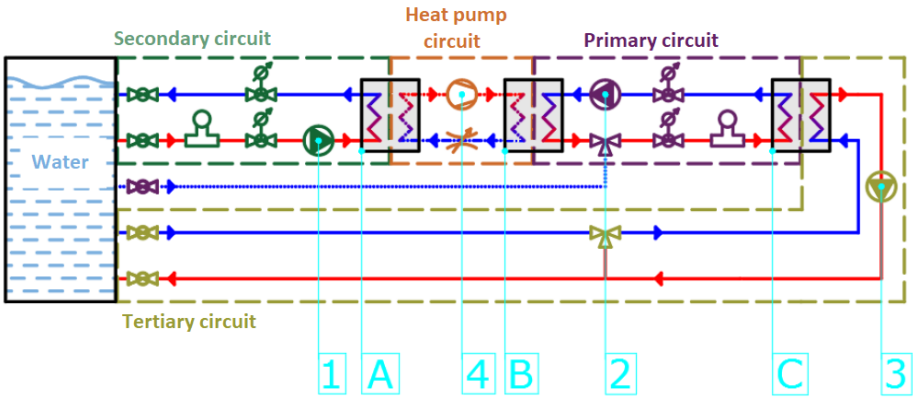


Fig. 1. The connection of the heat pump: 1) circulation pump of the secondary circuit, 2) circulation pump of the primary circuit, 3) cir-culation pump of the tertiary circuit, 4) compressor, A) condenser, B) evaporator, C) separating heat exchanger.

https://doi.org/10.5593/sgem2024/4.1/s19.56

The designed experimental device was constructed in an external company and later installed in the laboratory for more detailed analyzes of its properties. The device is shown in Figure 2. All pipes, where unwanted heat transfer would occur, are insulated with foam insulation with a thickness of 20 mm. Individual water temperatures were measured using PT100 temperature sensors at five different locations. The measuring points were located before the inlet to the evaporator and the condenser, at the outlet from the evaporator and the condenser, and in the water tank itself. The accuracy of the used temperature sensors was ± 0.01°C.

The volumetric flow of circulating water in the primary and secondary circuits was recorded using a Yokogawa AXF015G magnetic flow meter with a standard accuracy of ± 1%. Subsequently, using the calorimetric equation, we determined the heat output on both the primary and secondary sides. To determine the COP, we also needed to record the electricity consumption of the compressor itself. The electric current and the electric voltage at the input to the pumps before the heat pump and the compressor were sensed and subsequently processed into an output signal of 4-20mA for the datalogger with the help of electrical quantity converters. All temperature sensors and magnetic flowmeters were also connected to the datalogger.

The initial temperature of the heat source and storage tank was set at 10°C. In the container, the temperature was homogenized due to the location of the inlet and outlet openings and the stirrer used. Subsequently, the recording and the measurement itself started. Since the water in the container served as a source and at the same time as a consumer of heat, the temperature of the water increased more slowly. The increase in temperature in the vessel was dependent only on the energy supplied by the compressor.

b)

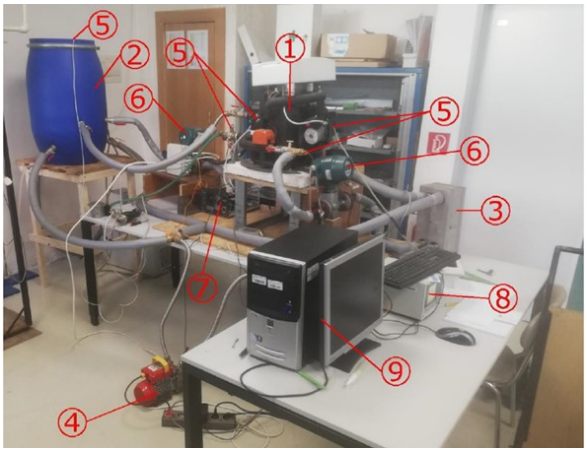


Fig. 2. The experimental setup: 1) heat pump, 2) water tank, 3) heat exchanger, 4) circulation pump of the tertiary circuit, 5) temperature sensor, 6) flow meter, 7) current and voltage converter, 8) data logger, 9) computer.

The efficiency of the heat pump is expressed using the power coefficient value. It is actually a ratio where the numerator shows the heat output obtained from the heat pump and the denominator shows the electricity consumption for the drive compressor. COP was calculated according to equations (1) and (2).

$$COP = \frac{Q_k}{P_{el}} \qquad (1)$$

Q_k is the heat transferred by the condenser and P_{el} is the electrical input of the heat pump.

$$Q_k = \frac{\rho_v \cdot \dot{V^{-1}}}{3600} \cdot c_v \cdot \triangle T \quad (2)$$

where ρ_v is the water density, V^{-1} is the volume flow of water, c_v is the specific heat capacity of water and $\triangle T$ is the temperature difference.

The regression statistical method was used to interpret all temperatures during the measurements according to the equation (3). The regression parameters of the polynomial function were found using Excel for each measured temperature. They express the dependence of the temperatures on the time passed since the beginning of the measurement. Time was chosen as the common variable x, and it was the only quantity with a linear course in the measurements. Polynomial regression of the 2nd degree was chosen for all temperatures, except for temperatures T1" and T2". Due to their more complex course, polynomial regression of the 6th degree was chosen for these temperatures in the second measurement.

$$y = a_n x^n + a_{n-1} x^{n-1} + \cdots + a_2 x_2 + a_0 \quad (3)$$

where y is the first known value, x is the second known value, and a_n is the regression parameter.

RESULTS

After measuring the operation parameters of the experimental equipment, all results were processed using regression statistical analysis, and the characteristics of the heat pump were then derived from these values. The results of the measured values and these derived parameters were individual graphs depending on the source temperature in the container.

The regression statistical method with a polynomial regression function of the 2nd degree was used with the aim of creating a functional mathematical model expressing the mutual correlation of T5 temperature and time since the beginning of the measurement. This method most closely corresponded to the development of T5 temperature. For all temperatures, except for temperatures T1" and T2", polynomial regression of the 2nd degree was chosen. They had a relatively continuous concave development. For temperatures T1" and T2" in measurement no. 2, polynomial regression of the 6th degree was chosen due to their more complex course.

Temperatures T1', T2', T3', T4', T1", T2", T3" and T4" as a function of time t' are also shown in Figures 3-4. The increase in temperature was continuous without significant fluctuations. The increase in temperature over time was dependent on the temperature of the heat source. The temperature of the source increased only by the value of the energy supplied by the compressor, because the heat source was also a heat consumer.

Regression analysis with a polynomial function was also performed on the measured volume flows. The courses in the primary and secondary circuits were recorded with a very small time interval. The recording interval was 1 second. For this reason, each measurement was more accurate, but the database contained a large number of measured quantities. The temperature did not change significantly during the time interval in realized measurements.

https://doi.org/10.5593/sgem2024/4.1/s19.56

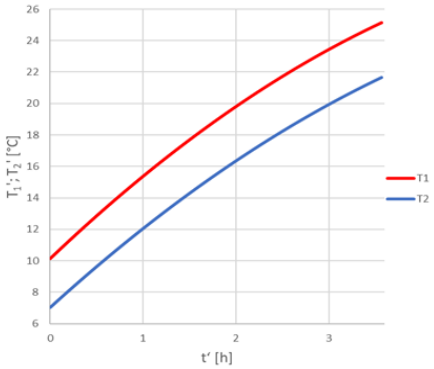


Fig. 3. Temperatures T_1' and T_2', as a function of time t'.

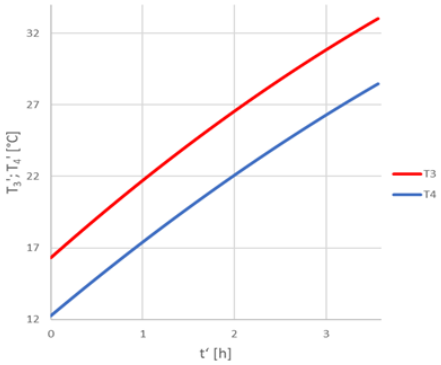


Fig. 4. Temperatures T3' and T4' as a function of time t'.

DISCUSSION

It can be observed that the COP value slowly decreased with the rising temperature of the heat source. It can be assumed that it could be caused by the overall overheating of the system. This resulted in a gradual reduction in the volume of refrigerant sucked in by the compressor and thus a gradual increase in the necessary work of the compressor itself. Another factor affecting the COP of the given mini heat pump was the gradual increase in temperature on the secondary side. The volume of water was constantly heated, which also increased the condensation temperature in the condensers of the heat pump. Such a state was caused on purpose. This mini heat pump is intended to accumulate heat in the massif and then consume the stored heat in the colder period. By constantly supplying heat to the accumulation layer, the temperature of this layer increases, which was actually simulated by the rising temperature of the water on the secondary side. Since the mini heat pump was connected according to Figure 1, the temperature of the source was also the condensation temperature and the rate of heating the water tank was dependent only on the work supplied by the compressor itself.

CONCLUSION

Humans should try to use renewable energy sources due to the limited natural energy sources used for heating. It should be also realized with the aim of the reduction of environmental burden. The low-potential heat of the environment can be converted into useful heat with the help of heat pumps. Another option for reducing heat production for the purpose of heating is heat accumulation in the summer time. Further, this heat can be used during the winter season. The base plate is located mostly directly under the heated object, thus a part of the heat can be transferred through the pipes. As the amount of heat stored in the accumulation layer decreases, the temperature of the layer itself also decreases. For this reason, a smart mini hybrid heat pump was put into heat circuit, which it increased the potential of the extracted heat and transformed it into heat with parameters usable for the heating system.

The goal of the measurements was to verify the suitability of using a mini heat pump for the purpose of heat accumulation in a massive concrete plate. By measuring and analyzing the results, it was found that the main parameter affecting the operating characteristics of the used heat pump was the temperature of the energy source T_1. The condensation heat Q_k, the extracted heat Q_o, the total electrical input of the circulation pumps (1, 2) and the compressor (4) increased with the increasing temperature T_1.

However, the COP of the experimental device decreased with the increasing T_1, because the thermal performance curve of the experimental device rose more slowly than the electrical input P_{el}. This phenomenon was caused by the insufficient thermal insulation of the storage tank. In the real case, the concrete storage layer would be placed in the ground, what it would mean a similar situation to the storage tank. Part of the heat would escape into the surrounding soil despite its isolation around the perimeter with polystyrene. Another aspect is the fact that, the compressor would have to deliver significantly more work with the increasing condensation temperature depending on the type of refrigerant. As a result, the ratio between transferred heat and supplied work would change.

The analysis of the results showed that the heat Q_o and Q_k, also the COP of the experimental device were closely related to the volume flow of all involved circulation pumps. The operation of these circulation pumps was partly uneven in this case, but they did not have a significant connection with the temperature T_1.

Based on the measurements and the evaluation of the individual quantities, it can be summarized that the smart mini hybrid heat pump can be used to accumulate heat into the accumulation layer and its subsequent removal for heating purpose. When using a combination with thermal solar panels, it is possible to replace the heat pump with a circulation pump in the summer mode. In the winter, it is possible to use photovoltaic panels to produce electricity that would drive the heat pump, which would have a positive effect on the overall energy and emission balance of facilities depending on the location of the building and his source of heat. The average production of CO_2 when burning solid fuels is around 0.25 - 0.35 kg CO_2 per 1 kWh. For more accurate data, it is necessary to know the specific type of fuel and its properties. In 2016, the average production of CO_2 in the production of electricity in Slovakia was approximately 0.133 kg CO_2/kWh. This figure includes all sources of energy used in Slovakia, including nuclear power, coal, gas and renewable sources. When using a heat pump and taking COP into account, CO_2 production will drop by more than 90% compared to solid fuel boilers.

ACKNOWLEDGEMENTS

This publication has been produced with the support of the project KEGA 032/ŽU-4/2022 "Implementation of knowledge about modern ways of reducing the environmental burden in the energy use of solid fuels and waste into the pedagogical process".

REFERENCES

[1] Esen, H., Inalli, M., Esen, M. Numerical and experimental analysis of a horizontal ground-coupled heat pump system. Building and Environment, 2007, Volume 42, Issue 3, Pages 1126-1134. DOI: 10.1016/j.buildenv.2005.11.027.

[2] Wang, R.Z., Xu, Z. Y., Hu, B., Du, S., Pan, Q. W., Jiang, L., Wang, L. W. Heat pumps for efficient low grade heat uses: from concept to application. Thermal Science & Engineering, 2019, Volume 27, No. 1.

[3] Valancius, R., Singh, R. M., Jurelionis, A., Vaiciunas, J. A review of heat pump systems and applications in cold climates: evidence from Lithuania. Energies, 2019, 12, 4331. DOI:10.3390/en12224331.

https://doi.org/10.5593/sgem2024/4.1/s19.56

[4] Kazjonovs, J., Sipkevics, A., Jakovics, A., Dancigs, A., Bajare, D., Dancigs, L. Performance analysis of air-to-water heat pump in Latvian climate conditions. Environmental and Climate Technologies, 2014. DOI: 10.1515/rtuect-2014-0009.

[5] Neubert, D.; Glück, C.; Schnitzius, J.; Marko, A.; Wapler, J.; Bongs, C.; Felsmann, C. Analysis of the operation characteristics of a hybrid heat pump in an existing multifamily house based on field test data and simulation. Energies 2022, 15, 5611. DOI:10.3390/en15155611.

[6] Nakos, H., Haglund Stignor, C., Andersson, K., Lidbom, P., Thyberg, S. Air-to-air heat pumps evaluated for Nordic climatestrends and standards. 11th IEA Heat Pump Conference, 2014, May 12-16 2014, Montréal (Québec) Canada.

[7] Michopoulos, A., Papakostas, K.T., Kyriakis, N. Potential of autonomous ground-coupled heat pump system installations in Greece. Applied Energy, 2011, 88, p. 2122–2129. DOI: 10.1016/j.apenergy.2010.12.061.

[8] Healy, P.F.; Ugursal, V.I. Performance and economic feasibility of ground source heat pumps in cold climates. Int. J. Energy Res. 1997, 21, p. 857–870.

[9] Zhou, A., Cui, W., Li, Z., Liu, X. Feasibility study on two schemes for alleviating the underground heat accumulation of the ground source heat pump. Sustainable Cities and Society, 24, 2016, p. 1-9. DOI: 10.1016/j.scs.2016.03.014

[10] Badescu, V. Model of a thermal energy storage device integrated into a solar assisted heat pump system for space heating. Energy Conversion and Management, 44, 2003, p. 1589-1604.

[11] Qi, Q., Deng, S., Jiang, Y. A simulation study on a solar heat pump heating system with seasonal latent heat storage. Solar Energy, 82, 2008, p. 669–675. DOI: 10.1016/j.solener.2008.02.017.

[12] Lizana, J., Chacartegui, R., Barrios-Padura, A., Valverde, J.M. Advances in thermal energy storage materials and their applications towards zero energy buildings: a critical review. Applied Energy, 203, 2017, p. 219-239. DOI:10.1016/j.apenergy.2017.06.008.

[13] Cabeza, L.F., Solé, A., Barreneche C. Review on sorption materials and technologies for heat pumps and thermal energy storage. Renewable Energy, 110, 2017, p. 3-39. DOI:10.1016/j.renene.2016.09.059.

[14] Yıldız, C., Seçilmiş, M., Arıcı, M., Mert, M. S., Nižetić, S., Karabay, H. An experimental study on a solar-assisted heat pump incorporated with PCM based thermal energy storage unit. Energy, 278, 2023, 128035. DOI: 10.1016/j.energy.2023.128035.

[15] Yu, M., Li, S., Zhang, X., Zhao Y. Techno-economic analysis of air source heat pump combined with latent thermal energy storage applied for space heating in China. Applied Thermal Engineering, 185, 2021, 116434. DOI: 10.1016/j.applthermaleng.2020.116434.

RECENT CHANGES IN THE SNOW COVER DURATION IN BULGARIA – PRELIMINARY RESULTS

Assist. Prof. Dr. Dimitar Nikolov[1]

Assist. Prof. Dr. Cvetan Dimitrov[1]

Msc. Radoslav Evgeniev[1]

[1] National Institute of Meteorology and Hydrology, **Bulgaria**

ABSTRACT

Snow cover is an indicator of the fluctuating climate, resulting from the change in the regime of winter precipitations and air temperatures. Our previous studies have revealed significant decreasing of the seasonal snow cover maxima and the precipitation amounts in the highest mountainous regions of Bulgaria, which is however not so strong at lower altitudes. Current research summarizes our last findings about one other characteristic of the snow cover – its duration. This is presented as annual number of days with snow cover with different heights. We have used 62 weather stations with altitudes ranging from 20 up to 2376 m a.s.l. Statistical analysis is performed in order to assess the variability and possible differences in the investigated characteristic from long-term data series for two main climatological periods 1961-90 and 1991-2020.

The general tendency for the whole country is a decreasing trend, more pronounced at the northwest and north parts of Bulgaria with some opposite exceptions with much smaller magnitude at some isolated places at northeast and south. Remarkable decreasing of the snow cover days in comparison with the period 1961-1990 has been encountered in the mountainous regions – in the regions of Koprivshtitza (Stara planina) and Cherni vrah (Vitosha Mountain) the decline is almost one month. We have investigated the mean annual number of snow cover days in three different height categories – all days with snow cover, and those above the limits 15 and 30 cm. Some of the results are presented graphically as maps of the current stage together with the deviation from the previous climatic periods.

This investigation is part of a project for investigation of the current variability of the snow cover and was funded by the Bulgarian National Science Fund in the call for young and post-doctoral researchers under contract number DM14/1.

Keywords: snow, snow cover duration, climate change

INTRODUCTION

Snow cover is an important meteorological variable acting as interface between the process in the atmosphere and under the ground. It can change the surface albedo and the thermal conditions of the underlying layers [1, 3, 11 and 17]. Snow cover keeps plants and other species from frost in coldest winter months [15], it serve as important water resources [13] and has significant importance for the winter sports and tourism [4, 5]. Many authors have reported shorter snow cover duration accompanied by increased

https://doi.org/10.5593/sgem2024/4.1/s19.57

winter air temperatures [2, 6-10, 12, 14, 16]. The main goal of the project has been to investigate the recent tendencies in all characteristics of the snow cover in Bulgaria but the current one has been limited only to the snow cover duration in terms of number of snow days.

MATERIALS AND METHODS

Data for the registered days with snow cover from 62 meteorological stations have been used in this study for the main period 1961- 2020. This time length covers two reference climatological periods – 1961-1990 and 1991-2020. However, several stations have not the full range and cover only until 2019. The tendencies in the mean seasonal number of days with snow cover (NDSC) were assessed by the Mann-Kendal test for linear trend. For more clear view of the picture of the changes, for few stations we have extended the investigated period back to 1930 and have estimated the monthly NDSC. We have investigated the NDSC in three categories – all registered days and those above the thresholds 15 and 30 cm. The study has been focused mainly on the stations from the lowland and that is way high mountain stations (above 1500 m) are only included in the first category.

RESULTS

NDSC – all registered days

The first examined snow height categories includes all registered days with snow cover. The results for the current climatic period (1991-2020) are presented on Figure 1. Mean seasonal NDSC varies between 10 on the coastal zones, through 20-30 in South Bulgaria, 40-54 to the north, above 55 in mid altitudes, up to 174 in the highest regions (around 2300 m).

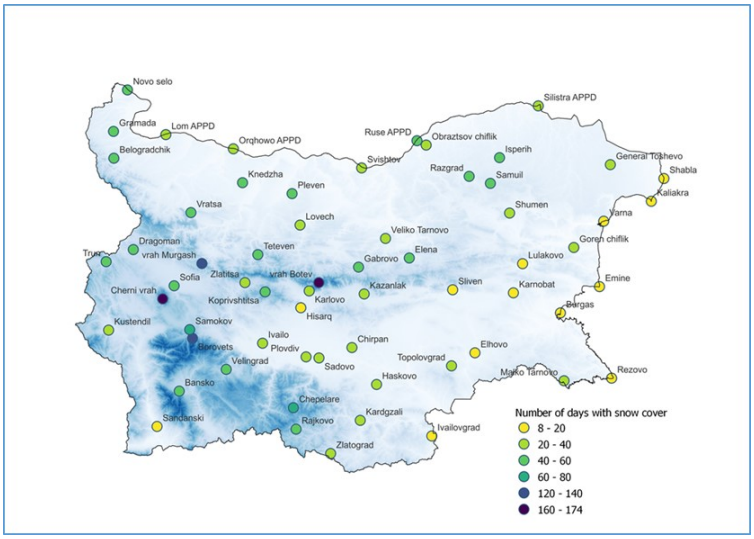


Fig. 1. All registered NDSC for the period 1991-2020

On next figure are depicted the deviations of the current norms of NDSC from the previous ones (1961-1990).

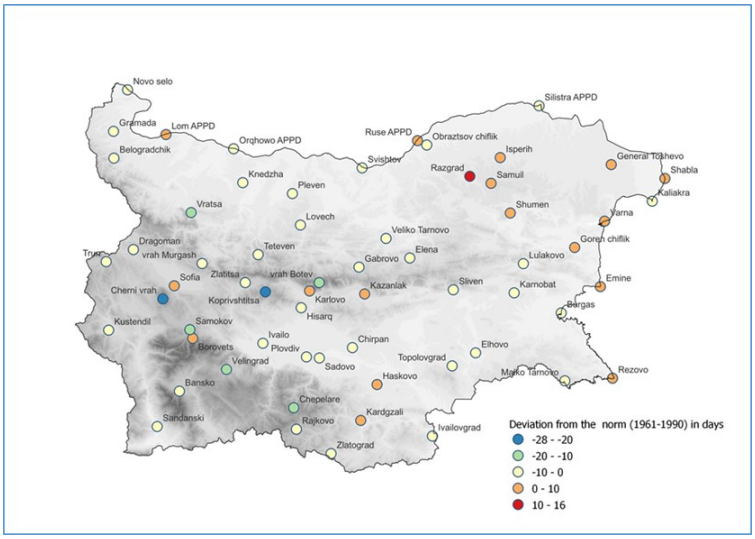


Fig. 2. Deviations in the current norms of NDSC from these for the period 1961-1990

It can be seen that the general tendency is decreasing of this characteristics, stronger in north Bulgaria with some isolated exceptions to the northeast. However, most pronounced and remarkable is the decreasing in the mountain regions. At stations Botev vrah (2376 m) it is nearly half a month (14 days) and at Koprivshtitza (1060 m) and Cheni vrah (2290 m) – almost a moth – 28 and 25 days correspondingly. Surprisingly is also the lower magnitude of the decreasing in the lowlands. The current popular feelings are that the snow has almost disappeared but this figure does not support it. Statistically significant at the 0.05 level are only the changes in NW Bulgaria. That is way, in order to get more detailed view on ongoing changes, we have extended the examined time back to 1930 for four selected stations – Vratza (NW), Shumen (NE), Sadovo (S) and Gramatikovo (SE coastal zones) and the results are shown on next 2 figures.

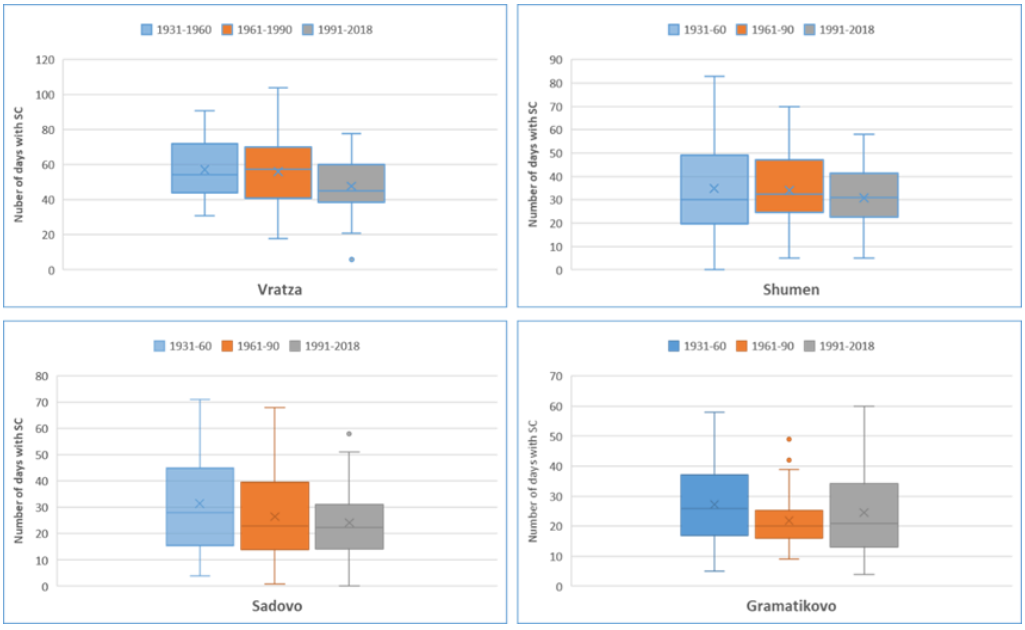


Fig. 3. Box-plots presentation of the statistical distribution of the NDSC for three reference periods – 1931-1960, 1961-1990 and 1991-2020

https://doi.org/10.5593/sgem2024/4.1/s19.57

On Figure 3 are presented as box-plots the comparisons of the statistical distributions of the NDSC for three climatological periods - 1931-1960, 1961-1990 and 1991-2020. It can be seen that, when including also the earliest period, the changes become significant also for the regions to the east (Shumen) and south (Sadovo), but remains almost with no changes for the south coastal regions (Gramatikovo).
We have also determined the monthly NDSC for the same stations and now the differences are more evident and as depicted below, it allows concluding that the strongest decreasing happens always in the coldest month – January. Stations from the north have strong declining also in next two months (Fabruary and March), while Sadovo shows greater lowering of the NDSC in November and December. Gramatikovo demonstrates this only for January.

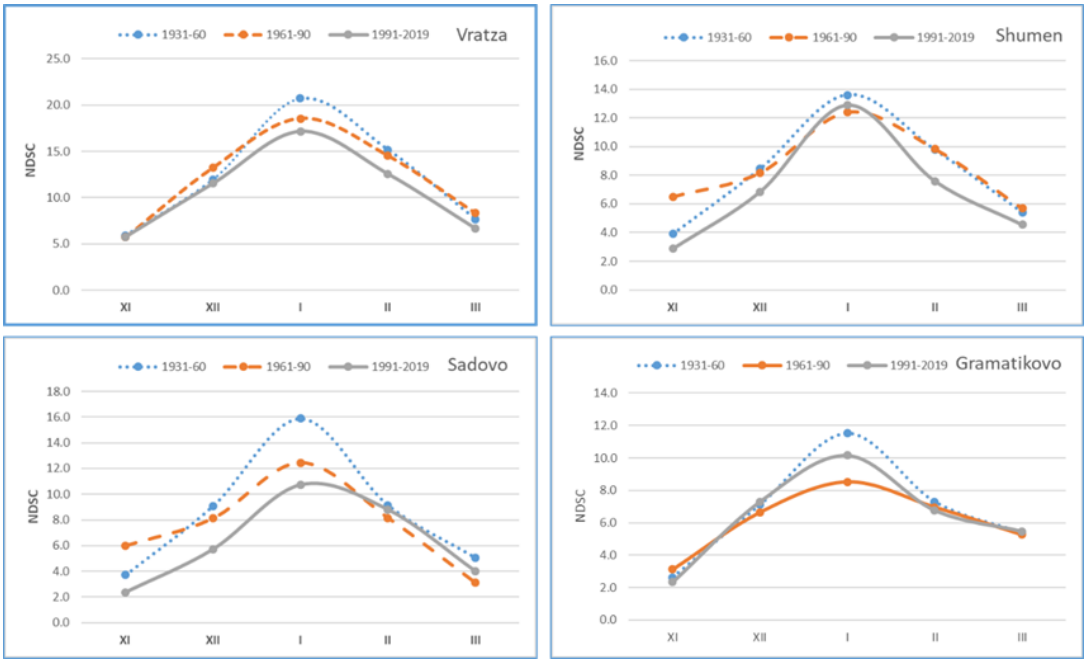


Fig. 4. Mean monthly values of the NDSC for 4 selected stations – Vratza, Shumen, Sadovo and Gramatikovo

NDSC – above 15 and 30 cm

The differences between NDSC above the thresholds 15 and 30 cm for the current climatic period and 1961-1990 are decreasing with increasing the thresholds. This is presented on next two figures – Figure 5 and Figure 6. The picture to the left depicts the spatial distribution of the corresponding above threshold NDSC and the right one the deviation from the previous period (1961-1990). The highest values of NDSC above used thresholds are in the mountains and in North Bulgaria. The greatest differences are again in the mountain areas. It should be mentioned again that only few of them have been included. We have selected two of them to illustrate this behaviour – Koprivshtitza and Chepelare (1232 m) – see figures 7 and 8. A clear decreasing trend can be observed on the data for the NDSC above 15 cm for both stations, for Koprivshtitza for the whole period and for Chepelare only after the 1980-s. No such trend can be found for the NDSC above 30 cm for both stations, rather it seems that there is periodicity in the data. This peculiarity is manifested also in the data for the stations from the lowland.

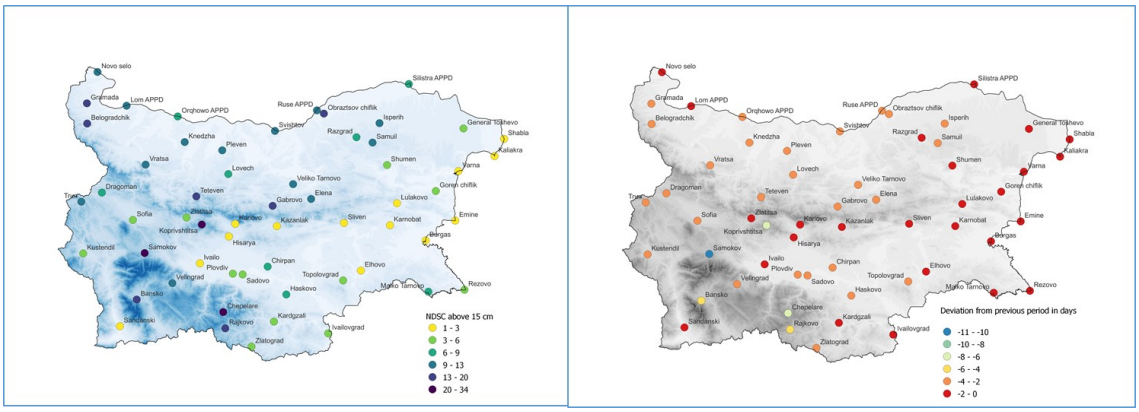


Fig. 5. Left – NDSC above 15 cm for the period 1991-2020; left – the corresponding deviation from the previous period (1961-1990)

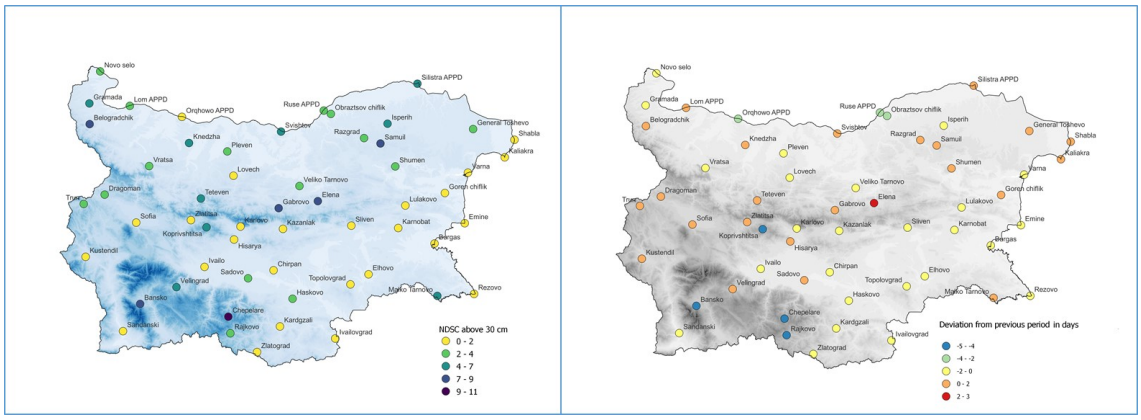
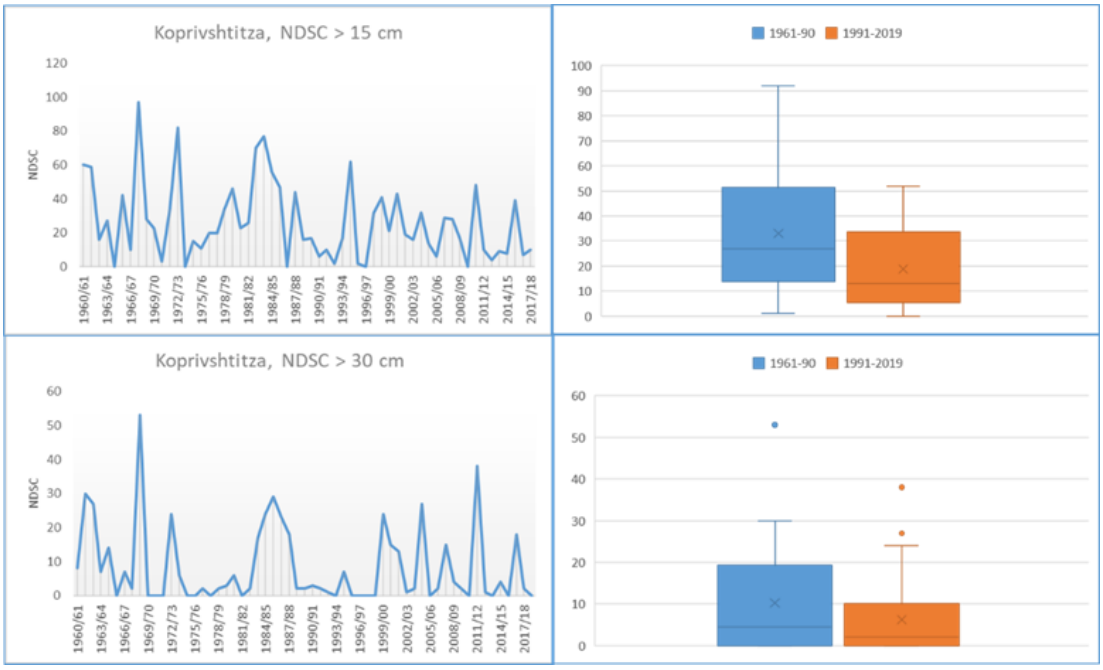


Fig. 6. The same as for Fig.5. but for NDSC above 30 cm



https://doi.org/10.5593/sgem2024/4.1/s19.57

Fig. 7. Change in NDSC for 1961-2019 above 15 and 30 cm for stations Koprivshtitza and comparison of the 2 periods

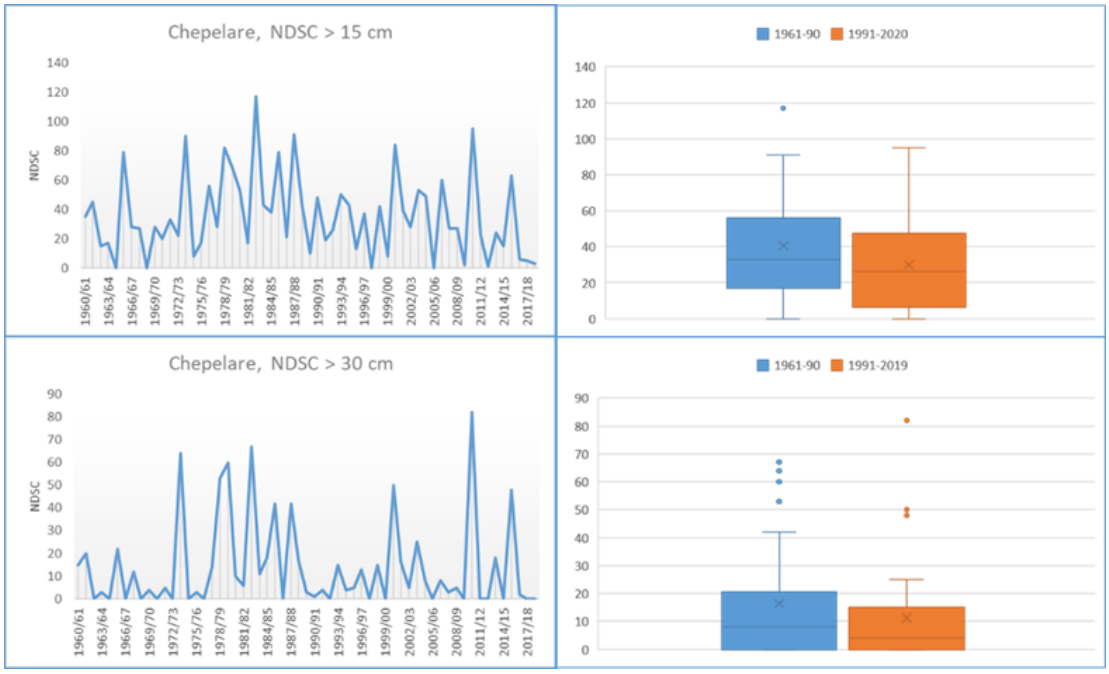


Fig. 8. Same as for fig. 5 but for stations Chepelare

DISCUSSION

The expectation that snow is being disappearing has not been confirmed so strong by the finding of this study. However, snow decreasing seems to be most pronounced in the very recent years, which were not included in the current research, because we have been focused on the comparison of the last two climatic periods. Now the need to extend the period to nowadays has been obviously rising.

Other surprising outcome was that the mountain regions of the country are the most affected by the decreasing of the snow cover duration. Another authors have reported results showing greater decline in snow height and snow duration for lowlands areas, with lower influence in high altitude [e.g. 8]. We need to check the behavior of the winter air temperatures and precipitation for searching for a possible explanation. Actually, we have already started this investigation.

CONCLUSION

A general tendency of decreasing of the snow cover duration in terms of days with snow cover has been found. It is strongest in Northwest Bulgaria and, surprisingly, in the mountain regions. In the northwest, the decreasing is of magnitude of several days, but in the highest zones, it reaches nearly a month.

In the north parts of the country, the most significant decreasing is in the coldest months – January and February, as well as in March. In south Bulgaria, it seems that such decreasing is happening in the beginning of the winter – November and March, but again January demonstrates the greatest decline. On the costal line this actually the only

months which possess any changes in the NDSC. All this imply the assumption that the decreasing of the snow cover duration in Bulgaria is rather due to an earlier snowmelt than to a delayed snow onset. However, it might be also explained by lower solid precipitation amounts in the coldest months. Both hypotheses need to be investigated further and our preliminary results show that probably both are acting combined.

The snow cover duration above 15 cm shows also a decreasing tendency but no so strong and is again most expressive in some mountain regions with altitudes about 1000 m. The NDSC with the threshold of 30 cm demonstrate even lower decline than this of 15 cm. Most of the stations manifested a picture, which implies probably periodicity in the seasonal trend.

ACKNOWLEDGEMENTS

This investigation is part of a project for investigation of the current variability of the snow cover and was funded by the Bulgarian National Science Fund in the call for young and post-doctoral researchers under contract number DM14/1.

REFERENCES

[1] Barry RG. 1992. Mountain Weather & Climate, 2nd edn. Routledge, Chapman and Hall: London. pp 402;

[2] Bednzorz. 2004. Snow cover in Eastern Europe in relation to temperature, precipitation and circulation, International Journal of Climatology, 24, pp. 591-601.

[3] Beniston M. 2006. Mountain weather and climate: A general overview and a focus on climatic change in the Alps. Hydrobiologia 562: 3–16;

[4] Beniston M., 1997. Variations of snow depth and duration In the Swiss Alps over the last 50 years:links to changes In large-scale slimatic forcings, Climate Change, 36, 281-300.

[5] Beniston M. Uhlmann B, Goyette S, Lopez-Moreno JI. 2011. Will snow-abundant winters still exist in the Swiss Alps in an enhanced greenhouse climate? International Journal of Climatology, 31:1257-1263;

[6] Beniston M, Farinotti D, Stoffel M, Andreassen LM, Coppola E, Eckert N, Fantini A, Giacona F, Hauck C, Huss M, Huwald H. 2018. The European mountain cryosphere: a review of its current state, trends, and future challenges. Cryosphere 12:759-794;

[7] Beniston M. Is snow in the Alps receding or disappearing? In: Wiley interdisciplinary reviews. Climate change, 2012, vol. 3, n° 4, p. 349–358. doi: 10.1002/wcc.179

[8] Brown I. 2020. Snow cover variability in Great Britain during a changing climate, International Journal of Climatology, 75,2, pp. 61-66, https://doi.org/10.1002/wea.3625;

[9] Brown RD. 2000. Northern Hemisphere snow cover variability and change, 1915–97. Journal of Climate 13:2339–2355;

[10] Brown RD, Mote PW. 2009. The response of Northern Hemisphere snow cover to a changing climate. Journal of Climate 22:2124–2145;

[11] Cohen J. 1994. Snow cover and climate. Weather 49:150-156;

https://doi.org/10.5593/sgem2024/4.1/s19.57

[12] Hantel M, Ehrendorfer M, Haslinger A. 2000. Climate sensitivity of snow cover duration in Austria. International Journal of Climatology 20:615–640;

[13] Helliwell RC, Soulsby C, Ferrier RC, Jenkins A, Harriman R. 1998. Influence of snow on the hydrology and hydrochemistry of the Allt a'Mharcaidh, Cairngorm mountains, Scotland. Science of the Total Environment 21: 59-70;

[14] Klein, G., Vitasse, Y., Rixen, C. et al. Shorter snow cover duration since 1970 in the Swiss Alps due to earlier snowmelt more than to later snow onset. Climatic Change 139, 637–649 (2016). https://doi.org/10.1007/s10584-016-1806-y

[15] Oke TR. 1987. Boundary layer climates. 2nd edition. Methuen, London.

[16] Wielke, Lucia-Maria; Haimberger, Leopold; Hantel, Michael. Snow cover duration in Switzerland compared to Austria, Meteorologische Zeitschrift Vol. 13 No. 1 (2004), p. 13 – 17, DOI: 10.1127/0941-2948/2004/0013-0013

[17] Zhang T. 2005. Influence of the seasonal snow cover on the ground thermal regime: An overview. Review of Geophysics 43: RG4002. doi:10.1029/2004RG000157

SOLUTIONS FOR REDUCING THE AIR POLLUTION GENERATED BY VEHICLE

Assoc. Prof. Dr. Eng. Mihai Gingarasu

Prof. Dr. Eng. Elena Mereuta

Assoc. Prof. Dr. Eng. Valentin Amortila

Assist. PhD. Ress.. Eng. George Balasoiu

"Dunarea de Jos" University of Galati, **Romania**

ABSTRACT

Reducing air pollution is a major objective of road transport, the most important consequence of this reduction being the decrease in the number of illnesses and, implicitly, a better quality of human life. To achieve this goal, researchers' efforts have been directed towards reducing the quantities and treating the exhaust gases of vehicles equipped with internal combustion engines. It is important to note that the reduction of environmental pollution must also aim at decreasing the emissions of particles that are not generated by the operation of internal combustion engines. The work aims to reduce the pollution generated by the malfunctioning of the steering systems of motor vehicles. Failures of this type cause additional friction between the tires and the roadway, generating additional amounts of NEE particles. The experiments focused on the detection of these faults during driving, using a Dacia Renault vehicle, a Samsung Galaxy brand mobile phone, type A71, with an accelerometer and iNVH-Bosch software for data processing. The analysis of the results revealed that the symptoms of failure of the steering systems, abnormal shocks and vibrations, can be detected while driving, inside the passenger compartment. The paper highlights the possibility of development of an electronic control system, with a software for vibration analysis, in order to implement a predictive maintenance system. The advantages of equipping vehicles with a system of this type are the early detection of faults and the reduction of environmental pollution.

Keywords: vehicle pollution, tire, particle matter, diagnosis, health

INTRODUCTION

Reducing air pollution is a major objective of road transport, the most important consequence of this reduction being the decrease in the number of illnesses and, implicitly, a better quality of human life. To achieve this goal, researchers' efforts have been directed towards reducing the quantities and treating the exhaust gases of vehicles equipped with internal combustion engines[1], [2], [3].

Another measure is represented by the implementation of advanced driver assistance systems (ADAS) on vehicles, which significantly contributes to reducing the number of road accidents, the indirect consequence being the reduction of pollution generated by

https://doi.org/10.5593/sgem2024/4.1/s19.58

the repair processes and the manufacturing of the components necessary for the maintenance[4]. Also, equipping vehicles with on-board diagnostic systems has an important role in increasing the quality of vehicle operation and reducing maintenance costs, the indirect result being the reduction of pollution through the early detection of defective systems and the decrease in the production of spare parts.

The development of electric and hybrid vehicle technology, combined with government subsidies for their commercialization, has led to an increase in the number of such vehicles in operation, resulting in direct consequences in the reduction of combustion gas pollution[5].

It is important to note that, in addition to the measures presented above, the reduction of environmental pollution must also aim at decreasing the emissions of particles that are not generated by the operation of internal combustion engines. These particles, ”non exhaust emissions” (NEE), released into the atmosphere by the wear of tires, brake system components and asphalt, are common to the operation of all road vehicles, regardless of their propulsion system[6], [7].

According to recent research, the particles resulting from the wear of tires and brake system components represent 60% of $PM_{2.5}$ particulate matter emissions and 73% of PM_{10} emissions generated by road transport[8], [9], [10]. Exposure of the population to these emissions, extremely small in comparison to visible matter (figure 1), is associated with a variety of adverse health effects, such as increased risks of cardiovascular, respiratory, developmental conditions and increases a person's chances of dying prematurely[7], [11], [12].

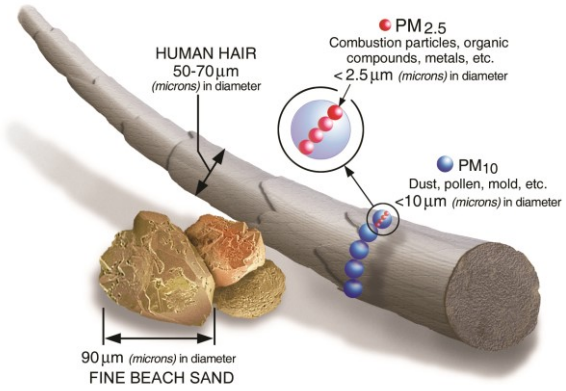


Figure 1. Size comparisons of PM particles[11]

This work aims to reduce the pollution generated by the malfunctioning of the steering systems of motor vehicles. Failures of this type cause additional friction between the tires and the roadway, generating additional amounts of NEE particles. Also, these failures generate increased resistance to movement, the effects being the increase in fuel consumption and the amount of combustion gases emitted into the atmosphere[13].

MATERIALS AND METHODS

International legislation requires periodic technical inspections of vehicles, including their steering systems, conducted at Vehicle Inspection Stations (VIS) under the authority and the control of the state government[14]. Between these inspections, defects may occur and their detection relies on the driver's experience. Wear of the

steering linkage, specifically of the spherical joints in the vehicle's steering mechanism, is accompanied by abnormal sounds, shocks and vibrations during operation[3], [13], [15]. Previous studies have shown that human perception of these symptoms of failure (vibrations and abnormal noises while driving) can be replaced by recording and analyzing vibrations at the defective tie rod ends[2], [3]. The aim of this study is to refine this diagnostic method for steering systems by recording and analyzing the symptoms of failure, abnormal shocks and vibrations while the vehicle is in motion, inside the driver's compartment.

The experiments were conducted on a passenger transport vehicle, of the Dacia Renault brand, with the following technical specifications: 5 seats, including the driver, engine power of 55 kW, 4-cylinder engine, cylinder capacity of 1.2 liters, hydraulic power-assisted steering system, tire dimensions of 185/65 R15, manual gearbox (5+1), maximum authorized total mass of 1586 kg. The tests were conducted under urban traffic conditions, with speeds of up to 50 km/h, tire load pressure of 2.2 bar, using summer tires and with an ambient temperature of 21°C.

For the analysis of abnormal vibration transmissibility in the driver's compartment, the tests were conducted in pairs, under similar conditions, the difference between each pair of tests being the installation of a tie rod end with or without defects. The comparative analysis focused on the symptoms perceived depending on the presence or absence of clearance in the spherical joint of the tie rod end (figure 2). The measurement equipment used consisted of a Samsung Galaxy A71 mobile phone equipped with an accelerometer and the iNVH BOSCH noise, vibration and harshness data processing software, an application developed by Robert Bosch GmbH. To record the vibrations transmitted through the kinematic chain of the steering system, the Samsung device was fixed on the steering wheel, as shown in figure 3. This mounting configuration positioned the X-axis of the accelerometer parallel to the intersection of the vehicle's horizontal and transverse planes. This direction coincided with the direction of measurement of the maximum clearance of 0.5 mm/radius in the defective spherical joint of tie rod end, installed on the vehicle.

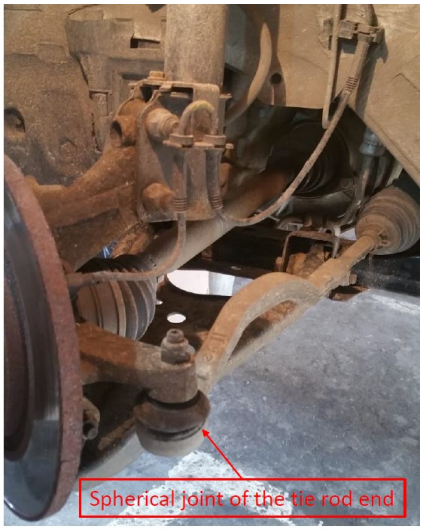


Figure 2. The tie rod end of the vehicle steering system

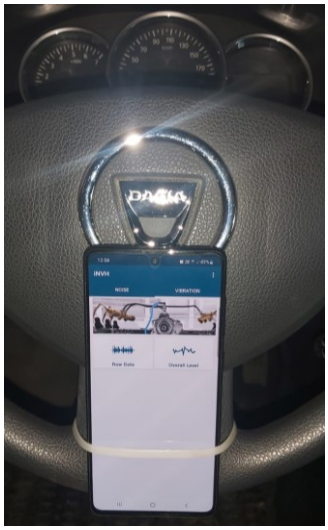


Figure 3. The device position on the steering wheel

https://doi.org/10.5593/sgem2024/4.1/s19.58

To induce the shocks and vibrations in the spherical joint of the tie rod end, the tested vehicle was driven over small bumps, specifically: roads and tram lines intersections, roadway sewer covers and asphalt bumps. The vibrations spectra in the time domain were achieved by recording the vibration accelerations, measured on three axes, at time intervals of 0.01 seconds.

RESULTS

The first pair of tests was conducted by crossing a tram line intersection at a speed of 20 km/h, using the second gear of the gearbox. In the first test, a flawless tie rod end was installed on the vehicle and the vibration accelerations measured on the X-axis of the device were highlighted in the graph in figure 4, shown in blue. In the second test, the conditions were similar to the first test, except that a defective tie rod end was installed on the vehicle. The vibration accelerations corresponding to the test with the defect, measured on the X-axis of the device, are also highlighted in the graph in figure 4, shown in green.

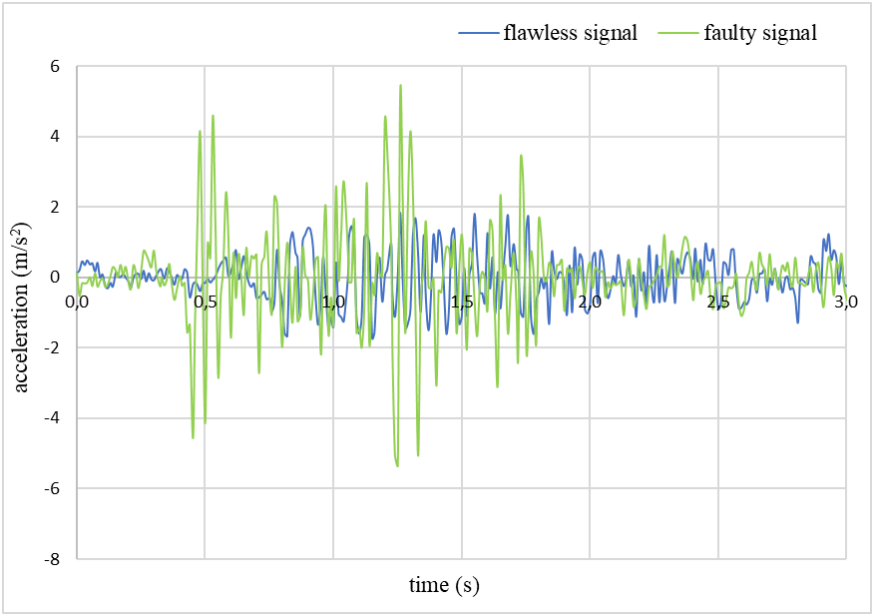


Figure 4. The overlap in time of vibrations spectra, with and without defect, X-axis, vehicle speed of 20 km/h

The variation of the recorded accelerations in a time interval, known as the second-order acceleration, reflects the slope of the acceleration signal over time. Overlaying the two vibrations spectra in the time domain highlights the maximum values of the acceleration slopes recorded in the defective signal scenario, reaching 1048.97 m/s^3, compared to the maximum values of the slopes in the flawless signal, which are 282.72 m/s^3 (figure 5). In the presence of a defect, compared to the flawless signal, traversing road irregularities leads to shocks between the worn components of the spherical joint. Consequently, during traversing road irregularities, the maximum values of the acceleration slopes are amplified, by approximately up to 4 times, due to the clearance in the worn spherical joint. Additionally, the analysis of the recorded data also reveals an increase in the average value of the acceleration slope from the value of the flawless signal, which is 62.36 m/s^3, to the corresponding value of the defective signal, which is 107.94 m/s^3 (figure 5). The ratio between the maximum slope and the average slope of

the accelerations recorded on the X-axis, corresponding to the first flawless test, presented in figure 6, is 4.53.

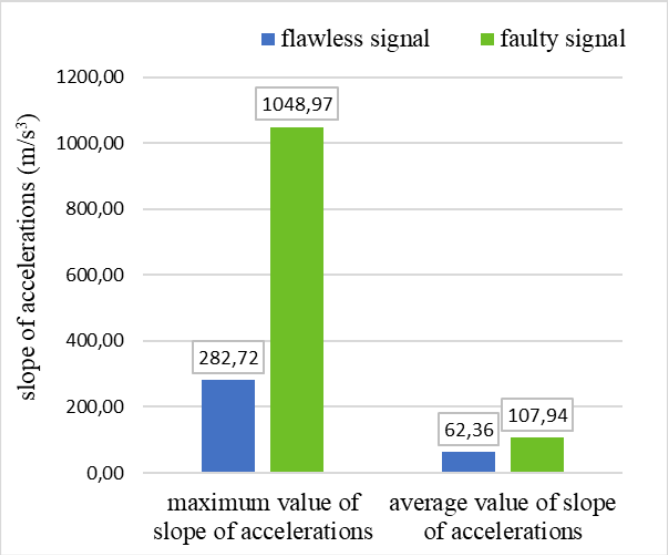


Figure 5. The maximum/average value of slope of accelerations, corresponding to first pair of tests

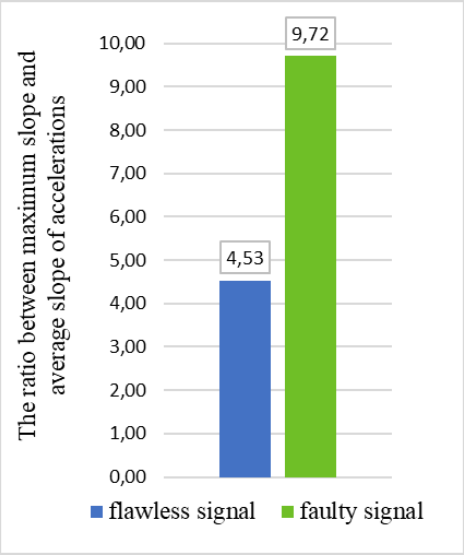


Figure 6. The ratio between maximum slope and average slope of accelerations

Corresponding to the second paired test, with a defect, the ratio between the maximum slope and the average slope of the accelerations recorded on the X-axis, presented in figure 6, is 9.72, showing an increase of over 2 times.

For the second pair of tests, the vehicle was driven over roadway sewer covers, at a speed of 30 km/h, using the third gear of the gearbox. The vibration accelerations corresponding to the flawless and faulty tests, measured on the X-axis of the device, are highlighted in the graph in figure 7, with the colors blue and green, respectively.

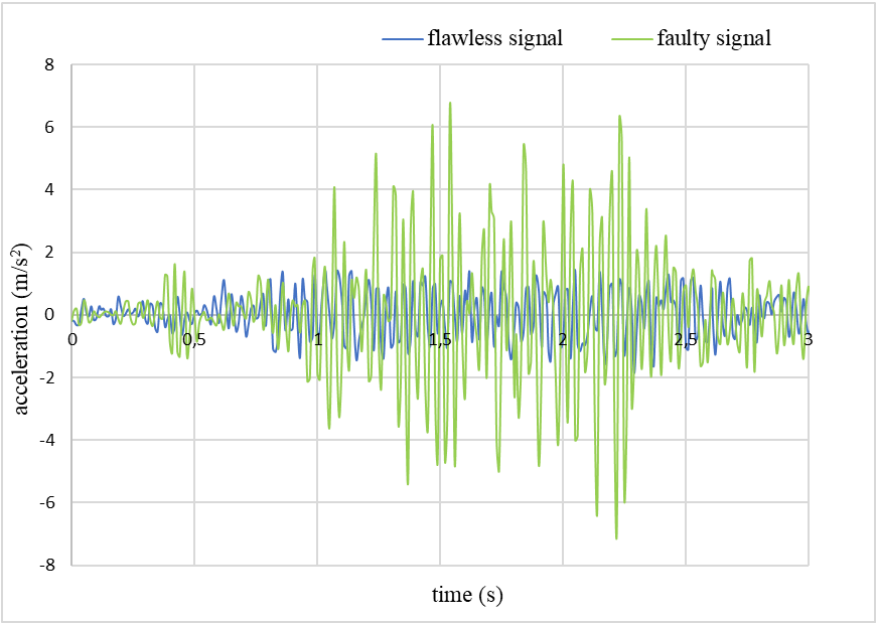


Figure 7. The overlap in time of vibrations spectra, with and without defect, X-axis, vehicle speed of 30 km/h

https://doi.org/10.5593/sgem2024/4.1/s19.58

The second pair of tests highlights the maximum value of the acceleration slopes recorded in the defective signal scenario at 1303.89 m/s^3, compared to the maximum value of the slopes in the flawless signal at 242.66 m/s^3 (figure 8). The maximum values of the acceleration slopes are amplified, by approximately over 5 times, due to the clearance in the worn spherical joint. Additionally, the analysis of the recorded data also reveals an increase in the average value of the acceleration slope from the value of the flawless signal, which is 76.18 m/s^3, to the corresponding value of the defective signal, which is 194.11 m/s^3 (figure 8).

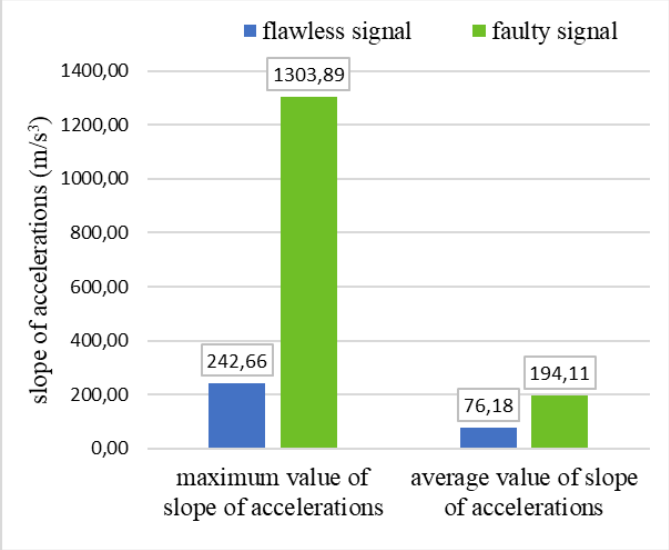


Figure 8. The maximum/average value of slope of accelerations, corresponding to second pair of tests

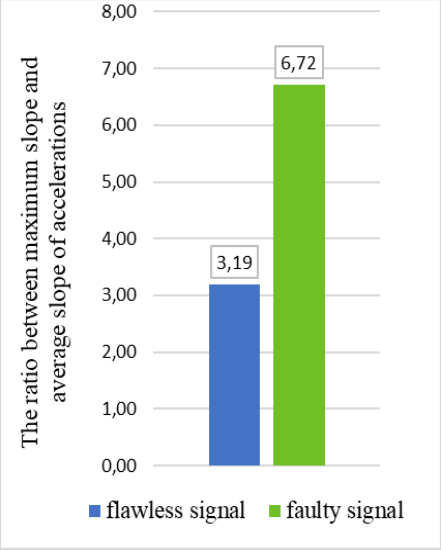


Figure 9. The ratio between maximum slope and average slope of accelerations

The ratio between the maximum slope and the average slope of the accelerations recorded on the X-axis, corresponding to the first test, without defect, presented in figure 9, is 3.19. Corresponding to the second paired test, with a defect, the ratio between the maximum slope and the average slope of the accelerations recorded on the X-axis, presented in figure 9, is 6.72, showing an increase of over 2 times.

CONCLUSION

In order to reduce air pollution generated by premature wear of tires, this paper analyzes the possibility of diagnosing defects in spherical joints based on the vibrations that propagate through the kinematic chain of the steering system, under different operating conditions and depending on the technical condition of the spherical joints (with or without defects of the tie rod end).

The analysis of the results revealed that symptoms of steering system failure, such as abnormal shocks and vibrations, can be detected while driving from inside the driver's compartment. The vibration accelerations measured with the accelerometer of a mobile phone, fixed on the steering wheel, show significant variations in driving situations with or without defects of the tie rod end.

From the comparative analysis of tests conducted on faulty or flawless systems, it is obvious that the ratio between the maximum acceleration slope and the average acceleration slope is considerably higher in defective systems compared to flawless

ones. From these comparisons it results that the doubling of the value of this ratio, compared to the values of the system without defect, can indicate the occurrence of the failure in the systems.

The paper highlights the possibility of development of an electronic control system, even using a simple one (smartphone for e.g.) with an appropriate software for vibration analysis, in order to implement a predictive maintenance system. The advantages of equipping vehicles with this kind of system include early detection of steering system failures and prevention of premature tire wear, thereby promoting cleaner air quality and reducing environmental impact.

REFERENCES

[1] J. Enzmann and M. Ringel, "Reducing Road Transport Emissions in Europe: Investigating A Demand Side Driven Approach †," *Sustainability*, vol. 12, no. 18, Art. no. 18, Jan. 2020, doi: 10.3390/su12187594.

[2] M. Gingarasu, E. Mereuta, V. Amortila, and C. Humelnicu, "The influence of the vehicle steering system missalignment on the environment," presented at the International Multidisciplinary Scientific GeoConference Surveying Geology and Mining Ecology Management, SGEM, 2019, pp. 295–302. doi: 10.5593/sgem2019V/4.2/S04.040.

[3] M. Gingarasu, E. Mereuta, V. Amortila, C. Humelnicu, and M. Novetschi, "The importance of vehicle steering system diagnosis in reducing environmental impact," presented at the International Multidisciplinary Scientific GeoConference Surveying Geology and Mining Ecology Management, SGEM, 2020, pp. 523–530. doi: 10.5593/sgem2020/4.1/s19.065.

[4] A. Ziebinski, R. Cupek, D. Grzechca, and L. Chruszczyk, "Review of advanced driver assistance systems (ADAS)," *AIP Conf. Proc.*, vol. 1906, no. 1, p. 120002, Nov. 2017, doi: 10.1063/1.5012394.

[5] A. Razmjoo *et al.*, "A Comprehensive Study on the Expansion of Electric Vehicles in Europe," *Appl. Sci.*, vol. 12, no. 22, Art. no. 22, Jan. 2022, doi: 10.3390/app122211656.

[6] J. C. Fussell *et al.*, "A Review of Road Traffic-Derived Non-Exhaust Particles: Emissions, Physicochemical Characteristics, Health Risks, and Mitigation Measures," *Environ. Sci. Technol.*, vol. 56, no. 11, pp. 6813–6835, Jun. 2022, doi: 10.1021/acs.est.2c01072.

[7] "WHO global air quality guidelines: particulate matter (PM2.5 and PM10), ozone, nitrogen dioxide, sulfur dioxide and carbon monoxide." Accessed: Apr. 23, 2024. [Online]. Available: https://www.who.int/publications-detail-redirect/9789240034228

[8] D. C. S. Beddows, R. M. Harrison, T. Gonet, B. A. Maher, and N. Odling, "Measurement of road traffic brake and tyre dust emissions using both particle composition and size distribution data," *Environ. Pollut.*, vol. 331, p. 121830, Aug. 2023, doi: 10.1016/j.envpol.2023.121830.

[9] "1907101151_20190709_Non_Exhaust_Emissions_typeset_Final.pdf." Accessed: Apr. 26, 2024. [Online]. Available: https://uk-air.defra.gov.uk/assets/documents/reports/cat09/1907101151_20190709_Non_Exhaust_Emissions_typeset_Final.pdf

https://doi.org/10.5593/sgem2024/4.1/s19.58

[10] B. Baensch-Baltruschat, B. Kocher, F. Stock, and G. Reifferscheid, "Tyre and road wear particles (TRWP) - A review of generation, properties, emissions, human health risk, ecotoxicity, and fate in the environment," *Sci. Total Environ.*, vol. 733, p. 137823, Sep. 2020, doi: 10.1016/j.scitotenv.2020.137823.

[11] O. US EPA, "Particulate Matter (PM) Basics." Accessed: Apr. 27, 2024. [Online]. Available: https://www.epa.gov/pm-pollution/particulate-matter-pm-basics

[12] European Court of Auditors, *Air pollution : our health still insufficiently protected*. in Special report No ... (European Court of Auditors. Online). LU: Publications Office, 2018. Accessed: Apr. 23, 2024. [Online]. Available: https://data.europa.eu/doi/10.2865/80097

[13] M. Wozniak, K. Siczek, G. Ozuna, and P. Kubiak, "A Study on Wear and Friction of Passenger Vehicles Control Arm Ball Joints," *Energies*, vol. 14, no. 11, Art. no. 11, Jan. 2021, doi: 10.3390/en14113238.

[14] L. Carvalho, S. Santos, and C. Ferreira, "A NEW METHODOLOGY FOR DETECTION OF A LOOSE OR WORN BALL JOINTS USED IN VEHICLES SUSPENSION SYSTEM," Jun. 2017.

[15] S. S. Chung, Y. Z. Lee, and S. O. Park, "Practical Evaluation of Ball Stud Plating Effects on the Increase of Free Gap of Ball Joints in the Vehicle," *Int. J. Automot. Technol.*, vol. 21, no. 5, pp. 1107–1111, Oct. 2020, doi: 10.1007/s12239-020-0104-x.

STUDY ON THE INFLUENCE OF THE ENERGY INDUSTRY ON THE LEVEL OF POLLUTION OF WASTEWATER IN ROMANIA

Assoc. Prof. Dr. Eng. Silvia Veresiu[1]

Assoc. Prof. Dr. Eng. Madalina Rus[1]

Prof. Dr. Eng. Elena Mereuta[1]

Assoc. Prof. Dr. Eng. Valentin Amortila[1]

Assoc. Prof. Dr. Eng. Mihai Gingarasu[1]

[1] „Dunarea de Jos" University of Galati, **Romania**

ABSTRACT

This research aims to conduct a detailed analysis of the necessity for generating electrical energy using conventional methods, simultaneously assessing the impact on water quality. Wastewater, originating from fluids used in industrial processes or households, contains various impurities and is discharged into the natural aquatic environment (such as rivers, lakes, or the Black Sea) or onto various lands, either with or without prior treatment.

The production and utilization of primary energy raw materials, such as coal, oil, natural gas, firewood, or the generation of energy through hydroelectric, nuclear, and unconventional sources, entail the need for water in associated technological processes. Consequently, wastewater becomes a potential source of pollution, even when subjected to treatment in a purification station or a complex of facilities developed or adapted to reduce pollutant concentrations.

This investigation was initiated with the objective of identifying the categories and methods of energy production that generate significant quantities of pollutants. The identification of a statistical correlation (Pearson coefficient) between primary fuels used in energy generation and the level of pollution in industrial waters suggests the imperative need to restrict or eliminate certain fuel sources in favor of environmental protection, as part of an effort to promote sustainable development.

The analysis was conducted over a period spanning from 2006 to 2022, encompassing the evaluation of various fuels, including coal, lignite, and others, which generate pollutants such as nitrogen, phosphorus, arsenic, mercury, etc. The information utilized in this analysis was sourced from official channels, specifically from the National Institute of Statistics in Romania.

Keywords: pollution, wastewater, fossil fuels, sustainable environment

INTRODUCTION

The use of fossil fuels for energy production as well as generating energy through hydroelectric power plants involves the necessity of water utilization in the associated processes.

https://doi.org/10.5593/sgem2024/4.1/s19.59

The use of water in technological production processes and energy production from various sources can vary significantly depending on the technology and resources available in a given region. Before undergoing treatment at a wastewater treatment plant, wastewater itself becomes a source of atmospheric pollution [1], [2].

There are several categories of energy sources that, during the production process, generate significant quantities of pollutants. These pollutants can have negative impacts on the environment and health. The main pollutants in wastewater can vary depending on their use in different types of industries and the specific processes carried out within them [3].

The most common contaminants found in industrial wastewater are:

- organic chemicals (oils, fats, solvents, hydrocarbons, pesticides, dyes, detergents, etc.); these can be toxic to the environment and can affect water quality and aquatic life;
- heavy metals (lead, mercury, cadmium, chromium, zinc); these are toxic to the environment and can have negative effects on human health and aquatic ecosystems;
- inorganic substances (salts, acids, bases);
- nutrients (nitrogen, phosphorus); these can cause water eutrophication and excessive growth of algae, affecting water quality and aquatic life;
- microorganisms and bacteria.

Limiting the level of pollution from wastewater in the energy industry in Romania is an important issue for protecting the environment and public health.

This paper analyzes how primary energy resources that generate pollutants such as nitrogen, phosphorus, cadmium, copper, nickel, lead, zinc, etc., influence the level of wastewater pollution with direct or indirect implications for air pollution.

The analysis was conducted for the period 2006 - 2022. The data used are sourced from the National Institute of Statistics of Romania (INSSE) [4].

MATERIALS AND METHODS

To assess the impact of wastewater pollution from the production and use of primary energy resources, we started by consulting the statistical database provided by INSSE. From there, data were collected regarding the categories of primary energy resources, the volume of wastewater, and the quantities of pollutants in wastewater, by sectors of activity.

From the analysis of the collected data, it can be observed that the mining and coal industry has undergone a significant decline in the last two decades due to the closure of economically unviable mines, low demand for coal, and current trends in green energy generation. Regarding coke production, it is important to mention that Romania had a fairly developed coke industry in the past, but it has undergone significant changes in recent decades due to market developments and changes in the energy sector.

The production of petroleum products from imports has been influenced by changes in the oil industry, domestic and international demand for petroleum products, fluctuations in international oil prices, government regulations and energy policy.

The production of firewood in Romania has undergone significant changes, influenced by a series of factors such as sustainable forest management, changes in demand and consumption, environmental protection factors, and climate change. The evolution of the main primary energy resources (coal, bituminous and anthracite coke, imported oil, firewood) during the analysed period is presented in figures 1(a), 1(b), 1(c), 1(d). It can be observed that all these primary energy sources show a declining trend or remain at approximately the same values, as is the case with firewood.

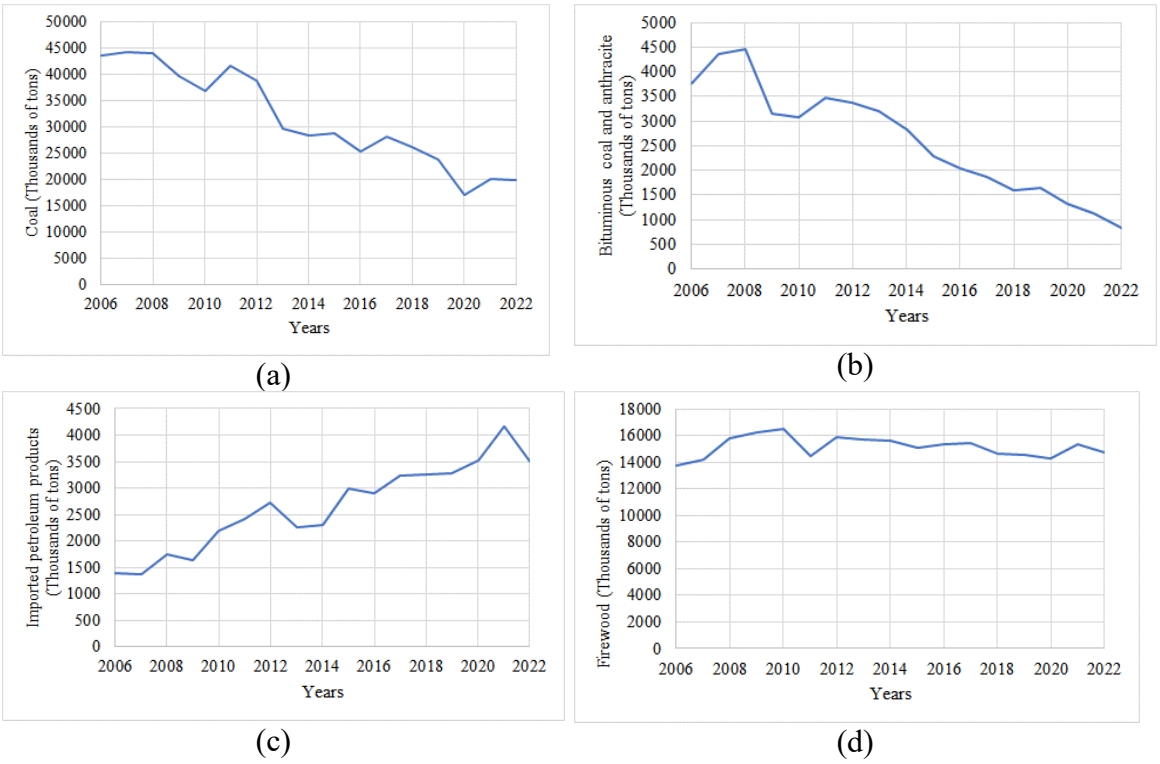


Figure 1 The evolution of the main primary energy resources

Regarding the volume of wastewater, its evolution based on origin is presented in figures 2(a), 2(b), 2(c), 2(d). For the analyzed period, based on the mentioned graphs, a somewhat different evolution can be observed in the sense that:

- Wastewater from the mining industry and those from the chemical and petrochemical industry show a constant decrease, with no significant variations observed, as shown in figures 2(a) and 2(b).
- On the other hand, wastewater from the production and distribution of energy, as well as industrial wastewater, experienced a significant decrease during the period 2012-2013 (approximately 3000 million cubic meters per year). However, from 2013 to 2022, the variations were not significant, remaining approximately at the same level as in 2013, as shown in figures 2(c) and 2(d).

https://doi.org/10.5593/sgem2024/4.1/s19.59

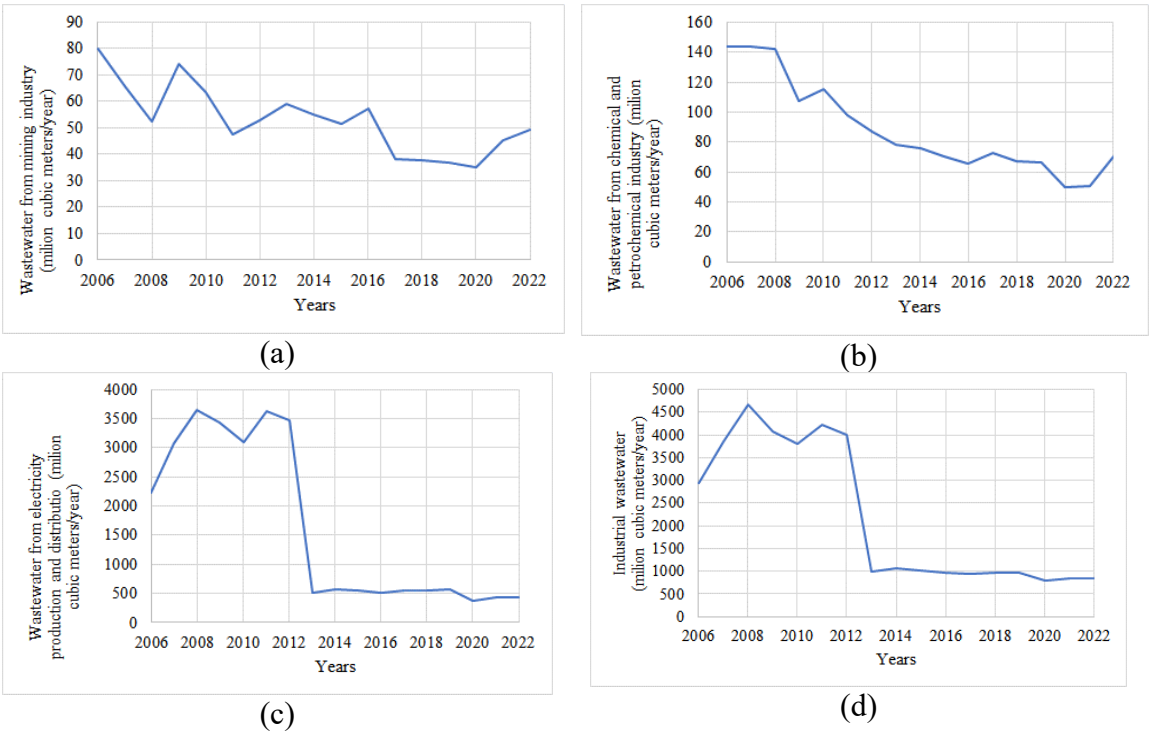


Figure 2 The evolution of wastewater by sector of activity

The distribution of average wastewater volume by source, in the total wastewater, is presented in figure 3. It can be observed that the majority of wastewater originates from industry, accounting for 55.17%, followed by wastewater from electricity production, which constitutes 41.24%. Wastewater from the mining industry and chemical industry accounts for a small percentage, but it must be considered due to the chemical compounds with which they are polluted.

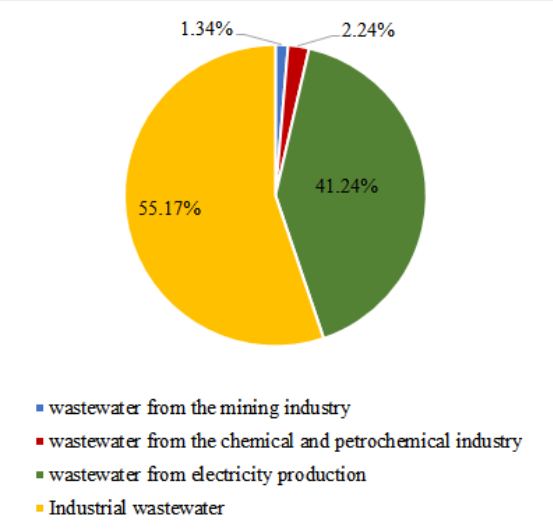


Figure 3 Distribution of wastewater

Among the contaminants present in wastewater are mentioned: nitrogen, phosphorus, cadmium, nickel, lead, zinc, and suspended matter. Their presence in wastewater can have negative effects on the environment and human health [5]. The distribution of

pollutants in wastewater, on average, for the analyzed period is presented in figure 4. It can be observed that the highest pollutant recorded is suspended matter, accounting for 72.46%, followed by zinc at 13.11%, and nitrogen at 7.48%. These pollutants found in wastewater are also atmospheric pollutants.

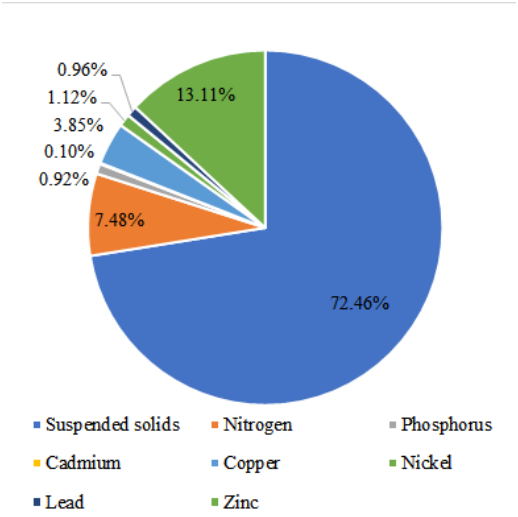


Figure 4 Distribution of polluants in wastewater

Due to the irregular variations observed during the analyzed period in both the volume of wastewater and the primary energy resources using water, it cannot be concluded that a decrease in production leads to a decrease in wastewater volume without finding a correlation between them. To establish a correlation between wastewater volume and primary energy resources, as well as pollutants, the Pearson correlation method was used. The Pearson correlation is a statistical measure used to evaluate the linear relationship between two continuous variables. It provides a measure of the direction and strength of the relationship between these variables. The Pearson correlation coefficient can vary between -1 and +1. A value close to +1 indicates a strong positive correlation, where the variables increase together in a positive relationship. A value close to -1 indicates a strong negative correlation, where one variable increases while the other decreases in a negative linear relationship. A value close to 0 indicates a weak or non-existent correlation between the two variables. It is important to mention that this correlation analysis does not necessarily imply a causal relationship.

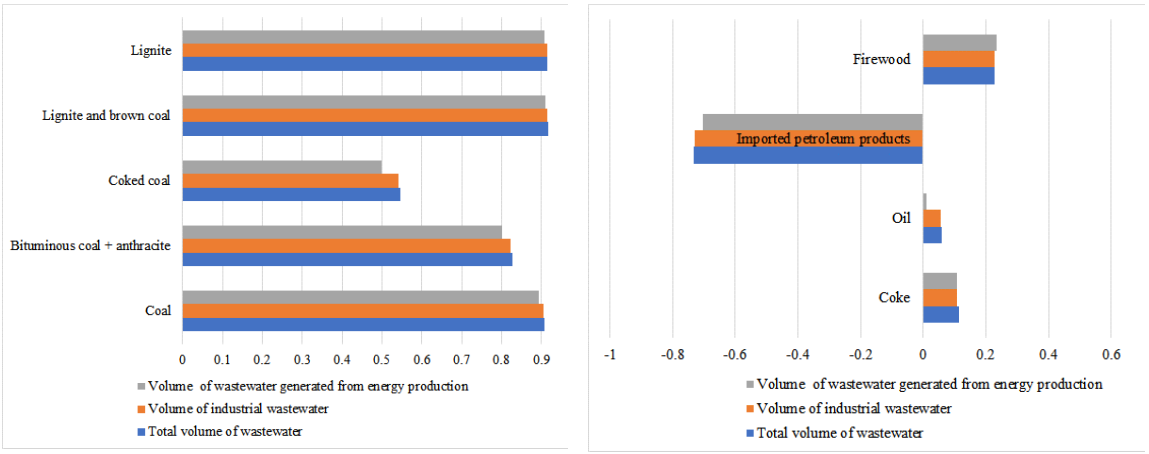
RESULTS AND DISCUSSION

In the analyzed case, regarding the relationship between the volume of wastewater and primary energy sources, using the Pearson correlation coefficient, it was determined whether there is an association between these two variables and, if so, how strong this association is based on the scale of the Pearson correlation coefficient values.

It can be said that there is a statistical correlation between the use of primary fuels in energy generation and the level of pollution in industrial waters, but this correlation can vary significantly depending on several factors such as the type of fuel used, adopted pollution control technologies, and water management practices of each industrial facility.

https://doi.org/10.5593/sgem2024/4.1/s19.59

The correlation between the volume of wastewater and primary energy resources is presented in figure 5. Thus, there is a strong correlation between the volume of wastewater and the use of fossil fuels such as lignite, brown coal, coke coal, and coal, which are the main factors polluting these waters, as shown in figure 5(a). A moderate correlation is recorded for the use of coke coal, as shown in figure 5(a), due to its reduced usage, given its use in the metallurgical industry, which has declined in Romania. Wood, oil, and coke have an insignificant influence on the volume of wastewater, as shown in figure 5(b). Regarding the association between the volume of wastewater and the use of imported petroleum products, it is observed that this correlation is negative. We can state that these used fuels have a low degree of pollution, which is why the decrease in the volume of wastewater is the result of the increased quantity of imported petroleum fuels used, as shown in figure 5(b).



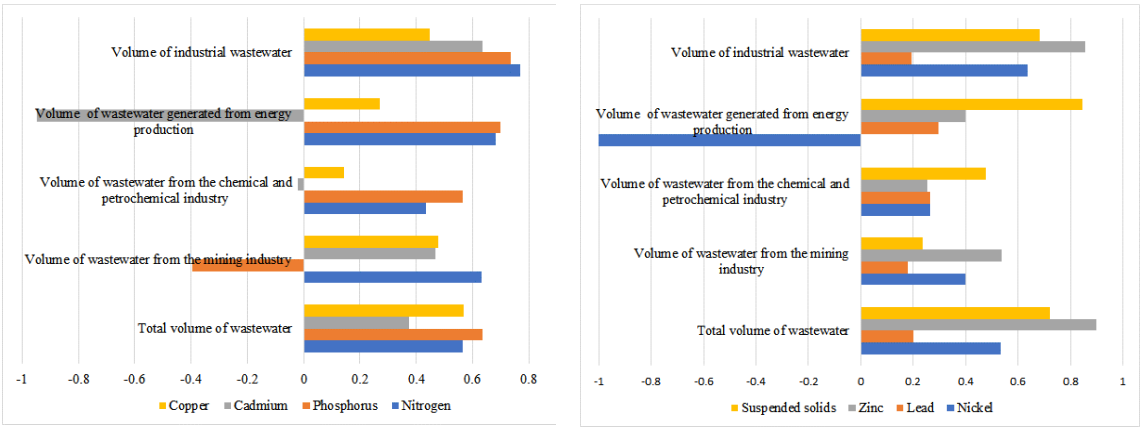
(a) (b)

Figure 5 The correlation between the volume of wastewater and primary energy resources

The adequate control of wastewater is essential for the elimination and reduction of pollutants to protect the environment and, especially, public health. Wastewater treatment processes, such as primary treatment, secondary treatment, and advanced treatment, are designed to remove or reduce pollutant concentrations before the water is discharged into the environment. The data obtained present a series of pollutants that pose a danger to the environment. By analyzing the association between the volume of wastewater and these pollutants, as presented in figure 6, we can conclude that:

- There is a strong direct association between water pollution and the quantities of nitrogen, phosphorus, and cadmium from industries, as shown in figure 6(a).
- Wastewater from industries has a very strong correlation with zinc, a substance that, when inhaled in high concentrations, can cause a condition called zinc fever, as shown in figure 6(b).
- Additionally, from the energy production industry, the Pearson correlation coefficient indicates a fairly strong association with pollutants such as nitrogen and phosphorus, as shown in figure 6(a). Although inhaling nitrogen is not very dangerous, inhaling phosphorus in high concentrations can cause lung conditions and skin and eye ailments.

- A perfect inverse correlation is observed between the volume of wastewater and nickel, indicating that water-based energy production technologies reduce the concentration of nickel in water. Therefore, an increase in wastewater volume may lead to nickel removal from water, as illustrated in figure 6(b).
- The volume of wastewater from the mining industry is the result of nitrogen pollution, while that from the chemical industry is the result of phosphorus pollution, as shown in figure 6(a).



(a) (b)

Figure 6 The correlation between the volume of wastewater and pollutants

CONCLUSION

Corelation analysis can indeed be a valuable tool in managing industrial wastewater, providing important insights for decision-making and improving the efficiency of wastewater treatment and management processes.

Following the analysis and study conducted, we can conclude that:

- There is a direct association between water pollution and concentrations of nitrogen, phosphorus, and cadmium from industries. Industrial wastewater influences water quality, aquatic ecosystems, with implications for atmospheric pollution.
- The strong association between wastewater from the energy-producing industry and nitrogen and phosphorus concentrations suggests that activities in the energy-producing industry can significantly contribute to nitrogen and phosphorus pollution in wastewater.
- The strong association between industrial wastewater and zinc concentration indicates that wastewater from industries has a very strong correlation level, concluding that industries can be significant sources of zinc contamination.
- Additionally, industrial wastewater may contain suspended particles and chemicals that can form aerosols in the atmosphere. These aerosols can affect air quality and may be responsible for the formation of fine particles or dust pollution.
- Identifying specific sources of pollution in wastewater from the mining industry, with nitrogen, and those from the chemical industry, with phosphorus, involves developing effective strategies to reduce pollutants from industries. Wastewater

https://doi.org/10.5593/sgem2024/4.1/s19.59

treatment processes can produce gases such as carbon dioxide, methane, or ammonia, which can contribute to air pollution.

These conclusions obtained using a statistical tool (Pearson correlation) underline the importance of adequate control of industrial wastewater to protect the environment and public health. They also highlight the necessity of implementing measures for preventing and treating pollution in various industrial sectors.

ACKNOWLEDGEMENTS

This scientific work was carried out within the Center for Interdisciplinary Research in Mechanical Engineering (CCIDIM) of the Department of Mechanical Engineering at the Faculty of Engineering of "Dunarea de Jos" University in Galati.

REFERENCES

[1] Vasiliu, D., Bucse, A., Lupascu, N., Ispas, B., Gheablau, C., & Stanescu, I., Assessment of the metal pollution in surface sediments of coastal Tasaul Lake (Romania), Environmental Monitoring And Assessment, 192(12), 2020, https://doi.org/10.1007/s10661-020-08698-0

[2] Romanescu, G., Cojoc, G. M., Sandu, I. G., Tirnovan, A., Dascalita, D., & Sandu, I., Pollution sources and water quality in the Bistrita Catchment (Eastern Carpathians). Revista de Chimie, 66(6), 2015, pp 855–863.

[3] Abdelwaheb, M., Nedeff, V., Dridi-Dhaouadi, S., Mosnegutu, E., Barsan, N., & Chitimus, A. D., Assessment of cadmium and copper adsorption by two agricultural soils from Romania and Tunisia: Risk of Water Resource Pollution, Processes, 10(9), 2022, https://doi.org/10.3390/pr10091802

[4] http://statistici.insse.ro:8077/tempo-online/#/pages/tables/insse-table

[5] Asano, T., Water from (Waste) Water—the Dependable Water Resource, Water Sci. Technol., 45(8), 2002, pp 24–33

THE PREDICTION AND OPTIMIZATION OF ALTERNATIVE FUEL CONSUMPTION IN VEHICLES USING ARTIFICIAL NEURAL NETWORKS WITH THE AIM OF REDUCING ATMOSPHERIC POLLUTION

Assoc. Prof. Dr. Eng. Amortila Valentin[1]

Prof. Dr. Eng. Mereuta Elena[1]

Assoc. Prof. Dr. Eng. Veresiu Silvia[1]

Assoc. Prof. Dr. Eng. Rus Madalina[1]

PhD Eng. Balasoiu George[1]

[1]" Dunarea de Jos" University of Galati, **Romania**

ABSTRACT

The purpose of this work is to explore the potential for predicting and improving the fuel efficiency of vehicles with thermal engines, especially in the context of reducing exhaust gas emissions that contribute to environmental pollution. With rising fuel costs, consumers need to make informed decisions about the fuel consumption and environmental impact of purchasing vehicles with internal combustion engines. To achieve this goal, the researchers utilized artificial intelligence and created a model using neural networks, drawing on data from vehicle manufacturers that incorporated various factors such as engine power, maximum torque, vehicle weight, engine cylinder volume, and the number of cylinders. The aim of this approach was to optimize fuel consumption for such vehicles. The study involved predicting and optimizing fuel consumption through the selection and fine-tuning of neural network architecture based on the data being analyzed. This included establishing the connections between input and output data, training the network to minimize errors, and validating the model to ensure high generalization. Various neural networks with 1, 2, or 3 layers were examined, taking into account the number of learning cycles, the sensitivity of input data, and the overall importance of each factor in order to minimize prediction errors. The findings of the study indicate that the construction parameters of vehicles significantly impact both fuel consumption and environmental pollution. The application of this fuel consumption prediction and optimization method could lead to the increased use of thermal engine vehicles that are chosen based on practical utility and transportation needs, while also helping to reduce pollution.

Keywords: neural network, air pollution, optimization, fuel.

INTRODUCTION

Man is at the basis of the emergence of artificial (anthropic) pollution sources through a diversity of human activities. These pollutants generated by human activity act upon the environment through a specific pollution with complex action. Anthropogenic sources of pollution can be grouped according to the domains that produce them as follows: anthropogenic sources from industry, anthropogenic sources from agriculture, anthropogenic sources from transport and anthropogenic sources from household

https://doi.org/10.5593/sgem2024/4.1/s19.60

activity. What do all these fields have in common? Precisely vehicles, which are also present in industry, agriculture, transport, and the daily activity of man. The European Road transport market is expected to grow by 4.9% in 2022 compared to 2021, which was already a year of very strong growth. In the medium term, until 2026, market expansion is expected to be more moderate: +3%. Thus, the increase in transport demand exceeds the improvements achieved in the energetic efficiency of the various means of transport [1], [2].
Despite the increase in transport, the associated emissions of harmful substances such as carbon monoxide, unburned hydrocarbons, particulate matter, and nitrogen oxides are decreasing as stricter emission standards are imposed on cars and trucks. However, the transports continue:

- to be the main atmospheric pollutants that cause atmospheric degradation.
- the chemical air pollution with harmful gas emissions released by internal combustion engines.
- to lead to harmful effects of pollutants upon the environment and upon health.

However, the concentrations of air pollutants continue to be very high and air quality problems persist. A significant proportion of Europe's population lives in areas, especially cities, where air quality standards are exceeded: pollution with ozone, nitrogen dioxide and particulate matter ($PM_{2.5}$, PM_{10}) induces serious health risks [3].
The polluting emissions of nitrogen oxides from transport can be reduced or eliminated by the introduction of vehicles with increased efficiency and low fuel consumption, the replacement of fossil fuels with sustainable alternative fuels (green) as well as the large-scale introduction of the electric motor into operation to vehicles. The reduction of fuel consumption must be done considering the destination of the transport, the destination of the vehicle, the area in which it moves, as well as the characteristics and constructive parameters of the vehicle. Depending on these parameters, the vehicles needed for transport can be chosen. Regarding cars, their purchase by the population should be done with prior information about the cylinder capacity, engine power, engine torque and the implication of fuel consumption upon the environment.
This information process can be done by predicting and optimizing the artificial intelligence-based fuel consumption, neural network modelling being the foundation of the artificial intelligence.

MATERIALS AND METHODS

Artificial neural networks are non-algorithmic computing systems capable of identifying and reproducing the complex relationships between a set of inputs and outputs, by making connections similar to those in the human brain.
Unlike algorithmic computing systems (usual computers), which work deductively, applying known solving rules to input data to obtain results, neural networks use an inductive method of computation. Starting from known input-output data pairs, the network establishes an optimal input-output equivalence, which equivalence can then be used to determine the output value for a given input value (prediction) or to investigate the influences of inputs on outputs (analysis). An artificial neural network consists of a number of elementary computing units – neurons (or "perceptrons") interconnected in different architectures, depending on the purpose for which it is used. The most general architecture is "feed forward MLP" (multi-layer perceptron – neurons organized on multiple layers with information flowing from input to output), figure 1.

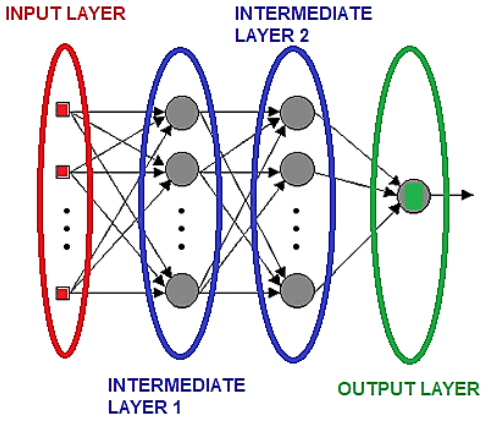


Figure 1 The general architecture of neural networks

Each neuron receives information from the previous ones, processes it based on a specific transfer function and transmits it further, to the neurons in the next layer, figure 2. The transfer function can have several expressions, the most used being the sigmoid function.

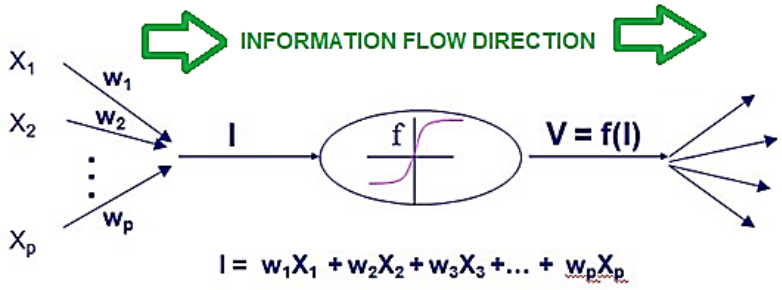


Figure 2 Information flow direction

x_i – anterior neurons; w_i – synaptic weights; I – input; f – transfer function; V – output.

Using a neural network implies a prior completion of the following steps:

- choosing and optimizing the architecture of the network.
- implementing the pairs of known input-output data.
- network training.
- network validation.

Fuel consumption is influenced by a number of factors, the most important of which are engine power, developed engine torque and vehicle mass. A series of other factors, aimed at optimizing the combustion processes (supercharging, computerized mixture control, etc.) can be considered by assessing the cylinder capacity. Thus, at the same developed power, a supercharged engine with a controlled mixture will have a lower cylinder capacity than a classic engine. As a result, fuel consumption data for a series of vehicles, presented in Table 1, were chosen, data that we used to build neural models using the EasyNN application. This data is provided by the vehicle manufacturers [4].

https://doi.org/10.5593/sgem2024/4.1/s19.60

Table 1 Input data for vehicles

Engine Power [HP]	Engine Torque [Nm]	Number of Cylinders	Volume of Cylinders [cm^3]	Mass [kg]	Mixed Consumption [l/100km]
272	400	6	2995	1740	8.1
450	550	8	3993	2565	9.3
156	200	4	1995	1360	7.9
286	580	6	2993	1645	7.5
431	550	6	2979	2100	8.3
450	650	8	4395	2885	10.5
1001	1250	16	7993	1888	24
432	569	8	6162	1769	14
141	176	4	1796	1365	6.8
115	150	4	1587	1790	7.1
75	107	4	1149	1505	5.9
75	114	4	1390	1395	6.7
105	290	4	1598	1290	5
130	221	5	2446	1750	9.7
60	109	4	1242	1035	5.4
150	370	4	1997	1655	4.4
160	188	4	1999	1165	7.8
240	216	2	1308	1330	8.4
550	632	6	3799	1815	11.8
195	400	4	1956	1780	5.1
110	280	4	1686	1690	4.5
105	250	4	1598	1480	4.5
150	320	4	1968	1350	4.5
64	125	4	1896	1125	4.8
230	350	4	1984	1382	6

Establishing the optimal architecture

A "Backpropagation - Feed Forward" network was chosen to build the neural model for fuel consumption analysis. In this type of networks, the establishment of the weights is done by propagating the error from the output to the input (backpropagation), while the input data moves from the input to the output of the network (feed forward) [5]. This type of networks lends itself best to prediction and optimization operations [6].

As input data, power, torque, number of cylinders, displacement and mass of the vehicle were chosen, according to table 1, and as output data - fuel consumption.

The parameters initially established in order to run the neural model are:

- learning rate: 0.9;
- moment: 0.8;
- maximum learning error: 0.01%.

Considering that for each modelled problem there is an optimal network architecture, in order to establish the optimal architecture, several network architectures were tested, with one, two and three layers, respectively. The networks were analyzed from the point of view of the number of learning cycles, sensitivity, and importance [5], [6].

The single-layer model was obtained by configuring the architecture for a single hidden layer, resulting in the network shown in figure 3.

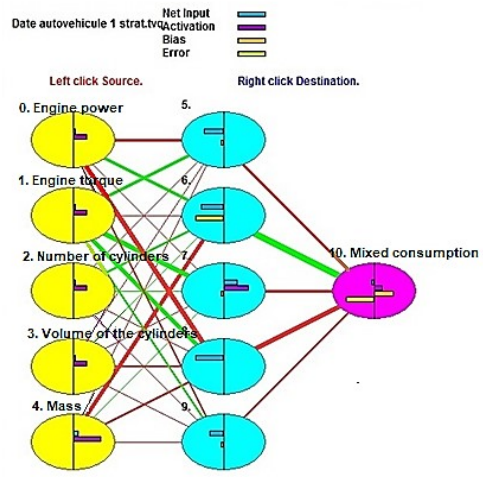


Figure 3 Single-layer neural network

After running the learning stage, it was observed that the number of cycles run until the predetermined learning error is obtained is 697. In the table 2 you can see both the order of importance of the input data and their sensitivity.

Table 2 Importance order of input sensitivity for the one-layer model

Column	Input Name	Importance	Column	Input Name	Sensitivity
0	Engine Power (HP)	14.1777	**0**	Engine Power (HP)	0.836263616
1	Engine Torque (Nm)	12.3498	**1**	Engine Torque (Nm)	0.720917834
4	Mass (kg)	8.9251	**4**	Mass (kg)	0.437804290
3	Volume of the cylinders (cm^3)	6.3420	**3**	Volume of the cylinders (cm^3)	0.427872904
2	Number of cylinders	4.7373	**2**	Number of cylinders	0.348919425

To obtain a two-layer model, the corresponding options in the architecture generator are activated, the result being shown in the figure 4.

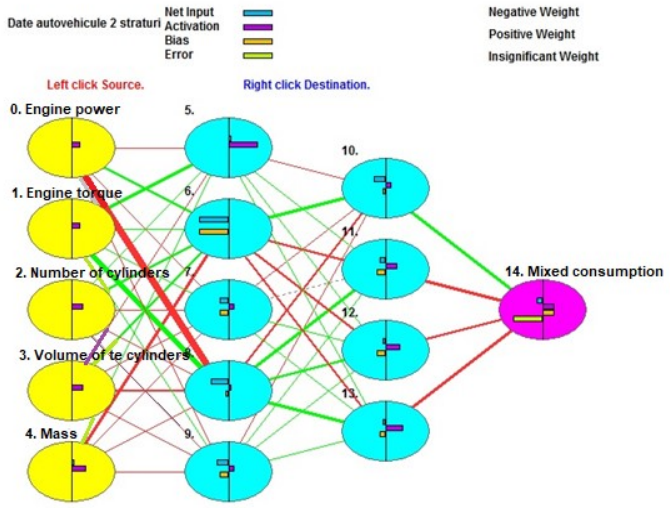


Figure 4 Neural network with 2 hidden layers

In the case of the model with two hidden layers, the number of cycles run until the predetermined learning error is obtained is 1440. The evolution of the learning error and the order of sensitivity and importance are presented in the table 3.

https://doi.org/10.5593/sgem2024/4.1/s19.60

Table 3 Order of Importance and Sensitivity of 2-layer model input data

Column	Input Name	Importance	Column	Input Name	Sensitivity
1	Engine Torque (Nm)	12.4970	**0**	Engine Power (HP)	0.695123285
0	Engine Power (HP)	10.8813	**1**	Engine Torque (Nm)	0.544121561
3	Volume of the cylinders (cm^3)	6.3219	**3**	Volume of the cylinders (cm^3)	0.475963764
2	Number of cylinders	5.6369	**4**	Mass (kg)	0.455951246
4	Mass (kg)	5.5719	**2**	Number of cylinders	0.403149600

Obtaining a three-layer model is done by appropriately modifying the settings in the architecture generator, the result being shown in the figure 5.

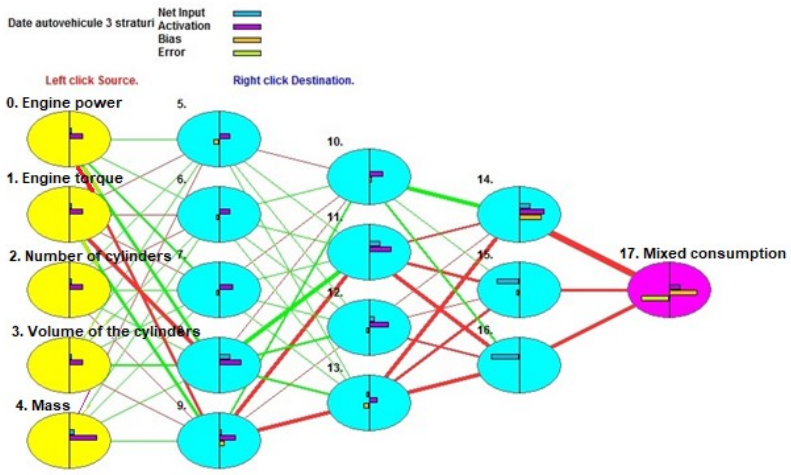


Figure 5 Neural network with 3 hidden layers

In the case of the model with two hidden layers, the number of cycles run until the predetermined learning error is obtained is 1429. The evolution of the learning error and the order of sensitivity and importance are presented in table 4.

Table 4 Order of importance and sensitivity of the 3-layer model input data

Column	Input Name	Importance	Column	Input Name	Sensitivity
0	Engine Power (HP)	9.3364	**0**	Engine Power (HP)	0.865886081
1	Engine Torque (Nm)	8.4944	**1**	Engine Torque (Nm)	0.85111500
3	Volume of the cylinders (cm^3)	5.9227	**3**	Volume of the cylinders (cm^3)	0.595385645
2	Number of cylinders	4.4247	**2**	Number of cylinders	0.554681808
4	Mass (kg)	2.2705	**4**	Mass (kg)	0.082160295

RESULTS AND DISCUSSION

In order to establish the optimal architecture for the neural model of fuel consumption, it is necessary to compare the performances of the previously presented models, following both the minimum number of learning cycles and the coincidence between the hierarchies of sensitivities and the importance of the input data upon the output data, as well as the shape of the variation curves of the error learning. Table 5 shows the results obtained by modeling fuel consumption with different neural network architectures (EP – Engine Power, ET – Engine Torque, VC - Volume of the cylinders, NC - Number of cylinders, M – Mass).

Table 5 Fuel consumption modeling with different neural network architectures

Neural model	Number of learning cycles	Importance	Sensitivity	Minimum number of cycles	Coincidence of importance and sensitivity hierarchies
1 layer	697	EP-ET-M-VC-NC	EP-ET-M-VC-NC	Yes	Yes
2 layers	1140	EP-ET-VC-M-NC	EP-ET-VC-M-NC	Not	Not
3 layers	1429	EP-ET-VC-NC-M	EP-ET-VC-NC-M	Not	Yes

After analyzing the data obtained, presented in the table, for the prediction and optimization of fuel consumption we chose the neural network with a single layer because the number of cycles is minimal, the learning graph has no jumps, and the order of importance and sensitivity of the input data coincide. Optimizing fuel consumption can be achieved by setting certain vehicle parameters that lead to minimum consumption in order to reduce air pollution. This can be done in two scenarios: changing all the constructive parameters of the vehicle or keeping some at preset values and changing others. For the first hypothesis, the value established in table 6 is valid.

Table 6 Optimization of fuel consumption by changing the constructive parameters.

Engine Power [HP]	Engine Torque [Nm]	Number of cylinders	Volume of the clinders [cm^3]	Mass [kg]	Minimum consumption [l/100km]	Maximum consumption [l/100km]
60	107	2	1149	1035	4.5619	-
1001	793	16	7993	2885	-	20.6951

Another possibility offered by the proposed neural model is to determine the influence of the input data (constructive parameters of the vehicle) upon the output - fuel consumption. The assessment of these influences is based on the value of the weights of the respective branches in the neural network, in the form of two graphic representations: importance and sensitivity, figure 6. It can be seen in the figure that the engine power and the engine torque imposed by the design conditions have the greatest influence upon the fuel consumption. Mass is in third place, followed by displacement, and in last place is the number of cylinders.

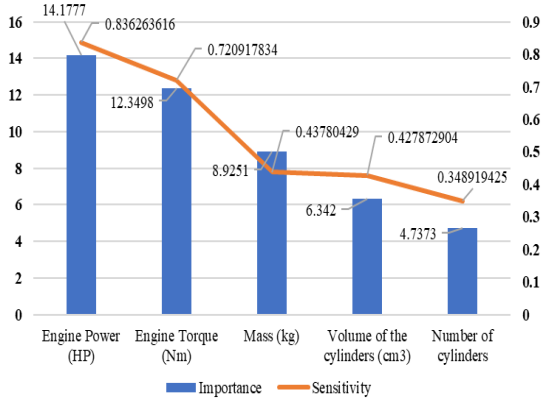


Figure 6 Importance and sensitivity plot of the input data for the optimal model

From this point of view, in order to obtain a minimum consumption, the values of these two parameters, which are constructively linked through the gearbox, can be modified accordingly. The appropriate choice of the type of gearbox can lead to optimal values of power and torque at the wheel, under the conditions of a reduced mass of the vehicle.

https://doi.org/10.5593/sgem2024/4.1/s19.60

By analyzing the hierarchies presented in the figure 6 starting from the constructive parameters of the vehicle imposed by the design requirements, it is possible to predict and optimize fuel consumption to protect the environment from the design phase.

CONCLUSION

Following the above, the following conclusions can be highlighted:

- in the design phase, all the constructive parameters of the vehicle are established, based on precise calculations.
- the constructive parameters of the vehicle have a major influence upon fuel consumption with implications on atmospheric pollution.
- the use from the design phase of a model for predicting fuel consumption is extremely useful, allowing the modification of certain constructive parameters with the aim of obtaining minimum consumption and implicitly reducing pollutants from fuel combustion.
- although there are currently a series of mathematical models for assessing fuel consumption according to the constructive characteristics of vehicles, they offer a low degree of precision due to the extremely complex interaction between them.
- models based on neural networks can handle prediction and optimization problems starting from known input-output data sets, acquired experimentally or statistically, the accuracy offered being according to the number of data sets used in the training stage.
- the model presented in this work can be used to predict and optimize fuel consumption, depending on the constructive parameters of the vehicle, minimizing the quantities of pollutants emitted by fuel combustion.

ACKNOWLEDGEMENTS

This scientific work was carried out within the Internal Grant of the 2024 Department of Mechanical Engineering at the Faculty of Engineering of "Dunarea de Jos" University in Galati and the Center for Interdisciplinary Research in Mechanical Engineering (CCIDIM).

REFERENCES

[1] https://www.eea.europa.eu/ro/articles/asigurarea-unui-transport-mai-durabil;
[2] https://logisticpost.ro/articole/cererea-de-transport-va-creste-cu-aproape-5-in-2022.html;
[3] George Balasoiu, Mihaela Buciumeanu, Sorin Ciortan, Valentin Amortila, A statistical analysis of the influence of the brake pads air pollution on the lung diseases of romanian population, International Multidisciplinary Scientific GeoConference: SGEM; Sofia, Vol. 20, Iss. 4.2, (2020). DOI:/10.5593/sgem2020V/4.2/s05.12];
[4] https://www.auto-data.net/ro/;
[5] Nandal M., Mor N., Sood H., An overview of use of artificial neural network in sustainable transport system, Advances in Intelligent Systems and Computing, (2021), 83-91, 1227;
[6] Fan W., Gurmu Z, Dynamic Travel Time Prediction Models for Buses Using Only GPS Data, International Journal of Transportation Science and Technology, vol 4, no. 4·2015, pp 353 – 366;

ANALYSIS OF DIFFERENT FACTORS IMPACT ON PARTICULATE MATTER FORMATION DURING THE REFUSED DERIVED FUELS COMBUSTION

Radovan Nosek[1]
Michal Sramka [1]
Nikola Čajová Kantová[2]
[1] Department of Power Engineering, Faculty of Mechanical Engineering, University of Žilina, **Slovakia**
[2] Research Centre, University of Žilina, **Slovakia**

ABSTRACT

The process of burning alternative materials such as refused derived fuels is an important topic in current scientific research and industry. Emissions and particulate matters are formatted during the combustion of refused derived fuels (RDF) and it is important to identify the ways of their reduction. This manuscript analyses the influence of factors such as fuel fraction and fuel moisture on particulate matter (PM) concentrations. The findings can assist to better understand the impact of individual factors on air quality. The main goal of this work is to conduct an experiment in laboratory conditions to determine the optimal conditions for the RDF combustion. Nine samples of RDF with the moisture from 0% to 6.5% were combusted in the experimental setup. Further measurements analyzed the effect of fuel fraction and PM concentration. The particulate matters were measured by TSI Scanning Mobility Particle Sizer and Aerodynamic Particle Sizer during the experiments. The concentration of particulate matters decreased up to 50.1% in the case of fractions ≤0.5 mm. The analysis of moisture effect shows that higher content of water has a negative effect on the mass concentration of PM. The greatest decrease in PM mass concentration by up to 69.4% was recorded for the RDF 7 sample when the moisture content changed from 6.18% to 0.0%. The obtained results show links between PM concentrations and mentioned conditions.

Keywords: Refused Derived Fuel (RDF), Particulate matter (PM), Combustion, Humidity, Fraction

INTRODUCTION

The combustion of biomass or RDF produce significant concentration of particulate matters [1, 2]. Particulate matters have negative impact on human health [3], as they consist of airborne PM with different chemical compositions [4]. In recent decades, the production of municipal waste has been constantly increasing, which represents adverse effects on the environment. Refused derived fuels, which are obtained from waste materials and serve as alternative fuels for energy production, have found great use in the cement industry. Refused derived fuels are non-conventional fuels that are used as a substitute for traditional fossil fuels. Over the last 20-30 years, the amount of fossil fuels replaced by alternative fuels has increased. Fuels from waste are obtained from a

https://doi.org/10.5593/sgem2024/4.1/s19.61

mixture of municipal waste that is mechanically or thermally processed to create energy. Reducing emissions from burning RDF is important not only from an environmental point of view, but also due to human health and sustainable development. Therefore, it is important to pay attention to this issue and look for innovative ways to improve combustion processes and minimize the negative impact on the environment. Analysis the factors affecting the formation of particulate matters from RDF combustion can bring new knowledge about options of their reduction. There are several devices for reducing the concentrations of particulate matters such as filters [5], electrostatic precipitators [6], or wet scrubbers [7].

In cement plant operations, various methods are used to reduce emissions produced into the air, such as various filters, but even these are not 100% effective, and in some cases they cannot capture particulate matters. One of the ways to reduce PM emissions is to change the operating conditions, such as the type and amount of fuel used, crushing the fuel into smaller size fractions or the decrease of fuel moisture.

The main purpose is to analyze the PM reduction during the burning of RDF under various operational factors. In this research, the influence of moisture and fuel fraction on PM concentrations was evaluated. The results of this work should be a valuable source of information for the optimization of combustion process and reduction of PM.

MATERIALS AND METHODS

This section describes the influence of various operating parameters on the formation of solid particles, such as the following parameters: fuel moisture and fraction. For combustion of RDF samples in real conditions, a tube furnace LT 50/750/13 was used. This device has electric coils that can heat the combustion chamber up to a temperature of 1300 °C. With this device, it is possible to monitor the current temperature and set it to the desired value using the regulator.

To measure the concentration of particulate matters, an aerodynamic particle counter TSI APS 3321 was used, which had to be supplemented with an Aerosol diluter. This is used to dilute the sample taken, as TSI APS 3321 is very sensitive to higher concentrations. Another device used in the measurement is the TSI SMPS 3938 particle mobility scanning spectrometer. The TSI APS 3321 device has the ability to measure particles in the range from 0.5 μm to 20 μm, while the TSI SMPS3938 device can measure in the range from 1 nm to 1000 nm. By connecting these two measuring devices in tandem, the particles in the range from 0.001μm to 20μm can be measured. Both devices were connected to a computer where the software for evaluating the measured outputs TSI aerosol instrument manager A.I.M 10.3 was installed. Temperatures were measured using thermocouples, which were installed in the following positions: at the fuel supply, in the tube furnace, at the outlet of the flue gas from the tube furnace, and the last position of the thermocouple was at the sampling probe to the TSI measuring devices (see Fig.1). At the fuel inlet, the speed of the air flow into the combustion chamber was measured using an anemometer.

The scheme of experimental setup is shown in Fig. 1. The real experimental device is presented in Fig. 2.

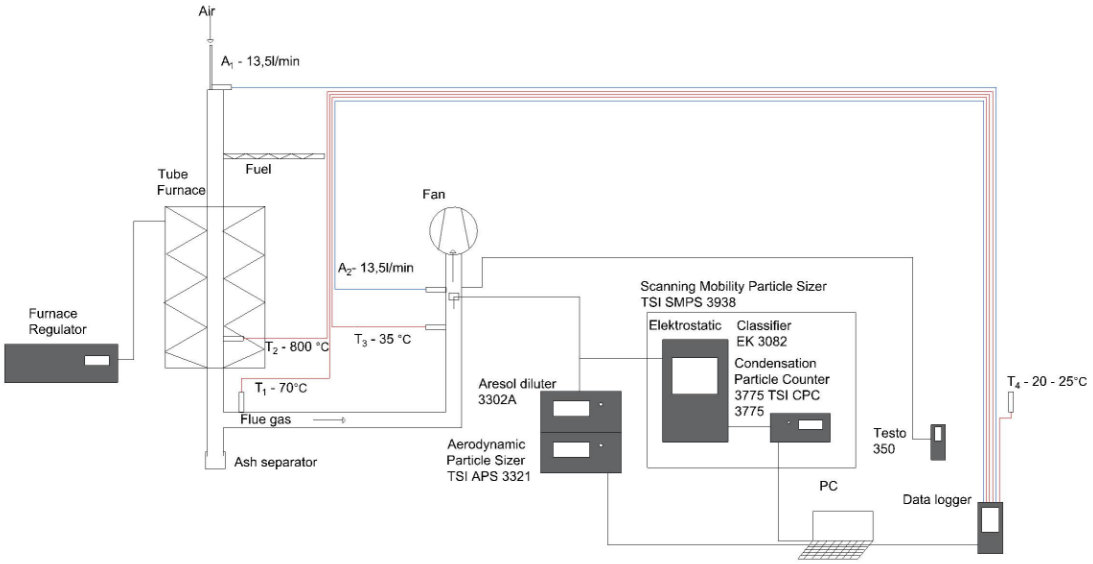


Figure 1 Scheme of experimental measuring system



Figure 2 Experimental setup: 1. Tube furnace LT 50/750/13; 2. TSI SMPS 3938 analyzer; 3. TSI APS 3321 analyzer

The weight of each sample is 0.1 g and was divided into 15 parts, due to the continuous feeding of the sample into the combustion chamber during the entire measurement process. The air flow during the analysis of different fractions and moisture was constantly maintained at the level of 13.5 $l.min^{-1}$ in an air atmosphere with 79% N_2 and 21% O_2. Temperature in the combustion chamber ranged from 820 °C to 860 °C.

Nine different RDF samples were tested in order to verify particulate matter concentrations during the combustion process. Each sample has its own unique composition and different effect on emissions formation. The samples were subjected to elemental analysis to better understand their chemical composition. This analysis can identify the main components and their concentrations. The samples were delivered in crushed form from the customer. One of the 9 samples is shown in Figure 3.

https://doi.org/10.5593/sgem2024/4.1/s19.61

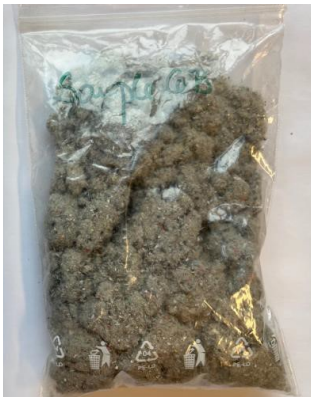


Figure 3. One of the tested RDF samples

The content of carbon, hydrogen, nitrogen, and sulphur in samples were measured using LECO CHNS 628 analyzer. The calorific value of samples was measured using the LECO AC 500 device. The analysis of fixed carbon, moisture, volatile matter, and ash in the samples was performed by thermogravimetric analyzer LECO TGA 701. The results of samples elemental analysis are summarized in Table 1.

Table 1 Elemental analysis of samples

Sample		1	2	3	4	5	6	7	8	9
Carbon	**[%]**	50.2	53.19	51.21	49.31	50.00	53.46	52.51	47.49	51.4
Hydrogen	**[%]**	10.74	13.04	12.38	11.19	11.83	13.04	12.29	11.56	12.12
Nitrogen	**[%]**	1.9	0.7	0.8	0.5	0.7	0.2	0.7	0.5	0.9
Sulphur	**[%]**	0.63	0.42	0.36	0.64	0.3	0.28	0.28	0.41	0.48
Calorific value	**[MJ.kg^{-1}]**	22.76	25.18	28.56	23.97	23.45	26.79	25.74	23.18	23.52
Fixed carbon	**[%]**	5.55	0.64	1.18	1.69	2.13	2.68	2.38	2.76	3.29
Moisture	**[%]**	6.5	3.83	4.52	3.61	4.42	4.31	6.18	4.04	4.76
Volatile matter	**[%]**	84.73	89.29	86.54	84.46	86.59	87.23	89.2	79.57	17.62
Ash	**[%]**	9.48	10.06	12.25	13.83	11.24	10.03	8.39	17.62	12.59

RESULTS

The results of the measurements present the mass concentration of particles released during the combustion process. In fig. 4 are presented the measured results of all 9 samples at an air flow of 13.5 l.min^{-1} and a temperature of around 800°C.

The highest concentration can be observed for particles with larger diameters. The vertical red line in Figure 4 shows the transition line between the two measuring analyzers SMPS 3938 and APS 3321. The highest PM values were recorded for sample RDF 9, and the lowest concentrations can be observed for sample RDF 4.

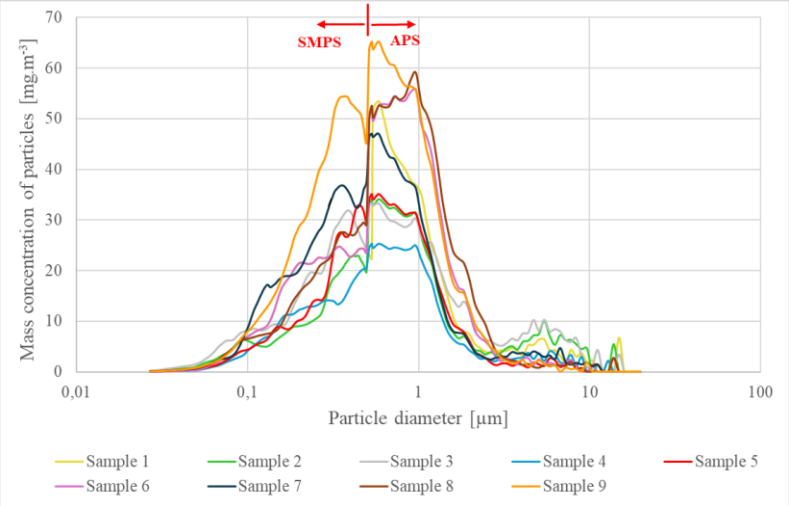


Figure 4. Distribution curve of particles mass concentration for the tested samples

Size fractions

The effect of size fractions on the formation of solid emissions was made only for RDF sample 1. The sample was prepared into the following three fractions:

1. Fraction smaller than 0.5 mm
2. Fraction in size of 0.5-1 mm
3. Fraction greater than 1 mm

The results of the mass of particles released from sample 1, during the combustion process for different size fractions are presented in Figures 5 and 6.

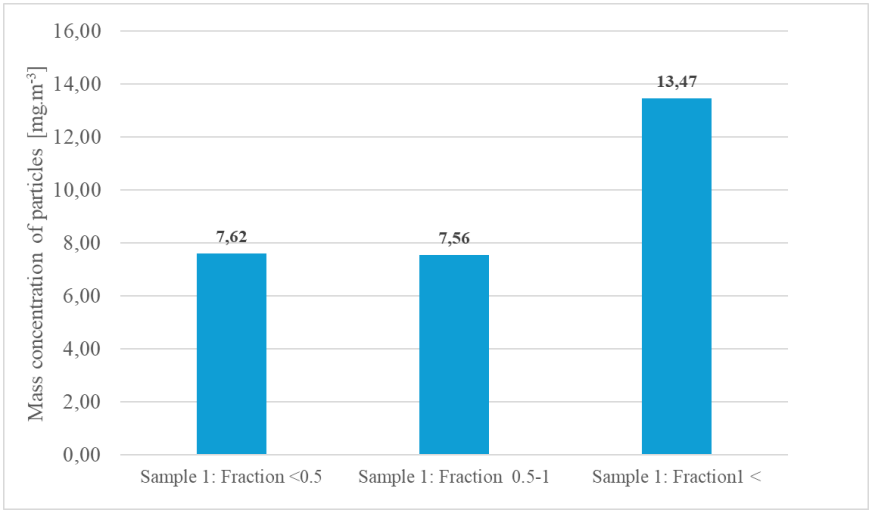


Figure 5. Mass concentration of particles for different size fractions (Sample 1)

The figures above show the effect of the smaller fraction on the lower PM concentrations. For sample 1 with a fraction smaller than 1 mm (Fig.6, red and blue lines), the largest decrease from 0.5 to 33.2 mg.m^{-3} in mass concentration was recorded. In Fig. 6, the highest concentration was recorded for the fraction greater than 1 mm for particles with a diameter of around 350 nm to 700 nm. A smaller size fraction led to a lower amount of released particles and their mass concentration was also lower.

https://doi.org/10.5593/sgem2024/4.1/s19.61

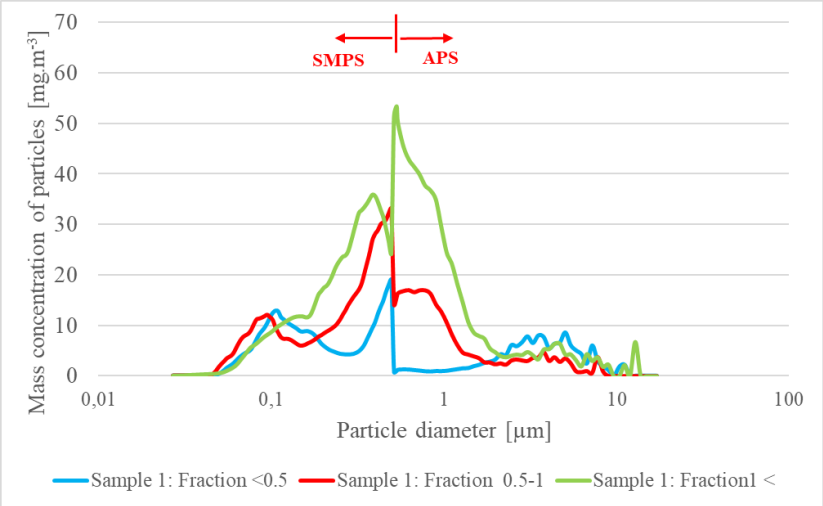


Figure 6. The effect of different size fractions on the mass concentration of particles (Sample 1)

Moisture

Fuel moisture can significantly affect the quality of combustion and the formation of solid particles. The presence of moisture in the fuel has consequences mainly on the combustion efficiency, the formation of emissions and ash. The original moisture values of the samples and after drying to 0% are shown in Tab.2.

Table 2 Moisture content of RDF samples

RDF Sample		**1**	**2**	**3**	**4**	**5**	**6**	**7**	**8**	**9**
Moisture – M1	**[%]**	6.5	3.83	4.52	3.61	4.42	4.31	6.18	4.04	4.76
Moisture – M0	**[%]**	0.0	0.0	0.0	0.0	0.0	0.0	0.0	0.0	0.0

Figure 7 shows that a higher moisture content has a negative effect on the mass concentration of PM. The highest mass concentration can be observed in sample 9, and on the contrary, the lowest can be seen in sample 2. The largest decrease in mass concentration was recorded in the case of Sample 7, the PM concentration changed from 23.5 to 7.2 mg.m^{-3}.

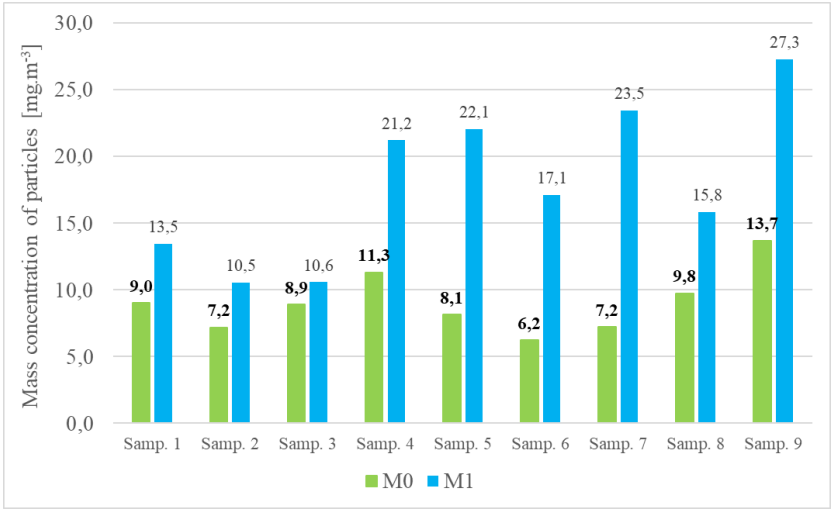


Figure 7. The effect of different moisture on the mass concentration of PM

DISCUSSION

The effect of a smaller fuel fraction indicates a reduction in PM formation. Crushing the fuel into smaller fractions increases the total area of the fuel so the combustion can take place and reduces the formation of incompletely burned residues that could otherwise form particulate matters. This process results in more efficient removal of organic and inorganic fuel residues, thereby reducing PM concentration. Based on these comparisons, it is recommended to crush the fuel into smaller fractions, as this can significantly contribute to the reduction of particulate emissions during the combustion process and improve the overall combustion efficiency. Based on this measurement can be concluded that the finer the fuel is broken down, the lower its ability to produce particles from combustion. This finding supports the research work of J. Stur et al. [8] which confirms the positive effect of a smaller fuel fraction on lower PM concentrations.

From the measurement results, it can be concluded that higher moisture has a negative effect on the formation of PM during RDF combustion. This phenomenon is caused by the fact that the water contained in the fuel absorbs heat during combustion, which lowers the combustion temperature. A lower combustion temperature subsequently causes incomplete combustion, which produces more PM particles.

CONCLUSION

The aim of the work was to build an experimental device in order to verify the influence of various aspects on PM formation during the combustion of RDF fuels in laboratory conditions. The influence of moisture and fuel fraction was analysed during the experimental measurements. The measured results show that one of the most positively significant factors influencing the formation of particulate matters can be the fraction of the given fuel. Based on the measurements, it was found out that smaller fuel size fractions produce fewer PM concentrations. The results show that the mass concentration of particles was reduced by 50.1% in the case of sample 1 with fraction smaller than 1 mm. Based on measured results is recommend modifying the fuel preparation to obtain smaller size fractions, which could significantly contribute to the reduction of particulates matter.

The moisture content of RDF also affects PM production. It was found out that higher fuel moisture supports the higher formation of solid particles. This phenomenon may be due to the higher moisture content of the fuel leading to heat absorption during combustion, which lowers the combustion temperature and causes incomplete combustion. The analyses show that the mass concentrations of particles in individual samples decreased in the range from 16.0% to 69.4% at zero moisture values M0 compared to the original value of samples moisture-M1. Incomplete combustion leads to a higher formation of PM. Therefore, is important to optimize the moisture content of RDF fuels.

Further research work should analyse the influence of amount of air flow and co-combustion of RDF with different materials.

https://doi.org/10.5593/sgem2024/4.1/s19.61

ACKNOWLEDGEMENTS

This research was funded by VEGA No. 1/0633/23: Optimization of the flow field preventing the spread of COVID-19 and other viruses and bacteria to the patient, KEGA No. 028ŽU-4/2023: Implementation of SMART solutions in energy regulation smachines and devices in the pedagogical process, VEGA No. 1/0150/22: Energy utilization of produced waste in connection with the COVID-19 pandemic through pellets as an alternative fuel.

REFERENCES

[1] Daellenbach, K.R., Uzu, G., Jiang, J. et al. Sources of particulate-matter air pollution and its oxidative potential in Europe. Nature 587, 414–419 (2020). https://doi.org/10.1038/s41586-020-2902-8

[2] Denise Pernigotti, Claudio A. Belis, Luca Spanò, SPECIEUROPE: The European data base for PM source profiles, Atmospheric Pollution Research, Volume 7, Issue 2, 2016, Pages 307-314, ISSN 1309-1042, https://doi.org/10.1016/j.apr.2015.10.007.

[3] Jiménez E, Linares C, Rodríguez LF, Bleda MJ, Díaz J. Short-term impact of particulate matter (PM2.5) on daily mortality among the over-75 age group in Madrid (Spain). Sci Total Environ. 2009 Oct 15;407(21):5486-92. doi: 10.1016/j.scitotenv.2009.06.038. Epub 2009 Jul 31. PMID: 19647288.

[4] Ki-Hyun Kim, Ehsanul Kabir, Shamin Kabir, A review on the human health impact of airborne particulate matter, Environment International, Volume 74, 2015, Pages 136-143, ISSN 0160-4120, https://doi.org/10.1016/j.envint.2014.10.005.

[5] Charan, Nerella & Krithiga, S. & Subudhi, Partha.. Review of Particulate Matter Filters. (2021) 10.1007/978-981-15-7241-8_30.

[6] Karunakaran M., Sivakumar P., Chira N. Electrostatic precipitator in ash removal system: A comprhensive review (2019) International Journal of Innovative Technology and Exploring Engineering, 8 (4S), pp. 321 - 324. https://www.scopus.com/inward/record.uri?eid=2-s2.0-85061725678&partnerID=40&md5=65528fd9acf7de0aff8673a79329d30c

[7] Jaworek A., Krupa A., Sobczyk A.T., Marchewicz A., Szudyga M., Antes T., Balachandran W., Di Natale F., Carotenuto C. Submicron particles removal by charged sprays. Fundamentals (2013) Journal of Electrostatics, 71 (3), pp. 345 - 350 DOI: 10.1016/j.elstat.2012.11.028 https://www.scopus.com/inward/record.uri?eid=2-s2.0-84875638140&doi=10.1016%2fj.elstat.2012.11.028&partnerID=40&md5=f4bc3b14c6ec5eaacb9bce118ef9a59b

[8] Štúr,J. 2023. Znižovanie produkcie tuhých častíc počas energetického zhodnocovania tuhých alternatívnych palív zmenou prevádzkových podmienok. [Diplomová práca] Žilina: Žilinská univerzita v Žiline, Fakulta strojnícka, Katedra energetickej techniky , 2023. 72 s.

VARIATION OF CRITICAL VELOCITY OF DOWNWARD VENTILATION IN INCLINED ROAD TUNNELS

Prof. Omar Lanchava[1]
Prof. Nino Ratiani[1]
Assoc. prof. Zaza Khokerashvili[1]
Assoc. prof. Nino Arudashvili[1]
[1] Georgian Technical University, **Georgia**

ABSTRACT

The paper presents the pattern of variation of critical velocity during longitudinal downward ventilation in an inclined road tunnel with its slope varying within 0-8 degrees. The results of both full-scale numerical modelling and laboratory experiments for a 1:10 scale tunnel models are presented. The effect of fire on the critical velocity and gradient factor was studied on the models. During the numerical modelling, the seat of fire, fans and tunnel portals were modelled with 0.1*0.1*0.1 m cells, while the cell sizes in the other areas were 0.5*0.5*0.5 m. Observations on the physical model, made of 2 mm thick stainless-steel sheets, were carried out considering the Froude number. The surface area of the source fire was 130X50 mm and 340X60 mm. Natural gas and air flow rates were measured with an accuracy of 1%. The heat release index was calculated based on air consumption. The ratio of tunnel width to tunnel height varied between 1.33 and 2 on the physical models. The results obtained show that the characteristic gradient factor of the critical velocity varies linearly with the tunnel slope to 6 %, and its numerical value depends on the heat release rate. The numerical simulation results show that after algebraically adding the ventilation and fire-induced drafts, the fire-induced draft becomes dominant when the tunnel slope exceeds 3% and the fire power exceeds 30 MW. In laboratory experiments, a similar effect was not observed due to the insufficient strength of the model fire.

Keywords: critical velocity, tilted tunnel, smoke control, positive ventilation flow.

INTRODUCTION

International recommendations to design emergency ventilation systems [1-3], as well as fire safety guidelines of the USA, one of the world leading countries [4-6], share the view that the critical velocity of a ventilation flow is an important technological parameter, which can be used to control smoke in traffic tunnels in case of any type of fire and heat release rate. The same opinion is given in scientific papers [7-17] following and based on the publication of work by Thomas “The movement of buoyant fluid against a stream and the venting of underground fires” in 1958 [18]. Today, accepting this point of view without criticism is a big mistake, at least according to our works [19, 20]. From the papers noted, it is obvious that fires often cause greater dynamic pressure than the most powerful tunnel fans. Therefore, there is a need to clarify this issue and scientifically differentiate the cases necessary for the implementation of vital emergency ventilation projects. The cases should be differentiated based on fire strength, tunnel geometry, and

https://doi.org/10.5593/sgem2024/4.1/s19.62

type of the ventilation flow. Solving this issue is an undoubtedly topical problem for further development of the given branch.
In mentioned our paper [19], using the Clapeyron equation, it was obtained that the dynamic pressure caused by a fire with a temperature of 1000 ℃ in the tunnels is 121.6 kPa, which is higher than the atmospheric pressure, and 8 times exceeds the maximal static pressure of the most powerful fans. At this time, the air density is reduced to 0.277 kg/m^3. Therefore, in the case of a strong fire, it will be practically impossible to control the ventilation flow through the fans, and the direction and consumption of the air movement will be determined by the depression caused by the fire. This provision contradicts the idea of critical velocity.
We obtained this result using the above equation, which had not been used before in the field of emergency ventilation. Then, through numerical simulations using PyroSim software, which was also not designed to study the movement of ventilation flows, and based on the laws of aeromechanics, we determined that the final sum of the currents induced by the fire and the fan can move in a previously unpredicted direction. This occurs when the indicated currents in the downward ventilation flow are in the opposite direction, when the tunnel slope is 3% or more, and the fire power is at least 30 MW. All of the above led to the need to deepen the knowledge about saving life in limited underground spaces in case of fire.
Based on the above, the essence of the problem lies in the critical analysis of the obsolete scientific concepts and in gaining novel results based on the concept introduced by us suggesting that fires cause dynamic pressure higher than the static pressure induced by tunnel fans is, as well as on the difference between the tunnel ventilation currents considering influence of the seat of fire, the type of its spreading under the ground, its heat release rate, tunnel geometry and other typical parameters. Thus, the essence of the problem is to differentiate the cases of fire scientifically and to develop adequate recommendations to rescue lives for different fire development scenarios in the confined underground areas.

MATERIALS & METHODS

Experimental modeling of fire scenarios

As mentioned above, experiments on the behavior of an underground fire were conducted at laboratory on a physical model made of 2 mm thick stainless steel sheets (Fig. 1). Air into the model tunnel was supplied by a duct fan. The surface area of the fire source was 130X50 mm and 340X60 mm. Natural gas and air flow rates were measured with an accuracy of 1%. Data acquisition and preprocessing were performed by Datataker DT85 central data acquisition module, which can simultaneously retrieve data from 40 points every second. Backlayering was accounted for by temperature change, the numerical values of which were taken from thermocouple data.

Experimental observations were made considering Froude Scaling Theory, which characterizes the relationship between inertia and buoyancy. Fire strength and air velocity on the model and in nature are calculated according to the formulas, respectively

$$\frac{Q_m}{Q_n} = \left(\frac{l_m}{l_n}\right)^{2.5} \quad (1)$$

$$\frac{U_m}{U_n} = \left(\frac{l_m}{l_n}\right)^{0.5} \quad (2)$$

where index m corresponds to the model; index n corresponds to the nature; Q is heat release power, kW; l is the length, m; U is air velocity, m/s; l_m=12 m; l_n= 120 m for scale 1:10. The other values are determined by formulas (1) and (2).

The fire source was located in the central part of the tunnel; its distance from the tunnel floor varied within 0.8-1.0 m. The dimensions of the fire surface are given above and will not be repeated here. Natural and liquefied gas was used for heating. The heat release intensity was determined by fuel consumption and specific heat release. The slope of the tunnel varied in the range of 0-8 degrees with a 1 degree step.

According to the results of experiments as well as numerical problems, the gradient factor was determined by the formula

$$k_g = {}^{u_{c,\vartheta}}/_{u_c} \quad (3)$$

where $u_{c,\vartheta}$ is the critical velocity for the tunnel inclined at ϑ, m/s; u_c is the critical velocity for a horizontal tunnel.



Fig. 1. A fragment of the tunnel model with thermocouples and measuring devices connected to it.

Numerical modeling of fire scenarios

Full-scale numerical modeling was performed in the FDS software environment using the finite volume method. Sections of 100 m and 400 m lengths of a typical two-lane inclined tunnel with a width of 8.5 m and a height of 5 m were selected. The effect of fire strength and tunnel slope on critical velocity was studied. The slope was also varied in the range of 0-8 degrees in 1 degree increments. In most of the fire simulations, the combustion reagent was gasoline. Individual observations were also made for diesel, fuel oil, and firewood. The modeling time was 120 s.

The dimensions of the individual cells of the numerical grid were 0.5*0.5*0.5 m. The seat of fire, fans and tunnel portals were modeled with 0.1*0.1*0.1*0.1 m cells. Preserving the scale on the models and when modeling with FDS, the mesh quality is best evaluated by the dimensionless parameter D*/δx rather than by the absolute mesh size δx. Here D* is the representative diameter of the fire, which is determined by the formula

$$D^* = \left(\frac{Q}{P_a c_P T_a \sqrt{g}}\right)^{2/5} \quad (4)$$

where P_a, c_P, and T_a are the characteristics of the outdoor air: pressure, isobaric heat capacity and temperature, respectively; g is the acceleration of a freely falling body.

https://doi.org/10.5593/sgem2024/4.1/s19.62

To model descending ventilation flows (**Fig. 2**), two jet fans with a capacity of 28 m^3/s and a pressure of 2000 Pa will be switched on for time moment τ= 0 s at the upper portal. The fans will eject additional air flow. At time moment τ = 20 s, fire will start on the model and the simulation continues with fire for the rest of the time.

The virtual gauges were placed in the middle of the tunnel in the longitudinal direction in two rows at 10 m intervals. The first row was placed at a height of 1.7 m from the tunnel roadway, and the second row was placed at a height of 4.7 m. The modeling used 4 groups of instrumentation that measured and recorded air velocity, temperature, air and soot density at the location point. In addition to point measurements, the model used virtual gauges that detected average values of air, carbon monoxide, carbon dioxide and soot densities in the tunnel section at 10 m intervals.

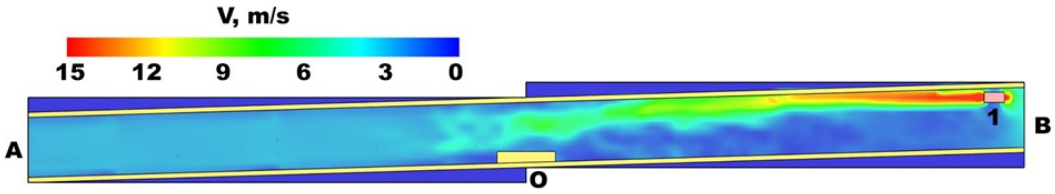


Fig. 2. Basic layout for modeling descending ventilation flows:
1 - jet fan, which will start at time moment τ = 0 s; O is the seat of fire, which will activate at time moment τ = 20 s (when the clean air jet front reaches the seat of the fire).

RESULTS & DISCUSSION

Individual models were run with 3 and 4 fans running in parallel. This was done in order to dramatically increase the numerical value of the modeled critical velocity. This does not mean that in real tunnels there will be enough space to accommodate four fans without significantly reducing the roadway of the tunnel.

In the numerical models, the heat transfer between the surrounding rock mass and the ventilation flow was assumed to be adiabatic. However, it is also clear that there is a pronounced nonstationary heat exchange, and the process itself is polytropic, and heat losses will be greater in real terms. As a result of this assumption, the numerical values of temperatures obtained by numerical modeling will be somewhat higher, but this is acceptable, since temperature prediction is not the main interest of this study. In the numerical problems, the pressure in the underground space near the portals was equal to atmospheric pressure.

The critical velocity was determined by the model of Danziger and Kennedy using the following formula [21]

$$u_c = \left(\frac{gQ_cH}{4.5\rho_0 c_P A T_f}\right)^{0.33} = 0.606\left(\frac{gQ_cH}{\rho_0 c_P A T_f}\right)^{0.33} \quad (5)$$

where, besides the values explained above, Q_c is the convection heat released from fire, which is 70% of the amount of heat calculated by fue consumption and specific heat capacity, kW; H is the height of the tunnel, m; ρ_0 is the density of the outdoor air, kg/m^3; A is the cross-sectional area of the tunnel, m2; T_f is the smoke temperature, K, and is determined by the formula

$$T_f = \left(\frac{Q_c}{\rho_0 c_P A U_c}\right) + T_a \quad (6)$$

Dimensionless heat release characteristic and dimensionless critical velocity are determined by the following formulas

$$Q^* = \frac{Q_c}{\rho_0 c_p T_a g^{1/2} H^{5/2}} \quad (7)$$

$$u^* = \frac{u_c}{(gH)^{1/2}} \quad (8)$$

It should be noted that the Danziger and Kennedy model is widely used to calculate the critical velocity. It is recommended in the US and PIARC design manuals [1-6]. Briefly note that the mentioned model utilizes the assumption of Thomas [18] that the critical Froude number in the fire zone is a constant value when clean air and fuel gases are mixed in equal proportions on the seat of fire, because in this case the smoke buoyancy and inertia of the clean jet balance each other. According to Thomas, if the critical Froude number $Fr_c \leq 1$, here is no smoke backlayering. If we denote the difference in density between smoke and outside air by $\Delta\rho$, then the critical Froude number is determined by the formula

$$Fr_c = \frac{\Delta\rho g H}{\rho_0 u_c^2} \quad (9)$$

The idea of the constancy of the Froude number was taken by Danziger and Kennedy from Thomas, and the numerical value $Fr_c = 4.5$ was taken from paper [22]. A coefficient of 0.606 is obtained from this value, which is included in formula (5) and, as already mentioned, is widely used to calculate the critical velocity. Although the Froude number is not a constant value for real fire scenarios [19], the use of 0.606 or another similar coefficient is unavoidable because the number of unknowns in the problem formulation exceeds the number of equations and there is no direct solution without assumption.

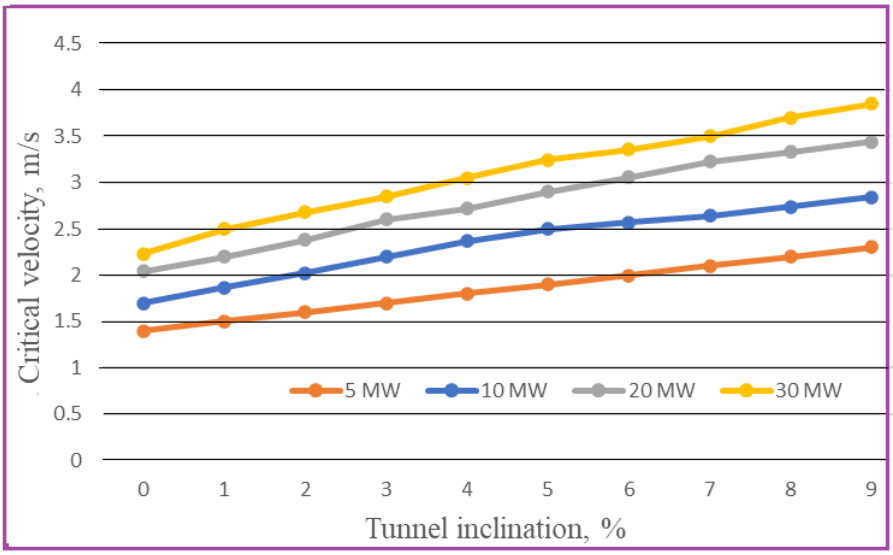


Fig. 3. Variation of critical velocity depending on tunnel slope and fire strength.

The critical velocity was determined by the backlayering, and the backlayering itself was determined by the thermocouple index in both physical and numerical models.
It is easy to see that in the case of numerical models, virtual measuring devices were used. The air velocity was assumed to be equal to the critical velocity at zero backlayering length. In the physical models, 15.81 kW corresponded to 5 MW of fire strength and 94.87 kW corresponded to 30 MW. In laboratory experiments, higher fire strength could not be achieved for safety reasons. The variation of the critical velocity in terms of

https://doi.org/10.5593/sgem2024/4.1/s19.62

descending longitudinal ventilation depending on tunnel slope and fire strength is given in Fig. 3. The presented results are obtained from full-scale numerical simulations.
The modeling results show that the critical velocity increases with increasing fire strength, which is caused by higher smoke temperature, increased buoyancy and higher propagation velocity of hot fuel gases.
There is a directly proportional relationship between the tunnel slope and the numerical value of critical velocity under the same fire strength conditions. Accordingly, as the tunnel slope is increasing, the critical velocity is inreasing as well and as it decreasing, the critical velocity is decreasing. Thus, the impact of the tunnel slope and the fire strength on the change in critical velocity have the same sign. It should be noted that the results obtained from the numerical and physical models should be considered almost identical, and the difference between them does not exceed 5% numerical value.

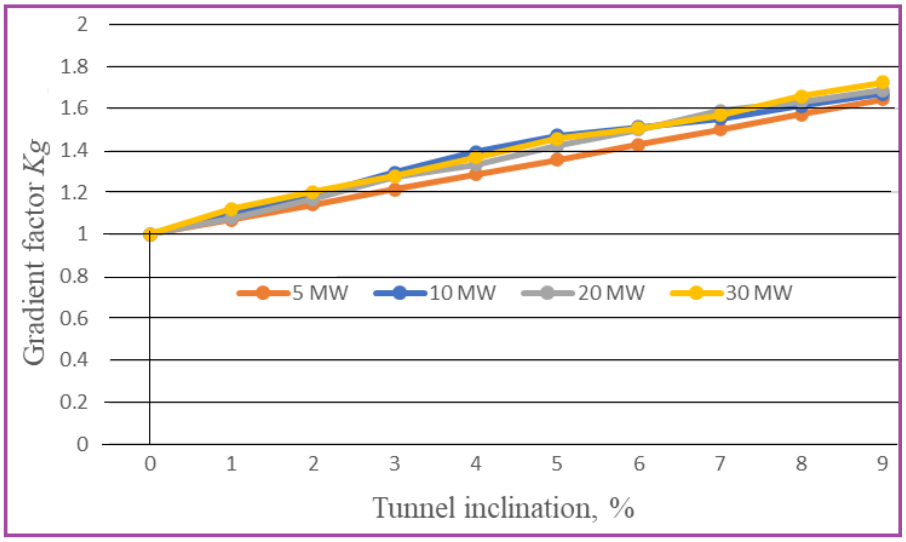


Fig. 4. The character of change of the gradient factor according to the results of numerical modeling as a function of tunnel slope and fire strength.

It should be especially noted that the character of change of the gradient factor demonstrating the rate of change of the critical velocity depending on the tunnel slope is according to the results of numerical simulation, which is presented in Fig. 4.
As can be seen from the presented results, the nature of the change in the gradient factor is linear. Moreover, to characterize fires with a power of 10-20 MW, it is possible to use the averaged numerical value of the gradient factor. In this case, the allowed error in the worst case does not exceed 7.5%, which is completely acceptable for practical purposes. For greater clarity, we provide the corresponding table.

Table 1. Change in gradient coefficient depending on the angle of inclination of the tunnel (%) and fire intensity: A – Average values; B – 10 MW; C – 20 MW.

0%	1%	2%	3%	4%	5%	6%	7%	8%	9%	
1	1.093	1.177	1.284	1.363	1.446	1.506	1.565	1.622	1.678	A
1	1.100	1.188	1.294	1.394	1.471	1.512	1.553	1.612	1.671	B
1	1.078	1.167	1.274	1.333	1.422	1.500	1.588	1.632	1.686	C

CONCLUSION

According to the presented results, we can conclude that the physical model of the tunnel used in this paper is convenient for experiments, because the use of the Froude criterion allows scaling strong fires, which on the one hand increases safety and on the other hand, makes the cost of experiments lower. By means of physical modeling it is possible to determine important process parameters: critical air flow velocity, length of backlayering and gradient coefficient. It is also possible to correlate their values in terms of tunnel slope, degree of tunnel filling with vehicles, fire strength and other important characteristic parameters. It should be noted specifically that the stated numerical value of the critical velocity of 3.0 m/s is not sufficient to prevent backlayering in terms of descending longitudinal ventilation, especially when the fire strength exceeds 30 MW and the tunnel slope exceeds 3%. This circumstance should be taken into account when determining safe parameters of tunnel ventilation in emergency fire ventilation projects. The change in the gradient factor depending on the power of the fire and the inclination of the tunnel is directly proportional and linear. At the same time, the rate of increase in the gradient factor is more noticeable with increasing angle of inclination of the tunnel. Therefore, to characterize fires with a power of 10-20 MW, the average numerical value of the specified coefficient can be used.

ACKNOWLEDGEMENTS

This work was supported by Shota Rustaveli National Science Foundation (SRNSF) [Grant number FR-22-12949, Project title “Study of critical velocity and fire induced backlayering to save lives in road tunnels”].

REFERENCES

[1] Vehicle Emissions and Air Demand for Ventilation. Technical Committee D5 of World Road Association. Road Tunnels, 2019, p. 62. www.piarc.organization

[2] UNITED NATIONS. TRANS/AC 7/9. RECOMMENDATIONS OF THE GROUP OF EXPERTS ON SAFETY IN ROAD TUNNELS, Economic and Social Council, Multidisciplinary Group of Experts on Safety in Tunnels, 2001 https://unece.org/DAM/trans/doc/2002/ac7/TRANS-AC7-09e.pdf

[3] UNITED NATIONS. TRANS/AC 7/11 REPORT OF THE AD HOC MULTIDISCIPLINARY GROUP OF EXPERTS ON SAFETY IN TUNNELS ON ITS FIFTH SESSION, Economic and Social Council, Multidisciplinary Group of Experts on Safety in Tunnels, 2002 https://unece.org/fileadmin/DAM/trans/doc/2002/ac7/TRANS-AC7-11e.pdf

[4] National Fire Protection Association. NFPA 502 Standard for road tunnels, bridges, and other limited access highways. National Fire Protection Association, Quincy, US, 2011.

[5] National Fire Protection Association. NFPA 502 Standard for road tunnels, bridges, and other limited access highways. National Fire Protection Association, Quincy, US, 2014.

[6] National Fire Protection Association. NFPA 502 Standard for road tunnels, bridges, and other limited access highways. National Fire Protection Association, Quincy, US, 2020.

https://doi.org/10.5593/sgem2024/4.1/s19.62

[7] Gannouni S., Maad R.B. Numerical study of the effect of blockage on critical velocity and backlayering length in longitudinally ventilated tunnel fires. Tunnelling and Underground Space Technology 48, pp. 147-155, 2015.

[8] Chow W. K., Gao Y., Zhao J.H., Dang J.F., Chow C.L., Miao, L. Smoke movement in tilted tunnel fires with longitudinal ventilation. Fire Safety Journal 75, pp. 14–22, 2015.

[9] Fan C.G., Yang J. Experimental study on thermal smoke backlayering length with an impinging flame under the tunnel ceiling. Experimental Thermal and Fluid Science 82, pp. 262–268, 2017.

[10] Fan C.G., Zhang L., Jiao S.C., Yang Z.W., Li M.H., Liu X.P. Smoke spread characteristics inside a tunnel with natural ventilation under a strong environmental wind. Tunnelling and Underground Space Technology 82, pp. 99–110, 2018.

[11] Kong J., Xu Z., You W., Wang B., Liang Y., Chen T. Study of smoke back-layering length with different longitudinal fire locations in inclined tunnels under natural ventilation. Tunnelling and Underground Space Technology 107, 103663, 2021.

[12] Lei P., Chen C., Zhang Y., Xu T., Sun H. Experimental study on temperature profile in a branched tunnel fire under natural ventilation considering different fire locations. International Journal of Thermal Sciences 159, 106631, 2021.

[13] Li Y.Z., Ingason H. Effect of cross section on critical velocity in longitudinally ventilated tunnel fires. Fire Safety Journal 91, pp. 303-311, https://doi.org/10.1016/j.firesaf.2017.03.069, 2017.

[14] Li J., Li Y.F., Cheng C.H., Chow W.K. A study on the effects of the slope on the critical velocity for longitudinal ventilation in tilted tunnels. Tunnelling and Underground Space Technology 89, pp. 262-267, 2019.

[15] Vaitkevicius A., Carvel R., Colella F. Investigating the Throttling Effect in Tunnel Fires. Fire Technology 52, pp. 1619–1628, 2016. DOI: 10.1007/s10694-015-0512-z

[16] Wan H., Gao Z., Han J., Zhang Y. A numerical study on smoke back-layering length and inlet air velocity of fires in an inclined tunnel under natural ventilation with a vertical shaft. International Journal of Thermal Sciences 138, pp. 293-303, 2019.

[17] Weng M.C., Lu X.L., Liu F., Du C.X. Study on the critical velocity in a sloping tunnel fire under longitudinal ventilation. Applied Thermal Engineering 94, pp. 422–434, 2016.

[18] Thomas P.H. The movement of buoyant fluid against a stream and the venting of underground fires. Fire Research Notes 351, 1958. http://www.iafss.org/publications/frn/351/-1

[19] Lanchava O., Javakhishvili G. Impact of strong fires on a road tunnel ventilation system. Bulletin of the Georgian National Academy of Sciences. 15(4), pp. 38-45, 2021.

[20] Lanchava O., Ilias N., Nozadze G. Some problems for assessment of fire in road tunnels. Quality Access to Success. 18(S1), pp. 69-72, 2017.

[21] Danziger N.H., Kennedy W.D. Longitudinal ventilation analysis for the Glenwood canyon tunnels. In: Proceedings of the 4th International Symposium of Aerodynamics and Ventilation of Vehicle Tunnels, York, UK, pp. 169–186, 1982.

[22] Lee C.K., Chaiken R.F., Singer J.M. Interaction between duct fires and ventilation flow: an experimental study. Combust. Sci. Technol. 20, pp. 59–72, 1979.